



Lyon 1



Leibniz-Institut für
Astrophysik Potsdam



N° d'ordre: 78-2014

Année 2014

THÈSE

délivrée par

L'UNIVERSITÉ CLAUDE BERNARD DE LYON 1, FRANCE

et préparée en cotutelle avec

L'UNIVERSITÉ DE POTSDAM, ALLEMAGNE

ÉCOLE DOCTORALE

Physique et Astrophysique - PHAST

pour l'obtention

DU DIPLÔME DE DOCTORAT

(arrêté du 7 août 2006 / arrêté du 6 janvier 2005)

soutenue publiquement le 12 06 2014

par

Jenny SORCE

From Spitzer Mid-InfraRed Observations and Measurements of Peculiar Velocities to Constrained Simulations of the Local Universe

Directeurs de thèse:

Mme COURTOIS Hélène (*Lyon*) et M STEINMETZ Matthias (*Potsdam*)

JURY:

Mme AUGIER Corinne (présidente du jury)

Mme COURTOIS Hélène (directrice de thèse)

M. GOTTLÖBER Stefan (examineur)

M. PORCIANI Cristiano (rapporteur)

M. STEINMETZ Matthias (directeur de thèse)

M. TULLY Brent (examineur)

M. YEPES Gustavo (rapporteur)

Published online at the
Institutional Repository of the University of Potsdam:
URL <http://opus.kobv.de/ubp/volltexte/2014/7248/>
URN <urn:nbn:de:kobv:517-opus-72486>
<http://nbn-resolving.de/urn:nbn:de:kobv:517-opus-72486>

From Spitzer Mid-InfraRed Observations and
Measurements of Peculiar Velocities to
Constrained Simulations of the Local Universe

by

Jenny Sorce

2011-2014

University of Lyon
Institut de Physique Nucléaire
4 rue Enrico Fermi
69100 Villeurbanne
FRANCE

University of Potsdam
Leibniz Institut für Astrophysik
An der Sternwarte 16
14482 Potsdam
DEUTSCHLAND

*I would like to dedicate this dissertation to my present and
hopefully future closest family. There is no doubt that without
their continued presence, support, love and encouragements,
none of this work would have happened.*

Abstract (long version)

Galaxies are observational probes to study the Large Scale Structure of the Universe. In the standard cosmological paradigm, their gravitational motions are *direct* tracers of the total (dark included) matter density and therefore of the Large Scale Structure. In this model, of an isotropic and homogeneous on large enough scales Universe, structure formation is the result of gravitational instabilities driven by primordial density perturbations generated during the early inflationary epoch just after the Big Bang. Analytical treatments of structure formation and galaxy evolution are complex. Thus, their studies rely on numerical cosmological simulations. Still, only one universe observable from a given position, in time and space, is available for comparisons with simulations. The related cosmic variance affects grandly our ability to interpret the results. Simulations constrained by observational data are a perfect remedy to this problem. Achieving such simulations requires the full extent of the international projects Cosmicflows and CLUES.

Cosmicflows aims at cartographing the matter in the Local Universe. In this regard, catalogs of accurate distance measurements to map deviations, due to baryonic and dark matters, from the overall Hubble expansion are built. These measures are mainly obtained with the galaxy luminosity-rotation rate correlation or Tully-Fisher relation. We present the calibration of that relation in the mid-infrared with observational data from Spitzer Space Telescope. The greatest advantage is an all-sky consistency of the measures, removing any systematics, due to the utilization of various observational instruments, which could create spurious cosmic flows. In addition, the mid-infrared band permits to obtain motions of galaxies very close to the obscured, by our galaxy disk, zone where major structures could be. From this calibration combined with the surface photometry of numerous galaxies, accurate distance estimates are derived. They will be included in the third catalog of the project. In the meantime, two catalogs up to 30 and 150 h^{-1} Mpc have been released.

We report improvements and applications of the CLUES' method on these two catalogs. The technique produces simulations, replicas of the Local Universe, constrained by observational data. It is based on the constrained realization algorithm. Beforehand, the cosmic displacement field is computed with the Zel'dovich approximation. This latter is then reversed to relocate reconstructed three-dimensional constraints to their precursors' positions in the initial field. The size, never equalled before, of a peculiar velocity catalogs such as *cosmicflows-2*, with 8000 galaxies within 150 h^{-1} Mpc, highlighted the importance of minimizing the different observational biases. The Local Universe, being neither isotropic nor homogeneous, developing a general corrective solution would be inadequate. By carrying out tests on mock catalogs, built from cosmological simulations, a method to minimize observational bias can be derived. Finally, for the first time in the field, cosmological simulations are constrained *solely* by peculiar velocities. The process is successful as the analysis of the resulting simulations shows that they resemble the Local Universe. The major attractors and voids are simulated at positions approaching observational positions by a few megaparsecs, thus reaching the limit imposed by the linear theory.

keywords: spatial mid-infrared observations, distance estimates, peculiar velocities, constrained cosmological simulations, dark matter, Local Universe

Abstract

(short version)

Galaxies are observational probes to study the Large Scale Structure. Their gravitational motions are tracers of the total matter density and therefore of the Large Scale Structure. Besides, studies of structure formation and galaxy evolution rely on numerical cosmological simulations. Still, only one universe observable from a given position, in time and space, is available for comparisons with simulations. The related cosmic variance affects our ability to interpret the results. Simulations constrained by observational data are a perfect remedy to this problem. Achieving such simulations requires the projects Cosmicflows and CLUES. Cosmicflows builds catalogs of accurate distance measurements to map deviations from the expansion. These measures are mainly obtained with the galaxy luminosity-rotation rate correlation. We present the calibration of that relation in the mid-infrared with observational data from Spitzer Space Telescope. Resulting accurate distance estimates will be included in the third catalog of the project. In the meantime, two catalogs up to 30 and 150 h^{-1} Mpc have been released. We report improvements and applications of the CLUES' method on these two catalogs. The technique is based on the constrained realization algorithm. The cosmic displacement field is computed with the Zel'dovich approximation. This latter is then reversed to relocate reconstructed three-dimensional constraints to their precursors' positions in the initial field. The size of the second catalog (8000 galaxies within 150 h^{-1} Mpc) highlighted the importance of minimizing the observational biases. By carrying out tests on mock catalogs, built from cosmological simulations, a method to minimize observational bias can be derived. Finally, for the first time, cosmological simulations are constrained *solely* by peculiar velocities. The process is successful as resulting simulations resemble the Local Universe. The major attractors and voids are simulated at positions approaching observational positions by a few megaparsecs, thus reaching the limit imposed by the linear theory.

Résumé (version longue)

Les galaxies sont des sondes observationnelles pour l'étude des structures de l'Univers. Dans le paradigme standard cosmologique, leur mouvement gravitationnel permet de tracer *directement* la densité totale de matière (noire incluse). Dans ce modèle, d'un univers isotropique et homogène aux grandes échelles, la formation des structures est le fruit d'instabilités gravitationnelles induites par des fluctuations de densité primordiales générées pendant la période d'inflation suivant le Big Bang. Les traitements analytiques de formation des structures et galaxies se révèlent complexes. C'est pourquoi leur étude s'appuie sur les simulations numériques cosmologiques. Cependant, un seul univers observable à partir d'une position donnée, en temps et espace, est disponible pour comparaison avec les simulations. La variance cosmique associée affecte fortement notre capacité à interpréter les résultats. Les simulations contraintes par les données observationnelles constituent une solution optimale au problème. Réaliser de telles simulations requiert toute l'ampleur des projets internationaux Cosmicflows et CLUES.

Cosmicflows a pour objectif de cartographier la matière dans l'Univers Local. Pour cela, des catalogues de mesures de distances précises, afin d'obtenir les déviations de l'expansion globale dues aux matières baryonique et noire, sont construits. Ces mesures sont principalement obtenues avec la corrélation entre la luminosité des galaxies et la vitesse de rotation de leur gaz, aussi appelée relation de Tully-Fisher. La calibration de cette relation est présentée dans le mi-infrarouge avec les observations du télescope spatial Spitzer. L'avantage majeur est une consistance des mesures dans tout le ciel, qui permet d'effacer les systématiques liées à l'utilisation de différents télescopes, pouvant engendrer de faux courants cosmiques. La bande mi-infrarouge permet également de sonder les mouvements des galaxies très proches de la zone obscurée, par le disque de notre galaxie, où d'importantes structures peuvent se trouver. Cette calibration, associée à la photométrie de surface de nombreuses galaxies, fournit des estimations de distances précises qui seront intégrées au troisième catalogue de données du projet. En attendant, deux catalogues de mesures atteignant 30 et 150 h^{-1} Mpc ont été publiés.

Les améliorations et applications de la méthode du projet CLUES sur les deux catalogues sont présentées. La technique permet d'obtenir des simulations, répliques de l'Univers Local, contraintes par les données observationnelles. Elle est basée sur l'algorithme de réalisation contrainte. Au préalable, l'approximation de Zel'dovich permet de calculer le champ de déplacement cosmique. Son inversion repositionne les contraintes tridimensionnelles reconstruites à l'emplacement de leur précurseur dans le champ initial. La taille, jamais égalée auparavant, d'un catalogue de vitesses particulières tel que *cosmicflows-2*, contenant 8000 galaxies jusqu'à une distance de 150 h^{-1} Mpc, a permis de mettre en évidence l'importance de minimiser les différents biais observationnels. L'Univers Local n'étant ni homogène, ni isotropique, le développement d'une solution corrective générale ne serait pas approprié. En réalisant des tests sur des catalogues de similis, issus des simulations cosmologiques, une méthode de minimisation des biais observationnels peut être dérivée. Finalement, pour la première fois dans le domaine, des simulations cosmologiques sont contraintes *uniquement* par des vitesses particulières de galaxies. Le procédé est une réussite car l'analyse des simulations obtenues montre leur grande ressemblance à l'Univers Local. Les principaux attracteurs et vides sont simulés à des positions approchant de quelques mégaparsecs les positions observationnelles, atteignant ainsi la limite fixée par la théorie linéaire.

mots-clefs: observations spatiales dans le mi-infrarouge, estimations de distances, vitesses particulières, simulations cosmologiques contraintes, matière noire, Univers Local

Résumé (version courte)

Les galaxies sont des sondes observationnelles pour l'étude des structures de l'Univers. Leur mouvement gravitationnel permet de tracer la densité totale de matière. Par ailleurs, l'étude de la formation des structures et galaxies s'appuie sur les simulations numériques cosmologiques. Cependant, un seul univers observable à partir d'une position donnée, en temps et espace, est disponible pour comparaison avec les simulations. La variance cosmique associée affecte notre capacité à interpréter les résultats. Les simulations contraintes par les données observationnelles constituent une solution optimale au problème. Réaliser de telles simulations requiert les projets Cosmicflows et CLUES. Cosmicflows construit des catalogues de mesures de distances précises afin d'obtenir les déviations de l'expansion. Ces mesures sont principalement obtenues avec la corrélation entre la luminosité des galaxies et la vitesse de rotation de leur gaz. La calibration de cette relation est présentée dans le mi-infrarouge avec les observations du télescope spatial Spitzer. Les estimations de distances résultantes seront intégrées au troisième catalogue de données du projet. En attendant, deux catalogues de mesures atteignant 30 et 150 h^{-1} Mpc ont été publiés. Les améliorations et applications de la méthode du projet CLUES sur les deux catalogues sont présentées. La technique est basée sur l'algorithme de réalisation contrainte. L'approximation de Zel'dovich permet de calculer le champ de déplacement cosmique. Son inversion repositionne les contraintes tridimensionnelles reconstruites à l'emplacement de leur précurseur dans le champ initial. La taille inégale, 8000 galaxies jusqu'à une distance de 150 h^{-1} Mpc, du second catalogue a mis en évidence l'importance de minimiser les biais observationnels. En réalisant des tests sur des catalogues de similis, issus des simulations cosmologiques, une méthode de minimisation des biais peut être dérivée. Finalement, pour la première fois, des simulations cosmologiques sont contraintes *uniquement* par des vitesses particulières de galaxies. Le procédé est une réussite car les simulations obtenues ressemblent à l'Univers Local. Les principaux attracteurs et vides sont simulés à des positions approchant de quelques mégaparsecs les positions observationnelles, atteignant ainsi la limite fixée par la théorie linéaire.

Zusammenfassung (lange Version)

Die Verteilung der Galaxien liefert wertvolle Erkenntnisse über die großräumigen Strukturen im Universum. Im kosmologischen Standardmodell ist ihre durch Gravitation verursachte Bewegung ein *direkter* Tracer für die Dichteverteilung der gesamten Materie. In diesem Modell ist die Strukturentstehung die Folge von Gravitationsinstabilitäten, welche ihren Ursprung in primordialen Dichtefluktuationen haben, die in der inflationären Phase der kosmologischen Expansion unmittelbar nach dem Big Bang entstanden sind. Die Strukturentstehung und die Bildung von Galaxien ist außerordentlich komplex und analytisch nicht behandelbar. Daher basiert ihre Erforschung auf kosmologischen numerischen Simulationen. Es gibt jedoch von einem gegebenen Ort aus nur ein einziges beobachtbares Universum, welches mit der Theorie und den Ergebnissen unterschiedlicher Simulationen verglichen werden muß. Die kosmische Varianz erschwert es, beobachtbare großräumige Strukturen mit Simulationen zu reproduzieren. Simulationen, deren Anfangsbedingungen durch Beobachtungsdaten eingegrenzt sind ("Constrained Simulations") stellen eine geeignete Lösung dieses Problems dar. Die Durchführung solcher Simulationen ist das Ziel der internationalen Projekte Cosmicflows und CLUES.

Die Zielsetzung von Cosmicflows ist eine Kartierung der Materieverteilung im lokalen Universum. Zu diesem Zweck werden Kataloge mit akkuraten Entfernungsbestimmungen erstellt, welche die durch das lokale Gravitationsfeld von baryonischer und dunkler Materie verursachte Abweichung von der allgemeinen Hubble-Expansion des Universums abbilden. Diese Messungen werden hauptsächlich aus der Korrelation zwischen Leuchtkraft und Rotationsgeschwindigkeit von Spiralgalaxien, der Tully-Fisher-Beziehung, gewonnen. In dieser Arbeit wird die Kalibrierung dieser Beziehung im mittleren Infrarot mithilfe von Daten vom Spitzer Space Telescope vorgestellt. Der größte Vorteil gegenüber anderen Datensätzen ist die Konsistenz der Messungen über den gesamten Himmel und damit eine wesentliche Verringerung systematischer Fehler durch die Verwendung unterschiedlicher Meßinstrumente. Außerdem ist es im mittleren Infrarot möglich, auch die Bewegung jener Galaxien zu messen, die sehr nah an dem durch die galaktische Scheibe der Milchstraße verdeckten Bereich liegen, in welchem massereiche Strukturen vermutet werden. Wird diese Kalibrierung mit Oberflächenphotometrie vieler Galaxien kombiniert, erhält man sehr genaue Entfernungsbestimmungen. Diese Entfernungsbestimmungen werden im dritten Katalog des Cosmicflows-Projekts enthalten sein. Bisher wurden zwei Kataloge veröffentlicht, mit Entfernungen bis zu 30 beziehungsweise $150 h^{-1}$ Mpc.

In dieser Arbeit wird die CLUES-Methode auf diese zwei Kataloge angewendet und Verbesserungen werden vorgestellt und diskutiert. Mit der CLUES-Methode kann man auf der Grundlage von Beobachtungsdaten des heutigen lokalen Universums seine Entstehung simulieren. Die Grundlage dafür bildet der Algorithmus der "Constrained Realizations". Zunächst wird das kosmische Verschiebungsfeld mithilfe der Zeldovich-Näherung bestimmt. In umgekehrter Richtung kann man damit die aus heutigen Beobachtungsdaten rekonstruierten dreidimensionalen Constraints an ihren Ursprungsort im frühen Universum zurückzusetzen. Der *cosmicflows-2* Katalog, welcher die Pekuliargeschwindigkeiten von 8000 Galaxien bis zu einer Entfernung von $150 h^{-1}$ Mpc enthält, bietet einen bisher unerreichten Datenumfang. Es ist daher eine besondere Herausforderung, den Einfluss verschiedener Beobachtungsfehler (Bias) zu minimieren. Da das lokale Universum weder homogen noch isotrop ist, reicht eine allgemeine Korrektur nicht aus. Eine für das lokale Universum angepasste Korrekturmethode läßt sich durch die Untersuchung von Mock-Katalogen finden, welche aus kosmologischen Simulationen gewonnen werden. Schließlich stellt diese Arbeit erstmals kosmologische Simulationen vor, die *ausschließlich* durch Pekuliargeschwindigkeiten eingegrenzt sind. Der Erfolg dieser Methode wird dadurch bestätigt, dass die daraus resultierenden Simulationen dem beobachteten lokalen Universum sehr ähnlich sind. Die relevanten Attraktoren und Voids liegen in den Simulationen an Positionen, welche bis auf wenige Megaparsec mit den beobachteten Positionen übereinstimmen. Die Simulationen erreichen damit die durch die lineare Theorie gegebene Genauigkeitsgrenze.

Schlüsselwörter: Beobachtungen im mittleren Infrarot, Abstandsmessungen, Pekuliargeschwindigkeiten, kosmologische Simulationen, Dunkle Materie, Lokales Universum

Zusammenfassung (kurze Version)

Die Verteilung der Galaxien liefert wertvolle Erkenntnisse über die großräumigen Strukturen im Universum. Ihre durch Gravitation verursachte Bewegung ist ein *direkter* Tracer für die Dichteverteilung der gesamten Materie. Die Strukturentstehung und die Entwicklung von Galaxien wird mithilfe von numerischen Simulationen untersucht. Es gibt jedoch nur ein einziges beobachtbares Universum, welches mit der Theorie und den Ergebnissen unterschiedlicher Simulationen verglichen werden muß. Die kosmische Varianz erschwert es, das lokale Universum mit Simulationen zu reproduzieren. Simulationen, deren Anfangsbedingungen durch Beobachtungsdaten eingegrenzt sind (“Constrained Simulations”) stellen eine geeignete Lösung dieses Problems dar. Die Durchführung solcher Simulationen ist das Ziel der Projekte Cosmicflows und CLUES. Im Cosmicflows-Projekt werden genaue Entfernungsmessungen von Galaxien erstellt, welche die Abweichung von der allgemeinen Hubble-Expansion abbilden. Diese Messungen werden hauptsächlich aus der Korrelation zwischen Leuchtkraft und Rotationsgeschwindigkeit von Spiralgalaxien gewonnen. In dieser Arbeit wird die Kalibrierung dieser Beziehung im mittleren Infrarot mithilfe von Daten vom Spitzer Space Telescope vorgestellt. Diese neuen Entfernungsbestimmungen werden im dritten Katalog des Cosmicflows-Projekts enthalten sein. Bisher wurden zwei Kataloge veröffentlicht, mit Entfernungen bis zu 30 beziehungsweise 150 h^{-1} Mpc. In dieser Arbeit wird die CLUES-Methode auf diese zwei Kataloge angewendet und Verbesserungen werden vorgestellt und diskutiert. Zunächst wird das kosmische Verschiebungsfeld mithilfe der Zeldovich-Näherung bestimmt. In umgekehrter Richtung kann man damit die aus heutigen Beobachtungsdaten rekonstruierten dreidimensionalen Constraints an ihren Ursprungsort im frühen Universum zurückzusetzen. Durch den großen Datenumfang des *cosmicflows-2* Katalogs (8000 Galaxien bis zu einer Entfernung von 150 h^{-1} Mpc) ist es besonders wichtig, den Einfluss verschiedener Beobachtungsfehler zu minimieren. Eine für das lokale Universum angepasste Korrekturmethode lässt sich durch die Untersuchung von Mock-Katalogen finden, welche aus kosmologischen Simulationen gewonnen werden. Schließlich stellt diese Arbeit erstmals kosmologische Simulationen vor, die *ausschließlich* durch Pekuliargeschwindigkeiten eingegrenzt sind. Der Erfolg dieser Methode wird dadurch bestätigt, dass die dadurch erzeugten Simulationen dem beobachteten lokalen Universum sehr ähnlich sind. Die relevanten Attraktoren und Voids liegen in den Simulationen an Positionen, welche bis auf wenige Megaparsec mit den beobachteten Positionen übereinstimmen. Die Simulationen erreichen damit die durch die lineare Theorie gegebene Genauigkeitsgrenze.

**From Spitzer Mid-InfraRed Observations and
Measurements of Peculiar Velocities to
Constrained Simulations of the Local Universe**

Contents

| | |
|---|--------------|
| Abstract | iv |
| Résumé | vi |
| Zusammenfassung | viii |
| List of Figures | xv |
| List of Tables | xviii |
| | |
| 1 Motivation | 1 |
| 2 Universe in Motion | 9 |
| 2.1 The Standard Cosmological Model | 9 |
| 2.1.1 An Universe in Expansion | 10 |
| 2.1.1.1 The Hubble Law | 10 |
| 2.1.1.2 Generalization | 11 |
| 2.1.1.3 Evolution of the Scale Factor | 12 |
| 2.1.2 Variations from the Hubble Expansion | 15 |
| 2.1.2.1 Bound Structures and Merging Processes | 15 |
| 2.1.2.2 Voids and Local Flows | 16 |
| 2.1.2.3 Effect on the Redshift | 21 |
| 2.2 The Linear Theory of Density Perturbations | 23 |
| 2.2.1 Continuity, Euler and Poisson Equations | 24 |
| 2.2.2 Comoving Equations | 25 |
| 2.2.2.1 Comoving Coordinates: Definition | 25 |
| 2.2.2.2 Comoving Coordinates: Equations | 26 |
| 2.2.3 Density Perturbation Field | 27 |
| 2.2.3.1 Linearization | 27 |
| 2.2.3.2 Fourier Analyses | 28 |
| 2.3 N-Body Simulations | 30 |
| 2.3.1 Dark Matter | 30 |
| 2.3.2 N-Body Codes | 31 |
| 2.3.2.1 The Modeling | 31 |
| 2.3.2.2 Collisionless Boltzmann and Poisson Equations | 32 |
| 2.3.2.3 GADGET: a TreeSPH Code | 34 |
| 2.3.3 Building Initial Conditions | 35 |

| | | |
|----------|--|-----------|
| 2.3.3.1 | The Zel'dovich Approximation | 35 |
| 2.3.3.2 | Redshift Surveys or Direct Distance Estimates? | 36 |
| 3 | Observed Universe | 37 |
| 3.1 | Distances | 37 |
| 3.1.1 | Luminosity Distance | 38 |
| 3.1.2 | Magnitudes | 39 |
| 3.1.3 | Distance Indicators | 41 |
| 3.1.3.1 | Primary Distance Estimators | 42 |
| 3.1.3.2 | Secondary Distance Estimators | 43 |
| 3.2 | Observations | 47 |
| 3.2.1 | RadioAstronomy: HI Observations | 47 |
| 3.2.2 | Photometry: Observational Band | 49 |
| 3.3 | Surface Photometry | 50 |
| 3.3.1 | Spitzer: an Instrument of Choice | 50 |
| 3.3.1.1 | The InfraRed Array Camera Channel 1 | 51 |
| 3.3.1.2 | The Observational Sample | 52 |
| 3.3.2 | Spitzer-Adapted ARCHANGEL: a Tool for Surface Photometry | 56 |
| 3.3.2.1 | Surface Photometry: Definition | 56 |
| 3.3.2.2 | ARCHANGEL | 58 |
| 3.3.2.3 | Some Analyses | 64 |
| 3.3.3 | Corrected Magnitudes and Surface Brightnesses | 66 |
| 3.3.3.1 | Galactic Extinction Correction | 67 |
| 3.3.3.2 | Internal Extinction Correction | 68 |
| 3.3.3.3 | K-Correction | 68 |
| 3.3.3.4 | Aperture Correction | 69 |
| 3.3.4 | Uncertainties | 70 |
| 3.3.5 | Comparisons with Other Pipelines | 75 |
| 3.3.6 | Bimodality in Disk Central Surface Brightness: a Study Example Based on Photometry Parameters | 77 |
| 3.3.6.1 | Introduction | 78 |
| 3.3.6.2 | Ursa Major: Testing Measurements of μ_0 at $3.6 \mu\text{m}$ | 79 |
| 3.3.6.3 | Sample Selection | 81 |
| 3.3.6.4 | A Lack of Intermediate Surface Brightness Galaxies | 82 |
| 3.3.6.5 | Why a Dip at Intermediate Surface Brightness? | 87 |
| 3.4 | Tully-Fisher Relation | 89 |
| 3.4.1 | Calibration at $3.6 \mu\text{m}$ | 89 |
| 3.4.1.1 | Calibrators | 90 |
| 3.4.1.2 | Slope and Zeropoint | 91 |
| 3.4.1.3 | A Color Dependence | 99 |
| 3.4.1.4 | Bias and an Hubble Constant Estimate | 102 |
| 3.4.2 | Robustness of the Calibration | 106 |
| 3.4.2.1 | Increasing the Calibrator Sample and Changing the Selection Band | 107 |
| 3.4.2.2 | Again a Color Term | 109 |
| 3.4.2.3 | Re-derivation of the Bias | 110 |
| 3.4.3 | Hubble Constant & Supernovae of Type Ia | 114 |

| | | |
|----------|--|------------|
| 3.5 | Catalogs of Accurate Distance Estimates | 122 |
| 3.5.1 | Cosmicflows-1 | 123 |
| 3.5.2 | Cosmicflows-2 | 124 |
| 3.5.3 | Cosmicflows-3: an Insight | 125 |
| 4 | Simulated Universe | 129 |
| 4.1 | Constrained Simulations | 130 |
| 4.1.1 | Constrained Initial Conditions | 130 |
| 4.1.2 | Constrained Realizations | 131 |
| 4.1.2.1 | The Wiener-Filter Technique | 131 |
| 4.1.2.2 | The Constrained Realization of Gaussian Fields | 133 |
| 4.1.3 | First CLUES Generation (2003 - 2009) | 135 |
| 4.2 | Reverse Zel'dovich Approximation | 136 |
| 4.2.1 | Method | 136 |
| 4.2.1.1 | RZA-radial (2009 - 2012) | 136 |
| 4.2.1.2 | RZA3D, CLUES Second Generation (2013 -) | 137 |
| 4.2.2 | Building Mocks | 138 |
| 4.2.3 | Application on Mocks | 140 |
| 4.2.3.1 | Wiener-Filter Reconstruction of the Mock Universe | 141 |
| 4.2.3.2 | Constrained Simulations: RZA-radial versus RZA3D | 143 |
| 4.3 | Constrained Simulations with Cosmicflows-1 | 148 |
| 4.3.1 | Wiener-Filter Reconstruction of the Local Universe | 149 |
| 4.3.2 | Constrained Simulations of the Local Universe | 149 |
| 4.3.2.1 | Constrained Simulations and WMAP7/ Λ CDM Cosmology | 150 |
| 4.3.2.2 | Constrained Simulations and Local Cosmography | 150 |
| 4.4 | Biases | 154 |
| 4.4.1 | Malmquist Biases | 154 |
| 4.4.2 | Error Bias | 156 |
| 4.4.3 | Minimizing Bias(es) | 159 |
| 4.4.3.1 | A Gaussian Distribution of Radial Peculiar Velocities | 159 |
| 4.4.3.2 | Very Realistic Mocks | 160 |
| 4.4.3.3 | The Method | 163 |
| 4.4.3.4 | Tests | 165 |
| 4.5 | CLUES with Cosmicflows-2 | 170 |
| 4.5.1 | Minimization of the Bias(es) | 170 |
| 4.5.2 | Reconstruction of the Local Universe Within $160 h^{-1}$ Mpc | 171 |
| 4.5.3 | Constrained Simulations of the Local Universe: Main Attractors and Voids | 175 |
| 4.5.3.1 | Increasing the Resolution | 175 |
| 4.5.3.2 | Local Cosmography, an Insight in the Zone of Avoidance | 175 |
| 4.5.3.3 | Recovering Clusters | 180 |
| 5 | Summary & Prospectives | 185 |
| 5.1 | Summary | 185 |
| 5.1.1 | Observed Universe | 185 |
| 5.1.2 | Simulated Universe | 188 |
| 5.1.3 | Conclusion | 191 |

| | | |
|----------|---|------------|
| 5.2 | Prospectives | 192 |
| 5.2.1 | Observations | 192 |
| 5.2.2 | Simulations | 194 |
| A | Extragalactic Distance Database: Spitzer [3.6] Band Photometry | 201 |
| B | Calibrator Parameters | 203 |
| C | Distance Estimates | 215 |
| D | Abbreviations and Acronyms | 270 |
| E | Physical Constants and Units | 272 |
| F | Symbols and Mathematical Functions | 274 |
| | Bibliography | 282 |
| | Acknowledgements | 302 |

List of Figures

| | | |
|------|---|----|
| 1.1 | Schematic Map of the Nearest Superclusters | 2 |
| 1.2 | Filaments in the Local Universe | 3 |
| 1.3 | Constrained Simulations Without and With the Reverse Zel'dovich Approximation | 7 |
| 2.1 | Motions Around and Within the Local Sheet | 17 |
| 2.2 | Push From the Local Void | 18 |
| 2.3 | Local Motion Patterns | 19 |
| 2.4 | Supergalactic Planes of the Wiener-Filter Reconstruction of the Local Universe Within $30 \text{ h}^{-1} \text{ Mpc}$ | 20 |
| 2.5 | Fingers of Gods in the 2MASS Redshift Catalog | 23 |
| 2.6 | Lagrangian, Eulerian and Comoving Coordinates | 26 |
| 2.7 | WMAP3, WMAP7 and Planck Power Spectra | 29 |
| 3.1 | The Cosmic Distance Ladder | 41 |
| 3.2 | HI Profiles of Two Galaxies | 49 |
| 3.3 | Comparative SED for Spirals of Types Sa, Sb and Sc. | 52 |
| 3.4 | Histogram of the Number of "Spitzer galaxies" per Cosmicflows Project's Sub-samples | 53 |
| 3.5 | Histograms of "Spitzer Galaxies" Type and Heliocentric Velocity | 53 |
| 3.6 | Repartition of the "Spitzer Galaxies" in the XY Supergalactic Plane | 55 |
| 3.7 | Example of Masking and Ellipse Fitting Obtained with ARCHANGEL | 59 |
| 3.8 | Example of Surface Brightness Profile and Growth Curve Obtained with ARCHANGEL | 61 |
| 3.9 | Outputs From the ARCHANGEL Software for Five Galaxies | 63 |
| 3.10 | Comparison Between d_{25} and $a_{26.5}$ at $3.6 \mu\text{m}$ | 64 |
| 3.11 | Histograms of the Isophotal, "Total" and "Extrapolated" Magnitudes at [3.6] Band | 65 |
| 3.12 | Histograms of the Extracted Photometry Parameters | 65 |
| 3.13 | Comparisons of Axial Ratios and Position Angles | 66 |
| 3.14 | Example of a Surface Brightness Profile Obtained with ARCHANGEL | 70 |
| 3.15 | Variation of Magnitude Uncertainty as a Function of Morphological Type | 72 |
| 3.16 | Variation of Magnitude Uncertainty as a Function of Magnitude | 73 |
| 3.17 | Variation of Magnitude Uncertainty as a Function of the Sky Value | 73 |
| 3.18 | Variation of Magnitude Uncertainty as a Function of Three Galaxy Characteristics | 74 |
| 3.19 | Comparisons Between CHP, S ⁴ G and ARCHANGEL Magnitudes | 76 |
| 3.20 | Disk Central Surface Brightnesses in Ursa Major | 80 |

| | | |
|------|---|-----|
| 3.21 | Histograms of Some Characteristics of Galaxies Selected From S ⁴ G for Bimodality Study Purposes | 81 |
| 3.22 | Angular Distribution on the Sky of Galaxies Selected From S ⁴ G for Bimodality Study Purposes | 82 |
| 3.23 | Histogram of the Aperture-Inclination Corrected Disk Central Surface Brightnesses | 83 |
| 3.24 | Disk Central Surface Brightness Variations with Morphological Types | 83 |
| 3.25 | Separation Between Galaxies With and Without Close Neighbors for Bimodality Study Purposes | 84 |
| 3.26 | Separation of Highly Inclined Galaxies From the Others for Bimodality Study Purposes | 85 |
| 3.27 | Separation of Galaxies with Highly Uncertain Axial Ratios From the Others for Bimodality Study Purposes | 86 |
| 3.28 | Rejection of Galaxies With Close Neighbors, Highly Inclined, Uncertain Axial Ratios for Bimodality Study Purposes | 86 |
| 3.29 | Tully-Fisher Relation at 3.6 μm for the Virgo Cluster | 93 |
| 3.30 | Tully-Fisher Relation at 3.6 μm for Twelve Clusters | 94 |
| 3.31 | Template Tully-Fisher Relation at 3.6 μm Obtained with 213 Galaxies in 13 Clusters | 96 |
| 3.32 | Tully-Fisher Relation for the Zeropoint Calibrators | 96 |
| 3.33 | Template Tully-Fisher Relation in the Mid-Infrared | 97 |
| 3.34 | Tully-Fisher Relation in B, R, I and [3.6] Bands | 99 |
| 3.35 | Representation of Fluxes at B, R, I and [3.6] Bands Normalized to Unity at I Band | 100 |
| 3.36 | Deviations From the Mean ITFR as a Function of Color | 101 |
| 3.37 | The Tully-Fisher Relation Adjusted for the Color Term | 102 |
| 3.38 | Simulated Tully-Fisher Relation and Estimated Bias | 105 |
| 3.39 | Hubble Parameter as a Function of Distance | 106 |
| 3.40 | Updated Tully-Fisher Relation for the Virgo Cluster and for the 13 Clusters (Robustness) | 108 |
| 3.41 | Updated Tully-Fisher Relation for the Zeropoint Calibrators and Universal Relation (Robustness) | 109 |
| 3.42 | Tully-Fisher Relation and Color (Robustness) | 110 |
| 3.43 | Bias Measured as a Function of Absolute Magnitude Cutoff (Robustness) | 112 |
| 3.44 | Hubble Parameter as a Function of Distance (Robustness) | 112 |
| 3.45 | Comparison Between Moduli Derived with SNIa and with "Other" Methods | 116 |
| 3.46 | Comparison Between TFR Distance Moduli Measured in I and [3.6] Bands | 117 |
| 3.47 | Comparison Between Moduli Derived with SNIa, with "Other" Methods, in I and [3.6] Bands (Robustness) | 118 |
| 3.48 | Histograms of Distances in Cosmicflows-1,-2 and Provisional Cosmicflows-3 | 127 |
| 3.49 | Cosmicflows with Spitzer and Provisional Cosmicflows-3 | 128 |
| 4.1 | Principle of the Constrained Realization of Gaussian Fields | 135 |
| 4.2 | Refinement of the WF/RZA Technique | 138 |
| 4.3 | Distributions of the Initial Perturbation Velocity Field | 141 |
| 4.4 | Cell-to-Cell Comparison Between Reconstructed and Original BOX160 Velocity Fields | 142 |
| 4.5 | Slices of the Reconstructed and Original BOX160 Fields | 143 |

| | | |
|------|--|-----|
| 4.6 | Distribution Functions of the Component Values of the Data-Data Correlation Vector | 145 |
| 4.7 | Slices of the Simulated and Original BOX160 Density Fields | 146 |
| 4.8 | Power Spectra and Mass Functions of Constrained and Random Simulations . | 150 |
| 4.9 | XY Supergalactic Slice of the Average of Ten Constrained Simulations Obtained with Cosmicflows-1 | 151 |
| 4.10 | Supergalactic Slices of the Wiener-Filter Reconstruction and Constrained Simulations of the Local Universe Obtained with Cosmicflows-1 | 153 |
| 4.11 | Histogram of Radial Peculiar Velocities in Cosmicflows-2 | 157 |
| 4.12 | Schematization of Bias Effects | 158 |
| 4.13 | Distribution of Selected Halos in the XY Plane of a Constrained Simulation . | 161 |
| 4.14 | Distribution of Radial Peculiar Velocities in Original, Bias and Corrected Mocks | 162 |
| 4.15 | Histograms of Fractional Errors on Distances and on Radial Peculiar Velocities | 163 |
| 4.16 | Distributions of Constraints in the XY Plane of the Original, Biased and Corrected Mocks | 164 |
| 4.17 | Slices of the Wiener-Filter Reconstructed Fields Obtained with the Original, Biased and Corrected Mocks | 166 |
| 4.18 | Cell-To-Cell Comparisons Between the Original, Biased and Corrected Mocks | 167 |
| 4.19 | Difference between Biased, Corrected and Original Reconstructed Velocity Fields | 168 |
| 4.20 | Difference between Biased, Corrected Reconstructed and Original Simulated Velocity Fields | 169 |
| 4.21 | Radial Peculiar Velocity Distributions in CF2- Biased, Catalog and Corrected | 171 |
| 4.22 | Supergalactic Planes of the Reconstructed Fields Obtained with CF2- Biased, Catalog and Corrected | 173 |
| 4.23 | Supergalactic Planes of the Reconstructed Overdensity Fields Obtained with Cosmicflows-2 Corrected | 174 |
| 4.24 | Supergalactic Planes of One Realization and of the Average of the Constrained Simulations Obtained with Cosmicflows-2 Corrected | 176 |
| 4.25 | Supergalactic Plane of the Simulated Density Field Obtained with the Whole Process Applied to Cosmicflows-2 | 178 |
| 4.26 | Superclusters within the Local Universe | 179 |
| 4.27 | Comparisons between Reconstruction (<i>top</i>) and Simulation (<i>bottom</i>) of the Local Universe | 180 |
| 4.28 | Abell Clusters on Top of a Constrained Simulation | 183 |
| 5.1 | Overview of Current and Envisaged Future Work | 199 |

List of Tables

| | | |
|------|---|-----|
| 2.1 | Cosmological Parameters | 15 |
| 3.1 | Photometric Observational Bands | 50 |
| 3.2 | Example of Extracted Photometry Parameters | 62 |
| 3.3 | Comparisons Between ARCHANGEL Magnitudes and Other Magnitudes | 77 |
| 3.4 | Characteristics of Simulations Evaluating the Probability to Obtain a Dip at Intermediate Surface Brightness by Pure Statistical Fluctuations | 87 |
| 3.5 | Properties of the Cluster Fits | 98 |
| 3.6 | Properties of the Cluster Fits (Robustness) | 113 |
| 3.7 | Tully-Fisher Relations' Parameters | 113 |
| 3.8 | Comparisons Between Cluster Distances Obtained with Tully-Fisher Relations | 114 |
| 3.9 | Properties of Clusters with Supernovae of Type Ia | 119 |
| 3.10 | Hubble Constant Estimates | 119 |
| 3.11 | Properties of Individual Type Ia Supernovae-Host Galaxies | 120 |
| 3.12 | Properties of Individual Type Ia Supernovae-Host Galaxies (Robustness) | 121 |
| 3.13 | Number of Measurements per Method in Cosmicflows-1 | 123 |
| 3.14 | Number of Measurements per Method in Cosmicflows-2 | 125 |
| 4.1 | Average Parameters of Look-Alikes of the Mock Halos | 148 |
| 4.2 | Average Parameters of Look-Alikes of Virgo | 151 |
| 4.3 | Abell Clusters and Matched Dark Matter Halos | 182 |
| A.1 | Extracted Photometry Parameters | 202 |
| B.1 | Calibrator Parameters | 207 |
| B.2 | Calibrator Parameters (Robustness) | 214 |
| C.1 | Distance Estimates | 268 |

*"Nothing happens
until something moves."
Albert Einstein*

Chapter 1

Motivation

With the emergence of modern cosmology came the cosmological principle which relies on the strong assumption that the distribution of matter, in the Universe, is homogeneous and isotropic about all locations when viewed on a large enough scale. This last part of the axiom is essential as observations soon revealed that nearby galaxies are distributed in an inhomogeneous way (e.g. Bahcall, 1984; Longair and Einasto, 1978). As a matter of fact, large scale structures which can extend up to $100 \text{ h}^{-1} \text{ Mpc}$ (Bahcall, 1984; Oort, 1982) can be observed in the whole observable Universe. Galaxies, which constitute themselves local inhomogeneities, have a tendency to gather in groups or even clusters, which can regroup to form superclusters, linked by filaments. The assumption of homogeneity on "small scales" had to be banished (Chincarini, 1981). Current maps of our neighborhood on Figures 1.1 and 1.2 show that indeed superclusters and clusters in the Universe are linked by filaments constituted of galaxies. These filaments delimit nearly empty regions or voids as large as $300 \text{ h}^{-1} \text{ Mpc}$ (e.g. Bahcall, 1984). The presence of such regions devoid of galaxies is striking. Mapping the Universe is essential to determine the limit of the cosmological principle. Besides, observations also revealed that the Universe undergoes an accelerated (Perlmutter et al., 1998; Riess et al., 1998) expansion (Hubble, 1929) suggesting the existence of a dark energy.

Beyond the simple acknowledgement of the existence of the Large Scale Structure, in an homogeneous and isotropic on a large enough scale Universe in accelerated expansion, is implied the study of its formation and evolution. There is no doubt that this dynamics of the Universe is gravitationally related (e.g. Peebles, 1980). Structures are the probable

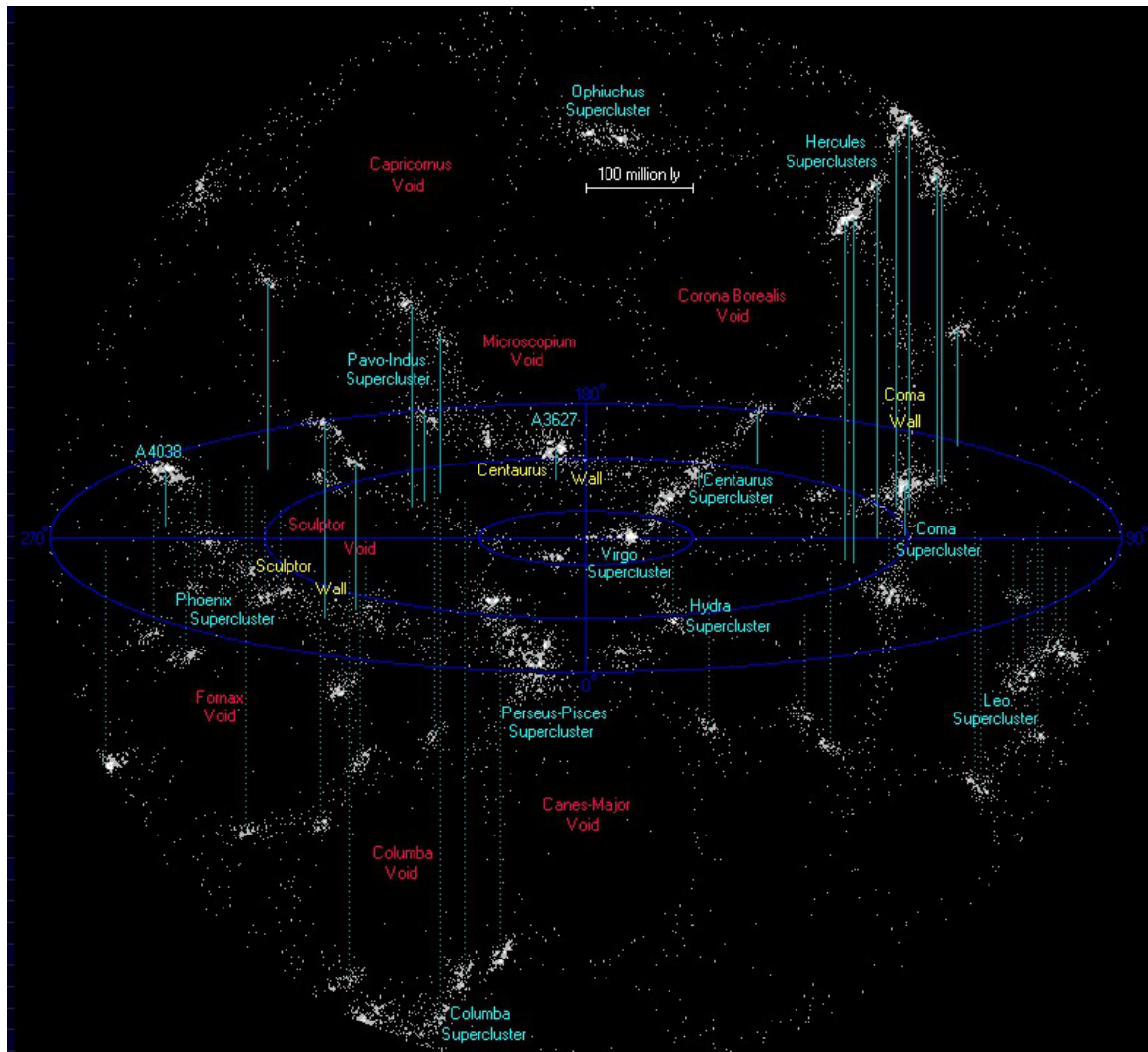


FIGURE 1.1: Schematic map of the nearest Superclusters centered on the Milky Way. Large structures of the Local Universe are visible: wide regions devoid of galaxies or voids (names written in red) are delimited by long filaments formed by galaxies (white dots). Superclusters (pale blue color) are at the nodes of these filaments. Their positions, with respect to the supergalactic plane in dark blue, is defined by pale blue lines either solid if their are above the plane or dotted if they are below it. The yellow color indicates walls (from <http://www.atlasoftheuniverse.com>).

results of irregularities in the primordial (early after the Big Bang) density field which have grown under the influence of gravity (e.g. [Press and Schechter, 1974](#); [Silk et al., 1983](#)). In that sense, the presence of a dipole in the Cosmic Microwave Background temperature map ([Fixsen et al., 1996](#)) is a compelling evidence of the motion of our Galaxy at high speed (over 600 km s^{-1}) because of gravity. However, the considerable majority ($\approx 70\%$) of this posited motion is due to the gravitational influence of large scales with origins that have yet to be understood.

Gravitational dynamics is too complex to be analytically studied in details. Thus, studies rely on simulations based on numerical methods. The recent development of large parallel

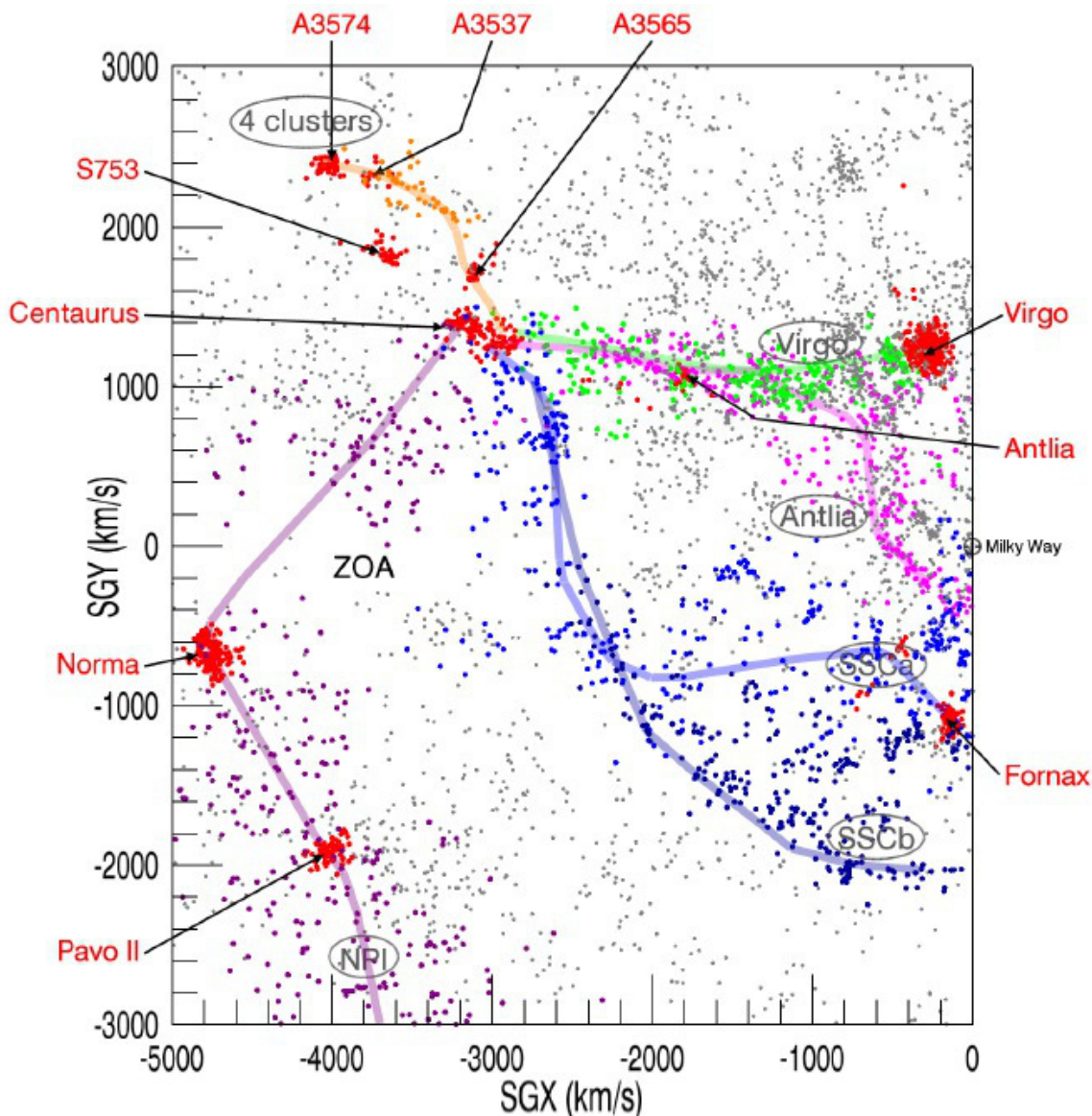


FIGURE 1.2: Supergalactic XY slice of 4000 km s^{-1} thickness in Z showing five filaments joining up in the Centaurus cluster. Red dots stand for the major clusters identified in red and filament names are in grey oval shapes. The five filaments and galaxies belonging to them are depicted with five different colors. Orphan galaxies are in grey (from [Courtois et al., 2013](#)).

supercomputers and of highly efficient numerical codes (e.g. [Kravtsov et al., 1997](#); [Springel, 2005](#); [Teyssier, 2002](#)), to simulate the gravitational clustering of dark matter, led to a better understanding of structure formation at all scales. Ordinary matter contributes to less than 20% of the total matter in the Universe, thus, accordingly, it can be neglected in simulations in a first approximation. The resulting scheme is 1) cosmic structures grow via the sole gravitational instabilities pre-existing in the initial density field in the form of Gaussian fluctuations ([Press and Schechter, 1974](#)) ; 2) in a dissipationless gravitational collapse, dark halos are shaped ([Gunn and Gott, 1972](#)) ; 3) and galaxies form with the halos following the

radiative cooling of baryons¹ (e.g. [Efstathiou, 2003](#)). Two powerful concepts can describe the formation of galaxies : 1- gasdynamical simulations (e.g. [Scannapieco et al., 2005](#)) ; 2- populating dark matter halos with semi-analytical models (e.g. [Cole et al., 2000](#)) or abundance matching techniques (e.g. [Klypin et al., 2013](#)). To summarize, to study a particular region or object, one can consider extracting a part of the larger box, resimulate it using higher resolution with or without adding baryonic particles. In this latter case, the simulation needs to be populated. This numerical progress has been accompanied by a huge amount of new observational data, which became available over the last decade. As a result, because on short distances tiny dwarf galaxies can be detected as well as big galaxies, structure formation in the nearby Universe can be observed on all possible scales ensuring that observations and simulations can be compared on every scale.

Resulting large simulations (e.g. [Alimi et al., 2012](#); [Angulo et al., 2012a](#); [Fosalba et al., 2013](#); [Klypin et al., 2011](#); [Springel et al., 2005](#)) have already widely contributed to establish the standard model of cosmology. Through comparisons with observations, it has become possible to decide between models and numerical algorithms. For instance, Hot Dark Matter was ruled out as the dominant matter component as it implies that large scale structures form first, before fragmenting, recently, into small structures in contradiction with observations of small scale structures at high redshifts (e.g. [Petry et al., 1998](#); [Rauch et al., 1999, 2001](#)). Still, while ensuing comparisons between (nearby) observations and simulations have revealed that Large Scale Structure formation can be well described within the Cold Dark Matter (CDM) scenario as a result of an accretion of small structures, there are several open problems related to the formation of these small scale structures. These problems are due to differences in the number of galaxy satellites ([Klypin et al., 1999](#); [Moore et al., 1999](#)), the size of voids ([Tikhonov and Klypin, 2009](#)) and the number of dwarfs between the observed and simulated local universes ([Zavala et al., 2009](#)). To compare more precisely theoretical predictions with observed nearby small scale structures, replicas of the Local Universe needs to be simulated to remove the dependence on the specificity of the environment, namely to avoid the cosmic variance contained in the random realizations. This can be done in the framework of simulations whose Initial Conditions are constrained by nearby observational data. Such constrained simulations are ideal laboratories to study the formation and evolution processes of the Universe in general but also of its constituents such as galaxies. By their constrained nature, they reduce effectively the cosmic variance related to the fact that as fixed observers in the Universe we can observe only one angle of our Universe, at one time.

Accordingly, the CLUES project² (Constrained Local UniversE Simulations, [Gottlöber et al.,](#)

¹The goal of this work is to study scales large enough for the influence of baryons to be negligible. Consequently, studies in this work are conducted in a dark matter only context.

²<http://www.clues-project.org/>

2010) developed the concept of constrained simulations. The first constrained Initial Conditions were produced by [Ganon and Hoffman \(1993\)](#), using the Mark III catalog of peculiar velocities ([Willick et al., 1996](#)). [Kolatt et al. \(1996\)](#) used these Initial Conditions to perform the first constrained simulations of the nearby Universe, more than ten years after the first standard numerical simulation was run within a Cold Dark Matter cosmological context ([Davis et al., 1985](#)). Later, [Bistolas and Hoffman \(1998\)](#) produced Initial Conditions constrained by redshift surveys. They were followed by [Mathis et al. \(2002\)](#) and [Lavaux \(2010\)](#) and very recently by [Heß et al. \(2013\)](#). There exists a real trade-off between the two sets of observational data available: radial peculiar velocities and redshift surveys. While measuring velocities is a tremendous challenge to the observers' community, on the theoretical side these velocities are unbiased tracers of the underlying gravitational field as they account for both baryonic and dark matter. On the other hand, very large and deep surveys of galaxy redshifts are more easily produced but galaxies constitute biased markers of the underlying mass distribution since they account only for the luminous matter. Moreover, the bias is poorly known (e.g. [Baugh, 2013](#)). Thus, radial peculiar velocity catalogs have inevitably a great potential and a promising future. The new project Cosmicflows³ (e.g. [Courtois and Tully, 2012a,b](#); [Tully and Courtois, 2012](#)) is an ideal constraints-supplier to perform constrained simulations of the nearby Universe.

Cosmicflows is an international project, with as many arms as an octopus, whose goal is to map the Local Universe. Within this context, the collaboration accumulates accurate distances of thousands of galaxies via observations and distance indicators such as the luminosity-linewidth rotation rate correlation or Tully-Fisher relation ([Tully and Fisher, 1977](#)), the Cepheid-period luminosity ([Freedman et al., 2001](#)), the Tip of the Red Giant Branch ([Lee et al., 1993](#)), the Surface Brightness Fluctuation ([Tonry et al., 2001](#)), the Fundamental Plane ([Colless et al., 2001](#)) and the Supernovae of type Ia ([Jha et al., 2007](#)) methods. A major part of the program involves exploitation of the Tully-Fisher relation. Activities in this regard began with the gathering of HI profiles for the necessary kinematic information using the Green Bank and Parkes Telescopes ([Courtois et al., 2009, 2011b](#)) and the accumulation of optical photometry for the necessary magnitude and inclination information using the University of Hawaii 2.24m telescope ([Courtois et al., 2011a](#)) and the available literature. The project has already supplied the community with two catalogs of accurate distances up to $30 \text{ h}^{-1} \text{ Mpc}$ ([Tully et al., 2008](#)) and $150 \text{ h}^{-1} \text{ Mpc}$ ([Tully et al., 2013](#)) respectively. Both are downloadable at the Extragalactic Distance Database website⁴ ([Courtois et al., 2009; Tully et al., 2009](#)) of the project. This work presents an extension of the optical part of the project with a shift to the mid-infrared wavelengths already partly published in ([Sorce et al., 2012a, 2013b, 2012b](#)). Results from this work will become part of another

³<http://www.ipnl.in2p3.fr/projet/cosmicflows/>

⁴<http://edd.ifa.hawaii.edu/>

catalog of the project with a greater accuracy. This third catalog will extend the coverage both in distances and close to the Zone of Avoidance (zone which looks devoid of data only because of the extinction of our Galactic disk) where our knowledge is still very limited. The holy grail of Cosmicflows is the use of these resulting distance estimates to determine radial peculiar velocities to be combined with the CLUES project.

First of all, these catalogs can be used with the Wiener-Filter technique (e.g. Zaroubi et al., 1995) to reconstruct the Local Universe. Still, if reconstructions of the velocity and density field of our neighborhood already enable the studies of the Bulk Flow and motions (e.g. Courtois et al., 2012), it presents us only with the linear part of the theory (e.g. Nusser, 2008; Zaroubi et al., 1999) and solely at redshift, z , null (namely the Universe today). Combined with the Constrained Realizations technique (e.g. Hoffman and Ribak, 1991), the catalogs can supply us with constrained Initial Conditions which, once run, can give insights into the evolution and formation of the Large Scale Structure from high redshifts up to today including non-linear events such as mergers. Studying the early history of our Universe will help decide between theoretical models which are all built to reproduce the observed expansion at late times (e.g. Xia et al., 2012). However, the first simulations output from the Constrained Realization method presented a shift in the position of structures of approximately $10 \text{ h}^{-1} \text{ Mpc}$ at $z = 0$ with respect to the observed Universe today. Moreover, additional density constraints were required to form the nearby clusters (Klypin et al., 2003). A new methodology has been developed to improve the simulations by taking into account the cosmic displacement field of data-points from high redshifts to $z = 0$ at first order (Doumler et al., 2013a,b,c). This methodology called the Reverse Zel'dovich Approximation, which works well on simple mocks on Figure 1.3, reveals itself to be insufficient when applied to observational data. This work presents tests on more realistic mocks to refine the process. Re-establishing the 3 directions of peculiar velocities is proved to be a satisfactory refinement for the process to work with observational datasets (work already published in Sorce et al., 2014). The resulting constrained dark matter only simulations are excellent replicas of our Universe, obtained for the first time *solely* with observational radial peculiar velocities from the first catalog of the project Cosmicflows. The uncertainty in positions has been reduced to $\sim 3 \text{ h}^{-1} \text{ Mpc}$ (the limit imposed by the linear theory) for the best realizations. This work concludes with the application of the whole process on the second catalog of the project Cosmicflows firstly analyzed to reduce bias effects which become more important with the increasing spatial extent of the catalog. A method is actually proposed in this work to minimize biases. The cosmological model considered in this work is the standard Λ CDM and the simulations have been run with the Lagrangian GADGET code (Springel, 2005).

This work aims at studying several processes both observational and numerical in analytical and quantitative ways in the loop defined by the combination of the Cosmicflows and CLUES

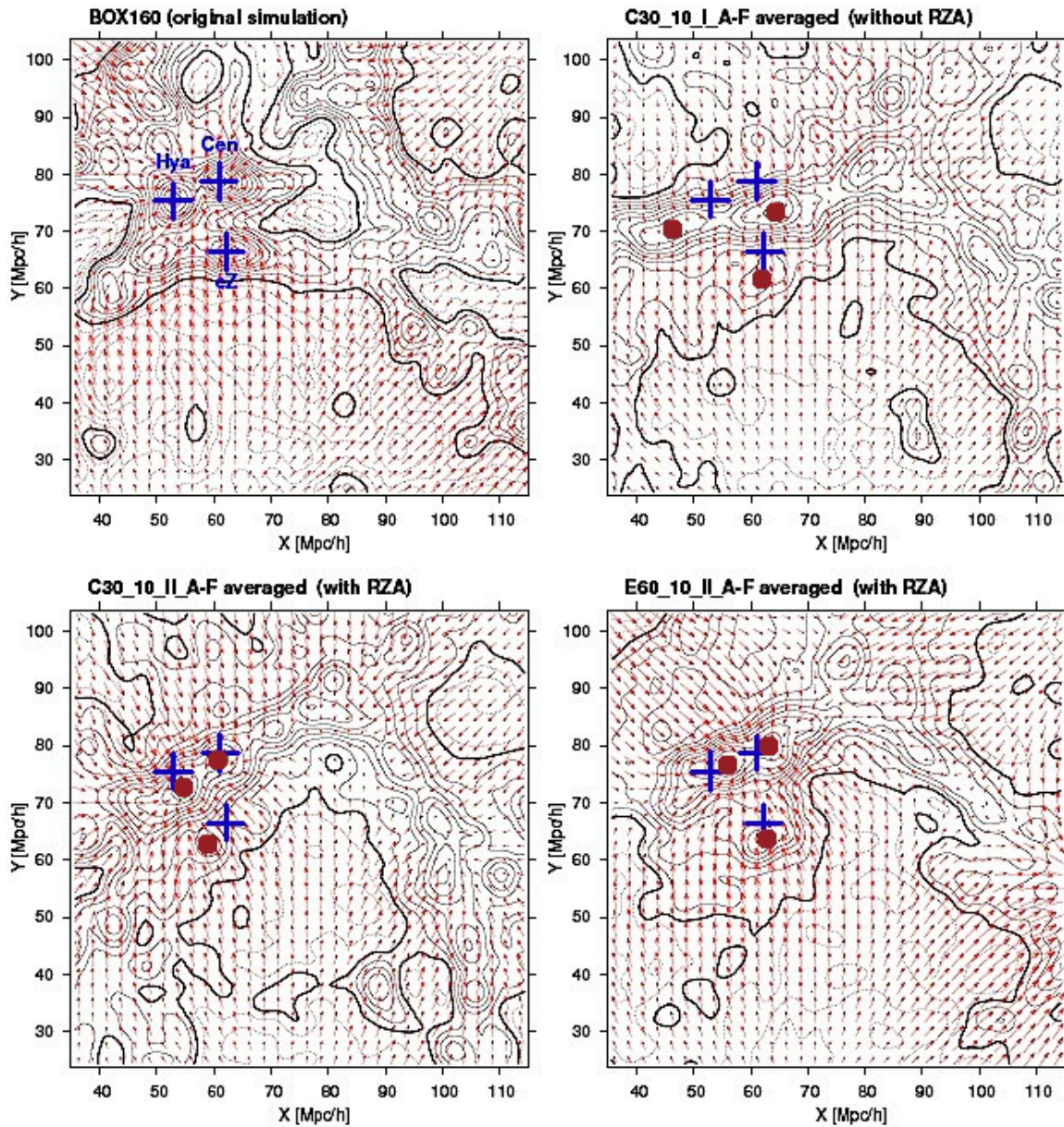


FIGURE 1.3: Density and velocity fields in a $10 h^{-1}$ Mpc thick slice of the original first constrained simulation, named BOX160, of the CLUES project (*top left quadrant*) and the averages of six constrained simulations obtained with mocks built out of BOX160. The constrained Initial Conditions have been obtained without (*top right*) and with the Reverse Zel'dovich Approximation applied to simple mocks mimicking the size and spatial extent of Cosmicflows' first (*bottom left*) and second catalogs (*bottom right*). Blue crosses show the positions of three clusters in the original simulation while red dots locates the clusters in the constrained simulations on average (adapted from [Doumler et al., 2013b](#)).

project. What is the quantitative quality of the observational data, of the measurements of luminosities, of the Tully-Fisher relation in the mid-infrared at $3.6 \mu\text{m}$? What is the performance of the newest CLUES technique applied to realistic mock and observational radial peculiar velocity catalogs? How can observations and simulations be intertwined to allow refinements of each other? How well and to which extent the simulations constrained by Cosmicflows' catalogs reproduce the Large Scale Structure of the Universe?

To answer these questions, this thesis manuscript is organized as follows. In Chapter 2, the fundamental knowledge about our Universe and especially our neighborhood is described from models to general methods and tools, through nearby observations, including: the standard Λ CDM cosmological model, the linear theory of density perturbations and the numerical cosmological simulation method. Chapter 3 presents the Observed Universe namely, the contribution of the Cosmicflows project to the global scheme. This Chapter includes the surface photometry of a large sample of galaxies up to the construction of a set of accurate distance measurements (in view of a future catalog for the Cosmicflows project) through the calibration of the Tully-Fisher relation and the determination of an Hubble Constant estimate. In Chapter 4, simulations obtained with Cosmicflows' catalogs in the context of the CLUES project are presented. To this end, the method to build constrained Initial Conditions is described and refined with tests on realistic mocks before being applied on the two first catalogs of the Cosmicflows project. The spatial extent of the second catalog of the Cosmicflows project leads us to analyze more thoroughly this catalog to propose a method to minimize biases before building Initial Conditions constrained with it. The last and fifth Chapter (5) summarizes the observational and numerical work accomplished before opening onto new perspectives for both projects.

Chapter 2

Universe in Motion

Cosmology aims at understanding the formation and evolution of structures in the Universe. For that purpose, galaxies constitute one of the sources of observational probes. However, they are only tips of the iceberg of a larger scheme involving more than 90 % of dark matter and energy. These two exotic components are elegantly accounted for in the widely accepted standard cosmological model, implying an homogeneous and isotropic on large enough scales Universe. Structure formation is the result of gravitational instabilities driven by primordial density perturbations. Their studies rely on numerical tools such as N-body methods. Accordingly, this Chapter presents the standard cosmological model in the context of an observed general expansion yet with visible local deviations from this widening. Then, these local variations are explained within the context of the linear theory of density perturbations. Finally, the numerical models used to simulate our Universe are described.

2.1 The Standard Cosmological Model

The standard cosmological model asserts that during the inflation that followed the big bang, the quantum fluctuations become classical such that particles and eventually nuclei were able to condense. Continuing expanding and cooling, the Universe experienced a transition from radiation-dominated era to a matter-dominated epoch. Baryons decoupled from radiations. This corresponds to the last scattering of photons, in other words to the Cosmic Microwave Background (CMB). Afterwards, structures began to form by collapse of small irregularities in an overall close to a homogeneous density distribution. Stars were born and soon reionized the Universe with their radiations while, larger scale structures, such as galaxies, clusters, etc formed. For a more complete description of the concept, we refer the reader to the wealth of the literature (e.g. [Binney and Tremaine, 1987](#); [Peacock, 1999](#); [Peebles, 1993](#)). To summarize, the Λ CDM scenario implies a hierarchical structure formation from small to

large scale structures, the latter forming by accretion of the former. This thesis work focus on this matter-dominated era of the Universe in expansion. The next subsections aims at establishing the theoretical framework of such an universe.

2.1.1 An Universe in Expansion

2.1.1.1 The Hubble Law

In 1929, Hubble observed that local galaxies are receding from us at a velocity proportional to their distance. The Hubble Law was born. In other words, any local galaxy at a distance D from us has a velocity v which follows:

$$v = H_0 D \quad (2.1)$$

where H_0 is the Hubble Constant usually expressed in $\text{km s}^{-1} \text{Mpc}^{-1}$.

To appreciate the importance of the adjective "local", let's consider a galaxy at a distance x with spatial coordinates fixed for simplicity. Because, photons travel along null geodesics, it follows from the Friedmann-Lemaître-Roberston-Walker metric (key to a solution of the equations of General Relativity written for an homogeneous isotropic Universe, [Friedmann, 1922](#); [Lemaître, 1931a,b](#); [Robertson, 1933, 1935, 1936a,b](#)) that:

$$ds^2 = 0 \Rightarrow c dt - a(t) \frac{dx}{\sqrt{1 - kx^2}} = 0 \quad (2.2)$$

where c is the vacuum velocity of light in km s^{-1} , ds is the geodesic followed by the light in a time dt , $a(t)$ is the scale factor due to the expansion and k is the curvature of space. Let's assume that the galaxy emits photons with a period $T = t_1 - t_0$ which propagates up to us (located at the distance x). We observe a period $T' = t'_1 - t'_0$. Integrating over time and space equation 2.2 gives:

$$\int_{t_0}^{t'_0} \frac{c}{a(t)} dt = \int_0^x \frac{dx'}{\sqrt{1 - kx'^2}} = \int_{t_1}^{t'_1} \frac{c}{a(t)} dt \quad (2.3)$$

which in turn gives:

$$\int_{t_0}^{t_1} \frac{c}{a(t)} dt + \int_{t_1}^{t'_0} \frac{c}{a(t)} dt = \int_{t_1}^{t'_0} \frac{c}{a(t)} dt + \int_{t'_0}^{t'_1} \frac{c}{a(t)} dt \quad (2.4)$$

If we make the reasonable approximation that T and T' are very small with respect to the expansion time, $a(t)$ varies only slightly during both periods. Thus, from equation 2.4:

$$\frac{T}{a(t_0)} \approx \frac{T'}{a(t'_0)} \quad (2.5)$$

In addition, if the galaxy is close enough to us (namely "local"), the scale factor can be assumed as unchanged between the emission and the reception of the signal and the curvature is negligible¹, then from the two first terms of equation 2.3:

$$t'_0 - t_0 \approx \frac{D}{c} \quad (2.6)$$

where $D \approx xa(t_0)$.

Since $v = c \frac{\lambda' - \lambda}{\lambda} = c \frac{T' - T}{T}$, it results from the relations 2.5 and 2.6 that at first order:

$$v = c \frac{a(t'_0) - a(t'_0 - \frac{D}{c})}{t'_0 - (t'_0 - \frac{D}{c})} \times \frac{\frac{D}{c}}{a(t'_0 - \frac{D}{c})} \approx \frac{\dot{a}(t'_0 - \frac{D}{c})}{a(t'_0 - \frac{D}{c})} D = \left. \frac{d \ln a}{dt} \right|_0 D \quad (2.7)$$

The Hubble Law in equation 2.1, valid solely for local galaxies, derives from 2.7 relation with $H_0 = \left. \frac{d \ln a}{dt} \right|_0 = \frac{\dot{a}_0}{a_0}$. The subscript 0 stands for "as measured today" and the "·" notation is the common writing for the derivative with respect to time. It results from this calculation that the discrepancies from the Hubble Law for galaxies far away from us enable the study of the scale factor history as a function of time.

In this respect, Edwin Hubble's observations of the Hubble Law consolidate the cosmological principle and the equations derived two years before by Lemaître. Namely, under the assumption that we are not privileged observers, the isotropy and homogeneity of the expanding Universe about all locations is confirmed. The rest of this subsection will generalize the Hubble Law in agreement with the cosmological principle and the observed expansion before giving the equations of evolution of the scale factor with time.

2.1.1.2 Generalization

A generalized version of the Hubble Law can be derived with the consideration that distances $D(t)$ between galaxies are simply resized by the scale factor $a(t)$ (the relative positioning is unchanged because of the cosmological principle). Accordingly:

$$D(t) = a(t)D_0 \quad v(t) = \dot{D}(t) = \dot{a}(t)D_0 = \frac{\dot{a}(t)}{a(t)} D(t) \quad (2.8)$$

¹In any case we will see later that our Universe is approximately flat.

One can verify that this general case contains the Hubble Law given in equation 2.1 for times t approximately equal to today time so that the corresponding scale factors $a(t)$ are close to a_0 .

2.1.1.3 Evolution of the Scale Factor

As a common consensus, the laws of gravity are described by the theory of General Relativity formulated by Einstein in 1915. This general formalism contains Newton's theory of gravity valid for gravitational fields on small scales solely. The Friedmann-Lemaître-Robertson-Walker metric can be shown to have a solution to Einstein's field equations for an homogeneous and isotropic Universe as a whole. However, such a derivation is beyond the scope of this work² and we rely on simple thermodynamical considerations (basically adiabatic processes) under the assumption of (relativistic) fluids to explain the equations governing the evolution of the scale factor with time.

Relativity implies that mass m and energy E are equivalent through the famous equation:

$$E = mc^2 \quad (2.9)$$

where c is the vacuum velocity of light.

A direct consequence of relation 2.9 resides in the fact that matter, in the general sense of the term, is not the sole actor of motions. Radiation fields, like the Cosmic Microwave Background, are also responsible for motions. Radiations are then considered similar to a matter with a density ρ and some pressure P which follow the first law of thermodynamics $dU = -PdV$ where dU and dV are the variations of energy and volume. More precisely, in an expanding context with a scale factor a , the first law of thermodynamics can be written:

$$d\rho + \left(\rho + \frac{P}{c^2}\right) \frac{dV}{V} = d\rho + 3 \times \left(\rho + \frac{P}{c^2}\right) \frac{da}{a} = d[\ln(\rho)] + 3 \times (1 + \omega)d[\ln(a)] = 0 \quad (2.10)$$

where the fact that $U = \rho c^2 V$ (from relations 2.9 and $m = \rho V$), $V \propto a^3$ (from relations 2.8 left and $V \propto D^3$) and $P = \omega \rho c^2$ (pressure related to thermal motion) have been used. ω is a constant depending on the object of study.

Let's consider three cases:

- in classical matter, the pressure is sufficiently smaller than ρc^2 for ω to be considered as null. Gravitational and inertial masses of classical matter are indistinguishable. As a result and as expected from the conservation of mass, the density of classical matter ρ_m is proportional to a^{-3} from equation 2.10,

²For a complete derivation of the equations of gravity, we refer the reader to the extensive literature on the subject (e.g. Binney and Tremaine, 1987; Peacock, 1999; Peebles, 1993).

- radiations are quite different since their pressure effect cannot be neglected. Hence, for massless and highly relativistic particles, ω equals $\frac{1}{3}$ from the relation between kinetic energy E_k and temperature T (typically $E_k = \frac{1}{2}mv^2 = \frac{3}{2}k_B T$ where k_B is the constant of Boltzmann). From equation 2.10, $\rho_r \propto a^{-4}$ which is expected because not only ρ_r decreases because of the Universe expansion but also radiations are subject to a loss of energy inversely proportional to a (increase of wavelength by a),
- considering $\omega = -1$, Carroll et al. (1992) defined the finite vacuum energy density or more generally the dark energy with a negative pressure. As expected, this term gathers the quality of a constant in space and time as it is independent of a from equation 2.10.

In such a defined homogeneous isotropic expanding Universe, the Friedmann-Lemaître-Robertson-Walker model describes the Universe with two equations of the scale factor a :

$$\frac{\ddot{a}}{a} = \frac{-4\Pi G}{3} \left(\rho + \frac{3P}{c^2} \right) + \frac{\Lambda}{3} \quad (2.11)$$

$$\left(\frac{\dot{a}}{a} \right)^2 = \frac{8\Pi G}{3} \rho - \frac{Kc^2}{a^2} + \frac{\Lambda}{3} \quad (2.12)$$

where G is the universal gravitational constant, c the vacuum velocity of light, P the pressure, K the scalar curvature and Λ stands for the cosmological constant which reproduces the expansion effect.

The first one of these two equations (2.11) is analogous to the classical equation of motion (after divisions by the scale factor a and the original coordinate x) which stipulates that the acceleration $\ddot{a}x$ equals the sum of the gravitational forces. In the presently defined Universe, the three types of components described above contribute to the gravitational field. Accordingly the sum of the forces can be written:

$$F_{total} = \frac{-G \frac{4\Pi(xa)^3}{3} \rho_m}{(xa)^2} + \frac{-G \frac{4\Pi(xa)^3}{3} \left(\rho_r + \frac{3P}{c^2} \right)}{(xa)^2} + \frac{-G \frac{4\Pi(xa)^3}{3} \left(-\frac{P}{c^2} \right)}{(xa)^2} \quad (2.13)$$

With $\rho = \rho_m + \rho_r$ and $\Lambda = 4\Pi G \left(-\frac{P}{c^2} \right)$ the analogy is complete.

The second equation 2.12 governing the scale factor evolution is comparable to the conservation of energy. It can be directly retrieved from equation 2.11 by first multiplying this latter by $\dot{a}a$. Then, a few relations have to be noticed:

$$\frac{d\dot{a}^2}{dt} = 2\dot{a}\ddot{a} \quad ; \quad \frac{da^2}{dt} = 2\dot{a}a \quad ; \quad \frac{d\left(\frac{-1}{a}\right)}{dt} = \frac{\dot{a}}{a^2} \quad (2.14)$$

and completed with

$$\frac{d(\rho a^2)}{dt} = 2\rho a\dot{a} + a^2\dot{\rho} = -a\dot{a}(\rho - 3\rho - \frac{a}{\dot{a}}\dot{\rho}) = -a\dot{a}(\rho + \frac{3P}{c^2}) \quad (2.15)$$

where the last equality derives directly from the first thermodynamical law 2.10. Finally, a division by a^2 and an equalization of the constant of integration to $-Kc^2$ gives 2.12. From the fact that K is the scalar curvature and the second equation of the standard cosmological model is similar to the conservation of energy, one can catch a glimpse at a link between energy density and geometry from the metric.

From relation 2.8, we have seen that $H(t) = \frac{\dot{a}}{a}$. The square of this ratio is given by equation 2.12. Setting today density parameters as follows:

$$\Omega_m = \frac{8\Pi G\rho_{m0}}{3H_0^2} \quad ; \quad \Omega_\Lambda = \frac{\Lambda}{3H_0^2} \quad ; \quad \Omega_K = \frac{Kc^2}{H_0^2} \quad ; \quad \Omega_r = \frac{8\Pi G\rho_{r0}}{3H_0^2} \quad (2.16)$$

where the subscript 0 stands for today time, it is possible to give an expression of $H(t)$ as a function of the components in the Universe today:

$$H(t) = H_0 \sqrt{\frac{\Omega_r}{a^4} + \frac{\Omega_m}{a^3} - \frac{\Omega_K}{a^2} + \Omega_\Lambda} \quad (2.17)$$

where matter and radiation have once again been separated as the expansion does not affect them in a similar way (density of radiation decreases faster than that of matter since $\rho_r = a^{-4}\rho_{r0}$ while $\rho_m = a^{-3}\rho_{m0}$).

Various observational programs over the past few years have contributed to the measurements of the density parameters. Table 2.1 recapitulates the different estimates. In this table, for conveniency, the Hubble Constant H_0 is replaced by the parameter h defined such that:

$$H_0 = 100 h \text{ km s}^{-1} \text{ Mpc}^{-1} \quad (2.18)$$

This parameter is convenient in the sense that, for example, any distance given in Megaparsec per unit of this parameter h is valid in any cosmological model. One remarkable characteristic of the ensemble of measures given in the table is that the sum of the matter and dark energy density parameters is always close to 1 up to a few hundreds of percents. Since today, $H = H_0$, $\Omega_r \approx 0$ ($\Omega_r \ll 1$ since z became less than 3000, end of the radiation dominated era, beginning of the matter dominated epoch) and the scale factor is the unity by definition, $\Omega_K = \Omega_m + \Omega_\Lambda - 1 \approx 0$ from equation 2.17. Namely, our Universe is likely to be flat. Accordingly, in the matter dominated era, the equation of evolution of the scale factor can be written:

$$\dot{a} = aH(t) = H_0 \sqrt{\Omega_m \left(\frac{1}{a} - 1\right) + \Omega_\Lambda (a^2 - 1) + 1} \approx H_0 \sqrt{\Omega_m \frac{1}{a} + \Omega_\Lambda a^2} \quad (2.19)$$

| Cosmological Parameters | WMAP3 | WMAP5 | WMAP7 | WMAP9 | Planck |
|--|-------|-------|-------|-------|--------|
| Ω_m (matter density) | 0.24 | 0.279 | 0.272 | 0.279 | 0.307 |
| Ω_Λ (dark energy density) | 0.76 | 0.721 | 0.728 | 0.721 | 0.693 |
| n_s (spectral index) | 0.95 | 0.960 | 0.961 | 0.972 | 0.962 |
| σ_8 (normalization parameter) | 0.75 | 0.817 | 0.807 | 0.821 | 0.834 |
| h (Hubble Constant / 100) | 0.73 | 0.70 | 0.702 | 0.700 | 0.677 |

TABLE 2.1: Cosmological Parameters measured with the Wilkinson Microwave Anisotropy Probe and Planck Observations: (1) Denomination of the cosmological parameters, (n_s and σ_8 are properties of the power spectrum, itself defined in section 2.2.3.2. The spectral index n_s is the relative distribution of power on large scales and the normalization parameter σ_8 scales the power spectrum to its today value), (2) Three-year WMAP measurements from [Spergel et al. \(2007\)](#), (3) Five-year WMAP measurements from [Komatsu et al. \(2009\)](#), (4) Seven-year WMAP measurements from [Komatsu et al. \(2011\)](#), (5) Nine-year WMAP measurements from [Hinshaw et al. \(2013\)](#), (6) First results obtained with Planck from [Planck Collaboration \(2013\)](#).

To summarize this subsection, the equations governing the evolution of the scale factor underlines the fact that space itself is in expansion. The apparent motion of galaxies receding from each other is solely a consequence of this dilatation of space. Yet, conserving the analogy with a Doppler effect is appropriate.

2.1.2 Variations from the Hubble Expansion

The cosmological principle implies that the Universe is homogeneous and isotropic about all locations. In addition, the expansion implies that the proper physical distance between two galaxies is bound to increase with time and does so at a velocity proportional to the distance. Yet a various set of small scale structures from single galaxies to structures extending over approximately $100 h^{-1}$ Mpc can be observed in our neighborhood. Gravitationally bound structures exist. Merging processes happen everywhere. These observations are corroborated by the presence of significative outliers in local Hubble diagrams.

2.1.2.1 Bound Structures and Merging Processes

The terminology "universal expansion" refers to the global motion of the cosmic matter, "global" in the sense when analyzing a large volume. However, galaxies close to each others tend to gather in structures possibly bound. Bound as they will not fall apart with increasing time because of the expansion. The local gravity wins over the global expansion effect preventing clusters of galaxies and even galaxies themselves to grow because of the universal expansion. Figures 1.1 and 1.2 in Chapter 1 reflect the existence of such bound structures

in the Local Universe. An extensive list of structures in the sole neighborhood of the Milky Way can be established. Only a few of them of different typical extents are mentioned here as examples: Virgo is the closest cluster of galaxies ; Coma, further away, is another bigger one. Coma is actually part of a larger structure called the Great Wall which extends over $100 h^{-1}$ Mpc. Our Galaxy, the Milky Way, is itself part of a small structure called the Local Group. The Shapley supercluster which extends at least over $30 h^{-1}$ Mpc is considered currently as the biggest bound structure in the Local Universe ([Reisenegger et al., 2002](#)). In definitive, the presence of an incommensurable number of structures on various scales confirms the role played by gravity.

Gravitational pulls inside and around structures shape motions. For instance, [Karachentsev et al. \(2009\)](#) observe the modification of the Hubble flow around the Local Group because of its mass. Galaxies of Coma I cloud move at large speed. Their motions are probably the result of an infall onto an attractor ([Karachentsev et al., 2011](#)). Models of the dynamics inside the Local Group show close passages between the Milky Way and M31 (Andromeda) suggesting a future merging event (e.g. [Peebles and Tully, 2013](#)). Actually numerous simulations have already found that the collision between our galaxy and M31 is likely to happen in a few billion years (e.g. [Cox and Loeb, 2008](#); [Hoffman et al., 2007](#)). Remnants of galaxy collisions and actual collisions are observed continuously (e.g. [Meyerdierks, 1991](#); [Schweizer, 1996](#)). Although this short subsection did not aim at explaining in details such processes, these latter are a proof of concept that the expansion is not the sole actor of observed motions in the Universe. Galaxies have also peculiar motions due to gravitational effects.

2.1.2.2 Voids and Local Flows

Reference frames and systems of coordinates:

To study more thoroughly local motions in our neighborhood it is essential to define a reference frame. Several reference frames exist such as heliocentric, galactocentric, Local Group, Local Sheet, Local Supercluster and CMB reference frames. Conversions from one reference frame to another are summarized in [Tully et al. \(2008\)](#). Their names are in general quite explicit. Usually we place ourselves in the CMB reference frame which consists in correcting for the dipole anisotropy in the Cosmic Microwave Background temperature map. Since this paragraph is prone to study local motions, it is quite appropriate to point out that the observed dipole anisotropy is a compelling evidence that our Galaxy has a peculiar motion with respect to the overall cosmic expansion. The Milky Way is moving in a well specified direction at approximately 630 km s^{-1} . Still, to study local motions, in particular our Galaxy's motion, the Local Sheet reference frame (a slight variant of the Local Group frame) can be more relevant.

In addition, the most used coordinate system is called supergalactic. It is defined by the supergalactic plane (e.g. [Lahav et al., 2000](#)), located at the null supergalactic latitude (SGB). The null supergalactic longitude (SGL) is at the intersection of the $SGB=0$ -plane with the galactic plane. Assuming D the distance of an object from us, the object is located in cartesian coordinates at:

$$\begin{aligned} SGX &= D \cos(SGB) \cos(SGL) \\ SGY &= D \cos(SGB) \sin(SGL) \\ SGZ &= D \sin(SGB) \end{aligned} \tag{2.20}$$

where SGX , SGY and SGZ are in the same unit as D .

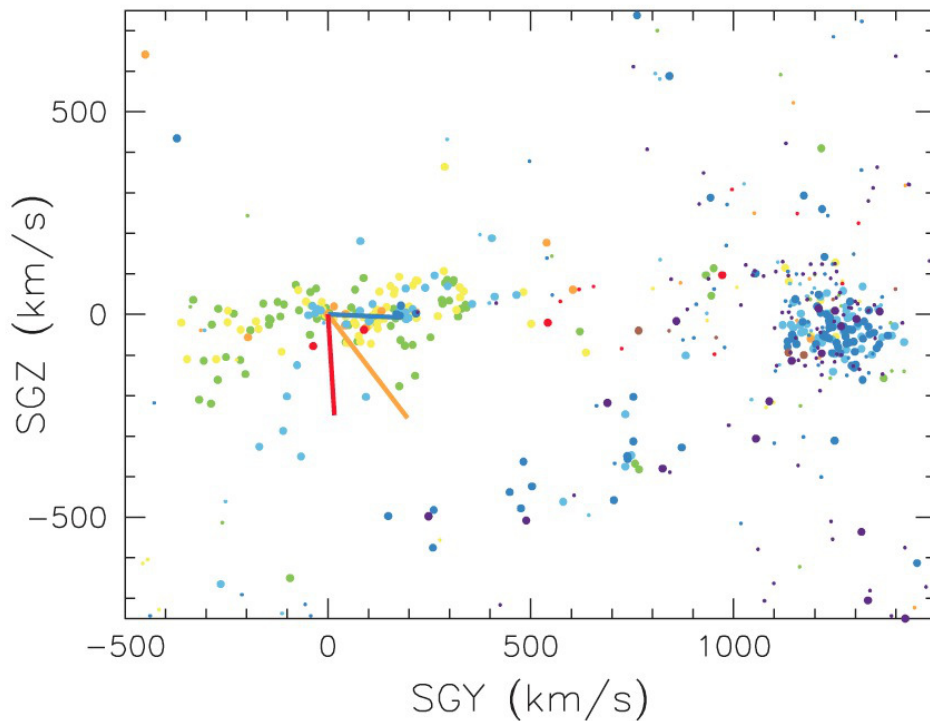


FIGURE 2.1: Motions around and within the Local Sheet. After accounting for a cosmic expansion of $74 \text{ km s}^{-1} \text{ Mpc}^{-1}$, yellow-orange-red dots indicate peculiar motions away from us while green-blue-purple dots stand for peculiar motion towards us. The orange vector is a motion with respect to the Local Supercluster reference frame at 320 km s^{-1} . The blue and red vectors are motions at 185 km s^{-1} towards Virgo (cluster of blue dots on the right) and at 260 km s^{-1} away from the Local Void in the Local Sheet reference frame (from [Tully et al., 2008](#)).

Observed peculiar motions:

[Lynden-Bell et al. \(1988a\)](#) were the first to discover that galaxies have peculiar motions pointing in a very specified direction near Centaurus cluster. They evoke the existence of a Great Attractor with probably an unusual large mass. This Great Attractor pull was confirmed later on by [da Costa et al. \(1996\)](#). These latter also observed a large infall towards the Perseus Pisces Supercluster located approximately across from us with respect to the

Great Attractor region. Furthermore, they noticed that galaxies are organized in filaments which delimit voids. Progress has been made over the past few years to better understand the motion of our Galaxy in this context. Figures 2.1 to 2.3 are a summary of our current knowledge. Our motion is the vector sum of gravitational pulls from many sources. The current understanding is that there are four to six dominant components on well separated spatial scales. The nearest of which are reasonably well understood probably because motion vectors are almost orthogonal (Tully, 2007, 2008a; Tully et al., 2008):

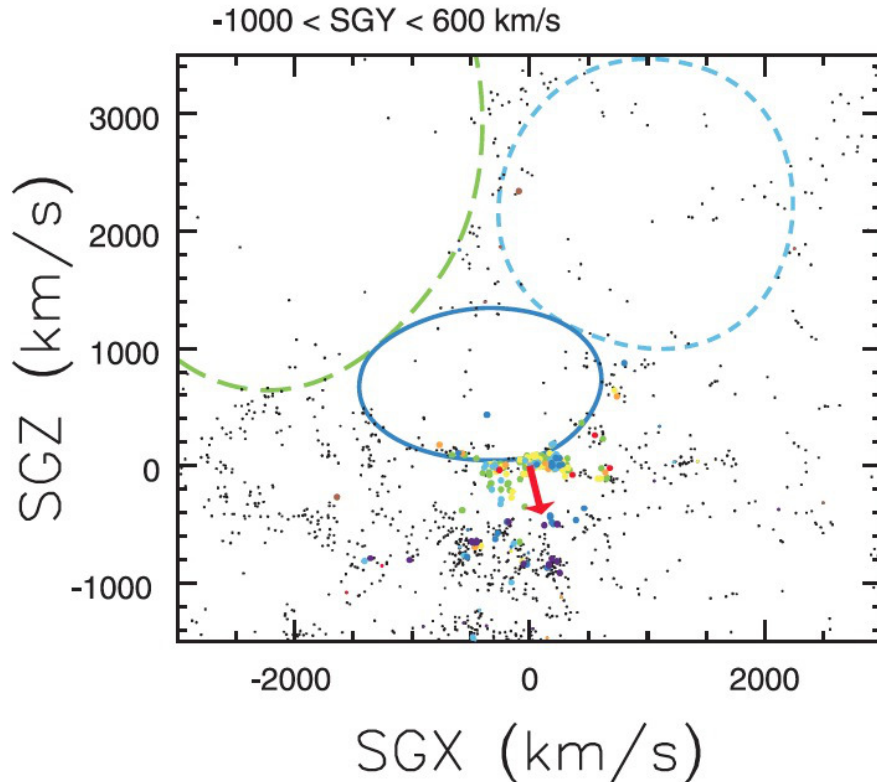


FIGURE 2.2: Region of the Local Void. The solid blue ellipse shows the Inner Local Void, bounded on one edge by the Local Sheet. North and South extensions are identified by blue and green dashed ellipses respectively. The red vector indicates the direction and amplitude of our motion away from the void. A galaxy, ESO 461-36 (blue dot in the Inner Local Void), is escaping from the void with a huge velocity of at least 350 km s^{-1} (approximately the sum of our motion away from the void and its motion towards us) (from Tully, 2008b; Tully et al., 2008).

- at the smallest scale, the Milky Way is falling at 135 km s^{-1} towards the galaxy M31,
- at slightly larger scales ($\approx 7 \text{ Mpc}$), the Local Sheet, that contains our Galaxy, is part of the wall delimitating a very large void (Local Void) which appears to expand at 260 km s^{-1} (see Figure 2.2),
- a bit farther ($\approx 17 \text{ Mpc}$), the Virgo Cluster, at the heart of the Local Supercluster, is found to pull the Local Sheet at 185 km s^{-1} ,
- after subtracting all these pulls individually from the CMB dipole vector, it remains to explain a motion of 445 km s^{-1} .

One could argue that the counterintuitive observed motions (galaxies drawing closer instead of receding) visible on Figures 2.1 and 2.3 left are due to the Hubble constant choice when decomposing total observed motions into cosmic expansion and peculiar motions. Selecting a larger value for H_0 would enhance a pattern of overall infalls after accounting for the expansion. On the opposite selecting a smaller value would create a trend towards outflows. Still, Figure 2.3 right confirms that overall patterns in peculiar motions are similar whatever reasonable H_0 value is considered.

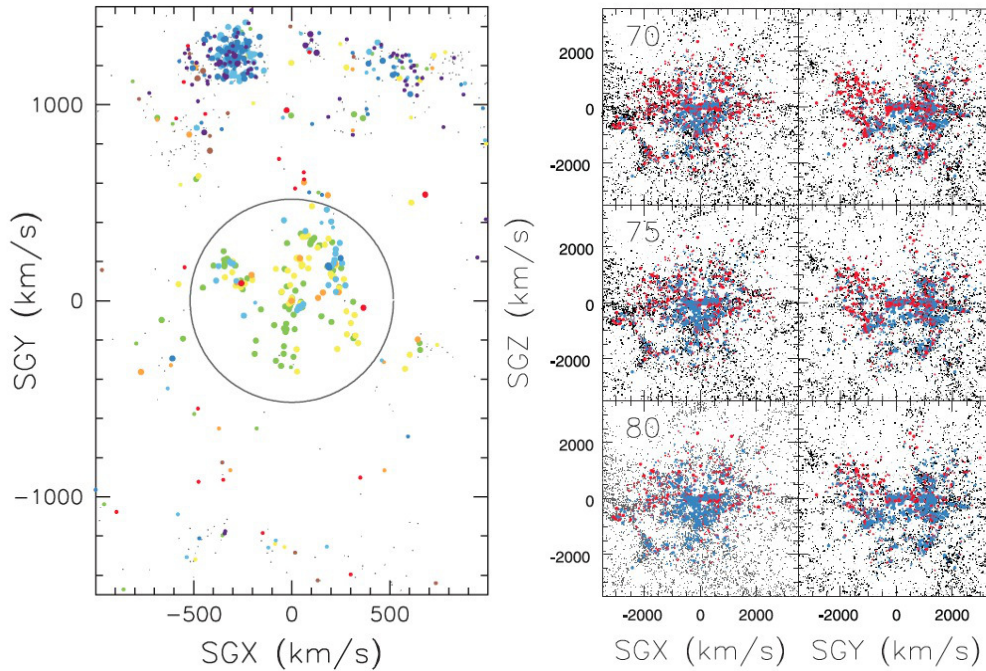


FIGURE 2.3: Local motion patterns. *Left:* The circle gives the outer projection of a 7 Mpc sphere centered at our position. After accounting for a cosmic expansion of $74 \text{ km s}^{-1} \text{ Mpc}^{-1}$, yellow-orange-red dots indicate peculiar velocities away from us, green-blue-purple dots indicate peculiar motion towards us. Virgo is the cluster of blue dots at the upper left. The local region has an overall peculiar velocity towards Virgo of approximately 200 km s^{-1} . *Right:* Red dots represents galaxies going away from us. Blue dots are galaxies coming towards us. Whatever value is adopted for H_0 (*top panel* 70 , *middle panel* 75 and *bottom panel* $80 \text{ km s}^{-1} \text{ Mpc}^{-1}$), the counterintuitive pattern of motions with respect to the knowledge of cosmic expansion still appears (from Tully et al., 2008).

Figure 2.4 shows supergalactic XY and YZ planes of the repartition of masses and motions in the Local Universe confirming the overall explanation for the motion of our Galaxy (Courtois et al., 2013). Courtois et al. (2012) also established the predominance of the role played by the Local Void over the Virgo cluster on the Local Flow.

Yet, in an era of "precision cosmology", only 30% of the motion of the Milky Way is understood exactly. In addition, peculiar motion estimates are not yet numerous or accurate enough to demonstrate whether other filaments have similar bulk motions with respect to voids. Moreover, bulk flow measurements are in apparent contradiction with each other. Two schools actually confront their ideas on the end of the bulk flow.

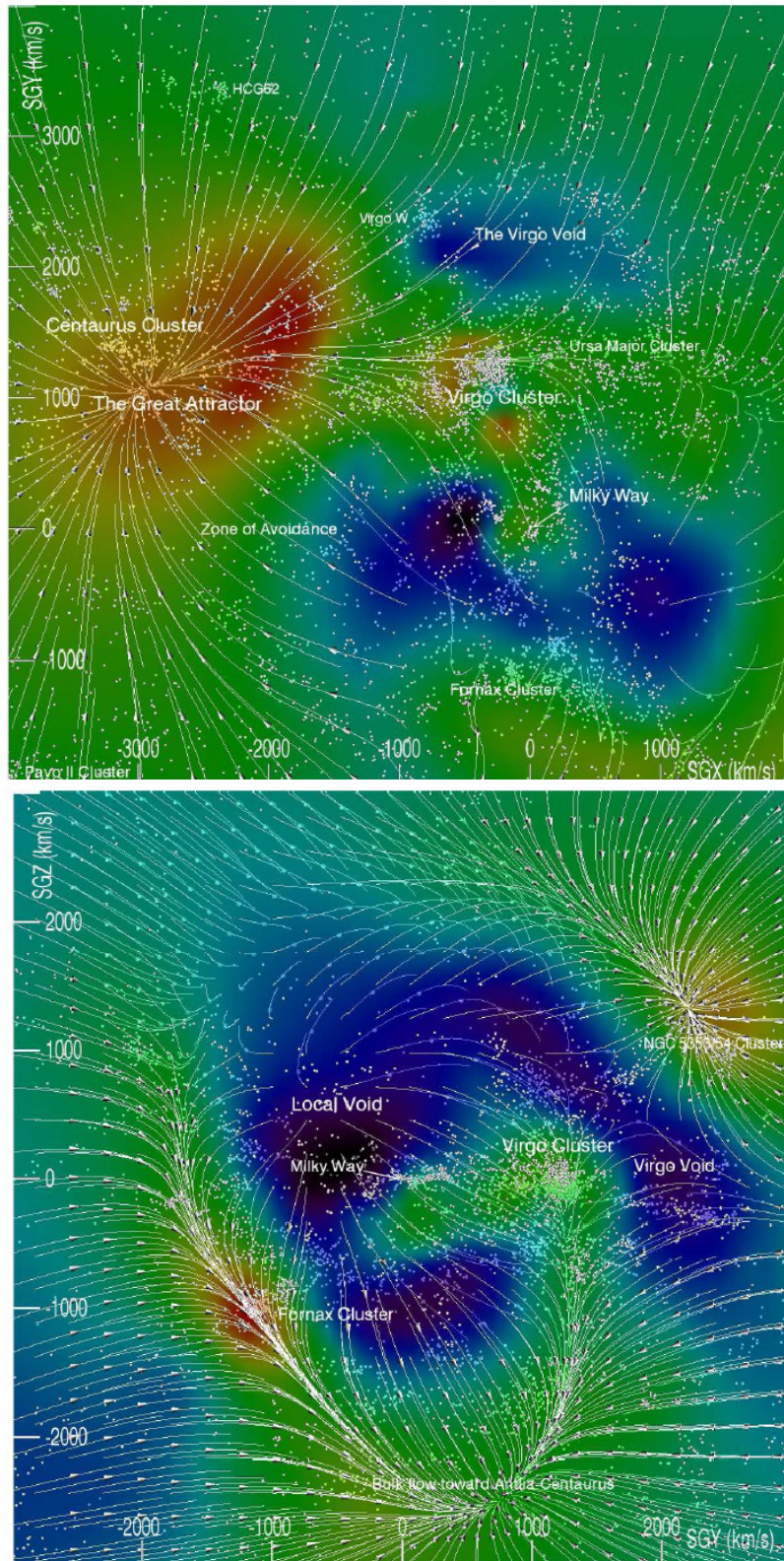


FIGURE 2.4: Supergalactic XY and YZ planes of the reconstruction of the mass distribution and motions in the Local Universe within $30 h^{-1}$ Mpc. Warm colors show high mass densities while cold colors stand for nearly empty regions or voids. White arrows represent motions. White dots stand for galaxies from a redshift survey called V8k and available at the Extragalactic Distance Database (<http://edd.ifa.hawaii.edu>) of the Cosmicflows project. A few structures are identified. In the *top panel*, the motion of the Milky Way towards Virgo itself falling onto the Great Attractor region is visible. In the *bottom panel*, the expulsion from the Local Void is visible (from Courtois et al., 2013).

The first school assumes the existence of a large bulk flow which extends up to distances greater than $500 \text{ h}^{-1} \text{ Mpc}$, they call it the dark flow (Kashlinsky et al., 2012, 2010). Their work relies on the measurement of the bulk flow of X-rays luminous clusters via the Sunyaev Zel'dovich effect (e.g. Sunyaev and Zeldovich, 1980, 1970). On the opposite, the second school does not envision the end of the bulk flow as far as $500 \text{ h}^{-1} \text{ Mpc}$. With supernovae of type Ia studies (e.g. Feindt et al., 2013; Turnbull et al., 2012), they assert that, although the Shapley supercluster is apparently not the end of the bulk flow, there is no such thing as a dark flow. This assertion seems confirmed by recent other measurements based on the Sunyaev Zel'dovich effect (Lavaux et al., 2013). Regardless, these multiple facts highlight a fundamental deficiency in our understanding of the Local Universe (composition) and explains the wealth of the Cosmicflows project.

2.1.2.3 Effect on the Redshift

Observations prove that galaxies have deviating motions from the Hubble expansion. Thus, their total velocities v_{tot} can be written as the sum of two terms, one due to the expansion HD , from equation 2.8 right, with D their distances and the other one due to gravitational effects, because of local variations of matter, called peculiar velocity v_{pec} . Accordingly, deriving peculiar velocities of galaxies supposes distances and total velocities to be known. Both can be estimated from observations. We will come back to the estimation of distances in Chapter 3, the observational part of this thesis work. Concerning total velocities, as we name them, close estimates can be obtained with the observational redshift. This redshift is derived from the shift of emitted wavelengths towards higher value because of the expansion or, more generally, because of the total motion (sum of the expansion and peculiar motion) of the emitting galaxy. It can be expressed in terms of wavelengths emitted λ_e and received λ_r :

$$z_{obs} = \frac{\lambda_r - \lambda_e}{\lambda_e} \quad (2.21)$$

Observers measure the redshifts of galaxies by identifying well defined series of lines in their emission or absorption spectra. The advantage of these ensemble of lines is that their values at rest are well known. Since these sequence of lines are unchanged but just shifted, redshifts can be computed from their shifts. An example of such a series of line is the Balmer series. This series consists in a set of spectral line emissions of the hydrogen atom due to transitions from level n (principal quantum number of the electron) greater or equal to 3 to the second level. These lines called H_α , H_β , H_γ , H_δ and H_ϵ are normally part of the visible spectrum. Their wavelength values can be computed with the formula $\lambda = \frac{1}{R_H} \left(\frac{1}{4} - \frac{1}{n^2} \right)$ where R_H is the Rydberg constant associated with the hydrogen. Hydrogen can be pointed out as a useful element in various fields of Astronomy because it is highly abundant in the Universe.

Such redshift estimates account for the expansion and the peculiar motions of the galaxies. To disentangle all these effects on the redshift, it is useful to introduce a cosmological redshift z_{cos} defined by the hypothetical shift in wavelength if expansion really bears sole responsibility for the shift:

$$z_{cos} = \frac{\lambda_{r_h} - \lambda_e}{\lambda_e} = \frac{1}{a} - 1 \quad (2.22)$$

where we have used $\lambda_{r_h} = a\lambda_e$ obtained with equation 2.8 left. λ_{r_h} is the hypothetical wavelength which would have been received by the observer in the case of pure expansion.

From the definitions of the observational and cosmological redshifts 2.21 and 2.22, an "extra redshift" z_{extra} can be defined:

$$1 + z_{obs} = \frac{\lambda_r}{\lambda_e} = \frac{\lambda_{r_h}}{\lambda_e} \frac{\lambda_r}{\lambda_{r_h}} = (1 + z_{cos})(1 + z_{extra}) \quad (2.23)$$

Then:

$$z_{extra} = \frac{z_{obs} - z_{cos}}{1 + z_{cos}} \quad (2.24)$$

This "extra redshift" is due to peculiar motions. Thus, non-relativistic peculiar velocity estimates v_{pec} are directly obtained with:

$$v_{pec} = cz_{pec} = c \frac{z_{obs} - z_{cos}}{1 + z_{cos}} \quad (2.25)$$

where c is the vacuum speed of light and $z_{pec} = z_{extra}$ is the "peculiar redshift". We will come back to the estimation of the cosmological redshift in Chapter 3 as distance definitions and estimates are required primarily.

It is pertinent to add that, as observers, only the line-of-sight of the coordinates is affected by peculiar motions or, in other words, only the radial component of the distant galaxies' peculiar velocities is accessible through redshift observations. This leads to distortions visible in maps of redshift surveys. Namely, galaxies positioned with redshift measurements on a map form "Fingers-of-God", as shown on Figure 2.5, resulting from the fact that while they are at the same distance from us, because of their different (random) peculiar motions, they appear to be located at different distances. The Kaiser effect (Kaiser, 1987) can also be mentioned although this effect can be detected only on large scales. It differs from the Fingers-of-God in the sense that it affects coordinates of galaxies which are coherently infalling onto a central mass to which they are bound.

In any case, the observations of such patterns are a proof of concept that deviations from the universal expansion, namely peculiar motions exist. These motions are due to local

gravitational fields which are generated by local density fluctuations. The study of primordial cosmological density inhomogeneities is required to understand the process that cause departure from a uniform density.

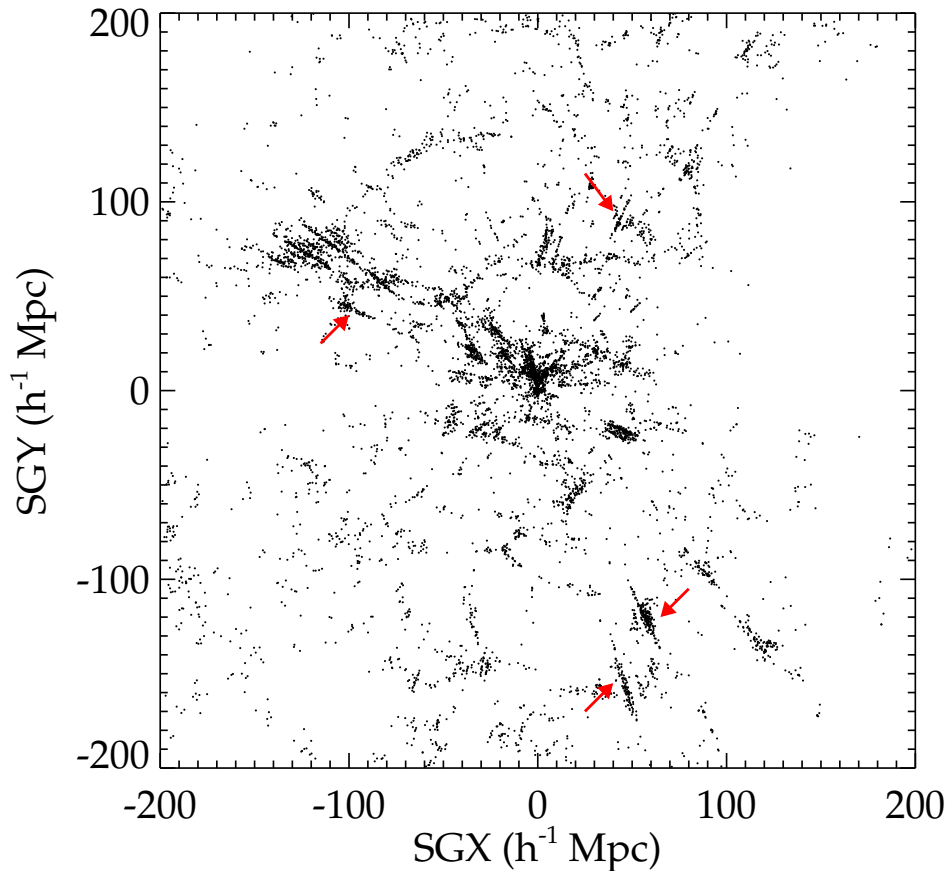


FIGURE 2.5: Supergalactic XY plane representing galaxies (black dots) of the Two-Micron All Sky Survey (2MASS) redshift catalog (Huchra et al., 2012) in a 5 Mpc thick slice. Numerous Fingers-of-God are visible, a few of them are pointed by red arrows.

2.2 The Linear Theory of Density Perturbations

The anisotropies observed in the Cosmic Microwave Background Temperature maps are witnesses of primordial density inhomogeneities. Our interest lies in the effect of these fluctuations which generate weak gravitational fields in addition to the overall gravitational potential. In this context, the overdensity δ defined as:

$$\delta = \frac{\rho - \bar{\rho}}{\bar{\rho}} \quad (2.26)$$

where $\bar{\rho}$ is the mean density and ρ the local density, is useful. Because the relation between matter density and gravitational potential is linear (Poisson equation), homogeneous matter distribution and density fluctuations can be considered separately. Thus, the total gravitational field can be seen as the sum of the average matter distribution and density

fluctuation effects. A simple explanation for the growth of structures because of these small initial perturbations can be presented as follows (e.g. [Einasto et al., 2011](#)): in overdense regions, meaning in regions where the overdensity is positive (density greater than the mean density), the density decreases more slowly than on average because the expansion effect is dimmed by the higher gravitational effect. Accordingly, the density contrast between these regions and mean density regions increases. This increased overdensity in turn produces an even stronger gravitational field and the process repeats itself. An opposite phenomenon happens in underdense regions. The expansion is less affected in these regions than in mean density regions by gravity, thus the density decreases faster. The gravitational effect is even weaker and the process continues. Hence, the evolution of structures can be described by the model of gravitational instability corresponding to an increase of density fluctuations.

2.2.1 Continuity, Euler and Poisson Equations

Because the growth of density perturbation length scales is substantially smaller than the Hubble radius ($\frac{c}{H_0} \approx 3000 \text{ h}^{-1} \text{ Mpc}$), working in the framework of Newtonian theory of gravity is acceptable. Matter is assumed to be solely in the form of dust which is described as a fluid. The equations of motions are then:

- the continuity or energy equation which states that the matter is conserved. The density decreases only if the fluid has a divergent velocity field meaning that the particles are moving away from each other, namely the total derivative of the density with respect to time t is null:

$$\left(\frac{\partial \rho(\mathbf{r}, t)}{\partial t}\right)_r + (\nabla)_r \cdot (\rho(\mathbf{r}, t) \mathbf{v}(\mathbf{r}, t)) = 0 \quad (2.27)$$

where ρ is the density and v the velocity. The r subscript signifies that derivatives are with respect to the coordinate \mathbf{r} fixed,

- the Euler equation which describes the conservation of momentum and the behavior of the fluid under the influence of forces (pressure P and gravitational potential Φ), analogous to Newton's first law:

$$\left(\frac{\partial \mathbf{v}}{\partial t}\right)_r + (\mathbf{v} \cdot \nabla_r) \mathbf{v} = -\frac{\nabla_r P(\mathbf{r}, t)}{\rho(\mathbf{r}, t)} - \nabla_r \Phi(\mathbf{r}, t) \quad (2.28)$$

where the gravitational potential follows the Poisson equation:

$$\nabla_r^2 \Phi = 4\pi G \rho \quad (2.29)$$

Since we consider only dust the pressure term P is null in the rest of this work.

Equations 2.27 and 2.28 are in general not solvable analytically. It is necessary to linearize these self-gravitating fluid equations for $|\delta| \ll 1$ (valid at very high redshifts, such as $z \approx 1000$ corresponding to the last time photons and matters interacted, it is the observed Cosmic Microwave Background) to find approximate solutions. One can note that the generalized Hubble law is a special exact solution of these equations for the homogeneous density field ρ . Thus, we can expect that physically relevant solutions are slight deviations from the homogeneous case comforting the prescribed linearization.

2.2.2 Comoving Equations

2.2.2.1 Comoving Coordinates: Definition

At this point, it is useful to introduce the comoving coordinates. These coordinates are a perfect compromise between the Eulerian and Lagrangian coordinates. While an Eulerian observer takes snapshots of the field at different times t , in other words he is more interested in the global variation of the field (grid) in time than in particular objects, a Lagrangian observer follows the chosen objects on the grid. Consequently, while the Eulerian observer can give the velocity in any point of the grid, the Lagrangian observer can locate the particles on the grid but not in time (the lagrangian coordinate is independent of time), thus, to him, it seems particle are immobile (no velocity). A comoving observer is in between. While he proceeds as the Eulerian observer, he forgets about the motion due to expansion. Namely, assimilating the Universe to a growing grid, the comoving observer resizes constantly the grid to its original size. As a result, he has (only) the *peculiar* velocity field in any point of the resized grid. Figure 2.6 schematizes the concept.

However, the Universe is homogeneous and isotropic only when smoothing out small irregularities. As a consequence, depending on the position of the observers, they are not necessarily comoving. That is one of the difficulty of being part of the system under study. A set of fundamental observers is considered comoving if observers are at rest with respect to the matter surrounding them. Since random velocities of galaxies and stars composing them are small (only a few hundreds of km s^{-1}) in comparison with receding velocities between galaxies separated by large distances (many thousands of km s^{-1}), on large scales (typically enough for the assumption of homogeneity to be accurate) any observer who moves with a typical star in a galaxy is considered at rest with respect to his environment and, as a result, is a fundamental observer. A cosmic time also needs to be defined (Gunn, 1978).

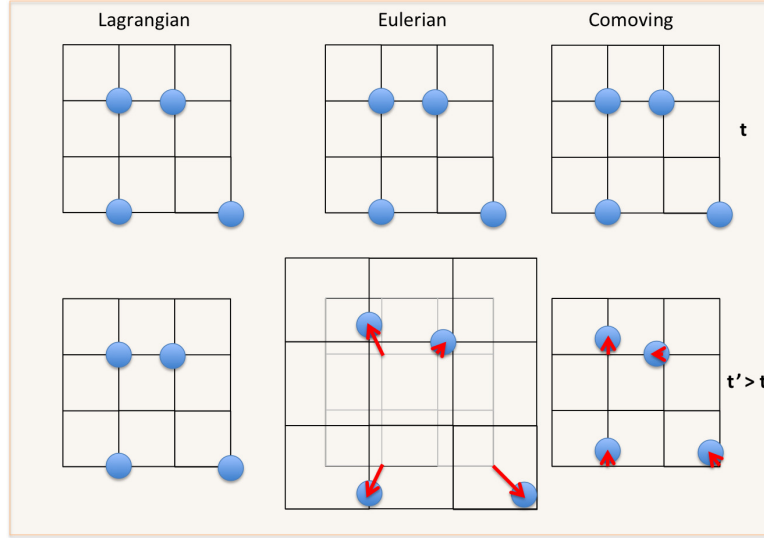


FIGURE 2.6: Schematization of the Lagrangian, Eulerian and Comoving coordinate principles: the Lagrangian observer follows the particles (blue filled circles) on the grid but not in time. Consequently, to him it looks like particles have no velocity. They do not move in time; the Eulerian observer, interested in the global value of the field at different times, takes the snapshot of the global field at times t and t' , he can trace the velocity field (red arrows) ; the comoving observer resizes the grid to remove the dependence on the expansion thus, he can give (only) the *peculiar* velocity field (red arrows).

2.2.2.2 Comoving Coordinates: Equations

Before any linearization of the continuity and Euler equations, changing to comoving coordinates is convenient. Let's define the proper coordinate r at time t by:

$$\mathbf{r} = a(t)\mathbf{x} \quad (2.30)$$

where a is the scale factor and x the comoving coordinate. From this definition, a velocity field v can be derived:

$$\mathbf{v} = \frac{\dot{a}}{a}\mathbf{r} + \mathbf{u}\left(\frac{\mathbf{r}}{a}, t\right) \quad (2.31)$$

where u is the deviation from the Hubble expansion, itself given by the first term of the formula by analogy with relation 2.8 right ; u is also called the peculiar velocity field since it would be null in absence of peculiar motion (x would stay unchanged with time in which case $u = a\frac{dx}{dt} = 0$).

Thus, in comoving coordinates using 2.30:

$$\left(\frac{\partial}{\partial t}\right)_r = \left(\frac{\partial}{\partial t}\right)_x + \left(\frac{\partial \mathbf{r}}{\partial t}\right)_x \cdot \nabla_x = \left(\frac{\partial}{\partial t}\right)_x - \frac{\dot{a}}{a}\mathbf{x} \cdot \nabla_x \quad ; \quad \nabla_r = \frac{\partial \mathbf{x}}{\partial \mathbf{r}} \nabla_x = \frac{1}{a} \nabla_x \quad (2.32)$$

where the subscript x stands for derivative with respect to the comoving coordinate x fixed.

From relations 2.30 to 2.32, the continuity and Euler equations 2.27 and 2.28 become:

$$\frac{\partial \rho}{\partial t} + \frac{3\dot{a}}{a}\rho + \frac{1}{a}\nabla \cdot (\rho \mathbf{u}) = 0 \quad (2.33)$$

$$\frac{\partial \mathbf{u}}{\partial t} + \frac{1}{a}(\mathbf{u} \cdot \nabla)\mathbf{u} + \frac{\dot{a}}{a}\mathbf{u} = -\frac{1}{a}\nabla\phi \quad (2.34)$$

where the pressure term has vanished, since we consider solely dust, and $\nabla_x \mathbf{x} = 3$ was used. For simplicity the x subscript is not written. In addition, both the definition 2.26 of the density δ and the equation of motion 2.11 in the Newtonian framework considering dust (namely P and Λ are null) were used. ϕ is now defined as $\Phi - \frac{2\Pi}{3}G\bar{\rho}|\mathbf{r}|^2$. Since it is the variation between the full gravitational potential Φ and the Newtonian gravitational potential $\frac{2\Pi}{3}G\bar{\rho}|\mathbf{r}|^2$, it corresponds to the gravitational potential of the density inhomogeneities. It satisfies the Poisson equation for the density inhomogeneities:

$$\nabla^2\phi(\mathbf{x}, t) = 4\Pi G a^2(t)\bar{\rho}(t)\delta(\mathbf{x}, t) \quad (2.35)$$

From equation 2.26 and $\bar{\rho}(t) \propto a^{-3}$ (namely, $\frac{\partial \bar{\rho}}{\partial t} = -3\frac{\dot{a}}{a}\bar{\rho}$), equation 2.33 can be written:

$$\frac{\partial \delta}{\partial t} + \frac{1}{a}\nabla \cdot [(1 + \delta)\mathbf{u}] = 0 \quad (2.36)$$

2.2.3 Density Perturbation Field

2.2.3.1 Linearization

The linearization of equations 2.34 and 2.36 consists in rejecting all terms other than the first order in δ and u . Accordingly, these equations become:

$$\frac{\partial \delta}{\partial t} + \frac{1}{a}\nabla \cdot \mathbf{u} = 0 \quad ; \quad \frac{\partial \mathbf{u}}{\partial t} + \frac{\dot{a}}{a}\mathbf{u} = -\frac{1}{a}\nabla\phi \quad (2.37)$$

Derivating the first of one of the two equations 2.37 with respect to the time and the second one with respect to x , subtracting them after division of the second by a , using the Schwarz theorem, the Poisson equation 2.35 and the left equation in 2.37, we obtain the second-order differential equation for the density perturbation field δ :

$$\frac{\partial^2 \delta}{\partial t^2} + \frac{2\dot{a}}{a}\frac{\partial \delta}{\partial t} = 4\Pi G \bar{\rho} \delta \quad (2.38)$$

Since only δ depends on x in this second-order differential equation, it is possible to find a solution of the form $\delta(\mathbf{x}, t) = D_{\pm}(t)\tilde{\delta}(\mathbf{x})$. From equation 2.38, after division by $\tilde{\delta}(\mathbf{x})$, D_{\pm} is solution of a second order differential equation with two linearly independent solutions.

While one of this solution decreases with time, the other one increases. It is logical to assume that at some later time, the increasing solution will dominate while the other one will have become irrelevant. Considering solely the increasing solution, hereafter D_+ , and normalizing it to unity today, $\delta(\mathbf{x}, t) = D_+(t)\delta_0(\mathbf{x})$ where δ_0 would be the distribution of density fluctuations at present if the evolution was linear until today. This is the linearly extrapolated density fluctuation field which approximation breaks down as soon as $|\delta|$ is not a lot smaller than the unity anymore. In comoving coordinates, this approximation implies that the spatial shape of the density fluctuations is frozen, only its amplitude can vary (e.g. [Heath, 1977](#)). The (linear) growth factor D_+ can be shown to be equal to:

$$D_+(a) = \frac{1}{D_{+0}} \frac{\dot{a}}{a} \int_0^a \frac{da}{\dot{a}^3} \quad (2.39)$$

where $D_{+0} = \frac{1}{H_0} \int_0^1 \frac{da}{\dot{a}^3}$.

This linear theory of density perturbations explain the observed structures in the Universe. Galaxies, clusters, etc result from the gravitational collapse of high peaks in the primordial density field. Current galaxy peculiar motions are proofs of concept that structures are continuously forming and evolving in the Universe. Studying analytically, in details, these motions via the perturbation density field appears to be a complex task. Statistical and numerical methods become resourceful.

2.2.3.2 Fourier Analyses

Before any comment on how to perform statistical measurements on the perturbation field, let's define its Fourier expansions:

$$\delta(\mathbf{k}) = \int \delta(\mathbf{x}) e^{-i\mathbf{k}\cdot\mathbf{x}} d\mathbf{x} \quad ; \quad \delta(\mathbf{x}) = \frac{1}{(2\pi)^3} \int \delta(\mathbf{k}) e^{-i\mathbf{k}\cdot\mathbf{x}} d\mathbf{x} \quad (2.40)$$

where k is the Fourier mode or wavevector.

Because in an homogeneous and isotropic universe the variance of the perturbation density field has to be the same from about all locations, statistical measurements can be performed. Namely, the gravitational instability yields patterns of inhomogeneities depending on the scale and on the precise matter content of the Universe. To define more precisely the scale-pattern or the variance in amplitude of the perturbation field at all scales, called the power spectrum, it is necessary to go back to the theory of inflation which predicts that the primordial fluctuations can be described by a Gaussian random field ([Kolb et al., 1990](#)). Because this field is not only Gaussian but also homogeneous from the cosmological principle, Fourier modes of the perturbation field are uncorrelated ([Bardeen et al., 1986](#)). Consequently, it is possible to define the variance in amplitude of the perturbation field at all scales, or power

spectrum P , as a function of the Fourier modes, or wavevectors, k such that the power spectrum is the ensemble of $P(\mathbf{k}) = \langle |\delta_k|^2 \rangle = |\delta_k|^2$ where the angle brackets stand for the average over the volume. From this definition, it appears that the amplitude of the power spectrum increases with time t . At t , the power spectrum is $D_+^2(t)P_0$ (from $\delta(\mathbf{x}, t) = D_+(t)\delta_0(\mathbf{x})$) where P_0 is the power spectrum today, normalized by σ_8 as given in Table 2.1. Figure 2.7 shows the three power spectra, i.e. cosmological models, which are used in Chapter 4 of this work.

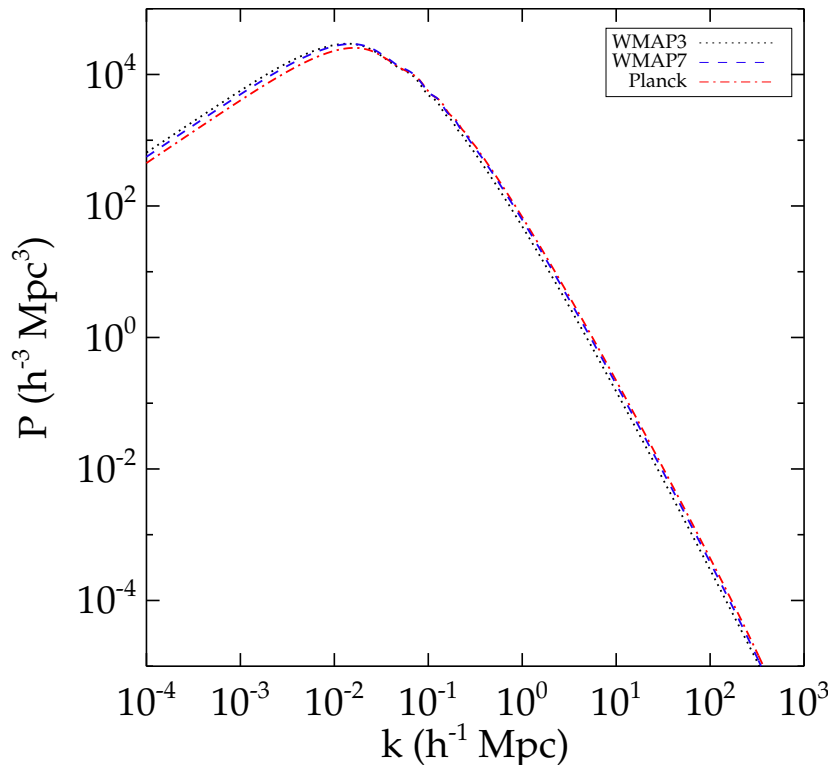


FIGURE 2.7: WMAP3, WMAP7 and Planck Power Spectra (linear part) in logarithmic scales.

Because of all the properties of homogeneity and isotropy from which is also derived the ergodicity (averages over several different random realizations and over a large volume of one realization are equivalent, Adler, 1981) and randomness of the perturbation field, the statistical properties of this latter are fully determined by the power spectrum. For instance, the autocorrelation function of the perturbation density field is defined by:

$$\xi(\mathbf{r}) = \langle \delta(\mathbf{x})\delta(\mathbf{x} + \mathbf{x}') \rangle = \frac{1}{(2\pi)^3} \int_0^\infty P(\mathbf{k})e^{-i\mathbf{k}\cdot\mathbf{r}} d\mathbf{k} \quad (2.41)$$

The remarkable fact that the perturbation density field is fully determined by the power spectrum, in other words by the Universe content, is at the basis of every simulation.

2.3 N-Body Simulations

All the equations of motions presented in the two first sections of this Chapter are non linear. A solution is given only in the limit of linear perturbations with the linearization. The evolution of the non linear density field can be obtained with N-body simulations of the density field represented by a set of particles.

2.3.1 Dark Matter

Zwicky (1933) noticed that the mass of the Coma cluster obtained with velocity dispersions is a lot greater than the total visible mass (light-emitting mass). Even the addition of the mass of X-ray emissive gases could not account for more than 20% of the total mass of the cluster obtained with gravitation. Most of the mass in the Universe is invisible. Fundamental laws of physics are affected when this invisible mass is not accounted for. For instance, rotation curve of galaxies fail to follow the Newtonian law of gravitation which predicts a decrease in rotational velocity beyond the disk of matter. As a matter of fact, observations at 21 cm (emission line due to the transition between the two hyperfine levels of the ground state of hydrogen, with different energies because of parallel and antiparallel spins) of the hydrogen disk reveal that galaxy masses are not concentrated within regions extending up to the hydrogen disk. If it was the case, from the first law of gravitation (here, $\frac{v^2}{r} = \frac{Gm}{r^2}$), the rotational velocity v of a galaxy beyond the hydrogen disk would decreased as $\frac{1}{\sqrt{r}}$ where r is the distance from the galaxy center. However, the rotational velocity beyond the hydrogen disk is a constant up to large galactocentric distances. The fact that the rotational velocity is a constant implies that the gravitational potential has to be inversely proportional to the distance. Namely, in a sphere of radius r , the mass m is proportional to r and the density is inversely proportional to r^2 . As a result, the invisible component of the Universe, called dark matter, is not a uniform mass in which ordinary matter is embedded. Its density is largely function of the galactocentric distance.

Still, the question of what englobes the terminology "dark matter" is not totally answered. The nature of the dark matter is only partly known. Going back to the linear theory of density perturbations, the relativistic hot dark matter particles can be ruled out at least if considered alone³. These relativistic particles are not gravitationally bound in the potential wells of density concentrations. Consequently, small scale density perturbations cannot form. This implies that large scale structures have to form first before fragmenting into smaller scale structures. This scenario contradicts observations of small scale structures at high redshifts (e.g. Petry et al., 1998; Rauch et al., 1999, 2001). Still, with the hot characteristic

³For more details on an extra hot dark matter component in addition to the dominant cold/warm dark matter component see e.g. Hamann and Hasenkamp (2013); Jeong et al. (2014) for the most recent progress.

dismissed, distinguishing warm from cold dark matter is yet to be done. While the adjective "warm" implies that particles decoupled while relativistic so that today velocities, densities and temperature relative to photons are reduced, the adjective "cold" suggests particle relics which decoupled while classical. The number density can be suppressed and the mass can be as large as desired, the thermal velocities being effectively zero. If decoupling happened at sufficiently high redshifts then the horizon scale was small at that time and free streaming had a negligible impact. As a result, structure formation is a hierarchical process in which large structures grow via the merging of smaller scale structures. In a warm dark matter dominated Universe, if particles decoupled at sufficiently early time (sufficient mass), small scale structures at high redshifts can also be found. The critical mass is around 1-10 keV. Regarding the baryonic characteristic of dark matter particles, from the primordial nucleosynthesis, the baryonic density parameter cannot exceed 0.07 for reasonable Hubble Constant value (e.g. Krauss, 1995). However, the estimate of the total matter density parameter Ω_m is at least 0.2 in Table 2.1. There is a necessity for dark matter to be (mostly) a non baryonic gravitationally dominant component of the Universe (e.g. Hattori, 1994). This work relies on the standard Λ CDM model, thus, cold dark matter is assumed to be the gravitationally dominant component of the Universe without any precision as to the nature of such particles. They could be Weakly Interacting Massive Particles (WIMPs, e.g. Bertone, 2010; Iocco, 2010) to give an example of current theories about dark matter particle nature. In any case, particles composing this dark matter dynamics can be studied with simulations.

2.3.2 N-Body Codes

2.3.2.1 The Modeling

The first problem encountered in the numerical cosmological field of research arises just by the complexity of simulating the entire Universe (probably infinite). We are constrained to simulate only a part of it. For the simulation to be statistically fair, the length L of the chosen cube, which will have to be resized permanently (comoving cube) because of the expansion particularity of the Universe, has to be large enough for the effect of the Large Scale Structure not to be neglected (e.g. Power and Knebe, 2006). The larger the box, the better it probably is, but, with it, comes the implication of a decrease in the mass and length scale resolutions. Because the total mass in the numerical volume is proportional to the cube of the length L times the matter density parameter, the minimum mass resolution which can be obtained for a number of particles n can be derived and a compromise can be achieved.

Still, a particle at the edge of the box has to feel gravitational forces beyond this edge. The box cannot be assumed to be embedded in nothing. From the assumption of the homogeneity of the Universe at scales larger than L , the cube is extended periodically. Thus, a particle

leaving from a boundary will re-enter the box from the opposite side and feel the gravitational effect of particles on the other side. Therefore, the mass distribution has a periodicity of L and quantitative analysis of the results have to be confined to approximately $\frac{L}{2}$.

Regarding matter modeling, since dark matter dominates the matter in the Universe, it is often sufficient to compute the behavior of this dark matter and to consider solely gravitational interactions at least as a first approximation. Baryonic physics can eventually intervene (e.g. Scannapieco et al., 2005) or dark matter only simulations can directly be galaxy populated (e.g. Cole et al., 2000; Klypin et al., 2013). The complete scheme is 1) structures grow via the sole gravitational instabilities pre-existing in the initial density field in the form of Gaussian fluctuations (Press and Schechter, 1974) ; 2) in a dissipationless gravitational collapse, dark halos are shaped (Gunn and Gott, 1972) ; 3) galaxies form with the halos following the radiative cooling of baryons. In this work, dark matter only simulations will be presented, namely, the third step is neglected which is a reasonable assumption on the scales of interests for the conducted studies (baryons have a negligible impact on such scales). Then dark matter halos will be assumed to represent galaxies or at least ensembles of galaxies such as clusters or groups. With this context established, particles of dark matter are represented by bodies of mass m . These macroscopic bodies are assumed to behave like microscopic dark matter particles in a volume $\frac{m}{\rho}$ where ρ is the density of bodies. N-body codes follow the motion of this large number of bodies of mass m under their mutual gravitational attraction. However, equations 2.33 to 2.35 are insufficient to solve properly the behavior of dark matter particles which is multi-streamed in any fixed discretization of the three-dimensional Euclidean space. To obtain a complete description of the behavior of dark matter, the whole phase space has to be considered. Usually, these systems are described with collisionless equations since the time coverage of simulations is much shorter than the relaxation time of these systems.

2.3.2.2 Collisionless Boltzmann and Poisson Equations

In an attempt to mimic the evolution of these systems with an infinite number of particles, the distribution can be seen as a continuum. Then, the gravitational field is not the result of a collection of mass points but that of a smooth mass distribution. Interactions between individual particles are indeed negligible in this large spatial extent context. This smooth mass distribution of non-interacting dark matter particles can be described by the collisionless Boltzmann and Poisson equations in an expanding Universe. The collisionless Boltzmann equation can be applied to the probability distribution function f of a particle to be at a given position. The conservation of this function in phase space implies $\frac{\partial f}{\partial t} + \frac{\partial f \dot{\mathbf{w}}}{\partial \mathbf{w}} = 0$ where $\mathbf{w} = (\mathbf{x}, \mathbf{v})$ with \mathbf{x} the position and \mathbf{v} the velocity. Using Hamilton's equations ($\dot{\mathbf{x}} = \frac{\partial H}{\partial \mathbf{v}}$ and

$\dot{\mathbf{v}} = -\frac{\partial H}{\partial \mathbf{x}}$) and Schwarz's theorem, the Boltzmann equation can be written:

$$\frac{\partial f}{\partial t} + \dot{\mathbf{x}} \frac{\partial f}{\partial \mathbf{x}} + \dot{\mathbf{v}} \frac{\partial f}{\partial \mathbf{v}} = 0 = \frac{\partial f}{\partial t} + [f, H] = \frac{df}{dt} \quad (2.42)$$

where the bracket notation denotes the Poisson Bracket (formulation from [Leeuwin et al., 1993](#)) and H is the Hamiltonian. In words, the flow of the probability fluid through phase space is incompressible which means that at any time even if the spatial extent increases (expansion) the probability distribution in phase space stays the same. An analogy would be an ideal set of runners who travel at different but constant speeds. Because of the variety of speeds some would recede faster than others from the departure point and the ensemble of runners will cover a larger area. Still because each one of the runners conserves its original speed, the spatial distribution of velocities and comoving positions stays unchanged. This means that sampling the density and velocity field at a time t , the resulting set of discrete particles will always be a uniform sample of the probability distribution function f . As a result, it is enough to solve the equations of motions for each one of these discrete particles.

The N-body method is based on this principle. In Cartesian comoving coordinates, the Hamiltonian H can be written:

$$H = \sum_{\alpha} \frac{\mathbf{v}_{\alpha}^2}{2a(t)} + \sum_{\alpha \neq \beta} \frac{\phi(\mathbf{x}_{\alpha} - \mathbf{x}_{\beta})}{a(t)} \quad (2.43)$$

where x_i and v_i (i stands for α or β) are the position and velocity of the particle i . Thus, for a discretized system, according to Hamilton's equations and because the gravitational field is conservative (this is usually written in the form of the Poisson equation):

$$\frac{dx_{\alpha}}{dt} = \frac{1}{a} v_{\alpha} \quad ; \quad \frac{dv_{\alpha}}{dt} = -\frac{1}{a} \nabla \phi(\mathbf{x}_{\alpha}) \quad \text{where} \quad -\nabla \phi(\mathbf{x}_{\alpha}) = \frac{F_{\alpha}}{m_{\alpha}} \quad (2.44)$$

where G is the universal gravitational constant and F_{α} is the force applied to the α particle by all the other particles of mass m_{β} defined by:

$$\text{For } \alpha = 1 \text{ to } n, \quad F_{\alpha} = \sum_{\beta \neq \alpha} G m_{\beta} m_{\alpha} \frac{\mathbf{x}_{\beta} - \mathbf{x}_{\alpha}}{|\mathbf{x}_{\beta} - \mathbf{x}_{\alpha}|^3} \quad (2.45)$$

As a result, the only major requirement is the derivation of the gravitational force exerted on each body α at their current positions by all the other bodies β . Bodies are moved accordingly to the application of the force after a short time and they are assigned the corresponding velocities (e.g. [Zemp et al., 2007](#)). To compute efficiently all these forces, Poisson solvers are used. The principle is to use the fact that each computed distance can be used twice in the set of forces 2.45. Thus, for n bodies, instead of n^2 operations, only $\frac{1}{2}n(n-1)$ are required. This number of operations can be reduced some more.

2.3.2.3 GADGET: a TreeSPH Code

Heitmann et al. (2008, 2005) studied the differences between various N-body codes such as RAMSES (Teyssier, 2002), ART (Kravtsov et al., 1997) and GADGET (Springel, 2005). They did not find any substantial variations between the Large Scale Structure obtained from the various codes down to the resolution limit. Because the CLUES collaboration uses widely the GADGET code, this work relies on the same code to facilitate comparisons with, and interactions between, present and future work. GADGET is capable of following a collisionless fluid with the N-body method and an ideal gas with smoothed particle hydrodynamics. For dark matter only simulations, only the N-body part of the code is of interest. GADGET combines different methods depending on the scale of computations to maximize the efficiency of the code. Hence, following Xu (1995), the "Tree method" is used at short range while Fourier techniques ("particle-mesh") are used at long-range.

The tree code method (e.g. Appel, 1985; Barnes and Hut, 1986; Dehnen, 2000) consists in dividing the cube in eight equal subcubes and each subcube containing more than one particle is in turn divided in eight. The process is repeated until each little cube hosts at most one particle. Then, the center of mass of the particles in each size cube is computed. Eventually, multipoles are evaluated so that forces acting on each one of the particles can be easily obtained. With only $n \ln n$ operations against $\frac{1}{2}n(n-1)$, this method effectively increases the performance of the code. Without any intrinsic resolution limit, the technique seems ideal but it is considerably slower than the particle-mesh technique. On the opposite, the particle-mesh relies on fastest computational schemes to obtain the gravitational field (e.g. Klypin and Shandarin, 1983; White et al., 1983). However, because forces at small scales are largely suppressed, the resolution is limited, hence the importance of combining the two techniques. The particle-mesh process consists in estimating the density for a set of points regularly spaced on the grid. The "mass assignment" method is used to allocate the mass of a particle to one or more grid nodes close to it. Several mass assignment schemes exist: 1) the NGP, for "nearest grid point", technique gives the mass of the particle to its closest node. This scheme is rarely used because assigned nodes changed discontinuously as particles move through the grid. 2) the CIC or "cloud-in-cell" method splits each mass into a homogeneous cube with side length equal to the grid spacing. 3) the TSC or "triangular shaped cloud" process splits the mass over more nodes than the CIC technique. CIC is usually a good compromise between the smoother TSC results and the noisier NGP results.

2.3.3 Building Initial Conditions

2.3.3.1 The Zel'dovich Approximation

With a large number of fundamental theoretical and numerical tools in hand to model our Universe, it is worth recalling and reminding the goal of this work: the production of simulations of our Universe. Initial Conditions for the GADGET code are required. These Initial Conditions are constituted of an ensemble of particles with given positions and velocities representing the primordial fields (discretization scheme, e.g. [Efstathiou et al., 1985](#)). Primordial and today fields are linked by the Zel'dovich approximation ([Zel'dovich, 1970](#)) which stays qualitatively valid even when the perturbations are large. Let's consider a particle at Lagrangian coordinates \mathbf{x}_L and the coordinates of the grid point occupied by the particle at a time $t = 0$, \mathbf{x}_E or Eulerian coordinates. At a later time t , the particle is located on the grid at $\mathbf{x}_E(t) = \mathbf{x}_L(\mathbf{x}_E) + \psi(\mathbf{x}_E, t)$ where $\psi(\mathbf{x}_E, t)$ is the displacement field from the initial position. The Zel'dovich approximation stipulates that this displacement field can be approximated by:

$$\psi(\mathbf{x}_E, t) = D_+(t)\psi_0(\mathbf{x}_E) \quad (2.46)$$

where $\psi_0(\mathbf{x}_E)$ is the initial displacement field. In other words, the displacement field behaves similarly to the perturbation density field. Its direction is frozen and it grows with time. This approximation is the first-order solution of the Lagrangian perturbation theory often referred to as LPT. Positions of particles at a time t can then be derived. This ensemble of particles approximates the primordial density perturbation field provided that the chosen time is small enough (or equivalently z is high enough).

Because the peculiar velocity field u is the time derivative of the Eulerian coordinates minus expansion:

$$\mathbf{u}(\mathbf{x}, t) = a \times \frac{\psi(\mathbf{x}, t)}{D_+(t)} \frac{dD_+}{dt} \times \frac{dt}{da} \dot{a} = \dot{a} f \psi(\mathbf{x}, t) \quad (2.47)$$

where $f = \frac{d(\ln D_+)}{d(\ln a)}$ is the growth rate, the displacement field can be reached through the peculiar velocity field.

Continuing our quest, the peculiar velocity field needs to be determined. From the continuity equation [2.37](#) left, the (linear) peculiar velocity field \mathbf{u} is directly available from the perturbation density field $\delta = \tilde{\delta} D_+$ provided that this latter is known:

$$\nabla \cdot \mathbf{u} = -a \frac{\partial(\tilde{\delta} D_+)}{\partial t} = -a \frac{\delta}{D_+} \frac{\partial D_+}{\partial t} \frac{\partial t}{\partial a} \dot{a} = -\dot{a} f \delta \quad (2.48)$$

where f is still the growth rate.

Both redshift surveys and peculiar velocity estimates can give access to the perturbation density field with reconstruction techniques such as the Wiener-Filter method (e.g. [Zaroubi et al., 1999, 1995](#)). This technique of reconstruction based on correlation functions will be described in more details in Chapter 4. Regardless, to measure the perturbation density field, there are thus two solutions. Either redshift surveys are directly used or they are combined with direct distance measurements to produce radial peculiar velocity measurements.

2.3.3.2 Redshift Surveys or Direct Distance Estimates?

Obtaining radial peculiar velocity measurements is clearly more demanding and one could argue that although it works it is not worth the effort. Still, since galaxies account only for the luminous matter while radial peculiar velocities from direct distance measurements account for both baryonic and dark matter, the trade-off between the two possible sets of observational data to produce constrained simulations is undeniable. Surely, the density field obtained from redshift surveys may be corrected for the bias. Comparisons between density perturbation fields obtained from large deep redshifts surveys and from independent peculiar velocities measurements have resulted in an estimate of this bias (e.g. [da Costa et al., 1998](#)) and methods based on redshift surveys flourished to produce constrained Initial Conditions ([Heß et al., 2013](#); [Lavaux, 2010](#); [Mathis et al., 2002](#)). However the bias is still poorly known (e.g. [Baugh, 2013](#)). Then, relying on *direct, unbiased* tracers of the underlying gravitational field (peculiar velocities) to derive the perturbation density field is highly relevant. The wealth of the Cosmicflows project is based on this last affirmation.

Chapter 3

Observed Universe

Peculiar velocities are departures from the cosmic mean Hubble expansion due to primordial density inhomogeneities. The overarching goal of the Cosmicflows project is to measure distances, to estimate such variations from the expansion, out to redshift $z \sim 0.05$ ($\sim 150 h^{-1}$ Mpc). Distance measurements are gathered from a multitude of methods. Of particular importance to the project are distances accrued from the correlation between the rotation rate of a galaxy and its luminosity or the Tully-Fisher Relation. There are methodologies that provide distance estimates that are individually more accurate but an abiding advantage of this relation is applicability to a large fraction of all galaxies over a wide range of environments and distances. Distances measured on a coherent scale around the sky are required to address properly the cosmological problems of the Hubble Constant and of departures from the mean cosmic flow. Mid-infrared ($3.6 \mu\text{m}$) photometry with the Spitzer Space Telescope is particularly valuable as the source of luminosities because it provides products of uniform quality across the sky. Accordingly, this Chapter presents observational data of the Cosmicflows projects, in particular surface photometry of Spitzer mid-infrared data. Subsequently, these data are used to calibrate the Tully-Fisher relation at $3.6 \mu\text{m}$ and to give an estimate of the Hubble constant. Finally, the accurate distance measurement catalogs of the project are presented.

3.1 Distances

Distances in the Universe are not accessible with everyday tools. Indicators like luminosity or size in the sky are required to estimate distances. Because distances are obtained through variables and methodological tools affected by the dynamics, geometry and compositions of the Universe, several definitions and explanations regarding fundamental bases of the tools are requested.

3.1.1 Luminosity Distance

Comoving Radial Distance:

From the definitions of the comoving coordinates 2.30 and cosmological redshift 2.22, the comoving radial distance x of a source with a cosmological redshift z_{cos} in our most likely flat Universe, today is:

$$x = \int \frac{1}{a} dr = \int \frac{-cdt}{a} = \int \frac{-cda}{a^2 H} = \int_0^{z_{cos}} \frac{cdz}{H} = \int_0^{z_{cos}} \frac{cdz}{H_0 \sqrt{(1+z)^3 \Omega_m + \Omega_\Lambda}} \quad (3.1)$$

where equation 2.19 and the metric 2.2 were used.

Luminosity Distance:

Among the variety of distances which can be measured, this work relies on the luminosity distance D_L . This latter is obtained measuring the flux F of celestial objects with the relation:

$$D_L = \sqrt{\frac{L}{4\pi F}} \quad (3.2)$$

assuming the total intrinsic luminosity L of the object is known.

The flux received from a galaxy at a comoving distance x today ($a = a_0=1$) is proportional to its luminosity distributed on a sphere of radius x . However, emitted particles such as photons are not received as such. They are affected by a double diminution of their frequency due to both the expansion and a loss of energy. Then the flux measured is:

$$F = \frac{L}{(1+z_{cos})^2} \frac{1}{4\pi x^2} \quad (3.3)$$

From relations 3.2 and 3.3, the luminosity distance D_L can be expressed very simply in function of the comoving distance x as:

$$D_L = (1+z_{cos})x \quad (3.4)$$

It is remarkable that because our Universe is most likely flat, the Friedmann-Lemaître-Robertson-Walker metric 2.2 is considerably simplified. When the relation between the measured and comoving distances could have involved (hyperbolic) sinus functions for a (negative) positive curvature of space, they are simply proportional in the case of a flat Universe.

Our final interest is in the estimation of peculiar velocities. In Chapter 2, the formula 2.25 enables the computation of non-relativistic radial peculiar velocities. However, equations to derive estimates of the cosmological redshift have yet to be discussed.

Relation 3.4 implies that the cosmological redshift can be estimated provided that the integral 3.1 can be calculated. Unfortunately, because of the presence of the cosmological constant, there is no simple solution. An approximation of the generalized Hubble constant is required. For small redshift, the development of H to the second-order in z is satisfactory. After a calculation, that we do not report here, Chiba and Nakamura (1998) give:

$$\frac{H(z)}{H_0} \approx [1 + (1 + q_0)z + \frac{1}{2}[(j_0 + 3q_0 + 2) - (2 + 3q_0 + q_0^2)]z^2] \quad (3.5)$$

$$D_L(z) \approx \frac{cz}{H_0} [1 + 0.5(1 - q_0)z - \frac{1}{6}(1 - q_0 - 3q_0^2 + j_0)z^2] \quad (3.6)$$

where $j_0 = \frac{\ddot{a}a^2}{\dot{a}^3}|_0$ is the jerk parameter and $q_0 = -\frac{\ddot{a}a}{\dot{a}^2}|_0 = 0.5(\Omega_m - 2\Omega_\Lambda)$ is the deceleration parameter obtained with equations 2.11, 2.12 and 2.16. Usually, we take the jerk parameter to be the unity.

Eventually, the cosmological redshift is solution of equation 3.6 where $D_L(z)$ is the measured luminosity distance. It leads to an estimate of the peculiar velocity with 2.25.

Very often, observers work with velocities from the start rather than redshifts. However, one has to be careful when working with velocities as the commonly seen relation $v_{tot} = cz_{obs}$ is inaccurate. From equations 2.23, 2.25, the generalized Hubble Law modified by peculiar motion 2.31 and the relation between cosmological redshift and distance luminosity 3.6, neglecting supplementary relativistic effects, if any, affecting the observational redshift, one finds:

$$\begin{aligned} v_{tot} = H_0 D_L + v_{pec} &\approx cz_{cos} [1 + 0.5(1 - q_0)z_{cos} - \frac{1}{6}(1 - q_0 - 3q_0^2 + j_0)z_{cos}^2] + cz_{pec} \\ &\neq cz_{obs} = c(z_{pec} + z_{cos} + z_{pec}z_{cos}) \end{aligned} \quad (3.7)$$

With these definitions settled, in the rest of this Chapter, distance stands for luminosity distance.

3.1.2 Magnitudes

Observations of brightnesses of stars and galaxies go back as far as the ancient world when lists of celestial objects and their magnitudes were compiled. Since the human eye relates magnitude and flux roughly logarithmically in base ten (denoted \log in this whole work), the logarithm scale has been kept over the years although, the relation is now much better defined. The apparent magnitude m of an object is given by:

$$m = -2.5 \log F + cst \quad (3.8)$$

where F is the flux and cst is a constant which depends on the chosen system. Multiple systems exist, two are used in this work:

- the *Vega system* which is built for the Vega star to have a zero magnitude in all filters. At only ~ 7 -8 parsecs from Earth, Vega, also called Alpha Lyrae, is the brightest star in the constellation Lyra. From the fifth brightest star in the night sky, it comes only second in the sole northern hemisphere after the Arcturus star. From the definition 3.8 of the apparent magnitude, the constant is $2.5\log(F_{Vega})$ plus an additional term depending on the observing telescope,
- the *AB system* which relies on the principle that an object with a constant flux (flat energy distribution) has the same magnitude in all bands. In that case, the constant in equation 3.8 is -48.6 to which the value corresponding to the response of the observational instrument has to be added.

Because objects are all at different distances (the desired variable), comparing their intrinsic luminosities with apparent magnitudes is not direct. Thus, the absolute magnitude M of an object is defined as the apparent magnitude which would be measured for the object if this latter was at 10 parsecs from us without any source of obscuration:

$$M = -2.5\log L + cst' \quad (3.9)$$

where L is the luminosity of the object and cst' a constant.

From the definitions 3.8 and 3.9 of the magnitudes and $F = \frac{L}{4\pi D^2}$ of the flux, apparent m and absolute M magnitudes of an object can be related to its distance D :

$$\mu = m - M = -2.5\log\left(\frac{4\pi \times 10^2}{4\pi \times [D(pc)]^2}\right) = 5\log[D(pc)] - 5 = 5\log[D(Mpc)] + 25 \quad (3.10)$$

where μ is called the distance modulus and (pc) and (Mpc) mean that the distance has to be converted either in parsecs or megaparsecs.

In 1934, relation 3.8 between the flux $F = \frac{L}{4\pi D^2}$ and the apparent magnitude m enabled Hubble to confirm the homogeneity of the Universe. For a homogeneous Universe, the number of galaxies with a flux greater than F in a steradian of the sky should follow the relation:

$$N(> F) = nV = \frac{nr^3}{3} = \frac{n}{3}\left(\frac{L}{4\pi F}\right)^{3/2} \propto F^{-3/2} \propto (10^{-0.4m})^{-3/2} = 10^{-0.6m} \quad (3.11)$$

Hubble counted and retrieved the proper relation. Note that in reality the homogeneity is confirmed only for the younger Universe as light received today has been emitted some time in the earlier history of the Universe. In addition, this relation is valid only nearby unless

some correction for the selection bias which affects it farther away is made (see section 4.4 in Chapter 4 for an explanation of the bias).

From this subsection, we learnt that measuring distances relies on obtaining distance modulus estimates, more precisely apparent and absolute magnitudes. The next subsection enlightens us on some of the methodological tools available to obtain such distance modulus measurements.

3.1.3 Distance Indicators

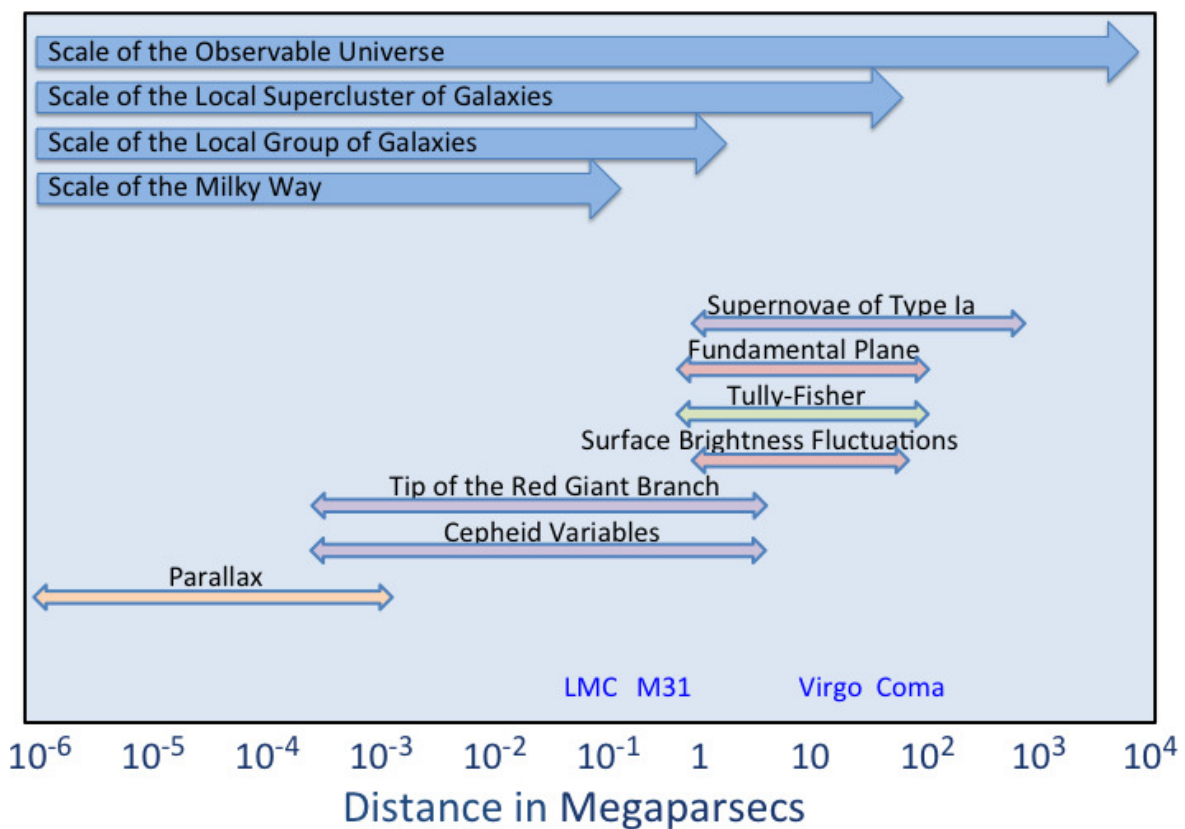


FIGURE 3.1: The cosmic distance ladder or extragalactic distance scale principle is presented here. Each technique from parallax to Supernovae of Type Ia through Cepheids, Tully-Fisher relation, etc is relevant to determine distances on varied scales. The most accurate ones, which can be used close to us, serves as scaler for the other ones. They are called primary distance indicators while the others are named secondary. The double head arrows underlying techniques' names show the range of distances on which methods are relevant. Their colors (except for the orange one) indicate the objects of study: purple for the stars, red for elliptical galaxies, green for spiral galaxies. The parallax is a geometrical method which applies to various but very close objects. A few object are identified in blue: the Large Magellanic Cloud (LMC), the galaxy M31 or Andromeda, the Virgo and Coma clusters. Their horizontal position in the diagram specifies their approximate distance. (This figure heavily borrows from one of Pr. Whittle's lessons, www.astro.virginia.edu).

The cosmic distance ladder or extragalactic distance scale is the ensemble of methods used by observers to determine distances in the Universe. The notion of ladder arises because none

of the techniques used to estimate distances can cover by itself the whole range of values. Distance indicators, as are called these methods, are separated into two groups: the primary distance estimators which are very accurate but can be used only locally and the secondary distance estimators which are less accurate but can provide distances much farther away. Figure 3.1 gives a non extensive list of distance estimators which are briefly described in the next paragraphs (see [Jacoby et al., 1992](#); [Rowan-Robinson, 1985](#), for a more complete review).

3.1.3.1 Primary Distance Estimators

Two primary distance estimators are of particular interests to the Cosmicflows project:

- the Cepheid Period Luminosity relation which is a very accurate method based on the relation between the distance modulus μ of the variable stars or Cepheids and their period P (amount of time necessary for their magnitude to be back to the initial value before repeating the same flux variation pattern again):

$$\mu = a[\log(P) - 1] \quad (3.12)$$

where a is a constant. [Freedman et al. \(2001\)](#) improved the calibration of this relation by taking into account the Cepheid-metallicity dependence of the relation. Distances are directly obtained from this relation and equation 3.10,

- the Tip of the Red Giant Branch (TRGB) method which relies on the fact that the red giant branch is well developed in stellar populations older than two gigayears. Stars at the tip of the branch are easily resolved if their distance is less than 10 Mpc. This method uses equation 3.13, a correlation between TRGB magnitudes and distance moduli:

$$\mu = m_{TRGB} + BC - M_{Bol,TRGB} \quad (3.13)$$

where BC is the bolometric correction (conversion from apparent to bolometric magnitudes where the bolometric magnitude is the magnitude that would be measured if all the wavelengths were observed simultaneously), $M_{Bol,TRGB}$ the bolometric luminosity function of metallicity and color and, m_{TRGB} the magnitude for which there is a discontinuity in the Color-Magnitude Diagram of the observed star population. At the core of low-mass star helium flashes, $M_{Bol,TRGB}$ varies only by approximately 0.1 magnitude. Thus, in a Color-Magnitude Diagram, which preserves a record of star formation history rich in details, low-mass stars accumulate along the red giant branch up to the tip as they evolve. The sudden discontinuity in the diagram indicates that

the tip is reached. Relation 3.13 and equation 3.10 enable a direct derivation of the distance.

These two primary distance indicators enable to set the zeropoint of the secondary distance estimators.

3.1.3.2 Secondary Distance Estimators

After observations revealed that kinematic properties and luminosities of galaxies are closely linked, relations have developed. A relation often applies to a particular type of galaxies. Let's first distinguish between the different galaxy types:

- the elliptical galaxies are smooth, featureless stellar systems containing little or no cool interstellar gas or dust and small or no stellar disk. Ten percents of these galaxies can be found in low density regions to over forty percent in dense clusters' centers. In the Hubble sequence, they are named $E0$ to $E7$ where the number 0 to 7 are related to a measure of the axial ratio at the effective radius or radius of the isophote (line of constant luminosity) delimiting half the total luminosity,
- the spiral galaxies, like the Milky-Way or M31, have prominent disks containing stars, gas and dust. Disks have spiral arms which are star forming filaments. These spiral arms are also visible in the old stars in disks. Arms are very variable in shape from one spiral galaxy to the other. About sixty percent of these galaxies can be found in low density regions while their number drops to ten percent in dense regions such as the core of clusters. Most spiral galaxies, like the Milky-Way, have also a bulge or central smooth and amorphous concentration of stars. In the Hubble sequence, spirals are called Sa to Sd . From a to d , the luminosity of their bulge decreases, their arms are less wound and show more individual clumps of young stars, their gas content increases. Spiral galaxies can also be barred like the Milky-Way. The bar is a long smooth stellar structure relic of a rigid system at the center of the disk. To distinguish normal from barred spirals, a "B" is added after the S (SBa,b,c,d),
- the lenticular galaxies (SO , SO^+ , SO^-) are galaxies in between ellipticals and spirals. Like ellipticals they do not have arms (so gas and young stars) and, they have a smooth appearance yet they have all the other characteristics of spirals. Found mostly at the center of clusters, they could be old spiral galaxies which interstellar gas has been streamed through different processes (e.g. Rawle et al., 2013),
- the irregular galaxies (Sm , Im), such as the two Magellanic clouds, are kind of spirals but with less sharply defined arms. They are rich in gas and could be the results of merging processes or could have been deformed by close encountering.

An old relic of the Hubble sequence, which was primarily assumed to be an evolutionary sequence of galaxies, left the denomination of early types for elliptical and lenticular galaxies and late types for spirals and irregular galaxies. These two different types of galaxies, mainly ellipticals and spirals, follow different relationships.

Relations for Elliptical Galaxies:

- Relations for elliptical galaxies are usually refinements of the Faber-Jackson relation (Faber and Jackson, 1976) which relies on the fact that on average the velocity dispersion σ_0 measured in the center of ellipticals is proportional to their luminosity L but with a large scatter. The Fundamental plane (Colless et al., 2001) is one of these refinements which supports the fact that not only luminosity and velocity dispersion are related but also the effective radius is proportional to the luminosity. As a result, the effective radius r_e is also proportional to the average effective surface brightness $\langle\mu_e\rangle$ defined as the brightness in magnitude per square arcsecond measured for the surface within the isophote of effective radius. As a matter of fact $L \propto r_e^2 \langle\mu_e\rangle \propto \langle\mu_e\rangle^{-cst}$, namely the more luminous the galaxy is, the smaller the effective surface brightness. Then, in a $(r_e, \langle\mu_e\rangle, \sigma_0)$ plane, hence the Fundamental Plane name, ellipticals are close to forming a plane:

$$\log r_e = a \langle\mu_e\rangle + b \log \sigma_0 + c \quad (3.14)$$

where a , b and c are constants. The radial stellar velocity dispersion is determined with spectroscopy measurements where absorption lines are broadened by internal motions of stars. Thus, the velocity dispersion is related to the Gaussian function necessary to match an assumed galaxy spectrum, with all stars at rest with respect to each other, to the observational galaxy spectrum.

The Fundamental Plane can be explained with the virial theorem which states:

$$2E_k + E_p = 0 \quad (\text{with } E_k = \frac{mv^2}{2} \text{ and } E_p = -\frac{Gm^2}{r}) \quad \iff \quad v^2 = \frac{Gm}{r} \quad (3.15)$$

Setting $r_e = k_r r$, $\sigma_0^2 = k_v v^2$ and $L = k_L \langle\mu_e\rangle r_e^2$, where k_x ($x = r, v$ and L) parameters reflect density, kinematic and luminosity structures of a given galaxy, the virial theorem 3.15 gives:

$$r_e = k_s \left(\frac{m}{L}\right)^{-1} \sigma_0^2 \langle\mu_e\rangle^{-1} \quad (3.16)$$

where $k_s = (Gk_L k_r k_v)^{-1}$. This relation is analogous to the relation 3.14, if the mass-to-light ratio is assumed to be constant (we will come back to this assumption at the end of this subsection).

- $D_n - \sigma$ (Dressler, 1987) is another variant of the Faber-Jackson relation which considering D_n as a function of $\langle \mu_e \rangle$ and r_e finds a relation with σ_0 . D_n is the diameter of the isophote encompassing 20.75 magnitude per square arcsecond.

- A quite different method is the Surface Brightness Fluctuations (Tonry et al., 2001) which measures the fluctuation of the number of bright stars per area element in a galaxy. This fluctuation can be described by a Poisson noise. Accordingly the farther away is the galaxy, the more stars there is in the observed areas, the smaller the relative fluctuation is. This measurement enables the definition of the fluctuation star counts $\bar{N} = \bar{m} - m$ with m the apparent magnitude and \bar{m} the fluctuation magnitude obtained with the flux of the fluctuation signal. Combining the correlation between absolute magnitude M and color (difference between magnitudes of two different Bands, or observational wavelength ranges, for a given galaxy) and the relation between that same color and the fluctuation star counts \bar{N} obtained with the observations of a larger number of galaxies, it is possible to write:

$$M = a + b\bar{N} \quad (3.17)$$

where a and b are again constants.

Relations for Spiral Galaxies:

- This work mainly relies on the Tully-Fisher relation (TFR, Tully and Fisher, 1977). In 1977, the virial theorem 3.15 had been the distance estimator up to the early 70s with what was usually called the "indicative mass" method. It was written, assuming a relation between mass and light, $L \propto v^2 r$ where v is the rotational velocity of the galaxy. Tully and Fisher (1977) suggested two alternatives: $L \propto v^\alpha$ (α ranges from 3 to 4) and $L \propto r^\beta$. They reduced the number of variables from 3 to 2 and departed from the virial theorem. Equation 3.18 is the resulting TFR as written nowadays:

$$M = a + b[\log(W) - 2.5] \quad (3.18)$$

with a and b constants, W is the linewidth of the 21-cm line which corresponds to twice the rotation rate of the galaxy.

This relation implies that more massive galaxies are both more luminous and rotate faster. It holds for galaxies with disks stabilized by rotation basically, spiral galaxies. There is no proper mathematical derivation for this relation, but an explanation can help make it plausible even to the cautious reader which remembers that flat ends of galaxy rotation curves imply the most probable existence of a dark matter. Because of this flat end, at a distance r sufficiently large from the center of the galaxy, the mass m can be written $m = v_{max}^2 \frac{r}{G}$. Since the mean surface brightness $\langle \mu \rangle$ is $\frac{L}{r^2}$, the luminosity becomes $L = (\frac{L}{m})^2 \frac{1}{G^2 \langle \mu \rangle} v_{max}^4$. This last equation is analogous to 3.18 assuming the mass-to-light ratio (the same assumption

was made for ellipticals) and the mean surface brightness to be identical for every spiral. Because of the existence of dark matter, this also implies that the ratio of luminous to dark matter is quite similar among spirals. The similarity between different rotational curves and the fact that the mass-to-light ratio of a stellar population should not depend strongly on its age (at least in the red and infrared wavelength) seem in agreement with this last implication. Another variation called the baryonic Tully-Fisher relation (McGaugh et al., 2000) exists which, instead of accounting only for the luminous mass, takes into account the total baryonic (stellar and gas) mass. We will come back to it in the prospectives (Chapter 5).

We close this section with the supernovae of type Ia (SNIa) which have remarkable properties such as their high luminosities ($10^9 L_{\odot}$) and their apparent homogeneous nature (Riess et al., 1995). Kowal (1968) established the first Hubble diagram that suggested SNIa could be used as extragalactic distance indicators. Two decades later, Phillips (1993) demonstrated the existence of a decline rate-absolute magnitude dependence for SNIa, validating that type Ia supernovae can act as standard candles. Namely the luminosity or absolute magnitude of these objects is always nearly the same. Work in subsequent years (Amanullah et al., 2010; Hamuy et al., 1995; Hicken et al., 2009; Jha et al., 2007) has produced alternate descriptions of the correlations between the intrinsic luminosities of SNIa and the shapes of their light curves. The properties of SNIa can be used to determine distances to galaxies at many hundreds of Megaparsecs. At such distances, objects are expected to have recessional velocities that individually differ from the mean by at most a few percent and collectively should define the cosmic expansion. Thanks to the great precision of SNIa distance estimates, high redshift SNIa revealed that the expansion of the universe is currently accelerating (Perlmutter et al., 1999; Riess et al., 1998). The SNIa method can provide the best estimate of the Hubble parameter once the zeropoint scale is set. Independent distances are needed to the hosts of low redshift SNIa (Folatelli et al., 2010; Riess et al., 2011, 2009) to establish the absolute scale. Then, measuring the apparent magnitude m and using the definition of the distance modulus 3.10, a distance estimate can be provided.

Actually, except for the Fundamental plane which provides the angular distance, all the above mentioned relations are based on this principle. They supply the absolute magnitude M which when combined with the measured apparent magnitude m enable the determination of the distance modulus μ , an estimate of the distance D with equation 3.10 closely follows. Still, measurements of apparent magnitudes are required and above all constants in all these relations need to be determined for each observational bands as they vary with it. Namely relations need to be calibrated. The constant which gives the zeropoint can only be obtained with primary distance indicators, hence the name of secondary distance indicators given to the estimators in this subsection. Because the interest of the Cosmicflows project goes mainly to the Tully-Fisher relation, the next two sections focus on the two types of observations and

on the surface photometry, performed to acquire apparent magnitudes, required to calibrate the Tully-Fisher relation and to compile an extensive list of accurate distances.

3.2 Observations

As theories can only be tested when directly confronted with observations or indirectly via simulations which are in turn compared with observations, these latter are essential to understand our Universe. To acquire optimal observational datasets, instruments need to be designed with care. Instruments are selected on their sensitivity which determines how dim a source can be and still be observable. This sensitivity depends on intrinsic properties of the telescope (aperture, sensitivity of the detectors, efficiency) but also on extrinsic parameters such as light or radio (depending on the wavelength of observations) pollution and atmospheric turbulences which decrease the angular resolution (minimal angular separation that can have two sources in the sky to be separately detected). The spectral resolution (capabilities to separate the different wavelengths) and the efficiency in terms of number of observations requested to observe a region (the larger the field-of-view, the less observations are required) are also of interests to the observers. For the Tully-Fisher relation, two kind of observations are needed: optical or infrared photometry and radio, precisely HI, observations. As a result two types of instruments are requested and described below along with observations.

3.2.1 RadioAstronomy: HI Observations

With the large number of radiotelescopes available (to date, Arecibo is the largest single dish and has the highest sensitivity, Greenbank is the largest fully steerable radio-instrument, Parkes has the advantage of being in the southern hemisphere unlike the two first mentioned telescopes), the Cosmicflows project has now analyzed HI profiles for over 14,000 galaxies in a consistent way, deriving a linewidth parameter W_{m50} with suitable precision (error estimate $\leq 20 \text{ km s}^{-1}$) for over 11,000 galaxies (Courtois et al., 2009, 2011b). These observations are mainly part of the Cosmicflows Large Program on the 100m Green Bank Telescope and complementary southern observations on the Parkes Telescope and the merging of various previous observations re-measured for consistency (Courtois et al., 2009, 2011b). The parameter W_{m50} is a measure of the HI profile width at 50% of the mean flux within the velocity range encompassing 90% of the total HI flux. It gives measures: 1) at a level low enough to capture the range of rotation motions while high enough to be above the noise, 2) with wings in profiles adequately observed, and 3) not sensitive to details of the profile shape (single or double peaked profiles, asymmetric peaks). All these new measurements are available for public use at the Extragalactic Distance Database (EDD, Tully et al., 2009)

website¹ of the Cosmicflows project alongside HI profiles. This observed parameter W_{m50} is transformed into the more physically motivated parameter W_{mx}^i through three steps that are justified in Courtois et al. (2009, 2011b); Tully and Fouque (1985). These transformations remove a slight relativistic broadening and a broadening due to finite spectral resolution, adjust to twice the projected maximum rotation velocity and de-project to edge-on orientation. Appropriate formulations of the adjustments of W_{m50} are given by:

$$\begin{aligned} W_{m50}^c &= \frac{W_{m50}}{1+z} - 2\Delta\nu\lambda \\ W_{mx}^2 &= W_{m50}^c{}^2 + W_{t,m50}^2(1 - 2e^{-(\frac{W_{m50}^c}{W_{c,m50}})^2}) - 2W_{m50}^c W_{t,m50}(1 - e^{-(\frac{W_{m50}^c}{W_{c,m50}})^2}) \\ W_{mx}^i &= \frac{W_{mx}}{\sin i} \end{aligned} \quad (3.19)$$

with z the redshift, $\Delta\nu$ the spectral resolution after smoothing, λ determined empirically (broadening is statistically described for $\lambda = 0.25$), $W_{t,m50}$ the turbulent broadening, $W_{c,m50}$ the transition from boxcar to Gaussian intrinsic profiles ($W_{c,m50} = 100 \text{ km s}^{-1}$ and $W_{t,m50} = 9 \text{ km s}^{-1}$ give the best fit), i the inclination from face-on. The final W_{mx}^i parameter statistically approximates twice the maximum rotation velocity of a galaxy. The inclination from face-on is defined by (Holmberg, 1958):

$$\cos i = \sqrt{\frac{(\frac{b}{a})^2 - q_0^2}{1 - q_0^2}} \quad (3.20)$$

where $\frac{b}{a}$ is the axial ratio and q_0 , chosen to be 0.20, is the statistical axial ratio of a galaxy viewed edge-on. Arguments can be made for a more complex dependence of q_0 . Fortunately, the choice of q_0 has a negligible effect on distance measurements if one is consistent between calibrators (galaxies used to calibrate the relation) and targets (galaxies to which the relation is applied) (Tully and Pierce, 2000). A q_0 value of 0.13 (0.20) yields an inclination of 81° (90°) for $\frac{b}{a} = 0.20$. This gives a $\frac{1}{\sin i}$ difference on the corrected linewidth of only 1.2%. As one progresses toward larger axial ratio, the difference in assigned inclination is reduced but the $\frac{1}{\sin i}$ correction is growing. The product of the two is a roughly constant shift of 1.2% in the corrected linewidth at all inclination $i > 45^\circ$. Still, the problem of de-projection is recurrent in observations. Accordingly within the Cosmicflows project, we have initiated a Citizen Science Project which should be opened soon to the public. It consists in sorting galaxies by their orientation from face-on to determine statistically and more precisely their inclination.

Linewidth error estimates are based on the level of the signal, S , at 50% of mean flux divided by the noise, N , measured beyond the extremities of the signal. Profiles with error estimates smaller than 20 km s^{-1} are retained. These profiles meet a minimum flux per channel

¹<http://edd.ifa.hawaii.edu>; catalog ‘All Digital HI’

requirement of signal-to-noise $S/N \geq 2$ and acceptance after visual inspection. Figure 3.2 shows two of such profiles. Errors in the logarithmic linewidth parameter tend to be larger for slow rotators since a typical measurement uncertainty of $10 - 20 \text{ km s}^{-1}$ causes a larger fractional uncertainty with a narrow profile. The largest uncertainties are associated with more face-on galaxies, those toward the 45° cutoff. At this limit, a 5° error in inclination results in an 8% error in linewidth.

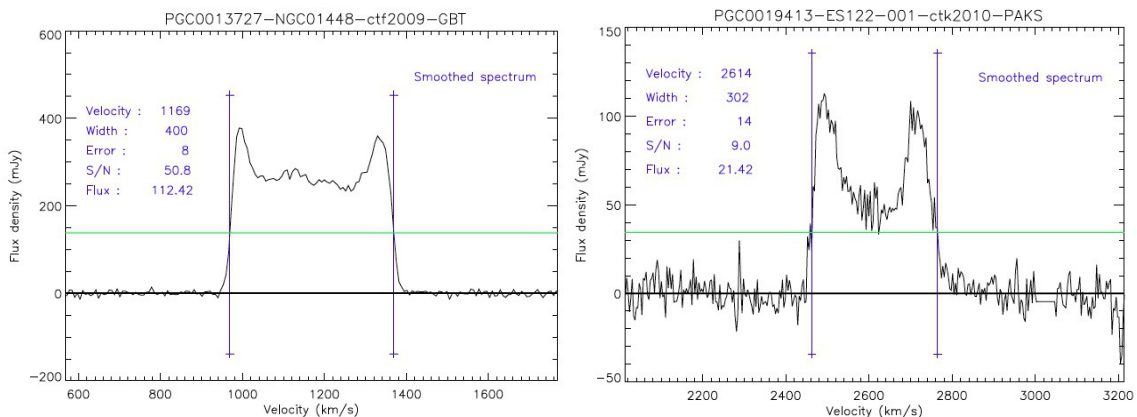


FIGURE 3.2: Suitable HI profiles of two galaxies obtained with the Green Bank (*left*) and Parkes (*right*) telescopes. The rotational velocities of these galaxies are half the given "Width" once corrected. "Width" corresponds to the linewidth parameter W_{m50} : a measure of the HI profile width at 50% of the mean flux within the velocity range encompassing 90% of the total HI flux (from Courtois et al., 2011b).

3.2.2 Photometry: Observational Band

Photometry raises the issue not only of the instrument choice but also of the wavelength of observation. Table 3.1 recapitulates the photometric letters usually attributed to each observational wavelength from the ultraviolet up to the limit with the mid-infrared. Numerous observations are already available in several bands from blue to red (B to R Bands) in the optical up to the near-infrared (e.g. I Band) through various observational surveys (e.g. the Sloan Digital Sky Survey, SDSS, Abazajian et al., 2003). The near-infrared up to its limit with the mid-infrared has even been explored with, for example, the J , H , K Bands of the Two Micron All Sky Survey (2MASS, Huchra et al., 2012). Yet, until recently, although it has long been appreciated that photometry in the infrared may offer advantages because of reduced extinctions, mid-infrared observations were mostly on hold. The difficulty arises from the fact that observations in the infrared from the ground are affected by high and variable sky foreground and by thermal radiations. As a result, much of the flux from galaxies, which lies in extended components with surface brightnesses that are well below the ground based sky level, is lost and very low surface brightness galaxies are not even seen. Observations from space remove the problem of the high contamination by Earth atmosphere. From a perch above the atmosphere, essentially the total magnitude of targets

can be recorded in exposures of a few minutes. Accordingly, the optimal instrument for our work is a spatial telescope observing in the mid-infrared. In addition, and a very important point, the photometry from such a telescope has consistent properties in all directions on the sky. Thus, acquisition of mid-infrared data from a spatial telescope contributes to great advances in photometry which were lacking to the Cosmicflows project to match the large progress achieved with HI observations.

| Ultraviolet | | | Near-infrared | | |
|-------------|-------|--------------------|-----------------------------|--------|---------------------|
| U | ~ 300 | u | I | ~ 800 | I _C , i |
| | | | Z | ~ 900 | z |
| Visible | | | Y | ~ 1020 | |
| B (blue) | ~ 400 | | J | ~ 1200 | |
| V (violet) | ~ 500 | | H | ~ 1600 | |
| G (green) | ~ 600 | g | K | ~ 2200 | K _s , K' |
| R (red) | ~ 700 | R _C , r | beyond: Mid-infrared | | |

TABLE 3.1: Photometric observational bands: (1) and (4) photometric letter, (2) and (5) approximate observational wavelength (depends on the filter), nm, (3) and (6) examples of specific filter-bands mentioned throughout this work.

3.3 Surface Photometry

Obscurations within the galaxies and due to the Milky Way which are minimized in the mid-infrared are not the sole advantage of infrared observations. Infrared flux arises in large measure from old stars that should optimally represent the baryonic mass that presumably couples to the rotation rate to give the TFR. Accordingly, it was suggested (Aaranson et al., 1979) that the TF methodology might be improved by moving to infrared bands, particularly when it is used to measure distances. Thus, although progress with infrared observations of galaxies was difficult because of the high and variable sky foreground at near-infrared wavelengths and overwhelming thermal emission at mid-infrared wavelengths with ground-based observations, several attempts to derive the TFR in the close to the mid-infrared band were made. The most modern serious attempt has drawn on the K_s magnitudes of 2MASS (Karachentsev et al., 2002). However, this shallow survey, like with the earlier work in the infrared, only registers the high surface brightness components of light from galaxies and can actually miss low surface brightness galaxies entirely.

3.3.1 Spitzer: an Instrument of Choice

The situation dramatically changed with the launch of *Spitzer Space Telescope* (Werner et al., 2004). With observations using the InfraRed Array Camera (IRAC, Fazio et al.,

2004) onboard *Spitzer Space Telescope*, the "sky" is far reduced from observations on the ground, now dominated by diffuse zodiacal light and the stochastic distribution of background high redshift galaxies. For example, integrating about four minutes in IRAC channel 1 permits area photometry at levels that can compete with ground-based optical imaging with comparable exposures, i.e. to levels that include all but a few percent of the total light of a galaxy.

3.3.1.1 The InfraRed Array Camera Channel 1

The Cosmicflows with Spitzer program concentrates on IRAC channel 1 observations in the $3.6 \mu\text{m}$ window that give magnitudes [3.6] in the AB system. This window provides observations with minimal dust extinction (Draine and Lee, 1984). It lies at a minimum of the zodiacal background radiation (Ootsubo et al., 1998).

Figure 3.3 provides examples of the spectral energy distribution of spiral galaxies (Silva et al., 1998). The Spitzer [3.6] band lies on the Rayleigh-Jeans tail of the spectral energy distribution of normal populations of stars, not yet strongly affected by flux from warm dust that starts to become a factor at longer wavelengths than $4 \mu\text{m}$. The discrete spectral features seen in the spectral energy distribution arise from Polycyclic Aromatic Hydrocarbon molecules (Tielens, 2008). The highest frequency Polycyclic Aromatic Hydrocarbon, at $3.3 \mu\text{m}$ is contained within the [3.6] bandpass. Meidt et al. (2012) have investigated the impact of various contributors to flux in the $3.6 \mu\text{m}$ window with six representative spiral galaxies observed with the Spitzer Survey of Stellar Structure in Galaxies (S⁴G, Sheth et al., 2010) program. They find contributions from 1) hot dust and Polycyclic Aromatic Hydrocarbons together at the level of $9 \pm 4\%$ of the global flux in the $3.6 \mu\text{m}$ band, 2) intermediate age asymptotic giant branch and red supergiant branch stars at the level of $3 \pm 2\%$ of the global flux, and 3) old stars, predominantly K and M giants for the rest, i.e. the great majority. These non-stellar and young stellar contributions should only slightly degrade the correlation between old stars and mass in normal spirals.

Using Spitzer IRAC channel 1, a point spread function with mean FWHM $1.66''$ is sampled with $1.2''$ pixels. The field of view is $5.2'$, adequate to encompass most galaxies to beyond twice d_{25} , the diameter at a B isophote of 25 magnitude per square arcsecond. Larger galaxies require mosaics. Integrations with the Cosmicflows with Spitzer (CFS) program involve the combination of 8×30 seconds slightly dithered exposures for a total of four minutes per field. As will be discussed, these integrations provide images that probe somewhat fainter limits than most ground-based optical photometry programs and much fainter limits than ground-based infrared photometry programs. Spitzer surface brightness levels reach ten magnitudes below typical ground-based infrared sky levels. No existing near-infrared ground survey

achieves the accuracy obtained with *Spitzer Space Telescope*. The outstanding advantages of space observations are background stability and all-sky consistency (Fazio et al., 2004).

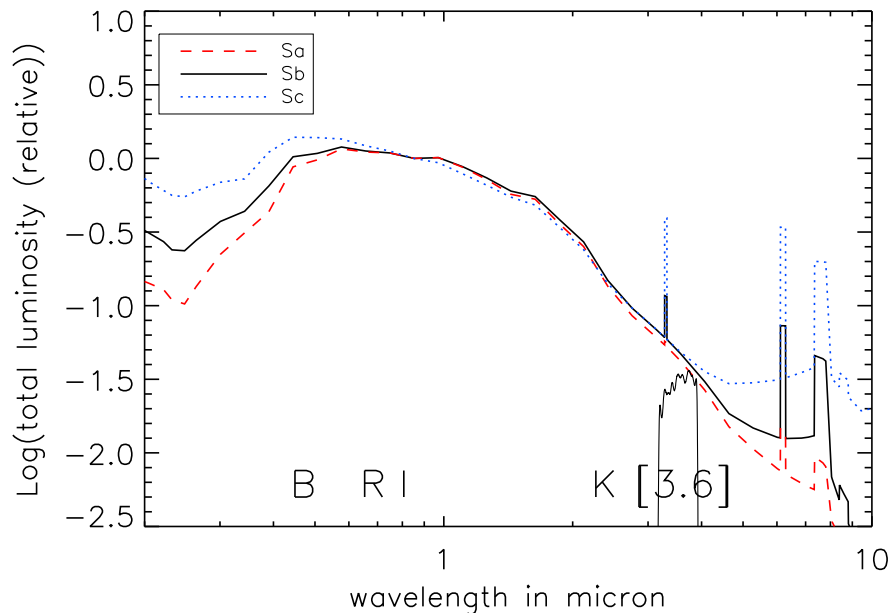


FIGURE 3.3: Comparative SED for spirals of types Sa (red, dashed), Sb (black, solid), and Sc (blue, dotted). The Spitzer [3.6] passband is illustrated along with the wavelengths associated with B , R , I , K bands. The relative scales of the SED are offset to match at $0.8 \mu\text{m}$. Features at $3.3 \mu\text{m}$ arise from Polycyclic Aromatic Hydrocarbon molecules.

3.3.1.2 The Observational Sample

The cycle 8 post-cryogenic program Cosmicflows with Spitzer avoids repetition of earlier Spitzer observations. Archival information is used where available. Major contributions from earlier programs come from SINGS, the Spitzer Infrared Nearby Galaxies Survey (Dale et al., 2005, 2007) and LVL, the Local Volume Legacy survey (Dale et al., 2009) carried out during the cryogenic phase, then S^4G , the Spitzer Survey of Stellar Structure in Galaxies (Sheth et al., 2010), and CHP, the Carnegie Hubble Program (Freedman et al., 2011), subsequently carried out during the post cryogenic phase. Smaller programs supply us with a few more fields. These data are available for public use at the Spitzer Heritage Archive website². The variety of source programs introduces variations in the details of the acquisition, particularly affecting total integrations, dithering procedures, and the extent of fields referenced to d_{25} . However, with all the data that will be considered the fields are large enough and the exposure times are long enough that at most only a few percent of the light from a target is lost.

In subsection 3.3.5, a comparison between 241 magnitudes from S^4G -pipeline (Muños-Mateos et al. in prep.) and from the Spitzer-adapted version of ARCHANGEL used in this work reveals the very good agreement between both magnitudes. As a result, S^4G -magnitudes are directly

²<http://irsa.ipac.caltech.edu/data/SPITZER/docs/spitzerdataarchives/>

used to derive distances for all the other, relevant to the Cosmicflows project, galaxies of the large S⁴G program.

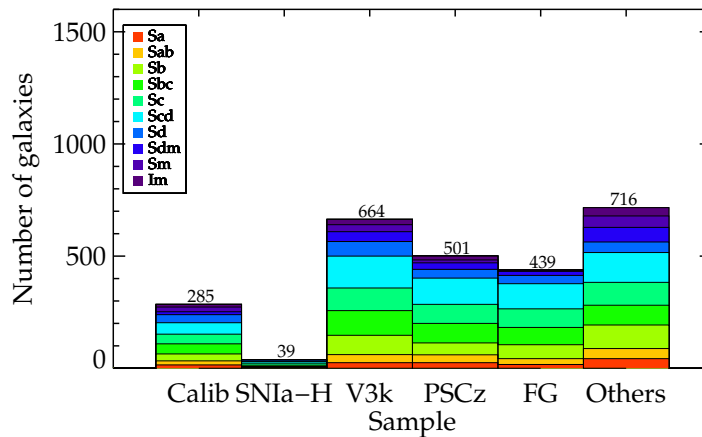


FIGURE 3.4: Histogram of the number of galaxies per subsamples in CFS and diverse programs, mostly S⁴G (65%). Calib is constituted of Tully-Fisher calibrators, SNIa-H contains hosts of Supernovae of Type Ia, V3k is built of galaxies with $v_{hel} < 3000 \text{ km s}^{-1}$, PSCz is derived from the Infrared Astronomical Satellite point-source Redshift Survey and FG is a catalog of flat galaxies. "Others" stands for galaxies of interests which do not fall into one of the previously cited categories. The gradient of colors shows the proportion of each morphological type from the HyperLeda Database in each sample.

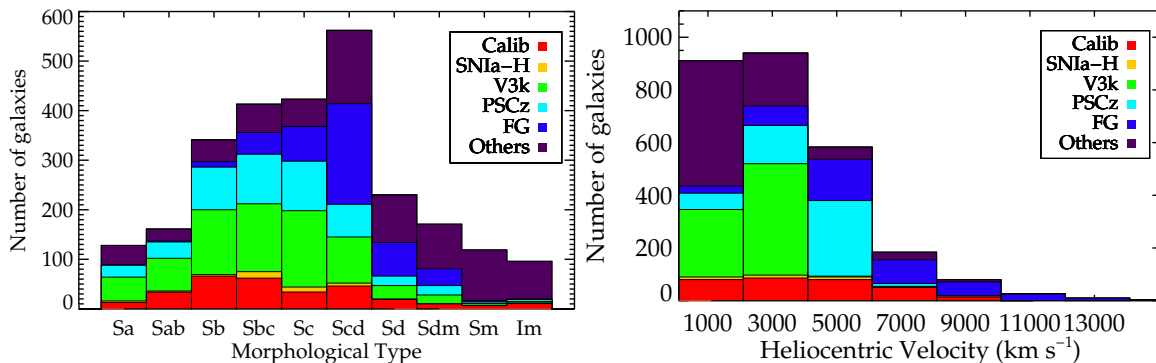


FIGURE 3.5: Histograms of the morphological type (*left*) from HyperLeda and of the heliocentric velocity (*right*) from EDD for the whole compilation of galaxies. The gradient of colors gives in which proportion each subsample contribute to a given type (*left*) and range of heliocentric velocities (*right*).

In Figure 3.4, galaxies which surface photometry has either been measured for the Cosmicflows project or that comes from S⁴G are distinguished by their occurrence in five subsamples: 1. the Tully-Fisher calibrators (Calib), 2. the hosts of Supernovae of Type Ia (SNIa-H), 3. the V3k, 3000 km s⁻¹ sample (V3k), 4. the Infrared Astronomical Satellite point source Redshift Survey sample (PSCz) and 5. the flat galaxy sample (FG). These subsamples are completed with galaxies from various surveys. If a galaxy lies within multiple samples, in the following the galaxy is assigned to the sample that includes it that is discussed first. Galaxies of interest of to the project but which do not fall into one of the previous categories constitute the sixth subsample. All these supplementary galaxies are mostly from

S⁴G (65%). Among the galaxies left, the majority has been observed by SINGS (2%), LVL (3%) and CHP (16%) programs.

- The first two of these subsamples have been already widely described (Courtois and Tully, 2012b; Tully and Courtois, 2012; Tully and Pierce, 2000). The first subsample constitutes a template for the calibration of the Tully-Fisher relation: galaxies in 13 clusters for the slope and galaxies with cepheids or Tip of the Red Giant Branch distances for the zeropoint. The second subsample is constituted of galaxies to set the zeropoint scale of the Supernovae of Type Ia method. The two subsamples will be discussed more precisely in subsections 3.4.1 and 3.4.3 when used at 3.6 microns. Approximately one third of the first subsample is constituted of galaxies observed for CFS with Spitzer. Others have been observed by previous Spitzer programs, mostly CHP and S⁴G. Half of the SNIa-H subsample is made of CFS observations while the other half contains mostly CHP observations.
- The third subsample is a catalog developed over the years called V3k (Tully et al., 2008) with the magnitude cutoff $M_K < -21$ mag. It extends up to the velocity limit, 3000 km s⁻¹, imposed by the capabilities of early-generation radio telescopes to obtain useable HI profiles and gives coverage of the traditional Local Supercluster (de Vaucouleurs, 1953). Figures 3.4 and 3.5 left shows that these galaxies are in majority of type later than Sa. Types come from the HyperLeda database (Paturel et al., 2003). Figure 3.5 right confirms that the heliocentric velocities, v_{hel} from EDD, of these galaxies are mostly less than 3300 km s⁻¹. Among the 683 galaxies available for this third subsample about a quarter comes from the CFS survey. This sample provides a high density and precision map of the Local Supercluster centered on Virgo.
- The next subsample is based on the redshift survey PSCz (Saunders et al., 2000) of sources drawn from a flux-limited sample at 100 μ m obtained with the InfraRed Astronomical Satellite. This point source-redshift sample is constituted of galaxies with far infrared - 60-100 μ m - colors such that their flux arises predominantly from cirrus. The sample is dominated by normal spirals distributed around the Sc type as Figures 3.4 and 3.5 show. The heliocentric velocity limit is 6000 km s⁻¹ to obtain reasonable HI lines with current radio telescopes. This subsample includes the Norma-Hydra-Centaurus and the Perseus-Pisces superclusters in opposite directions and many low latitude galaxies b - offering good coverage above $|b| = 5^\circ$. The bifurcation between our flow direction and a motion towards Perseus-Pisces, highlighted by Erdoğdu et al. (2006), will be located thanks to this subsample. The PSCz sample will also strongly constrain the CMB dipole component within 6000 km s⁻¹. CFS contains the majority (445) of these galaxies.

- The last subsample is constituted of flat galaxies from the catalog of [Karachentsev et al. \(1999\)](#). These edge-on systems have a major to minor axis ratio greater than 7 implying minimal de-projection of their HI linewidths. The flat galaxies are principally of type Scd, as shown in Figures 3.4 and 3.5 left. They constitute a homogeneous class of HI rich systems but they have a low space density because of the strong inclination constraint. Extinction problems existing at optical bands and for ground-based telescopes are practically removed with IRAC channel 1. The whole flat galaxy subsample comes from CFS observations.

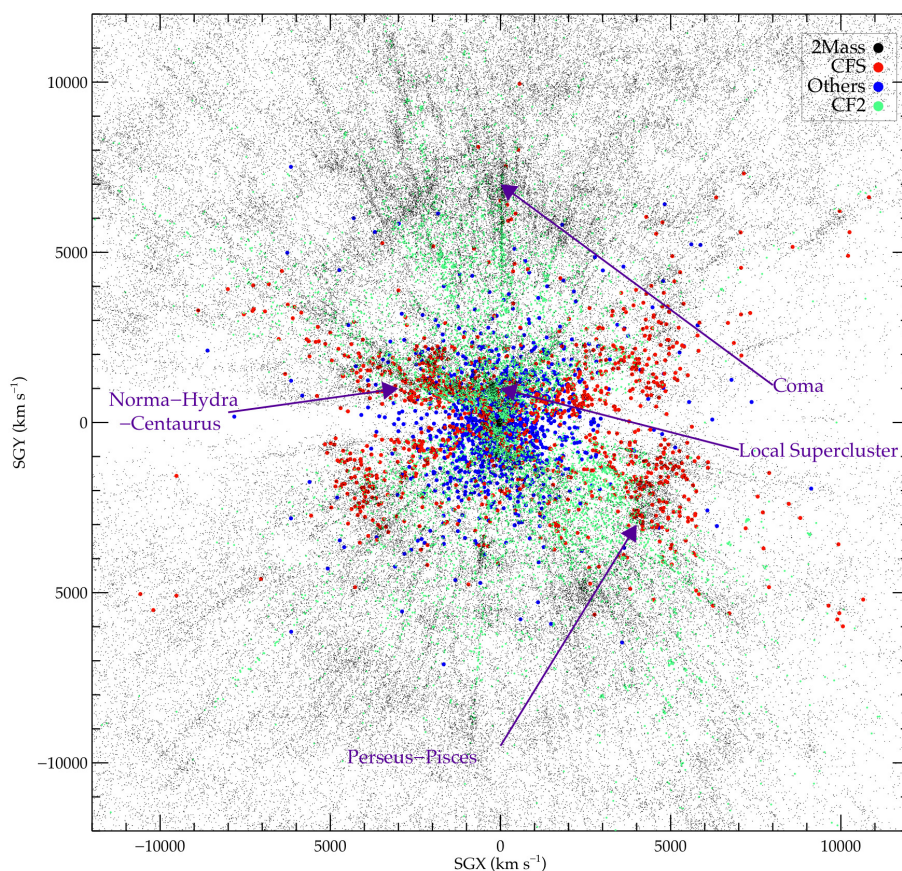


FIGURE 3.6: In the XY supergalactic plane (no restriction on Z), galaxies of the CFS survey (red dots) are superimposed to the 2MASS redshift catalog (tiny black dots) available at EDD. Blue dots stand for galaxies of interests to the Cosmic Flows project but observed by different programs, mostly S⁴G. A few superclusters are identified by violet arrows. CFS gives special attention to galaxies at low galactic latitudes. Green dots represent the second catalog of the Cosmicflows project. Future catalogs of the Cosmicflows project will have a better coverage near the Zone Of Avoidance, reconstructions of the Local Universe will be more accurate in that region.

Figure 3.6 illustrates the combined coverage of CFS and other relevant surveys with *Spitzer Space Telescope*. CFS complements previous surveys with galaxies at low galactic latitudes

for two reasons. First, CFS complements the important S⁴G survey that has a $|b| = 30^\circ$ lower limit. Second, we recognize that photometry from WISE, the Wide-Field Infrared Survey Explorer (Wright, 2008), will be useful but be at a competitive disadvantage to Spitzer in the crowded star fields at lower galactic latitudes because of resolution issues. With Spitzer observations, future catalogs of the Cosmicflows project will contain more data close to the Zone Of Avoidance than the second catalog of the project. This catalog will be discussed at the end of this Chapter but is already superimposed on the same figure.

3.3.2 Spitzer-Adapted ARCHANGEL: a Tool for Surface Photometry

3.3.2.1 Surface Photometry: Definition

Large numbers of pixels complicate simple parameter extractions. A galaxy is spread over a large area of the sky. At some point outer pixels have more sky luminosity (zodiacal light and background contaminants) than galaxy luminosity. Then determining the "sky" level dominates the total magnitude error budget. An analysis of a large galaxy (extending across many pixels) requires surface photometry involving fits of isophotes, lines of constant luminosity. Isophotes are often set to be ellipses (Milvang-Jensen and Jørgensen, 1999). Our interest is with spiral galaxies with types typically between Sa and Scd. A well behaved spiral is approximated by an oblate spheroid that appears circular when viewed face-on and projects to an ellipse when viewed toward edge-on. Galaxy 2D images described by elliptical isophotes can be summed in annuli to reduce to a 1D description. Then, the 1D profiles are fitted by various functions in order to extract the radial surface brightness (SB) distribution, global structure or geometrical characteristics, spatial orientation, stellar populations, characteristics of dust, etc. To obtain apparent magnitudes, de Vaucouleurs (1977) introduced the growth curve, a plot of magnitude within a radius as a function of radius. With an adequate signal to noise ratio, it could be enough to place large apertures around galaxies and sum the total amount of light, minus the sky contribution. In practice, a galaxy luminosity distribution decreases towards larger radii so larger apertures catch more galaxy light but also introduce more sky noise. Some light is inevitably lost below the sky level. Isophotal intensities associated with the galaxy light at large radii are sensitive to the sky setting. Restriction to a smaller radius leads to underestimates of total light. The problem is that galaxies do not have discrete edges.

It is never possible to measure 100% of the light of a galaxy. Measurements are made to an isophotal level dictated by telescope optics, detector, exposure times, and sky brightness. Different authors measure magnitudes to different isophotal levels then often extrapolate to total magnitudes. Our interest is with spiral galaxies for TF use. These galaxies characteristically decay exponentially in luminosity with radius. In an ideal case, light contained within

a specified isophotal level is a simple function of the disk central surface brightness and of the exponential decay scale length. To extrapolate in such a case one can assume that the light at large radii falls off like an exponential disk with a central surface brightness and scale length characterized by a fit to the main body of the galaxy. The estimated contribution lost below the sky level can be added to what is observed to give an extrapolated magnitude (Tully et al., 1996).

The total luminosity in some passband λ is given by:

$$L_T^\lambda = L_{lim}^\lambda + 2\Pi\frac{b}{a}\mu_0 \int_{r_{lim}}^{\infty} r e^{-\frac{r}{\alpha}} dr \quad (3.21)$$

where L_{lim} is the observed luminosity within a limiting isophote, $\frac{b}{a}$ is the isophote axial ratio, μ_0 is the exponential disk central surface brightness, α is the disk scale length, and r is the radius from the center. Performing the integration by parts gives:

$$L_T^\lambda = L_{lim}^\lambda - 2\Pi\frac{b}{a}\mu_0\alpha^2\left[\left(1 + \frac{r}{\alpha}\right)e^{-\frac{r}{\alpha}}\right]_{r_{lim}}^{\infty} \quad (3.22)$$

Relation 3.22 can be transformed to logarithmic units. From definition 3.8, the total magnitude m_T (no limit) is:

$$m_T^\lambda = \mu_0^\lambda - 2.5\log 2\Pi\frac{b}{a} - 5\log\alpha \quad (3.23)$$

where $\mu_0^\lambda = -2.5\log\mu_0$. Then, the magnitude within an isophote corresponding to the radius r is:

$$m_r^\lambda = m_T^\lambda - 2.5\log\left[1 - \left(1 + \frac{r}{\alpha}\right)e^{-\frac{r}{\alpha}}\right] \quad (3.24)$$

At n scale lengths, $\frac{r}{\alpha} = n$, the surface brightness drops by $-2.5\log(e^{-n}) = 1.086 n$. The number of scale lengths observed between μ_0 and $\mu_{r_{lim}}$ is $\Delta n = \frac{\mu_{r_{lim}} - \mu_0}{1.086}$. This gives the extrapolation Δm_{ext} beyond the observed m_r^λ that has to be added to the measured magnitude m_r^λ :

$$\Delta m_{ext} = 2.5\log[1 - (1 + \Delta n)e^{-\Delta n}] \quad (3.25)$$

The fraction of the total light above or below a given isophote depends only on Δn . There is no dependency on α or $\frac{b}{a}$. This exponential fitting model might give an overestimate because: 1) of an additional bulge component so additions to the disk contribute fractionally less to the total light, in that case, profiles deviate at small radii and 2) the disk may truncate at large radii, in that case growth curves deviate from the exponential relation at large radii. These situations are well known (e.g. De Vaucouleurs 1959, Kent 1985). Fortunately, given that Spitzer photometry is already fairly deep, profile extrapolations add only a few percent of the total light. The only extrapolations significant are either for galaxies that extend beyond the field of the instrument or for extremely low surface brightness galaxies which is overall not the case in this work.

3.3.2.2 ARCHANGEL

Schombert (2007); Schombert and Smith (2012) developed ARCHANGEL, a flexible tool for galaxy surface photometry built of a combination of FORTRAN and Python routines. ARCHANGEL performs procedures such as: 1) masking of stars and flaws, 2) ellipse fitting at expanding radii from the galaxy center, 3) compression of 2D information into 1D surface brightness and magnitude growth curves as a function of radius, and 4) extrapolation via fits to the magnitude growth curve at large radii involving rational functions. Position angles and ellipticities are freely determined at each radial step in the development of the growth curve. At large radii noise dominates and position angle and ellipticity are frozen for the remaining outward steps in radius. An interesting feature was implemented in ARCHANGEL in this work concerning the flexibility in where these parameters become frozen so that they may be frozen at all radii. Total magnitudes, the most important product of this analysis, are found to be negligibly affected by position angle and ellipticity details at intermediate radii. Still, an added feature enables to give, directly from the start of the process, position angle and/or ellipticity, would ARCHANGEL not succeed in fitting the galaxy properly otherwise. Comparisons with alternative photometry are discussed in subsection 3.3.5. Figure 3.7 provides an example of masking and ellipse fitting with the Spitzer-adapted ARCHANGEL. Not to underestimate the total luminosity, masked pixels are then filled with the isophote mean luminosity to which they belong.

A significant source of uncertainty arises from the setting of the sky level and will be discussed thoroughly in subsection 3.3.4. In ARCHANGEL the sky is taken as the median of sky boxes placed around the galaxy. This method gives realistic initial sky background estimates (Hall et al., 2012). If targets are modest in size there is reasonable control of the sky level. If the sky is set properly then the magnitude growth curve should go asymptotically flat at large radii. One can also evaluate the sky setting by looking at the Surface Brightness as a function of radius. Surface Brightnesses are not expected to flare or drop precipitously at the sky level, although such occurrences are not phenomenologically excluded (Erwin et al., 2008; MacArthur et al., 2003). Visual inspections of the magnitude growth curve and Surface Brightness dependence with radius ensure an optimal sky setting. Fortunately, sky values are low in Spitzer data, even if we will show in the last section that this problem remains our major source of uncertainty.

An issue related to the sky problem is the matter of the terminal radius of an analysis. A limit to the fitting process can be imposed by signal-to-noise considerations. Integration times permit us to reliably reach a radius $a_{26.5}$ at the isophotal level 26.5 mag arcsec⁻² in the [3.6] band. We try to extend the ellipse fitting to 1.5 $a_{26.5}$ in the [3.6] band. A goal of the program is to assure that the ellipse fitting extends to at least 1.5 $a_{26.5}$, with mosaics if necessary. This [3.6] band dimension is not available before the observation so we rely on a

substitution found to be comparable based on the B band diameter d_{25} , requiring that the observed area extend to a radius $1.5 d_{25}$ (Sheth et al., 2010). ARCHANGEL is then run twice on each galaxy, at first with $1.5 d_{25}$ to obtain a first estimate of $a_{26.5}$ and then again but with the first estimate of $a_{26.5}$. We found the process to be robust as first and second estimates of $a_{26.5}$ are very similar (so are other parameters) except in a few cases (mostly low surface brightness galaxies).

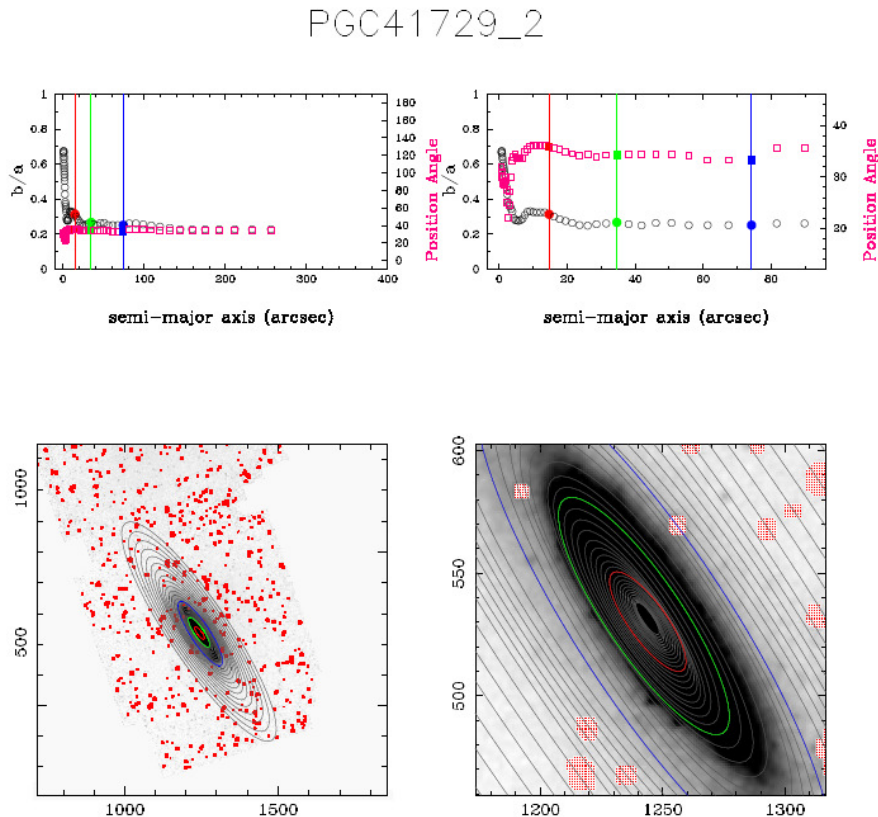


FIGURE 3.7: Output of the ARCHANGEL software showing the axial ratio $\frac{b}{a}$ and the position angle in the two *top* panels and the fitted ellipses and the masking in the two *bottom* panels for PGC41729 or NGC4522.

The mean Surface Brightness in magnitudes per square arcsecond in an annulus at radius r depends on the mean flux in a pixel at that radius $F(r)$ and the mean sky flux in a pixel S :

$$\mu(r) = -2.5 \log\left(\frac{F(r) - S}{0.6}\right) + 21.585 \quad (3.26)$$

where the constant in the denominator provides a conversion from pixels to arcseconds. The other constant 21.585 comes from the fact that pixel size and zeropoint ($F_0 = 280.9$ Jy) for Spitzer Post Basic Calibrated data are constant. The conversion factor C for the flux, from MJy sr $^{-1}$ to Jy per pixel, is equal to 8.461595×10^{-6} for Channel 1 and a pixel size of $0.6''$. As a result, the constant (or zeropoint for the AB system in that precise case) value

is $2.5 \log(\frac{F_0}{C}) = 18.8$ (value for $0.6''$ per pixel) + 2.785 (conversion Vega to AB system from the IRAC Instrument handbook³ and Caputi et al., 2006). At optical bands it is common practice to quote magnitudes in the Vega photometric system but working in the mid-infrared it is more useful to use the AB system. Where comparisons are made between optical and mid-infrared, we use the following transformations (Frei and Gunn, 1994):

$$\begin{aligned} B(Vega) &= B(AB) + 0.163 \\ R_C(Vega) &= R_C(AB) - 0.117 \\ I_C(Vega) &= I_C(AB) - 0.342 \end{aligned} \tag{3.27}$$

ARCHANGEL allows to describe the Surface Brightness as the sum of disk and bulge components. Instead, we choose to restrict to disk fits only. With multiple component fits there are frequently trade-offs such that the overall fit may be satisfactory but the physical meanings of parameters are ambiguous. Usually the dominant radial Surface Brightness characteristic of spiral galaxies is an exponential decay of projected luminosity with radius. Deviations are most frequently seen toward the center where a bulge may become dominant. It is beyond the scope of this program to dissect galaxy images into detailed morphological components because such dissection has negligible effect on the product that most interests us: total magnitudes. We restrict fitting to a rough characterization of the exponential fall-off. Accordingly, surface brightness profiles as a function of radius are fitted by simple straight lines between a_e (radius of the isophote encompassing half of the total light in the [3.6] band) and $a_{26.5}$ (radius of the 26.5 mag arcsec⁻² isophote in the [3.6] band). In rare cases, fits are adjusted by eye, if they are clearly inappropriate between a_e and $a_{26.5}$ after checking that the background brightness variation is not causing any unexpected surface brightness profile changes. Figure 3.8 displays an example of surface brightness fit obtained with ARCHANGEL. μ_0 is obtained by extrapolation as shown by the following relationship:

$$\mu^{[3.6]}(r) = \mu_0^{[3.6]} + 1.0857 \frac{r}{\alpha} \tag{3.28}$$

This corresponds to an exponential profile $L^{[3.6]}(r) = L_0^{[3.6]} e^{-r/\alpha}$. $L_0^{[3.6]}$ and $\mu_0^{[3.6]}$ are the disk central surface brightnesses in intensity and magnitude units respectively. α is the disk scale length and r is the distance from the galactic center. Some concerns may arise about the disk-only fitting technique for bulge galaxies. However, de Jong (1996a) showed that disk-only fits gave unbiased disk parameters relative to a 2D fit decomposition parameters within only 0.5 mag arcsec⁻².

Surface brightness values between two isophotes are then added up to constitute the growth curve. An example of a magnitude growth curve as a function of semi-major axis is shown in

³<http://irsa.ipac.caltech.edu/data/SPITZER/docs/irac/iracinstrumenthandbook/>

Figure 3.8. The light from each succeeding annulus contributes to the (negatively) increasing magnitude with increasing radius. If the sky value is properly set then the growth curve will asymptotically flatten. Should the curve turn over it would be inferred that the sky level is set too high - flux from the galaxy is being attributed to the sky and being removed. Conversely, the sky set too low causes flux from the sky to be attributed to the galaxy and the growth curve will fail to flatten. Given a growth curve as seen in Figure 3.8 it is straightforward to define the useful parameters a_{20} , a_e , and a_{80} enclosing 20%, 50%, and 80% of the light respectively. The associated surface brightnesses, magnitudes and semi-major radii are illustrated in Figures 3.7 and 3.8.

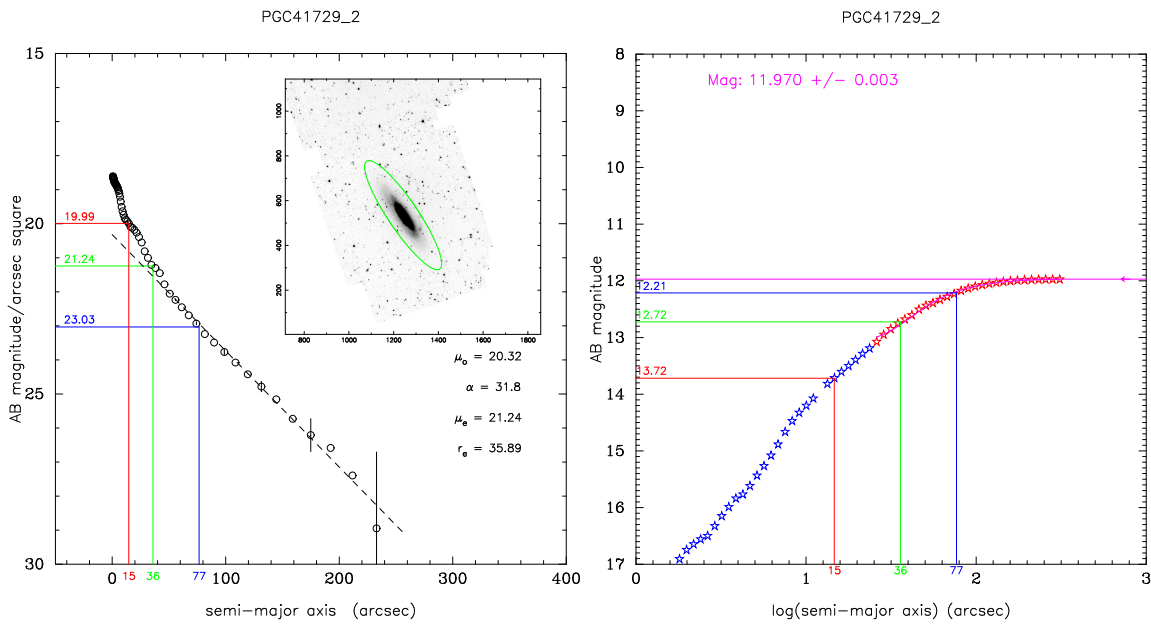


FIGURE 3.8: Example of an ARCHANGEL output surface brightness profile and its disk-only fit between a_e and $a_{26.5}$ at 3.6 microns (*left*) and growth curve (*right*) for PGC41729 or NGC4522. *Left*: parameters of the fit, disk central surface brightness (μ_0) and scale length (α) are listed on the figure. Two more parameters also listed are the effective surface brightness (μ_e) and radius ($r_e = a_e$). No correction has been applied yet to the data. The green ellipse on the inset image represents the 26.5 mag arcsec⁻² isophote at 3.6 microns. *Right*: the incremental growth of the apparent magnitude of the galaxy with radius is shown by the progression of stars. The fit providing an extrapolation to a total magnitude is generated over the domain of the red stars. The level of the total magnitude is shown in magenta. In both panels, red, green and blue lines show the radii enclosing 20%, 50% and 80 % of the total light.

The Spitzer photometry is sufficiently deep that magnitudes in the growth curve approach the total magnitude of the galaxy. One way to extend to the total magnitude uses the procedure built into ARCHANGEL based on interpolations and extrapolations with rational functions. Such functions have a wide range in shape and have better interpolating properties than polynomial functions. They suit data where an asymptotic behavior is expected. The quadratic form/quadratic form, meaning a degree of two in both numerator and denominator is the simplest choice. The asymptotic magnitude is the ratio of the second order coefficients of the

numerator and denominator. However, rational functions are non-linear. They can produce vertical asymptotes due to roots in the denominator that are to be ignored. Fit uncertainties are given by the standard error of the estimate $SEE = \sqrt{\frac{1}{n} \sum_{i=1}^n (m(r_i)_{fit} - m(r_i)_{measured})^2}$. Because of the convergence problem that can occur with rational functions, we provide in total three magnitudes that approximate the global magnitude of the galaxy: $[3.6]_{26.5}$, an isophotal magnitude that directly measures the light within a reliably attained radius, $[3.6]_{tot}$, a "total" magnitude given by the asymptote of the ARCHANGEL rational function extrapolation, and $[3.6]_{ext}$, an "extrapolated" magnitude assuming a continuation of the exponential disk beyond the radius of the isophote 26.5 mag arcsec⁻² obtained with equation 3.25. The relative merits of these magnitudes will be discussed in subsection 3.3.4. Other products are the average Surface Brightness within a_e and a_{20} and a concentration index $C_{82} = a_{80}/a_{20}$. Table 3.2 gives the parameters that are extracted for the galaxy used as an example in Figures 3.7 and 3.8 and illustrates what is seen in a single row in the catalog "Spitzer [3.6] Band Photometry" at EDD and in Appendix A (although restricted to twenty entries and simplified: common name, date and exposure time are absent). Capabilities within EDD allow a user to link to other catalogs, thereby accessing all manner of information about each target.

Figure 3.9 gathers as examples the three outputs obtained with ARCHANGEL for five galaxies, each one of them belonging to at least one of the five subsamples of the CFS program.

| 1 | 2 | 3 | 4 | 5 | 6 | 7 | 8 | 9 | 10 |
|-------|---------|-------------------------|-----|------------|----------------|---------------|------------|---------------|---------|
| PGC | Name | Date | Exp | $a_{26.5}$ | $[3.6]_{26.5}$ | $[3.6]_{tot}$ | σ_m | $[3.6]_{ext}$ | μ_0 |
| 41729 | NGC4522 | 2007.02.14T14:46:36.378 | 240 | 181 | 11.98 | 11.970 | 0.003 | 11.957 | 20.32 |

| 11 | 12 | 13 | 14 | 15 | 16 | 17 | 18 | 19 | 20 | 21 | 22 | 23 | 24 |
|----------|------|----------------|----|----------|------------|-------|---------|-------------------------|----------|------------|----------------------------|----------|---------|
| α | b/a | $\sigma_{b/a}$ | PA | a_{80} | μ_{80} | a_e | μ_e | $\langle \mu_e \rangle$ | a_{20} | μ_{20} | $\langle \mu_{20} \rangle$ | C_{82} | RefLink |
| 31.8 | 0.26 | 0.01 | 34 | 77 | 23.04 | 36 | 21.24 | 20.31 | 15 | 19.99 | 19.53 | 5.2 | SSOV |

TABLE 3.2: Extracted photometry parameters. (1) Principal Galaxies Catalog number, (2) common name, (3) date of Spitzer observation, (4) nominal total integration, seconds (actual time collecting photons somewhat less), (5) $a_{26.5}$: major axis radius at isophote 26.5 mag arcsec⁻², (6) $[3.6]_{26.5}$: AB magnitude within $a_{26.5}$, (7) $[3.6]_{tot}$: total AB magnitude from rational function asymptote, (8) σ_m : root mean square deviations, rational function fit, (9) $[3.6]_{ext}$: total AB magnitude by extrapolating flux beyond $a_{26.5}$ assuming continuance of exponential disk, (10) μ_0 : central disk surface brightness from inward extrapolation of disk fit, mag arcsec⁻², (11) α : exponential disk scale length, arcsec, (12) b/a: ratio of minor to major axes, (13) $\sigma_{b/a}$: uncertainty in axial ratio, (14) PA: position angle of major axis, deg. (15) a_{80} : major axis radius of annulus enclosing 80% of total light, arcsec, (16) μ_{80} : surface brightness at a_{80} , mag arcsec⁻², (17) a_e : 'effective radius', major axis radius of annulus enclosing 50% of total light, arcsec, (18) μ_e : surface brightness at a_e , mag arcsec⁻², (19) $\langle \mu_e \rangle$: average surface brightness within a_e , mag arcsec⁻², (20) a_{20} : major axis radius of annulus enclosing 20% of total light, arcsec, (21) μ_{20} : surface brightness at a_{20} , mag arcsec⁻², (22) $\langle \mu_{20} \rangle$: average surface brightness within a_{20} , mag arcsec⁻², (23) C_{82} : concentration index, a_{80}/a_{20} , (24) Spitzer program link.

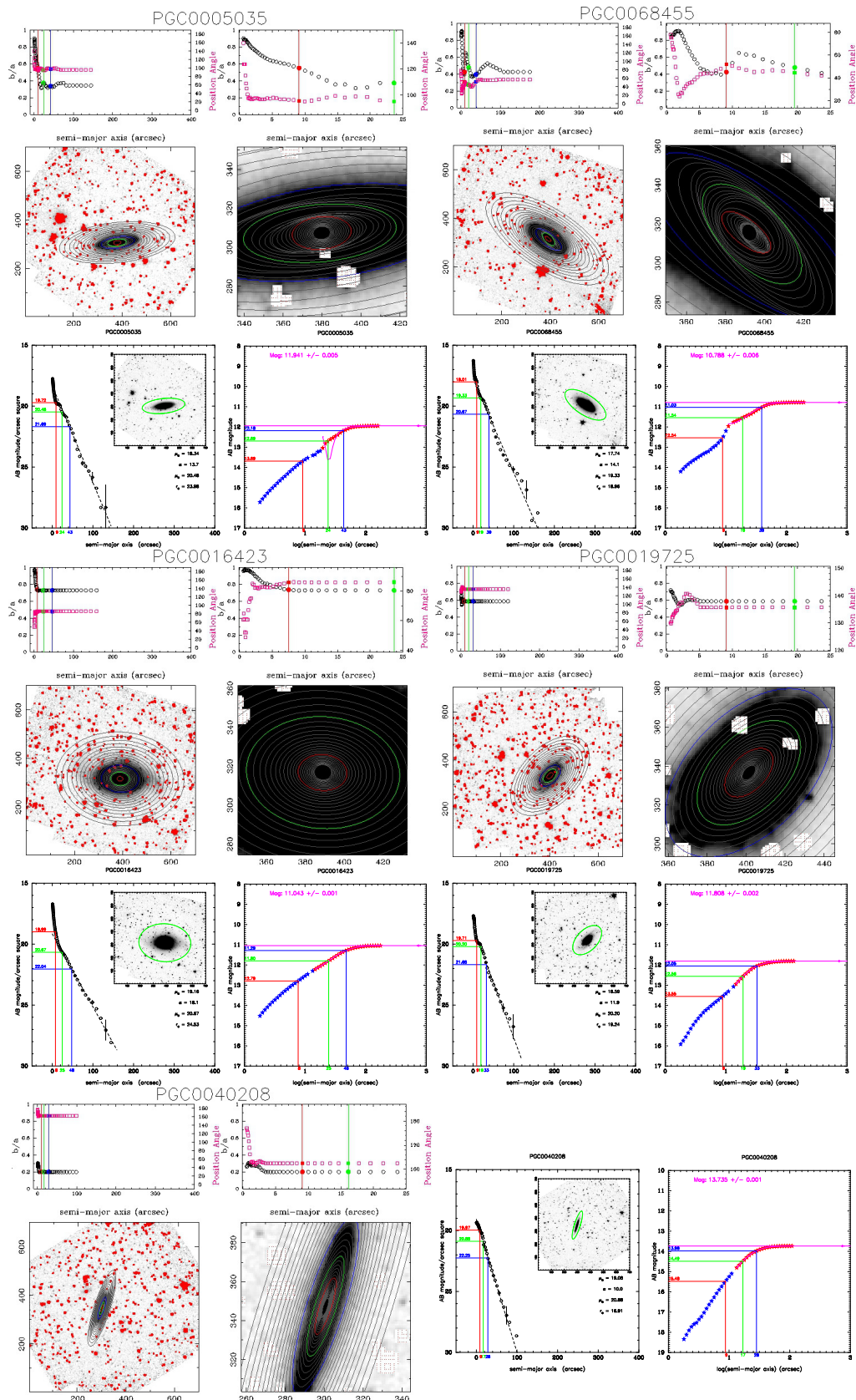


FIGURE 3.9: Surface photometry outputs from the ARCHANGEL software. PGC0005035 is from the Calib subsample. PGC0016423 has hosted at least one supernovae of Type Ia. PGC0068455 and PGC0019725 are in the V3k and PSCz catalogs respectively. PGC0040208 is a flat galaxy. For each galaxy, the variations of the position angle and of the b/a ratio are given as a function of the radius in arcsec. The masks is shown in red on top of the galaxy images and the fitted ellipses are in black. Surface brightness profiles, growth curves and their fits are represented. In every plot, except for the insert in the growth curve plot, red, green and blue colors show the annuli encompassing 20, 50 and 80% of the light. On the insert, the green ellipse is the isophote at $26.5 \text{ mag arcsec}^{-2}$ in the $[3.6]$ band.

3.3.2.3 Some Analyses

In this subsection, we focus mostly on the Cosmicflows with Spitzer sample although the additional Spitzer archival galaxies minus S⁴G's are processed equally. We present the different parameters derived with the software ARCHANGEL for each one of the CFS galaxies. We claim at the beginning of subsection 3.3.1.2 that we choose to observe each galaxy to within at least twice d_{25} to capture most of galaxy lights and to minimize magnitude measurement uncertainties. Then, we force ellipse fitting up to $1.5 \times a_{26.5}$. Figure 3.10 confirms that d_{25} from the third reference catalog (RC3) in EDD, used to set observations, and $a_{26.5}$ obtained after reduction are comparable representatives of size. The scatter is only 41 arcseconds around a 1:1 linear relation. The observational sensitivity is sufficient for our ultimate goal since at 26.5 mag arcsec⁻² the isophotal magnitude is already very close to extrapolated ones on Figure 3.11. We will show this in more details in subsection 3.3.4.

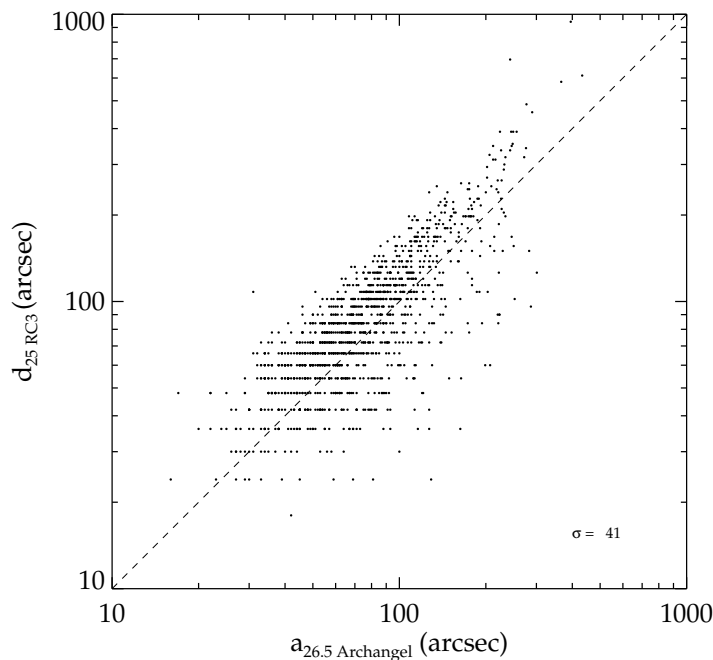


FIGURE 3.10: Comparison between the radius in arcsecond of the isophote at 26.5 mag arcsec⁻² in the [3.6] band, obtained after reduction with ARCHANGEL, and the radius at 25 mag arcsec⁻² at B band used beforehand to set observational parameters. These parameters are proportional to each other. In the case of an optimal 1:1 linear relation, the scatter is only 41 arcseconds.

Histograms of the other parameters are given in Figure 3.12 in mag arcsec⁻² for surface brightnesses and in arcseconds for corresponding radii. For all these parameters there is no outliers.

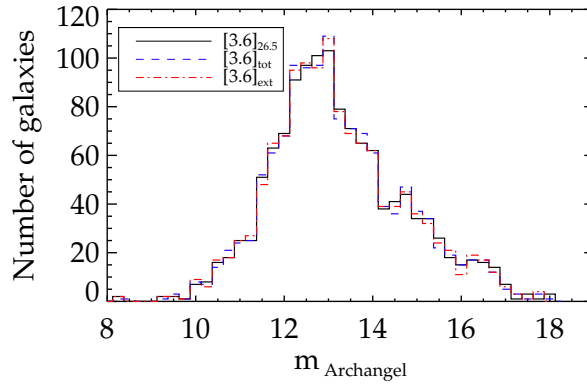


FIGURE 3.11: Histograms of the three magnitudes derived with ARCHANGEL. The magnitude at the 26.5 mag arcsec⁻² isophote at 3.6 μ m, $[3.6]_{26.5}$ (black straight line), the magnitude obtained by the extrapolation of the growth curve, $[3.6]_{tot}$ (blue dashed line) and the magnitude assuming a continuous exponential disk, $[3.6]_{ext}$ (red dotted-dashed line).

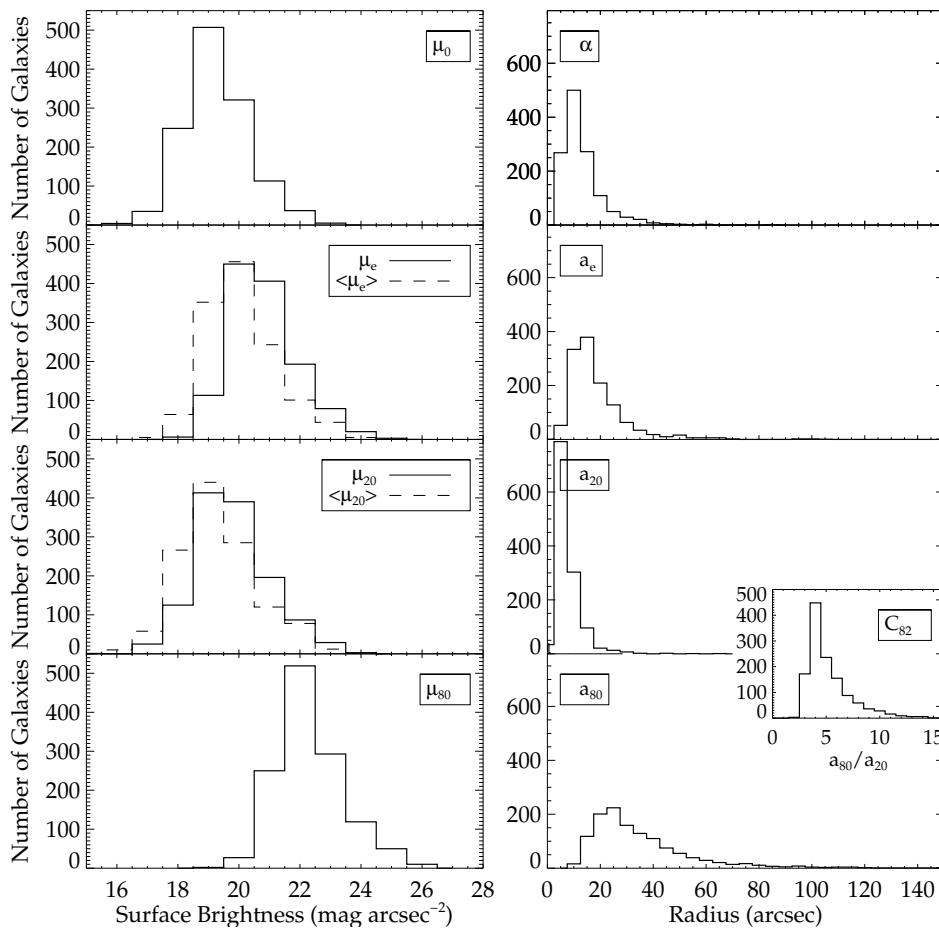


FIGURE 3.12: Histograms of some of the parameters computed with the ARCHANGEL software. *Left, from top to bottom*, histograms in solid lines of the central disk surface brightness μ_0 and of the surface brightnesses at 50, 20 and 80% of the total light μ_e , μ_{20} and μ_{80} (mag arcsec⁻²). Histograms of the average of the surface brightnesses between 0 and 50 and 20% of the light, $\langle \mu_e \rangle$ and $\langle \mu_{20} \rangle$ respectively, are overplotted in dashed lines. *Right, from top to bottom*, disk scale length α and annuli encompassing 50, 20 and 80% of the light a_e , a_{20} and a_{80} , in arcseconds. The histogram of the concentration index, $C_{82} = a_{80} / a_{20}$ is overplotted in a small panel on the right side of the a_{20} and a_{80} histograms.

One specificity of the adapted version of ARCHANGEL is the computation of the minor to major axis, b/a , ratio which is defined as the mean of the b/a ratios between 50% and 80% of the light. Measuring b/a ratios is not an easy task and a comparison with the ratios from the HyperLeda Database in B-band on Figure 3.13 left shows that at least one b/a source cannot be trusted. Each value needs to be checked before any usage. The initiated Citizen Science Project to order galaxies by inclinations to which we contribute will be most useful. Position angles on the other hand are in good agreements on the right of the same Figure.

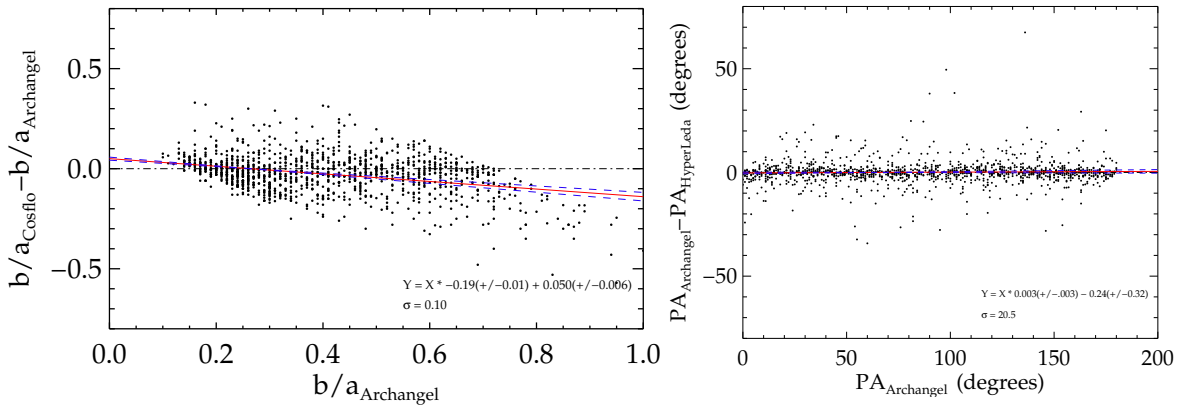


FIGURE 3.13: *Left*: Residual between Cosmicflows program b/a ratios and the b/a ratios obtained with ARCHANGEL versus ARCHANGEL's b/a ratios. *Right*: Differences between ARCHANGEL-derived position angles and HyperLeda's versus ARCHANGEL's. The black dotted-dashed lines show the perfect case $y=0$, the red straight lines are linear fits to the data (with a 3σ clipping (20 galaxies) in the right panel), the blue dashed lines are the 1σ uncertainties.

3.3.3 Corrected Magnitudes and Surface Brightnesses

Several effects affect light as it travels towards us. Apparent magnitude measurements [3.6] need to be corrected for these effects. Corrected apparent magnitudes [3.6]^{*b,k,i,a*} for Spitzer IRAC channel 1 data are given by:

$$[3.6]^{b,i,k,a} = [3.6] - A_b^{[3.6]} - A_i^{[3.6]} - A_k^{[3.6]} + A_a^{[3.6]} \quad (3.29)$$

with $A_b^{[3.6]}$ galactic extinction correction, $A_i^{[3.6]}$ internal extinction correction, $A_k^{[3.6]}$ k -correction, and $A_a^{[3.6]}$ aperture correction. All these terms are described in details hereafter in different subsections. Briefly, extinction is due to the reduction in a source apparent brightness by absorption, scattering or radiation as light travels towards us. Only in extreme cases, light is totally extinguished. Attenuation would be a more appropriate term. There are several potential sources of extinction such as Earth atmosphere, Milky-Way and target galaxy dust. Spitzer is in space which prevents any atmospheric extinction. The k -correction is a term to correct for the reddening of light due to the universe expansion and the aperture correction is a particularity of the instrument.

Disk central surface brightnesses will be the object of study in subsection 3.3.6 and its measurements also need to be corrected. Inclination effects are quite confusing at optical band because the path length of observed surface brightnesses, varying with the line-of-sight, and extinction, work in opposite way on measured μ_0 values. At 3.6 microns we can assume the obscuration to be negligible and therefore only the geometric effect of the inclination on surface brightnesses needs to be taken into account. We measure the face-on $\mu_0^{[3.6],a,i}$ as follows:

$$\mu_0^{[3.6],a,i} = \mu_0^{[3.6],a} - 2.5C^{[3.6]}\log\left(\frac{b}{a}\right) \quad (3.30)$$

with $C^{[3.6]}=1$ accordingly (intrinsic extinction negligible), $\frac{b}{a}$ the axial ratio and $\mu_0^{[3.6],a}$ the disk central surface brightness corrected for aperture as described in the following subsections.

3.3.3.1 Galactic Extinction Correction

The InterStellar Medium consists of small dust particles with diameters between 0.01 and 1 μm . They scatter, absorb and re-emit light. Blue light is more strongly scattered and absorbed than red light. Sources appear dimmer and redder. Schlegel et al. (1998) mapped this effect. The resulting galactic extinction and reddening map is an exquisite tool to compute extinction correction. To obtain this map, they combine the far-infrared emission (100 μm) of InfraRed Astronomical Satellite, the Diffuse InfraRed Background Experiment on COsmic Background Explorer satellite and the colors of background galaxies from Automated Plate Measurement Galaxy Survey. The colors allow dust normalization to E(B-V) reddening in magnitudes. Diffuse InfraRed Background Experiment provides absolute calibration across several passbands. It maps the dust color temperature and converts the 100 μm emission to dust column density. The relationship between ultraviolet/optical extinction and far-infrared emission depends on the grain size distribution. Then, assuming that the dust grain size distribution is everywhere the same and using the mean value in the diffuse InterStellar Medium given by Cardelli et al. (1989), galactic extinction depends only on object coordinates and observational wavelengths λ . The InfraRed Science Archive provides an online tool at <http://irsa.ipac.caltech.edu/applications/DUST/> with these 100 μm cirrus maps that supply us with the differential reddenings $E(B - V)$. We use the correction term given by Cardelli et al. (1989) accounting for a small shift to the centroid of the Spitzer passband:

$$A_b^{[3.6]} = R_{[3.6]}E(B - V) \quad (3.31)$$

with $R_{[3.6]} = 0.20$. Galactic extinction magnitude corrections at [3.6] are only 9% compared to those at I_C and 4% of the corrections at B . Corrections at latitudes above 15° are almost always 0.05 magnitude or less, with uncertainties around 0.01 magnitude.

3.3.3.2 Internal Extinction Correction

Internal extinction is usually the greatest concern. Galaxies of the same intrinsic size and luminosity appear dimmer when seen edge-on because path lengths through their own absorbing dust increase. Fortunately, in the infrared such extinction is very small. [Giovanelli et al. \(1997b, 1995\)](#) showed that there is a luminosity dependence to galaxy internal obscurations (high-luminosity cases are more reddened). [Tully et al. \(1998\)](#) confirmed and provided an alternative description of the effect. There is a subtle problem because absolute magnitudes (luminosities) are not known a priori. They are a product of the analysis. [Tully et al. \(1998\)](#) framed magnitude corrections in term of a distance-independent surrogate, the linewidth parameter, W_{mx}^i . Accordingly, the internal extinction correction can be written:

$$A_i^{[3.6]} = \gamma_{[3.6]} \log(a/b) \quad (3.32)$$

where $\gamma_{[3.6]}$ is:

$$\gamma_{[3.6]} = 0.10 + 0.19(\log W_{mx}^i - 2.5) \quad (3.33)$$

if $W_{mx}^i > 94 \text{ km s}^{-1}$ and $\gamma_{[3.6]} = 0$ otherwise. W_{mx}^i is defined by equations [3.19](#).

There is an advantage to this formulation of the internal extinction. If the inclination is underestimated, $\log(a/b)$ is underestimated driving $A_i^{[3.6]}$ low but then W_{mx}^i is overestimated which drives $\gamma_{[3.6]}$, hence $A_i^{[3.6]}$ up. The two terms in $A_i^{[3.6]}$ are affected in opposite directions. Regardless, internal absorption corrections are always small, rarely reaching 0.1 magnitude at $3.6 \mu\text{m}$. Uncertainties in these corrections are less than 0.02 magnitude.

3.3.3.3 K-Correction

A wavelength emitted at a redshift z increases by a factor $(1+z)$ by the time it reaches us. As galaxy emissions depend on the wavelength (confer non-flat spectral energy distributions), the received amount of light in a given finite band might be incorrect. It is over/underestimated unless some k -correction is applied (e.g. [Oke and Sandage, 1968](#)). k -correction depends on spectral energy distribution, redshift and observing passband. The derivation of k -corrections are generally based on the template fitting of observed spectral energy distributions. They require redshift and color photometry (at least one) or morphological type to build a template (e.g. [Blanton and Roweis, 2007](#); [Chilingarian et al., 2010](#); [Cowie et al., 1994](#); [Han, 1992a](#)). Our interest lies with spiral galaxies, a k -correction based on morphological type is ideal. [Huang et al. \(2007\)](#) happened to develop eleven model Spectral Energy Distributions ranging from a pure early template, i.e. an old "early-type" stellar population as might be found in an elliptical galaxy or spiral bulge, to a pure late template, i.e. a mix of stars and interstellar emission as might be found in "late-type" spiral galaxy disk. Convolving each one of the

spectral energy distributions with IRAC filter functions, they show a linear dependence of the k -correction with redshift at $3.6 \mu\text{m}$. In addition, this linear dependence is independent of the galaxy type at small redshifts, at this position on the Rayleigh-Jeans tail of the spectral energy distribution of star light. We use the low- z formulation by [Huang et al. \(2007\)](#):

$$A_k^{[3.6]} = -2.27 z \quad (3.34)$$

with z the galaxy redshift. Uncertainties are at the level of 0.01 magnitude or less.

3.3.3.4 Aperture Correction

The fourth and last adjustment is the aperture correction. Aperture corrections are required for extended source photometry with Spitzer (e.g. galaxies) because their absolute calibrations are tied to point sources with IRAC observations. There is extended emission from the Point Spread Function outer wings, and the scattering of the diffuse emission across the focal plane that is captured by the extended source photometry but not by the calibrations on point sources. Since the photometry is normalized to $12''$ apertures, a correction must be applied for large apertures ([Reach et al., 2005](#), and IRAC Instrument Handbook)⁴. For an effective aperture radius r in arcseconds, the channel 1 IRAC extended source aperture correction recommended is:

$$F_{IRAC\ true} = F_{IRAC\ measured} \times (ae^{-r^b} + c) \quad (3.35)$$

where $a = 0.82$, $b = 0.37$ and $c = 0.91$. Then the extended source aperture correction in magnitudes is:

$$A_a^{[3.6]} = -2.5 \log(ae^{-r^b} + c). \quad (3.36)$$

The average correction for galaxies of interest to our program is 0.10. The variations on this correction from source to source for our galaxies, which are typically larger than $1'$, is 0.01 magnitudes and 10% relative uncertainties in the adjustment are negligible.

Regarding surface brightnesses, fluxes need to be corrected directly with equation 3.35 before using relations 3.26, 3.28 and 3.30. The correction is very small for IRAC channel 1. For example, the disk central surface brightness of PGC7544 shown in Figure 3.14 becomes 18.10 after correction against 18.06 before. This is largely within the retained uncertainty ($0.5 \text{ mag arcsec}^{-2}$) on disk central surface brightness measurements for the project developed in subsection 3.3.6.

⁴<http://irsa.ipac.caltech.edu/data/SPITZER/docs/irac/iracinstrumenthandbook/>

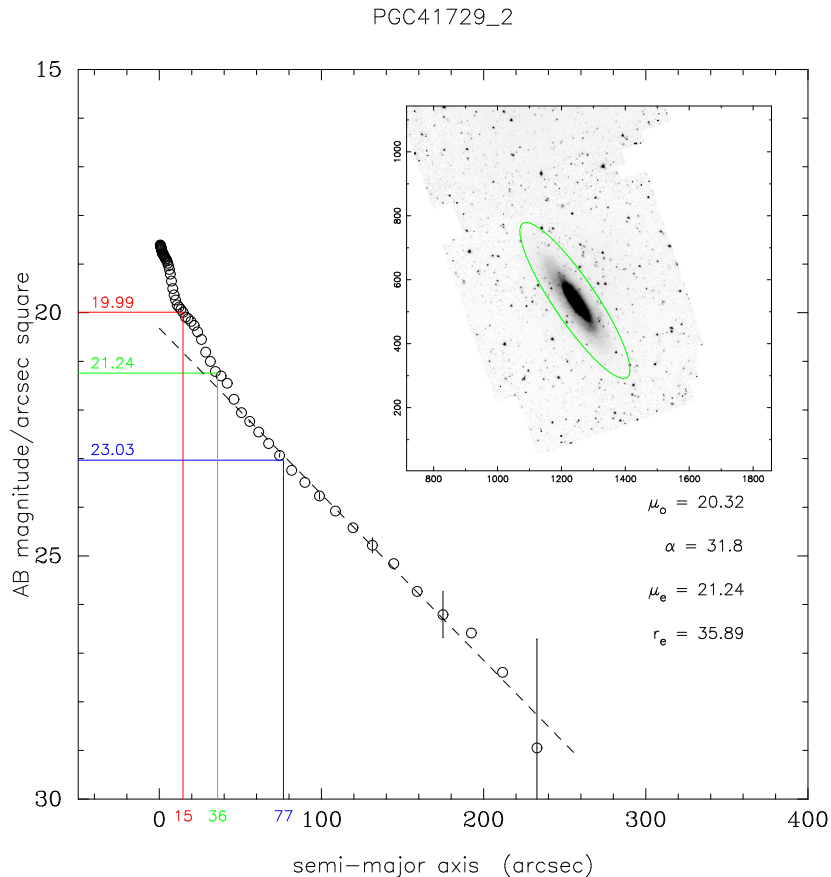


FIGURE 3.14: Example of an ARCHANGEL output surface brightness profile and its disk-only fit between a_e and $a_{26.5}$ at 3.6 microns for PGC7554. Parameters of the fit, disk central surface brightness (μ_0) and scale length (α) are listed on the figure. Two more parameters also listed are the effective surface brightness (μ_e) and radius ($r_e = a_e$). No correction has been applied yet to the data. Radii enclosing 20%, 50% and 80 % of the total light are given by red, green and blue lines. The green ellipse on the inset image represents the 26.5 mag arcsec⁻² isophote at 3.6 microns.

3.3.4 Uncertainties

An extremely important virtue of the Spitzer [3.6] band photometry is the robustness of the luminosity measurements (a) with uniformity across the sky, (b) with inclusiveness of target light because of the sensitivity, and (c) because adjustments are small. There was a discussion of uncertainties associated with the different corrections in the previous subsections and it can be summarized that as long as sources are not in extremely obscured regions of our Galaxy ($A_b^{[3.6]} < 1$) then the global *uncertainty* in adjustments is at the level of 0.03 magnitude or less, with internal absorption within sources dominant in the error budget. The IRAC handbook gives a 2 – 3% error on the absolute flux calibration (excluding the aperture correction), but more importantly for this program, it claims photometry is repeatable across the sky at the 1% level.

Among our parameters we determine isophotal, "total", and "extrapolated" magnitudes. The latter two both approximate the global magnitude, the "total" from the rational function asymptote of the growth curve and the "extrapolated" from the extension of the exponential disk fit beyond the radius of the isophotal magnitude. By construction, $[3.6]_{26.5}$ is fainter than $[3.6]_{ext}$ and should be fainter than $[3.6]_{tot}$. The average difference $\langle [3.6]_{26.5} - [3.6]_{ext} \rangle = 0.016$ magnitude corresponds to a typical disk fit of 6.2 exponential scalelengths at the 26.5 mag arcsec⁻² isophote. The typical *uncertainty* in this extrapolation is below 0.01 magnitude except if the target is extremely low surface brightness. Surface Brightness profiles of spirals can depart from a pure exponential at large radii, either with flares or truncations and because of the interplay between bulges and disks (Kent, 1985). Yet because such a large fraction of the flux is captured by the deep Spitzer integrations the differences between measured isophotal and extrapolated magnitudes are so small as to leave little room for uncertainty in the extrapolation.

By comparison, $\langle [3.6]_{26.5} - [3.6]_{tot} \rangle = 0.007$ magnitude, that is, $[3.6]_{tot}$ is fainter than $[3.6]_{ext}$ by 0.009 magnitude on average. The root mean square scatter is 0.018 magnitude between these alternative measures. The differences are primarily due to a slight instability in the rational function fits. We give preference to the *exponential disk extrapolations*.

We turn to what is probably the largest source of error, the determination of the "sky" level. With observations in space at [3.6] band this noise level is dominated by diffuse zodiacal light and discrete high redshift galaxies. The discrete contaminants can be easily seen to very faint levels in regions beyond the galaxy. They are less easy to see and exclude if they are superimposed on the target galaxy. A major task before running a surface photometry analysis is the removal of contaminants like foreground stars and background galaxies. Our approach is to not be too aggressive with the removal of contaminants. We remove contaminants as best we can on the target and remove contaminants in the adjacent sky to the same level, leaving in place fainter sources since such sources must also be hidden within the galaxy.

It was described in the section on ARCHANGEL photometry that sky settings were established from the median of pixel fluxes in boxes placed around the galaxy and validated by the nature of the magnitude growth curve (it should go asymptotically flat) and the surface brightness profiles (flares or cutoffs as noise dominance are approached as suspicious but not considered a conclusive sign of bad sky setting). In order to generate a quantitative test of the effects of sky variance we have run Spitzer-adapted ARCHANGEL on 235 galaxies, part of the Tully-Fisher calibrator sample defined in Tully and Courtois (2012). This sample contains only a few low surface brightness and irregular galaxies.

A first run gives us the sky value S and its uncertainty σ_{sky} . We run ARCHANGEL two more times with sky values of $S \pm \sigma_{sky}$ respectively for each one of our selected galaxies. This

gives us three extrapolated magnitudes that we call $[3.6]_0$, $[3.6]_+$, and $[3.6]_-$. Figures 3.15 and 3.16 show the variation of $(|[3.6]_0 - [3.6]_-| + |[3.6]_0 - [3.6]_+|)/2$ as functions of type and apparent magnitude. These plots show the sensitivity to the choice of sky value and that this sensitivity becomes particularly acute for low surface brightness systems. The galaxies of type Sd, identified in the plots as low surface brightness galaxies, and the Magellanic irregular galaxies are clear outliers. There are also three galaxies with very bright objects nearby that could influence the sky level with stray light and might explain their position in Figure 3.16. These three are retained in the calculations of the offset and scatter since they are typical spiral galaxies but the low surface brightness and irregular galaxies are excluded. Magnitude uncertainties due to the sky error are of the order 0.04 ± 0.02 . Uncertainties with low surface brightness and irregular galaxy magnitudes tend to be more important which is understandable. Low surface brightness galaxies have by definition surface brightness values closer to that of the sky and irregular galaxies not only tend to be low surface brightnesses but in addition might not be well described by elliptical isophotes. Changing the sky value a little might change the measured flux considerably toward the external part of such galaxies. Low surface brightness and irregular galaxies apart, Figure 3.16 indicates that uncertainties do not strongly increase at fainter magnitudes.

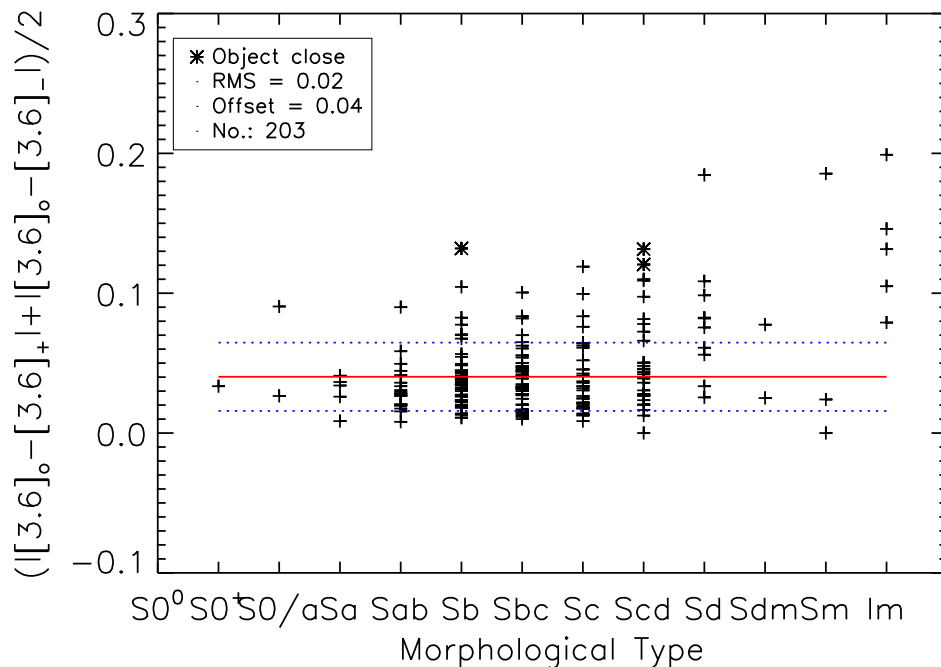


FIGURE 3.15: Variation of magnitude uncertainty as a function of morphological type. The mean offset of 0.04 magnitude and root mean square scatter of 0.02 magnitude indicated by the solid red and dotted blue lines respectively excludes types Sd and later. Three cases with contamination from nearby bright objects are indicated by asterisks. The scatter is asymmetric about the mean since an absolute value difference from the fiducial value cannot be less than zero.

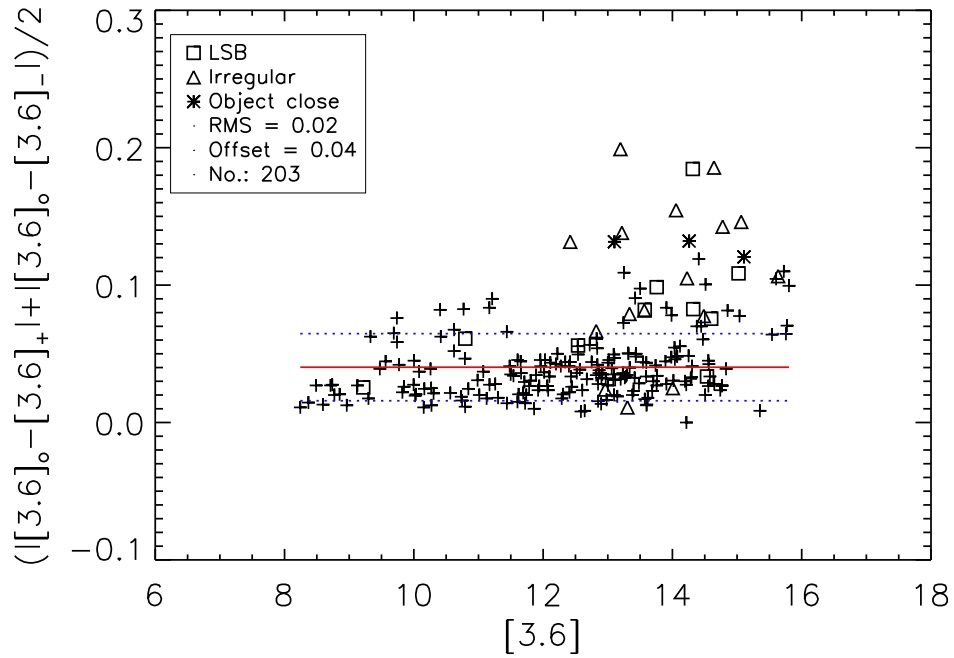


FIGURE 3.16: Variation of magnitude uncertainty as a function of magnitude. Type Sd systems, here referred to as low surface brightness galaxies, are represented by squares and types Sdm-Sm-Im irregular galaxies are represented by triangles. Asterisks locate galaxies with a very bright object close to them. The mean offset and scatter lines have the same meaning as in the previous figure.

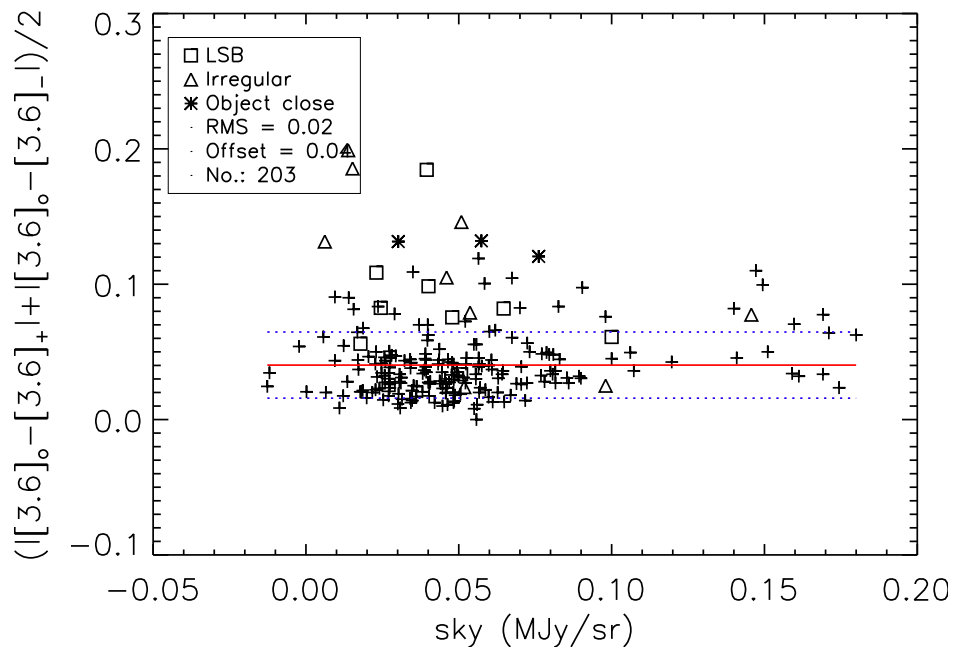


FIGURE 3.17: Variation of magnitude uncertainty as a function of the sky value in MJy sr^{-1} . Squares represent low surface brightness galaxies while triangles stand for irregular ones. Galaxies represented by asterisks are galaxies with a very bright object close to them. Sky values can be four times higher than on average without resulting in abnormally high uncertainty in magnitudes.

Next we test for uncertainties in magnitude due to the sky against the sky value itself, as well as against the isophotal semi-major axis in the [3.6] band $a_{26.5}$, inclination from face-on, and apparent area defined as the area of the ellipse at $a_{26.5}$ to see if any trends exist. The results in Figures 3.17 and 3.18 show no correlation. In Figure 3.17, we can see that the uncertainty in magnitude does not depend on the sky value. We checked for a dependence on sky uncertainty and find no correlation. These results suggest that the total and extrapolated disk apparent magnitudes are adequate (we do not show the plots for both magnitudes here as they are very similar). In any case, the highest sky values are relatively moderate (< 0.20 MJy sr $^{-1}$). One can also notice that sky values and sky uncertainties are not correlated, evidently a reflection of the relative uniformity of background across dimensions of 5 – 10 arcminutes. Structure in the background could be a worse problem when the sky setting is very low. Perhaps it is a surprise that the uncertainty is not proportional on the galaxy apparent area (Figure 3.18, bottom). The more pixels that are affected by changing the sky value, the more the magnitude might change. In any case, these tests indicate that magnitude uncertainties can be taken to be approximately constant for all normal spiral galaxies.

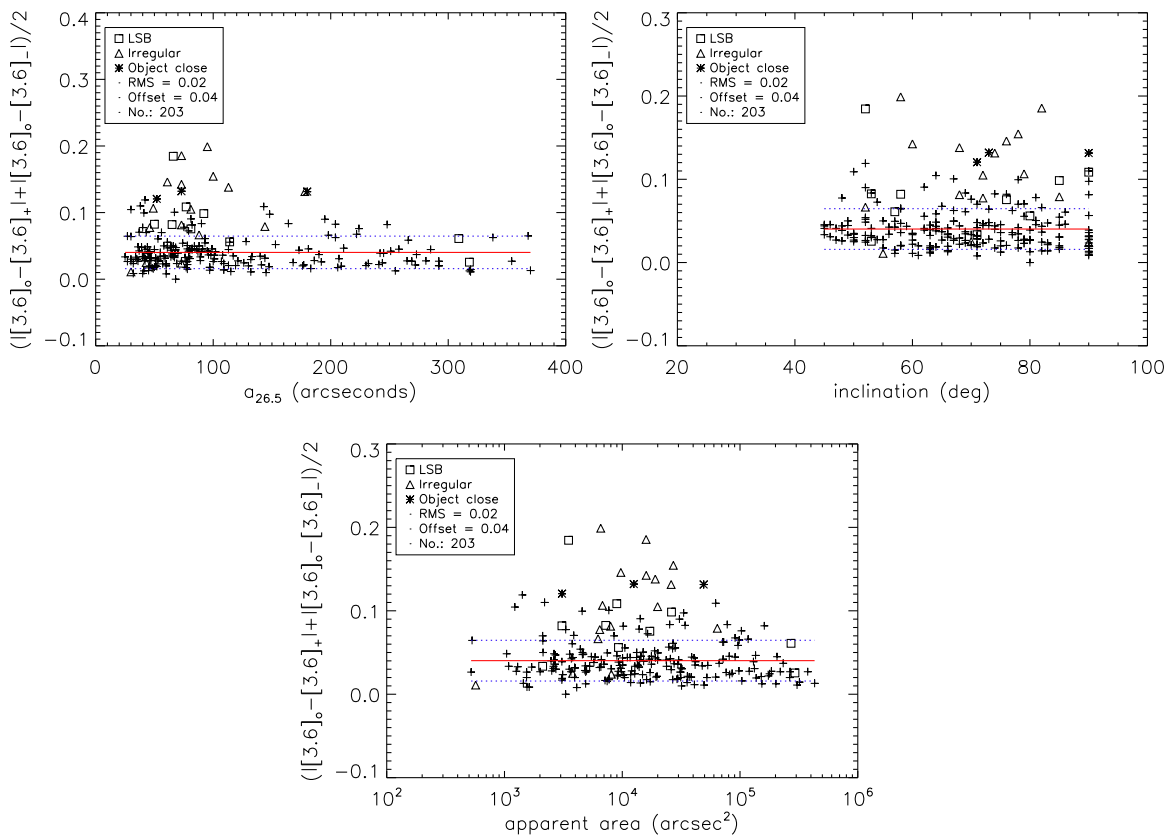


FIGURE 3.18: Variation of magnitude uncertainty as a function of three galaxy characteristics: (*top left*) semi-major axis, (*top right*) inclination, and (*bottom*) apparent area. Squares, triangles and asterisks represent low surface brightness, irregular, and possibly contaminated galaxies respectively. There is no apparent correlation between the magnitude uncertainty and the radius, inclination, or apparent area of a galaxy.

Regarding surface brightness uncertainties, we have seen that concerns, which might have arise about the disk-only fitting technique, are not very relevant. Since [de Jong \(1996a\)](#) showed that disk-only fits gave unbiased disk parameters relative to a 2D fit decomposition parameters within $0.5 \text{ mag arcsec}^{-2}$ and because the background (distant galaxies and zodiacal light) uncertainties lead to a small magnitude uncertainty even for IRAC channel 1, we retain an uncertainty budget of $0.5 \text{ mag arcsec}^{-2}$ for $\mu_0^{[3.6]}$ measurements.

3.3.5 Comparisons with Other Pipelines

Our ARCHANGEL analysis procedures can be compared with other reductions of Spitzer observations. Comparisons with magnitudes found by the projects SINGS ([Muñoz-Mateos et al., 2009](#)), CHP ([Freedman et al., 2011](#), private communication) and S⁴G ([Muñoz-Mateos, in prep.](#)) show that the Cosmicflows project is on the same magnitude scale as all these projects. In the case of CHP we give special attention to a comparison because CHP and CFS, have the common ambition of measuring galaxy distances. We do the same with S⁴G as we take directly magnitudes derived from their pipeline. As we go forward, we want to understand to what degree the alternative photometry analyses are interchangeable. A comparison is given between the sources in [Figure 3.19](#). There is a slight tendency for CHP values to be brighter for the largest galaxies, with essentially no difference faintward of $[3.6] = 12$. The most likely explanation for a difference with the bright and large galaxies is small differences in the way sky values are set. The root mean square scatter in the differences (6 deviant points rejected) is ± 0.052 which, if attributed equally, implies an uncertainty in an individual measurement of ± 0.037 magnitude for each source. S⁴G values tend to be dimmer for the smallest galaxies. Again probably because of the way sky values are set which is in this case quite different from us. Instead of using sky boxes, they compute sky values out of annuli located just at the extremity of what they estimate to contain the totality of the galaxy light. This different sky setting might also explain the slight increase in the root mean square scatter (4 galaxies rejected) which reaches ± 0.1 giving an uncertainty about ± 0.07 magnitude for each source. Regardless, it is reassuring that our magnitudes are in agreements with these two alternative computations.

Comparisons with other projects give comparable results. Typical zeropoint differences are ± 0.015 and root mean square uncertainties are $\pm 0.05 - 0.07$ magnitude. A summary of comparisons are given in [Table 3.3](#). These results provide an estimate of the internal errors of alternate fitting procedures with the same data. We recall that our two measures of magnitude agree at the level of 0.01 with scatter ± 0.02 . In summary of errors, the dominant contributions are sky settings (0.04 magnitude), flux calibration (0.02 magnitude), and extinction (0.02 magnitude), leading to total uncertainties in magnitudes of $\sim 0.05 \text{ mag}$. The great interest with the CFS program is to use TFR to measure distances to galaxies and

the typical scatter in TFR is 0.4 magnitude, 20% in distance. With errors on photometry after corrections held to 0.05 magnitude the contribution to the distance error budget from photometry is minor.

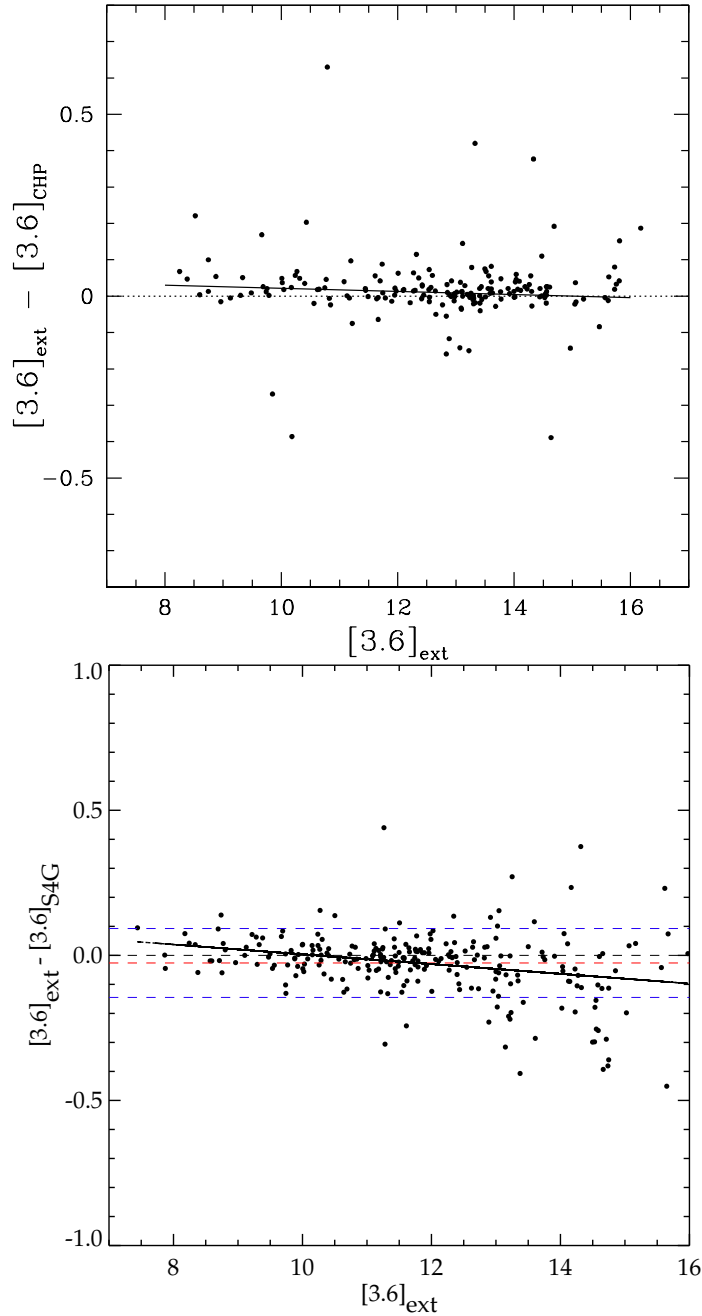


FIGURE 3.19: Comparisons between exponential disk extrapolated magnitudes $[3.6]_{\text{ext}}$ of ARCHANGEL and asymptotic total magnitudes from CHP (*top*) and S⁴G (*bottom*) programs. *Top*: the slight tilt of the thick line best fit, and the offset of $\langle [3.6]_{\text{ext}} - [3.6]_{\text{CHP}} \rangle = 0.01$ from the dotted line null value, have only 2 – 2.5 σ significance. Both the tilt and the offset have been computed rejecting 6 deviant points. *Bottom*: the fit at 3 σ clipping (4 galaxies rejected) has a slope of -0.02 ± 0.004 and a zeropoint of 0.17 ± 0.04 . The red dashed thick line stands for the offset at -0.02 magnitude and the blue dashed lines represent the scatter at 0.1 magnitude. Deviant cases except for 2 are low surface brightness galaxies and we find no reason to reject ARCHANGEL values.

| Program | N | Range | $m_{other} - m_{Archangel}$ | scatter |
|----------|-----|-------|-----------------------------|---------|
| S4G | 241 | 7-16 | -0.02 | 0.10 |
| CHP | 171 | 8-16 | -0.01 | 0.05 |
| SINGS | 12 | 8-10 | 0.02 | 0.07 |
| Various* | 5 | 9-11 | 0.01 | 0.03 |

TABLE 3.3: Comparisons between ARCHANGEL magnitudes and other magnitudes: (1) program name (* measurements from a small number of programs focused on large galaxies, Jarrett, private communication) (2) number of galaxies compared, (3) range of magnitudes over which the comparison is made, mag, (4) difference ARCHANGEL magnitude – other magnitude, mag, and (5) scatter, mag.

Finally, from the comparisons we consider that CHP, S⁴G and ARCHANGEL magnitudes can be used indifferently. For a better precision they are averaged when more than one of them is available in section 3.4.

3.3.6 Bimodality in Disk Central Surface Brightness: a Study Example Based on Photometry Parameters

In this subsection, we report on measurements of the disk central surface brightnesses (μ_0) at 3.6 microns for 438 galaxies selected by distance and absolute magnitude cutoffs from the more than 2350 galaxies in the Spitzer Survey of Stellar Structure in Galaxies (S⁴G), one of the largest and deepest homogeneous mid-infrared datasets of nearby galaxies. Our sample contains nearly three times more galaxies than the most recent study of the μ_0 distribution. We demonstrate that there is a bimodality in the distribution of μ_0 . Between the low and high surface brightness galaxy regimes there is a lack of intermediate surface brightness galaxies. Caveats invoked in the literature from small number statistics to the knowledge of the environmental influences, and possible biases from low signal to noise data or corrections for galaxy inclination are investigated. Analyses show that the bimodal distribution of μ_0 cannot be due to any of these biases or statistical fluctuations. It is highly probable that galaxies settle in two stable modes: a dark matter dominated mode where the dark matter dominates at all radii - this gives birth to low surface brightness galaxies - and a baryonic matter dominated mode where the baryons dominate the dark matter in the central parts - this gives rise to the high surface brightness disks. The lack of intermediate surface brightness objects suggests that galaxy evolution does not favor a mode where dark matter and baryons are equally present in the central parts of galaxies.

3.3.6.1 Introduction

Observational surveys of the distribution of galaxy parameters in diverse environments provide essential constraints for theoretical models of galaxy formation and evolution (e.g. [Thompson, 2003](#)). The sample selection in these surveys needs to be as bias-free as possible to conduct an appropriate analysis. Recently a number of large surveys (e.g. [Dale et al., 2009](#); [Sheth et al., 2010](#); [Stoughton et al., 2002](#)) have been conducted with various telescopes that have led to multiple findings of bimodal distributions of galaxies in terms of color ([Baldry et al., 2004](#); [Brammer et al., 2009](#); [Martínez et al., 2006](#); [Whitaker et al., 2011](#)), star formation ([Wetzell et al., 2012](#)) and disk central surface brightnesses (μ_0 , e.g. [McDonald et al., 2009a,b](#)). [Bailin and Harris \(2008\)](#) have even suggested a trimodal distribution for galaxy concentrations.

Surface brightness profiles were first studied in 1948 by De Vaucouleurs and later on by [Sersic \(1959\)](#) and [Freeman \(1970\)](#). However, the first convincing evidence of a μ_0 bimodal distribution was published only a long time after by [Tully and Verheijen \(1997\)](#). This study revealed that the μ_0 distribution in Ursa Major was discontinuous with a lack of galaxies of intermediate surface brightness, or alternatively that there was an excess of low and high surface brightness (L/HSB) galaxies. The authors suggested two stable modes for galaxy formation: a dominant dark matter component at all radii giving birth to LSB galaxies and a dominant baryonic matter in the center giving rise to HSB galaxies. They suggested that the low number of Intermediate Surface Brightness (ISB) galaxies could be the result of galaxies avoiding the situation where baryonic and dark matters are co-dominant in the center. The very few ISB galaxies could also indicate that there is a small probability for LSB galaxies to turn into HSB galaxies at some point. However, the authors expressed concerns because of possible large errors in fitting galaxy disks due to shallow K'-band observations which could lead to premature truncation of disks. As a result bulges could be partially included in fits leading to a bias in μ_0 . Later [Bell and de Blok \(2000\)](#) argued that the bimodality could also be an artifact due to incorrect inclination-corrections applied to the μ_0 values. They noted that the bimodality could also result from small number statistics. [McDonald et al. \(2009b\)](#) studied a larger number of galaxies in the Virgo cluster to overcome the problem of small number statistics and found a bimodal distribution too. However, they were hesitant to claim that bimodality is inherent to all environments because they had studied only one cluster and felt that different environments could show different behavior of μ_0 .

The goal of this section is to address all of these issues with a study of 438 galaxies selected from the *Spitzer Survey of Stellar Structure in Galaxies* (S^4G , [Sheth et al., 2010](#)). We study the μ_0 distribution to confirm the evidence of the gap found in the Ursa Major and Virgo clusters. The confirmation of a gap can place constraints on present day galaxy distributions

which are essential to the comprehension of galaxy formation and evolution. Post-Basic Calibrated Data used for measurements are publicly available at the Spitzer Heritage Archive website. We show that the 438 galaxies constitute a representative sample to an absolute magnitude of -15 in the $3.6 \mu m$ band of the *Spitzer Space Telescope* (Fazio et al., 2004; Werner et al., 2004). The sample extends up to 20 Mpc and includes all morphological types later than SO^- . The key attributes of the sample are that it is a homogeneous dataset with a large number of galaxies from the field and cluster environments imaged with excellent photometry (Reach et al., 2005). The mid-infrared wavelengths also offer a view of galaxies at very low extinction (Draine and Lee, 1984) and with 4 minutes of integration time per pixel, the data are significantly deeper than anything that can be obtained from the ground for a large sample of galaxies. In the rest of this section, after testing ARCHANGEL measurements of μ_0 at $3.6 \mu m$, we discuss the sample selection, the bimodal distribution of $\mu_0^{[3.6]}$ and the likelihood of obtaining a dip at ISBs from statistical fluctuations of a flat μ_0 distribution selection.

3.3.6.2 Ursa Major: Testing Measurements of μ_0 at $3.6 \mu m$

To test ARCHANGEL measurements of μ_0 at $3.6 \mu m$ to that obtained in previous papers, we retrieve the available 43 of 78 previously used Ursa Major galaxies (Tully and Verheijen, 1997) from the Spitzer archive. Sixteen of these galaxies are from the Carnegie Hubble Program (Freedman et al., 2011) and 27 are from the S^4G survey. Disk central surface brightness values obtained with our procedure at 3.6 microns in the AB system are compared to values obtained in the K' band in the Vega system from the 1997 paper in the top panel of Figure 3.20. We find a good agreement between K' and [3.6] band values. Bottom panels of the same figure show μ_0 distributions for the 43 galaxies in common with the previous studies. The bottom right panel also shades the galaxies according to their type - one immediately sees that the early type galaxies have a higher μ_0 (ie, are usually HSBs) compared to the usually lower surface brightness late type galaxies demonstrating the known strong correlation between morphological type and the disk central surface brightness. The previous studies found values for LSB and HSB peaks in the K'-band at about 19.7–20.0 for LSBs and 17.3–17.5 for HSBs (mag arcsec⁻² in the Vega system). We find values of 22.5 and 19.5 for LSBs and HSBs at $3.6 \mu m$ but in the AB system as shown in Figure 3.20. A conversion between the Vega and AB systems re-establishes the proper relative positions between peaks in the K' and [3.6] bands. Namely, at 3.6 microns, peaks are located at smaller values in the Vega system ($[3.6](Vega) = [3.6](AB) - 2.785$) than in the K' band in the same system. A single Gaussian model of the μ_0 distribution can be rejected at more than the 99% confidence level while the significance of a double Gaussian modeling is quite high (54%). However these 43 galaxies do not constitute a complete sample and cannot lead to a universal conclusion

about the bimodality we seek to test. Still the comparisons show that our procedure gives results similar to the previous studies and does not introduce any particular bias.

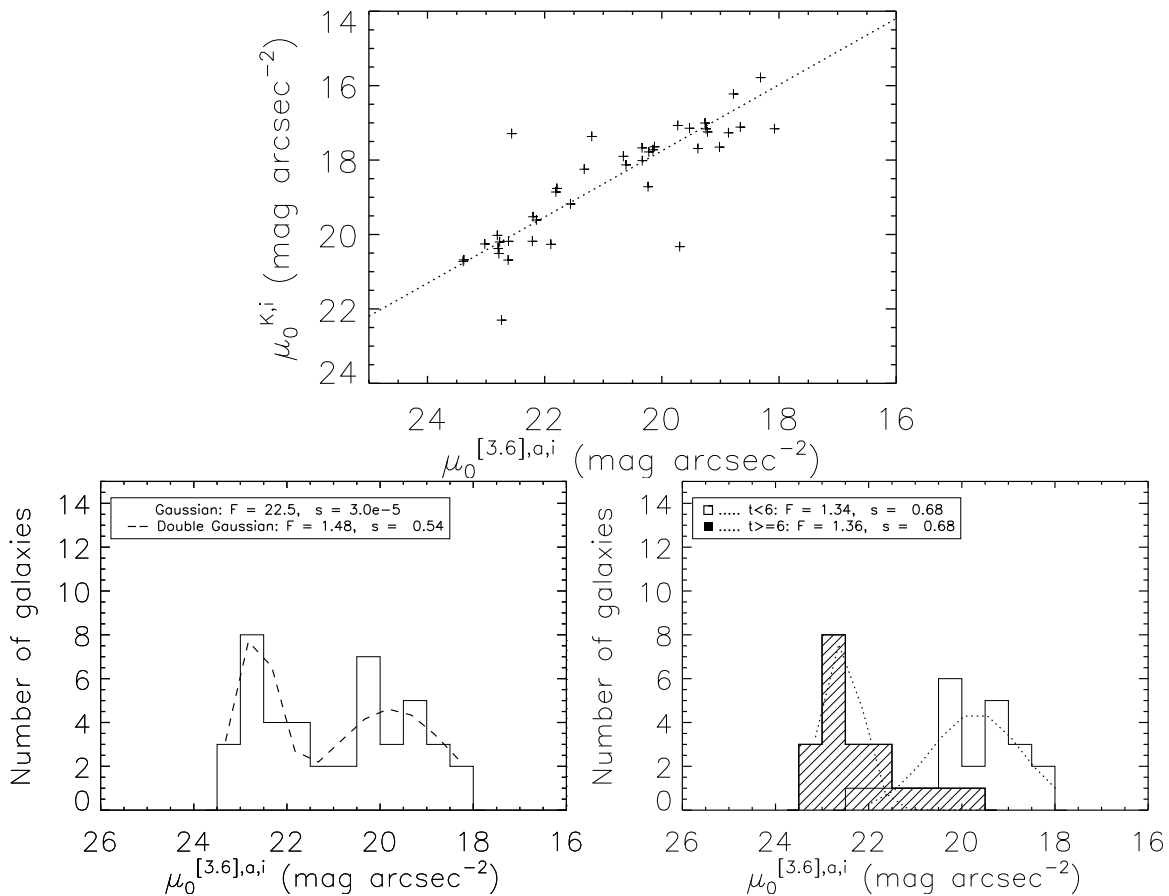


FIGURE 3.20: *Top*: Comparison between disk central surface brightnesses from Tully & Verheijen 1997 in the K'-band, Vega system and this work, AB system. The dotted line is the 1:1 relation shifted by the average K'(Vega)-[3.6](AB) value of the sample. *Bottom left*: Histogram of the disk central surface brightnesses corrected for inclination and aperture of 43 Ursa Major galaxies. The dashed line represents the sum of two Gaussian fits from LSB and HSB subsample modelings. While the significance level (s) of the F-Test (F) for the double Gaussian is high, the single Gaussian modeling can be rejected at more than the 99% confidence level. *Bottom right*: Distributions of type greater than 6 galaxy disk central surface brightnesses (dashed histogram) and type smaller than 6 galaxy disk central surface brightnesses (plain histogram) for the available galaxies of the Ursa Major cluster.

As stipulated in subsection 3.3.2.2, surface brightnesses are fitted with disk-only. Tully and Verheijen (1997) and McDonald et al. (2009a) were concerned about the disk-only fitting technique for bulge galaxies. However, they respectively showed that neither dropping bulge galaxies nor making a bulge-disk decomposition removed the bimodality. They also asserted that their results were not significantly affected by alternative decompositions. We have retained in subsection 3.3.4 an uncertainty budget of $0.5 \text{ mag arcsec}^{-2}$ for $\mu_0^{[3.6]}$ measurements. This leads to a choice of bin sizes of $0.5 \text{ mag arcsec}^{-2}$ for histograms of $\mu_0^{[3.6]}$ distributions.

3.3.6.3 Sample Selection

The S^4G survey is a volume-, magnitude-, and diameter-limited ($d < 40$ Mpc, $|b| > 30^\circ$, $m_{Bcorr} < 15.5$ and $D_{25} > 1'$) survey of over 2,350 galaxies observed with channels 1 and 2 (3.6 and 4.5 μm respectively) of the IRAC instrument (Fazio et al., 2004) aboard the Spitzer Space Telescope (Werner et al., 2004). It is a very large extremely deep, representative and homogeneous sample of nearby galaxies containing all Hubble types. We use only the 3.6 μm band data that we preferred for the Cosmicflows project based on the knowledge that 4.5 μm fluxes have a higher contribution from hot dust than fluxes at 3.6 μm (Meidt et al., 2012). We extracted from the S^4G survey every galaxy of type later than SO^- up to a distance of roughly 20 Mpc according to the Extragalactic Distance Database. At low redshift, surface brightnesses are independent from distances. Thus, distances used here are simple estimates derived from redshifts tethered to a Virgo infall model constrained by distance measurements. The resulting sample goes down to an absolute magnitude limit of -16 in the B band in the Vega magnitude system. This faint magnitude limit prevents the loss of low surface brightness galaxies (LSB, Zhong et al., 2008) from the volume surveyed and guarantees the presence of galaxies of intermediate surface brightnesses.

Figure 3.21 shows histograms of the sample as function of 1) numerical morphological type, which increases with the "lateness" of the literal type (E to Im through S), 2) absolute 3.6 μm magnitude and 3) distance. The left panel in Figure 3.21 shows a deficit of Type-7/8 galaxies and a small excess of Type-5/6 galaxies but this is not a bias from the selection – the distribution of the full S^4G sample shown with the dashed line also displays the same behavior. Moreover, the morphological T-type assignments from HyperLeda (Paturel et al., 2003) are qualitative with an uncertainty of $\delta T=1$. There is also no a priori expectation of similar numbers of galaxies in each category in a given volume.

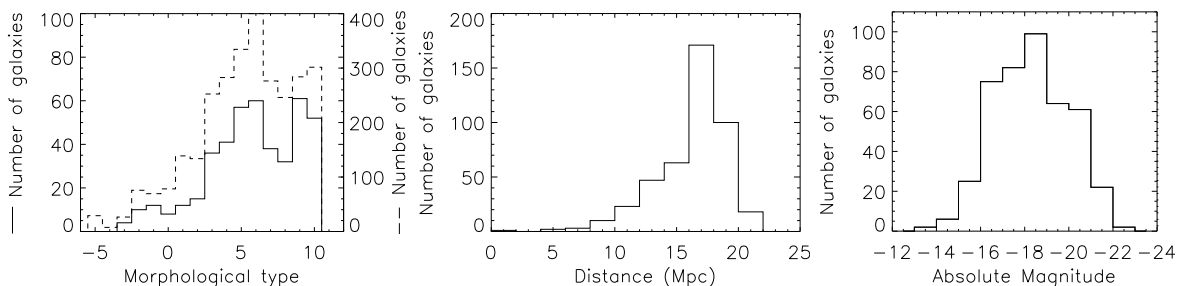


FIGURE 3.21: Histograms showing the distributions of the 438 galaxies extracted from the S^4G sample. *From left to right:* Morphological type from HyperLeda database (we chose all galaxies with $T > -3$ or later than SO^-). The dashed histogram is the distribution of HyperLeda types for the whole S^4G sample ; Distance to the galaxies from the Extragalactic Distance Database ; Absolute Magnitude ($M_{[3.6]} < -16$ in the AB system).

Figure 3.22 shows the angular distribution across the sky of the 438 galaxies; point sizes are set according to their distances from us. We perform aperture photometry for the 438 Post

Basic Calibrated Data of the galaxy sample using the adapted for this work ARCHANGEL software following the process detailed in subsection 3.3.2.2.

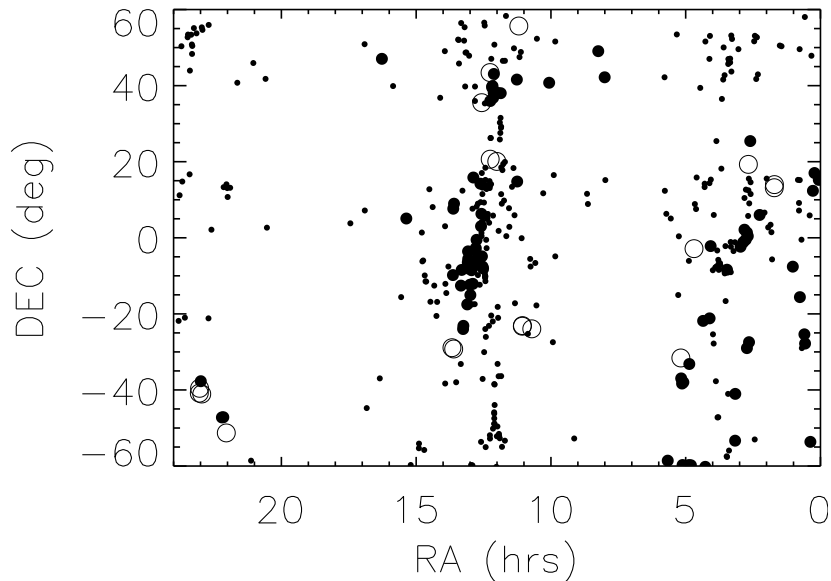


FIGURE 3.22: Angular distribution on the sky of the 438 S^4G galaxies. Size of the symbols represents the distance to the galaxy. The largest symbols show galaxies closer than 10 Mpc, the medium sized symbols stand for galaxies between 10 and 15 Mpc, and the smallest symbols show galaxies farther than 15 Mpc.

3.3.6.4 A Lack of Intermediate Surface Brightness Galaxies

The entire $\mu_0^{[3.6],a,i}$ distribution for the 438 galaxy sample from S^4G is shown in Figure 3.23. It reveals a hint of bimodality – There is a lack of galaxies between 21 mag arcsec $^{-2}$ and 22 mag arcsec $^{-2}$ (less than 45 galaxies versus more than 60 galaxies at the peaks). We fit this distribution with a double Gaussian assuming a population with μ_0 greater than 21.5 mag arcsec $^{-2}$ and a population with μ_0 less than 21.5 mag arcsec $^{-2}$ - roughly reflecting a LSB and HSB population respectively (see top panel in Figure 3.24) . This model has a much higher significance (can only be rejected at a 21% confidence level) compared to a simple Gaussian model which can be rejected at a 55% confidence level.

As shown in the top panel of Figure 3.24, the ad-hoc limit of 21.5 mag arcsec $^{-2}$ matches well with the well known fact that LSB galaxies are in general of late Hubble type while HSB galaxies are in general of early Hubble type (e.g. de Jong, 1996b). In this figure, the LSB galaxies appear only for types later than the Scd type. The bottom panel of Figure 3.24 shows the $\mu_0^{[3.6],a,i}$ distribution for each morphological type in the 438 galaxy sample. The histogram peak shifts to the left (higher $\mu_0^{[3.6],a,i}$) with increasing morphological types, supporting the correlation between types and the disk central surface brightnesses.

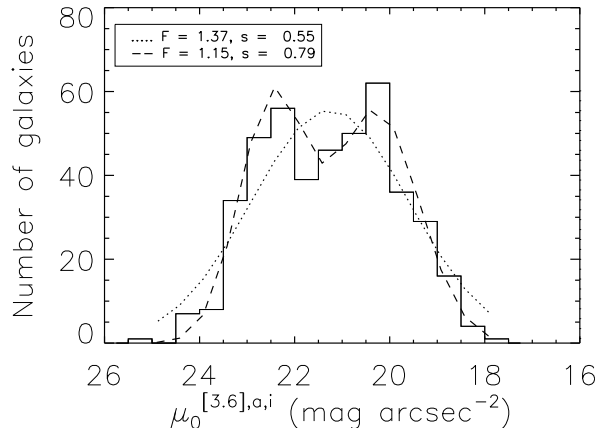


FIGURE 3.23: Histogram of the aperture-inclination corrected disk central surface brightnesses. A Gaussian fit (dotted line) to the distribution can be rejected at the 55 % confidence level ($F=F$ -Test, s =significance level) while a sum of two Gaussians respectively from the modelings of LSB and HSB disk central surface brightness subsample distributions can be rejected only at the 21% confidence level (dashed line) supporting the bimodality seen previously.

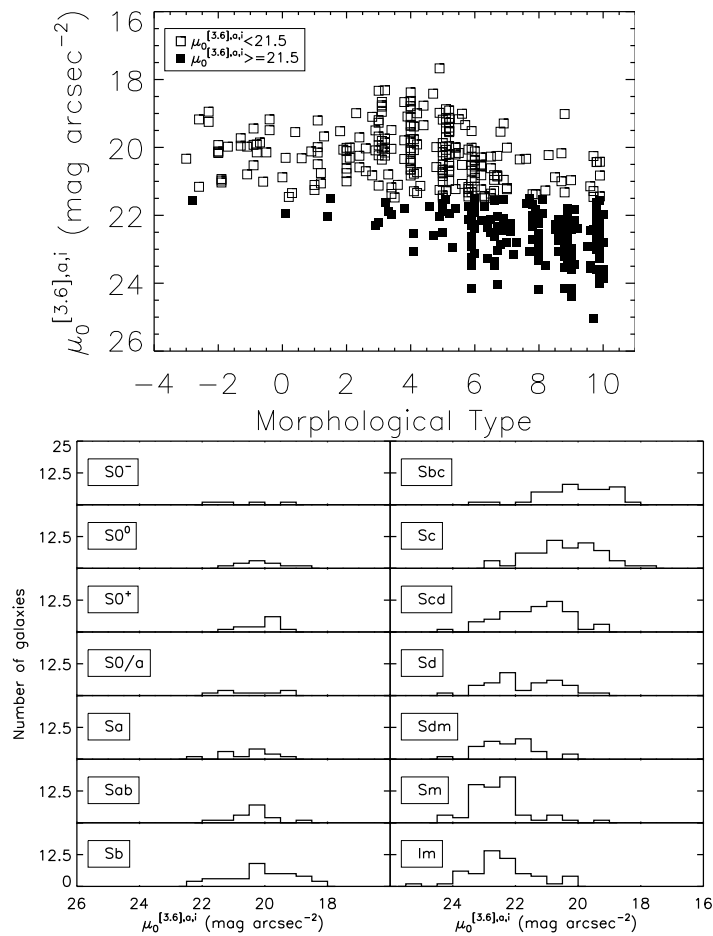


FIGURE 3.24: *Top*: disk central surface brightness versus morphological type. An ad-hoc limit set at $\mu_0^{[3.6],a,i} = 21.5 \text{ mag arcsec}^{-2}$ shows that galaxies with $\mu_0^{[3.6],a,i} > 21.5 \text{ mag arcsec}^{-2}$ appear for types greater than ~ 6 (later than Scd). *Bottom*: Peaks of the $\mu_0^{[3.6],a,i}$ distributions shift to the left with increasing morphological type.

Since the double Gaussian modeling can be rejected as a model for the total sample at the 21% (against 55% for the single Gaussian modeling) confidence level, we next define selection criteria to understand better which galaxies are in the gap and what might be causing a bimodality.

Close neighbor: galaxies with a close neighbor ($D < 80 \text{ kpc}$) can undergo interactions which can potentially modify their μ_0 values. If there are only two parent populations (HSB and LSB types), then mergers / interactions could move galaxies into the gap separating the HSB and LSB galaxies (Tully and Verheijen, 1997). We remove galaxies with close neighbors to test the postulate that this will increase the bimodal nature of the μ_0 distribution. We assume that a galaxy with a velocity, v , has a "close neighbor" whenever there is another galaxy within 80 kpc with a velocity equal to $v \pm 200 \text{ km s}^{-1}$. We find only a few galaxies with close neighbors as shown on Figure 3.25. The remaining "isolated" sample consists of 411 galaxies. The distribution of the 27 galaxies with close neighbors looks quite flat - although the numbers are too small to investigate the nature of the distribution. Quite a few of the 27 galaxies are in the gap. This agrees with the hypothetical scenario proposed by Tully and Verheijen (1997) in which LSB galaxies tend to turn into HSB galaxies progressively going through a stage as intermediate surface brightness galaxies due to an interaction with a neighbor.

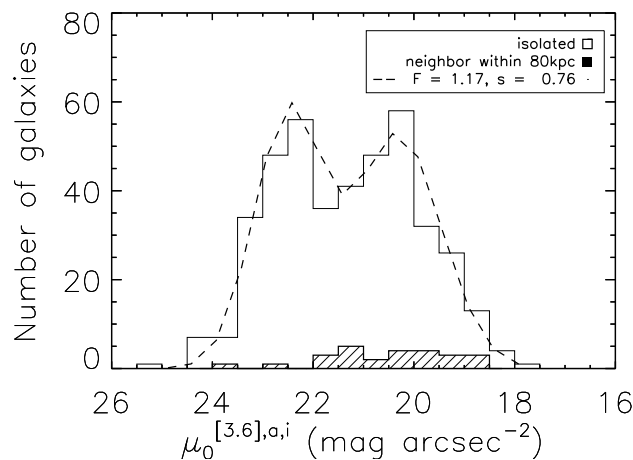


FIGURE 3.25: Separation between galaxies with at least one neighbor closer than 80 kpc (dashed histogram) and without a neighbor within 80 kpc (plain histogram). The velocity of the neighbor has to be within $\pm 200 \text{ km s}^{-1}$ of the galaxy velocity. The dashed line is the sum of two Gaussians. It cannot be rejected at more than the 24 % confidence level (1 σ significance level (s)) with a F-Test (F).

Inclination: next we explore the effect of inclination corrections as noted by Bell and de Blok (2000). According to them, the effects of dust and projection geometry may not be negligible, even in the mid-infrared: 1) averaging ellipse surfaces at high inclinations to obtain μ_0 may result in a systematically smaller value (Huizinga, 1994), 2) assuming a thin, uniform, slab disk at high inclinations may lead to incorrect conclusions because three

dimensionality of stellar structures affects the inclination correction in non-trivial ways. It is difficult to characterize the surface brightnesses of edge-on galaxies because integrating along the line of sight may hide the effects of sub-structures like bars and spiral arms (e.g. [Mosenkov et al., 2010](#)). No precise method exists for correcting such effects and the coefficient $C^{[3.6]}$ in equation 3.30 itself may vary with galactic radius. In absence of a proper (or even better) method to correct for inclination and because numerically obtained inclinations are quite uncertain (see for example, Figure 3.13), we decided to remove every galaxy with an inclination greater than $\sim 73^\circ$ ($\frac{b}{a}=0.35$)⁵ leaving us with 292 galaxies. Figure 3.26 displays the bimodal distribution of this refined sample along with the distribution for the "edge-on" galaxies. The inclined galaxies are well-described by a single Gaussian that peaks in the previously observed gap between the HSB and LSB galaxies. The remainder of the sample is well-fitted with a double Gaussian model which cannot be rejected at more than the 16 % confidence level with the F-Test (based on the ratio of model and data variances).

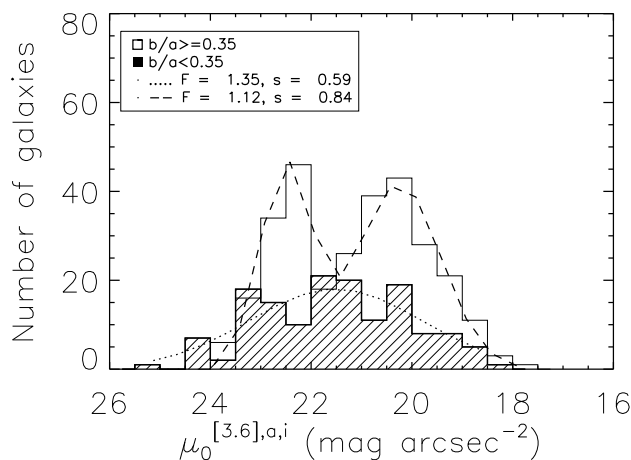


FIGURE 3.26: Distribution of disk central surface brightnesses of highly inclined galaxies ($i > 73^\circ$, dashed histogram) against the others ($i < 73^\circ$, plain histogram). The $\mu_0^{[3.6],a,i}$ distribution of highly inclined galaxies is fitted by a Gaussian (dotted line) whereas the less inclined galaxy $\mu_0^{[3.6],a,i}$ distribution is fitted by a double Gaussian (dashed line) (F=F-Test, s=significance level).

Axial Ratio: an error in the axial ratio is another source of error in the inclination correction we apply to get the face-on $\mu_0^{[3.6],a}$ value. An error of 0.2 in the axial ratio leads to an error of about $0.5 \text{ mag arcsec}^{-2}$ (namely a change of bin in our histograms). We remove every galaxy whose ARCHANGEL derived ratios differ from that found in HyperLeda database ([Paturel et al., 2003](#)) by more than 0.2. The resulting distribution of $\mu_0^{[3.6],a,i}$ is shown in Figure 3.27. Where the axial ratio between the HyperLeda values and that measured by ARCHANGEL in the S⁴G data are similar (408 galaxies), the bimodal distribution is still visible. There are fewer LSB galaxies in this plot compared to the original because LSB galaxies are the

⁵0.4 instead of 0.35 was the choice of [Bell and de Blok \(2000\)](#). Because of the uncertainties on inclinations ($\sim 4 - 5^\circ$), choosing 0.35 (73°) over 0.4 (69°) does not change the conclusions.

ones most affected by a change in observations (optical versus mid-infrared). The double Gaussian modeling cannot be rejected at more than the 19% confidence level.

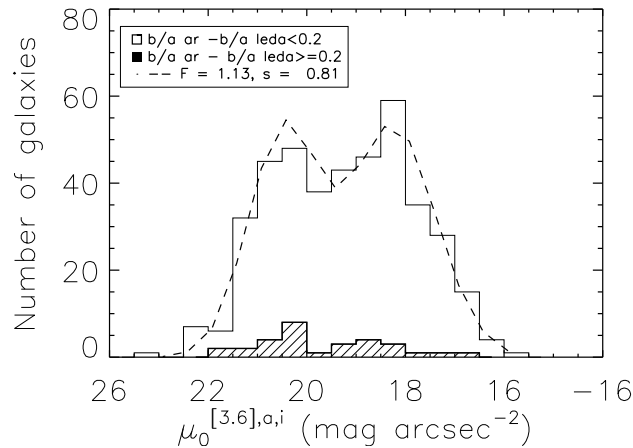


FIGURE 3.27: Distribution of $\mu_0^{[3.6],a,i}$ separating galaxies which "ARCHANGEL axial ratios" differ by more than 0.2 from "HyperLeda axial ratios" (dashed histogram) from which that do not (plain histogram). The total sample is modeled by a sum of two Gaussians (dashed line) (F =F-Test, s =significance level).

Combination of selection criteria: if we now combine the three selection criteria (isolated, non-inclined galaxies, with similar axial ratios in the optical and mid-infrared) we get a sample of 249 galaxies. On Figure 3.28, the $\mu_0^{[3.6],a,i}$ distribution for this highly refined sample clearly shows the bimodality. The double Gaussian modeling now cannot be rejected at more than the 19% confidence level according to the F-Test. On the contrary, the single Gaussian modeling can be rejected at a 81% confidence level with the same test. Thus we conclude that the $\mu_0^{[3.6],a,i}$ distribution of the sample is bimodal and that there is a lack of intermediate surface brightness galaxies.

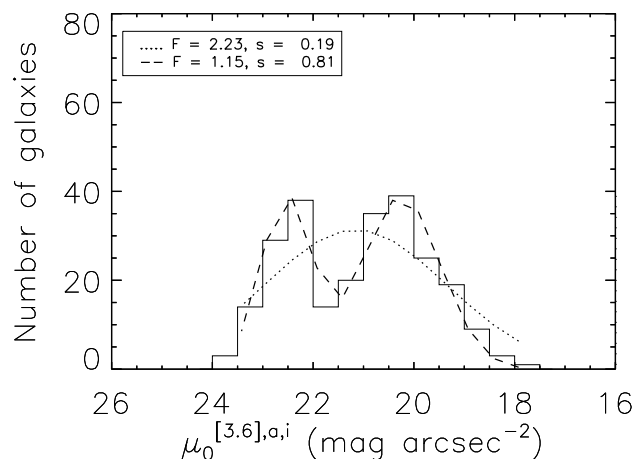


FIGURE 3.28: $\mu_0^{[3.6],a,i}$ histogram after dropping galaxies inclined by more than 73° , with a neighbor closer than 80 kpc and with an axial ratio different by more than 0.2 between HyperLeda and S⁴G data. A double Gaussian (dashed line) clearly fits the distribution far better than a single Gaussian (dotted line) (F =F-Test, s =significance level).

3.3.6.5 Why a Dip at Intermediate Surface Brightness?

The different results of previous sections demonstrate strongly that the $\mu_0^{[3.6],a,i}$ distribution is bimodal. Is it possible that the bimodality is from statistical fluctuations? To obtain the likelihood of getting a dip at intermediate surface brightness from a statistical fluctuation, we simulated a flat $\mu_0^{[3.6],a,i}$ distribution of 700 galaxies with μ_0 between 19 and 24 mag arcsec⁻². We chose a flat distribution in agreement with the current description of disk central surface brightness distribution (McGaugh, 1996; McGaugh et al., 1995). This flat distribution has an upper brightness limit to disk central surface brightnesses that must have a physical origin (Freeman, 1970) and a lower brightness limit due to observational limitations in the simulations. Each 1 mag arcsec⁻² size bin contained the same number of galaxies. We randomly selected 249 galaxies from that distribution and looked at the likelihood of obtaining a gap between two peaks. We repeated the selection 10,000 times and retained only simulations with a gap between two peaks and a number of galaxies in the gap no greater than 50 % the number of galaxies in the peaks. This is approximately what we observe in Figure 3.28. Table 3.4 lists the histogram parameters of the 9 simulations out of the 10,000 simulations which showed a distribution similar to the observed bimodality we observed in the 249 galaxy sample. The last line corresponds to the mean values for the 9 simulations. Thus the likelihood of randomly obtaining the observed bimodality is only ~ 0.1 %.

| Simulations | peak ₁ | pos. peak ₁ | peak ₂ | pos. peak ₂ | gap | position gap | % ₁ | % ₂ |
|-------------|-------------------|------------------------|-------------------|------------------------|-----|--------------|----------------|----------------|
| 431 | 71 | 24.0 | 62 | 22.0 | 31 | 23.0 | 44 | 50 |
| 870 | 63 | 23.0 | 61 | 21.0 | 27 | 22.0 | 43 | 44 |
| 2603 | 64 | 24.0 | 63 | 21.0 | 30 | 22.0 | 47 | 48 |
| 3923 | 65 | 20.0 | 59 | 23.0 | 28 | 22.0 | 43 | 48 |
| 4852 | 66 | 24.0 | 61 | 22.0 | 23 | 23.0 | 35 | 38 |
| 4887 | 64 | 23.0 | 63 | 20.0 | 28 | 21.0 | 44 | 44 |
| 8330 | 66 | 22.0 | 62 | 24.0 | 30 | 23.0 | 46 | 48 |
| 8421 | 67 | 23.0 | 60 | 20.0 | 30 | 22.0 | 45 | 50 |
| 9233 | 63 | 23.0 | 62 | 21.0 | 30 | 22.0 | 48 | 48 |
| Mean | 65 | 23 | 61 | 21 | 28 | 22 | 44 | 46 |

TABLE 3.4: Kept simulations: (1) Number characterizing the simulation out of 10,000. Only simulations with two peaks and a gap in between are selected. The number of galaxies in the gap has to be at most 50 % the galaxy number in peaks. Only 9 out of 10,000 simulations are similar to the observed bimodality. In other words, there is only a ~ 0.09 % probability that the bimodality is due to a statistical fluctuation. (1) - (2) Value (number of galaxies) and Position (mag arcsec⁻²) of the first peak, (3) - (4) Value (number of galaxies) and Position (mag arcsec⁻²) of the second peak, (5) - (6) Value (number of galaxies) and Position (mag arcsec⁻²) of the gap, (7) - (8) Percentage of galaxies in the gap with respect to the number of galaxies in the first and second peaks respectively.

In the Vega system, peaks have been found at 17.5-18 and 20 mag arcsec⁻² for both Virgo and Ursa Major Clusters in the K' band and in the H band respectively (McDonald et al., 2009a,b; Tully and Verheijen, 1997). The gap found in between has a width of one unit in magnitude per square arcsecond and is located at ~ 19 mag arcsec⁻². In this study, at 3.6 μm in the AB system, the observed bimodal distribution shows two peaks at 20.5 and 22.5 mag arcsec⁻² and a gap of width 1 mag arcsec⁻² at 21.5 mag arcsec⁻² in between. This excellent agreement between the studies, including the shift to smaller values when moving towards longer wavelengths (visible after applying the AB-Vega system conversion) already shown in Figure 4 of the 1997 paper, is a strong evidence for an inherent bimodality in the local galaxy population.

The results reveal a clear separation between $\mu_0^{[3.6]}$ of HSB and LSB galaxies. The former are probably dominated by baryonic matter at their centers whereas the latter are likely dark matter dominated at all radii (Tully and Verheijen, 1997). Along with a lack of intermediate surface brightness galaxies, the data suggest that the two (L/HSB) peaks signify two stable configurations of galaxy formation (Mestel, 1963). Systems that retain large angular momentum from their formation may prevent the baryonic matter from collapsing to form a stellar disk that could dominate the dark halo at the galaxy center. These systems may reach a rotational equilibrium at densities where the dark matter halo remains dominant and the galaxies appear as LSB galaxies. On the other hand, galaxies with low angular momentum, either because of their formation or because they transferred their angular momentum away from much of their gas, allow baryonic matter to collapse and form disks that can dominate the dark matter halo at the center. This hypothesis is supported by the differences between typical LSB and HSB rotation curves. LSB galaxies reach flat rotation at very large radii from their centers (Swaters et al., 2010) whereas HSB galaxies reach their maximal rotation speed at, or within, $r=2.15 \alpha$ where α is the disk scale length (Courteau, 1997).

The gap between the two peaks suggests that galaxy formation does not favor a situation where the dark matter and the baryonic matter have equal weight in the center. The few galaxies present in this gap may be transitioning from LSB to the HSB galaxies as suggested by the experiment with the close neighbor pairs. Eventually all galaxies that undergo interactions may end up as HSB galaxies so that the peak of HSB systems should be higher than the LSB peak in environments where interactions are common.

Our 438 galaxy sample is representative of all galaxies later than SO^- in the half of the sky at the Galactic poles within the volume extending to 20 Mpc and brighter than $M_B = -16$. The galaxies lie in clusters, groups, and the field. The bimodality in disk central surface brightnesses first found in moderate and high density regions is found to be pervasive. Galaxies are mostly HSB or LSB but rarely ISB. This phenomenon must have a physical explanation, one that probably will give an important clue regarding the process of galaxy

formation. Seeking for such a bimodality to be present in disk central surface brightness distributions of simulated galaxies could unravel some mystery about the process of galaxy formation.

3.4 Tully-Fisher Relation

This section expounds the calibration of the Tully-Fisher relation in the mid-infrared. It results from a commonality of interests between the overall Cosmicflows project (subprogram Cosmicflows with Spitzer, initiated in cycle 8) and the Carnegie Hubble Program (CHP, initiated in Spitzer proposal cycle 6). The intent of CHP is to reduce systematics arising in the determination of the Hubble Constant by giving attention to a mid-infrared calibration of the Cepheid Period-Luminosity relation and a second part addresses the properties of the rotation rate–luminosity correlation of galaxies or Tully-Fisher Relation (TFR). Cosmicflows seeks to obtain accurate distance measurements for thousands of galaxies using the mid-infrared TFR in order to map deviations from Hubble flow. Since the TFR zeropoint is established by the Cepheid distance measurements, the Cepheid Period-Luminosity relation calibration is required. [Freedman et al. \(2011\)](#) describe the goals of CHP and [Freedman et al. \(2012\)](#) report on the results of the Cepheid calibration that gives a distance modulus for the Large Magellanic Cloud of 18.48 ± 0.03 magnitudes.

3.4.1 Calibration at 3.6 μm

The ensuing discussion about the Tully-Fisher calibration borrows on the recent re-calibration of the I band correlation by [Tully and Courtois \(2012\)](#) (hereafter TC12). The strategy consists in forming a template relation using samples from 13 galaxy clusters and the establishment of a zeropoint using nearby galaxies with independent Cepheid period-luminosity or Tip of the Red Giant Branch (TRGB) distances. [3.6] magnitudes are obtained mostly with ARCHANGEL and are eventually combined with CHP measurements. HI profile and inclination information are the same as in TC12. The significant difference is the replacement of mid-infrared for optical luminosities. It turns out that although the new photometry has high fidelity and the photometry correction terms are small there is an intrinsic color term in the [3.6] band TFR. Scatter in the relation will be reduced upon application of a color correction. We will conclude the section with an estimate of the Hubble Constant.

3.4.1.1 Calibrators

The slope and zeropoint calibrator samples are described in detail in TC12. The correlation slope is established from a template built from galaxies in 13 clusters from the closest Virgo cluster up to Abell clusters, the farthest being Abell 2634. As a matter of fact, the only departure in terms of an extension from the *I* band calibration occurs precisely in the case of Abell 2634. The CHP program included observations of a larger region including Abell 2666. The two clusters are close in projection and, evidently, in distance. We find no discernible difference in distance between galaxies closest on the sky to Abell 2634 versus those closest to Abell 2666. We propose to average over the entire complex.

Each cluster sample is comprised of galaxies likely to be at similar distances. There was an attempt to include all galaxies with suitable properties down to a defined faint luminosity level to have an unbiased sampling of the cluster volume to a magnitude limit. Candidates are chosen out of a projection-velocity window. We care about minimizing relative distance effects in the TFR so it is more important to minimize interlopers than maximize true members. Cluster members that are "window outsiders" would not be expected to lie in any preferred part of the TF diagram. The selection criteria are:

- morphological types earlier than Sa are excluded (SO types are similar to spirals but have been shown not to lie on the same Tully-Fisher relation, e.g. [Bedregal et al., 2006](#); [Williams et al., 2010](#)),
- HI profiles with adequate signal-to-noise are required,
- HI profiles should present no evidence of confusion or tidal disruption,
- inclinations less than 45° are rejected to limit large linewidth de-projection errors. Tests with samples that satisfy this limit have not revealed that this selection gives rise to a distance bias (TC12).

Criteria for inclusion of zeropoint calibrators are similar, with the additional requirement that they have very well known distances from either Cepheid or TRGB measurements. In TC12, the Cepheid scale had been set by a distance modulus for the Large Magellanic Cloud of 18.50 magnitude ([Freedman et al., 2001](#)). Here we adopt the slightly modified modulus $18.48 \pm [0.03 - 0.06]$ magnitude based on mid-infrared photometry of Cepheids in the Large Magellanic Cloud and in our Galaxy, the latter anchored with trigonometric parallaxes ([Monson et al., 2012](#)). The TRGB distances are based on a Population II calibration but have been demonstrated to be on a consistent scale ([Rizzi et al., 2007](#); [Tully et al., 2008](#)).

At the time of this calibration work, Cosmicflows with Spitzer observations were incomplete, still already 230 of 314 galaxies (73%) used in the *I* band calibration (plus 9 other galaxies

introduced with the extension of the Abell 2634 sample to include Abell 2666) had Spitzer [3.6] photometry, including 26 of 36 (72%) that set the zeropoint. The completion was greater than 60% with each of 12 of the 13 template clusters (the Pisces filament is the exception). Consequently, we proceeded with the TFR calibration with the available material. The data that are used in the following discussion are collected into Table B.1 of Appendix B. This table includes CFS and CHP total magnitudes, each including the four corrections described in subsection 3.3.3, and averages of the two methods. The table also gives inclination and linewidth information drawn from TC12 and color terms for color corrections described in subsection 3.4.1.3. The galaxies in Table B.1 of Appendix B are either part of the zeropoint calibration sample (ZP) or a member of a cluster contributing to the slope template.

3.4.1.2 Slope and Zeropoint

The TFR calibration requires the definition of a slope and the establishment of an absolute scale. The slope is the trickiest item because there is a correlation between its value and a form of Malmquist bias. Given two galaxies at the same distance with the same linewidth, the brighter galaxy might be chosen but not the fainter one. The potential bias depends on the slope of the correlation because with a relatively flat slope most intrinsically luminous galaxies lie above the correlation while with a very steep slope these same galaxies tend to lie below the correlation. Consider a target for a distance measurement in the field that intrinsically lies above the assumed mean relation, the trend for distant galaxies if the relation is flat. With the distance measurement the target is assigned the mean luminosity of the correlation at the target's linewidth so given a distance that is too small. This bias has repeatedly been discussed at length, most recently by TC12. The salient point is that the so-called "inverse" relation (ITFR), the least squares regression where errors are taken to be in linewidth only, gives results that are close to bias free. Willick (1994) pointed out that, while in his experiments the ITFR bias was reduced by a factor 6 from that incurred using the direct relation, yet a small bias remained because the sample selection was not made in the band he considered. We have the same problem. Our strategy is to use the ITFR and then evaluate the bias with simulations anticipating that, like with the *I* band calibration, the effects will be small. The bias tests are discussed in a later subsection 3.4.1.4. The calibration process has been described in detail by Tully and Pierce (2000) and TC12. With the *I* band relation there was no clear evidence for scatter due to a third parameter but the situation at [3.6] is different. A color term is found and that matter will be discussed in subsection 3.4.1.3.

The measurement of distances requires the hypothesis of a universal correlation. To begin, we make inverse fits to each one of the clusters separately. We use the least square fitting mathematical procedure which consists in finding the best-fitting curve to a set of point by

minimizing the sum of the residual squares (given points minus model). Squares are used as they can be assimilated to a continuous differentiable quantity contrary to absolute values. The condition for the sum of the residual squares to be an extremum (minimum in our case) for a linear fit of n points (x, y) is given by:

$$\frac{\partial \sum_{i=1}^n [y_i - (a + bx_i)]^2}{\partial a} = 0 \quad \text{and} \quad \frac{\partial \sum_{i=1}^n [y_i - (a + bx_i)]^2}{\partial b} = 0 \quad (3.37)$$

where y_i are the variables to fit as a function of the x_i variables and a, b are constants. Because we want inverse fits, y_i are to be assimilated to logarithms of linewidths, more precisely to $\log W_{mx}^i - 2.5$ and x_i to magnitudes m .

In matrix form, equations 3.37 can be written:

$$\begin{bmatrix} n & \sum_{i=1}^n x_i \\ \sum_{i=1}^n x_i & \sum_{i=1}^n x_i^2 \end{bmatrix} \begin{bmatrix} a \\ b \end{bmatrix} = \begin{bmatrix} \sum_{i=1}^n y_i \\ \sum_{i=1}^n x_i y_i \end{bmatrix} \quad (3.38)$$

which gives:

$$\begin{bmatrix} a \\ b \end{bmatrix} = \frac{1}{n \sum_{i=1}^n x_i^2 - (\sum_{i=1}^n x_i)^2} \begin{bmatrix} \sum_{i=1}^n y_i \sum_{i=1}^n x_i^2 - \sum_{i=1}^n x_i \sum_{i=1}^n x_i y_i \\ n \sum_{i=1}^n x_i y_i - \sum_{i=1}^n x_i \sum_{i=1}^n y_i \end{bmatrix} \quad (3.39)$$

where we have used the relation between a 2x2 matrix and its inverse:

$$\begin{bmatrix} a_1 & a_2 \\ a_3 & a_4 \end{bmatrix}^{-1} = \frac{1}{a_1 a_4 - a_3 a_2} \begin{bmatrix} a_4 & -a_2 \\ -a_3 & a_1 \end{bmatrix} \quad (3.40)$$

The correlation coefficient $corr$ is the ratio of the covariance cov over the product of variances σ_x, σ_y :

$$corr = \frac{cov}{\sigma_x \sigma_y} = \frac{\sum_{i=1}^n (x_i - \bar{x})(y_i - \bar{y})/n}{\sum_{i=1}^n (y_i - \bar{y})^2/n \sum_{i=1}^n (x_i - \bar{x})^2/n} \quad (3.41)$$

where barred quantities stand for the means. With the definitions of variances and covariance, $b = \frac{cov}{\sigma_x^2}$ and $a = \bar{y} - b\bar{x}$.

Standard errors on b and a can be derived with:

$$err_a = \sqrt{\frac{n\sigma_y^2 - n b cov}{n-2} \left(\frac{1}{n} + \frac{\bar{x}^2}{n\sigma_x^2} \right)} \quad \text{and} \quad err_b = \sqrt{\frac{n\sigma_y^2 - n b cov}{n-2} \frac{1}{n\sigma_x^2}} \quad (3.42)$$

However, once a and b are computed, the relation needs to be inverted to find the Tully-Fisher relation: $[x_i (= m)] = -\frac{b}{a} + \frac{1}{b}[y_i (= \log W_{mx}^i - 2.5)]$. We define the errors on such an "inverse" slope ($\frac{1}{b}$) as the product of the standard error on the "direct" slope by the "inverse" slope divided by the "direct" slope. The standard error on the "direct" slope is obtained with the

relation 3.42 but this time with y_i assimilated to magnitudes m and x_i to $\log W_{mx}^i - 2.5$ in the procedure.

Dotted lines in Figures 3.29 and 3.30 illustrate the inverse fits of the TFR for each cluster. Slopes are quite similar between clusters. Slopes and their uncertainties are given for each cluster in Table 3.5. The individual fits are consistent with the soon to be derived best fit and hence with the universal correlation hypothesis⁶. As cluster distances increase, the faint luminosity limits decrease in magnitudes. However, no dependence of the slope with distance is seen, as would be a marker of Malmquist bias (we still make a tiny correction for bias to cluster moduli as described in subsection 3.4.1.4).

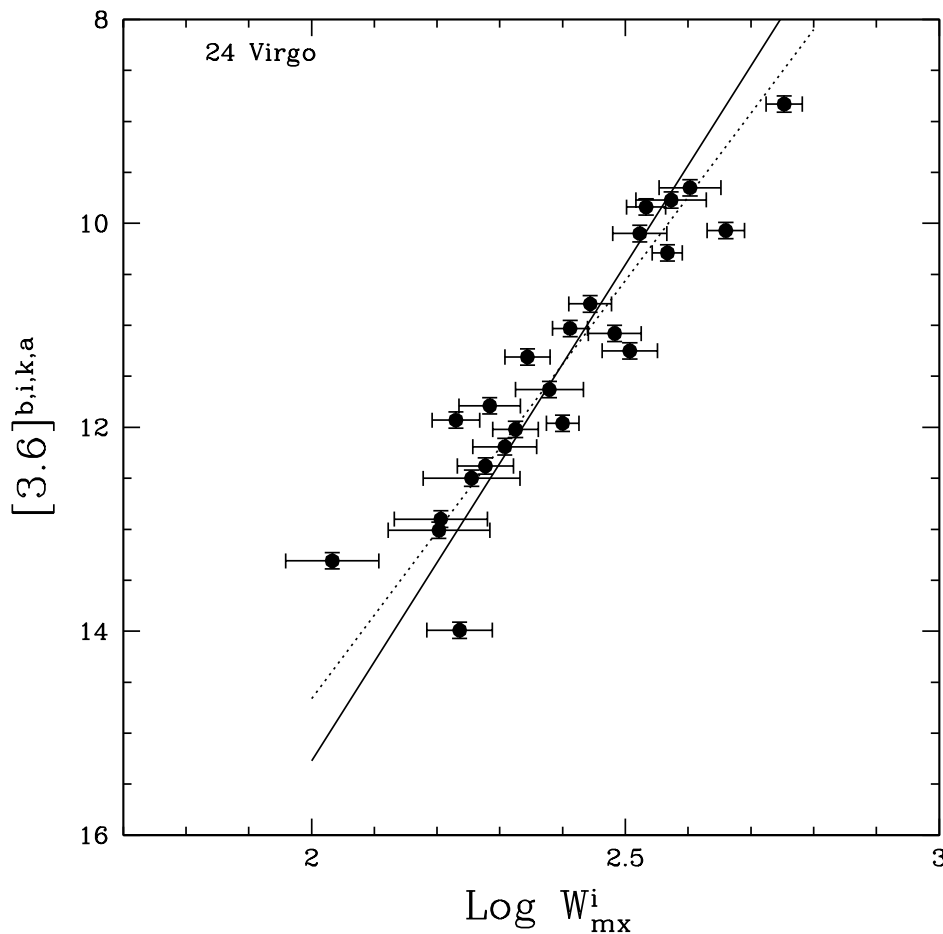


FIGURE 3.29: Tully-Fisher relation at $3.6 \mu\text{m}$ for the Virgo Cluster. The solid line gives the inverse fit of the universal template correlation. The dotted line is the inverse fit of the correlation for the Virgo Cluster alone.

⁶Note that Mocz et al. (2012) calibrated the TFR in u, g, r, i, z bands of SDSS for over 25,000 galaxies and found no dependence on the environment. If there is one it would be only at the 3% level. This comforts our assumption.

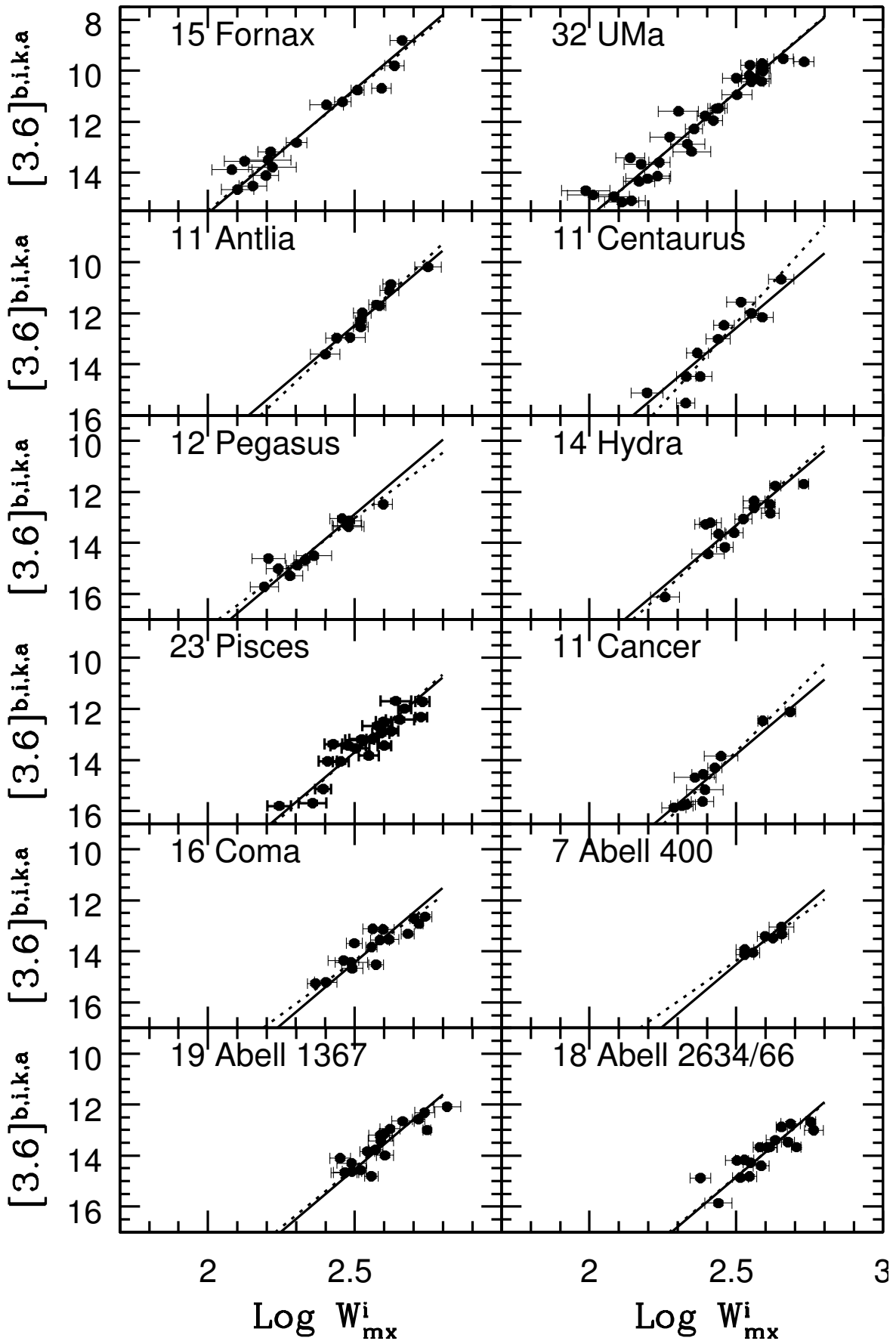


FIGURE 3.30: Tully-Fisher relation at $3.6 \mu\text{m}$ for the Fornax, Ursa Major, Antlia, Centaurus, Pegasus, Hydra, Pisces, Cancer, Coma, Abell 400, Abell 1367 and Abell 2634/66 clusters. Solid lines give the inverse fit of the universal template correlation. Dotted lines are the inverse fits of the TF correlation for each cluster.

The next step is to combine the 13 individual cluster correlations by vertical translations. The Virgo Cluster is used as a reference. Each preliminary zeropoint from the individual fits ($-\frac{b}{a}$) provides us with a first estimate of the relative distance between the Virgo Cluster and the cluster in question. Apparent magnitude zeropoints confirm that Virgo, Fornax and Ursa Major are the closest clusters. Then come Antlia-Centaurus-Pegasus, then Hydra-Pisces-Cancer, and finally Coma and the three Abell clusters A1367, A400 and A2634/66. To establish the best universal slope and the best relative distances between clusters, we follow an iterative procedure. We initially consider the nearest three clusters because they are observed to comparable depths in intrinsic magnitude. The Fornax and Ursa Major magnitudes are shifted according to the difference in zeropoint with respect to Virgo. A least squares fit of the ITFR is made to this ensemble. The slope obtained from this fit is then assumed in a fit to the three clusters separately with only the zeropoint as a free parameter in each case. The first assumed offset for a cluster is corrected for the deviation of the mean zeropoint $z_{\bar{p}t} = \frac{1}{n} \sum_{i=1}^n (x_i - slope \times y_i)$ of that cluster from Virgo's zeropoint. Given the new zeropoint offsets the cycle is repeated, leading to rapid convergence. This procedure is repeated with the addition of each distance group in turn. Again, convergence is rapid. It is to be stressed that this procedure works because, following expectations, the slope of the ITFR is not affected by the magnitude level of truncation. This procedure would manifestly *not* work with the direct or bi-variate relations where the slopes vary with the level of truncation. In the end we obtain a slope of -9.74 ± 0.22 for the template ITFR. Zeropoint offsets with this "universal" slope are shown in Figure 3.31 and give relative distance moduli of clusters referenced to the Virgo Cluster. The universal slope of the ITFR is displayed in Figure 3.31 as well as by the solid lines in Figures 3.29 and 3.30. The error on each cluster zeropoint (offset + Virgo's zeropoint) is obtained by the standard deviation, *stddev* (scatter), of the galaxy zeropoints, $z_{pt} = x_i - slope \times y_i$, divided by the square root of the number n of galaxies in the cluster:

$$err_{z_{pt}} = stddev \sqrt{\frac{1}{n}} = \sqrt{\sum_{i=1}^n \frac{(z_{pt} - z_{\bar{p}t})^2}{n-1} \frac{1}{n}} \quad (3.43)$$

At the time of this calibration work, [3.6] photometry was available for 26 nearby galaxies with suitable morphologies, inclinations, and linewidths that also have well measured distances from either the Cepheid period-luminosity or TRGB methodologies. These 26 are a subset of the 36 absolute calibrator galaxies used in the I band calibration (TC12). Their luminosity-linewidth correlation is seen in Figure 3.32 where now the ordinate is absolute magnitude from the established distances. The line is a least squares fit with the slope -9.74 prescribed by the template. The zeropoint is -20.34 ± 0.10 where the error is the sum in quadrature of the standard deviations (scatters) of all the calibrators together and of the zeropoint calibrators divided by their respective number. The most deviant point is the fastest rotator, NGC

2841, with a deviation of 2.7σ with respect to the template dispersion. This galaxy was a 2.3σ deviant in the I band calibration. There is nothing unusual about this galaxy other than its extreme rotation rate so we see no reason to disregard it as a calibrator.

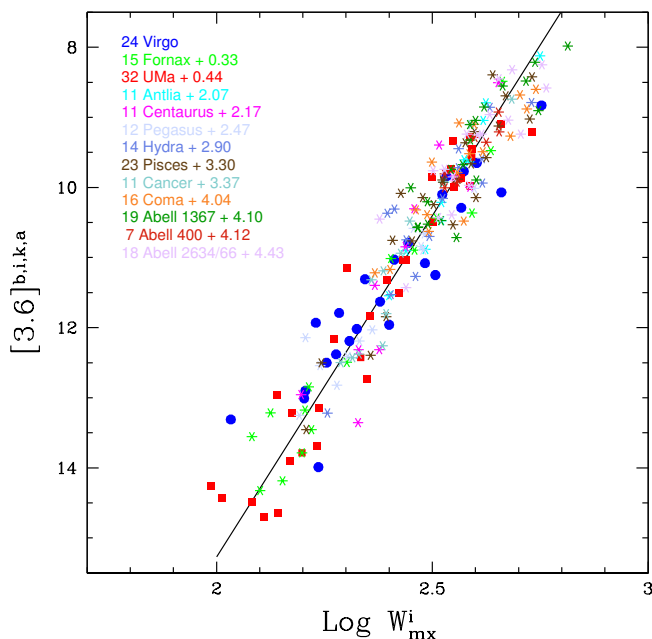


FIGURE 3.31: Template Tully-Fisher relation in the $[3.6]$ band obtained with data from 213 galaxies in 13 clusters. Offsets given with respect to the Virgo Cluster represent distance modulus differences between each cluster and Virgo. The solid line is a least squares fit to all the galaxies with errors entirely in linewidths, the ITFR.

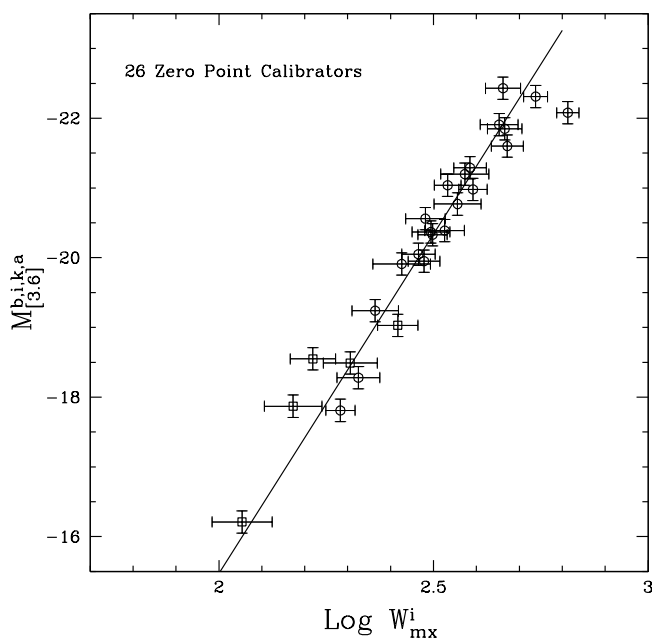


FIGURE 3.32: TFR for the 26 galaxies with distances established by observations of Cepheid stars (circles) or Tip of the Red Giant Branches (squares). The solid line is the least squares fit with the slope established by the 13 cluster template. The zeropoint of the TFR is set at the value of this fit at $\log W_{mx}^i = 2.5$.

The distance to the Virgo Cluster is given by the zeropoint of the constrained slope shown in Figure 3.31 minus the zeropoint of the absolute calibration shown in Figure 3.32. Application of this shift allows both cluster template and zeropoint calibrator galaxies to be plotted together as seen in Figure 3.33. The ITFR expression in the [3.6]-band is given by:

$$M_{[3.6]}^{b,i,k,a} = -(20.34 \pm 0.10) - (9.74 \pm 0.22)(\log W_{mx}^i - 2.5) \quad (3.44)$$

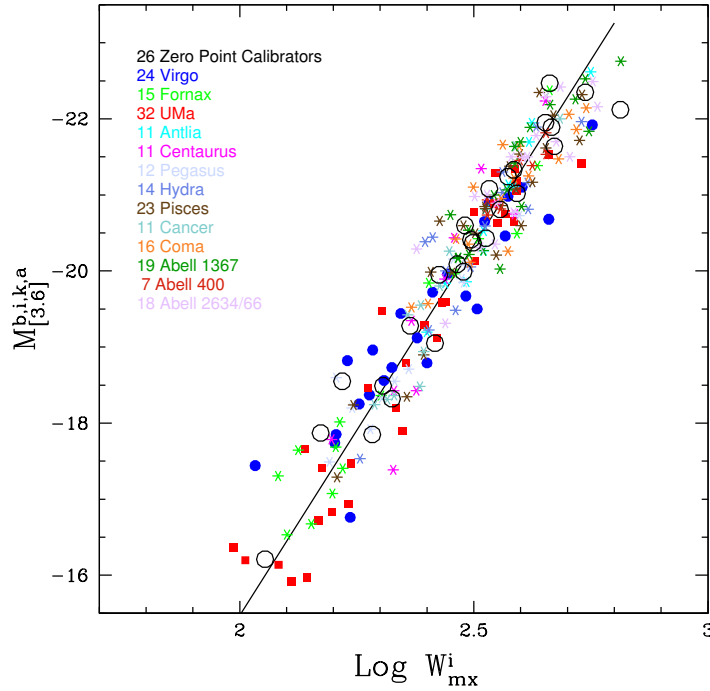


FIGURE 3.33: The template of the [3.6] band - HI linewidth correlation is built with 213 galaxies in 13 clusters extending in range from 1000 to 10,000 km s⁻¹ with the absolute magnitude scale set by 26 zeropoint calibrators.

The TFR scatter in magnitudes (relevant for distance measurements) for the entire cluster template sample is ± 0.49 magnitude from the universal ITFR, corresponding to a scatter in distance of 25%. The scatter for the 26 zeropoint calibrators is a similar 0.44 magnitude. Dispersion increases toward fainter magnitudes as well documented at *I* band by [Giovanelli et al. \(1997a\)](#). The sample presented here is still limited but the dispersion is consistent with a Gaussian distribution. With large samples ([Tully et al., 2008](#)) one finds that about 3% of candidates are more deviant than anticipated by Gaussian statistics. The causes are not always evident.

Scatter may arise from:

- measurement uncertainties affecting magnitudes, inclinations, and linewidths but observational errors are not likely to account for the whole scatter (e.g. [Bothun and Mould, 1987](#)),

- correction uncertainties applied to measured parameters,
- "cosmic" scatter, e.g. cluster depth effects or interlopers, deviations from disk planarity, other gravitational and photometric asymmetries, variations in the stellar population make-up, variations in disk-to-bulge ratios, etc.

Whatever the sources, we have a standard to meet set by the I band analysis. The sample used in the current analysis involve more than 70% of the sample used in the I -band calibration (TC12). Inclinations and linewidths are the same, the factors mentioned associated with cosmic scatter are the same, corrections to photometric parameters are reduced in the mid-infrared, and the integrity of the magnitude measurements must be at least as good or better with the Spitzer observations since observations are made all-sky with the same instrumental configuration. Error bars on magnitudes are reduced compared with those in I band to the degree that observational errors in magnitudes are a minimal component of uncertainties. Yet the scatter found at I band is less: ± 0.41 magnitude for the cluster template sample, lower with a significance of 2σ , and 0.36 magnitude for the zeropoint calibrators. As much as half of the increase in magnitude scatter will occur because the slope of the correlation is steeper in the mid-infrared. However there could be an additional explanation for the increased scatter found at [3.6].

| | v_{CMB} | N | Slope | ZP | scatter | ZP_{color} | scatter | bias | DM | Dist | V/D |
|----|-----------|----|-------------------|------------------|---------|------------------|---------|------|------------------|-----------------|----------------|
| V | 1410 | 24 | -8.21 ± 0.71 | 10.40 ± 0.14 | 0.67 | 10.49 ± 0.11 | 0.56 | 0.00 | 30.83 ± 0.14 | 14.7 ± 0.9 | 96.2 ± 6.9 |
| F | 1484 | 15 | -9.39 ± 0.66 | 10.73 ± 0.13 | 0.49 | 10.86 ± 0.12 | 0.47 | 0.00 | 31.20 ± 0.14 | 17.4 ± 1.2 | 85.4 ± 6.4 |
| U | 1101 | 32 | -9.83 ± 0.52 | 10.84 ± 0.10 | 0.55 | 10.94 ± 0.08 | 0.44 | 0.00 | 31.28 ± 0.11 | 18.0 ± 0.9 | 61.1 ± 4.2 |
| An | 3119 | 11 | -10.79 ± 0.79 | 12.47 ± 0.07 | 0.23 | 12.44 ± 0.06 | 0.21 | 0.04 | 32.82 ± 0.10 | 36.6 ± 1.7 | 85.1 ± 4.2 |
| Ce | 3679 | 11 | -12.69 ± 1.76 | 12.57 ± 0.19 | 0.62 | 12.58 ± 0.18 | 0.59 | 0.01 | 32.93 ± 0.20 | 38.5 ± 3.5 | 95.4 ± 8.8 |
| Pe | 3518 | 12 | -8.55 ± 0.94 | 12.87 ± 0.13 | 0.44 | 12.89 ± 0.12 | 0.42 | 0.01 | 33.24 ± 0.14 | 44.5 ± 3.0 | 79.1 ± 5.4 |
| H | 4121 | 14 | -10.48 ± 1.49 | 13.30 ± 0.14 | 0.53 | 13.35 ± 0.14 | 0.52 | 0.05 | 33.74 ± 0.16 | 56.0 ± 4.2 | 73.6 ± 5.5 |
| Pi | 4779 | 23 | -10.15 ± 0.82 | 13.70 ± 0.10 | 0.47 | 13.69 ± 0.08 | 0.40 | 0.02 | 34.05 ± 0.11 | 64.6 ± 3.4 | 74.0 ± 3.9 |
| Ca | 4940 | 11 | -11.46 ± 1.17 | 13.77 ± 0.12 | 0.39 | 13.78 ± 0.10 | 0.34 | 0.02 | 34.14 ± 0.13 | 67.3 ± 4.0 | 73.4 ± 4.4 |
| Co | 7194 | 16 | -8.49 ± 1.10 | 14.44 ± 0.12 | 0.49 | 14.50 ± 0.10 | 0.39 | 0.06 | 34.90 ± 0.13 | 95.4 ± 5.6 | 75.3 ± 4.5 |
| A4 | 7108 | 7 | -8.03 ± 1.40 | 14.52 ± 0.08 | 0.21 | 14.50 ± 0.08 | 0.21 | 0.10 | 34.94 ± 0.11 | 97.3 ± 5.1 | 73.1 ± 3.8 |
| A1 | 6923 | 19 | -9.38 ± 1.16 | 14.50 ± 0.11 | 0.47 | 14.50 ± 0.11 | 0.42 | 0.08 | 34.92 ± 0.14 | 96.4 ± 6.0 | 71.8 ± 4.5 |
| A2 | 8381 | 18 | -9.55 ± 1.38 | 14.83 ± 0.12 | 0.51 | 14.85 ± 0.10 | 0.44 | 0.05 | 35.24 ± 0.13 | 111.7 ± 6.6 | 75.0 ± 4.4 |

TABLE 3.5: Properties of the Cluster Fits: (1) Cluster name (V Virgo, F Fornax, U Ursa Major, An Antlia, Ce Centaurus30, Pe Pegasus, H Hydra, Pi Pisces, Ca Cancer, Co Coma, A4 Abell 400, A1 Abell 1367 and A2 Abell 2634 and 2666), (2) Mean velocity of the cluster with respect to the CMB, km s^{-1} , (3) Number of studied galaxy per cluster, (4) Slope of the inverse fit, (5) Zero point relative to Virgo's zeropoint, no color adjustment, mag, (6) Scatter, no color adjustment, (7) Zero point relative to Virgo's zeropoint after color adjustment, mag, (8) Scatter after color adjustment, mag, (9) Bias, mag, (10) Bias corrected Distance Modulus, mag, (11) Cluster Distance, Mpc, (12) Hubble parameter, $\text{km s}^{-1} \text{Mpc}^{-1}$

3.4.1.3 A Color Dependence

It has long been known that the TFR steepens toward longer wavelengths (e.g. Courteau et al., 2007; Tully et al., 1982). The effect is seen in Figure 3.34 (Note: in the discussions in this section all optical photometry values have been transferred from Vega system to AB system according to relations 3.27). There is a strong color correlation with linewidth, more rapidly rotating galaxies tend to be redder, so at longer wavelengths the high rotation end of the TFR rises with respect to the low rotation end. Within a small linewidth interval, redder galaxies will rise more than bluer galaxies. It follows that red and blue galaxies cannot be well mixed in the TFR at all wavelengths. The trends that could be anticipated are shown in Figure 3.36 (only a portion of the sample have photometric measurements at B band). The comparison of fluxes at four bands from B to $[3.6]$ for individual sources given in Figure 3.35 confirms the well known linkage between galaxy type and color. Early type galaxies have relatively more infrared flux relative to late type galaxies. This point was also illustrated with the representative spectral energy distribution plots in Figure 3.3. Galaxies that are more luminous and earlier in type are dominated by older, more metal enriched red giant stars emitting more in the infrared.

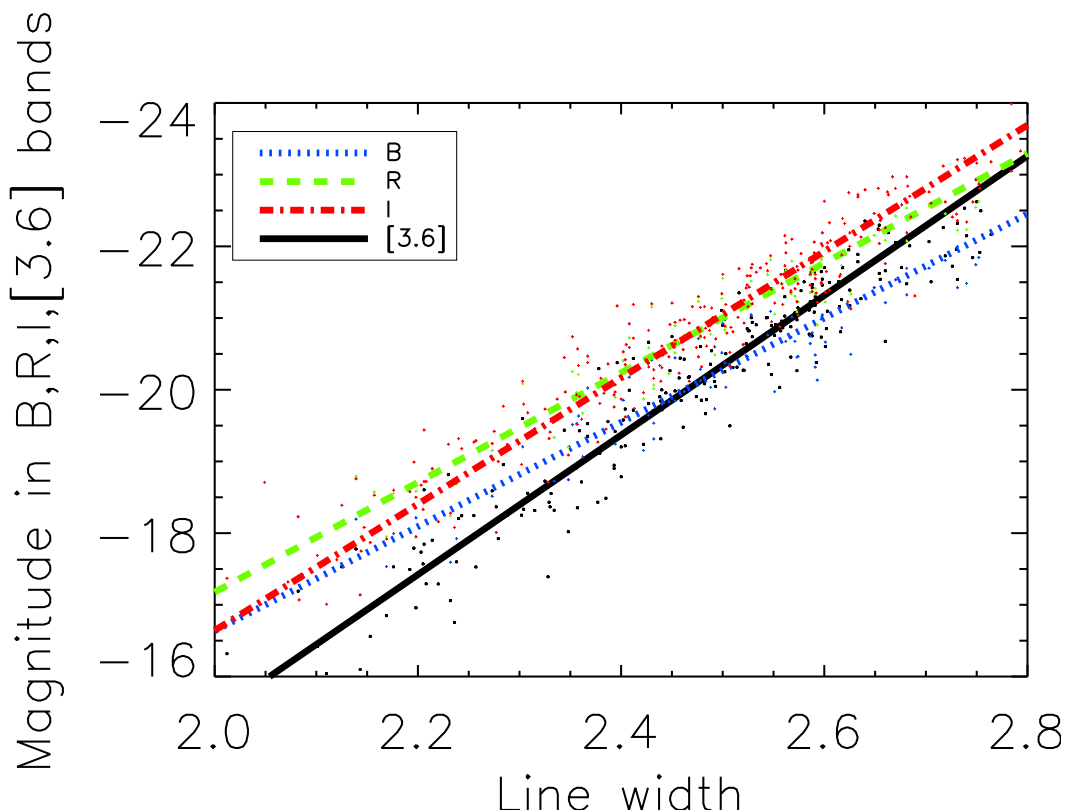


FIGURE 3.34: TFR in B , R , I and $[3.6]$ bands. B and R bands data are from Tully and Pierce (2000), I band data are from TC12 and $[3.6]$ band data are from section 3.3. Linewidths are the same as used by TC12. The slopes steepen from blue to red, with values -7.27 at B , -7.65 at R , -8.81 at I , and -9.74 at $[3.6]$.

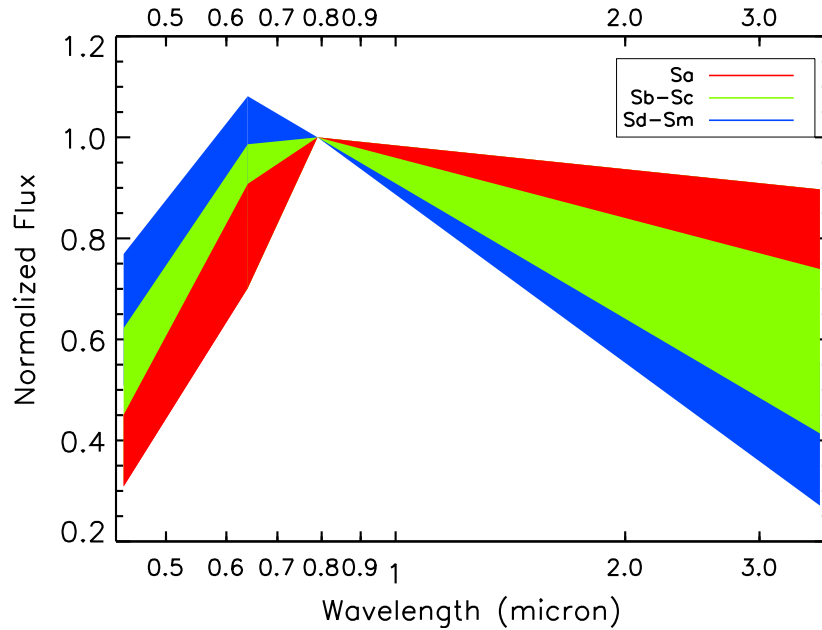


FIGURE 3.35: Representation of fluxes at B , R , I , $[3.6]$ bands normalized to unity at I band. Type Sa: red; types Sb-Sc: green; types Sd-Sm: blue. The extrema are defined by members of our sample and color swaths indicate the domains dominated by the different types.

There have been long standing suggestions that the dispersion in the TFR might be reduced by inclusion of additional parameters. In an early instance (Rubin et al., 1985), when only photographic or photoelectric magnitudes were available, the case was framed in terms of galaxy types which are strongly correlated with color. Masters et al. (2006) have maintained the use of a type separation with I band work. Tully and Pierce (2000) acknowledged the hint of a type dependence in the I band relation but concluded that the evidence remained too weak to warrant adding complexity to the TFR analysis. The situation changes with the mid-infrared information. In spite of superior photometry the scatter in the TFR is increased and there is a significant color signature. The variations in spectral energy distribution implicit in the range of representative colors shown in Figure 3.35 provide a natural explanation given the extended lever arm from the optical to the $[3.6]$ band.

There is also the possibility that some flux in the $[3.6]$ band may come from other than old stars. Meidt et al. (2012) determined that $12 \pm 5\%$ of $[3.6]$ flux arises from hot dust, Polycyclic Aromatic Hydrocarbon emission, or young to intermediate age stars in six representative spiral galaxies observed with *Spitzer Space Telescope*. However the variance of 0.05 mag is small compared with the ITFR scatter. Moreover, it can be anticipated that the galaxies most affected by manifestations of star formation are later, bluer types, whence augmented flux will tend to diminish a color term arising from old stars. Whatever the cause, it can be anticipated that the scatter can be decreased with the introduction of a color correction. To address this issue we consider the straight line fits included in the top and bottom left panels of Figure 3.36. The fits are least squares minimizations on the ordinate parameter;

the difference in magnitude of a target from the mean TFR. The bottom right panel shows the concordant variation of color with linewidth. Faster rotators tend to be redder.

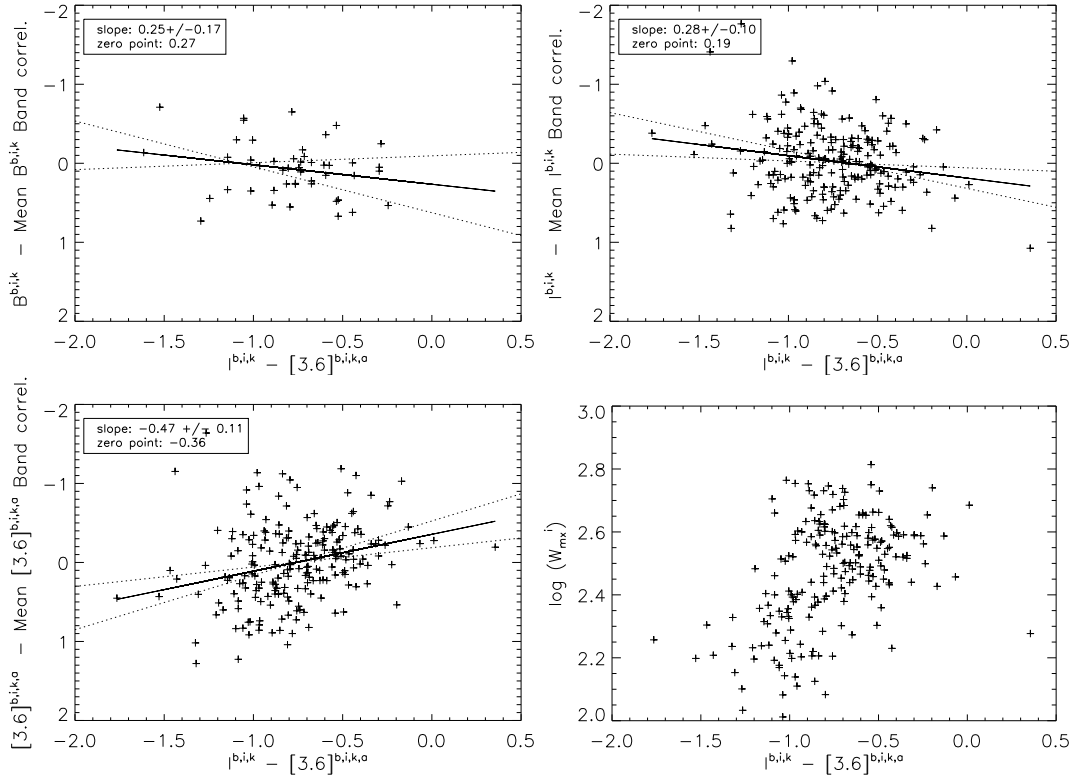


FIGURE 3.36: *Top and left bottom panels:* Deviations from the mean ITFR relation as a function of $I - [3.6]$ color. Solid and dotted lines are best fits and 95% probability limits. *Top left:* At B band red galaxies tend to lie below the mean relationship. *Top right:* At I band there is a hint that red galaxies lie low although the correlation fit is dominated by a few extreme cases. *Bottom left:* At $[3.6]$ band the sense of the correlation has flipped and red galaxies tend to lie above the mean relation. *Bottom right:* The correlation between linewidth and color.

In the mid-infrared case, the offset for an individual galaxy from the mean fit in Figure 3.36 is:

$$\Delta M_{[3.6]}^{color} = M_{[3.6]}^{b,i,k,a} + 20.34 + 9.74(\log W_{mx}^i - 2.5). \quad (3.45)$$

An equivalent correction can be constructed with apparent magnitudes rather than absolute magnitudes, $\Delta [3.6]^{color} = \Delta M_{[3.6]}^{color}$, with an appropriate replacement of the zeropoint constant in equation 3.45. The correction term commensurate with the fit in the third panel of Figure 3.36 is:

$$\Delta [3.6]^{color} = \Delta M_{[3.6]}^{color} = -(0.47 \pm 0.11)[(I^{b,i,k} - [3.6]^{b,i,k,a}) + 0.77]. \quad (3.46)$$

where both $I^{b,i,k}$ and $[3.6]^{b,i,k,a}$ band magnitudes are in the AB system. $I^{b,i,k,a}$ is the corrected I-band apparent magnitude. We introduce a new color adjusted magnitude parameter $C_{[3.6]} = [3.6]^{b,i,k,a} - \Delta [3.6]^{color}$ where the distinct nomenclature emphasizes the composite

nature of this pseudo-magnitude. Next, the analysis discussed in subsection 3.4.1.2 leading to the construction of Figure 3.31 is repeated. Likewise, the adjustments are applied to the calibrators with independently established distances and the procedures that lead to Figure 3.33 are repeated. The adjusted relations are shown in Figure 3.37. The new correlation is described by the formula:

$$M_{C_{[3.6]}} = -(20.34 \pm 0.08) - (9.13 \pm 0.22)(\log W_{mx}^i - 2.5) \quad (3.47)$$

The flattening of the adjusted relation comes about since redder systems move downward and redder galaxies tend to have larger linewidths. The overall magnitude scatter in the new relation is ± 0.44 magnitude (corresponding to a scatter in distance of 22%), down from 0.49 magnitude before adjustment, and comparable with 0.41 found at I band with an otherwise comparable analysis (TC12). The comparable numbers for the zeropoint calibrators alone are a scatter of 0.37 with the adjusted parameter $C_{[3.6]}$, 0.44 before the adjustment, and 0.36 at I band. The comparisons between [3.6] and I have some imprecision because the sample sizes for the latter are 25% greater. The TFR parameters derived from alternative samples and bandpasses are summarized in Table 3.7.

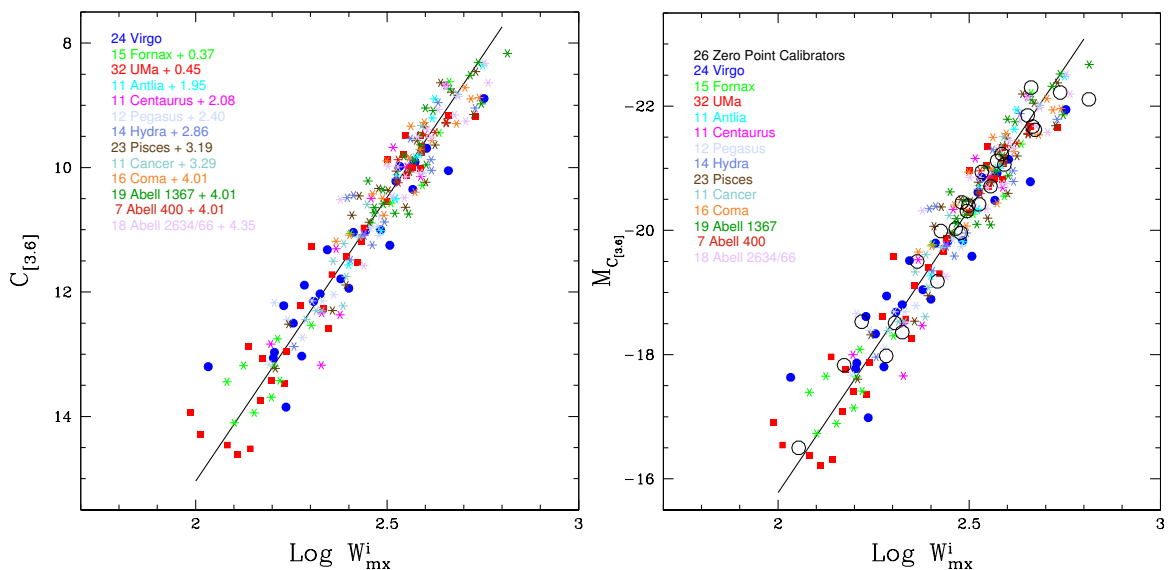


FIGURE 3.37: The ITFR after adjustments for the color term. *Left*: Color adjusted apparent magnitudes translated to the relative distance of the Virgo Cluster. *Right*: Color adjusted absolute magnitudes with the absolute distance scale established by the galaxies with independent distances represented by large open circles.

3.4.1.4 Bias and an Hubble Constant Estimate

Willick (1994) showed that a small Malmquist bias exists in the use of the ITFR, although reduced from the direct TFR by a factor of 6 in the situation he explored (Willick et al.,

1995). Reducing the bias reflects on the Hubble Constant (e.g. Bottinelli et al., 1986). The bias arises from two effects:

- sample selection departs from an idealized case of a flat magnitude limit because samples have been selected in blue bands and color terms translate to a slope in the limiting magnitude in the infrared: slower rotators which tend to be bluer are favored for inclusion over faster rotators which tend to be redder (see Figure 3.38, left). It is the so-called Gould’s effect (Gould, 1993),
- the shape of the galaxy luminosity function contributes to the bias because there are more intrinsically fainter galaxies that scatter bright-ward through errors than intrinsically brighter galaxies that scatter faint-ward (Eddington, 1913). The bias increases with distance as the effect of the exponential cutoff of the luminosity function plays an increasing role while for the direct fit it is a constant whatever the completeness of the cluster considered is (e.g. Teerikorpi, 1990, 1993).

The Schechter luminosity function is written:

$$\Phi(L) = \left(\frac{\Phi^*}{L^*}\right)\left(\frac{L}{L^*}\right)^\alpha \exp\left(\frac{-L}{L^*}\right) \quad (3.48)$$

where L^* is a characteristic luminosity above which the distribution decreases exponentially, α is the slope for "small" luminosity L , and Φ^* specifies the normalization. Since $\frac{dL}{L} = -0.4 \ln 10 dM$ from the definition of the absolute magnitude 3.9, it can be rewritten as a function of magnitude:

$$\Phi(M) = \Phi(L) \left| \frac{dL}{dM} \right| = \Phi(L) 0.4 \ln 10 L = (0.4 \ln 10) \Phi^* 10^{0.4(\alpha+1)(M-M^*)} \exp(-10^{0.4(M^*-M)}) \quad (3.49)$$

where $M^* \propto -2.5 \log L^*$. This equation depends both on galaxy type and environment.

The amplitude of the bias from the two effects was explored with the calibration at I band (TC12). The situation now with the [3.6] band sample is slightly worse than at I because the wavelength interval from selection at B is larger. The bias analysis carried out in the case of the I band calibration is repeated here, tailored to the current situation. We first combine the Virgo, Fornax, and Ursa Major samples to improve statistics and include contributions from a range of environments. This ensemble is described by a Schechter (1976) function with faint end slope $\alpha = -0.9$ and a bright end cutoff at $M_{[3.6]}^* = -22$. Then we randomly populate an artificial TFR to match the observed [3.6] band relation in terms of slope and zeropoint, drawing from the Schechter luminosity function. We fake a scatter of 0.4 magnitude. The faint limit or cutoff is determined empirically to roughly obey the relation $M_{[3.6]}^{lim} = C_\ell - 2.70(\log W_{mx}^i - 1.8)$ where C_ℓ couples with distance. The artificial TFR and the cutoff for

the nearest clusters is shown in the left panel of Figure 3.38. The dashed blue line indicates the cutoff experienced at a distance modulus of 31. The cutoff, characterized by C_ℓ , slides to brighter (more negative) magnitudes linearly with increasing distance modulus. The bias $\langle \Delta M \rangle_{measured}$ is determined at intervals of C_ℓ corresponding to increasing distance. More precisely, for each successive sample with a different cutoff C_ℓ , the inverse slope is determined and compared to the expected slope without any bias (namely, slope given to the artificial TFR). Then $\langle \Delta M \rangle_{measured}$ is the average deviation in magnitudes obtained with the inverse slope from the fiducial relation with the expected slope where $\langle \Delta M \rangle_{true} = 0$ by construction. The growth of the bias as a function of cutoff magnitude is seen in the right panel of Figure 3.38. The solid curve, normalized to zero at a distance modulus $\mu = 31$ where even the faintest of useful candidates are included, is described by the formula between bias, b , and distance modulus, μ :

$$b = -0.0065(\mu - 31)^2 \quad (3.50)$$

By comparison, the coefficient in the case of the I band analysis is -0.005 . The letters at the bottom of the figure are codes for the 13 calibrating clusters (see Table 3.5 to decipher codes) and their horizontal placements indicate the respective sample limits and projection upward gives the corresponding biases. These biases are recorded in Table 3.5 and are reflected in the adjusted cluster moduli and distances. For a galaxy in the field, the corrected distance modulus μ^c can be expressed as

$$\mu^c = (C_{[3.6]} - M_{C_{[3.6]}}) + 0.0065[(C_{[3.6]} - M_{C_{[3.6]}}) - 31]^2 \quad (3.51)$$

The last column in Table 3.5 records the "Hubble parameter" for each cluster: the velocity of the cluster in the CMB frame divided by the measured distance. These quantities are plotted against distance in Figure 3.39. A similar figure was presented as a summary of results from the I band calibration with the same 13 clusters (TC12: distances compared in Table 3.7). Here, as there, we see a large scatter in the Hubble parameter for the nearer clusters and small scatter for the more distant clusters. It can be anticipated that the measures for the nearer clusters are strongly affected by peculiar motions. The five clusters within 40 Mpc are all part of our extended supercluster complex: either within the historic Local Supercluster or the so-called Great Attractor region. The low scatter among the seven clusters more distant than 50 Mpc ($v_{CMB} > 4000 \text{ km s}^{-1}$) suggests that the relative contributions of peculiar velocities have a modest effect on redshifts at such large distances.

In the case of the I band calibration, the mean value of the Hubble parameter for the seven most distant clusters was $75.1 \pm 2.7 \text{ km s}^{-1} \text{ Mpc}^{-1}$ where the error is just the root mean square scatter of the seven contributions. That value would increase to 75.8 with the revised Large Magellanic Cloud distance from Monson et al. (2012). With the present calibration, including the new Large Magellanic Cloud distance, the fit shown in Figure 3.39 gives a value

of $H_0 = 73.8$ with a root mean square scatter of 1.1 and a standard deviation of $0.4 \text{ km s}^{-1} \text{ Mpc}^{-1}$ for the same seven clusters considered previously. If the fit is extended to include the Pegasus Cluster at 44.5 Mpc then $H_0 = 74.4$ and the scatter is $2.0 \text{ km s}^{-1} \text{ Mpc}^{-1}$. The effect of a deviant radial motion of 200 km s^{-1} is illustrated in the figure as a function of distance.

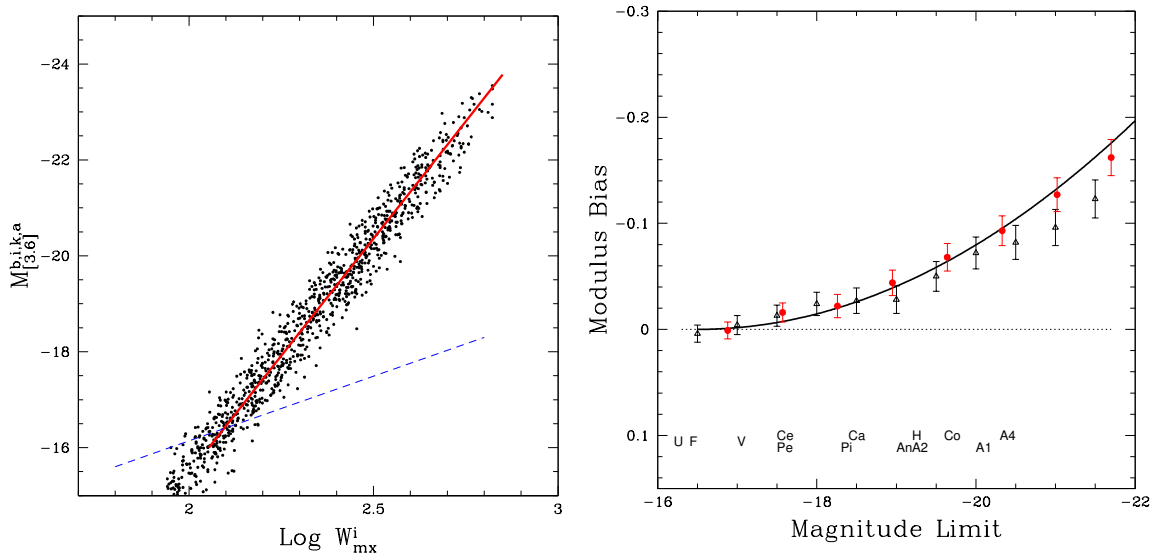


FIGURE 3.38: *Left*: Simulated TFR drawing randomly from a Schechter luminosity function with slope $\alpha = -0.9$ and cutoff $M^* = -22$. The ITFR has slope -9.13 and scatter 0.4 magnitude. The dashed blue slanting line illustrates the color dependence at the faint limit resulting from sample selection in the blue. *Right*: Bias $\langle \Delta M \rangle_{measured}$ as a function of absolute magnitude limit which increases with distance. Black triangles: flat faint limit; red circles: faint limit increasing with increasing linewidth in accordance with the blue line in the left panel. Solid curve: the empirical bias fit $b = -0.0065(\mu - 31)^2$. Letters at the bottom are codes for the 13 calibrating cluster (see Table 3.5 for translation of codes). Their horizontal positions indicate sample limits and vertical intercepts with the solid curve give the corresponding biases.

The uncertainty from the fit in Figure 3.39 is given by the statistics of the deviations of the seven contributions. It is unrealistically low. This error is what is expected if there is perfect Hubble expansion. If peculiar motions of 200 km s^{-1} are the norm, and given the expected statistical errors on the distance D of each cluster (4-5 % according to Table 3.5), the anticipated scatter around the mean Hubble value is $\pm 2.6 \text{ km s}^{-1} \text{ Mpc}^{-1}$. We have used the propagation of error formula giving in this case:

$$err_{H=\frac{v}{D}} = \sqrt{\left(\frac{\partial H}{\partial v} err_v\right)^2 + \left(\frac{\partial H}{\partial D} err_D\right)^2} = \frac{1}{D} \sqrt{200^2 + (v \times 0.045)^2} \quad (3.52)$$

where the error on the velocity v was assimilated to the peculiar motions and $0.045 = \frac{err_D}{D}$ is a compromise between the 4-5 % statistical error on distances. The scatter is half this value. We consider this to be our 1σ random error. We have several sources of systematic error. The dominant component, creating almost 4% uncertainty in H_0 , comes from the

uncertainty in the TFR zeropoint with just 26 calibrators. Combined with a small uncertainty from the finite population of the template, the uncertainty in H_0 associated with the TFR calibration (assuming the zeropoint calibrator distances are perfect) is typically $\pm 2.9 \text{ km s}^{-1} \text{ Mpc}^{-1}$. We have used 1) the error on the zeropoint (and distance modulus μ) 0.08 mag, 2) $err_D = err_\mu \frac{\ln(10)}{5} D$ from the definition of the distance modulus 3.10 and 3) formula 3.52 reduced to errors on distances D solely. However, the zeropoint calibrator distances are not perfect. Freedman et al. (2012) and Riess et al. (2011) report that with new Milky Way parallaxes for Cepheid stars and mid-infrared Spitzer photometry the uncertainty in the Cepheid scale is in the range $\pm[1.9 - 2.5] \text{ km s}^{-1} \text{ Mpc}^{-1}$. The TRGB zeropoint calibration which concerns 4 of the 26 calibrators, has similar or smaller systematics. The cumulative systematic error (sum in quadrature) in H_0 is $\pm[3.5 - 3.8] \text{ km s}^{-1} \text{ Mpc}^{-1}$. Combining random and systematic components we find $H_0 = 73.8 \pm 2.6(\text{ran}) \pm [3.5 - 3.8](\text{sys}) \text{ km s}^{-1} \text{ Mpc}^{-1}$.

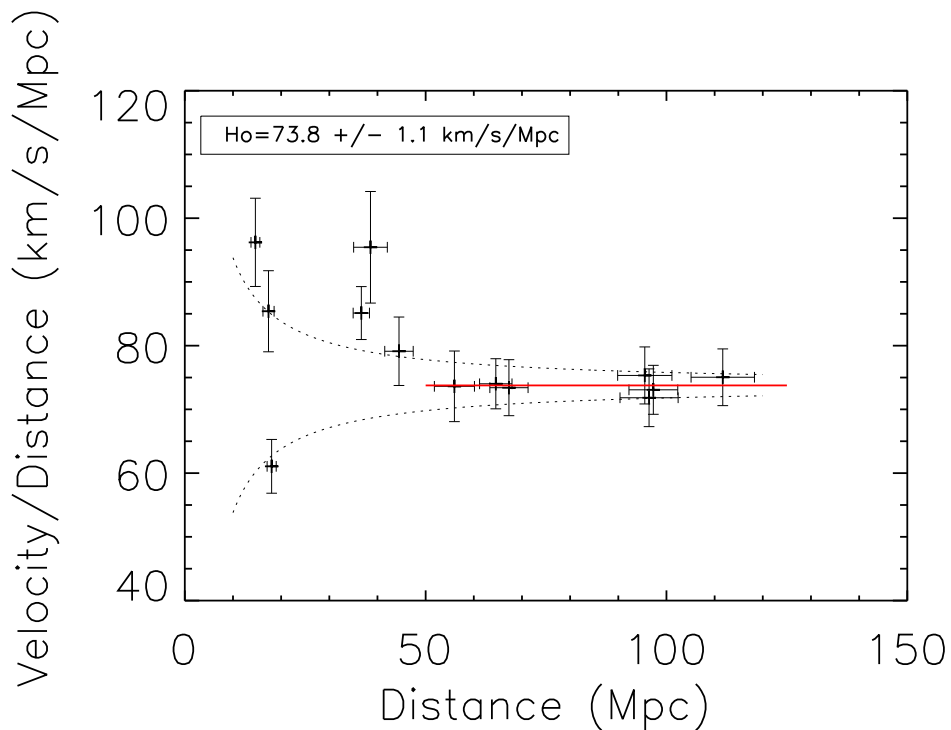


FIGURE 3.39: Hubble parameter as a function of distance. The red solid line is a fit to cluster points at distances greater than 50 Mpc ($v_{CMB} > 4000 \text{ km s}^{-1}$). The fit gives $H_0 = 73.8 \pm 1.1 \text{ km s}^{-1} \text{ Mpc}^{-1}$. Curved dotted lines illustrate deviations in velocity of 200 km s^{-1} from the fit.

3.4.2 Robustness of the Calibration

In this section, the robustness of both the calibration method and the mid-infrared TFR presented in the previous subsections is shown. The previously expounded calibration was indeed presented at the time of its release as preliminary, especially because of the lack of completeness of the calibrator sample. Still, this subsection confirms this first calibration.

Magnitudes used in this subsection come from ARCHANGEL (Cosmicflows with Spitzer survey completed in the mean time). They are combined with this time S⁴G-pipeline (magnitudes publicly released in the mean time) or CHP-pipeline magnitudes (as earlier) or both when they are available.

3.4.2.1 Increasing the Calibrator Sample and Changing the Selection Band

The previously derived template TFR made use of 213 galaxies in 13 clusters. The zero point calibration was given by 26 additional galaxies. The inverse fit was used to calculate the slope of the relation and a very small correction was computed to remove a bias. The same analysis is done here but using an updated sample of template and zeropoint calibrators. This sample is improved with respect to the previous one by two aspects:

- the number of calibrators is increased from 213+26 to 287+32. The list of these calibrators and characteristics are given in the second table (Table B.2) of Appendix B,
- galaxies are now selected in K Band which decreases the selection bias. The selection of calibrators is extended to be complete to K=11.75 magnitude, the limit of the 11.75-2MASS Redshift Survey (Huchra et al., 2012)

This new set of calibrators follows the same rules as the previous one. Typically, candidates are chosen out of a projection-velocity window, morphological types earlier than Sa are excluded, profiles with visible confusion or tidal disruption are disregarded and inclinations must be greater than 45°. Zeropoint calibrators also need to have a very well known distance from Cepheid or Tip of the Red Giant Branch measurements.

Then, we proceed exactly as described in subsection 3.4.1:

- an inverse TFR is fitted to each one of the clusters separately. Figure 3.40 left shows the example of the Virgo cluster. Parameters for every cluster are given in Table 3.6. The inverse fit assumes errors only in linewidth to obtain results close to free of Malmquist magnitude selection bias. Yet, there will be a tiny bias residual because of the bright end cutoff of the luminosity Schechter function although it should be somewhat smaller than for the previous calibration where, in addition, the selection was made in the B band. We investigate this bias relic at the end of this subsection,

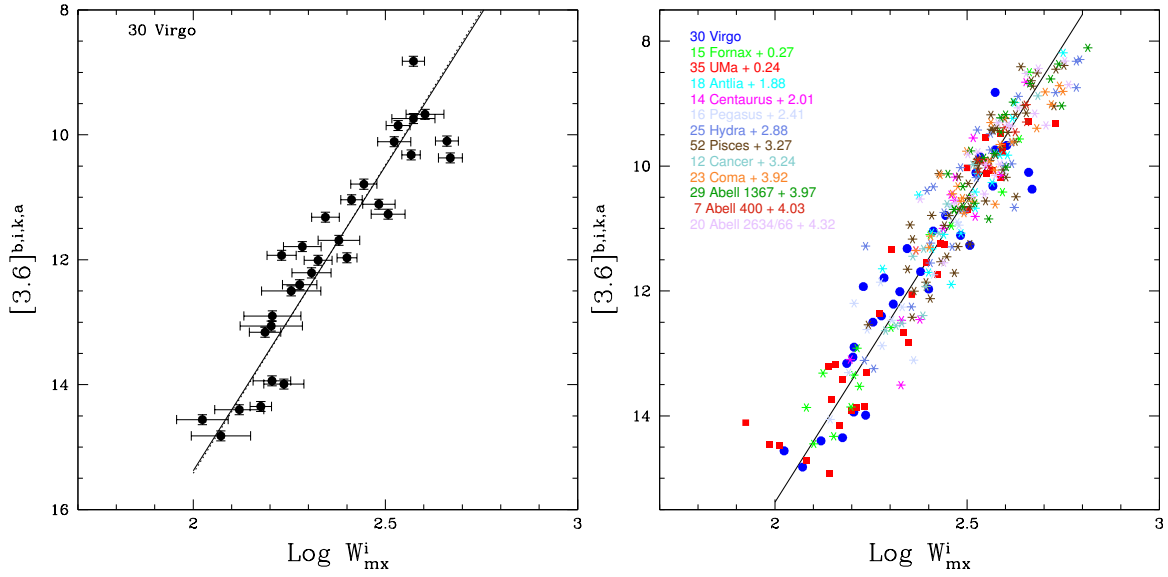


FIGURE 3.40: *Left*: Inverse Tully-fisher relation at 3.6 microns for the Virgo cluster in dotted line. The solid line stands for the inverse Tully-Fisher of the template cluster. *Right*: Universal inverse TFR at 3.6 microns obtained with 287 galaxies in 13 clusters. Numbers of galaxies selected for the calibration per clusters are given in front of clusters' names while distance modulus differences between each cluster and Virgo are visible after clusters' names.

- because slopes are quite similar between clusters in Table 3.6, individual fits are consistent with the postulate of a universal TFR. Thus the 13 clusters are combined into one template cluster. Virgo is taken as the reference cluster and each one of the 12 other clusters is shifted to be on the same scale. Three by three, clusters are inserted into the template and offsets between them and Virgo are found by an iterative process which relies on least squares fits of the inverse TFR. Convergence is quick. We obtain a slope of -9.77 ± 0.19 , insignificantly different from the previous slope -9.74 confirming the robustness of the previous calibration and of the method. The universal slope and the offsets with respect to Virgo are shown on Figure 3.40 right,
- the zeropoint scale is set by the distance modulus of the Large Magellanic Cloud, $18.48 \pm [0.04-0.07]$ magnitude (Monson et al., 2012; Riess et al., 2011). Then, the 32 zeropoint calibrators give the zeropoint of the universal TFR assuming the slope of the cluster template. Their correlation is visible on Figure 3.41 left where now absolute magnitudes replace apparent magnitudes. The zeropoint of the TFR is the difference between the zeropoint given by zeropoint calibrators on Figure 3.41 left and by Virgo in Figure 3.40 right: -20.31 ± 0.09 . The zeropoint is once again insignificantly larger than that of the previous calibration, -20.34 ,
- the universal relation at 3.6 microns is visible on Figure 3.41 right and is given by a slightly updated version of the previous calibration 3.44:

$$M_{[3.6]}^{b,i,k,a} = -(20.31 \pm 0.09) - (9.77 \pm 0.19)(\log W_{mx}^i - 2.5) \quad (3.53)$$

with a scatter of 0.54 for the 13 clusters and 0.45 for the 32 zeropoint calibrators. The causes of such a scatter have already been discussed. We will again apply a color correction in the next subsection to confirm the color corrected TF relation derived before and the robustness of such a process.

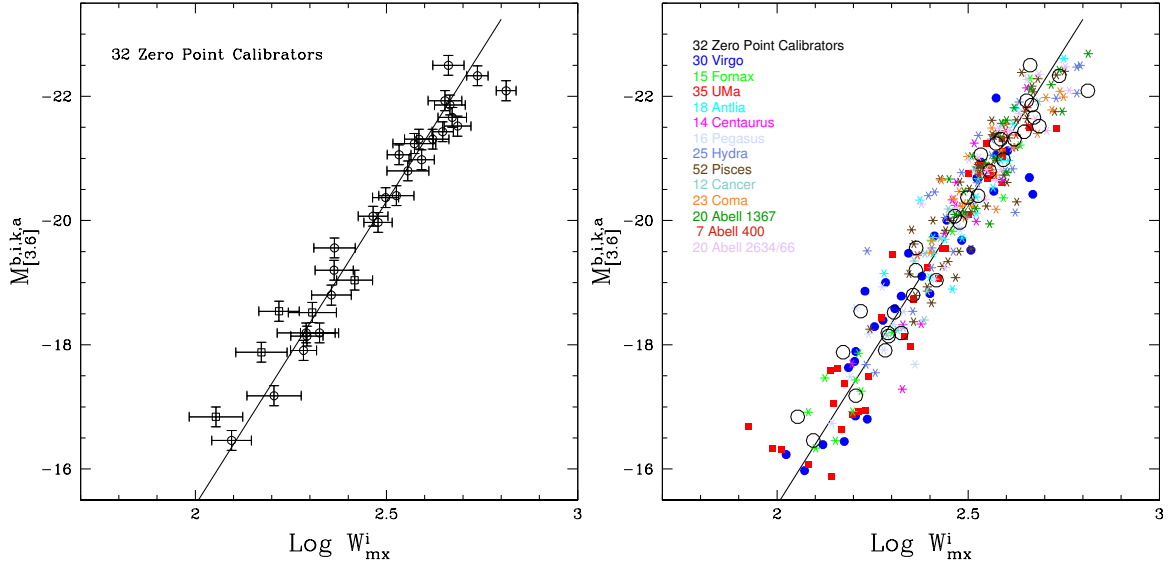


FIGURE 3.41: *Left*: Inverse TFR for the 32 zeropoint calibrators with distances obtained with Cepheids (circles) or Tip of the Red Giant Branch (squares). The slope of the solid line is given by the luminosity-linewidth correlation of the template cluster while the zeropoint is obtained with the least squares fit to the 32 galaxies. The zeropoint is set at $\log W_{mx}^i = 2.5$. *Right*: Inverse Tully-Fisher relation at 3.6 microns with the slope built out of 287 galaxies in 13 clusters and the zeropoint set by 32 galaxies with very accurate distances.

3.4.2.2 Again a Color Term

Because of the increased number of data, we double check the color term deriving a new estimate. The straight line fit given in Figure 3.42 left is again a least squares minimization with respect to the difference in magnitude of a galaxy from the derived TFR. In the [3.6] band, a galaxy is offset from the TFR by:

$$\begin{aligned} \Delta M_{[3.6]}^{color} &= M^{b,i,k,a} + 20.31 + 9.77(\log W_{mx}^i - 2.5) \\ &= -(0.52 \pm 0.10)[(I^{b,i,k} - [3.6]^{b,i,k,a}) + 0.73] \end{aligned} \quad (3.54)$$

Note that I Band magnitudes have been shifted from the Vega to the AB system by 0.342 magnitude. Slope and zeropoint are slightly smaller than those obtained before (-0.47 and -0.36) but within the uncertainty. Still, for completeness, we use this new estimate. Color

adjusted parameters, $C_{[3.6]} = [3.6]^{b,i,k,a} - \Delta[3.6]^{color}$, are derived accordingly and then, considered as pseudo-magnitudes to produce the "control" color corrected calibration. The procedure described in the previous subsection is reiterated with a number of galaxies slightly decreased due to a lack of I Band measurements (273+31).

This color corrected calibration is visible on Figure 3.42 right and given by:

$$M_{C_{[3.6]}} = -(20.31 \pm 0.07) - (9.10 \pm 0.21)(\log W_{mx}^i - 2.5) \quad (3.55)$$

with 0.45 and 0.37 as new scatters. A summary of the derived parameters for this TFR are given in Table 3.7 as well as in Table 3.8 along those of the previous calibration and those of TC12 for the I Band. Although a direct comparison has some imprecision because of the different galaxy samples, the agreement is excellent. The robustness of the procedure and of the derived TF relations is confirmed. Namely, no major bias affects the relation as it is almost independent of the calibrator sample in terms of completeness and band selection.

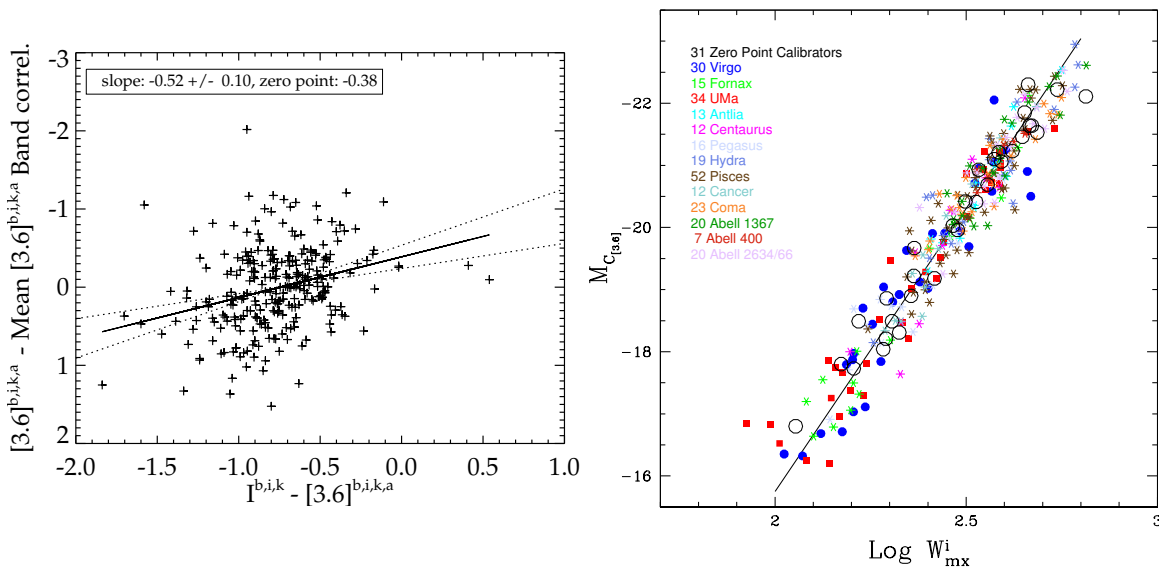


FIGURE 3.42: *Left:* Deviation from the universal inverse TFR as a function of $I^{b,i,k} - [3.6]^{b,i,k,a}$ color. The solid line stands for the best fit while the dotted lines represent the 95% probability limits. Red galaxies tend to lie above the relation while blue galaxies are preferentially below the relation. *Right:* Relation for pseudo-absolute magnitudes with the zeropoint set by galaxies with independent very accurate distance estimates (open circles).

3.4.2.3 Re-derivation of the Bias

Although all TFRs derived are again inverse fits (errors solely in linewidths), a small Malmquist selection bias residual still remains. The situation is improved in this case because galaxies are selected in K (instead of B) band. This change in wavelength selection reduces the interval between sample selection and photometry bands. However, because of the morphology

of the luminosity function, the amplitude of the bias still increases with distance as the selection limit approaches the exponential cutoff of the luminosity function. Consequently, the bias analysis is reiterated but without consideration of a faint end cutoff color dependence. Virgo, Fornax and Ursa Major are this time modeled with a [Schechter \(1976\)](#) function with a faint end slope of -1.0 and a bright end cutoff at -22. Then, a random population is built out of this Schechter function to match the TFR at 3.6 microns in terms of slope, zeropoint and scatter. The bias is estimated as the average deviation of sampled distances from the input TFR for successive brighter cutoffs but we take the opposite convention with respect to before for conveniency. The corresponding curve normalized to zero at a distance modulus of 31 is shown in [Figure 3.43](#) and can be written:

$$bias = 0.004(\mu - 31)^{2.3} \quad (3.56)$$

where μ is the distance modulus. The coefficient 0.004 is smaller than before (0.0065) because of the previous color dependence. However, the 2.3 exponent is larger than before because of a larger assumed scatter (0.45 against 0.4) which confirms that the scatter dominates the bias relic ([Giovanelli et al., 1997a](#)). At the bottom of [Figure 3.43](#), letters standing for the 13 clusters are positioned at their cutoffs while the corresponding biases are given by projection onto the curve. Bias corrections for each cluster are given in [Table 3.7](#) alongside the letters to match them with the names of clusters. Corrections are already included in moduli and distances given in this same table. As for an individual galaxy, the bias corrected distance modulus μ is obtained by adding $0.004(\mu - 31)^{2.3}$. For completeness, the bias correction for the *non* color adjusted relation, obtained similarly, is given by $bias = 0.006(\mu - 31)^{2.3}$.

Distances obtained for the 13 clusters are compared with previous estimates in [Table 3.8](#). Overall distances are in good agreement with each other and within uncertainties. Combining these distances with velocities with respect to the cosmic microwave background, but this time corrected for a cosmological model assuming $\Omega_m = 0.27$ and $\Omega_\Lambda = 0.73$ with the approximative formula in [Tully et al. \(2013\)](#) (to account for the fact that the real total velocity is given by formula [3.7](#)), it is possible to derive a "Hubble parameter" for each cluster. These values are given in [Table 3.7](#) and plotted in [Figure 3.44](#). A straight line fit to the logarithms of these parameters for clusters at a distance greater than 50 Mpc gives a Hubble value of $75.0 \pm 3.9 \text{ km s}^{-1} \text{ Mpc}^{-1}$ where 3.9 correspond to twice the statistical scatter. Proceeding with equation [3.52](#) as before, we found $2.0 \text{ km s}^{-1} \text{ Mpc}^{-1}$. Then 2.0 stands for the 1σ random error and the cumulative systematic error is the same as before (the only change is the error on the zeropoint that is insignificantly decreased from 0.08 to 0.07). Then, combining all the uncertainties $H_0 = 75.0 \pm 2.0 \text{ (ran)} \pm [3.5-3.8] \text{ (sys)} \text{ km s}^{-1} \text{ Mpc}^{-1}$. This value is somewhat different to that obtained before principally because of the use of better estimates of total velocities. Still, first and second estimates are within uncertainties and differ only at the level of $1.2 \text{ km s}^{-1} \text{ Mpc}^{-1}$. The change in total velocities

brings the Hubble Constant estimate close to the value found in the I Band (75.1) and to the value found including the sample of supernovae (75.2, that we derived using the previous calibration and which is presented in the next subsection, 3.4.3).

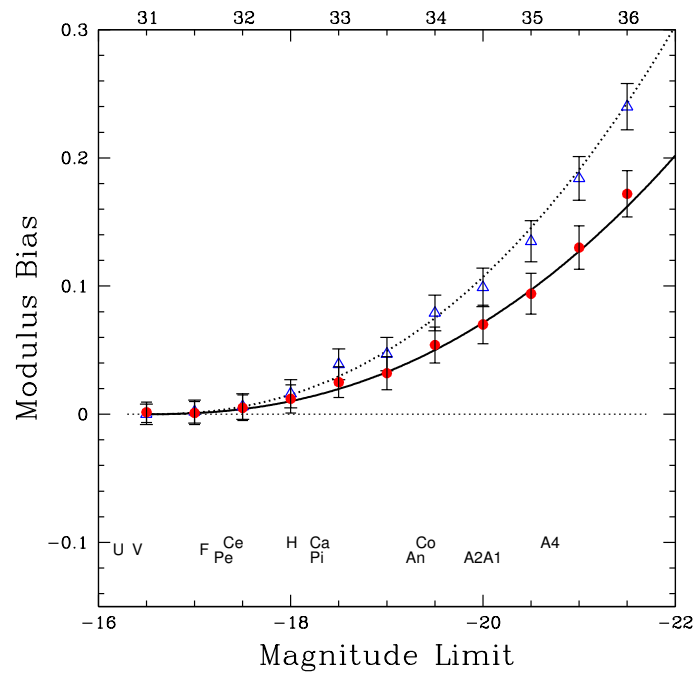


FIGURE 3.43: Bias measured as a function of absolute magnitude cutoff. The dotted and solid black curves are fits to the blue triangles and red filled circles which are bias estimates at successive cutoffs for the [3.6] TF calibration and for the color adjusted TF relation. The formulas are $0.004(\mu - 31)^{2.3}$ for the red curve and $0.006(\mu - 31)^{2.3}$ for the blue curve. Letters at the bottom stand for the 13 clusters given in Table 3.7. They are positioned at the magnitude limits of clusters and their vertical projections onto the curve give the corresponding biases. The bias for an individual galaxy with a measured modulus is given by projection onto the curves from the top axis.

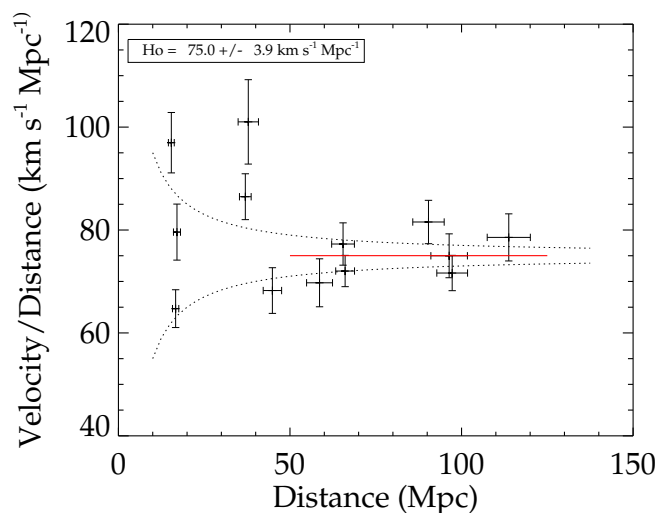


FIGURE 3.44: Hubble parameter as a function of distance. The solid red line at 75.0 ± 3.9 $\text{km s}^{-1} \text{Mpc}^{-1}$ is a fit to the logarithms of cluster "Hubble parameters" at distances greater than 50 Mpc. Dotted lines show the expected values for a deviation of ± 200 km s^{-1} from the mean Hubble flow.

| | v_{mod} | eV | N | Slope | ZP | scatter | ZP _{color} | scatter | bias | DM | Dist | V/D |
|----|-----------|-----|-------|-------------|------------|---------|---------------------|---------|------|------------|-----------|----------|
| V | 1495 | 37 | 30-30 | -9.88±0.73 | 10.50±0.12 | 0.64 | 10.63±0.10 | 0.55 | 0.00 | 30.94±0.12 | 15.4±0.9 | 97.0±5.9 |
| F | 1358 | 45 | 15-15 | -9.56±0.63 | 10.77±0.12 | 0.46 | 10.85±0.11 | 0.42 | 0.00 | 31.16±0.13 | 17.1±1.0 | 79.6±5.4 |
| U | 1079 | 14 | 35-34 | -9.32±0.52 | 10.74±0.11 | 0.64 | 10.80±0.10 | 0.57 | 0.00 | 31.11±0.12 | 16.7±0.9 | 64.7±3.7 |
| An | 3198 | 74 | 18-13 | -10.07±1.33 | 12.37±0.12 | 0.52 | 12.48±0.07 | 0.27 | 0.05 | 32.84±0.10 | 37.0±1.7 | 86.5±4.5 |
| Ce | 3823 | 82 | 14-12 | -12.92±1.74 | 12.51±0.16 | 0.60 | 12.58±0.16 | 0.55 | 0.00 | 32.89±0.17 | 37.8±3.0 | 101±8.2 |
| Pe | 3062 | 78 | 16-16 | -9.84±1.03 | 12.91±0.14 | 0.55 | 12.94±0.11 | 0.44 | 0.01 | 33.26±0.13 | 44.9±2.7 | 68.2±4.4 |
| H | 4088 | 72 | 25-19 | -9.12±0.94 | 13.38±0.14 | 0.71 | 13.52±0.13 | 0.55 | 0.01 | 33.84±0.14 | 58.6±3.8 | 69.7±4.7 |
| Pi | 4759 | 39 | 52-52 | -11.02±0.75 | 13.77±0.07 | 0.50 | 13.76±0.06 | 0.45 | 0.03 | 34.10±0.09 | 66.1±2.7 | 72.0±3.0 |
| Ca | 5059 | 82 | 12-12 | -11.65±1.02 | 13.74±0.11 | 0.39 | 13.75±0.10 | 0.31 | 0.02 | 34.08±0.11 | 65.5±3.3 | 77.3±4.1 |
| Co | 7370 | 76 | 23-23 | -7.97±0.67 | 14.42±0.10 | 0.49 | 14.40±0.09 | 0.42 | 0.07 | 34.78±0.11 | 90.4±4.6 | 81.6±4.2 |
| A4 | 7228 | 97 | 7-7 | -8.00±1.38 | 14.47±0.11 | 0.48 | 14.46±0.09 | 0.42 | 0.15 | 34.92±0.12 | 96.4±5.3 | 75.0±4.3 |
| A1 | 6969 | 93 | 20-20 | -9.32±0.92 | 14.53±0.08 | 0.21 | 14.53±0.07 | 0.19 | 0.10 | 34.94±0.10 | 97.3±4.5 | 71.6±3.4 |
| A2 | 8938 | 164 | 20-20 | -9.55±0.97 | 14.82±0.11 | 0.50 | 14.88±0.10 | 0.43 | 0.09 | 35.28±0.12 | 113.8±6.3 | 78.6±4.6 |

TABLE 3.6: Properties of the Cluster Fits (Robustness): (1) Cluster name (V Virgo, F Fornax, U Ursa Major, An Antlia, Ce Centaurus30, Pe Pegasus, H Hydra, Pi Pisces, Ca Cancer, Co Coma, A4 Abell 400, A1 Abell 1367 and A2 Abell 2634 and 2666, (2) Mean velocity of the cluster with respect to the CMB corrected for the cosmological model, km s⁻¹, (3) Error on the velocity, km s⁻¹, (4) Number of studied galaxy per cluster for the original TFR and for the color-corrected TFR, (5) Slope of the inverse fit, (6) Zero point relative to Virgo’s zeropoint, no color adjustment, mag, (7) Scatter, no color adjustment, (8) Zero point relative to Virgo’s zeropoint after color adjustment, mag, (9) Scatter after color adjustment, mag, (10) Bias, mag, (11) Bias corrected Distance Modulus, mag, (12) Cluster Distance, Mpc, (13) Hubble parameter, km s⁻¹ Mpc⁻¹.

| Sample | Ngal | Slope | Scatter | Zero Point |
|--|------|------------|---------|--------------------|
| <i>I</i> template | 267 | -8.81±0.16 | 0.41 | – |
| <i>I</i> zeropoint | 36 | – | 0.36 | -21.39±0.07 (Vega) |
| [3.6] template | 213 | -9.74±0.22 | 0.49 | – |
| [3.6] zeropoint | 26 | – | 0.44 | -20.34±0.10 (AB) |
| <i>M_C</i> template | 213 | -9.13±0.22 | 0.44 | – |
| <i>M_C</i> zeropoint | 26 | – | 0.37 | -20.34±0.08 (AB) |
| Control [3.6] template | 287 | -9.77±0.19 | 0.54 | – |
| Control [3.6] zeropoint | 32 | – | 0.45 | -20.31±0.09 (AB) |
| Control <i>M_C</i> template | 273 | -9.10±0.21 | 0.45 | – |
| Control <i>M_C</i> zeropoint | 31 | – | 0.37 | -20.31±0.07 (AB) |

TABLE 3.7: TFR parameters in TC12 for the I Band obtained with the B band selected calibrator sample, in subsection 3.4.1 for the [3.6] calibration derived with part of the B band selected calibrator sample and in subsection 3.4.2 for the calibration computed with K band selected calibrators.

| Cluster | Control | Calib. | TC12 | Cluster | Control | Calib. | TC12 |
|------------|----------|----------|----------|------------|---------|--------|-------|
| Virgo | 15.4±0.9 | 14.7±0.9 | 15.9±0.8 | Pisces | 66±3 | 65±3 | 64±2 |
| Fornax | 17.1±1.0 | 17.4±1.2 | 17.3±1.0 | Cancer | 66±3 | 67±4 | 65±3 |
| Ursa Major | 16.7±0.9 | 18.0±0.9 | 17.4±0.9 | Coma | 90±5 | 95±6 | 90±4 |
| Antlia | 37±2 | 37±2 | 37±2 | Abell 400 | 96±5 | 97±5 | 94±5 |
| Centaurus | 38±3 | 39±4 | 38±3 | Abell 1367 | 97±5 | 96±6 | 94±5 |
| Pegasus | 45±3 | 45±3 | 43±3 | A 2634/66 | 114±6 | 112±7 | / |
| Hydra | 59±4 | 56±4 | 59±4 | Abell 2634 | / | / | 121±7 |

TABLE 3.8: Comparisons between cluster distances from subsections 3.4.2, 3.4.1 and TC12: (1)-(4) Cluster name, (2)-(5) control calibration distance, Mpc, (3) calibration distance, Mpc (4) TC12 distance, Mpc

3.4.3 Hubble Constant & Supernovae of Type Ia

This subsection builds on a calibration of the SNIa absolute distance scale begun with a core of distances based on the correlation between galaxy rotation rates and optical I_C band photometry. This work extends the calibration to the use of mid-infrared photometry acquired at 3.6 μm with Spitzer Space Telescope. The great virtue of the satellite observations is constancy of the photometry at a level better than 1% across the sky. This calibration is based on 39 individual galaxies and 8 clusters that have hosted well observed SNIa. The 3.6 μm calibration at time of this work was not yet as extensively based as the I_C band calibration but was already sufficient to justify a report. Regardless, it has been shown to be robust in the previous subsection. Distances based on the mid-infrared photometry are insignificantly different than reported at I_C band. The I_C band result is confirmed with only a small adjustment. Incorporating a 1% decrease in the Large Magellanic Cloud distance, the study indicates $H_0 = [75.2 - 75.9] \pm 3.3 \text{ km s}^{-1} \text{ Mpc}^{-1}$.

In subsection 3.1.3, the SNIa method was expounded as the potential supplier of the best Hubble parameter estimate once the zeropoint scale is set. Independent distances are needed to the hosts of low redshift SNIa (Folatelli et al., 2010; Riess et al., 2011, 2009) to establish that absolute scale. The Cosmicflows project had already contributed to the establishment of the SNIa scale (Courtois and Tully, 2012b) primarily using constraints imposed by distances acquired with the correlation between the luminosities and rotation rates of galaxies (Tully and Fisher, 1977), the Tully-Fisher relation (TFR). Optical I_C band luminosities were used in that study. Now there is the opportunity to refine the calibration with the use of photometry at 3.6 μm obtained with *Spitzer Space Telescope* (Werner et al., 2004). The great advantage with Spitzer observations is photometric integrity to better than 1% across the sky. Additional advantages are minimal obscuration either within hosts or from our Galaxy,

magnitude measures approximating total magnitudes because of low backgrounds, and fluxes dominated by light from old stars which presumptively correlates with galaxy mass. Roughly 4000 galaxies have been observed with *Spitzer* and at the time of this work already, 39 galaxies had been observed that have hosted SNIa and are appropriate for an application of the TFR methodology. The present discussion parallels the paper by [Courtois and Tully \(2012b\)](#) with the important difference being the use of mid-infrared [3.6] photometry in place of optical I_C photometry.

Three parameters are needed to obtain distances with the TFR: a luminosity, a measure of rotation, and an inclination to account for projection effects. Our sample in this study is a subset of the sample used for the same purpose of a determination of SNIa host absolute luminosities by [Courtois and Tully \(2012b\)](#). Consequently, we use the same information on rotation rates, from HI profile information, and inclinations, from optical band imaging. The difference in this work is the replacement of I_C luminosities with [3.6] luminosities from observations using *Spitzer Space Telescope* IRAC channel 1. At the time of this work we had 39 galaxies (close to our current number of 45) that have hosted SNIa from the list of 56 galaxies given by [Courtois and Tully \(2012b\)](#). Their parameters are accumulated in Table 3.11. Using the TFR, we obtain their distance estimates.

Distance measurements obtained via the TFR are individually uncertain. Averaging over a cluster provides a more robust distance so we include clusters in our analysis. Thirteen clusters were used to form the calibration template for the [3.6] band TFR so there is a good distance determination for each of these clusters. Suitably observed SNIa have been observed in eight of these clusters. Pertinent information is provided in Table 3.9. With the two nearest clusters (Virgo and Fornax) high quality distance measures are available from Cepheid and Surface Brightness Fluctuation observations and these measures contribute to (indeed, dominate) the values of the moduli in column 3 of the table. The averaging over multiple contributions follows [Courtois and Tully \(2012b\)](#). When there were more than one SNIa observed per galaxy or cluster, or more than one observation per SNIa, we take averaged SNIa modulus estimates.

Distances determined with the TFR enable us to set a zeropoint for the SNIa distance scale. Consideration of a large sample of SNIa in the redshift range $0.03 < z < 0.5$ leads us to an estimate of the Hubble Constant. [Courtois and Tully \(2012b\)](#) discuss the accumulation of a sample of SNIa from five sources ([Amanullah et al., 2010](#); [Folatelli et al., 2010](#); [Hicken et al., 2009](#); [Jha et al., 2007](#); [Prieto et al., 2006](#)) with scale shifts as appropriate to match the scale of the last of these sources, a compilation referred to as UNION2. Relevant distance moduli are gathered from these five sources and recorded in Tables 3.9 and 3.11 with averaging in the case of clusters with multiple recorded SNIa events. Moduli drawn from the tables are compared in Figure 3.45.

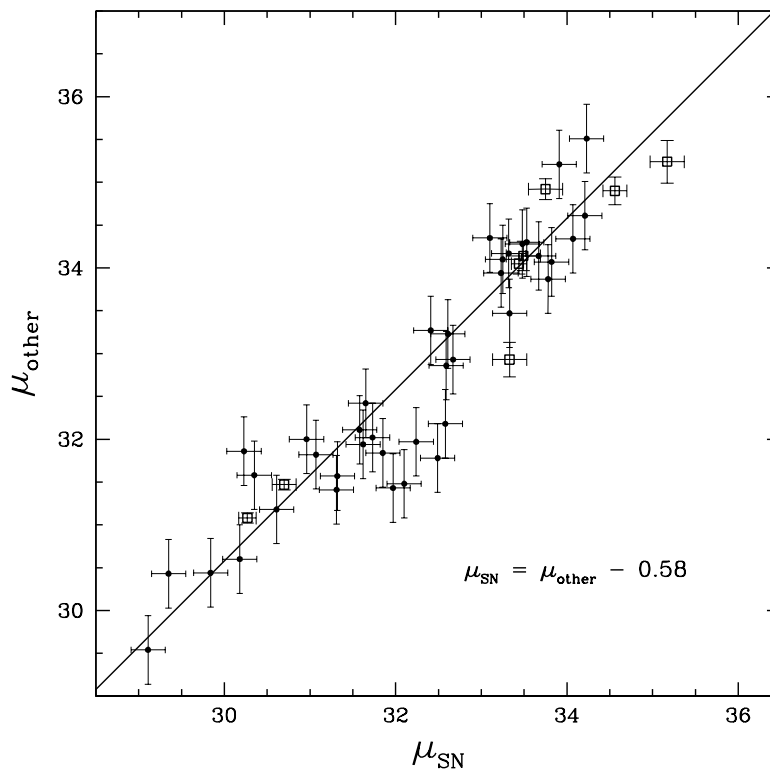


FIGURE 3.45: Comparison between moduli derived with SNIa and with "other" methods: the TFR, with Cepheid and Surface Brightness Fluctuation supplements. The comparisons include 39 individual galaxies with TFR measurements (filled points) and eight clusters (open squares). The straight line is a weighted fit to the 39 galaxies with TFR distances and six of the eight clusters.

The straight line in this figure is a fit, assuming slope unity, to the 39 individual galaxies each with weight 1 and six clusters each with weight 9. The locations of two clusters are deviant (Centaurus at 5σ under the fit in Figure 3.45 and A1367 at 3σ over the fit). These two clusters were deviant and rejected from the optical SNIa calibration (Courtois and Tully, 2012b) and for consistency in the comparison are again rejected from the fit. The offset between the newly determined distance moduli (other) and the SNIa moduli on the UNION2 scale is $\mu_{other} - \mu_{SN} = 0.58$. The comparable fit with I_C band material was shown in Figure 5 of Courtois and Tully (2012b). The offset in that earlier case was 0.56. It is instructive to compare results using only identical galaxies and clusters rather than using the ensemble. Figure 3.46 compares distance moduli measured alternatively with mid-infrared [3.6] photometry and optical I_C photometry observed from the ground, using the same line width and inclination parameters. The comparison involves the 13 clusters used to establish the TFR template at I_C (Tully and Courtois, 2012) and [3.6] (this work) and the 39 individual galaxies that have hosted SNIa (Courtois and Tully (2012b) and this work). With the individual SNIa hosts there is a hint of an increase in the difference between moduli for the more distant cases but the trend is not statistically significant. No such trend is seen

with the clusters. Overall the [3.6] moduli are greater than the I_C moduli by 0.02 ± 0.02 mag. The difference of 1% in distance is not statistically significant. The [3.6] calibration increases distances by 1% so reduces H_0 by 1%. It is to be noted, though, that the new mid-infrared calibration is tied to a distance to the Large Magellanic Cloud that is 1% closer than assumed in I Band. With a common choice of Large Magellanic Cloud distance, the [3.6] band distances are 2% greater than those at I_C band.

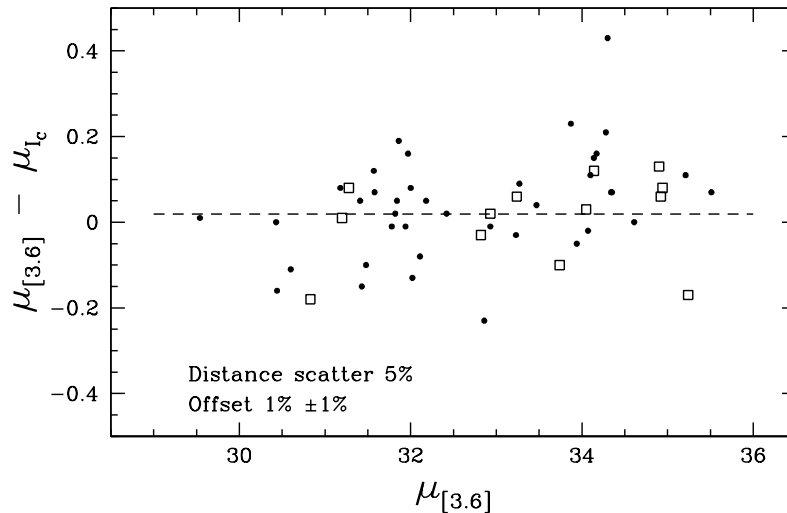


FIGURE 3.46: Differences in TFR distance moduli measured at [3.6] and at I_C plotted against the [3.6] moduli. Filled points: the 39 galaxies that have hosted SNIa ; Open squares: the 13 TFR template calibrator clusters.

The final calibration of the SNIa distance scale in the I_C band analysis of Courtois and Tully (2012b) leads to the determination of the Hubble Constant shown in their Figure 8. It is based on a fit over the redshift range $0.03 < z < 0.5$ to the UNION2 sample (Amanullah et al., 2010), with cosmological parameters $\Omega_m = 0.27$, and $\Omega_\Lambda = 0.73$. The result obtained in that paper was $H_0 = 75.9 \pm 3.8 \text{ km s}^{-1} \text{ Mpc}^{-1}$. In the present work, distances are decreased by 1% due to a revised Large Magellanic Cloud modulus and increased 2% with the switch from optical I_C to mid-infrared [3.6] magnitudes. The present calibration is in statistical agreement with the earlier work though formally gives a result 1% lower. An error budget was discussed by Courtois and Tully (2012b). Their 5% uncertainty is a combination of the 3% error budget discussed at length by Freedman and Madore (2010); Freedman et al. (2011); Riess et al. (2011) and 4-4.5% due to some concerns regarding 1) the scatter in SNIa measurements, 2) the effect of peculiar velocities which are not null although peculiar velocities are low with respect to the mean expansion at such distances and, 3) the absence of all-sky consistency. Uncertainties are reduced with this new work in two respects. First, there is increased confidence in the absolute scale set by the distance to the Large Magellanic Cloud (Freedman and Madore, 2010). Second, the mid-infrared calibration of the TFR removes latent concerns about possible photometric differences in different parts of the sky.

These two improvements warrant a decrease in our total error estimate to reach 4.3-4.5%, the major part of the decrease is due to the all-sky consistency. As a result, our best estimate for the Hubble Constant was at that time $H_0 = 75.2 \pm [3.2 - 3.4] \text{ km s}^{-1} \text{ Mpc}^{-1}$.

However, as mentioned before, at the time of this work only 39 hosts of SNIa had been observed with Spitzer. Now, 45 host galaxies have all the required parameters to be compared with SNIa measurements. The new information extends the previous work by only six galaxies and we do not expect much change with regard to the offsets between SNIa and TF distance moduli estimates, neither do we between I and [3.6] band measurements especially because the calibration at $3.6 \mu\text{m}$ has been shown to be very robust. Still, for the sake of completeness, Figure 3.47 shows the results when the six additional galaxies are included in the sample and the newest TFR is used to derive moduli. Characteristics of these galaxies are in Table 3.12 in red, exactly like the color they have been attributed in the Figure, alongside the slightly different magnitudes and moduli for all the other host galaxies with the last calibration. For the clusters, new parameters are alongside the first parameters in Table 3.9.

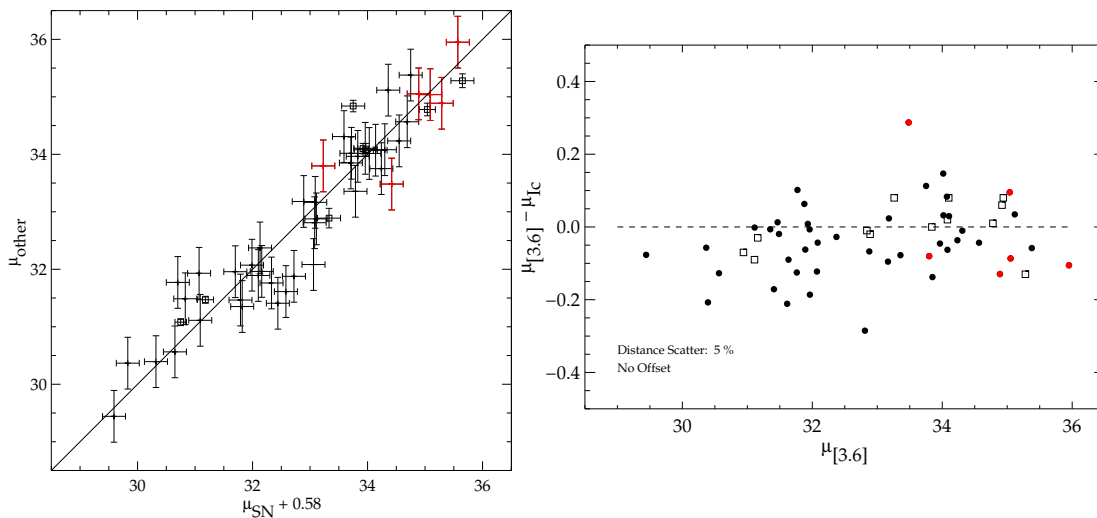


FIGURE 3.47: *Left*: Comparison between moduli derived with SNIa and with "other" methods (TFR, with Cepheid and Surface Brightness Fluctuation supplements). The solid line is the weighted fit to the 45 galaxies (filled points) with TFR distances and six of the eight clusters (open squares). *Right*: Differences in TFR distance moduli measured at [3.6] and at I_C in function of the [3.6] moduli. The 45 galaxies that have hosted SNIa are represented by filled points while the open squares stand for the 13 TFR template calibrator clusters. In both panels, red points stand for the late obtained photometric data.

Overall, the offset between SNIa distance moduli and other distance moduli is unchanged while the offset between TF distance moduli from the [3.6] and I band is slightly decreased to zero but that is within the uncertainty of the previously derived offset ($1\% \pm 1\%$). The trend of increase in the difference between the two band moduli is more pronounced than before. This is probably due to the fact that, in the latest calibration, the bias correction (with a higher exponent but a smaller multiplicative coefficient) increases first more slowly

than the first derived bias correction with the distance but then, around 32.6-32.7 mag, roles are reversed. Because clusters as their are less affected by the change of sign observed in the difference between the two bias corrections due to their sole exponents, the offset was computed giving a higher weight to these latter. The [3.6] band distances are greater than the I band distances but only by 1% due to the Large Magellanic Cloud distance estimate change. Regardless, the Hubble Constant estimate about 75-76 km s⁻¹ Mpc⁻¹ we gave before is still correct. Table 3.10 recapitulates Hubble Constant estimates of this section.

| Cluster | v_{CMB} | v_{mod} | $\mu_{other 1}$ | $\mu_{other 2}$ | μ_{SN} | SNIa names |
|----------|-----------|-----------|-----------------|-----------------|------------|--|
| Virgo | 1410 | 1495 | 31.08*±0.06 | 31.08*±0.06 | 30.27±0.10 | 1991bg, 1994D, 1999cl, 2006X |
| Fornax | 1484 | 1358 | 31.47*±0.06 | 31.47*±0.06 | 30.70±0.14 | 1980N, 1992A |
| Cen30 | 3679 | 3823 | 32.93±0.20 | 32.89±0.17 | 33.33±0.20 | 2001cz |
| Pisces | 4779 | 4759 | 34.05±0.11 | 34.07±0.09 | 33.44±0.09 | 1998ef, 1999ej, 2000dk, 2001en, 2006td |
| Cancer | 4940 | 5059 | 34.14±0.13 | 34.06±0.11 | 33.49±0.20 | 1999aa |
| Coma | 7194 | 7370 | 34.90±0.13 | 34.71±0.11 | 34.56±0.14 | 2006cg, 2007bz |
| A1367 | 6923 | 6969 | 34.92±0.14 | 34.84±0.10 | 33.75±0.20 | 2007ci |
| A2634/66 | 8381 | 8938 | 35.24±0.13 | 35.19±0.17 | 35.17±0.20 | 1997dg |

TABLE 3.9: Properties of clusters with SNIa: (1) Cluster name, (2) Mean velocity of the cluster with respect to the CMB, km s⁻¹, (3) Mean velocity of the cluster with respect to the CMB corrected for the cosmological model, km s⁻¹, (4) TFR distance modulus corrected for bias, mag, (5) Latest TFR distance modulus corrected for bias, mag, (6) SNIa distance modulus, mag, (7) SNIa identifications. *Virgo and Fornax are special cases discussed in the text.

| | Computation from | H ₀ (km s ⁻¹ Mpc ⁻¹) |
|----|-----------------------------|--|
| 1. | I Calib. | 75.1 ± 2.7 (ran) (75.8*) |
| 2. | [3.6] Calib. | 73.8 ± 2.6 (ran) ± [3.5-3.8] (sys) |
| 3. | [3.6] Control Calib. | 75.0 [†] ± 2.0 (ran) ± [3.5-3.8] (sys) |
| 4. | I Calib. + SNIa | 75.9 ± 3.8 |
| 5. | [3.6] Calib. + SNIa | 75.2 ± [3.2-3.4] |
| 6. | [3.6] Control Calib. + SNIa | 75.9 ± [3.2-3.4] |

TABLE 3.10: Hubble Constant Estimates: 1.,2.,3. obtained with distance measurements derived from the TFRs in I band (Tully and Courtois, 2012) and at 3.6 μm (subsections 3.4.1, 3.4.2), 4. obtained with scaling the type Ia supernovae method (Courtois and Tully, 2012b) using distance moduli derived from the TFR in I band among others, 5.,6. obtained with comparisons between distance moduli derived from the I and [3.6] band TFRs and the scaling of the type Ia supernovae method (subsection 3.4.3). * adopting a closer (by 0.02 mag) distance modulus for the Large Magellanic Cloud, [†] using velocities with respect to the cosmic microwave background corrected for the cosmology.

| Name | PGC | SNIa | v_{CMB} | W_{mx}^i | $[3.6]^{b,i,k,a}$ | $C_{[3.6]}$ | $M_{C_{[3.6]}}$ | μ_{TF} | μ_{SN} |
|------------|-------|--------|-----------|------------|-------------------|-------------|-----------------|------------|------------|
| UGC00646 | 3773 | 1998ef | 5011 | 389 | 12.89 | 12.88 | -21.16 | 34.10 | 33.25 |
| PGC005341 | 5341 | 1998dm | 1663 | 236 | 12.91 | 12.79 | -19.18 | 31.97 | 32.24 |
| NGC0673 | 6624 | 1996bo | 4898 | 445 | 12.04 | 12.19 | -21.69 | 33.94 | 33.23 |
| NGC0958 | 9560 | 2005A | 5501 | 584 | 11.09 | 11.24 | -22.77 | 34.07 | 33.82 |
| ESO300-9 | 11606 | 1992bc | 5918 | 323 | 14.69 | 14.67 | -20.42 | 35.21 | 33.91 |
| NGC1148 | 13727 | 2001el | 1092 | 386 | 10.05 | 10.05 | -21.13 | 31.18 | 30.61 |
| UGC03329 | 17509 | 1999ek | 5277 | 525 | 12.13 | 11.89 | -22.35 | 34.30 | 33.53 |
| UGC03375 | 18089 | 2011gc | 5792 | 535 | 11.82 | 11.78 | -22.42 | 34.28 | 33.48 |
| PGC018373 | 18373 | 2003kf | 2295 | 234 | 12.72 | 12.69 | -19.15 | 31.84 | 31.85 |
| UGC03432 | 18747 | 1996bv | 5015 | 289 | 14.20 | 14.12 | -19.98 | 34.17 | 33.32 |
| UGC03576 | 19788 | 1998ec | 6013 | 393 | 13.03 | 13.07 | -21.20 | 34.34 | 34.07 |
| UGC03370 | 20513 | 2000fa | 6525 | 371 | 13.48 | 13.56 | -20.97 | 34.61 | 34.21 |
| UGC03845 | 21020 | 1997do | 3136 | 257 | 13.35 | 13.39 | -19.52 | 32.93 | 32.67 |
| NGC2841 | 26512 | 1999by | 804 | 650 | 8.68 | 8.66 | -23.20 | 31.86 | 30.23 |
| NGC3021 | 28357 | 1995al | 1797 | 303 | 11.68 | 11.84 | -20.17 | 32.02 | 31.73 |
| NGC3294 | 31428 | 1992G | 1831 | 431 | 10.77 | 10.84 | -21.57 | 32.42 | 31.65 |
| NGC3368 | 32192 | 1998bu | 1231 | 428 | 8.80 | 8.89 | -21.54 | 30.43 | 29.35 |
| NGC3370 | 32207 | 1994ae | 1609 | 312 | 11.68 | 11.81 | -20.29 | 32.11 | 31.58 |
| NGC3627 | 34695 | 1989b | 1061 | 385 | 8.33 | 8.40 | -21.12 | 29.54 | 29.11 |
| NGC3663 | 35006 | 2006ax | 5396 | 443 | 12.44 | 12.41 | -21.68 | 34.14 | 33.67 |
| NGC3672 | 35088 | 2007bm | 2223 | 399 | 10.59 | 10.68 | -21.26 | 31.94 | 31.62 |
| NGC4501 | 41517 | 1999cl | 2601 | 570 | 8.84 | 8.90 | -22.68 | 31.58 | 30.35 |
| NGC4527 | 41789 | 1991T | 2072 | 362 | 9.34 | 9.56 | -20.88 | 30.44 | 29.84 |
| NGC4536 | 41823 | 1981B | 2144 | 341 | 9.81 | 9.96 | -20.64 | 30.60 | 30.18 |
| NGC4639 | 42741 | 1990N | 1308 | 336 | 11.18 | 11.23 | -20.58 | 31.82 | 31.07 |
| NGC4680 | 43118 | 1997bp | 2824 | 237 | 12.09 | 12.23 | -19.20 | 31.43 | 31.97 |
| NGC4679 | 43170 | 2001cz | 4935 | 427 | 11.83 | 11.90 | -21.53 | 33.47 | 33.33 |
| NGC5005 | 45749 | 1996ai | 1178 | 601 | 9.05 | 9.11 | -22.89 | 32.00 | 30.96 |
| ESO576-040 | 46574 | 1997br | 2385 | 170 | 13.82 | 13.69 | -17.88 | 31.57 | 31.32 |
| PGC47514 | 47514 | 2007ca | 4517 | 285 | 14.03 | 13.89 | -19.93 | 33.87 | 33.78 |
| NGC5584 | 51344 | 2007af | 1890 | 267 | 11.75 | 11.74 | -19.67 | 31.41 | 31.31 |
| IC1151 | 56537 | 1991M | 2274 | 242 | 12.91 | 12.88 | -19.28 | 32.18 | 32.58 |
| NGC6063 | 57205 | 1999ac | 2950 | 308 | 13.06 | 13.01 | -20.24 | 33.27 | 32.41 |
| UGC10738 | 59769 | 2001cp | 6726 | 585 | 12.52 | 12.61 | -22.78 | 35.51 | 34.23 |
| UGC10743 | 59782 | 2002er | 2574 | 206 | 12.74 | 12.83 | -18.64 | 31.48 | 32.10 |
| NGC6962 | 65375 | 2002ha | 3936 | 633 | 11.11 | 11.19 | -23.09 | 34.35 | 33.10 |
| IC5179 | 68455 | 1999ee | 3158 | 444 | 10.86 | 11.15 | -21.69 | 32.86 | 32.59 |
| NGC7329 | 69453 | 2006bh | 3143 | 461 | 11.24 | 11.36 | -21.83 | 33.23 | 32.61 |
| NGC7448 | 70213 | 1997dt | 1838 | 316 | 11.37 | 11.44 | -20.34 | 31.78 | 32.49 |

TABLE 3.11: Properties of individual SNIa-host galaxies: (1) Common name, (2) PGC name, (3) SNIa identification, (4) Mean velocity of host galaxy with respect to the CMB, km s⁻¹, (5) Corrected rotation rate parameter corresponding to twice the maximum velocity, km s⁻¹, (6) Corrected 3.6 μ m magnitude in the AB system, mag, (7) Color adjusted magnitude, mag, (8) Absolute color adjusted magnitude, mag, (9) TFR distance modulus corrected for bias, mag, (10) SNIa distance modulus, mag.

| Name | PGC | v_{CMB} | v_{mod} | W_{mx}^i | $[3.6]^{b,i,k,a}$ | $C_{[3.6]}$ | $M_{C_{[3.6]}}$ | μ_{TF} | μ_{SN} |
|------------|-------|-----------|-----------|------------|-------------------|-------------|-----------------|------------|------------|
| UGC00139 | 963 | 3975 | 3626 | 311 | 13.43 | 13.51 | -20.25 | 33.80 | 33.33 |
| UGC00646 | 3773 | 5348 | 4898 | 389 | 12.85 | 12.84 | -21.13 | 34.02 | 33.82 |
| PGC005341 | 5341 | 1964 | 1601 | 236 | 12.84 | 12.72 | -19.15 | 31.88 | 32.82 |
| NGC0673 | 6624 | 5241 | 5051 | 444 | 11.96 | 12.15 | -21.66 | 33.85 | 33.81 |
| NGC0958 | 9560 | 5732 | 5623 | 592 | 11.09 | 11.23 | -22.79 | 34.08 | 34.40 |
| UGC01993 | 9618 | 8005 | 7967 | 485 | 12.97 | 12.94 | -22.00 | 35.04 | 35.19 |
| IC1844 | 10448 | 6846 | 6693 | 309 | 13.55 | 13.23 | -20.22 | 33.48 | 34.52 |
| ESO300-009 | 11606 | 6045 | 6017 | 321 | 14.67 | 14.64 | -20.37 | 35.12 | 34.46 |
| PGC011767 | 11767 | 8701 | 8671 | 422 | 13.16 | 13.35 | -21.46 | 34.89 | 35.39 |
| NGC1448 | 13727 | 1194 | 1062 | 388 | 9.97 | 9.99 | -21.12 | 31.11 | 31.19 |
| UGC03329 | 17509 | 5253 | 5668 | 524 | 11.74 | 11.65 | -22.31 | 34.01 | 34.13 |
| UGC03375 | 18089 | 5783 | 5879 | 534 | 11.63 | 11.67 | -22.38 | 34.10 | 34.06 |
| PGC018373 | 18373 | 2168 | 2281 | 239 | 12.45 | 12.54 | -19.22 | 31.76 | 32.43 |
| UGC03432 | 18747 | 4996 | 5080 | 289 | 13.93 | 13.96 | -19.96 | 33.96 | 33.93 |
| UGC03576 | 19788 | 5966 | 6009 | 392 | 12.94 | 13.01 | -21.17 | 34.23 | 34.65 |
| UGC03770 | 20513 | 6378 | 6646 | 371 | 13.48 | 13.55 | -20.95 | 34.57 | 34.79 |
| UGC03845 | 21020 | 3034 | 3166 | 257 | 13.33 | 13.36 | -19.50 | 32.88 | 33.21 |
| NGC2841 | 26512 | 637 | 810 | 650 | 8.63 | 8.61 | -23.16 | 31.77 | 30.80 |
| NGC3021 | 28357 | 1515 | 1781 | 302 | 11.64 | 11.82 | -20.14 | 31.96 | 32.26 |
| NGC3294 | 31428 | 1567 | 1838 | 431 | 10.76 | 10.82 | -21.54 | 32.37 | 32.23 |
| NGC3368 | 32192 | 906 | 1332 | 427 | 8.77 | 8.86 | -21.50 | 30.37 | 29.93 |
| NGC3370 | 32207 | 1367 | 1622 | 311 | 11.69 | 11.81 | -20.26 | 32.07 | 32.09 |
| NGC3627 | 34695 | 723 | 1454 | 384 | 8.26 | 8.36 | -21.08 | 29.44 | 29.69 |
| NGC3663 | 35006 | 5040 | 5389 | 443 | 12.42 | 12.37 | -21.65 | 34.07 | 34.24 |
| NGC3672 | 35088 | 1860 | 2210 | 399 | 10.57 | 10.66 | -21.23 | 31.89 | 32.20 |
| NGC4501 | 41517 | 2268 | 1740 | 570 | 8.75 | 8.85 | -22.64 | 31.49 | 30.93 |
| NGC4527 | 41789 | 1736 | 2090 | 361 | 9.32 | 9.56 | -20.84 | 30.39 | 30.42 |
| NGC4536 | 41823 | 1808 | 2162 | 341 | 9.81 | 9.95 | -20.61 | 30.56 | 30.75 |
| NGC4639 | 42741 | 1003 | 1740 | 348 | 11.25 | 11.26 | -20.69 | 31.96 | 31.80 |
| NGC4680 | 43118 | 2491 | 2811 | 237 | 12.10 | 12.24 | -19.17 | 31.41 | 32.54 |
| NGC4679 | 43170 | 4665 | 3824 | 426 | 11.72 | 11.84 | -21.49 | 33.36 | 33.89 |
| NGC5005 | 45749 | 1011 | 1177 | 601 | 9.01 | 9.08 | -22.85 | 31.93 | 31.17 |
| ESO576-040 | 46574 | 2095 | 2407 | 169 | 13.72 | 13.61 | -17.85 | 31.47 | 31.89 |
| PGC047514 | 47514 | 4217 | 4577 | 284 | 13.96 | 13.82 | -19.89 | 33.75 | 34.34 |
| NGC5584 | 51344 | 1655 | 191 | 266 | 11.74 | 11.72 | -19.64 | 31.35 | 31.92 |
| IC4423 | 51549 | 9115 | 9691 | 470 | 13.73 | 13.92 | -21.88 | 35.95 | 35.67 |
| IC1151 | 56537 | 2176 | 2287 | 241 | 12.83 | 12.83 | -19.25 | 32.08 | 33.16 |
| NGC6063 | 57205 | 2841 | 2958 | 308 | 12.98 | 12.95 | -20.21 | 33.18 | 32.99 |
| UGC10738 | 59769 | 6716 | 6850 | 584 | 12.37 | 12.53 | -22.74 | 35.38 | 34.85 |
| UGC10743 | 59782 | 2744 | 2581 | 218 | 12.59 | 12.76 | -18.85 | 31.61 | 32.68 |
| NGC6962 | 65375 | 4200 | 3695 | 639 | 11.05 | 11.15 | -23.09 | 34.31 | 33.69 |
| IC5179 | 68455 | 3400 | 3108 | 444 | 10.80 | 11.14 | -21.66 | 32.81 | 33.18 |
| UGC12133 | 69428 | 7391 | 7213 | 442 | 13.17 | 13.32 | -21.64 | 35.05 | 34.99 |
| NGC7329 | 69453 | 3245 | 3150 | 461 | 11.19 | 11.34 | -21.80 | 33.16 | 33.19 |
| NGC7448 | 70213 | 2170 | 1752 | 309 | 11.32 | 11.40 | -20.23 | 31.63 | 32.72 |

TABLE 3.12: Properties of individual SNIa galaxies (latest results): (1) Common name, (2) PGC name, (3) Mean velocity of host galaxy with respect to the CMB, km s^{-1} , (4) Mean velocity of host galaxy with respect to the CMB corrected for the cosmological model, km s^{-1} , (5) Corrected rotation rate parameter corresponding to twice the maximum velocity, km s^{-1} , (6) Corrected 3.6 μm magnitude in the AB system, mag, (7) Color adjusted magnitude, mag, (8) Absolute color adjusted magnitude, mag, (9) TFR distance modulus corrected for bias, mag, (10) SNIa distance modulus, mag. Supplementary galaxies with respect to the first work are in red.

3.5 Catalogs of Accurate Distance Estimates

Near, intermediate, and far TFR samples in the Cosmicflows program were described by [Courtois et al. \(2011b\)](#) and in subsection 3.3.1.2. To summarize:

- the "near" sample is intended to achieve dense coverage of a volume extending to 3300 km s^{-1} with inclusion of all galaxies later than Sa that are brighter than $M_K = -21$, inclined greater than 45° , and not obscured, disrupted, or confused,
- the "intermediate" sample is drawn from flux and color limits applied to an Infrared Astronomical Satellite Redshift Survey ([Saunders et al., 2000](#)). The flux limit at $60 \mu\text{m}$ is 0.6 Jy, the color criterion to separate normal spirals from active nuclei is a ratio of $100 \mu\text{m}$ to $60 \mu\text{m}$ flux greater than one, there is a velocity cutoff at 6000 km s^{-1} , and there is the same inclination restriction as with the near sample,
- the "far" sample is restricted to extreme edge-on systems drawn from Flat Galaxy catalogues ([Karachentsev et al., 1999](#); [Mitronova et al., 2004](#)). Candidates in the sample that lie at declinations accessible to Arecibo Telescope have velocities extending to $15,000 \text{ km s}^{-1}$.

These are the well defined samples. In addition distances are derived to all other suitably observed galaxies. A quite separate and active component of Cosmicflows is a program with *Hubble Space Telescope* to obtain Tip of the Red Giant Branch distances to nearby, spatially resolved galaxies ([Jacobs et al., 2009](#); [Makarov et al., 2006](#); [Rizzi et al., 2007](#)). Exquisite distances (5% accuracy) are available for approaching 300 galaxies within $\sim 10 \text{ Mpc}$. Still, generally the information for the additional systems comes from archives. Thus, distances for Cosmicflows encompass measures by other methodologies discussed in the literature. Foremost among these are Cepheid Period-Luminosity Relation (e.g. [Freedman et al., 2001, 2012](#)), Surface Brightness Fluctuation (e.g. [Blakeslee et al., 2010](#); [Tonry et al., 2001](#)), Fundamental Plane (e.g. [Colless et al., 2001](#)), and Supernova Ia ([Amanullah et al., 2010](#); [Folatelli et al., 2010](#)) procedures. The diverse material is drawn together in the Extragalactic Distance Database ([Tully et al., 2009](#)). EDD goes beyond the compilation of catalogs relevant to extragalactic distances to include redshift catalogs, that with various levels of completion describe the distribution of galaxies in the Local Universe, and group catalogs, that help identify entities where averaging over velocities or distances is reasonable. The first assembly of distances in this program ([Tully et al., 2008](#)) has now been given the name *cosmicflows-1*. A core team was involved in the assembly of *cosmicflows-2* ([Courtois and Tully, 2012b](#); [Tully and Courtois, 2012](#); [Tully et al., 2013](#)). This work increases the size of this second catalog by 20% in spatial regions not necessarily accessible from the ground (like very close to the Zone Of Avoidance). It will help constitute the third catalog of the project, *cosmicflows-3*.

In the three subsequent subsections, the two first catalogs are described and an insight into the third one is given.

3.5.1 Cosmicflows-1

Cosmicflows-1 is the first catalog of the Cosmicflows project. Publicly released by [Tully et al. \(2008\)](#), it is available at the Extragalactic Distance Database. This catalog contains accurate distance measurements of 1797 galaxies up to 3000 km s^{-1} . These distances are given on the Cepheid reference scale from the Hubble Space Telescope Key Project ([Freedman et al., 2001](#)) with which Tip of the Red Giant Branch (TRGB) and Surface Brightness Fluctuation (SBF) measurements from the literature are in agreement. Distance estimates obtained with the SBF indicator come in majority from [Tonry et al. \(2001\)](#). These three methods Cepheid Period-Luminosity (PL), TRGB and SBF claim comparable accuracies. Consequently, an uncertainty about 10% is assigned to distance measurements obtained with these estimators. Tully-Fisher (TF) distance estimates from [Tully and Pierce \(2000\)](#) and [Karachentsev et al. \(2002\)](#) are added to this ensemble after a small adjustment to be on the same reference scale. A 20% uncertainty is allocated to these last measures.

Some of these 1797 galaxies have two or three (even four for PGC2557) distances estimates but the majority of them has solely TF estimates (1199), giving the reason for keeping distance estimates from this method although it is less accurate than other distance indicators: the Tully-Fisher relation gives access to a large number of galaxy distance measurements. The double-entry Table 3.13 gives the number of galaxies which have estimates from SBF, TRGB, PL, TF methods or a combination of them. These galaxies are part of clusters such as Virgo (142 galaxies), Fornax (34), Centaurus (13), Antlia (11) and Ursa Major (51, often mentioned as a cluster, it is more probably a cloud, see for example [Karachentsev et al., 2013](#)), while some belong to groups like ComaI (12), Maffei (13) and VirgoW (11). A total of 437 galaxies are lonely at this point, either because they are in the field or because of the restricted number of measures available in the group/cluster to which they belong. We denote 152 pairs of galaxies, again some are the pure result of the limited number of data points. Other galaxies can be gathered by 3 or more, the maximum is reached for Virgo.

| | SBF | TRGB | PL | TF | PL-TF | TRGB-TF | TRGB-PL-TF |
|------|-----|------|----|------|-------|---------|------------|
| SBF | 334 | 9 | 1 | 8 | 5 | 1 | 1 |
| TRGB | - | 184 | 11 | 13 | 2 | - | - |
| PL | - | - | 10 | 19 | - | - | - |
| TF | - | - | - | 1199 | - | - | - |

TABLE 3.13: Number of Measurements per Method in *cosmicflows-1*, double-entry table: (*Line*) Number of galaxies with First Distance Estimates obtained with the SBF, TRGB, PL or TF methods and (*Column*) Potential Second, Third and Fourth Distance Estimates obtained with a combination of SBF, TRGB, PL and TF relations. Only PGC2557 has four distance estimates.

3.5.2 Cosmicflows-2

The second catalog of the Cosmicflows project was publicly released by [Tully et al. \(2013\)](#). It gathers over 8000 accurate distance measurements obtained from various methods from the Cepheid Period Luminosity (PL) to the Tully-Fisher (TF) relations going through the Surface Brightness Fluctuation (SBF), the type Ia Supernovae (SNIa), the Tip of the Red Giant Branch (TRGB), the Fundamental Plane (FP) and other miscellaneous methods such as RR Lyrae, Horizontal Branch, Eclipsing Binary. This catalog extends up to 30,000 km s⁻¹, ten times the extent of the first catalog, and it enhances the density of measurements within the first catalog spatial coverage. The scale is still given by Cepheids but from a slightly refined version ([Freedman et al., 2012](#); [Riess et al., 2011](#)). TRGB measurements are on the same scale (e.g. [Rizzi et al., 2007](#)). With its all-sky consistency, the work presented in this Chapter contributed to slightly re-evaluate the I-band TFR scale ([Tully and Courtois, 2012](#)) in agreement with the tiny difference found between I and [3.6] distance estimates at the time of the second catalog release. Regardless, above all, the Spitzer work confirms the results found in I band which were lacking an all-sky consistency as the I band work is a gathering of several telescope data.

Among the galaxies constituting the catalogs approximately half of them are isolated galaxies. The others are mostly in clusters such as Virgo (160), Coma (132), Abell 2151 or Hercules (87), Pisces (74), Hydra (71), Abell 2196/99 (66), Abell 400 (63), Fornax (54), Abell 2634 (54), Centaurus (49), Abell 0426 or Perseus (47), Klemola44 (46), Ursa Major (45), Cancer (42), Abell 0548 (42), Pegasus (41) etc. In total, they can be gathered in approximately 500 groups and clusters. Again the TFR supplies most of the measurements (5856 of the galaxies have a unique TF distance estimate, see Table 3.14) then comes Fundamental plane (FP), SBF (S) closely followed by SNIa (SN), TRGB (T), PL (P) and finally a few miscellaneous (M) methods. It is to be noted that galaxy distances obtained with different methods are not necessarily compared and averaged over each galaxies. In the case of measurements from both SBF and TF methods, distances are averaged after grouping. It is also frequently the case for distances obtained with both SNIa and TF methods.

With this variety of different distance estimates, the remarkable property of *cosmicflows-2* is the distribution of uncertainties which is strongly bimodal with peaks at around 8-10% and 20% uncertainties on distances. A higher uncertainty is attributed to galaxies with solely FP estimates (25%) producing another small peak. In the grouped version of the catalog, the distribution of uncertainties has an additional feature: groups and clusters with several distance measurements from the TF / FP relations produce another peak at around 15% but also contribute to the 8-10% peak.

| | P | T | M | S | SN | TF | FP | T-TF | S-TF | SN-TF | T-S | T-M. | T-M-S-TF | S-FP | SN-FP |
|----|---|-----|----|-----|-----|------|------|------|------|-------|-----|------|----------|------|-------|
| P | 3 | 14 | - | - | 4 | 11 | - | 9 | 4 | 5 | 3 | 6 | 1 | - | - |
| T | - | 192 | 10 | 12 | - | 20 | - | - | 2 | - | - | - | - | 1 | - |
| M | - | - | 3 | - | - | - | - | - | - | - | - | - | - | - | - |
| S | - | - | - | 270 | 1 | 10 | 75 | - | - | - | - | - | - | - | 3 |
| SN | - | - | - | - | 216 | 50 | 7 | - | - | - | - | - | - | - | - |
| TF | - | - | - | - | - | 5856 | 3 | - | - | - | - | - | - | - | - |
| FP | - | - | - | - | - | - | 1370 | - | - | - | - | - | - | - | - |

TABLE 3.14: Number of Measurements per Method in *cosmicflows-2*, double-entry table: (Line) Number of galaxies with First Distance Estimates obtained with the PL (P), TRGB (T), SBF (S), SNIa (SN), TF and FP methods and various distance indicators (M) ; (Column) Second, Third, Fourth and Fifth Distance Estimates potentially obtained with a combination of all the distance estimators at hand. Only PGC39600 has five distance estimates.

3.5.3 Cosmicflows-3: an Insight

This Chapter has been the occasion to expound the observational campaign Cosmicflows with Spitzer (CFS), a photometric component of the Cosmicflows project. The primary goal of this observational survey is to increase the number of distance estimates close to the Zone Of Avoidance using the Tully-Fisher relation. The first channel ($3.6 \mu\text{m}$) of the InfraRed Array Camera onboard the Spitzer Space Telescope is indeed the instrument of choice to obtain the required excellent photometry. At this wavelength the Zone of Avoidance and uncertainties on measurements are considerably reduced. Surface photometry of 1270 galaxies constituting the CFS sample observed in cycle 8 with IRAC channel 1 and over 400 additional galaxies observed in various other surveys have been presented in section 3.3. The Spitzer Survey of Stellar Structure in Galaxies supplies many more galaxies of interests to the Cosmicflows project. The final set is constituted of about 2,000 galaxies with required parameters (heliocentric velocity or redshift, W_{mx} , b/a , $E(B-V)$, R_λ at $[3.6]$ (and I), γ_λ at $[3.6]$ (and I), $[3.6]$ and if available I), to derive an estimate of their distance with the mid-infrared (color adjusted) TFR, all available. Axial ratios come either from previous estimates of the Cosmicflows program or from HyperLeda if they are from [Paturel et al. \(2003\)](#). Galaxies without estimates of their axial ratios will be added later on thanks to the Citizen Science project. Inclination have been obtained with formula 3.20 to correct linewidths and magnitudes. The compilation of I band magnitudes is described in [Tully et al. \(2013\)](#). It gathers magnitudes used in [Tully and Pierce \(2000\)](#); [Tully et al. \(2008\)](#), themselves borrowing from [Giovanelli et al. \(1997b\)](#); [Mathewson et al. \(1992\)](#); [Pierce and Tully \(1988\)](#); [Tully et al. \(1996\)](#), but also recent derivations from [Courtois et al. \(2011a\)](#); [Springob et al. \(2007\)](#) and [Hall et al. \(2012\)](#). [Tully et al. \(2013\)](#) showed that these I-band magnitudes are on a consistent scale after small adjustments with the exception of those of [Hall et al. \(2012\)](#) because they use a significantly different filter. Accordingly these latter are

adjusted with the formulas prescribed by [Smith et al. \(2002\)](#) and [Tully et al. \(2013\)](#). These corrections involve a translation from Sloan g, r, i band (Gunn i band) to Cousins I band:

$$I = i - 0.14(g - r) - 0.35 \quad (3.57)$$

where cases with $r-i \geq 0.95$ are excluded, and account for a slight tilt between I and I_c , from the Cosmicflows project, magnitudes.

$$I_c = 1.017 I - 0.221 \quad (3.58)$$

I -band magnitudes are corrected with the following formula ([Chilingarian et al., 2010](#); [Schlafly and Finkbeiner, 2011](#); [Tully and Pierce, 2000](#)):

$$\begin{aligned} I^{b,i,k} &= I - A_i^I - A_k^I - A_b^I \quad \text{where :} \\ A_i^I &= (0.92 + 1.63(\log W_{\text{mx}}^i - 2.5))\log(b/a) \quad (\text{if } A_1^I < 0 \text{ then } A_1^I = 0) \\ A_b^I &= 1.94 \times E(B - V) \\ A_k^I &= 0.302z + 8.768z^2 - 68.680z^3 + 181.904z^4 \end{aligned} \quad (3.59)$$

where the terms have the same signification as those in the relation [3.29](#) for $[3.6]$ magnitudes. Besides, these latter are corrected with that relation.

When available, I -band magnitudes are converted to the AB system with equation [3.27](#) and pseudo-magnitudes are derived with formula [3.54](#). Combined with the (color corrected) Tully-Fisher relation [3.55](#) applied to linewidths, they enable the derivation of distance moduli with relation [3.10](#). These latter are corrected for the selection bias with equation [3.56](#) before deriving distance estimates with formula [3.10](#) used in reverse. Eventually distance estimates given in the table of Appendix [C](#) will be incorporated into a new data release of the Cosmicflows project, increasing the size of the previous catalog by 20%, including in spatial regions close to the Zone Of Avoidance.

In addition, EDD contains a bit more than 10,000 linewidths (with an error below 20 km s^{-1}) of galaxies which inclinations are greater than 45° . Acquiring the photometry for the galaxies without any photometric measurement to be matched with their linewidth is accordingly the next top priority of the Cosmicflows project. This photometry supplied by all sky surveys such as the Wide-field Infrared Survey (WISE, [Wright, 2008](#)) combined with the ongoing TF calibration (Neil et al. in prep. for WISE) will result in the compilation of *cosmicflows-3* which will gather all the distance material available. At present, we estimate that this third catalog of accurate distance estimates could contain in total (including distance estimates from Cepheids, TRGB, etc) around 14,000 measures, almost twice the size of the latest *cosmicflows-2* catalog. It will have approximately the same coverage as the second catalog

but with an enhanced density, especially next to the Zone Of Avoidance thanks to Spitzer observations. Figures 3.48 and 3.49 give an overview of the provisional *cosmicflows-3*.

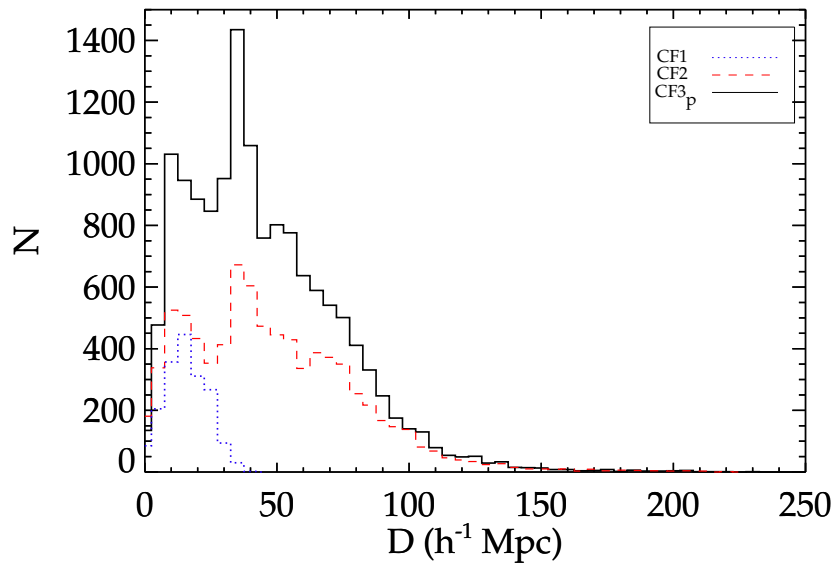


FIGURE 3.48: Histograms of distances in cosmicflows-1 (blue dotted line),-2 (red dashed line) and provisional *cosmicflows-3* (black solid line).

We have closed this Chapter with catalogs of Cosmicflows which gather peculiar motions of galaxies in the Local Universe. These peculiar velocities are departures from the cosmic mean expansion and it is assumed that they arise due to density irregularities. Two regimes require separate attention. The high density environments in and around collapsed halos are at the extreme of non-linear dynamics. Within the collaboration, a Numerical Action Method was developed that provide an optimal description of the distribution of mass affecting galaxies on curved orbits on first approach to an attractor (Peebles et al., 2001; Peebles and Tully, 2013; Shaya et al., 1995). The other extreme is the regime of linear dynamics. A procedure used that is appropriate with redshift data sets of 10^5 or more objects is based on the action principle (Lavaux et al., 2010). However the methodology that most interests us starts with Wiener filtering of the peculiar velocity field resulting in descriptions of the density and velocity fields independent of information provided by redshift surveys (Courtois et al., 2012; Zaroubi et al., 1995). The fields can then be mapped back to initial conditions that are then the starting point for constrained simulations that attempt to approximate the observed universe with a computer model (Courtois and Tully, 2012a; Doumler et al., 2013b; Gottlöber et al., 2010; Klypin et al., 2003). Such constrained simulations constitute the second course of this work in the framework of the CLUES collaboration.

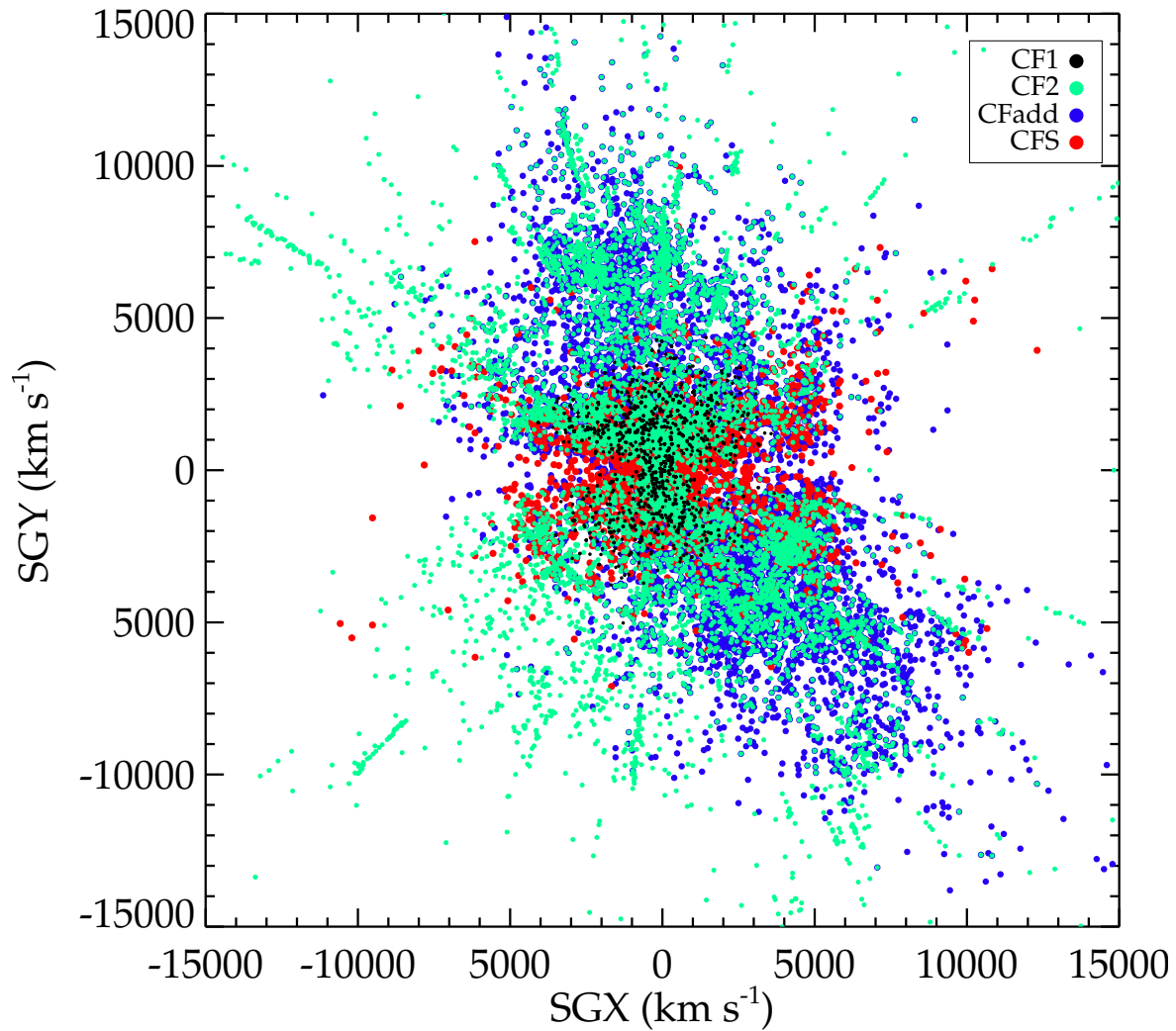


FIGURE 3.49: XY supergalactic plane showing the provisional *cosmicflows-3* catalog. Black dots stand for the contribution of *cosmicflows-1* (available since 2008), green dots represent *cosmicflows-2* (available since the end of 2013), red dots are galaxies analyzed in this work with Spitzer and blue dots are galaxies which will be studied with all sky surveys such as WISE. The ensemble of all these dots (galaxies) constitutes the provisional *cosmicflows-3* catalog with over 14,000 accurate distance estimates. Spitzer observations contribute to *cosmicflows-3* by considerably increasing the number of distance estimates near the Zone Of Avoidance.

Chapter 4

Simulated Universe

Numerical simulations provide the opportunity to develop studies of the formation and evolution of structures. The overarching goal of the CLUES project is to produce constrained simulations which best approximate the observed nearby Universe by reducing the so-called cosmic variance. Such constrained simulations stem from initial conditions obeying a set of observational constraints in addition to the random component. Constraints can either be peculiar velocities or galaxy distributions. Peculiar velocities, obtained from direct distance measurements, are data of choice to achieve constrained simulations of the Local Universe reliable down to a scale of a few Megaparsecs. Unlike redshift surveys, peculiar velocities are direct tracers of the underlying gravitational field as they trace both baryonic and dark matter. Yet, the method, designed over the past few years to produce initial conditions constrained by peculiar velocities, necessitated additional density constraints to result in simulations that resemble the Local-Universe. Accordingly, this Chapter presents the first attempt to use solely observational peculiar velocities to constrain cosmological simulations of the nearby universe. First the general method to produce constrained initial conditions is reviewed. Then, the process, as it was at the beginning of this work, is augmented and tested on realistic mocks before being applied to the first catalog of the Cosmicflows project. Finally the process is reiterated with the second catalog of the Cosmicflows project after minimizing observational biases in this latter. The second generation of constrained simulations of the Local Universe is unveiled.¹

¹This Chapter makes use of the ICECORE code and we refer the reader to "TH2012_Doumler_Timur.pdf" downloadable at "<http://phd-physics.universite-lyon.fr>" for more details on this code.

4.1 Constrained Simulations

Under the assumption of a dark-matter only Universe, even the simplest problem of the emergence of structures defies a proper and detailed analytical treatment. As a result, the study of the formation of the Large Scale Structure of the Universe relies heavily on numerical simulations. Actually, large scale dark matter simulations (e.g., [Alimi et al., 2012](#); [Angulo et al., 2012b](#); [Klypin et al., 2011](#); [Prada et al., 2012](#); [Watson et al., 2013](#)) constitute the backbone of the study of structure formation in the Universe. The standard model of cosmology asserts that the primordial fluctuations are constituted by a Gaussian random field whose statistical properties are determined by its power spectrum. An accurate determination of the power spectrum is enabled by the cosmological parameters. These latter are obtained from observations of the fluctuations in the cosmic microwave background radiation combined with Baryonic Acoustic Oscillations and supernova measurements ([Komatsu et al., 2011](#); [Larson et al., 2011](#); [Planck Collaboration, 2013](#)). Standard cosmological computations use then Initial Conditions drawn from random realizations of the primordial Gaussian perturbation field which properties correspond to a given power spectrum. By contrast, *constrained simulations* stem from Initial Conditions obeying a set of observational constraints in addition to the random component. They provide a different approach to cosmological simulations to better approximate the observed nearby Universe to study it more thoroughly. Namely, they aim at reducing the so-called cosmic variance due to our fixed position in the Universe combined with the fact that we can only observed one realization (one universe) of the theoretical model at one time. This cosmic variance affects greatly the results. For example, [Garrison-Kimmel et al. \(2014\)](#) reveal the importance of the surrounding environment (in particular the approaching M31) to derive a proper stellar halo mass relation in the Local Group.

4.1.1 Constrained Initial Conditions

Initial conditions can either be constrained by peculiar velocities or galaxy distributions:

- the first constrained initial conditions were produced by [Ganon and Hoffman \(1993\)](#), using the Mark III catalog of peculiar velocities ([Willick et al., 1996](#)). These initial conditions were then used to perform the first constrained simulation of the nearby universe by [Kolatt et al. \(1996\)](#). The CLUES (Constrained Local UniversE Simulations) project has been ever since running a variety of pure dark matter and hydrodynamical constrained simulations of the Local Universe, aiming mostly at studying a variety of issues concerning the Local Group (for a general review [Gottlöber et al., 2010](#), and references therein),

- galaxy redshift surveys provide a different source of constraints. This was first pioneered by [Bistolas and Hoffman \(1998\)](#) and followed later on by [Mathis et al. \(2002\)](#) and [Lavaux \(2010\)](#) and very recently by [Heß et al. \(2013\)](#).

There is a considerable tradeoff between using peculiar velocities and spatial distributions of galaxies from redshift surveys. Galaxy redshifts are quite easy to measure accurately. Very large and deep surveys are now routinely produced. However, galaxy distributions constitute biased tracers of the underlying density field. The mass-to-light bias has yet to be completely modeled and corrected for. On the other hand, measuring peculiar velocities poses formidable challenges to observational cosmologists. The observations are susceptible to systematic biases, and the resulting catalogs are noisy, sparse and with an incomplete sky coverage. Still, on the theoretical side, peculiar velocities are unbiased tracers of the underlying mass distribution. As long as virial motions inside clusters can be suppressed, the construction of the underlying density and velocity fields can be easily performed. The procedure to reconstruct underlying density and velocity field (and eventually to build initial conditions) with peculiar velocities is based on the linear Wiener-Filter and Constrained Realization of Gaussian fields algorithms ([Hoffman, 2009](#); [Hoffman and Ribak, 1991](#); [Zaroubi et al., 1995](#)). These techniques are described more thoroughly in the next section.

4.1.2 Constrained Realizations

4.1.2.1 The Wiener-Filter Technique

The Wiener-Filter (WF) technique is a very efficient and straightforward method to recover from sparse and noisy data the Gaussian underlying fields assuming a prior model. Developed in 1949 by Wiener for the field of signal processing, it consists in reducing the amount of noise in a dataset to generate an estimate of the underlying true signal. Introduced in 1992 by [Rybicki and Press](#), in the astrophysical and cosmological fields of research, it was soon after used to reconstruct fields from observational datasets (e.g. [Zaroubi et al., 1995](#)). This technique requires only the computation of a correlation matrix and its inverse. More precisely, the Wiener-Filter corresponds to the minimal variance estimator of the data with respect to the assumed prior model. This function is obtained by minimizing the square of the residuals R_i between the underlying field $f_i = \sum_{j=1}^n F_{ij}C_j$ and the model $f'_i = \sum_{j=1}^n F'_{ij}C_j$ where F' is the Wiener-Filter of the data (best fit to the data) after the minimization process and C_j are the n constraints, either galaxy redshift surveys, i.e densities ([Erdoğdu et al., 2006](#); [Fisher et al., 1995](#); [Kitaura et al., 2009](#)), or peculiar velocities like for the Cosmicflows project ([Courtois et al., 2012](#); [Zaroubi et al., 1999](#)). Namely, $\langle R_i R_j \rangle = \langle (f_i - f'_i)(f_j - f'_j) \rangle$ needs to be minimized. Processing in a similar way to the derivation of the least square

fitting method explain in Chapter 3, subsection 3.4.1.2, but with higher order matrixes, it is then possible to write:

$$f_i = \sum_{j=1}^n \sum_{i=1}^n \langle f_i C_i \rangle \langle C_i C_j \rangle^{-1} C_j \quad (4.1)$$

where $\langle AB \rangle$ notations stand for the correlation functions involving the assumed prior model.

In subsection 2.2.3.2 of Chapter 2, we have seen that from their statistical properties, the underlying fields are fully determined by the power spectrum. Assuming the power spectrum as the prior model, replacing f_i by either $\delta(\mathbf{r})$ or $v_{x,y,or z}(\mathbf{r})$, equation 4.1 seems sufficient to obtain both the full underlying density δ and velocity \mathbf{v} fields from a dataset constituted of n constraints $\{C_0, C_1, \dots, C_n\}$ (the Wiener-Filter can inter/extrapolate in absence of data). On the practical side, observational data contain uncertainties. Data points can thus be re-written $C_i = c_i + \epsilon_i$ where ϵ_i is the error on the data. Two approximations can be made regarding these errors:

- they constitute a purely statistical noise which results in an absence of correlation with the data. Then, $\langle f_i C_j \rangle = \langle f_i c_j \rangle$ and $\langle C_i C_j \rangle = \langle c_i c_j \rangle + \langle \epsilon_i \epsilon_j \rangle$,
- they have a Gaussian distribution². Then, $\langle \epsilon_i \epsilon_j \rangle = \delta_{ij}^K \epsilon_j$ where δ_{ij}^K is the Kronecker function which can take only two values, 1 if $i = j$ and 0 otherwise.

From these two approximations and equation 4.1, the perturbation density and velocity fields can be estimated with:

$$\delta^{WF}(\mathbf{r}) = \sum_{i=1}^n \langle \delta(\mathbf{r}) c_i \rangle \eta_i \quad (4.2)$$

$$v_\alpha^{WF} = \sum_{i=1}^n \langle v_\alpha(\mathbf{r}) c_i \rangle \eta_i \quad \text{with } \alpha = x, y, z \quad (4.3)$$

where $\eta_i = \sum_{j=1}^n \langle C_i C_j \rangle^{-1} C_j$ are the components of the correlation vector η with $C_i = c_i + \epsilon_i$ and $\langle C_i C_j \rangle = \langle c_i c_j \rangle + \langle \epsilon_i \epsilon_j \rangle$.

Regarding the associated correlation functions, they are given by:

$$\begin{aligned} \langle \delta(\mathbf{r}') v_\alpha(\mathbf{r}' + \mathbf{r}) \rangle &= \frac{\dot{a}f}{(2\Pi)^3} \int_0^\infty \frac{ik_\alpha}{k^2} P(\mathbf{k}) e^{-i\mathbf{k}\cdot\mathbf{r}} d\mathbf{k} \\ &= -\dot{a}f \hat{r}_\alpha \zeta(r) \end{aligned} \quad (4.4)$$

$$\begin{aligned} \langle v_\alpha(\mathbf{r}') v_\beta(\mathbf{r}' + \mathbf{r}) \rangle &= \frac{(\dot{a}f)^2}{(2\Pi)^3} \int_0^\infty \frac{k_\alpha k_\beta}{k^4} P(\mathbf{k}) e^{-i\mathbf{k}\cdot\mathbf{r}} d\mathbf{k} \\ &= (\dot{a}f)^2 \Psi_{\alpha\beta} \end{aligned} \quad (4.5)$$

²Note that this hypothesis is not actually fully valid because distances are logarithmically linked to distance moduli by equation 3.10. Consequently, errors have a lognormal distribution. We will more thoroughly explain and investigate this matter when confronted with the extended *cosmicflows-2* dataset in section 4.4.2.

where

- P is the assumed prior power spectrum, $\hat{\mathbf{r}} = \frac{\mathbf{r}}{r}$, the superscript WF specifies that these are Wiener-Filter estimates of the true fields,
- $\zeta = \frac{1}{2\Pi^2} \int_0^\infty k^2 j_0(\mathbf{k}\mathbf{r}) P(\mathbf{k}) d\mathbf{k}$,
- $\Psi_{\alpha\beta} = [\Psi_T \delta_{\alpha\beta}^K + (\Psi_R - \Psi_T) \hat{r}_\alpha \hat{r}_\beta]$,
with $\Psi_T = \frac{1}{2\Pi^2} \int_0^\infty \frac{j_1(\mathbf{k}\mathbf{r})}{\mathbf{k}\mathbf{r}} P(\mathbf{k}) d\mathbf{k}$ and $\Psi_R = \frac{1}{2\Pi^2} \int_0^\infty [j_0(\mathbf{k}\mathbf{r}) - \frac{2j_1(\mathbf{k}\mathbf{r})}{\mathbf{k}\mathbf{r}}] P(\mathbf{k}) d\mathbf{k}$.
The " j_i s" denote the common Bessel functions.

To summarize, in the Wiener-Filter technique, data dominate the reconstruction in region where they are dense and accurate. On the opposite when they are noisy and sparse, the reconstruction is a prediction based on the assumed prior model. Schematically data are multiplied by $\frac{P}{P+\epsilon^2}$ and the reconstruction tends to the null overdensity field when data degrade. Consequently, the Wiener-Filter field estimates are non-power preserved. They cannot be used to build initial conditions as these latter need to be Gaussian fields with statistical properties given by the power spectrum. In cause is the variance of the residual which is minimized but not negligible. As a result, the true field is the sum of the mean field (or Wiener-Filter estimate) and of the residual. Unfortunately, this residual is not known but it can be approximated to produce initial conditions with the proper statistical properties. This technique relies on the Constrained Realization (CR) of Gaussian fields.

4.1.2.2 The Constrained Realization of Gaussian Fields

Evaluating the residual, required to complete the Wiener-Filter obtained mean field to produce proper initial conditions, needed some ingenuity. Bertshinger (1987) suggested first the utilization of constrained realizations to derive initial conditions, yet the algorithm used at that time revealed to be unpractical due to a slow convergence. Hoffman and Ribak (1991, 1992) were the first one to present the exact optimal algorithm to evaluate the residual. Their procedure relies on the fact that the variance of the residual is independent of the constraints. Basically, $\langle RR' \rangle = \langle f f' \rangle$ is fully determined by the assumed prior model. Thus, considering a set of mock constraints \tilde{C}_i of a random generated field \tilde{f}^{RR} , which statistics are characterized by the same assumed prior model as the observational constraints, the Wiener-Filter of the random field can be written:

$$\tilde{f}^{WF} = \sum_{j=1}^n \sum_{i=1}^n \langle f_i \tilde{C}_i \rangle \langle \tilde{C}_i \tilde{C}_j \rangle^{-1} \tilde{C}_j = \sum_{j=1}^n \sum_{i=1}^n \langle f_i C_i \rangle \langle C_i C_j \rangle^{-1} \tilde{C}_j \quad (4.6)$$

since the correlation functions are independent of the values of the constraints, they depend solely on the assumed prior model. This gives by definition of the residual:

$$\tilde{R} = \tilde{f}^{RR} - \tilde{f}^{WF} = \tilde{f}^{RR} - \sum_{j=1}^n \sum_{i=1}^n \langle f_i C_i \rangle \langle C_i C_j \rangle^{-1} \tilde{C}_j \quad (4.7)$$

Finally, from equations 4.1 and 4.7 the constrained realization field is:

$$f^{CR} = f^{WF} + \tilde{R} = \tilde{f}^{RR} + \sum_{j=1}^n \sum_{i=1}^n \langle f_i C_i \rangle \langle C_i C_j \rangle^{-1} (C_j - \tilde{C}_j) \quad (4.8)$$

Applying relation 4.8 to the perturbation fields and keeping the same approximations as before for the errors:

$$\delta^{CR}(\mathbf{r}) = \delta^{RR}(\mathbf{r}) + \sum_{i=1}^n \langle \delta(\mathbf{r}) c_i \rangle \eta_i \quad (4.9)$$

$$v_\alpha^{CR} = v_\alpha^{RR}(\mathbf{r}) + \sum_{i=1}^n \langle v_\alpha(\mathbf{r}) c_i \rangle \eta_i \quad \text{with } \alpha = x, y, z \quad (4.10)$$

where the components of the correlation vector are now $\eta_i = \sum_{j=1}^n \langle C_i C_j \rangle^{-1} (C_j - \overline{C}_j)$. Here again, the constraints can be either densities or velocities. The combination of the projects Cosmicsflows and CLUES, namely this work, uses *solely* peculiar velocities obtained from direct distance measurements. The similarity between the Wiener-Filter equations (4.2 and 4.3) and the Constrained Realization equations (4.9 and 4.10) can be summarized by pointing that "without the random field, the results of the computation are the Wiener-Filter or mean fields ; with the random field, the resulting fields are precursors to build constrained initial conditions as they have the characteristics of the assumed prior model". Figure 4.1 gives another summary.

A small detail is left to be taken care of. At redshift zero, namely today, radial peculiar velocities are not all linear as assumed in the technique. Assimilating non-linearities with a statistical scatter, it is in principle possible to account for non-linear effects. On the basis that data sample a typical realization of the prior model, i.e. the power spectrum, $\frac{\chi^2}{d.o.f}$, where $\chi^2 = \sum_{i=1}^n \sum_{j=1}^n C_i \langle C_i C_j \rangle^{-1} C_j$ and d.o.f is the degree of freedom, should be close to 1. Then, adding a "sigma non-linear" σ_{NL} in the model to drive $\frac{\chi^2}{d.o.f}$ close to 1 is sufficient to compensate for the non-linearities. The σ_{NL} is inserted in the data such that $\langle C_i C_j \rangle = \langle c_i c_j \rangle + \delta_{ij}^k \epsilon_j^2 + \delta_{ij}^k \sigma_{NL}^2$.

Ultimately, assuming that the observed peculiar velocities are not strongly affected by non-linear dynamics (curl free field above the scale of virial motions), and assuming a prior cosmological model (here growth rate constant with time), the initial conditions are readily

calculated from the constrained realization fields with the procedure described in subsection 2.3.3 of Chapter 2.

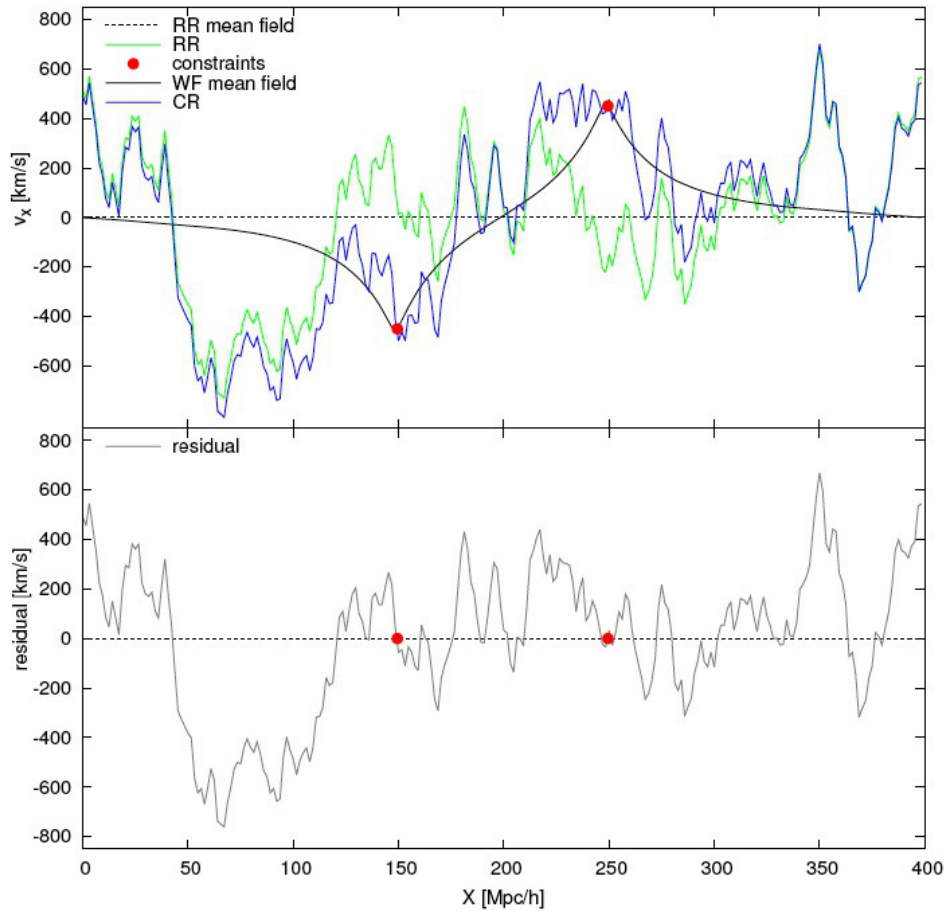


FIGURE 4.1: Principle of the Constrained Realization of Gaussian fields in one dimension. *Top*: the constrained realization field (blue solid line) equals the Wiener-Filter mean field (black solid curve) at the location of the constraints (red dots). The constraints have been put atop a random realization (green solid line). *Bottom*: the residual \tilde{R} is zero at the positions of constraints (red dots). Anywhere else, it is close to the random realization (from Doumler's thesis).

4.1.3 First CLUES Generation (2003 - 2009)

Following the development of the methodology, the first constrained initial conditions were produced by [Ganon and Hoffman \(1993\)](#), using the Mark III catalog of peculiar velocities ([Willick et al., 1996](#)). Later on, [Kolatt et al. \(1996\)](#) used these initial conditions to perform the first constrained simulations of the nearby Universe, more than ten years after the first standard numerical simulation was run within a Cold Dark Matter cosmological context ([Davis et al., 1985](#)). However, the first simulations output from this method, shown on the left top panel of Figure 1.3 of Chapter 1, did not meet the standards required to fulfill the aims of the CLUES project on two aspects :

- these simulations presented a shift in the position of structures of approximately $10 \text{ h}^{-1} \text{ Mpc}$ at $z=0$ with respect to the today observed Universe. In other words, constrained simulated halos were, at $z=0$, located $10 \text{ h}^{-1} \text{ Mpc}$ away from the reference objects' original positions,
- additional density constraints were required to form nearby clusters (Klypin et al., 2003).

4.2 Reverse Zel'dovich Approximation

The major drawback of the Constrained Realization method is the fact that it is formulated in an Eulerian way at a precise time. As a result the cosmic displacement field is neglected, although galaxies observed today are at different comoving positions from their progenitors at higher redshifts. A first attempt to improve this shortcoming has been recently suggested by Doumler et al. (2013a,b,c) who tested the remedy against simple mock catalogs. They recover positions up to a few Megaparsecs, typically approximately $5 - 6 \text{ h}^{-1} \text{ Mpc}$. The technique, described in the following subsection, was yet to be tested on realistic mocks and on observational dataset. Accordingly this work takes three additional steps:

- the whole process to produce initial conditions from peculiar velocities is tested on more realistic mocks which include a zone of galactic extinction and errors on distances,
- the technique is refined, tested against the same realistic mocks and compared with results from the previous chain of processes,
- in a subsequent section, the refined technique is applied to the *cosmicflows-1* catalog of observational peculiar velocities (Tully et al., 2008, and subsection 3.5.1).

Throughout this section, distances are in $\text{h}^{-1} \text{ Mpc}$. All figures are presented after a Gaussian smoothing of the fields at $2 \text{ h}^{-1} \text{ Mpc}$, which is the intrinsic floor value validity of the linear theory, as it will be re-measured.

4.2.1 Method

4.2.1.1 RZA-radial (2009 - 2012)

Evaluating exactly the cosmic displacement field is not feasible because of the numerous non-linear events on small scales which have occurred over time, yet in subsection 2.3.3, we presented the Zel'dovich approximation (equation 2.46) which stays valid even when

perturbations are large. Then, evaluating the Zel'dovich linear displacement field from the Wiener-Filter reconstructed overdensity field (using equations 2.48 and 2.47) gives a solution to the problem: reversing this displacement in time to move the constraints from $z = 0$ backwards to their progenitors' approximated positions at higher redshifts enable to account for the cosmic displacement field. Called the Reverse Zel'dovich Approximation (RZA) by its designers (Doumler et al., 2013a,b,c), in the framework of Lagrangian perturbation theory, it can be written directly from the Zel'dovich approximation 2.46, equation 2.47 and the fact that today $\dot{a}|_0 = \frac{\dot{a}_0}{[a_0=1]} = H_0$:

$$\mathbf{x}_{L\,init}(\mathbf{x}_E) = \mathbf{x}_E(t) - \mathbf{\Psi}(\mathbf{x}_E, t) = \mathbf{x}_E(t) - \frac{\mathbf{u}(\mathbf{x}_E, t)}{H_0 f} \quad (4.11)$$

where \mathbf{x}_E is the (Eulerian) position of a data point at time t , $\mathbf{x}_{L\,init}$ is the initial (Lagrangian) position, $\mathbf{\Psi}$ is the displacement field, \mathbf{u} is the perturbation or peculiar velocity field and f is the growth rate.

Once re-located at their precursors' approximated positions, the constraints are inserted into the Constrained Realization method to set initial conditions. Tested against simple mocks, positions are recovered up to a few Megaparsecs, typically $\approx 5 - 6 \text{ h}^{-1} \text{ Mpc}$ (Doumler et al., 2013a,b,c). Still, the first application of the process to the first observational catalog of the Cosmicflows project reveals that the method can be refined.

4.2.1.2 RZA3D, CLUES Second Generation (2013 -)

Because observed constraints have uncertainties (and are probably also affected by biases), the peculiar velocity field is not accurately described by solely one (radial) component (unique component accessible from direct observations). An additional step can thus be added to the initial technique called RZA-radial from now on. In the refined technique (RZA3D) constraints are not only moved to their progenitors' positions but, also, the *observed uncertain* peculiar velocities are replaced by fully WF-reconstructed three component vectors. Such resulting constraints have already been given by the Wiener-Filter a weight according to their precision. Typically, the Wiener-Filter field goes to the null value when there is no coherent signal or when data points have too large errors. Thus, no error should be allocated to RZA3D derived constraints when input in the Constrained Realization algorithm³. Initial conditions are then produced in the standard way.

In other words, RZA3D differs from the initial RZA-radial on two points:

- instead of observed radial peculiar velocities, the constraints are now the Wiener-Filter estimated peculiar velocities,

³This is in a sense similar to an unbiased minimal variance estimator (Zaroubi, 2002)

- initial conditions are constructed under the assumption of null statistical errors to prevent the double signal suppression resulting from the successive application of the Wiener-Filter (to obtain 3D velocities) and of the Constrained Realization (to produce initial conditions).

Figure 4.2 provides a schematic presentation of the WF/RZA method which prepares the constraints to be input into the Constrained Realization algorithm.

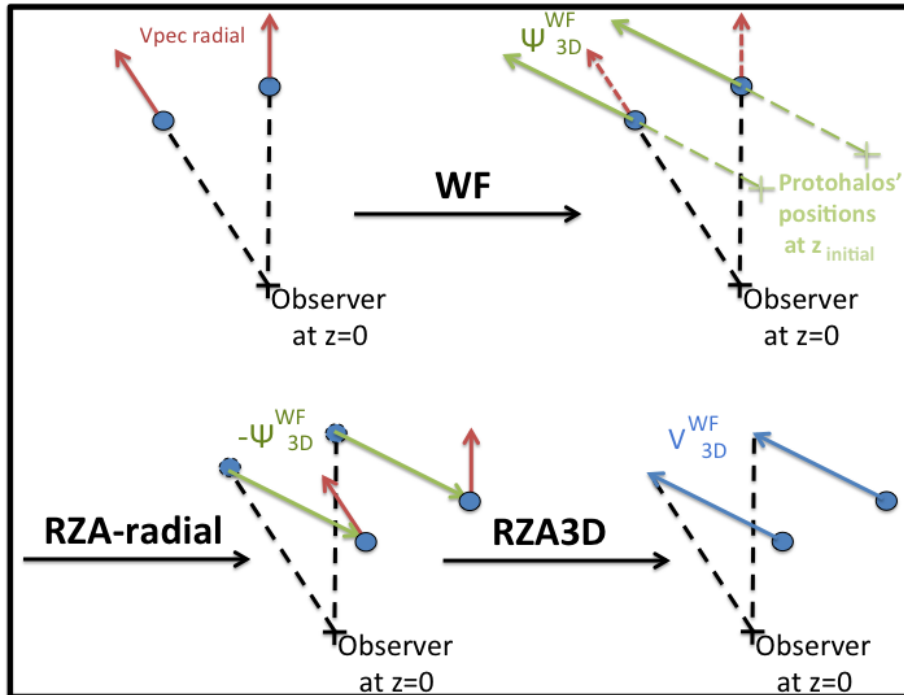


FIGURE 4.2: The refinement of the WF/RZA technique. The Wiener-Filter applied to observed radial peculiar velocities provides full 3D reconstructed peculiar velocity field v_{3D}^{WF} which allows to derive the cosmic displacement field Ψ_{3D}^{WF} (see equation 2.47). In the initial RZA-radial technique the observational (radial) constraints at $z = 0$ are re-located by $-\Psi_{3D}^{WF}$ to their progenitors' positions at higher redshifts. Since the peculiar velocity field is curl free (above the scale of virial motions) it is supposed to be fully defined by only one component. However, because observed peculiar velocities have uncertainties (and are probably affected by biases), RZA-radial is insufficient. The proposed refinement in RZA3D takes care of this flaw by using the full 3D Wiener-Filter reconstructed peculiar velocities v_{3D}^{WF} as constraints.

4.2.2 Building Mocks

When working on scales of a few tens of Megaparsecs (enclosing a volume we call the Local Universe), the cosmic variance is a major concern because these scales are far smaller than the scale of homogeneity of the Universe. As a matter of fact, the observational dataset used in this section only reaches once to twice the size of our filament (from Ursa-Major to Centaurus clusters, the distance is roughly $40 h^{-1} \text{Mpc}$). This leads to a bias:

- our position (as observers) is unique (peculiar) and impacts highly the data collections. In other words since we are living in a supercluster bounding a very large void, the observed peculiar velocities are very much dominated by a specific local structure dynamics,

Thus we must:

- test the methodology against a replica of the actual nearby Universe to be in the same particular dynamical conditions (including the presence of a nearby very large void),
- run several constrained numerical simulations to estimate the confidence level at which the observed large scale structures are recovered with a given methodology whatever the random component.

Accordingly, mock catalogs are drawn from a previous constrained simulation of the Local Universe (Klypin et al., 2003). This particular simulation, hereafter BOX160, is a dark matter only simulation of 1024^3 particles in a computational box of side length $L = 160 h^{-1} \text{ Mpc}$ constrained by peculiar velocity catalogs and a sample of positions and masses of X-ray selected nearby clusters. Since this simulation was computed in the WMAP3 framework, tests on the mock are also conducted in the WMAP3 framework. WMAP3, described in Table 2.1, is a flat universe with a matter density of $\Omega_m = 0.24$, a $\sigma_8 = 0.75$ normalization and $H_0 = 73 \text{ km s}^{-1} \text{ Mpc}^{-1}$.

BOX160 reproduces many of the key structures of the nearby universe, such as Virgo, Coma and Centaurus clusters, Perseus-Pisces supercluster and the Great Attractor region. A Local Group-like structure has been identified in the simulation and a mock observer is attached to that object. The catalog is built with respect to this observer. We assume that galaxies follow the peculiar velocities of dark matter halos in which they reside. Consequently, a mock catalog of dark matter halos has been extracted from BOX160 with the Amiga halo finder (Knollmann and Knebe, 2009). A comparison between the various halo-finders by Knebe et al. (2013) did not reveal any substantial difference between the resulting list of halos and their characteristics. Consequently, the halo finder choice should not impact our work. The output list of parameters contains halo coordinates in $h^{-1} \text{ Mpc}$, peculiar velocities in km s^{-1} and masses in $h^{-1} M_\odot$. Halos are selected in a sphere of $30 h^{-1} \text{ Mpc}$ radius around the mock observer to mimic as much as possible the extent of the Cosmicflows project's first catalog to be used later on. Two novelties with respect to the mocks of Doumler et al. (2013a,b,c) are introduced. To simulate a zone without data similar to that produced by the extinction of our galaxy's disk (Zone of Avoidance), every halo with a latitude in between $\pm 10^\circ$ is removed. Major players in the local dynamics, such as the mock Great Attractor, are thus (partly) masked by this extinction zone. The mock catalog is also designed to reproduce

the current observational limits: a 20% uncertainty on galaxy distances, and thereby on derived radial peculiar velocities. For simplicity the relative errors are assumed to follow a normal distribution around the true distances D . Resulting distances D' correspond to the observational measured distances with their uncertainties. The mock radial peculiar velocities are then computed as the difference between the total velocity (expansion+peculiar motion) and the modified distances D' multiplied by 100 (Hubble Constant $\times h^{-1}$ as distances are in h^{-1} Mpc). This procedure takes place in the Cosmic Microwave Background frame of reference, namely in the framework of the computational box.

The reconstruction of the Large Scale Structure, and of its initial conditions, from peculiar velocities is hampered by virial motions of galaxies in clusters. Such motions cannot be accounted for in the present proposed WF/RZA/CR framework. Grouping distance measurements of galaxies at the same distance (belonging to a same cluster) into a single data point with a reduced error could provide a partial remedy to the problem. However, the issue of grouping a given catalog constitutes a formidable challenge that has not been adequately solved yet. Fortunately late-type galaxies constitute roughly 80% of *cosmicflows-1* data (Tully et al., 2008). Such galaxies reside mostly in the field where virial motions do not dominate cosmic flows, thus they are less affected by this problem. The mock catalog is quite similar on this matter. The halo selection procedure described earlier give 1467 halos. Still, 95% of these halos that serve as mock data points are isolated. As a result, virial motions do not dominate cosmic flows in the mock either. Such a mock catalog is a reasonable proxy to the first catalog of the project Cosmicflows.

4.2.3 Application on Mocks

In this subsection, the full machinery to obtain constrained simulations is tested on the mock built in subsection 4.2.2. The WF/RZA/CR algorithm is first applied using both variants of the RZA to obtain precursors of initial conditions. A σ_{NL} term is used to account for the non-linear contributions of the radial peculiar velocities, which are not included in the model. From these precursors, initial conditions are set and input in GADGET-2 (Springel, 2005) N-body code to perform dark matter only simulations. The boxsize, $160 h^{-1}$ Mpc long on each side, is almost three times the extent of the mock. Periodic boundary conditions can be assumed without any risk of spurious phenomena in the central $60 h^{-1}$ Mpc region to be analyzed. In addition, the distribution of the peculiar velocity field values at high redshifts (in the initial conditions) is quite Gaussian in Figure 4.3. This implies that there are enough modes to define large scale flows (and velocities through large scale correlations). As a result, the $160 h^{-1}$ Mpc box has a large enough size for computations. The grid size is $N = 256^3$. Knebe et al. (2009) showed that the choice of the initial redshift value has no

substantial impact on the resulting dark matter halo properties at $z = 0$. Thus, we only seek to avoid shell-crossing. Hence, simulations are started at $z = 60$.

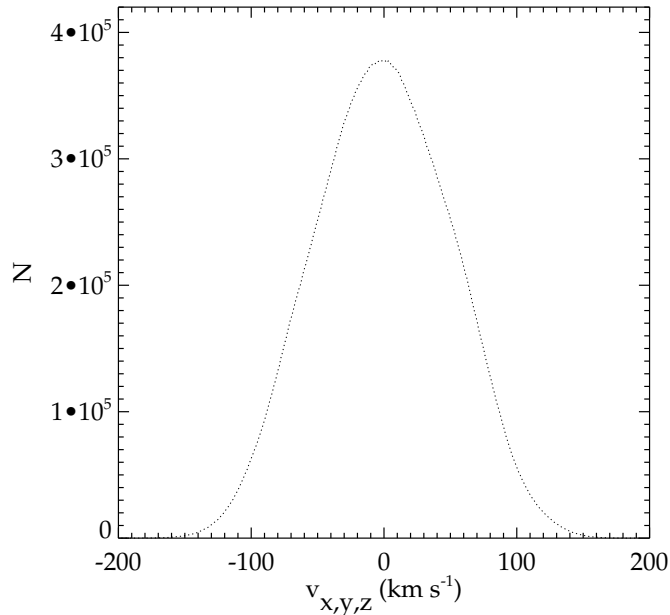


FIGURE 4.3: Distribution of the velocity field components, at $z = 60$, in the initial conditions. The distribution is quite Gaussian implying that there are enough modes to define large scale flows (and velocities through large scale correlations) within a boxsize of 160 h^{-1} Mpc long on each side.

4.2.3.1 Wiener-Filter Reconstruction of the Mock Universe

To facilitate the comparisons between the initial BOX160 and its Wiener-Filter reconstruction from a mock, the BOX160 velocity field is interpolated on a 256^3 grid using a Cloud-In-Cell interpolation scheme. Figure 4.4 displays the confidence level zones of the reconstruction with respect to the original BOX160. The zones result from a cell-to-cell comparison, within the central 60 h^{-1} Mpc region, between the velocity grids of the Wiener-Filter reconstruction and of the reference simulation. The total scatter around the 1:1 relation is 201 km s^{-1} or 1.7σ . The Wiener-Filter velocity field is thus a good reconstruction of the BOX160 source.

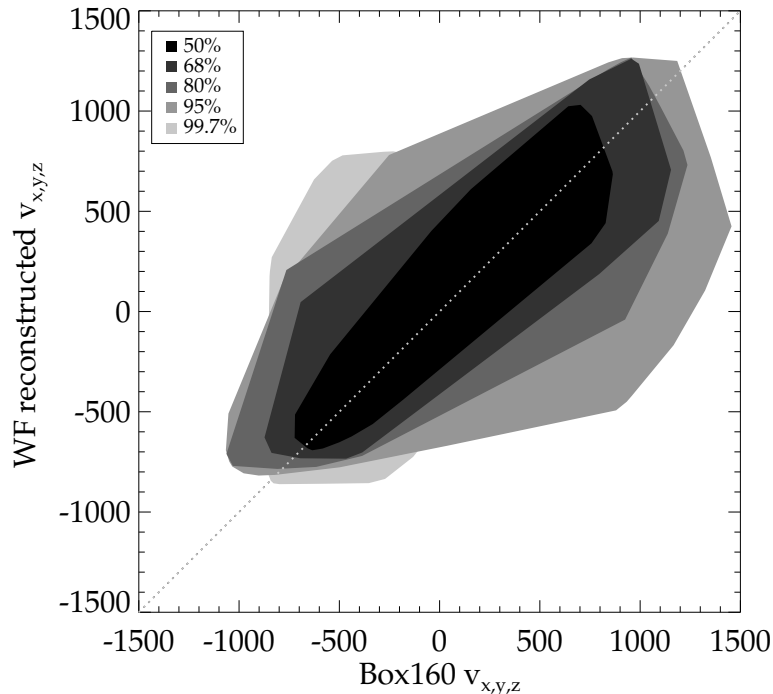


FIGURE 4.4: Confidence level zones obtained with a cell-to-cell comparison between the velocity grids of the reference simulation BOX160 and its Wiener-Filter reconstruction within a $30 \text{ h}^{-1} \text{ Mpc}$ radius sphere. For example, 50 % of the peculiar velocity pairs, $(\text{value}_{\text{cell } xyz \text{ BOX160}} ; \text{value}_{\text{cell } xyz \text{ WF}})$ can be found in the darker zone. This zone, slightly scattered around a 1:1 relation, shows the good agreement between the velocity values in a cell from the reference simulation and in the very same cell from the reconstruction. 68 % of the pairs are in the sum of the two internal zones and so on. 68, 95 and 99.7 % correspond to 1, 2 and 3 σ uncertainties.

Figure 4.5 shows two planes centered on the look-alike of the Milky-Way of the reference simulation and of its reconstruction obtained with the Wiener-Filter technique applied to the mock. Velocity (black arrows) and density (contours) fields are plotted. The green contour displays the mean density level. The main features - direction of the cosmic flows and attractors' positions - are properly reconstructed. The feature, in the XY plane, is the Great Attractor region look-alike with three density peaks from the reference simulation marked by red crosses in both quadrants. In YZ, the red cross locates the density peak of the mock Virgo halo in the reference simulation. These qualitative analyses illustrate the claim that, with a sparse and noisy mock similar to *cosmicflows-1* (in terms of number of constraints, zone of extinction without data and large errors on peculiar velocities), the Wiener-Filter is an optimal reconstruction tool in the linear regime of the gravitational instability. Structures are not necessarily reconstructed at their exact positions since the intrinsic accuracy is about $2 \text{ h}^{-1} \text{ Mpc}$. Still, overall, the density field is recovered when considering only the linear theory on all scales.

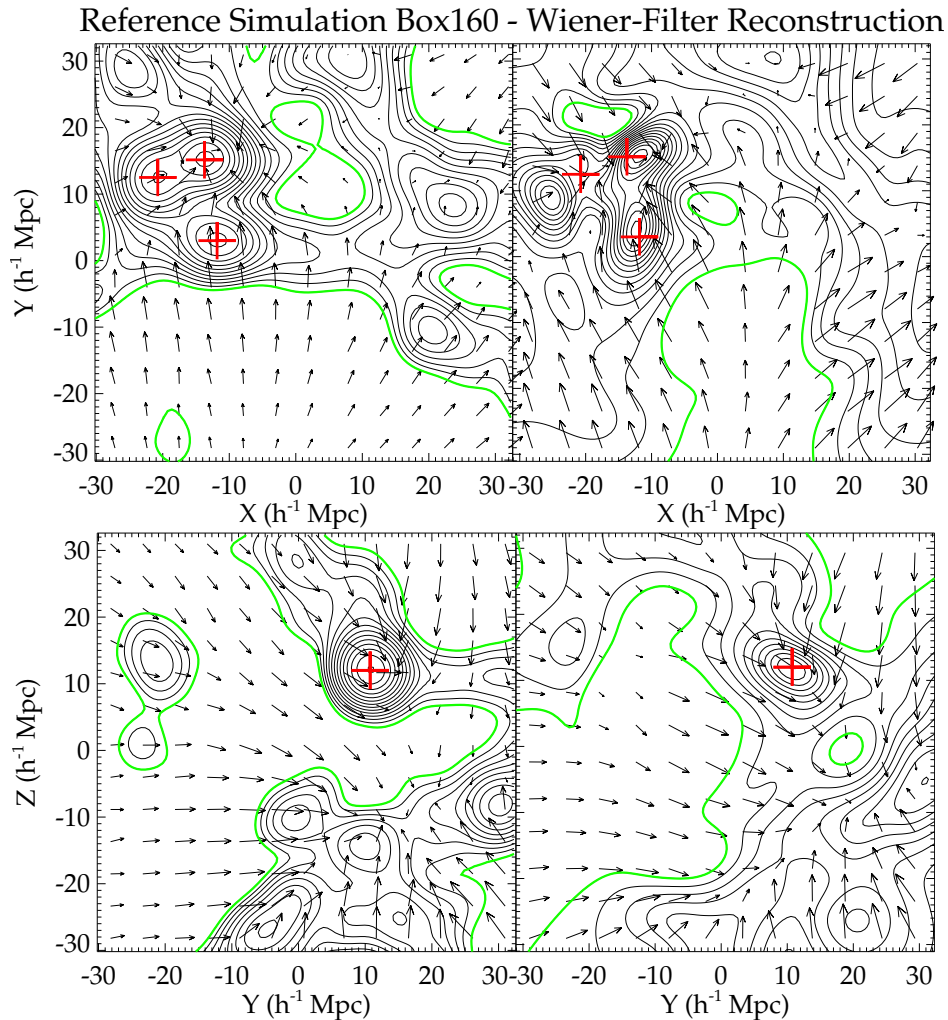


FIGURE 4.5: XY and YZ views of the reference simulation BOX160 (*left*) and its Wiener-Filter reconstruction (*right*) restricted to the central $60 h^{-1}$ Mpc zone. The reconstruction has been obtained using only radial peculiar velocity data from a realistic mock catalog containing about the same errors and same number of data-points as the observational *cosmicflows-1* catalog. The cosmic flows are represented by black arrows. Overdensity isocontours are delimited by solid black lines. The green contour delimitates the mean density. Red crosses show the positions of the major density peaks in the reference simulation. Even with this sparse and noisy realistic mock, the Wiener-Filter has enough signal to properly recover the original cosmic flows and density peaks with a precision of about $2\text{-}3 h^{-1}$ Mpc in position.

4.2.3.2 Constrained Simulations: RZA-radial versus RZA3D

Once the continuous fields obtained with the Wiener-Filter technique have been extrapolated at the data points' positions, constraints are displaced from their $z = 0$ location to their progenitors' position at higher redshifts. In addition, constraints are replaced by their full Wiener-Filter reconstruction in the RZA3D technique. Since simulations are run with periodic boundary conditions, only the divergent part of the velocity field (velocities due to

densities inside the box solely) is used to generate initial conditions. Hence, any tidal motion due to densities outside of the box is removed.

A major objective of this subsection is to compare RZA-radial and RZA3D algorithms. However, cosmic variance can affect the comparison between methods. To take care of this effect:

- each RZA-radial derived Initial Condition shares the same random component with one of the RZA3D obtained Initial Condition. Hence, the simulations resulting from the same random seed initial conditions are expected to reproduce the same Large Scale Structure,
- ten constrained initial conditions are built to estimate the confidence level on structure positions for each procedure.

Resulting simulations are also compared with the reference BOX160 to estimate the average misplacement of simulated structures at $z = 0$ with respect to original locations. The comparison between the constrained simulations and BOX160 is done on a 256^3 Cloud-In-Cell interpolated grid after smoothing the density and velocity fields with a Gaussian kernel of $2.0 \text{ h}^{-1} \text{ Mpc}$. When averaging over an increasing number of constrained simulations, the standard deviation with respect to BOX160 starts at 0.47 in logarithmic unit of density for one simulation and decrease to a plateau value of 0.37 when considering eight or more simulations. Adding more than ten simulations would not produce, on average, other high and deep density zones that could be compared between the two methods and with BOX160 (or the 0.37 value would have continued to decrease). The standard deviation of RZA3D simulations around their average is smaller than that of RZA-radial both in terms of velocity and density (0.34 against 0.35 in logarithmic unit of density and 246 against 258 km s^{-1}). Although there is a random component, constrained simulations of BOX160 obtained with RZA3D method have stronger features, reproduced at very similar positions, than RZA-radial constrained simulations. The cosmic variance is reduced with RZA3D because constraints are stronger than in the RZA-radial case as seen on Figure 4.6. The η_i components of the data-data correlation vector η have higher absolute values with RZA3D than with RZA-radial.

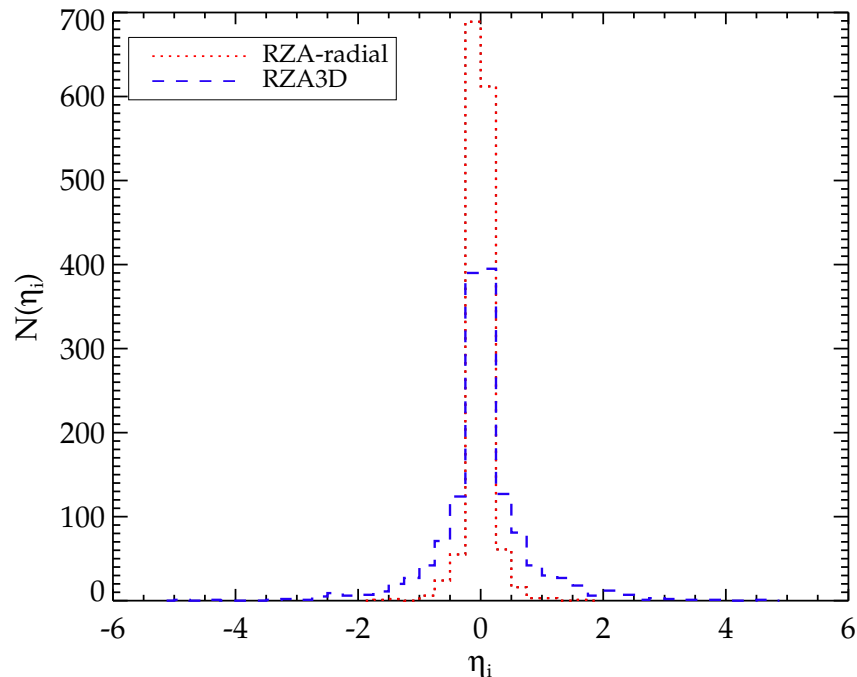


FIGURE 4.6: Distribution functions of the component values η_i of the data-data correlation vector η computed with RZA-radial (dotted red line) and RZA3D (dashed blue line) constraints. The higher the absolute value of η_i , the more the corresponding constraint contributes in the constrained Initial Condition. Since the distribution obtained with RZA3D is wider than that resulting from RZA-radial, RZA3D constraints are stronger than RZA-radial ones.

BOX160 contains some replicas of prominent nearby structures such as Virgo, Hydra and Centaurus. These halos are named hereafter s-Virgo, s-Hydra and s-Centaurus to distinguish them from the observed ones. BOX160 contains also a halo called s-Cz (in accord with [Doumler et al., 2013b](#)). These target objects are used to monitor the quality of the simulations. Figure 4.7 shows the density field in the planes containing these objects of the actual simulation BOX160 (top panel), of RZA-radial (middle panel), and RZA3D (bottom panel) with simulations averaged on ten different realizations. The main dark matter halos from BOX160 used as tracers are marked by red crosses in the six panels. There is a recurrent overdensity at the expected location of s-Virgo (high density peak in the YZ plot) only in the RZA3D simulations.

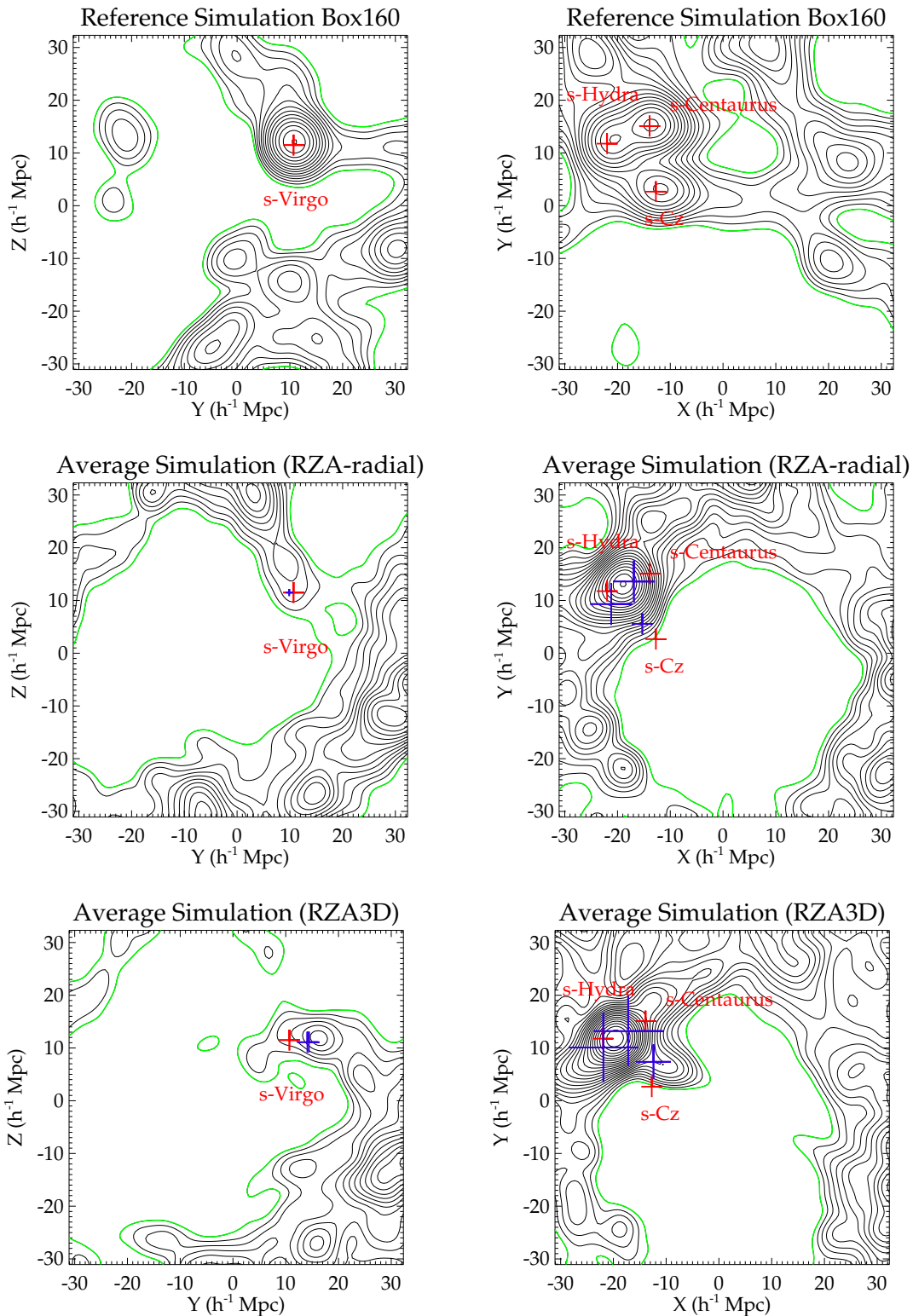


FIGURE 4.7: Visualization of planes containing main simulated attractors (positioned at $X=7$ and at $Z=-6 h^{-1}$ Mpc). Solid black iso-contours delimit overdensities. The green color stands for the mean density in the box. *Top*: Reference simulation. *Middle*: Average over ten constrained simulations using RZA-radial on the mock. *Bottom*: Average over ten constrained simulations applying RZA3D on the mock. Red crosses show original positions of *s-Virgo*, *s-Hydra*, *s-Centaurus* and *s-Cz* in the reference simulation. Positions of the averaged replicas in the constrained simulations are shown in blue. Crosses' sizes are proportional to the number of replicas found out of ten simulations.

For a more quantitative analysis, dark matter halos are obtained with the Amiga halo finder for each one of the simulations and the s-halos are identified when recovered. A halo in a constrained simulation is considered to be a replica of a BOX160 halo when the difference in position is smaller than approximately $6 \text{ h}^{-1} \text{ Mpc}$ and when masses are of the same order. The search is restricted to a sphere of $6 \text{ h}^{-1} \text{ Mpc}$ since the scope of this work is to find a method resulting in an error below $6 \text{ h}^{-1} \text{ Mpc}$ (3σ). Blue crosses on Figure 4.7 are located at the average position of the look-alikes of s-Virgo, s-Hydra, s-Centaurus and s-Cz halos in the constrained simulations. The cross sizes are proportional to the number of simulations (out of ten) in which a replica has been found. Table 4.1 recapitulates the characteristics of the targeted halos and of their look-alikes: virial masses, positions and standard deviations. RZA-radial fails to recover s-Hydra and s-Centaurus as separate individual objects in five out of ten simulations, thus they are not reported in the table. In these five out of ten simulations, they are collapsed into a single object. The table also records the average of each replicas distance to the genuine halo. The typical difference is about $5 \text{ h}^{-1} \text{ Mpc}$ for the RZA3D technique against $6 \text{ h}^{-1} \text{ Mpc}$ for RZA-radial. However, because with RZA-radial more halos are not found in the $6 \text{ h}^{-1} \text{ Mpc}$ sphere (they are outside of the sphere so farther away) than with RZA3D, the value for RZA-radial is more biased (lowered) by the restricted search than that of RZA3D. Still, studying the standard deviations of the position errors shows that it is possible to reach the floor value imposed by the linear regime, $2\text{-}3 \text{ h}^{-1} \text{ Mpc}$ with some random seeds for RZA3D while it is always impossible with RZA-radial. The table proves an enhanced accuracy of the RZA3D method in terms of position errors (when compared with BOX160). The gain is also clear in term of reliability-robustness of the results since more replicas (out of ten different random seed simulations) are found at a similar location (smaller standard deviations in positions) with RZA3D than with RZA-radial.

We can also consider a comparison between high density peaks in the Wiener-Filter and in the constrained simulations. The density peak reconstructed by the Wiener-Filter in the bottom right quadrant of Figure 4.5 is also present in six RZA3D simulations out of ten when looking within a $\sim 6 \text{ h}^{-1} \text{ Mpc}$ sphere centered on the Wiener-Filter peak. By contrast, there is a peak in only three RZA-radial simulations out of ten within the same sphere. In both cases, the typical misplacement is $4\text{-}5 \text{ h}^{-1} \text{ Mpc}$ with a standard deviation about $1 \text{ h}^{-1} \text{ Mpc}$.

RZA3D applied to a mock *cosmicflows-1* catalog outperforms RZA-radial applied to the same mock. The stronger the constraints, the more the cosmic variance that exists over ten constrained simulations because of a different random component is reduced. The number and accuracy of constraints in a *cosmicflows-1*-like catalog are adequate to simulate properly a look-alike of the Local Universe, within a $30 \text{ h}^{-1} \text{ Mpc}$ radius sphere, with a precision reaching the intrinsic limitation of the technique.

| Simulation case | Mass | Average Position X, Y, Z | Average Distance to reference halo | Nb of occurrences |
|---|------------------------|--|---|---|
| Box160 s-Virgo | 3.3 | 7.12, 10.7, 11.5 | | |
| <u>RZA-radial</u> s-Vir. | 0.25 | 3.40, 9.88, 17.2 | <u>6.9</u> | <u>1/10</u> |
| RZA3D s-Vir. | 0.34 ; $\sigma = 0.05$ | 7.78, 14.4, 11.1 ; $\sigma = 2.4$ | 5.4 ; $\sigma = 1.6$ | 5/10 |
| Box160 s-Centaurus | 6.07 | -13.9, 15.1, -8.81 | | |
| <u>RZA-radial</u> s-Cent. | 3.1 ; $\sigma = 2.8$ | -16.9, 13.6, -9.62 ; <u>$\sigma = 3.0$</u> | <u>6.0</u> ; <u>$\sigma = 0.4$</u> | <u>5/10</u> |
| RZA3D s-Cent. | 7.9 ; $\sigma = 4.0$ | -17.2, 13.2, -10.5 ; $\sigma = 1.9$ | 5.0 ; $\sigma = 1.5$ | 10/10 |
| Box160 s-Hydra | 5.18 | -22.0, 11.8, -3.35 | | |
| <u>RZA-radial</u> s-Hyd. | 4.7 ; $\sigma = 2.3$ | -21.2, 9.32, -4.87 ; <u>$\sigma = 1.9$</u> | 3.1 ; $\sigma = 1.5$ | <u>5/10</u> |
| RZA3D s-Hyd. | 4.7 ; $\sigma = 2.0$ | -21.9, 10.1, -4.58 ; $\sigma = 1.3$ | 3.0 ; $\sigma = 1.2$ | 10/10 |
| Box160 s-Cz | 0.96 | -12.7, 2.68, -6.36 | | |
| <u>RZA-radial</u> s-Cz | 0.80 ; $\sigma = 0.44$ | -15.3, 5.56, -10.1 ; $\sigma = 2.3$ | 6.3 ; <u>$\sigma = 0.57$</u> | <u>3/10</u> |
| RZA3D s-Cz | 0.40 ; $\sigma = 0.19$ | -12.4, 7.37, -7.20 ; $\sigma = 2.3$ | 6.0 ; $\sigma = 1.9$ | 5/10 |

TABLE 4.1: Average parameters and standard deviations σ for target halos looked for in a $6 \text{ h}^{-1} \text{ Mpc}$ sphere centered on their original positions in the reference simulation. (1) simulation in which the halos are looked for, (2) dark matter mass in $10^{14} \text{ h}^{-1} \text{ M}_{\odot}$, (3) average coordinates X, Y and Z and standard deviations, $\text{h}^{-1} \text{ Mpc}$, (4) average distance to the genuine halo and standard deviation, $\text{h}^{-1} \text{ Mpc}$, (5) number of simulations (out of ten with a different random seed) which contain a replica.

4.3 Constrained Simulations with Cosmicflows-1

Cosmicflows-1, catalog of peculiar velocities (Tully et al., 2008, and subsection 3.5.1), is used to perform constrained simulations of the Local Universe. For every simulation, we assume a Λ CDM model in the 7-year Wilkinson and Microwave Anisotropy Probe (WMAP7) framework (Komatsu et al., 2011). The cosmological parameters are $H_0 = 70 \text{ km s}^{-1} \text{ Mpc}^{-1}$, $\Omega_m = 0.272$ and $\Omega_{\Lambda} = 0.728$ (see Table 2.1). Figure 4.10 recapitulates the main results of this section:

- the left column is the first step of the WF/RZA/CR technique, namely the Wiener-Filter,
- the middle column represents the outcomes of one single simulation,
- the last (right) column shows the average over ten different realizations.

These results are described in the subsequent subsections. Note that we perform in parallel the same work within the WMAP3 framework to evaluate the impact of a change in cosmology. Finding no substantial difference, we decided to present only fields obtained within the WMAP7 framework to match previous work conducted with *cosmicflows-1*.

4.3.1 Wiener-Filter Reconstruction of the Local Universe

Reconstructions of the Local Universe obtained with the Wiener-Filter applied to *cosmicflows-1* have already been presented at length in [Courtois et al. \(2012, 2013\)](#) (see Figure 2.4 for some of the results). This work only uses the Wiener-Filter as a step in the process to reach the ultimate goal, namely the constrained simulations. Regardless, in absence of access to the full fields of the Local Universe to compare our final products with, the Wiener-Filter maps of *cosmicflows-1* are taken as proxies to the actual Universe and, thus, are worth presenting. In the reconstruction, supergalactic cartesian coordinates are centered on the Milky-Way and the XY supergalactic plane contains the Local Structure. The three main planes are shown at the supergalactic $Z=0$, $Y=12.5$ and $X=-2.5 \text{ h}^{-1} \text{ Mpc}$ coordinates to fit the location of the Virgo cluster. For a direct comparisons between the real Universe and the Wiener-Filter reconstructed large scale structure the V8k galaxy redshifts catalog is overplotted as grey dots. This catalog contains 30,124 galaxies with distances modified by a numerical action model of the Virgo infall for $v < 3000 \text{ km s}^{-1}$. It is available at the Extragalactic Distance Database website. Qualitatively, the real Virgo cluster and the void behind are reconstructed in the supergalactic XY plane. Virgo is also visible next to the Local Void in the YZ supergalactic plane. It can also be found in the XZ supergalactic slice.

4.3.2 Constrained Simulations of the Local Universe

The Wiener-Filter reconstructed velocity field is then extrapolated at the location of the data points. Next, RZA-radial and RZA3D methods are applied to *cosmicflows-1* constraints in order to construct initial conditions with the constrained realization algorithm. Ten random seeds are used to build initial conditions with periodic boundary conditions for both methods. It is to be noted that observational radial peculiar velocities are measurements of motions related to the whole gravitational potential. However, simulations are here run in a relatively small box, with periodic boundary conditions, where not all the attractors responsible for the entire motions are present. Thus, replacing velocities that result from the entire gravitational potential by velocities related to the gravitational potential in the box (namely RZA3D instead of RZA-radial) is more accurate and constitutes another advantage of the RZA3D method. Resulting initial conditions are then run from redshifts 60 to 0. The cosmic variance in terms of standard deviations of ten simulations with respect to their average is 1.45 against

1.40 in logarithmic unit of density and 303 against 291 km s^{-1} for RZA-radial and RZA3D respectively. Values are in agreement with results found previously in subsection 4.2.3 for mock constrained simulations. RZA3D constraints are stronger than RZA-radial ones.

4.3.2.1 Constrained Simulations and WMAP7/ Λ CDM Cosmology

In order to check the compatibility of *cosmicflows-1* constrained simulations with the standard model of cosmology, random simulations are run with the same seeds used to set up the constrained initial conditions. Figure 4.8 compares the final power spectra and mass functions at $z = 0$ of ten RZA3D constrained simulations and corresponding random ones (RZA-radial results in very similar, if not identical, plots which are thus not shown). A clear overlap is seen, which leads to conclude that the methodology preserves the cosmology. As the method does not modify the cosmology, its validity is not altered.

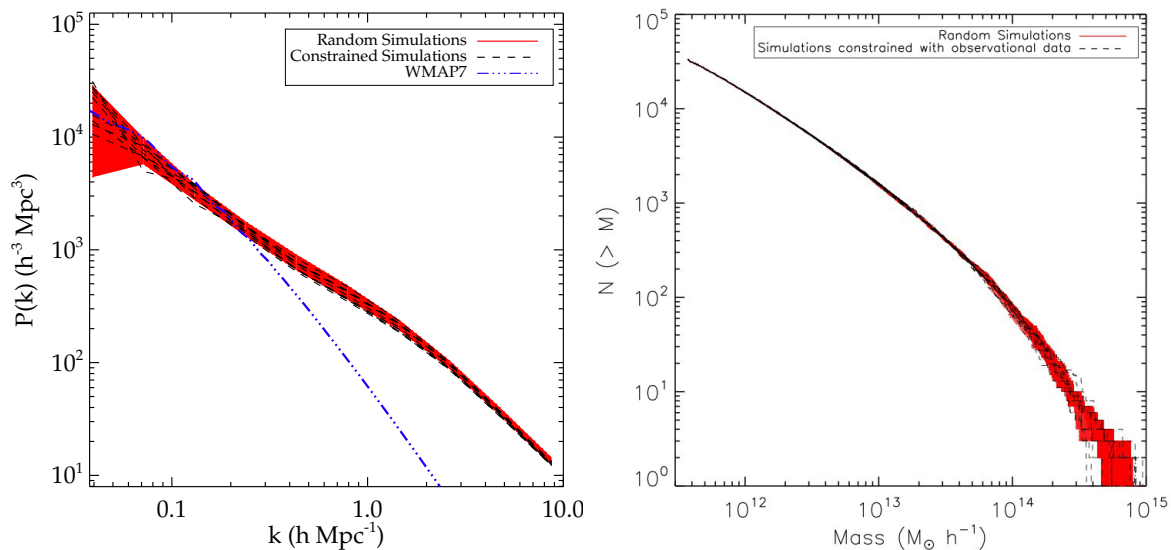


FIGURE 4.8: Power spectra (*left*) and mass functions (*right*) of the ten constrained simulations of the Local Universe obtained with RZA3D applied to *cosmicflows-1* (black dashed lines). The red shaded areas correspond to the range within which the ten random simulations, with the same cosmology as constrained simulations (same assumed prior model), are contained. The dashed-dotted blue line in the left panel stands for the linear part of WMAP7. Both constrained and random power spectra and mass functions overlap each other.

4.3.2.2 Constrained Simulations and Local Cosmography

In the simulations, the supergalactic coordinates are parallel to the box coordinates with the origin at the center of the box where ideally there is a Milky-Way-like. Table 4.2 and Figure 4.9 are proofs that no Virgo cluster is simulated at the expected location out of ten RZA-radial simulations constrained by the observational peculiar velocity catalog assuming

either WMAP7 or WMAP3 (choice which results in negligible differences). Accordingly and in agreement with the theoretical study which advocate the utilization of RZA3D, the rest of the section focuses only on the analysis of RZA3D constrained simulations. The compatibility of the constrained simulations with the observed local cosmography is presented.

| Case | Mass | Average supergalactic X,Y,Z position | Average distance to the observed Virgo cluster | Nb of oc- curences |
|--------------------|----------------------|---|---|-----------------------|
| Observed | 4* | -2.74, 12.0, -0.518 | | |
| Virgo cluster | | | | |
| RZA3D (WMAP7) | 0.7 ; $\sigma = 0.3$ | 1.23, 13.8, 2.2 ; $\sigma = 1.2$ | 5.4; $\sigma = 1.2$ | 8/10 |
| RZA3D (WMAP3) | 0.5 ; $\sigma = 0.2$ | 1.30, 13.8, 0.70 ; $\sigma = 1.0$ | 4.7; $\sigma = 0.8$ | 8/10 |
| RZA-radial (WMAP7) | | | | 0/10 |
| RZA-radial (WMAP3) | | | | 0/10 |

TABLE 4.2: Average parameters and standard deviations σ for the halos representative of Virgo. (1) simulations in which the halos are looked for, (2) mass in $10^{14} h^{-1} M_{\odot}$. *Estimation of the total (baryonic + dark matter) mass (e.g. Ekholm et al., 2000; Karachentsev and Nasonova, 2010). (3) average supergalactic coordinates X, Y and Z and their standard deviations, h^{-1} Mpc, (4) distance from the simulation halo to the observed Virgo location and standard deviation σ , h^{-1} Mpc, (5) number of occurrences in ten different simulations (if a halo similar to Virgo was found in a $6 h^{-1}$ Mpc sphere).

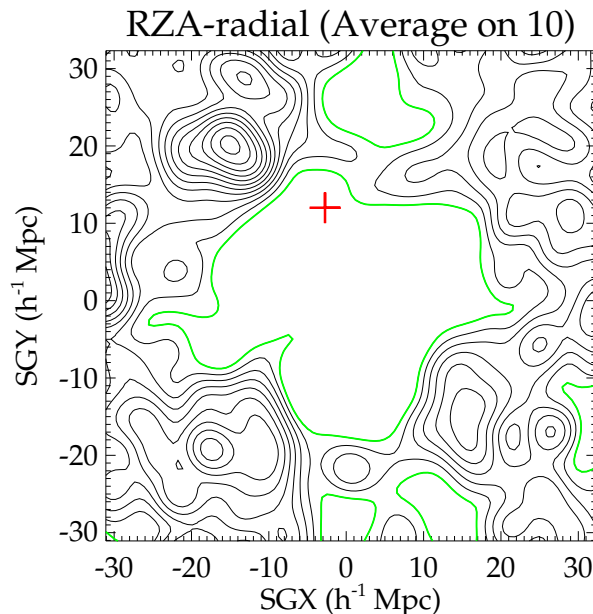


FIGURE 4.9: Average of ten constrained simulations obtained with RZA-radial applied to the observational catalog of peculiar velocities *cosmicflows-1*. Virgo is never simulated at the expected location, a void stands at its position.

Figure 4.10 displays the Wiener-Filter reconstruction of the *cosmicflows-1* catalog (left), one single RZA3D simulation (middle column) and an average of ten RZA3D constrained

simulations (right). Fields are smoothed by a Gaussian kernel of $2 \text{ h}^{-1} \text{ Mpc}$. Red crosses mark the position of the Virgo cluster in the observed Universe (see Table 4.2 for the exact position). The Local Void and Virgo Void are also indicated. The Wiener-Filter serve as targets for the constrained simulations, with the caveat that the Wiener-Filter provides only the linear overdensity field. The inner $R = 30 \text{ h}^{-1} \text{ Mpc}$ volume is dominated by the Local Supercluster. The general structure of the Local Universe including positions of the voids are quite well reproduced by a constrained simulation. The average over ten different realizations shows that in general the Virgo cluster region is well simulated at a similar location whatever random component is used.

To quantify the reliability of the RZA3D technique in simulating the Virgo cluster and the area surrounding it:

- the high density peak of the Wiener-Filter reconstruction is identified in each RZA3D simulation,
- the Amiga halo finder is used to identify replicas of the cluster in the constrained simulations.

To proceed, we use the same process as with the mock catalog. There is a density peak at a similar location to the Wiener-Filter peak in the ten RZA3D constrained simulations. The typical misplacement with respect to the Wiener-Filter peak is about $8\text{-}9 \text{ h}^{-1} \text{ Mpc}$ with a standard deviation about $2 \text{ h}^{-1} \text{ Mpc}$. Although the supergalactic Y and Z components are very similar in the Wiener-Filter (~ 13 and $1 \text{ h}^{-1} \text{ Mpc}$) and in the simulations ($\sim 13 \pm 1$ and $3 \pm 2 \text{ h}^{-1} \text{ Mpc}$), the error in position is quite high because in the supergalactic X direction the shift in position, with respect to *cosmicflows-1* Virgo cluster, is negative in the Wiener-Filter ($\sim -3 \text{ h}^{-1} \text{ Mpc}$) while it is positive in the simulations ($\sim 4 \text{ h}^{-1} \text{ Mpc}$). Still, there is absolutely no density peak in the RZA-radial constrained simulations even when looking in a $10 \text{ h}^{-1} \text{ Mpc}$ sphere centered on the Wiener-Filter density peak. The blue crosses in Figure 4.10 stand for the positions (average positions, in the right column) of the Virgo-like halos. Table 4.2 provides details about masses, positions, errors in position and standard deviations. For completeness, the table presents the results obtained in both WMAP7 and WMAP3 frameworks although differences are negligible. A Virgo-like halo is present in eight out of ten simulations. By comparison, with RZA-radial, no replica of Virgo in $6 \text{ h}^{-1} \text{ Mpc}$ spheres centered on the observational position was found.

A synthetic Local Universe with a Virgo cluster using *only observational peculiar velocities* is produced for the first time thanks to the WF/RZA/CR technique described in this work. This is a proof of concept that the WF/RZA/CR method can be applied to observational peculiar velocities to successfully build constrained Initial Conditions.

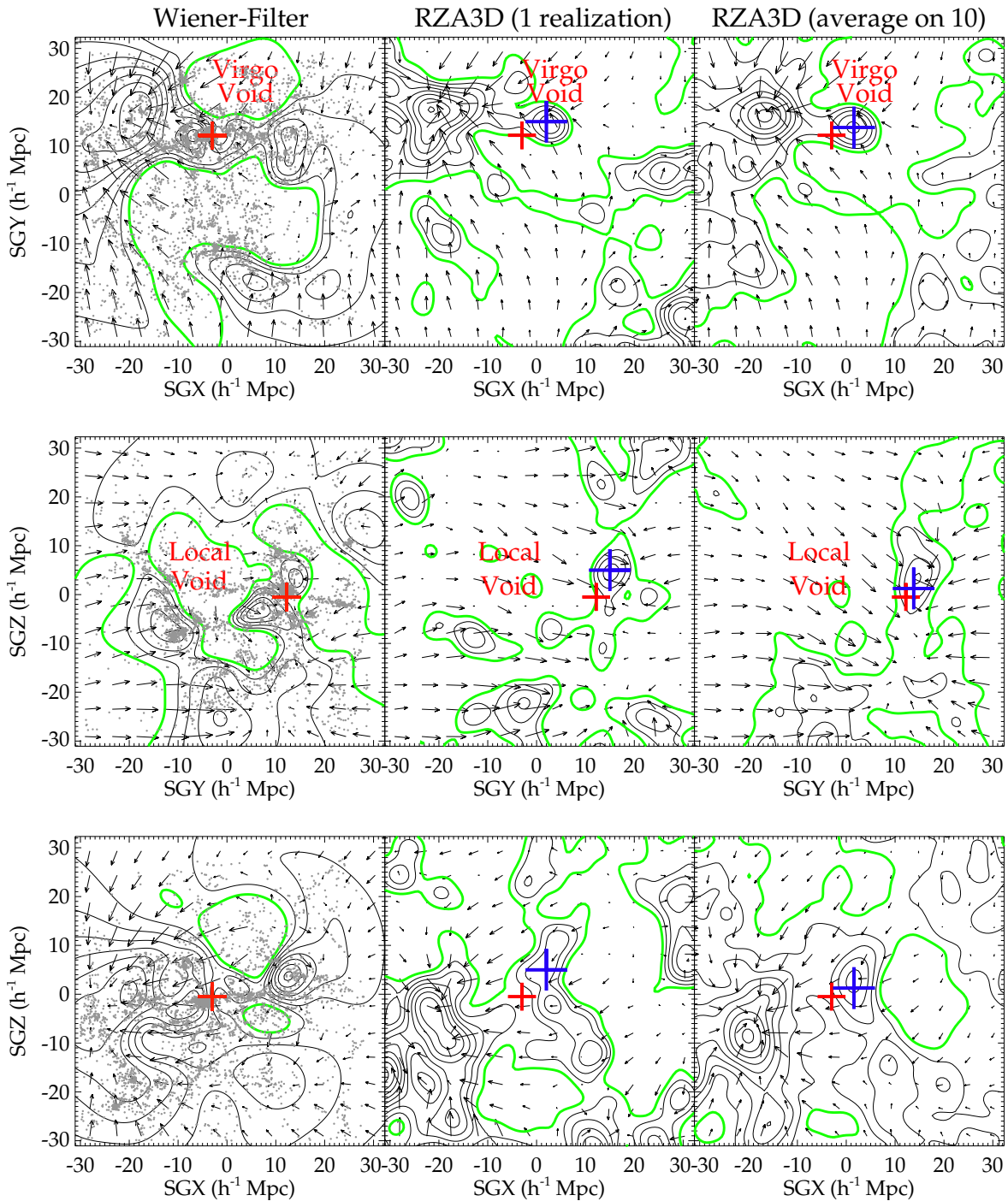


FIGURE 4.10: XY, YZ and XZ supergalactic slices of the Wiener-Filter reconstruction (*left*), of one constrained simulation (*middle*) and of the average of ten constrained simulations (*right*) of the Local Universe within a $30 \text{ h}^{-1} \text{ Mpc}$ radius sphere. The supergalactic slices are located at $Z = 0$, $X = -2.5$ and $Y = 12.5 \text{ h}^{-1} \text{ Mpc}$ to fit the location of the Virgo cluster. The overdensity, at $2 \text{ h}^{-1} \text{ Mpc}$ Gaussian smoothing, is represented with black isocontours. The green contour stands for the mean density. The flows are shown with black arrows. In the XY supergalactic plane, the Virgo cluster and the Virgo Void are both reconstructed (*left column*) and simulated (*middle column*). Virgo is also visible next to the Local Void in the YZ supergalactic slice. In general Virgo is well simulated, at a similar location, whatever random component is used (*right column*). V8k (catalog of redshifts) galaxies are shown for reference as grey dots in a $\pm 10 \text{ h}^{-1} \text{ Mpc}$ thick slice on the Wiener-Filter reconstruction. The red crosses locate Virgo in *cosmicflows-1*. The bigger blue crosses represents the (average) location of the Virgo-like halos.

4.4 Biases

A preliminary study of the second catalog of the Cosmicflows project (Tully et al., 2013, and subsection 3.5.2) revealed that although superior in size (number of constraints and spatial coverage) than *cosmicflows-1*, some bias effects cannot be ignored anymore at this level. This section aims at presenting the different biases that can affect observational catalogs like *cosmicflows-2*. This section and the subsequent one do not have the pretension to correct for the whole lot of biases but try to minimize their effects proposing some recipes to be applied to the observational catalog.

4.4.1 Malmquist Biases

Distance estimates are subject to severe systematic biases which affect the derived radial peculiar velocities. Almost always all gathered under the term "Malmquist Bias", in reality three types of Malmquist Bias can be distinguished:

- the most often mentioned Malmquist Bias, successively called Problem I, Selection Effect/Bias, "r against V", Distance-dependent, Frequentist, Calibration problem, M-bias of the second kind (Kaptney, 1914; Malmquist, 1922; Han, 1992b; Hendry and Simmons, 1994; Sandage, 1994; Teerikorpi, 1990, 1993, 1995, 1997; Willick, 1994), is analogous to a selection effect in magnitude resulting in underestimated distances. A magnitude limit in a selected sample result in a mean apparent magnitude smaller than it should be. As the limit decreases, in unit of magnitudes with the distance, the bias increases. Namely, dwarfs and other dimmer galaxies are more and more under-represented in the sample with respect to brighter galaxies as the observer looks farther and farther. Consequently, their contribution to the mean apparent magnitude is increasingly reduced. Thus, the mean increases slower than it would have, with the distance or redshift, would all the galaxies have really been included. This explains why equation 3.11 is not valid at higher redshift unless some corrections are made. In this work, this bias affects principally the calibration of the Tully-Fisher relation: as some faint galaxies are "missing" in the sample, the absolute slope of the relation is underestimated so are distances (data points are lacking in the Tully-Fisher diagram below the fitted relation. Where they to be present, the absolute slope would have been higher). In this work, this selection effect was minimized with two successive processes: 1) inverse fits were used to calibrate the Tully-Fisher relation and 2) a correction to be applied on distance modulus estimates was derived to minimize the bias relic (Tully and Courtois, 2012, and section 3.4). This relic is due principally to the fact that galaxies are more likely to be scattered towards brighter "regions" in the diagram than the opposite because of the shape of the Schechter luminosity function,

- the second bias is called the Homogeneous Malmquist Bias and gathers terminology such as Problem II, General Malmquist Bias, Geometry Bias, "V against r", Classical, Bayesian, Inferred-distance problem, M-bias of the first kind (Kapteyn, 1914; Malmquist, 1920; Han, 1992b; Hendry and Simmons, 1994; Lynden-Bell et al., 1988b; Sandage, 1994; Strauss and Willick, 1995; Teerikorpi, 1990, 1993, 1995, 1997). Because our observations are restricted to a sphere centered on us, from the homogeneity of the Universe, the number of observable galaxies increases with the distance. Then considering a true distance $\langle r \rangle$, there is a higher probability to observe a galaxy at $\langle r \rangle + dr$ than at $\langle r \rangle - dr$. Consequently, the probability for a galaxy which distance estimate is r to have been put closer is higher than the opposite. Namely, we are more likely to underestimate the distance. In practice, it is even more complicated than that because of the presence of small scale structures. The bias is a function of the direction of observation. This leads us to the third Malmquist Bias,
- the last of the Malmquist Bias is called the Inhomogeneous Malmquist Bias (e.g. Dekel, 1994; Hudson, 1994; Landy and Szalay, 1992). It is the result of the small scale structures, namely of the fluctuations of the number of galaxies. To apprehend this bias, let's consider a group of galaxies at $\langle r \rangle$ with null radial peculiar velocities for simplicity. Because of observational uncertainties, these galaxies are randomly scattered to the foreground and background of $\langle r \rangle$. For all galaxies at the same redshift, their estimated radial peculiar velocities obtained on either side of $\langle r \rangle$ result in an inaccurate infall towards $\langle r \rangle$ giving birth to spurious structures and flows. In other words, galaxies are more likely to be scattered from high density regions towards low density regions than the opposite. Reducing this bias and the previous one (which are highly related) is a complicated task and we suggest that grouping galaxies in groups and clusters might reduce this bias as recommended by e.g. Burstein et al. (1990) and Nusser and Davis (2011): because galaxies in a same cluster or group are approximately at the same distance, averaging over galaxy distance estimates (to keep only distance estimates of groups and clusters) reduces errors on distances, thus on radial peculiar velocities, of clusters and groups by the square root of the number of estimates. Retracing the footsteps of the methods proposed for instance by Dekel et al. (1999) for the POTENT technique or by Hudson (1994), in addition to grouping, we can envisage to correct the distances or more appropriately, we can minimize their uncertainties. We will propose a method to reduce uncertainties on distances devised during this work in the next section. However, unlike the above mentioned methods, ours is based on correcting peculiar velocities. Before explaining the proposed method, we define another bias.

4.4.2 Error Bias

This last bias results from the assumption that fractional errors on distances, hence errors on radial peculiar velocities, have a Gaussian distribution (see subsection 4.1.2). In reality, because distances are obtained via a logarithmic function applied to distance moduli (equation 3.10), a Gaussian (symmetric) distribution of errors on distance moduli results in a lognormal (asymmetric) distribution of fractional errors on distances and as a result of errors on peculiar velocities. This asymmetric bias associated with the Gaussian weight distribution, by assumption, in the bayesian Wiener-Filter technique, results in a spurious overall velocity infall onto the Local Volume. After assessing the existence of this bias, a method is proposed to minimize it. This technique based on probabilities and Gaussian distributions is similar to bayesian methods. It is developed and tested with very realistic mock catalogs, look-alikes of the second data release of the Cosmicflows project. To control the cosmic variance, mocks are built out of ten different realizations of constrained cosmological simulations of the Local Universe. The method is then applied to cosmicflows-2 in the last section.

Errors on observed peculiar velocities grow linearly with the distance. Although these errors can soon be larger than the peculiar velocities themselves, the bayesian Wiener-Filter technique applied to radial peculiar velocities reconstruct overall the overdensity and velocity fields (e.g. Courtois et al., 2012, and subsection 4.3.1). More importantly this distribution of errors is not symmetric when considering two constraints one located closer to the observer than it should be and the other one positioned farther away. This asymmetry introduces a strong bias in the final recovered velocity field. As a matter of fact, observed distances D of galaxies are derived from the distance modulus μ . Thus even if distance errors in magnitudes are distributed evenly around the modulus value, since a logarithmic function is used to derive the distance in Megaparsecs from the modulus μ in magnitudes, the error in megaparsecs is not anymore distributed symmetrically around the distance value D , as shown by the following set of equations derived from the definition of the distance modulus 3.10:

$$\begin{aligned} \Delta\mu &= \sqrt{\Delta m^2 + \Delta M^2} \approx \Delta M \quad \text{symmetric around } \mu \\ \Delta D &= (\Delta\mu \times \ln(10) \times D)/5 \quad \text{asymmetric around } D \end{aligned} \tag{4.12}$$

where Δ notations stand for the uncertainties.

Since radial peculiar velocities and their uncertainties are derived from distances by the classical equation 3.7, the asymmetric distribution propagates onto peculiar velocity errors via $\Delta v_{pec} = H_0 \times \Delta D$. This asymmetrical error distribution results in a bias in peculiar velocities. Large negative peculiar velocities have an abnormal large error which cannot be properly propagated in the Wiener-Filter because the sign of the error on a particular

distance modulus is unknown. As an example, let's consider a galaxy at 100 Mpc, with $v_{pec}=0 \text{ km s}^{-1}$, $H_0=75 \text{ km s}^{-1} \text{ Mpc}^{-1}$. A 2σ error on the distance modulus gives either 34.2 or 35.8 mag instead of $\mu = 35$. The derived distance is either 69 or 145 Mpc, giving a radial peculiar velocity of 2311 or -3338 km s^{-1} . As a result, a larger error is made by allocating a radial peculiar velocity of -3338 km s^{-1} to this galaxy than when assuming 2311 km s^{-1} . However, the sign of the error on the distance moduli is unknown, hence, although -3338 km s^{-1} is assigned to this galaxy, proportionally the same uncertainty is attributed to that peculiar velocity as it would have been if the value 2311 km s^{-1} was given. Since, the Wiener-Filter technique uses the errors on peculiar velocities as an indication of the strength of the signal in the correlation matrixes, it results in giving the same weight to both values although the absolute negative value is more incorrect than the positive value. This asymmetrical bias results in a spurious overall large infall seen in the velocity field. Figure 4.11 reveals a skewness towards negative peculiar velocities in *cosmicflows-2* confirming the presence of the asymmetry which impacts the reconstruction.

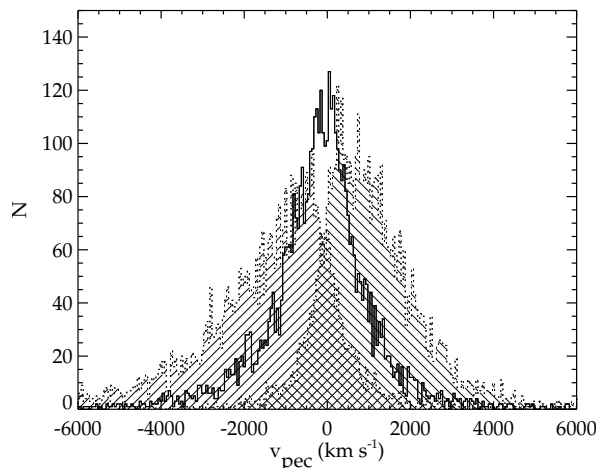


FIGURE 4.11: Histogram (solid line) of radial peculiar velocities in *cosmicflows-2* dataset. The dashed histograms stand for the possible variations of the histogram shape because of uncertainties on radial peculiar velocities. A larger tail is visible in the negative side of this diagram due to the error bias.

Yet, before continuing, it is legitimate to question the relationship between all the above mentioned biases. If they are intertwined, then we can assume that minimizing one we will also drive the others closer to their minimum. Surely, minimizing all of them is better but in absence of such a possibility, it is interesting to define the relations between the biases. As a matter of fact, Homogeneous and Inhomogeneous Malmquist Biases are related. If the first one is due to a larger probability of scatter from farther distances to closer distances, the second one is the result of a larger probability of scatter from high density regions towards low density regions. In addition, Sandage (1994) highlighted the connection between Selection Bias (also a higher probability of scatter from fainter to brighter "regions" than the opposite) and the Homogeneous Malmquist Bias. As for Landy and Szalay (1992), they proved that the error lognormal distribution influences the Inhomogeneous Malmquist Bias affecting grandly

the conclusion on the backside infall onto an attractor. Figure 4.12 recapitulates the bias effects in the form of a diagram. Minimizing a bias, thus decreasing distance uncertainties, we potentially decrease all the others as they all have effects proportional to distance errors. The selection effect has already been minimized, we choose to approach the last presented bias and we propose a method to minimize it too.

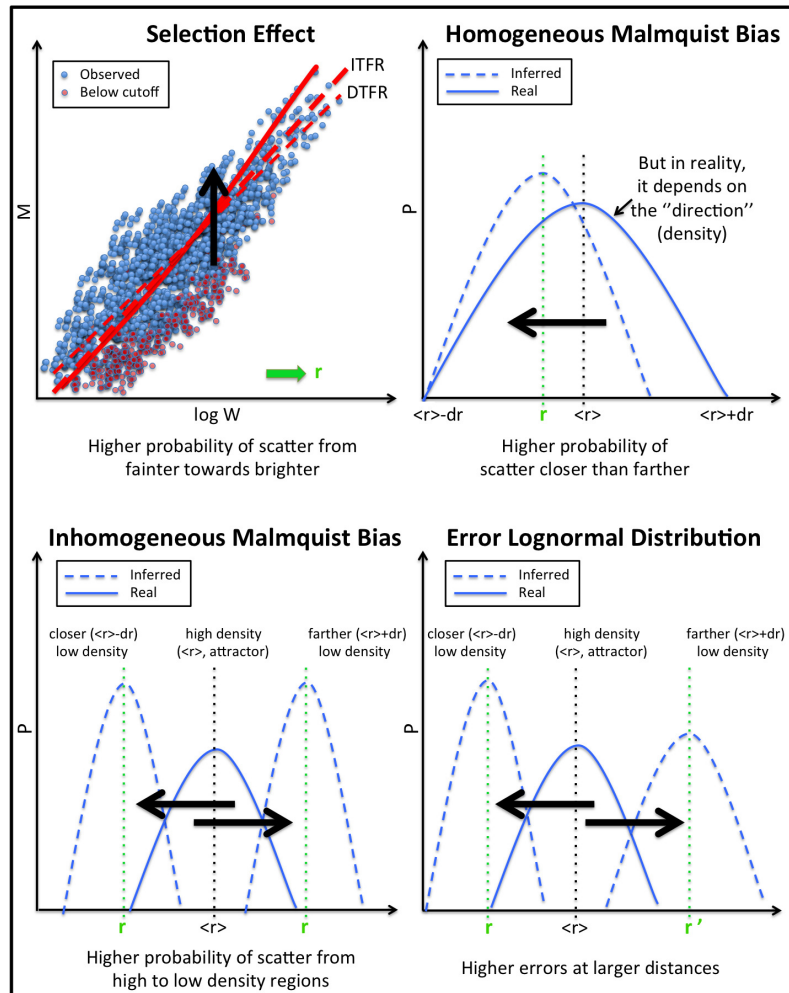


FIGURE 4.12: Schematization of the different bias effects on individual distance estimates, hence on individual inferred radial peculiar velocities. *From left to right, top to bottom:* selection effect, galaxies are more likely to be scattered towards brighter "regions", as a result without appropriate correction distance estimates are too small; homogeneous Malmquist bias, the probability to find a galaxy at $\langle r \rangle + dr$ is higher than at $\langle r \rangle - dr$, consequently without correction distances are again underestimated; inhomogeneous Malmquist bias, it is even more complicated than that because the distribution of galaxies is not homogeneous on small scales, thus galaxies are more likely to be scattered from high to low density regions resulting in spurious flow patterns; another complication comes from the lognormal distribution of errors on distance measurements which results on larger errors at larger distances. The big black arrows in each panel show the "direction" in which galaxies are more likely to be scattered. The dashed red and blue lines give an example of what we could measure and infer for an individual galaxy with a given uncertainty, while the red and blue solid lines mimic the distance range of where the galaxy is more likely to be. Biases are highly related. Minimizing one potentially helps minimizing another. Above all, reducing errors on distances probably drives all of them down.

4.4.3 Minimizing Bias(es)

We can advocate that the effects of all the above mentioned biases were reduced (thus negligible) in *cosmicflows-1* for at least two reasons:

- the coverage of *cosmicflows-1* was smaller than that of *cosmicflows-2* and we know that bias effects increase with the distance (errors are proportional to distances),
- *cosmicflows-1* was in majority constituted of spiral galaxies which are mostly in the field. On the opposite, *cosmicflows-2* contains a large fraction of elliptical galaxies because it uses, in particular, distance estimates from the Fundamental Plane relation (see section 3.5). Ellipticals populate in majority dense regions unlike spirals. *Cosmicflows-2* is then more likely to suffer from non-linear motions and from the Inhomogeneous Malmquist Bias due to high concentrations of single measurements in dense regions.

It is important to note that these biases are by definition highly dependent on the studied sample (e.g. [Landy and Szalay, 1992](#)). Thus, mocks built to test correction methods have to be very realistic especially since these correction methods rely only on the information at hand.

4.4.3.1 A Gaussian Distribution of Radial Peculiar Velocities

Instead of correcting distances as widely proposed in previous methods (e.g. [Dekel et al., 1999](#); [Hudson, 1994](#)), we propose to adjust first peculiar velocities and then go back to distances to correct them. Our process is then based on the distribution of radial peculiar velocities rather than on the radial distribution of galaxies (e.g. [Hudson, 1994](#); [Landy and Szalay, 1992](#)). [Sheth and Diaferio \(2001\)](#) proved that the distribution of radial peculiar velocities considering groups and clusters (namely removing virial motions) should be a Gaussian. Consequently, unless we are located at a particular position in the Universe, which is highly improbable, the distribution of radial peculiar velocities obtained from our position should be close to a Gaussian too. As a matter of fact, Gaussianity is found in mock peculiar velocity catalogs drawn from N-body simulations described in subsection 4.4.3.2. Namely, dark matter halos (what we can actually have access to with dark matter only simulations and which are themselves well described by the linear theory) are equivalent to groups, clusters or isolated galaxies. To derive a method to minimize the error bias in observational datasets, this Gaussianity will be the initial assumption. Yet, if studying simulations, [Bhattacharya \(2008\)](#) confirmed the overall Gaussian distribution of radial peculiar velocities, he also warns us that:

- the cosmic variance due to the particularity of our neighborhood,
- Poisson noise due the restricted size of the sample of peculiar velocities,

both affect the distribution. Still, a major advantage of our study comes from the fact that:

- we use constrained simulations of the Local Universe to produce a set of mocks on which we test our method,
- our mocks mimic as much as possible the characteristics of the observational catalog under study.

As a result, both cosmic variance and Poisson noise are reduced.

4.4.3.2 Very Realistic Mocks

To test our method to be discussed in the next subsection, we need to build even more realistic mocks than those built to test the augmented Reverse Zel'dovich Approximation (RZA3D). These mocks need to match *cosmicflows-2* on several aspects which are:

- the repartition of the data points (number, spatial coverage and distribution including the Zone Of Avoidance),
- the distribution of errors which is highly bimodal in *cosmicflows-2* (see [Tully et al., 2013](#), and subsection [3.5.2](#)),
- the asymmetry bias (namely the errors need to be inserted at the level of the distance moduli not directly on distances anymore),
- the exact error on a distance is unknown, only its 1σ uncertainty is available.

Several realizations are tested to measure the robustness and the accuracy of the method discussed in the next subsection. Because results are similar, if not identical, for every mock tested, only one mock built out of one of the ten simulations is discussed in full length and breadth in this work. The simulation has 512^3 particles and is $320 \text{ h}^{-1} \text{ Mpc}$ wide. It was computed within the framework of the CLUES project (Constrained Local Universe Simulations, [Gottlöber et al., 2010](#)) using the method described in section [4.2](#). A look alike for all the major structures of the Local Universe can be found in this chosen simulation. Figure [4.13](#) allows to identify in the XY plane: the Shapley supercluster in the top left corner, Coma in the top middle, Virgo is close to the center and the Centaurus-Great Attractor region is on Virgo's left side. Using Amiga halo finder ([Knollmann and Knebe, 2009](#)), a list of halos is

drawn from this simulation. Halos are then selected to match *cosmicflows-2* grouped catalog in terms of size (number of constraints), distance extent and spatial distribution (including a Zone Of Avoidance). On Figure 4.13, this compiled list of halos is visible as blue dots in a $10 \text{ h}^{-1} \text{ Mpc}$ thick slice in the XY plane.

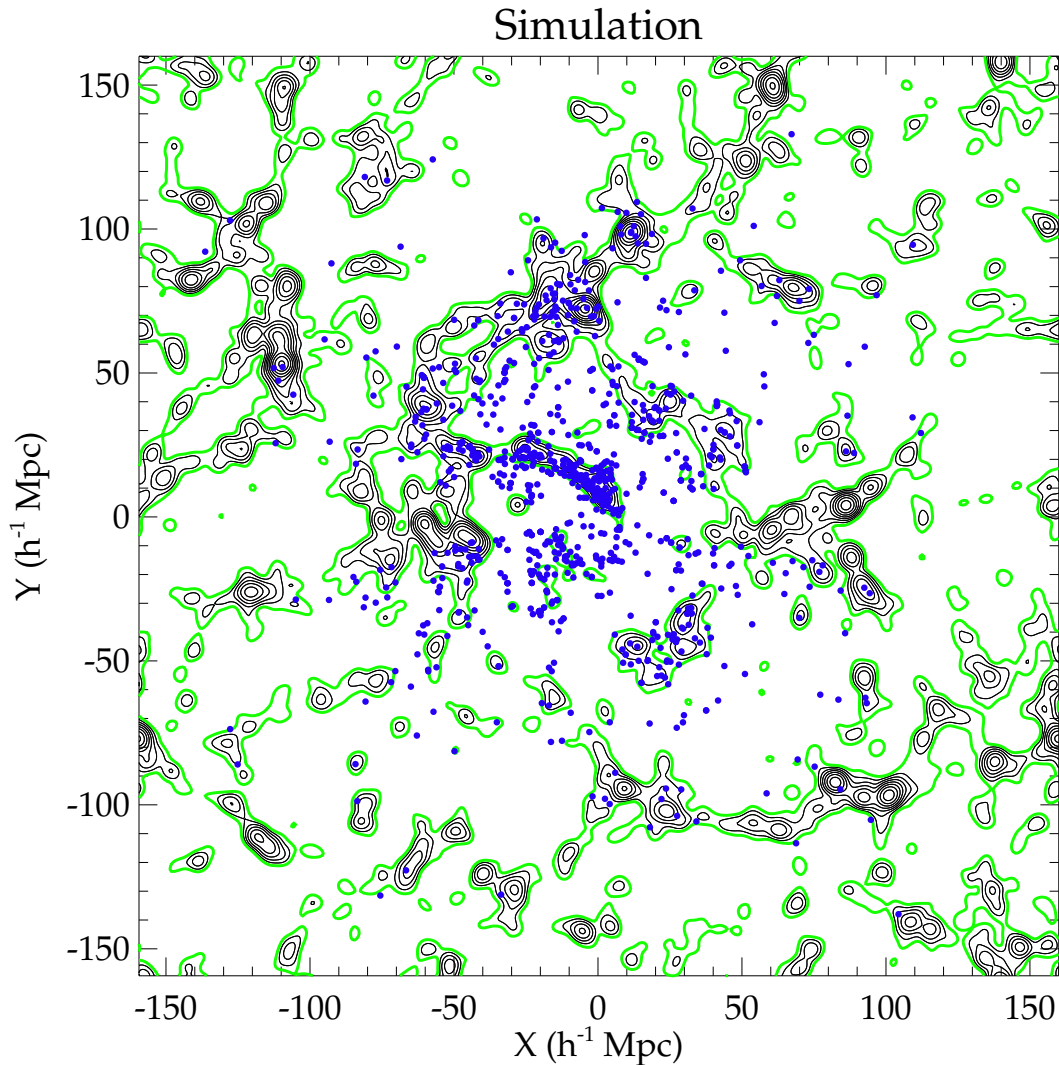


FIGURE 4.13: Distribution of selected halos (blue dots) in the XY plane ($\pm 5 \text{ h}^{-1} \text{ Mpc}$ slice in Z) of a cosmological simulation which is similar to the Local Universe. Halos are selected to build a mock similar to the second catalog of the Cosmicflows project. Black and green contours show the density field and the mean density.

As predicted by [Sheth and Diaferio \(2001\)](#), the distribution of halo radial peculiar velocities (computed with respect to the center of the box, where the Milky-Way like is assumed to be) of this mock catalog can be modeled by a Gaussian visible in Figure 4.14 in blue. This mock is called original in the sense that it has no error on galaxy distances yet. To match *cosmicflows-2* observed catalog as closely as possible, errors need to be inserted into the mock. To preserve the asymmetry problem, a Gaussian distribution of errors with 0.2 magnitude scatter (as on average in the observational catalog) is added to distance moduli. Then to

preserve the strongly bimodal distribution of errors visible in *cosmicflows-2*, constraints at large distances from the center of the box which were attributed a (close to) zero error are reassigned to have a 1σ (0.42 magnitude) error on distance moduli. Disrupted distances and corresponding radial peculiar velocities are then computed. Figure 4.14 displays the distribution of radial peculiar velocities for this "biased mock" by a dotted black line. This distribution is flatter than a theoretical Gaussian with a larger tail on the negative side and, in that sense, is very similar to *cosmicflows-2* distribution on Figures 4.11 and 4.21. Figure 4.15 also presents the histograms of fractional errors on distances (left) and of errors on radial peculiar velocities (right) in black. Then, because in the observed universe, the exact error made on a particular measurement is unknown, distances are attributed either a 9%, 15%, 20% or 25% uncertainty in accordance with their real inserted errors to match the distribution of uncertainties in *cosmicflows-2*.

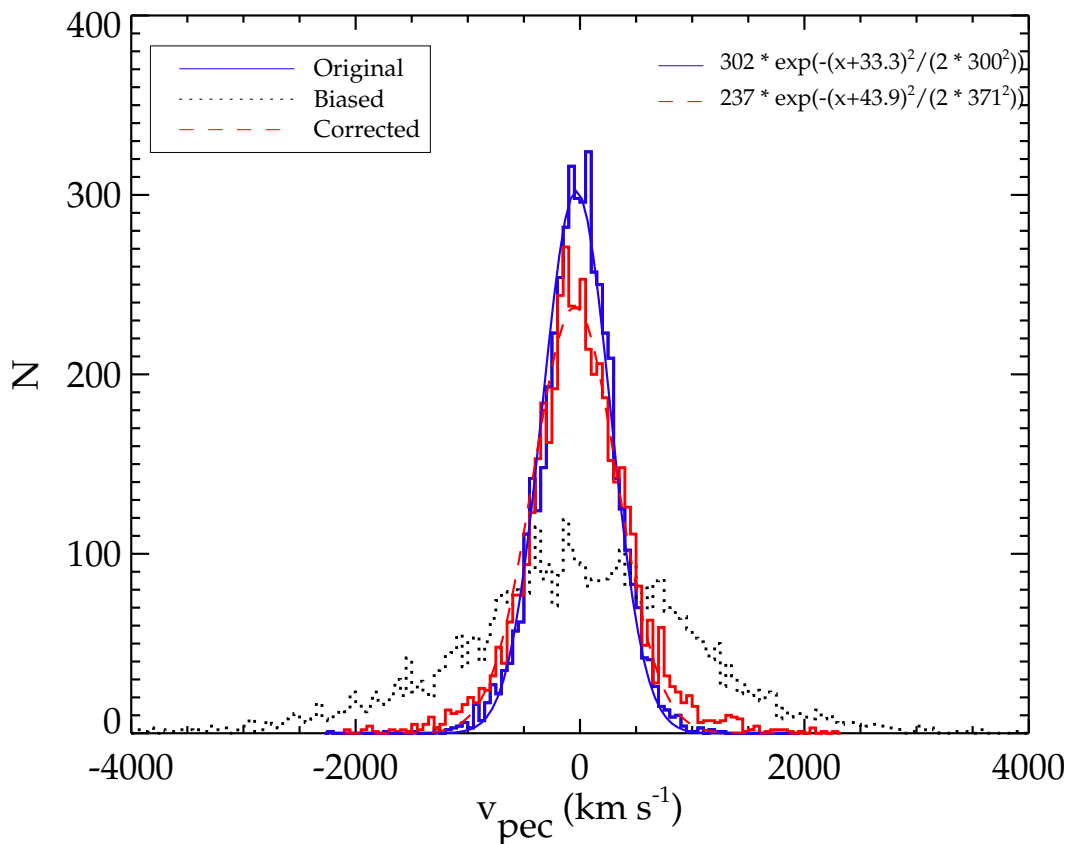


FIGURE 4.14: Distribution of radial peculiar velocities in the original mock catalog (blue solid histogram) and in the mock containing the asymmetry bias (black dotted histogram). The original distribution of radial peculiar velocities can be modeled by a normal distribution (blue solid curve). The distribution of corrected radial peculiar velocities (red solid line) is shown by the red histogram. A Gaussian can also fit this distribution (red dashed line).

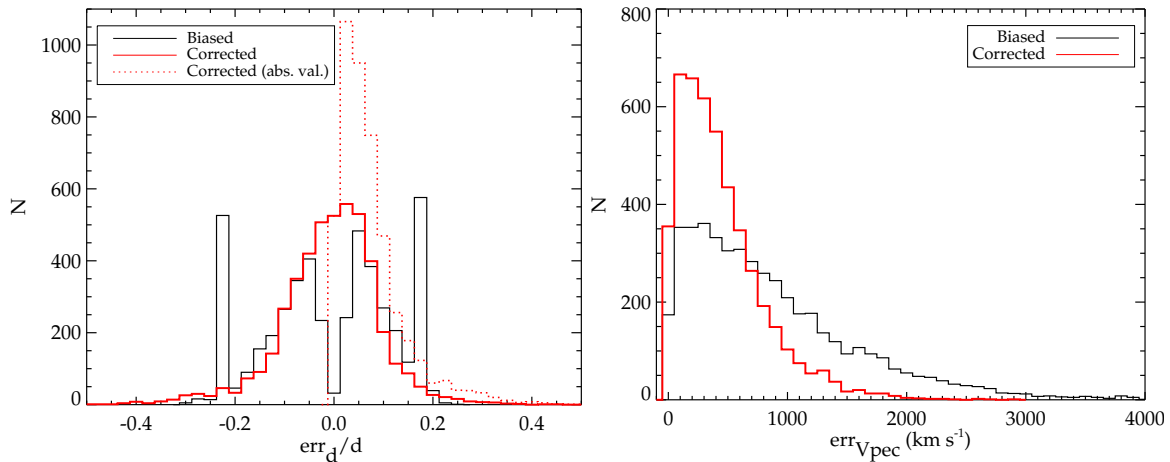


FIGURE 4.15: Histograms of fractional errors on distances (*left*) and on radial peculiar velocities (*right*) in the biased mock (solid black lines) and in the corrected mock (solid red lines). The bimodal distribution of fractional errors on distances with two peaks at 8-10% and 20% errors (absolute values) similar to *cosmicflows-2* is visible. The dotted red histogram shows the distribution of absolute fractional errors on distances after minimization of the bias with a median at 0.06.

4.4.3.3 The Method

To minimize the bias in the mock catalog, an approach similar to a bayesian way is taken. After application of the process, the mock should have a Gaussian radial peculiar velocity distribution with variance and location peak similar to the original ones. In the mock case, variance and peak are determined by the mock with the original positions, hence velocities. Regardless, in the ten different realizations, the standard deviation of the Gaussian fitted to the radial peculiar velocity distributions for mocks similar to *cosmicflows-2* is always around $300 \pm 50 \text{ km s}^{-1}$. As a result, a peculiar velocity is modified according to its probability of belonging to the theoretical Gaussian (with a typical standard deviation of 300 km s^{-1}) and according to its uncertainty. Two cases can be distinguished, either the radial peculiar velocity is positive or it is negative. Then corrected radial peculiar velocities are derived with equations 4.13 and 4.14 devised in this work:

if $v_{pec} > 0$,

$$v_{pec c} = f[p(v_{pec} - \Delta) + (1 - p)(v_{pec} + \Delta)] + (1 - f)v_{pec} \quad (4.13)$$

if $v_{pec} < 0$,

$$v_{pec c} = f[p(v_{pec} + \Delta) + (1 - p)(v_{pec} - \Delta)] + (1 - f)v_{pec} \quad (4.14)$$

where Δ is the radial peculiar velocity uncertainty (Δv_{pec}); p is the probability that a radial peculiar velocity does not belong to the theoretical Gaussian (thus it needs to be corrected and it should either be reduced if it is highly positive or increased if it is highly negative); f is the probability that the radial peculiar velocity estimate is wrong. Namely, f is proportional

to the fractional uncertainty on distances (peculiar velocities) normalized to the maximum fractional uncertainty plus 0.05 (best parameter in our different realizations to retrieve a distribution close to the theoretical Gaussian) to keep a minimum of trust towards the initial measurements.

These corrected radial peculiar velocities enable us to compute distances for constraints using the classical formula 3.7 in reverse order. After corrections, the distributions of radial peculiar velocities, fractional errors on distances, and errors on radial peculiar velocities are all shown on Figures 4.14 and 4.15 in red. The distribution of absolute fractional errors on distances shown by the red dotted line reveals that, after correction, the distribution of errors is poissonian with a median at 0.06. These distributions and median values are typical for all the mocks built out of the ten different realizations. The distribution of radial peculiar velocities can now be approximated by a Gaussian with variance and peak similar to the original one. Fractional errors on distances are distributed on an approximate Gaussian and the distribution of uncertainties on radial peculiar velocities is less flat and contained in a smaller interval of values.

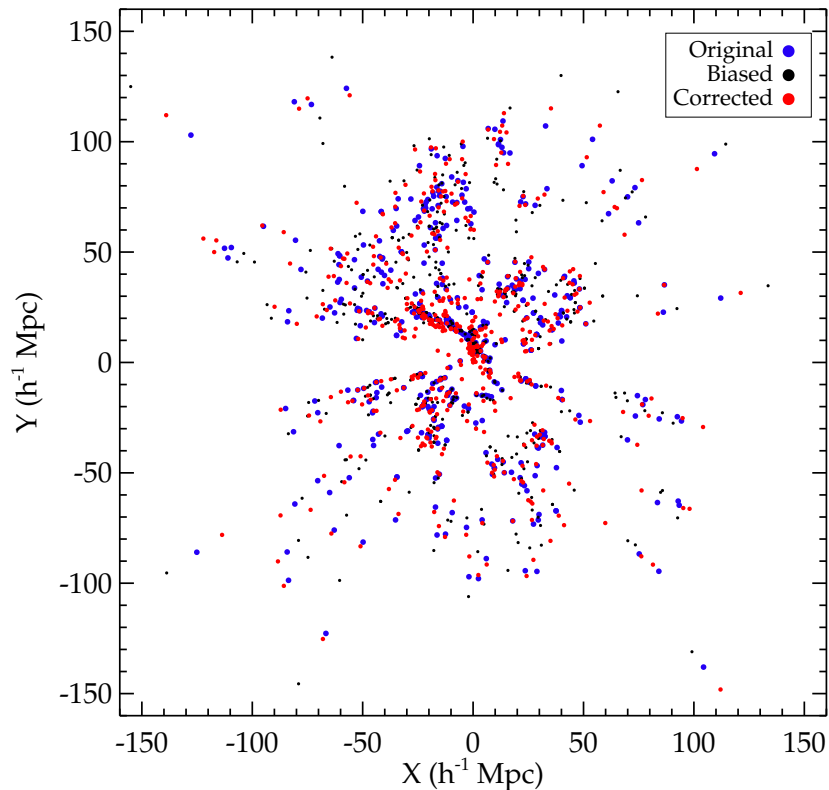


FIGURE 4.16: Distribution of constraints in the XY plane in a $\pm 5 h^{-1}$ Mpc thick slice. Blue dots stand for constraints at their true positions. Black dots are constraints from the biased mock. Constraints located at corrected positions are shown as red dots. These latter are overall closer to blue dots than black ones. Namely, after correction, positions (hence distances and radial peculiar velocities) are more accurate than previous ones.

Figure 4.16 is a proof of concept that, after correction, positions (hence distances and corrected radial peculiar velocities) are overall closer to the true positions than biased ones. On this figure, blue dots stand for the true positions in the XY plane of halos in a $\pm 5 \text{ h}^{-1} \text{ Mpc}$ thick slice. Red dots represent constraints at corrected positions while black dots show halos at their location before correction. Red dots are overall closer to blue dots than dark ones. Namely, in the corrected mock, positions (distances and velocities) attributed to constraints are closer to true ones than biased positions are. Other slices have been looked at resulting in the same conclusion. Moreover, no additional bias is created since, after correction, positions are not always closer to / farther from the center of the box than original ones. Namely, distances are not all under/over-estimated. The reconstruction technique is put into practice in the next subsection on this minimized biased mock. Fractional errors of 6% on distances are assumed in agreement with the upper limit of fractional error medians found in the various corrected mocks.

4.4.3.4 Tests

For purposes of completeness, the Wiener-Filter technique is applied to three mock catalogs: biased, corrected and, as a mean of control, original with positions and 3D peculiar velocities, to remove any bias due to an increasing smoothing with distance. The reconstruction obtained with the original mock represents the best overdensity and velocity fields we can expect from the Wiener-Filter method would the data be perfect. As the goal of this subsection is not to test the accuracy of the Wiener-Filter technique already widely tested (e.g. Courtois et al., 2012; Zaroubi, 2000; Zaroubi et al., 1999, 1995, and subsection 4.3.1), it is in a sense easier to compare the reconstruction obtained with biased and corrected mocks to that former reconstruction to determine to which extent the bias is properly minimized. The three reconstructions are on Figure 4.17. The reconstruction obtained with the biased mock (middle column) present what is expected from the asymmetry problem, namely a large infall in contradiction with the simulation. In addition, structures are extended and very round. On the opposite, the strict infall has disappeared from the reconstruction resulting from the corrected mock (last column). Structures are more sharply defined in good agreement with the best result we can obtain using the Wiener-Filter technique on a catalog similar to *cosmicflows-2* but ideal (first column). After this qualitative analysis, a quantitative one can be derived from cell-to-cell comparisons between reconstructions obtained with the original and the two other mocks. Such comparisons are visible on Figure 4.18 between cells within $200 \text{ h}^{-1} \text{ Mpc}$.

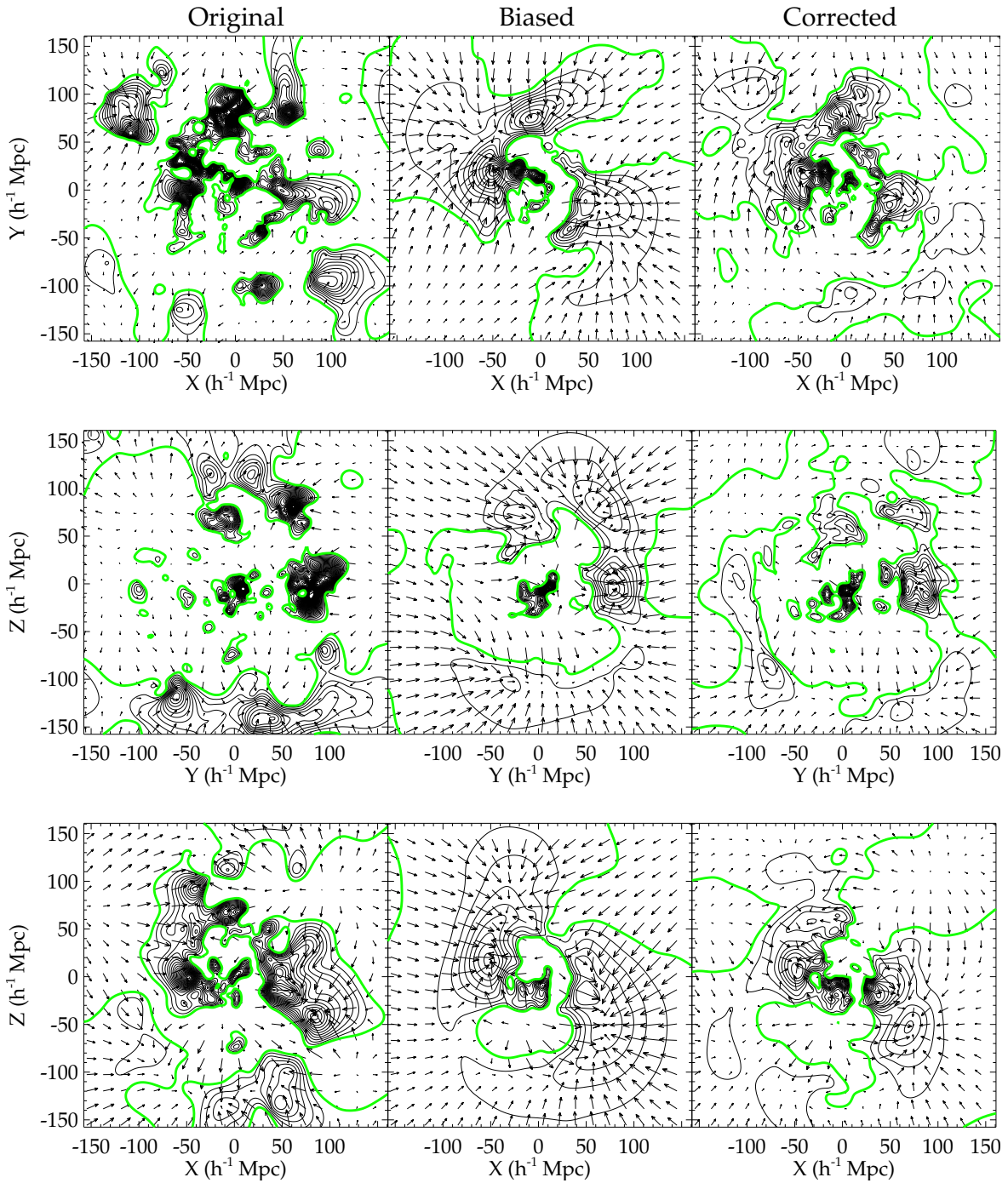


FIGURE 4.17: XY (*top*), YZ (*middle*) and XZ (*bottom*) slices of the overdensity (black contours) and velocity (black arrows) fields reconstructed with the Wiener-Filter technique applied to the original (*left*), biased (*middle*) and corrected (*right*) mocks. The green contours show the mean density. The net spurious infall onto the volume is clearly visible in the velocity field reconstructed from the biased mock and structures are round. On the opposite, structures are more sharply defined (for instance, the look-alike of Shapley in the top left corner of the XY plane) in the reconstruction obtained with the corrected mock and the strong infall has disappeared (for instance, the expulsion from the void in the top right corner of the XZ plane).

The scatter around the 1:1 linear relation is smaller when comparing all but 0.3% of the cells within $200 \text{ h}^{-1} \text{ Mpc}$ between reconstructions obtained with original and corrected mocks than between those obtained with original and biased mocks. Even when considering the whole box, standard deviations are 378 km s^{-1} (2.1σ) for the reconstruction obtained with the corrected mock against 433 km s^{-1} (2.4σ) for that obtained with the biased mock. This is probably the results of the flatter radial peculiar velocity distribution in the biased mock rather than a close to a Gaussian distribution in the corrected mock. The slight tilt, observed in the comparisons, is due to the fact that the Wiener-Filter smooths according to given errors. Since no error was attributed to constraints in the original mock while some were given to velocities in the biased and corrected mocks, the reconstructed velocity fields resulting from the Wiener-Filter applied to these two last mocks are smoother than the velocity field obtained with the original mock. A point which is important to notice as a large lack of power will lead to simulations (the final goal) lacking some power on all scales. Namely, the random field added by the Constrained Realization technique would not suffice to re-establish the proper power. Thus, once a process is applied to an observational catalog, checking the power left in the data is required.

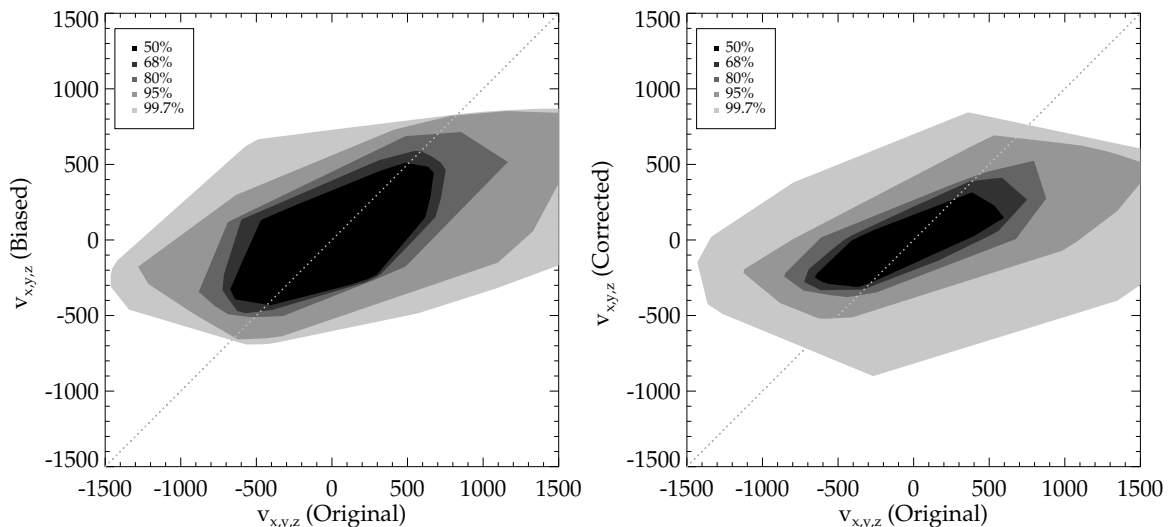


FIGURE 4.18: Cell-to-cell comparisons within $200 \text{ h}^{-1} \text{ Mpc}$ between reconstructions obtained with original and biased mocks (*left*) and between those obtained with original and corrected mocks (*right*). The gradient of grey delimits the 50, 68, 80, 95 and 99.7 % confidence zones. Apart from the 0.3% cells which cannot be find in the 95% confidence zone, all the other cells are less scattered around the 1:1 ideal relation when comparing original and corrected mocks than when comparing original and biased mocks.

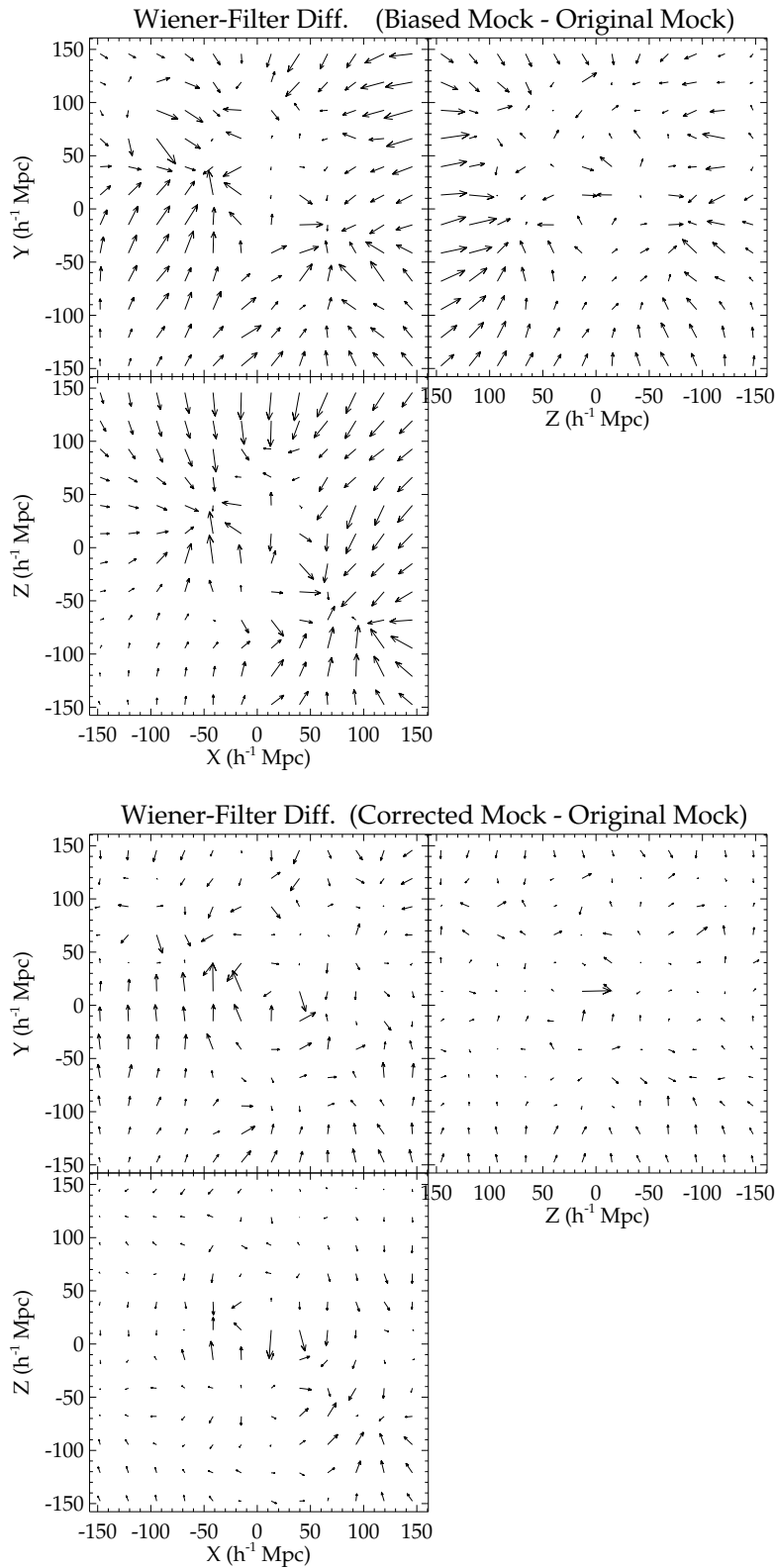


FIGURE 4.19: Residual velocity fields in the XY, YZ and XZ planes when subtracting the Wiener-Filter reconstructed fields obtained with the original mock to those obtained with biased (*top*) and corrected (*bottom*) mocks. Velocity fields have been first normalized by their maximal value. While the spurious infall due to the bias is clearly visible in the residual between reconstructions obtained with biased and original mocks, the effect is minimized when looking at the difference between the fields obtained with corrected and original mocks. As no major pattern in the *bottom* panel is missing in the *top* panel, the correction process does not lead to additional false patterns in the velocity field.

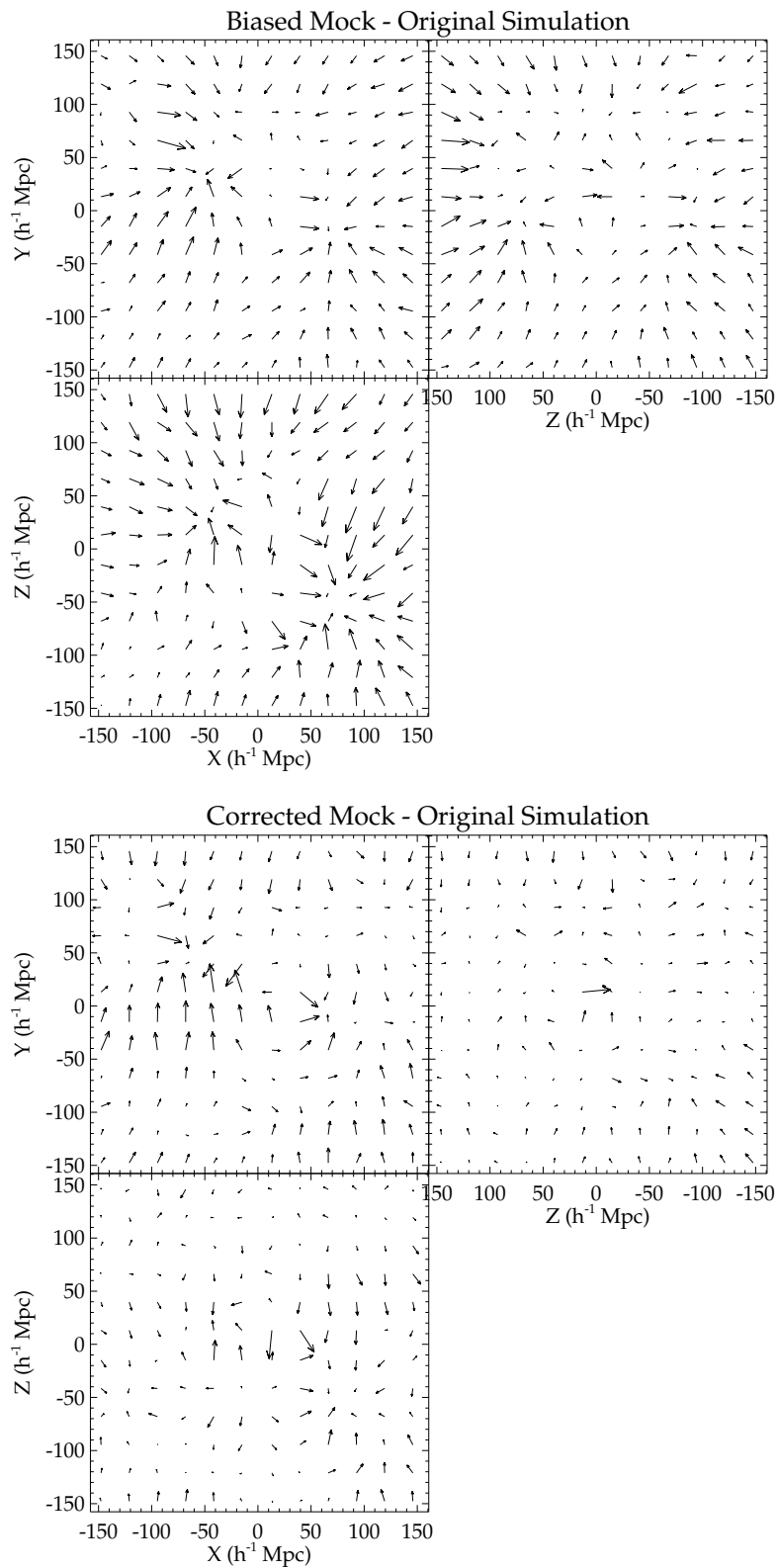


FIGURE 4.20: Same as the previous figure except for the reconstructed velocity field obtained with the original mock. It is replaced by the velocity field from the original simulation. Conclusions are unchanged.

To check that the infall bias into the box is indeed minimized without creating additional spurious patterns in the velocity field, Figure 4.19 shows the residual between velocity fields normalized by their maximal value obtained with biased, corrected and original mocks. On this figure, the spurious infall present in the reconstruction derived with the biased mock is visible while it is largely minimized in the field reconstructed from the corrected mock. No flow which was not in the biased reconstruction appears in the velocity field obtained after application of the correction process. Residual flows are dimmed or in another word minimized. For completeness, Figure 4.20 represents the residual between reconstructions and the original simulation. Standard deviations between original simulated and reconstructed velocity fields are 191 km s^{-1} and 225 km s^{-1} when corrected and biased mocks are used respectively. The exact same conclusions can be drawn. The process devised in this work contributes to decrease the bias in the mock catalog.

Because our procedure also decreases errors on distances, in addition to the latent relationship between the biases, we can suggest that it also contributes to some extent to the minimization of the Malmquist Biases. Regardless, our main concern is with the constrained simulations which are not affected as much as the reconstruction by the bias (since the precursory simulation used to test the proposed correction is itself based on a preliminary version of *cosmicflows-2*), probably because RZA3D, through the Wiener-Filter, is capable of removing itself most of the biases by replacing noisy radial peculiar velocities with noise-filtered 3D peculiar velocities. Argumentations can be made in favor of more mathematical derivations but, because of the cosmic variance, biases, and thus the required correction, highly depend on the catalog at hand. Thus, we found the method we propose here to be satisfactory to reach our ultimate goal.

4.5 CLUES with Cosmicflows-2

In this last section, we apply the whole process to the observational catalog *cosmicflows-2* within the framework of Planck cosmology but with a slightly modified normalization, than that given in Table 2.1, in agreement with the value chosen in other works of the CLUES project ($\sigma_8 = 0.829$). From the bias minimization up to the RZA3D method, *cosmicflows-2* is adjusted before being input in the Constrained Realization of Gaussian Fields algorithm to produce initial conditions which are run with GADGET.

4.5.1 Minimization of the Bias(es)

For comparison purposes, the Wiener-Filter is first applied to three versions of *cosmicflows-2* (CF2). The primary or biased version which can be compared with the biased mock, the

corrected version to be linked with the corrected mock and the version released in [Tully et al. \(2013\)](#). This *cosmicflows-2* version, hereafter CF2-catalog, contains a small correction made at that time to reduce the asymmetry bias. That correction consists in shrinking large negative radial peculiar velocities to make the radial peculiar velocity distribution more symmetric as it is visible on Figure 4.21. However, both distances and uncertainties are kept in the process.

4.5.2 Reconstruction of the Local Universe Within $160 h^{-1}$ Mpc

Figure 4.22 shows the reconstruction obtained out of CF2-biased, CF2-catalog and CF2-corrected. This figure shows that the small correction previously made goes in the proper direction. The spurious infall is less pronounced although the correction is not quite strong enough to minimize the effect of the asymmetry bias. The correction proposed in this work on the other hand reveals that the reconstructed velocity field resulting from the Wiener-Filter applied to CF2-corrected does not suffer from the spurious infall anymore. For instance in the top left corner of the supergalactic YZ plane on Figure 4.22, there is an eviction from the void.

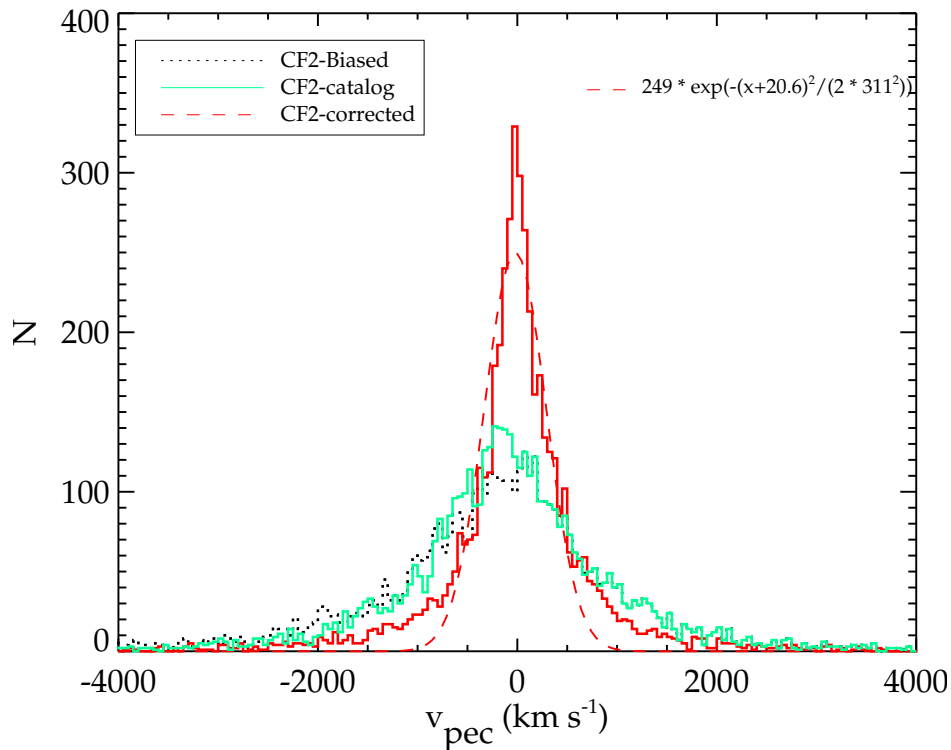


FIGURE 4.21: Radial peculiar velocity distributions in CF2-biased (dotted black line), CF2-catalog (solid green line) and CF2-corrected (solid red line). After correction, the distribution of radial peculiar velocities in CF2-corrected can be fitted by a Gaussian (dashed red line) with variance and peak close to the original ones (obtained with mocks).

Moreover, it appears that the $\chi^2/\text{d.o.f}$ (with d.o.f the degree of freedom) value of the CF2-catalog is below 1. As this value measures the adequacy between the data and the power spectrum, a value less than 1 reveals that the dataset is missing some power probably because the allocated error budget is too large when applying the Wiener-Filter. For instance, considering TF distance estimates, since they do not all have a 20 % error (this is the TFR scatter or 1σ uncertainty), assigning to each one of them such an error does not constitute the optimal solution. Still, in absence of another solution, these large uncertainties are allocated to every TF distance measurements of isolated galaxies in CF2-biased and CF2-catalog. The signal is oversmoothed by the Wiener-Filter. On the opposite, a value greater than 1 is due to the non-linear part of the dataset which is not taken into account a priori in the linear bayesian Wiener-Filter technique. As explained before in subsection 4.1.2, a sigma non-linear added in quadrature to the radial peculiar velocity errors can re-establish a value close to 1. As Initial Conditions can be derived solely from catalogs with value close to 1 or resulting simulations will lack some power at all scales, the $\chi^2/\text{d.o.f}$ value should be controlled. Namely the power spectrum of the resulting simulations will not match a measured power spectrum, such as Planck power spectrum, if $\chi^2/\text{d.o.f}$ is not close to 1.

To estimate the quality of the reconstruction of the Local Universe obtained with the Wiener-Filter applied to CF2-corrected, Figure 4.23⁴ shows the reconstructed overdensity field to which is superimposed the 2MASS redshift catalog as white dots. The gradient of colors gives an estimate of the overdensity in the reconstruction with an increase from blue to red. Typically, voids are in blue and overdensities are in red/orange. Structures of the Local Universe are reconstructed.

⁴This figure was made with the SDvision software (e.g. Pomarède et al., 2013).

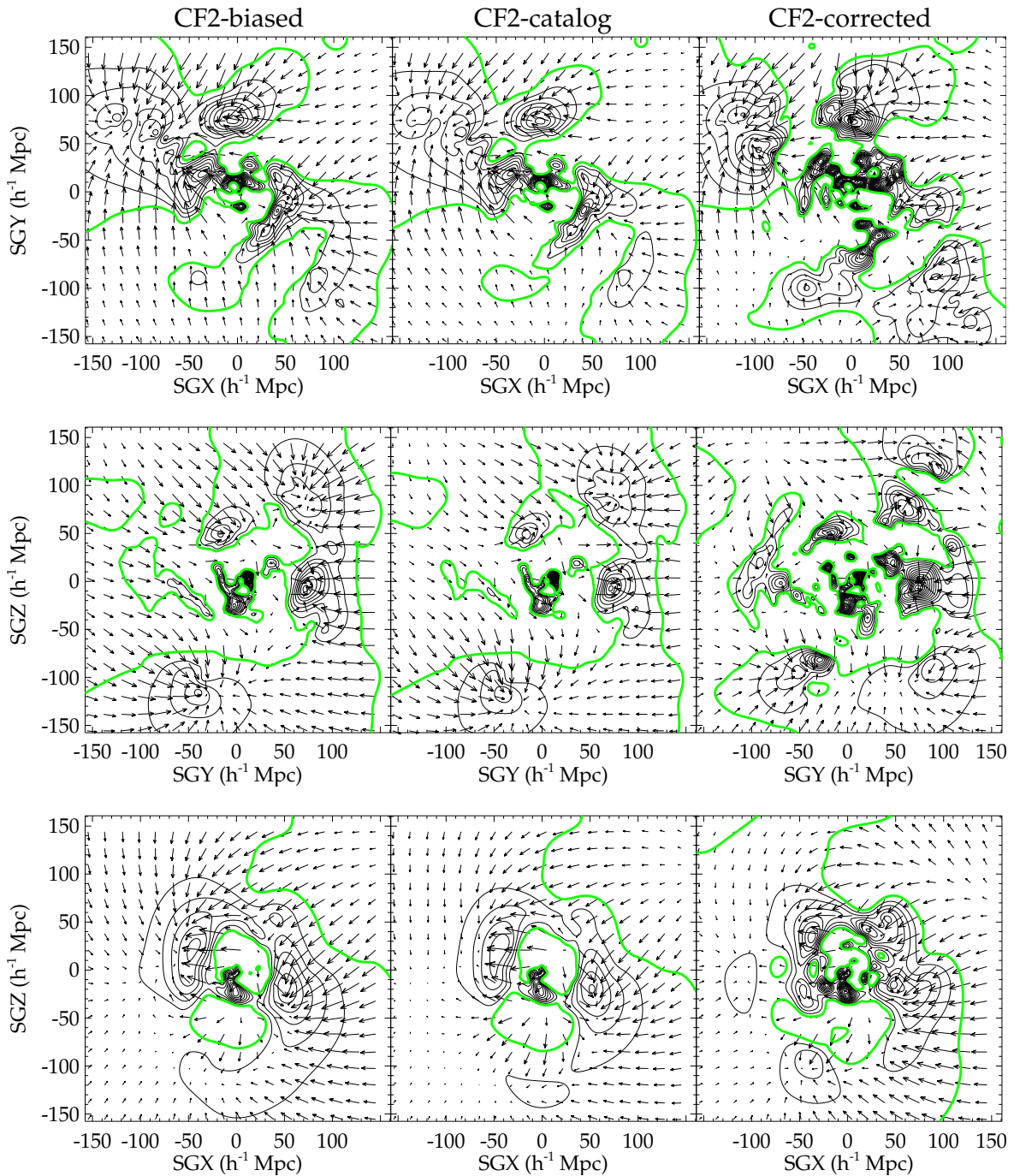


FIGURE 4.22: Supergalactic XY (*top*), YZ (*middle*) and XZ (*bottom*) slices of the overdensity (black contours) and velocity (black arrows) fields reconstructed with the Wiener-Filter technique applied to CF2-biased (*left*), CF2-catalog (*middle*) and CF2-corrected (*right*). The green contours show the mean density. The net spurious infall onto the volume is clearly visible in the velocity field reconstructed from CF2-biased and structures are quite extended. On the opposite, structures are more sharply defined in the reconstruction obtained with the corrected mock (for instance, the great wall on the left of the supergalactic YZ plane) and the strong infall has disappeared (for instance, evictions from regions at the top left and right corners of the supergalactic YZ and XZ planes are clearer).

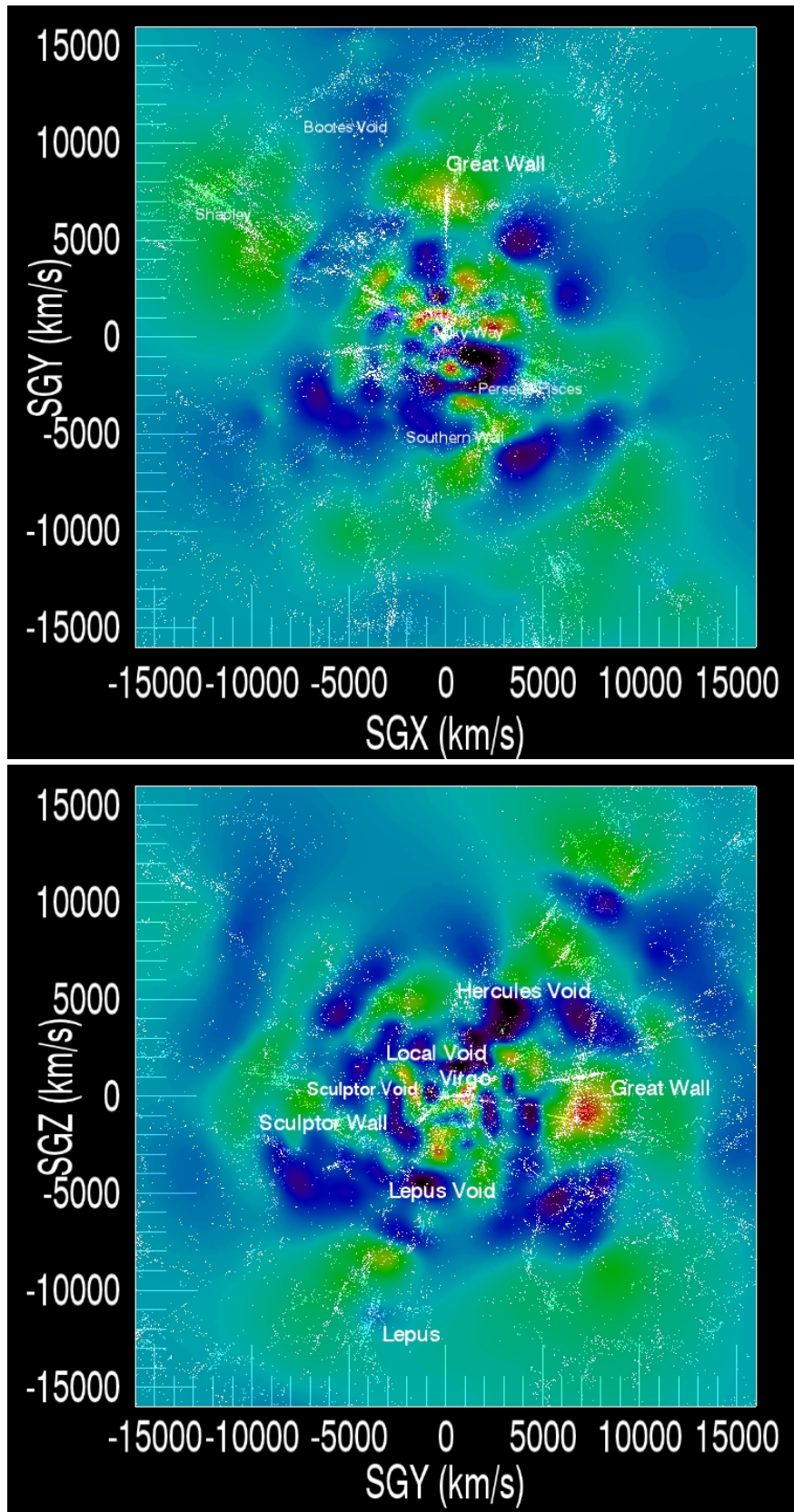


FIGURE 4.23: XY and YZ supergalactic planes of the reconstructed overdensity field smoothed at $2 \text{ h}^{-1} \text{ Mpc}$ of the Local Universe obtained with the Wiener-Filter applied to CF2-corrected. The color gradient represents the overdensity field: from blue to red, the overdensity increases. Typically blue regions stand for voids while red/orange zones are overdensities. Galaxies from the 2MASS redshift survey are superimposed as white dots for comparison purposes only. Structures of the Local Universe are well recovered. The "finger-of-Gods" mentioned in subsection 2.1.2.3 of Chapter 2 are clearly visible in 2MASS, thus the comparison has its limitation.

4.5.3 Constrained Simulations of the Local Universe: Main Attractors and Voids

4.5.3.1 Increasing the Resolution

The spatial coverage of the *cosmicflows-2* catalog has required an extent in boxsize that would drastically reduce the resolution of any simulation based on a 256^3 grid. Consequently, constrained realization fields cannot be transformed in initial conditions for GADGET as such. To increase the number of particles from 256^3 to 512^3 , we use the software GINNUNGAGAP, developed within the CLUES project by Steffen Knollmann. This package requires the white noise of the constrained realization fields, the power spectrum and the assumed cosmology. With all these parameters, it is capable of increasing the size of the grid to then produce primordial fields to build initial conditions for GADGET.

The white noise field $\omega(\mathbf{x})$ is generated with the density perturbation field $\delta(\mathbf{x})$ and the power spectrum $P(\mathbf{x})$ which follow the relation in Fourier space:

$$\delta(\mathbf{k}) = \sqrt{P(\mathbf{k})} \cdot \omega(\mathbf{k}) \quad (4.15)$$

Note that this method applied in reverse enable the production of a random field with the statistics of the power spectrum for the constrained realization technique: it is enough to generate a Gaussian white noise field with zero-mean and unity-variance and to combine it with the power spectrum according to formula 4.15 (Bertschinger, 2001; Prunet et al., 2008).

4.5.3.2 Local Cosmography, an Insight in the Zone of Avoidance

With a series of ten constrained simulations, containing 512^3 particles, produced with the observational data, *cosmicflows-2*, within the framework of Planck cosmology, following the whole process described in this Chapter, we can study in more details the Local Universe. We choose to present the result for the best realization we have for a boxsize of $500 \text{ h}^{-1} \text{ Mpc}$ and a grid of 512^3 . Regardless, the ten realizations are very similar. They have all variances about 0.44 in unit of density around their average. This latter is visible in Figure 4.24 alongside the chosen realization.

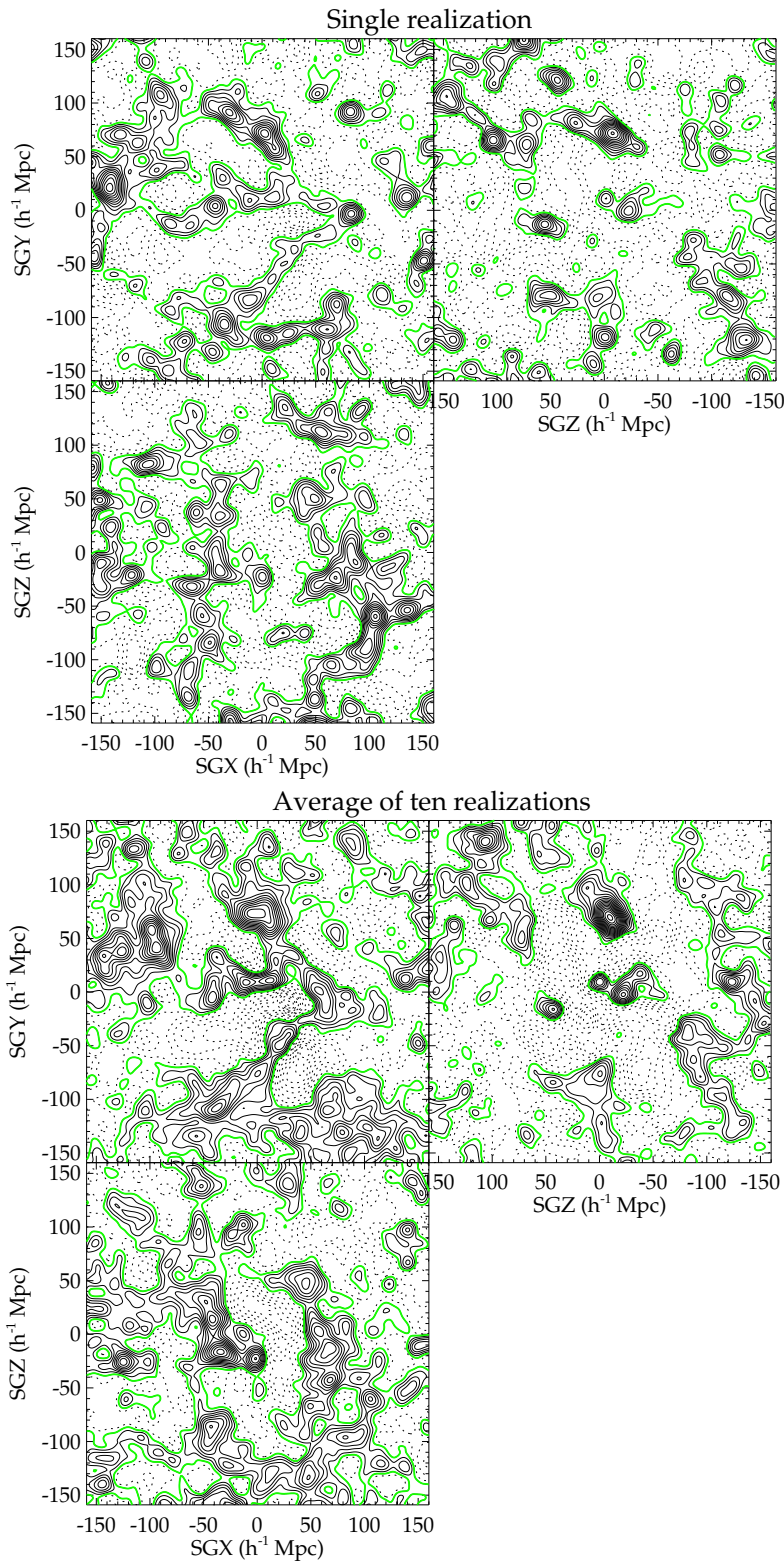


FIGURE 4.24: Supergalactic XY, YZ and XZ planes of one realization (*top*) and of the average of ten constrained simulations (*bottom*) of the Local Universe obtained with *cosmicflows-2*. Solid black contours show overdensities while dashed black contours are underdensities. The mean density is in green. Underdensities in the average have to be present in most of the simulations. In other words, there cannot be in any simulation a major peak at their locations (if there is any overdensity it cannot be higher than half the value of the highest peaks). The most underdense regions have to be underdense in all the simulations. Regarding the highest peaks, they have to be present at least in approximately half the simulations to show up as high as they are. The highest peaks and the largest voids in the unique realization are present in the average revealing they are stable in the different realizations. These peaks and large voids correspond to large overdensities (superclusters) and underdensities (major voids) in the Local Universe.

This average shows the voids and the peaks with the highest probability. In other words, large voids and high density peaks are visible in the average only if they are formed in the majority of the ten realizations. For instance, the highest peaks in the different realizations have values around 16-20 in unit of density. Since the highest peak values in the average are approximately 8-10 in unit of density, the highest peaks have to be present at least in approximately half of the ten realizations ($0.5 \times [16-20]$) at the exact same location. As for underdense regions (including voids), their value in unit of density is necessarily below 1, thus underdensities need to be present in approximately all the simulations. If there is any exception, the overdensity at this location cannot be higher than approximately half the value of the highest peak ($[8-10]$ in unit of density). This value quickly decreases with the number of peaks to reach underdensity values. In other words, in this average of ten realizations, the major overdensities are representative at 2σ and voids at more than 3σ . Back to the $500 \text{ h}^{-1} \text{ Mpc}$ boxsize, it is a compromise between a better resolution but a greatly reduced zone of possible study due to boundary conditions and, a decreased resolution but a zone of study which extends just at the limit of the Shapley supercluster where no spurious effect should appear because of boundary conditions.

In the chosen realization, on Figure 4.25, a look alike for most superclusters and voids in the Local Universe can be found. Maps of superclusters and voids to assess the quality of the constrained simulation are given in Figures 4.26 and 1.1 (Chapter 1). Little is known about structures in the Zone of Avoidance but, from what can be found in the literature, the simulation reproduces quite well the observations also in this zone:

- a connection between the Perseus-Pisces supercluster below the the Zone of Avoidance to a Abell cluster (Abell 569) above the zone of obscuration around $\text{SGX} \approx 6000 \text{ km s}^{-1}$ (Chamaraux et al., 1990; Focardi et al., 1984) is recovered,
- the Perseus-Pisces chain folding back into the zone of obscuration around $\text{SGX} \approx 7500 \text{ km s}^{-1}$ (Marzke et al., 1996; Pantoja et al., 1997) phenomenon is also visible,
- a filament extends from Hydra and Antlia *clusters* across the Zone Of Avoidance around -3000 km s^{-1} to reach the region of the Great Attractor (\sim Centaurus Supercluster, Kraan-Korteweg et al., 1994). A potential supercluster is on an extension of the filament around -6000 km s^{-1} in the zone of obscuration (Kraan-Korteweg et al., 1994),
- and last but not least, Kraan-Korteweg et al. (1994) noted a clustering around $-15,000 \text{ km s}^{-1}$ in the zone hidden by our galaxy dust, a potential connection between the Horologium and Shapley Superclusters. The simulation contains this high density zone. Actually more than half of our ten constrained simulations has a high density zone at this position. Consequently, although it is slightly beyond the maximum zone of study we established ($L/2$ where L is the boxsize, or $[-L/4, L/4]$), it looks like it is a robust structure not an artifact of periodic boundary conditions.

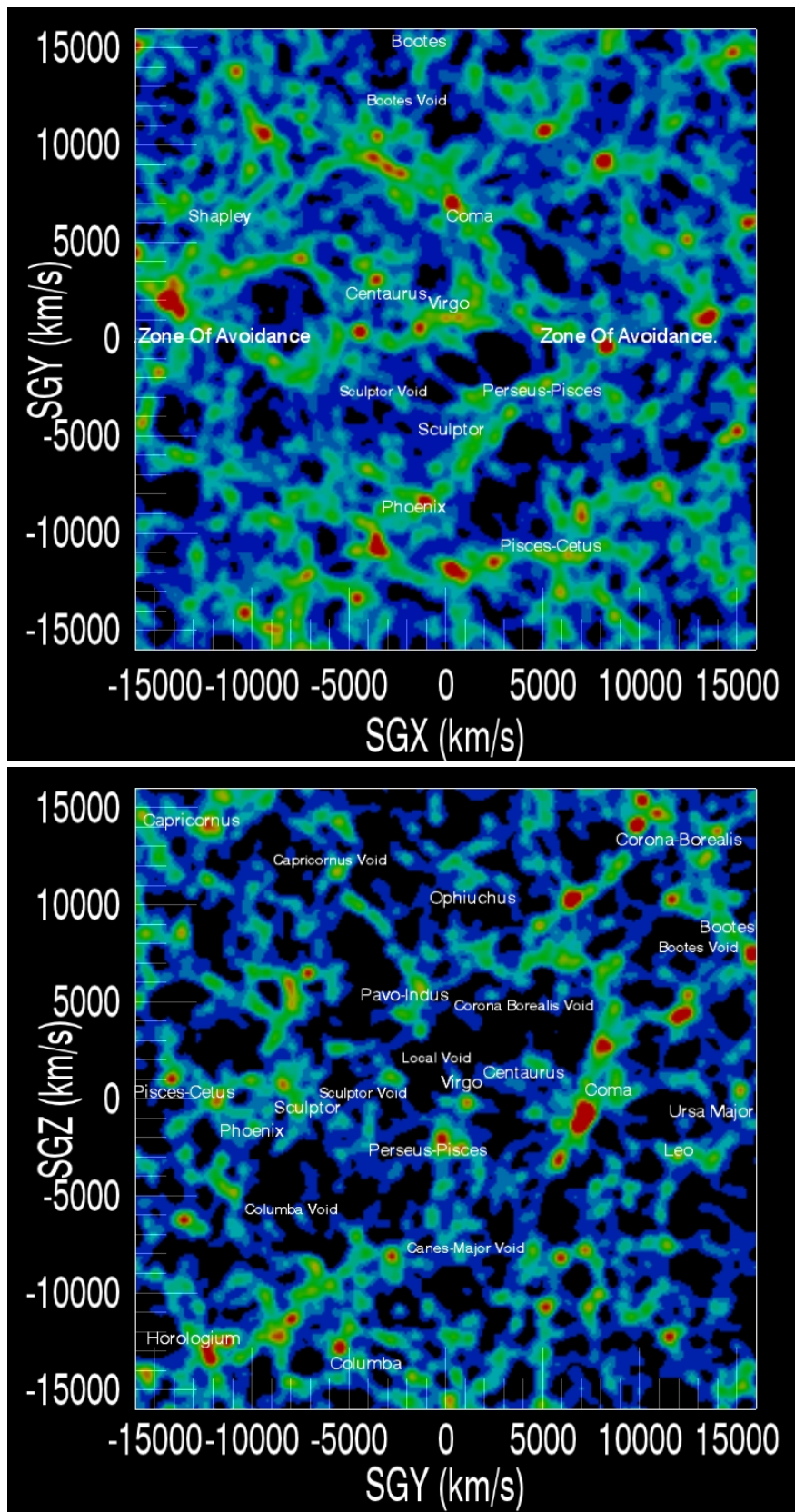


FIGURE 4.25: XY and YZ supergalactic planes of the smoothed at $2 h^{-1}$ Mpc simulated density field of the Local Universe for the best realization obtained with *cosmicflows-2* catalog. The color gradient represents the density field: from blue to red, the overdensity increases. Typically the darkest regions stand for voids while red/orange zones are large overdensities and green are filaments. Major overdensities and voids in the simulation can be paired with a major supercluster or void in the Local Universe (white color names). Note that in the XY plane Sextans and Bootes superclusters are not in the plane.

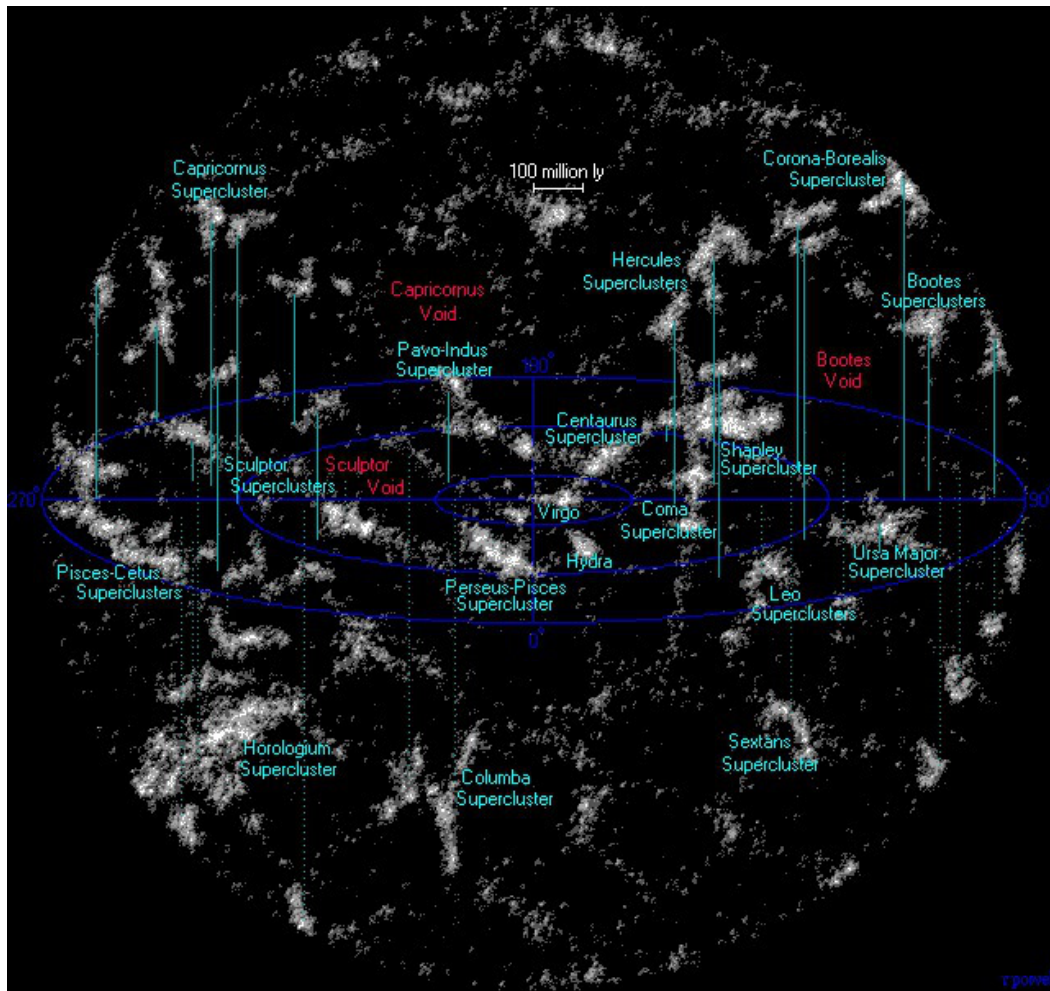


FIGURE 4.26: Representation of the superclusters and major voids in the Local Universe (from www.atlasoftheuniverse.com).

Before going into a more quantitative analysis, Figure 4.27 shows side by side reconstruction and simulation. On that figure, the simulation has been smoothed at $5 h^{-1}$ Mpc to facilitate the comparison with the smoothed at $2 h^{-1}$ Mpc Wiener-Filter field computed on half the grid size. Although the Wiener-Filter shows only the linear field, reconstruction and simulation agree very well. The reconstruction presents more feature in the center but the increasing smoothing with the distance to the center of the box is probably the cause for such an observation. The simulation allows to go deeper into the Zone of Avoidance and to extend further the study of the Large Scale Structure and, more importantly, it supplies the whole density field (including non-linearities).

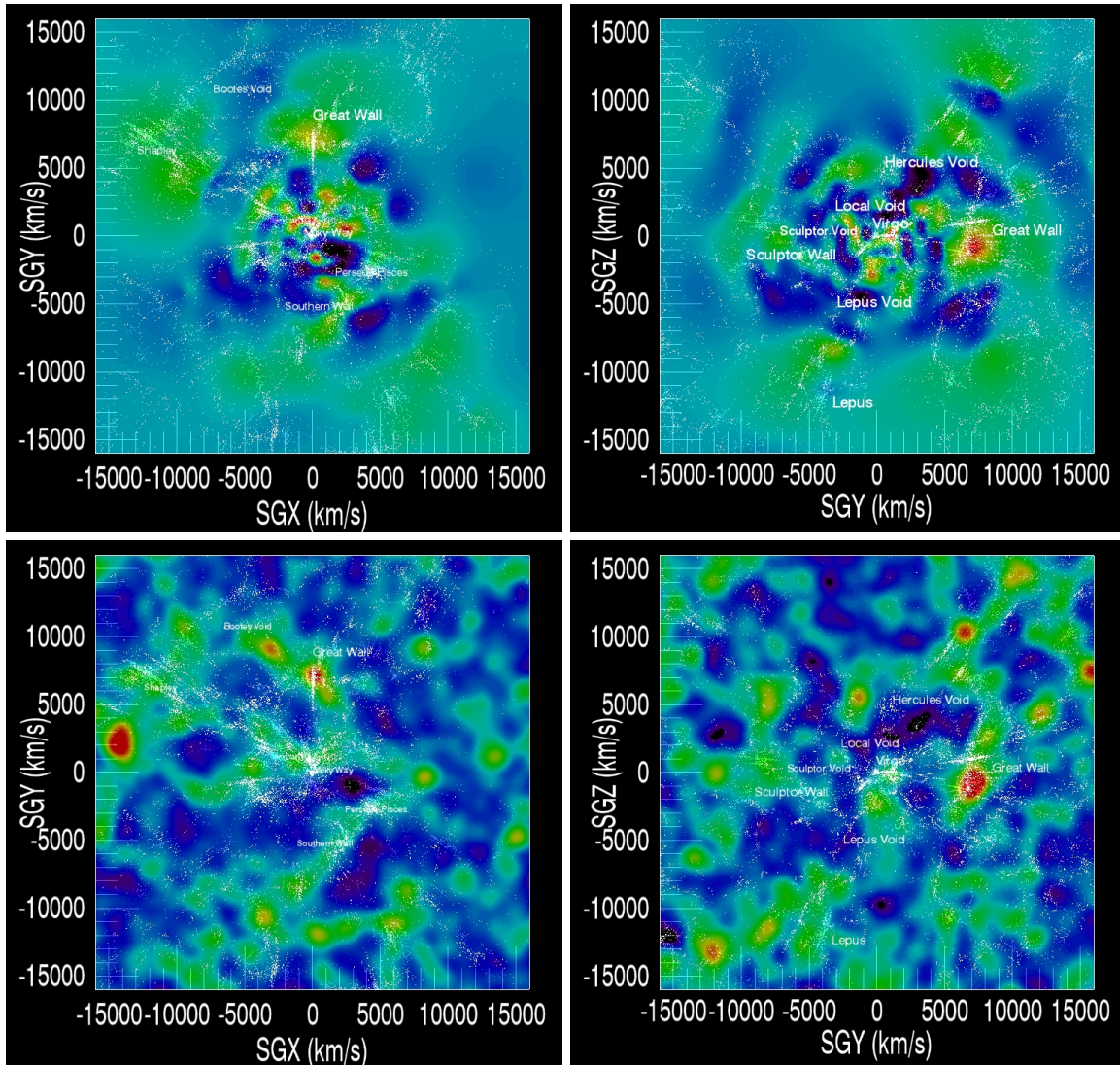


FIGURE 4.27: Comparisons between reconstruction and constrained simulation of the Local Universe obtained both with *cosmicflows-2* modified by the process explained in this work. To facilitate the comparison, the simulation has been smoothed at $5 \text{ h}^{-1} \text{ Mpc}$ and the reconstruction at $2 \text{ h}^{-1} \text{ Mpc}$. Galaxies from the 2MASS redshift survey, in a $\pm 10 \text{ h}^{-1} \text{ Mpc}$ thick slice, are superimposed as white dots for comparison purposes only. Structures of the Local Universe are well recovered in both cases. A few of them are identified (white names). While the Wiener-Filter reconstructs fairly well the Local Universe in the center of the box, the simulation allows to go farther in distances and deeper into the Zone of Avoidance and, more importantly, it supplies the whole density field (including non-linearities).

4.5.3.3 Recovering Clusters

Finally, we turn our attention to the study of halos. To match halos in the simulation with clusters in the Local Universe, we use first Amiga halo finder to compile the list of halos in the simulation. Then, we look for look-alikes of known Abell clusters (Tully et al. private communication) and we add to the list Virgo and, as another example, Ursa Major. We did not look especially for the Coma Supercluster because it is surely fragmented and regardless

it is composed of Abell clusters. Thirteen Abell clusters in addition to Virgo, Ursa Major and their paired halos alongside their distance, their supergalactic coordinate, their mass and their shift in position are given in Table 4.3. The ability to found dark matter halos at so close positions (about $3\text{-}4\ h^{-1}\ \text{Mpc}$ for a search restricted to a $6\ h^{-1}\ \text{Mpc}$ sphere) to that of observed clusters is remarkable. Masses are not always satisfactory but two parameters can be in cause, first simulations are run with dark matter only; second and probably with the most effect, the mass resolution of the simulation is not exceptionally high. The process is repeated for Virgo and Ursa Major in the nine other realizations. Including the tenth chosen realization, we found nine Virgo-like and ten Ursa Major-like dark halos in a $6\ h^{-1}\ \text{Mpc}$ radius sphere. The look-alikes of Virgo have masses ranging between 1.04 and $4.29\ 10^{13}\ h^{-1}\ M_{\odot}$ with a median at $2.23\ 10^{13}\ h^{-1}\ M_{\odot}$. As for the Ursa Major-like halos, their masses are about 1.39 (median) and varies between 1.05 and $3.74\ 10^{13}\ h^{-1}\ M_{\odot}$. More remarkable than masses, are the small shifts in positions in intervals like $[3.03\text{-}5.58]$ (median 3.53) and $[1.39\text{-}4.2]$ (median 2.5) in $h^{-1}\ \text{Mpc}$ for replicas of Virgo and Ursa Major respectively.

In any case, Figure 4.28 is a proof of concept that densities are overall recovered at the positions of Abell clusters. We can conclude with the remarkable agreement between reconstructions, simulations and observations of the Local Universe. This is the first time that such simulations are produced using *solely* peculiar velocities to reproduce all the major attractors and voids in the Local Universe at positions shifted by a few megaparsecs. Even the assumptions and observations regarding the content of the Zone of Avoidance seem to be recovered. The next step is inevitable: increasing the resolution to 1) better recover halos and pursue with more detailed studies of the Local Universe and 2) run gas simulations.

| Name | Mass | D | SGX | SGY | SGZ | δ_{SGX} | δ_{SGY} | δ_{SGZ} | δ_{SG} |
|------------|-----------------------|--------|--------|--------|--------|----------------|----------------|----------------|---------------|
| Virgo | 4e+14* | 12.26 | -2.79 | 11.93 | -0.56 | | | | |
| 19219 | 2.23e+13 | 12.15 | 0.74 | 12.08 | -1.04 | 3.54 | 0.16 | -0.48 | 3.57 |
| Ursa Major | 3.4e+13* | 12.27 | 5.06 | 11.16 | 0.58 | | | | |
| 15991 | 2.60e+13 | 13.85 | 7.38 | 11.64 | 1.34 | 2.32 | 0.48 | 0.76 | 2.49 |
| 100005 | 4.58e+14* | 69.8 | -2.45 | 68.59 | -12.71 | | | | |
| 580 | 2.16e+14 | 70.82 | -0.75 | 69.59 | -13.17 | 1.68 | 1.00 | -0.45 | 2.00 |
| 200046 | 2.92e+14* | 96.8 | 70.18 | -54.65 | -38.19 | | | | |
| 6499 | 5.11e+13 | 92.13 | 67.39 | -51.68 | -35.73 | -2.79 | 2.97 | 2.47 | 4.76 |
| 100041 | 2.49e+14* | 94.3 | 10.34 | 59.96 | 72.05 | | | | |
| 4935 | 6.16e+13 | 92.92 | 5.30 | 59.16 | 71.46 | -5.04 | -0.80 | -0.58 | 5.13 |
| 100018 | 2.36e+14* | 74.7 | -4.27 | 74.18 | -7.67 | | | | |
| 25 | 7.60e+14 [†] | 73.33 | 0.24 | 73.00 | -6.96 | 4.51 | -1.19 | 0.72 | 4.72 |
| 100083 | 1.55e+14* | 99.7 | -45.52 | 31.60 | 82.88 | | | | |
| 4425 | 6.67e+13 | 98.60 | -45.87 | 29.18 | 82.26 | -0.35 | -2.42 | -0.63 | 2.53 |
| 120005 | 1.35e+14* | 72.1 | -2.42 | 71.25 | -10.75 | | | | |
| 6052 | 5.35e+13 | 74.20 | -3.11 | 73.70 | -8.01 | -0.70 | 2.44 | 2.74 | 3.74 |
| 200022 | 1.12e+14* | 48 | -36.84 | -27.28 | 14.23 | | | | |
| 1095 | 1.56e+14 | 43.68 | -33.54 | -22.99 | 15.94 | 3.31 | 4.29 | 1.72 | 5.68 |
| 100175 | 1.10e+14* | 99.7 | -91.89 | 34.42 | -17.65 | | | | |
| 936 | 1.70e+14 | 97.86 | -91.28 | 30.88 | -17.02 | 0.61 | -3.54 | 0.63 | 3.65 |
| 200252 | 1.07e+14* | 85.8 | 48.88 | -55.70 | -43.24 | | | | |
| 4161 | 6.94e+13 | 85.72 | 49.74 | -53.71 | -44.60 | 0.86 | 1.99 | -1.36 | 2.56 |
| 200052 | 9.88e+13* | 64.5 | 34.57 | -47.57 | -26.50 | | | | |
| 5462 | 5.74e+13 | 69.25 | 39.50 | -49.45 | -28.10 | 4.93 | -1.88 | -1.59 | 5.51 |
| 200032 | 9.61e+13* | 58.1 | -36.00 | -32.27 | 32.22 | | | | |
| 608 | 2.09e+14 | 54.15 | -35.02 | -29.10 | 29.31 | 0.98 | 3.17 | -2.91 | 4.41 |
| 100337 | 7.58e+13* | 95.4 | 15.48 | 42.12 | -84.18 | | | | |
| 5762 | 5.55e+13 | 101.13 | 17.46 | 44.55 | -89.10 | 1.97 | 2.43 | -4.91 | 5.83 |
| 100061 | 6.97e+13* | 71.2 | 1.30 | 71.06 | -4.28 | | | | |
| 436 | 2.49e+14 | 71.52 | 4.01 | 71.35 | -2.77 | 2.72 | 0.29 | 1.51 | 3.13 |

TABLE 4.3: Virgo, Ursa Major and 13 Abell cluster look-alikes in the best realization: (1) name of the cluster/halo, (2) mass, $h^{-1} M_{\odot}$ within Planck cosmology. *Estimation of the total (baryonic + dark matter) mass (e.g. [Ekholm et al., 2000](#); [Karachentsev and Nasonova, 2010](#); [Karachentsev et al., 2013](#); [Tully, 2010](#)) and Tully et al. private communication. [†] is likely to be a component of the Coma supercluster (this halo accounts for approximately half the total mass of Coma), (3) distance from the center of the box, h^{-1} Mpc, (4) to (6) supergalactic coordinates, h^{-1} Mpc, (7) to (9) shift in position on the supergalactic coordinates, h^{-1} Mpc and (10) total shift in position (sum in quadrature), h^{-1} Mpc.

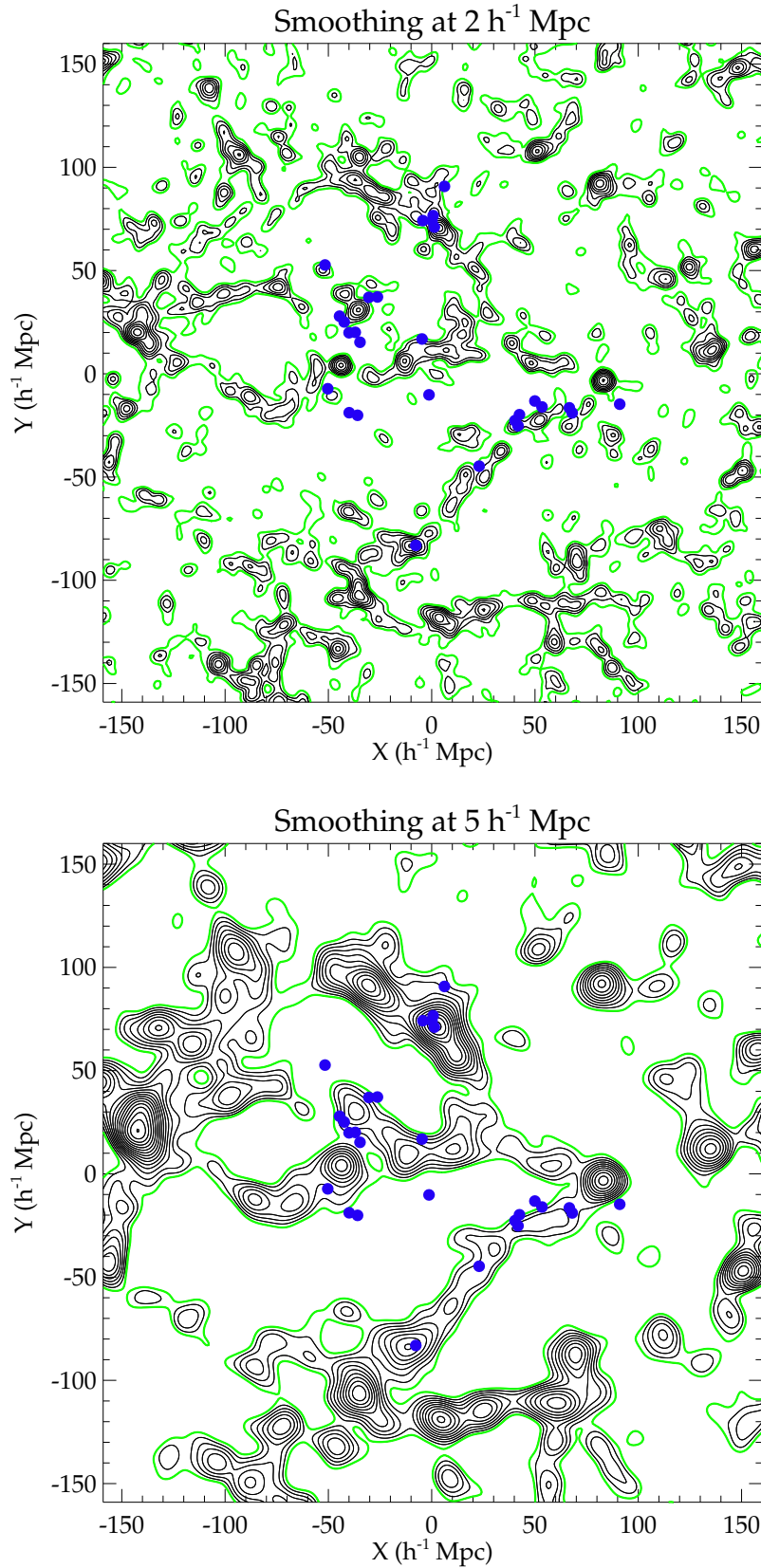


FIGURE 4.28: Superposition of Abell clusters (blue dots, Tully et al. private communication), located in a $\pm 10 h^{-1} \text{ Mpc}$ thick slice in Z in the XY supergalactic plane, on top of a constrained simulation of the Local Universe. Black and green contours stand for the overdensities and mean density. The simulation has been obtained with the process described in this work applied to *cosmicflows-2* catalog. *Top*: simulation smoothed at $2 h^{-1} \text{ Mpc}$, *bottom*: smoothing at $5 h^{-1} \text{ Mpc}$. Overdensities are overall simulated at the positions of Abell clusters. No Abell cluster lie at the center of a major void.

Chapter 5

Summary & Prospectives

The work presented in this manuscript results from the combination of two international projects: The observational project Cosmicflows which goal is to cartography the Local Universe. In this regard, this project's accomplishment consists in catalogs of accurate distance measurements to map local deviations from the Hubble expansion. These distance estimates are mainly obtained with the Tully-Fisher distance indicator ; The CLUES project which produces constrained simulations of the Local Universe with, in this case, the observational catalogs of peculiar velocities built by the first project. These velocities are ideal tracers of the underlying gravitational field at the origin of the formation of structures as they account for both baryonic and dark matter. Resulting constrained simulations of the Local Universe enable to apprehend our environment with exquisite tools to better understand the formation and evolution of our neighborhood. In this closing Chapter, we summarize the work accomplished within these two projects and propose some perspectives.

5.1 Summary

5.1.1 Observed Universe

A great concern with studies of motions on large scales with the correlation between galaxy luminosities and their rotation rates or Tully-Fisher relation (TFR, [Tully and Fisher, 1977](#)) has been the possibility that systematic errors in photometry could create spurious flows. Small offsets between different observers, instruments, conditions, hemispheres, or seasons could be sky-sector dependent. With the new generation of telescopes both in the radio field and in the photometric domain, cosmic flow studies have received an impetus. The space-base Spitzer telescope ([Werner et al., 2004](#)) is an example of such a telescope with

enhanced capacities. Probably the single most important advantage of the use of space-based photometry such as offered by the Spitzer mission comes from the confidence that measurements are on the same scale at better than 1% in all parts of the sky. There are other advantages. Obscuration is minimal both within targets and from our Galaxy and backgrounds are very low. This latter point is especially significant because studies of galaxy flow patterns can now reach high levels of completion across the sky. Then it is a considerable advantage that the great majority of flux at [3.6] band arises from old stars that are good representatives of the baryonic mass, mainly those on the red giant branch. It can be surmised from the modest scatter in the Tully-Fisher relation that there is a close coupling between the mass in stars and the dynamical mass. There is also an advantage, at least vis à vis ground infrared observations, with the sensitivity achieved because of very low sky noise. All but a few percent of the total flux is measured within isophotes resolved from the noise.

Our photometric procedures for the semi-automated analysis of Spitzer IRAC (Fazio et al., 2004) channel 1 data at 3.6 μm have been described. The galaxy surface photometry was carried out with the ARCHANGEL software (Schombert, 2007; Schombert and Smith, 2012) adapted for Spitzer data input. Material of interests for the project was available for about 2000 galaxies from the Spitzer Heritage Archive including the subprogram Cosmicflows with Spitzer. We have demonstrated the ability to use *Spitzer Space Telescope* mid-infrared data to perform surface photometry with a relatively high accuracy. No correlation was found between magnitude uncertainties and other important galaxy parameters such as inclination, apparent area, or semi-major axis. We concluded that, after all corrections, uncertainties on magnitudes are of the order ± 0.05 for the regular spiral galaxies at the heart of the project. These uncertainties are small compared with the typical overall scatter in the Tully-Fisher relation. Low surface brightness galaxies or very irregular ones require special attention but these classes of galaxies are not of principal interest to us.

The current goal of the project is to measure distances, hence map peculiar velocities, across the local universe within 10,000 km s^{-1} using mainly the Tully-Fisher relation. The Extragalactic Distance Database (EDD, Tully et al., 2009) contains HI profile information (Courtois et al., 2009) that provides useful linewidths for over 11,000 galaxies. Spitzer observations provided the complementary photometric information required for a dense, detailed map of structure and motions in the near part of the Universe especially close to the Zone of Avoidance due to the obscuration by our galactic disk dust.

First, galaxies selected as part of the calibrator sample were used to calibrate the mid-infrared Tully-Fisher relation. Then, using the calibrated relation, distance estimates have been derived for the rest of the galaxies with acceptable inclinations and available linewidths that either we have reduced or that come from the S⁴G analysis. A small disadvantage with the mid-infrared TFR calibration has been revealed with the documentation of a color term.

This color term is understood as the natural consequence of the correlation between galaxy rotation rate or luminosity and color (Tully et al., 1982). At a given linewidth, red galaxies progressively become brighter relative to blue galaxies as one considers the TFR at longer wavelengths. Evidence is accumulating that intrinsic scatter in the simple two parameter-TFR is minimal with photometry at about 1 μm . A consequence of the color dependence is a steepening of the TFR toward the infrared. At the expense of the requirement of extra knowledge in the form of a color, the TFR in the [3.6] band was reformulated in a form with scatter that matches the best optical formulations. The correction is small and not acutely dependent on the color measurement. The appropriate inverse TFR equation for the measurement of distances is, after checking the robustness deriving two relations with two different calibrator samples (selection in B and K bands):

$$M_{C_{[3.6]}} = -(20.31 \pm 0.07) - (9.10 \pm 0.21)(\log W_{mx}^i - 2.5) \quad (5.1)$$

where $M_{C_{[3.6]}}$ is derived from the corrected apparent magnitude $[3.6]^{b,i,k,a}$ of a source minus the color term $\Delta[3.6]^{color} = -(0.52 \pm 0.10)[(I^{b,i,k} - [3.6]^{b,i,k,a}) + 0.73]$ with I Band magnitude shifted to the AB system. The slope of this formulation has been derived from a sample of 273 galaxies distributed in 13 clusters, while the zeropoint is established from 31 calibrators with Cepheid or tip of the red giant branch distances. The root mean square scatter in distances found with these galaxies (cluster template and zeropoint calibrators combined) of 0.43 mag, 22% in distance, is close to the accuracy found with the overlapping I band study (Tully and Courtois, 2012).

Distance measures derived with this calibration are subject to a small Malmquist bias or selection effect (Willick, 1994), requiring the distance modulus correction $\mu^c = \mu + 0.004(\mu - 31)^{2.3}$. After application of bias and color corrections, a preliminary estimate of the Hubble Constant can be made from the velocities and distances to seven clusters at $V_{CMB} > 4000$ km s^{-1} . Accounting for all error sources (sum in quadrature), the determination is $H_0 = 75.0 \pm 5.5$ km s^{-1} Mpc $^{-1}$. The difference between the value determined with this mid-infrared analysis compared with the I band value found with the same procedures and an overlapping sample is $\Delta H_0 < 1$ km s^{-1} Mpc $^{-1}$, not a formally significant difference. We reiterate that the great strength of the present calibration is the high confidence in uniformity over the entire sky. Nevertheless the present sample of only seven clusters beyond the domain of known extreme peculiar velocities was unsatisfactorily small. Subsequently, the [3.6] band calibration was extended to a calibration of the Type Ia supernova (SNIa) scale, analogous to what has been done at I band (Courtois and Tully, 2012b), permitting a determination of H_0 at $z \sim 0.1$.

The mid-infrared TFR calibration of the SNIa distance scale led to a result for the Hubble Constant that is not significantly different from the earlier optical TFR calibration. The

earlier calibration made use of a considerably larger collection of material. Besides using over 50% more individual TFR galaxies, it gave consideration to 61 groups or clusters hosting SNIa with distances not only from the TFR but also with Cepheid, surface brightness fluctuation, and fundamental plane measurements (Courtois and Tully, 2012b). Nevertheless we contend that the present confirming work has value because it puts to rest a concern with the optical study. The optical photometry was acquired by a diverse community of observers on several telescopes with a variety of detectors and filters and subject to the vagaries associated with ground-based observations. This mid-infrared photometry has been acquired with a single observing configuration in space advertising photometric consistency across the sky to better than 1%. The study has extended the calibration to distances where peculiar velocities should have negligible impact and we found $H_0 = 75.5 \pm 3.3 \text{ km s}^{-1} \text{ Mpc}^{-1}$.

Distances for Cosmicflows encompass measures by other methodologies than the TFR either from the literature or from other subprograms of the project. Foremost among these are Cepheid Period-Luminosity Relation (Freedman et al., 2001, 2012), Tip of the Red Giant Branch (Lee et al., 1993; Makarov et al., 2006; Rizzi et al., 2007), Surface Brightness Fluctuation (Blakeslee et al., 2010; Tonry et al., 2001), Fundamental Plane (Colless et al., 2001), and Supernova Ia (Jha et al., 2007; Riess et al., 2011) procedures. The diverse material is drawn together in EDD which goes beyond the compilation of catalogs relevant to extragalactic distances to include redshift catalogs, that with various levels of completion describe the distribution of galaxies in the Local Universe, and group catalogs, that help identify entities where averaging over velocities or distances is reasonable. The first assembly of distances in this program (Tully et al., 2008) has now been given the name *cosmicflows-1*. This work has contributed to build the second catalog of the Cosmicflows project (*cosmicflows-2*, Tully et al., 2013) and has initiated the development of a third one with Spitzer observations which will be completed with other measurements in the mid-infrared (WISE, Wright, 2008, Neil et al. in prep.). With two catalogs ready *cosmicflows-1* and *cosmicflows-2* and a third one in preparation, a collaboration with the CLUES project has been established to pursue reconstructions (e.g. Courtois et al., 2012) and constrained simulations (e.g. Gottlöber et al., 2010) of the Local Universe.

5.1.2 Simulated Universe

A great concern with numerical simulations to be compared with observations to study the Local Universe is cosmic variance. This cosmic variance is due to the fact that there is only one universe that we can observe only, at one time, from our "particular" position within the Large Scale Structure environment. Namely, the surrounding environment of the object of study is as important as the object (e.g. Garrison-Kimmel et al., 2014). To minimize the cosmic variance effect, the CLUES collaboration works within the framework

of numerical cosmological constrained simulations of the Local Universe. The first CLUES simulations based on the Mark III catalog of peculiar velocities (Klypin et al., 2003) were not very precise: 1) structures in the simulation at $z=0$ were shifted by $10 \text{ h}^{-1} \text{ Mpc}$ from their observed positions and 2) density constraints were used to simulate nearby clusters. The main deficiency of the Constrained Realization of Gaussian fields algorithm (Hoffman and Ribak, 1991, 1992) used to produce the initial conditions was not to account for the cosmic displacement field whereas galaxies observed today are at different locations from their precursors at higher redshifts. A partial remedy to the problem, called the Reverse Zel'dovich Approximation, was suggested and tested by Doumler et al. (RZA, 2013a,b,c). This approximation consists in shifting constraints back in time from their positions at redshift $z=0$ to the locations of their precursors at higher redshifts. The technique was yet to be tested on more realistic mocks and on an actual observational catalog of the Cosmicflows project. The work presented in this manuscript is thus the first attempt to produce simulations constrained *solely* by an observational catalog of peculiar velocities from the Cosmicflows project.

Since *cosmicflows-1* (peculiar velocity catalog) extends only out to about $30 \text{ h}^{-1} \text{ Mpc}$ (radius), derived constrained simulations are subject to the cosmic variance inherent to the particularities of our neighborhood. Accordingly to test either a reconstruction or a generator of initial conditions method, mock catalogs have to be drawn from a previous constrained simulation which looks like the Local Universe and an ensemble of initial conditions has to be produced. The mock catalogs used in this work have been designed to mimic the observational catalog by including distance measurement errors and a large continuous zone without data (Zone of Avoidance due to our Galaxy extinction). Tests on these mocks and on *cosmicflows-1* revealed that the original RZA, from now-on called RZA-radial, method could be refined. We suggested that *observational* radial peculiar velocities are subject to uncertainties and probably also biases which prevent them from completely defining the curl free velocity field. Thus, the RZA algorithm with its additional feature, which replaces original observed radial peculiar velocity vectors by their full 3D reconstructions provided by the Wiener-Filter estimator (Zaroubi et al., 1999, 1995), should be a remedy to this flaw. The augmented RZA method (called RZA3D) has been tested against the same mocks and resulting simulations have been compared with RZA-radial and original simulations. The enhanced precision and reliability of RZA3D has been validated. The RZA3D methodology has been subsequently applied to the actual *cosmicflows-1* catalog. Only after such a process of the observational dataset, the Constrained Realization of Gaussian fields technique was applied to build various realizations of the initial conditions. The different ensuing simulations recover the observed Large Scale Structure with a typical accuracy of $5 \text{ h}^{-1} \text{ Mpc}$ in position, the best realizations reaching a $2\text{-}3 \text{ h}^{-1} \text{ Mpc}$ precision, i.e. the limit imposed

by the linear theory. The methodology succeeded in performing robust constrained simulations using *only observational peculiar velocities* as constraints. However, *cosmicflows-1* was too shallow to enable constrained simulations that could reproduce all the main attractors and voids of the local dynamics. *Cosmicflows-2* catalog which contains more than 8,000 galaxy distances (1,800 in *cosmicflows-1*) and extends out to about $150 \text{ h}^{-1} \text{ Mpc}$ was more appropriate.

Yet, reiterating the process with the second catalog of the Cosmicflows project revealed that this greater spatial extent catalog suffered from biases (Kapteyn 1914 ; Malmquist, 1920 and e.g. Dekel, 1994; Han, 1992b; Hendry and Simmons, 1994; Hudson, 1994; Landy and Szalay, 1992; Sandage, 1994; Teerikorpi, 1990, 1993, 1995, 1997) that needed to be minimized before pursuing with the work. First, *cosmicflows-2* was grouped. Second, a correction devised in this work to minimize in particular the asymmetry bias observed in the second catalog of the international Cosmicflows project was proposed. This bias is due to the fact that distance errors have a lognormal distribution rather than a Gaussian one resulting in an asymmetric radial peculiar velocity distribution. This asymmetric distribution inserted in the bayesian Wiener-Filter technique results in a spurious infall onto the Local Volume as, by assumption, a Gaussian weight distribution is assigned to radial peculiar velocities. The correction was developed and tested on mocks closely matching *cosmicflows-2* in terms of size (coverage, number, spatial distribution including the Zone of Avoidance), lognormal errors, uncertainties (quasi bimodal distribution) and absence of exact knowledge of errors. The method to minimize the bias, similar to bayesian ways as it relies on probabilities and Gaussian distributions, corrects velocities according to the following formula proposed in this work:

if $v_{pec} > 0$,

$$v_{pec c} = f[p(v_{pec} - \Delta) + (1 - p)(v_{pec} + \Delta)] + (1 - f)v_{pec} \quad (5.2)$$

if $v_{pec} < 0$,

$$v_{pec c} = f[p(v_{pec} + \Delta) + (1 - p)(v_{pec} - \Delta)] + (1 - f)v_{pec} \quad (5.3)$$

where Δ is the radial peculiar velocity uncertainty (Δv_{pec}) ; p is the probability that a radial peculiar velocity does not belong to the theoretical Gaussian (thus it needs to be corrected and it should either be reduced if it is highly positive or increased if it is highly negative) ; f is the probability that the radial peculiar velocity estimate is wrong. Namely, f is proportional to the fractional uncertainty on distances (peculiar velocities) normalized to the maximum fractional uncertainty plus 0.05 (best parameter in our different realization to retrieve a distribution close to the theoretical Gaussian) to keep a minimum of trust towards the initial measurements. After correction, distances are computed accordingly and a 6% fractional error on distances is assumed in agreement with the upper limit of the fractional error medians measured for the corrected mocks. As this method reduces the error on distances,

we can expect that it also minimizes other Malmquist Biases to some extent especially since biases are all related to distance errors (Landy and Szalay, 1992; Sandage, 1994).

The whole process has then been applied to the second catalog of the Cosmicflows project from the minimization of the asymmetry bias up to RZA augmented, both devised in this work. Then the resulting dataset was input in the Constrained Realization of Gaussian fields algorithm to produce constrained simulations of the Local Universe. The second generation of constrained simulations of the Local Universe performed in this work, *solely from observational peculiar velocities*, has finally been presented and shown to reproduce the Large Scale Structure of the Local Universe. The majority of the superclusters of the Local Universe within $200 \text{ h}^{-1} \text{ Mpc}$ are recovered so are the filaments interconnecting them, even across the Zone Of Avoidance. Major voids are also simulated. Looking for specific clusters like the Abell clusters a handful of them are found with appropriate masses. Regardless, these halo-replicas are found at locations approaching by a few megaparsecs, typically $3\text{-}4 \text{ h}^{-1} \text{ Mpc}$, the observational positions of Abell clusters.

5.1.3 Conclusion

Galaxies are sources of observations. Still, they are only tips of the iceberg of a larger scheme which involves a mysterious dark component: the dark matter and energy. The standard cosmological model is currently accepted as an elegant theory in which are included these two necessary exotic dark components. Subsequently, although it can be far from the truth, this cosmological model enables to simulate the formation and evolution of the Universe in a remarkable agreement with observations. From initial perturbations to growth of structures, the Universe seems to be understood to a great extent. Comparisons and synergies between observations from the Cosmicflows project and constrained simulations from the CLUES project presented in this work confirm the largely accepted scheme at least on large scales. The only missing component to perfect comparisons between observations and simulations are baryons. They still need to be analyzed and studied in thorough details in simulations to reconcile entirely observations with theories. Yet, before taking this step, 1) observational catalogs are improvable especially in terms of coverage, *cosmicflows-3* is an example, and potentially reduction of uncertainties and biases, 2) resulting dark matter constrained simulations have yet to be studied more thoroughly to deliver some aspects of the Local History before adding any gas material. The constant back-and-forth between observations and simulations provides us with a way to refine our numerical methods but also to better exploit our observational data (e.g. removing biases, Lavaux et al., 2008, and section 4.4.3).

5.2 Prospectives

The main goal of the combined "CosmicCLUES"¹ project is to study the Local Universe formation and evolution to better understand the cosmology of our Universe and as a result the nature of dark matter. To this end, carrying on developing the synergy between the theoretical, observational and numerical fields of research is essential. The direct comparisons between the observed and the simulated universes will enable to confirm, to refine and to develop the current theoretical understanding of structure formation.

5.2.1 Observations

In the observational field, there are two main points which might be worth looking into:

- first and foremost, there is the increase in size of the future catalogs both in coverage and in density (spatial extent and number of measurements),
- second, the improvement in distance estimate accuracies.

Actually, the collaboration has already begun to work on both points. The first point has begun with the collection of data to build cosmicflows-3. Spitzer has already supplied part of it and, for instance, WISE (Wright, 2008) will provide the rest of it. The calibration of the Tully-Fisher relation for WISE bands is already in progress (Neil et al. in prep). Gathering even more data from archives regarding HI profiles and re-measurements in a consistent way are also ongoing (Courtois et al. in prep). Photometric data will then be collected from other all-sky surveys like PanStarrs (Kaiser et al., 2002). *Cosmicflows-4* can be envisaged with 100,000 observations, up to 500 h⁻¹ Mpc, from the Australian Square Kilometre Array Pathfinder and Apertif (Johnston and Deboer, 2008; Verheijen et al., 2008). Regarding the second point, the collaboration has taken three paths, 1) one which tries to improve grouping of galaxies (Tully et al. private communication). As a reminder, grouping improves group distance estimate accuracies as the square root of the number of grouped galaxies, 2) one which aims at reducing the uncertainty on galaxy inclinations with the soon to be launched Citizen Science project (alternatively, a recent paper by Obreschkow and Meyer (2013) proposes a method to derive the Tully-Fisher relation without galaxy inclinations. This process can indirectly be used to constrain inclinations of galaxies with unknown inclinations, this matter could be look into more thoroughly) and 3) the last one which concentrates on reducing the scatter in the Tully-Fisher relation (Zaritsky et al., 2014) using the Baryonic Tully-Fisher relation. That is now deemed appropriate to explain in more detail this Baryonic Tully-Fisher relation (BTFR) and the results found. This

¹Note that this name is not official and is just given here for conveniency.

relation relies on the observations that the scatter in the TFRs varies with the use of another parameter (color, half light radius, concentration index, size, morphology, see e.g. [Pizagno et al., 2007](#)) which probably means that the ratio of dark-luminous matter varies within the disk populations. Perhaps so, but what about the relation baryonic-dark mass? As the baryonic mass is the sum of the stellar and gas mass (formula 5.4), a tighter correlation between the baryonic mass and the rotation rate of galaxies would imply that the classic TF is valid because luminosity approximates quite well the stellar mass and the gas mass is negligible in most galaxies. Deviant galaxies from the classic TF are indeed gas dominated galaxies and special galaxies in the sense that they are not classic disk dominated spirals. The BTFR is able to reconcile disagreements which can be found between such different systems, namely they do lie on the same BTFR but have their own classic TFR (e.g for massive disk galaxies and for Hickson compact group galaxies, [Noordermeer and Verheijen, 2007](#); [Torres-Flores et al., 2013](#)). The Faber-Jackson relation (FJR) has also its equivalent the BFJR ([Catinella et al., 2012](#)).

$$M_{gas} = \underbrace{1.4}_{\text{accounts for } H_e \text{ \& metals}} \times \underbrace{[(3.7 - 0.8T + 0.043T^2) + 1]}_{\text{corrects for } M_{H_2}} \times \underbrace{(2.36 \times 100000 \times D_L^2 \times F_{HI})}_{\text{gives } M_{HI}}$$
(5.4)

$$M_* = 10^{5.65} F_{[3.6]}^{2.85} F_{[4.5]}^{-1.85} \left(\frac{D_L}{0.05}\right)^2 M_\odot$$

$$M_{baryonic} = M_* + M_{gas}$$

from [McGaugh and de Blok \(1997\)](#); [Zaritsky et al. \(2014\)](#) with T the numerical morphological type, between approximately 0 and 10 for late type galaxies, and from [Eskew et al. \(2012\)](#). M_{gas} is in units of $10^5 M_\odot$, F_X are fluxes (integrated within the HI profile in units of Jy km s^{-1} or in [3.6] and [4.5] Spitzer bands in Jy) and D_L the luminosity distance. [Zaritsky et al. \(2014\)](#) noted that the baryonic content of the galaxy considered, $M_{baryonic}$ as above defined, accounts only for the condensed fraction of baryons onto the central region of spiral galaxies (both extremely cold and hot material and far from the center baryons are not considered). A fraction found to be a constant 40% ([Zaritsky et al., 2014](#)).

In any case, the BTFR relation is found to have a reduced scatter with respect to the classic TF in various bands (e.g. [Zaritsky et al., 2014](#), at $3.6 \mu\text{m}$). However, stellar masses are still to be better determined. For instance, some tensions between BTFR slopes found by [McGaugh \(2012\)](#) and [Zaritsky et al. \(2014\)](#) might be due partially to stellar normalizations. As a matter of fact, gas-dominated galaxies and stellar-dominated galaxies if fitted separately share the same BTFR slope but when fitted together result in a higher BTFR slope. The

slope can be driven up more or less depending on the different stellar-normalizations affecting the stellar-dominated galaxy zeropoint. A reconciliation is absolutely necessary because the slope value influence the derived distance estimates. On another matter, a higher slope (≈ 4) privileges the MODified Newtonian Dynamics model (Milgrom, 1983a,b,c) over the standard Λ CDM model.

Although the BTFR has a quite reduced scatter with respect to the classic TFR in the dwarfs regime, it is not null or small enough to be yet accounted for by the sole observational errors. Among the possible effects, we note the concentration of dark matter that may vary differently from the center to the edge (Dutton, 2012) or some interaction between baryonic and dark matter that may come into play (Desmond, 2012). These are even more reasons to test the relations with simulations, to compare simulated and observed galaxies to better understand galaxy formation.

5.2.2 Simulations

Large scales are well reproduced by dark matter only simulations but on small scales because of the complexity of star and galaxy formation, the baryonic physics cannot be neglected. Accordingly, for the CLUES project, the next step after reproducing the local Large Scale Structure is to dig into the matter of galaxy formation and evolution in the Local Universe. However, running a full hydrodynamical simulation including star formation within the Large Scale volume with the necessary resolution is currently unconceivable. Then, the CLUES project can follow different paths:

- running gasdynamical simulations in a smaller volume with higher resolution. Such simulations can be envisaged within the framework of zoomed simulations. To this end, the method presented and refined in this work to build constrained initial conditions could be used to produce constrained density fields. These density fields could then be converted into white noise fields which would ultimately be input in GINNUNGAGAP to produce multi-scale initial conditions or, alternatively, into the publicly available MUSIC (Multi-Scale initial conditions) code developed by Hahn and Abel (2011) which, to date, has been more tested. These codes both use the popular "zoom-in" technique (see Bertschinger, 2001, for the precursor of the technique) which consists in increasing the resolution in region of interests (clusters of galaxies, specific objects) selected in the simulation at $z = 0$. To this end, the corresponding peak patch in the initial white noise field from which the region of interest is going to emerge has to be identified. Then, the resolution is increased in the white noise field in this particular patch while the large scale is left at low resolution. Large scale modes have to be kept to preserve their tidal influences on the particular region of interests. Assuming that the baryon

distribution at the initial redshift follows that of dark matter, a Boltzmann solver (e.g. [Birrell and Rafelski, 2014](#)) allows then to compute velocity and density fields. Resulting multi-scale hydrodynamical initial conditions could then be input in GADGET,

- running high resolution dark matter only simulations of the full box so that halos of $10^9 h^{-1} M_{\odot}$ could be resolved. At this point, parameters of the simulations could be tuned by first testing intermediate resolutions (for instance a simulation box of approximately $320 h^{-1} \text{Mpc}$ side length with 2048^3 particles, in a Planck cosmology, results in a particle mass around $3.3 \times 10^8 h^{-1} M_{\odot}$. Thus, dark matter halos of $10^{10} h^{-1} M_{\odot}$ are resolved with 30 particles). Regardless, the same pre-required white noise as before could be input in GINNUNGAGAP to increase the resolution but homogeneously (not locally anymore). Objects in these resulting simulations could then be identified with a spherical overdensity halo finder (Amiga Halo finder, [Knollmann and Knebe, 2009](#)) as well as friends-of-friends algorithms. Outputs from these algorithms would enable to populate these simulations with galaxies using the abundance matching techniques which consist in attributing observed galaxies to simulated dark matter halos. The more massive the host halo, the more massive the galaxy is assumed to be. Then, a stellar-to-halo mass relation could be derived from this observation/simulation combination (e.g. [Behroozi et al., 2010](#); [Moster et al., 2010](#)). However, the derived stellar-to-halo mass relation depends widely on the observational limits of the galaxy survey used to pair dark matter halos with galaxies (e.g. [Garrison-Kimmel et al., 2013](#)). In addition, even if these different stellar-to-halo mass relations could be reconciled and could be extended at low mass ends, they might depend on the environment. Therefore, the development of a stellar-to-halo mass relation in each one of the specific region of the Local Universe to study would have to be privileged to, eventually, conclude on the (non)-universality of such a relation. For example, within the CLUES project, the stellar-to-halo mass relation was derived for Local Group galaxies ([Brook et al., 2013](#)). Thus, it could be first checked that the same relation for Local Group-like galaxies is found. Since running, a full gasdynamical simulation with the same resolution and the same boxsize is currently impossible, thorough comparisons with the full box would not be possible but chosen specific regions could be compared. For instance, the stellar-to-mass halo relation could be derived for the Local Group-like galaxies in the gas simulation in order to be compared with the result obtained in the dark matter simulations combined with the abundance matching technique,
- running a series of lower resolution simulations (for instance 1024^3 particles with the same typical boxsize as used for the high resolution simulation, results in a mass particle about $2 \cdot 10^9 h^{-1} M_{\odot}$). These dark matter only constrained simulations could then be used to study the cosmic variance in terms of scatter in positions of structures and in merging histories of the replicas of local clusters. The merging history with the higher

statistical probability could give clues as to where to look for radio relics produced during merger events or, at least, provide an estimate of the number of radio relics which could be observed by future surveys obtained with LOw-Frequency ARray and Westerbork Synthesis Radio telescopes (Nuza et al., 2012). Studying the mass accretion history (defined by formation, assembly and last major merging times) of several nearby groups-like, mass accretion history which has been find to be quiet in the Local Group case (Forero-Romero et al., 2011), might solve the question of how large and mid scale environments around groups induce different mass accretion history. Currently, it is clear that low density environment and isolation criteria are both not adapted to end up, after selection, with only quiet mass accretion history groups-like (Forero-Romero et al., 2011). This work would answer the question "how unique is the Local Group in a given cosmological context?" to better distinguish between models. For instance, Libeskind et al. (2013) has shown that within Warm Dark Matter, the Local Group is more likely to be more diffuse than observed today than within cold dark matter. This leads to an increased trust towards the cold nature of the dark matter although it is not impossible to find the proper Local Group in a warm context, excluding the eviction of the Warm Dark Matter from theories.

In parallel, the theoretical approach might also be improved. For instance, the first order linear approximation used to compute the cosmic displacement field in the RZA could be refined up to the second order using the second order Lagrangian Perturbation Theory (e.g. Kitaura, 2013; Kitaura et al., 2012) or even the Augmented Lagrangian Perturbation Theory proposed by Kitaura and Heß (2013). This method builds on the difference between the long and short range components of the displacement. Namely, at small scales the second order fails because of shell crossing, it is then replaced by a spherical collapse model. Finally, a comparison between simulations constrained with different types of constraints, peculiar velocities and distribution of galaxies (Heß et al., 2013) could also give the advantages and the limitations of each method. Regardless, the variety of simulations expounded above would need to be performed in between.

We conclude this manuscript with an overview, Figure 5.1, of this work, realized within the context of the global "CosmicCLUES" project scheme, and we extend it to the future work which can be envisaged.

Figure 5.1 ⇒

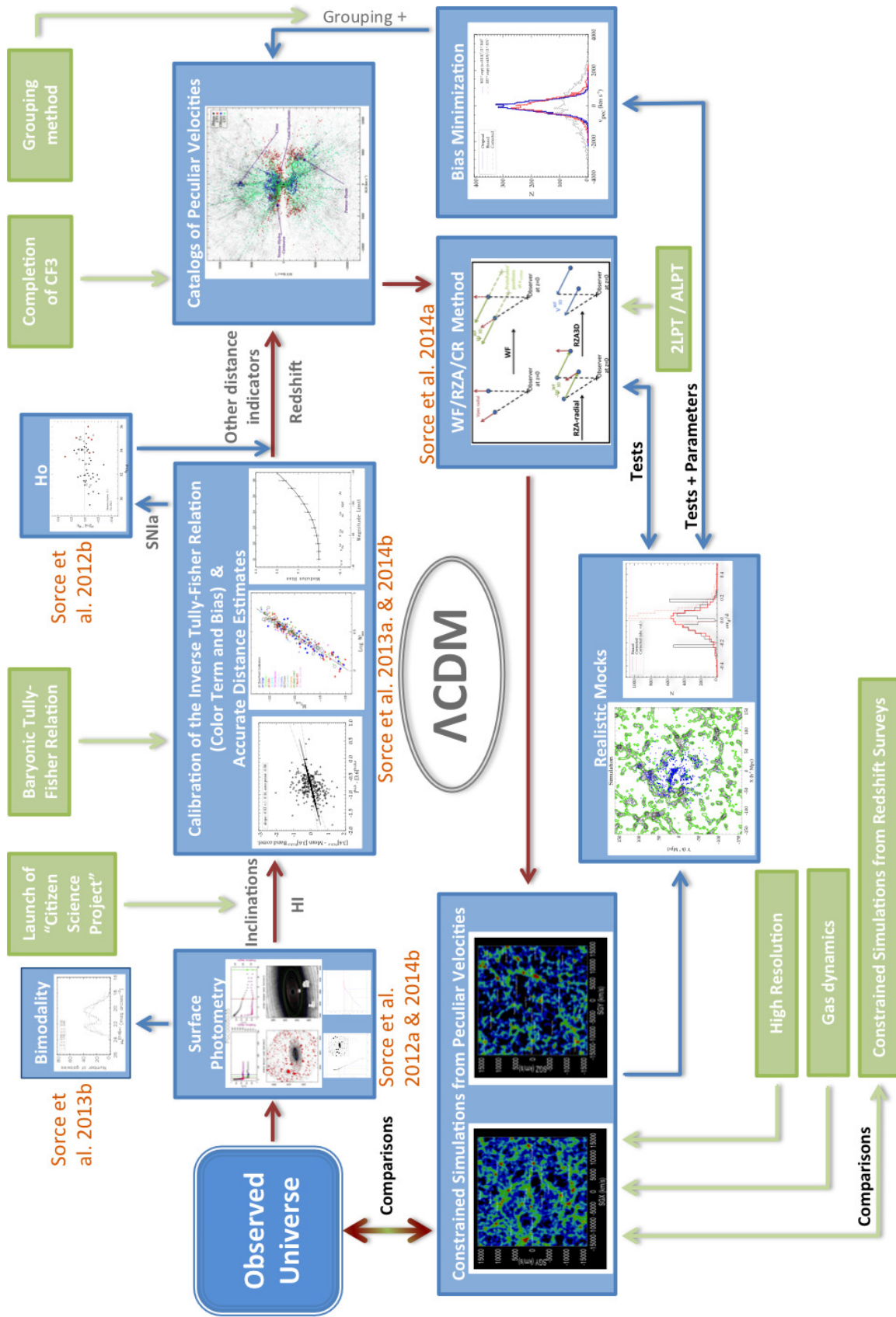


FIGURE 5.1: Outlines of current and envisaged additional future work are presented. The blue color shows this work (outputs from outside are in grey) from the observations to the constrained simulations through, the calibration of the Tully-Fisher relation and the refinement of the process to build constrained initial conditions (red path) with, parallel work to estimate the Hubble constant, to confirm bimodality in disk central surface brightnesses of galaxies, to build realistic mock to tests methods and to devise a correction to minimize the bias(es) (blue path). This work results from, and, enables a synergy between, simulated and observed universes. Namely, the back-and-forth between observations and simulations provides a way to refine the methods but also to better exploit the observational data to, finally, study the Local Universe, the formation and evolution of structures. In green are the envisaged extensions to this work which will enable a thorough study of the Local Universe thanks to detailed comparisons between observed and simulated universes to better understand the nature of dark matter via its influence on structure formation and galaxy evolution. The proposed future work goes from the baryonic Tully-Fisher relation - to obtain even more accurate distance estimates - up to the addition of gas in simulations through, the launch of the Citizen Science project - to obtain better inclination estimates - the refinement of the grouping technique, the production of higher resolution constrained simulations, a higher order development in the computation of the cosmic displacement field and the completion of the cosmicflows-3 catalog in addition to, comparisons with simulations constrained with redshift surveys. Basically, the prospective work proposes to augment the quality of the now fully functional red path.

Appendix A

Extragalactic Distance Database: Spitzer [3.6] Band Photometry

| 1 | 2 | 3 | 4 | 5 | 6 | 7 | 8 | 9 | 10 | 11 | 12 | 13 | 14 | 15 | 16 | 17 | 18 | 19 | 20 | 21 | |
|------|------------|-----------------------|----------------------|------------|----------------------|---------|----------|------|----------------|-----|----------|------------|-------|---------|-------------------------|----------|------------|----------------------------|----------|-------|--|
| PGC | $a_{26.5}$ | [3.6] _{26.5} | [3.6] _{tot} | σ_m | [3.6] _{ext} | μ_0 | α | b/a | $\sigma_{b/a}$ | PA | a_{80} | μ_{80} | a_e | μ_e | $\langle \mu_e \rangle$ | a_{20} | μ_{20} | $\langle \mu_{20} \rangle$ | C_{82} | Prog. | |
| 94 | 49 | 15.93 | 15.932 | 0.004 | 15.913 | 19.73 | 7.9 | 0.20 | 0.00 | 53 | 30 | 23.70 | 17 | 22.39 | 22.37 | 8 | 22.15 | 21.79 | 3.9 | CFS | |
| 143 | 405 | 11.72 | 11.467 | 0.001 | 11.437 | 23.45 | 144.4 | 0.44 | 0.00 | 3 | 430 | 27.87 | 230 | 25.09 | 24.38 | 107 | 24.12 | 23.91 | 4.0 | CHP | |
| 527 | 48 | 16.11 | 16.001 | 0.002 | 15.962 | 22.59 | 13.2 | 0.29 | 0.00 | 33 | 34 | 25.46 | 17 | 24.01 | 22.87 | 8 | 22.41 | 22.09 | 4.4 | CFS | |
| 698 | 124 | 11.24 | 11.209 | 0.003 | 11.201 | 20.71 | 23.2 | 0.63 | 0.00 | 171 | 30 | 21.67 | 11 | 19.45 | 17.90 | 4 | 16.77 | 16.36 | 8.4 | CHP | |
| 701 | 223 | 11.38 | 11.329 | 0.075 | 11.360 | 19.74 | 35.9 | 0.26 | 0.00 | 44 | 113 | 23.14 | 58 | 21.45 | 20.70 | 29 | 20.43 | 20.15 | 3.8 | SINGS | |
| 767 | 68 | 12.78 | 12.769 | 0.024 | 12.776 | 18.96 | 9.9 | 0.51 | 0.06 | 149 | 29 | 21.92 | 14 | 20.60 | 19.93 | 6 | 19.67 | 19.00 | 5.1 | CFS | |
| 963 | 77 | 13.47 | 13.453 | 0.007 | 13.438 | 20.66 | 14.2 | 0.44 | 0.02 | 80 | 33 | 23.51 | 16 | 21.36 | 20.54 | 7 | 20.27 | 19.83 | 4.9 | CFS | |
| 1315 | 50 | 13.09 | 13.082 | 0.003 | 13.088 | 18.68 | 7.0 | 0.69 | 0.05 | 154 | 23 | 22.25 | 15 | 20.96 | 20.37 | 7 | 20.34 | 20.00 | 3.5 | CFS | |
| 1592 | 121 | 11.78 | 11.771 | 2.410 | 11.778 | 18.64 | 16.8 | 0.21 | 0.01 | 3 | 62 | 22.80 | 22 | 19.78 | 18.82 | 9 | 18.38 | 18.04 | 6.9 | CFS | |
| 1658 | 105 | 12.71 | 12.713 | 0.009 | 12.705 | 18.15 | 13.7 | 0.13 | 0.03 | 170 | 35 | 21.25 | 13 | 18.99 | 18.62 | 5 | 18.48 | 18.06 | 6.5 | CFS | |
| 1713 | 57 | 14.68 | 14.667 | 0.003 | 14.650 | 20.61 | 10.4 | 0.36 | 0.00 | 126 | 35 | 23.93 | 21 | 22.74 | 22.14 | 10 | 21.99 | 21.49 | 3.6 | CHP | |
| 2098 | 40 | 15.97 | 15.928 | 0.002 | 15.962 | 19.36 | 6.1 | 0.23 | 0.00 | 84 | 23 | 23.21 | 14 | 22.39 | 22.06 | 8 | 21.87 | 21.68 | 2.9 | CFS | |
| 2578 | 77 | 14.73 | 14.650 | 0.001 | 14.655 | 21.77 | 17.7 | 0.41 | 0.00 | 1 | 64 | 25.59 | 42 | 24.31 | 23.77 | 30 | 23.65 | 23.36 | 2.2 | LVL | |
| 2747 | 102 | 13.18 | 13.200 | 0.002 | 13.177 | 17.98 | 13.0 | 0.11 | 0.00 | 178 | 46 | 21.69 | 28 | 20.42 | 19.98 | 15 | 19.75 | 19.66 | 3.0 | CFS | |
| 2781 | 47 | 13.09 | 13.091 | 0.002 | 13.086 | 18.91 | 6.7 | 0.65 | 0.09 | 8 | 20 | 22.14 | 13 | 20.96 | 19.96 | 5 | 19.32 | 18.84 | 3.9 | CFS | |
| 2865 | 190 | 13.07 | 12.844 | 0.237 | 13.056 | 19.68 | 30.2 | 0.14 | 0.03 | 108 | 115 | 23.95 | 24 | 20.37 | 20.10 | 8 | 20.08 | 19.15 | 14.4 | CFS | |
| 2899 | 45 | 15.20 | 15.169 | 0.003 | 15.167 | 20.78 | 8.5 | 0.43 | 0.01 | 41 | 28 | 24.17 | 16 | 22.89 | 22.24 | 6 | 22.17 | 21.70 | 4.3 | CFS | |
| 2928 | 50 | 14.76 | 14.730 | 0.003 | 14.738 | 20.37 | 8.9 | 0.38 | 0.00 | 104 | 25 | 23.38 | 14 | 22.04 | 21.44 | 6 | 21.26 | 20.88 | 4.3 | CFS | |
| 2964 | 41 | 14.83 | 14.826 | 0.010 | 14.817 | 19.39 | 6.2 | 0.27 | 0.01 | 139 | 18 | 22.43 | 10 | 21.28 | 20.54 | 4 | 20.22 | 19.91 | 4.6 | CFS | |
| 2992 | 29 | 15.52 | 15.500 | 0.020 | 15.468 | 21.16 | 6.0 | 0.81 | 0.04 | 49 | 18 | 24.41 | 9 | 22.91 | 22.21 | 5 | 22.15 | 21.65 | 3.3 | LVL | |
| ... | | | | | | | | | | | | | | | | | | | | | |

TABLE A.1: Extracted photometry parameters. (1) Principal Galaxies Catalog number, (2) $a_{26.5}$: major axis radius at isophote 26.5 mag arcsec⁻², (3) [3.6]_{26.5}: AB magnitude within $a_{26.5}$, (4) [3.6]_{tot}: total AB magnitude from rational function asymptote, (5) σ_m : rms deviations, rational function fit, (6) [3.6]_{ext}: total AB magnitude by extrapolating flux beyond $a_{26.5}$ assuming continuance of exponential disk, (7) μ_0 : central disk surface brightness from inward extrapolation of disk fit, mag arcsec⁻², (8) α : exponential disk scale length, arcsec, (9) b/a: ratio of minor to major axes, (10) $\sigma_{b/a}$: uncertainty in axial ratio, (11) PA: position angle of major axis, deg. (12) a_{80} : major axis radius of annulus enclosing 80% of total light, arcsec, (13) μ_{80} : surface brightness at a_{80} , mag arcsec⁻², (14) a_e : 'effective radius', major axis radius of annulus enclosing 50% of total light, arcsec, (15) μ_e : surface brightness at a_e , mag arcsec⁻², (16) $\langle \mu_e \rangle$: average surface brightness within a_e , mag arcsec⁻², (17) a_{20} : major axis radius of annulus enclosing 20% of total light, arcsec, (18) μ_{20} : surface brightness at a_{20} , mag arcsec⁻², (19) $\langle \mu_{20} \rangle$: average surface brightness within a_{20} , mag arcsec⁻², (20) C_{82} : concentration index, a_{80}/a_{20} , (21) Spitzer program.

Appendix B

Calibrator Parameters

Table B.1

| PGC | Name | $[3.6]_{ext}^{b,i,k,a}$ | $[3.6]_{CHP}^{b,i,k,a}$ | $[3.6]_{ave}^{b,i,k,a}$ | Diff | b/a | Inc | W_{mx} | W_{mx}^i | W_{mxt}^i | S |
|-------|---------|-------------------------|-------------------------|-------------------------|--------|------|-----|----------|------------|-------------|----|
| 9332 | NGC0925 | 10.866 | 10.231 | 10.549 | -1.589 | 0.57 | 57. | 194 | 231. | 2.364 | ZP |
| 13179 | NGC1365 | 8.818 | 8.812 | 8.815 | -0.725 | 0.61 | 54. | 371 | 459. | 2.662 | ZP |
| 13602 | NGC1425 | 10.693 | 10.700 | 10.697 | -1.197 | 0.46 | 65. | 354 | 391. | 2.592 | ZP |
| 17819 | NGC2090 | 10.477 | 10.287 | 10.382 | -1.052 | 0.43 | 67. | 277 | 301. | 2.478 | ZP |
| 21396 | NGC2403 | 8.558 | 8.370 | 8.464 | -1.354 | 0.53 | 60. | 226 | 261. | 2.417 | ZP |
| 23110 | NGC2541 | / | 11.949 | 11.949 | -1.189 | 0.49 | 63. | 188 | 211. | 2.325 | ZP |
| 26512 | NGC2841 | 8.644 | 8.644 | 8.644 | -1.114 | 0.45 | 66. | 592 | 650. | 2.813 | ZP |
| 28120 | NGC2976 | 9.904 | / | 9.904 | -0.924 | 0.53 | 60. | 129 | 149. | 2.173 | ZP |
| 28357 | NGC3021 | 11.693 | / | 11.693 | -0.773 | 0.57 | 57. | 254 | 303. | 2.481 | ZP |
| 30197 | NGC3198 | 10.368 | 10.326 | 10.347 | -1.177 | 0.39 | 70. | 296 | 315. | 2.498 | ZP |
| 30819 | IC2574 | 11.750 | / | 11.750 | -1.630 | 0.40 | 69. | 106 | 113. | 2.054 | ZP |
| 32007 | NGC3351 | 9.208 | 9.210 | 9.209 | -0.879 | 0.70 | 47. | 262 | 359. | 2.556 | ZP |
| 32207 | NGC3370 | 11.739 | / | 11.739 | -0.889 | 0.56 | 58. | 264 | 312. | 2.494 | ZP |
| 34554 | NGC3621 | 8.989 | 9.035 | 9.012 | -1.002 | 0.45 | 66. | 266 | 292. | 2.465 | ZP |
| 34695 | NGC3627 | 8.314 | 8.254 | 8.284 | -0.894 | 0.53 | 60. | 333 | 385. | 2.585 | ZP |
| 39422 | NGC4244 | 10.333 | / | 10.333 | -1.413 | 0.20 | 90. | 192 | 192. | 2.283 | ZP |
| 40692 | NGC4414 | 9.368 | 9.367 | 9.368 | -0.638 | 0.60 | 55. | 378 | 463. | 2.666 | ZP |
| 41812 | NGC4535 | 9.783 | 9.751 | 9.767 | -0.817 | 0.72 | 45. | 265 | 374. | 2.573 | ZP |
| 41823 | NGC4536 | 9.840 | 9.856 | 9.848 | -0.818 | 0.38 | 71. | 322 | 341. | 2.533 | ZP |
| 42408 | NGC4605 | 10.161 | / | 10.161 | -0.971 | 0.41 | 69. | 154 | 165. | 2.219 | ZP |
| 42510 | NGC4603 | 10.682 | 10.663 | 10.673 | -0.913 | 0.64 | 52. | 353 | 450. | 2.653 | ZP |
| 42741 | NGC4639 | 11.250 | 11.255 | 11.253 | -1.073 | 0.60 | 55. | 274 | 336. | 2.526 | ZP |
| 43451 | NGC4725 | 8.922 | 8.893 | 8.908 | -1.068 | 0.56 | 58. | 397 | 470. | 2.672 | ZP |
| 51344 | NGC5584 | 11.763 | 11.819 | 11.791 | -1.171 | 0.73 | 44. | 186 | 267. | 2.426 | ZP |
| 69327 | NGC7331 | 8.409 | 8.377 | 8.393 | -0.873 | 0.44 | 66. | 501 | 547. | 2.738 | ZP |
| 73049 | NGC7793 | 9.298 | / | 9.298 | -1.048 | 0.62 | 53. | 162 | 202. | 2.306 | ZP |
| 40095 | NGC4312 | 11.307 | / | 11.307 | -1.087 | 0.27 | 79. | 217 | 221. | 2.344 | V |
| 40105 | NGC4313 | 11.029 | / | 11.029 | -1.079 | 0.22 | 85. | 257 | 258. | 2.412 | V |
| 40201 | NGC4330 | 11.956 | / | 11.956 | -1.156 | 0.17 | 90. | 251 | 251. | 2.400 | V |
| 40507 | NGC4380 | 11.084 | / | 11.084 | -1.274 | 0.52 | 61. | 265 | 304. | 2.483 | V |
| 40516 | NGC4383 | 11.628 | / | 11.628 | -0.768 | 0.58 | 56. | 199 | 239. | 2.379 | V |
| 40581 | NGC4388 | 10.294 | / | 10.294 | -0.984 | 0.26 | 80. | 364 | 369. | 2.567 | V |
| 40622 | NGC4396 | 12.381 | / | 12.381 | 0.279 | 0.35 | 73. | 181 | 189. | 2.277 | V |
| 40644 | NGC4402 | 10.816 | 10.772 | 10.794 | -0.634 | 0.34 | 74. | 267 | 278. | 2.444 | V |
| 40644 | NGC4402 | 10.816 | 10.772 | 10.794 | -0.634 | 0.34 | 74. | 267 | 278. | 2.444 | V |

| PGC | Name | $[3.6]_{ext}^{b,i,k,a}$ | $[3.6]_{CHP}^{b,i,k,a}$ | $[3.6]_{ave}^{b,i,k,a}$ | Diff | b/a | Inc | W_{mx} | W_{mx}^i | W_{mxl}^i | S |
|-------|------------|-------------------------|-------------------------|-------------------------|--------|------|-----|----------|------------|-------------|---|
| 41024 | NGC4450 | 9.648 | / | 9.648 | -1.028 | 0.67 | 49. | 304 | 401. | 2.603 | V |
| 41061 | IC3392 | 11.789 | / | 11.789 | -0.889 | 0.42 | 68. | 178 | 192. | 2.284 | V |
| 41472 | NGC4498 | 12.193 | / | 12.193 | -1.203 | 0.48 | 64. | 182 | 203. | 2.308 | V |
| 41504 | IC0797 | 13.010 | / | 13.010 | -1.010 | 0.69 | 48. | 118 | 160. | 2.203 | V |
| 41517 | NGC4501 | 8.827 | / | 8.827 | -0.967 | 0.48 | 64. | 507 | 566. | 2.753 | V |
| 41608 | IC3476 | 12.901 | / | 12.901 | -0.951 | 0.64 | 52. | 126 | 161. | 2.206 | V |
| 41729 | NGC4522 | 12.022 | / | 12.022 | -1.082 | 0.25 | 81. | 209 | 211. | 2.325 | V |
| 41812 | NGC4535 | 9.785 | 9.753 | 9.769 | -0.819 | 0.72 | 45. | 265 | 374. | 2.573 | V |
| 41823 | NGC4536 | 9.828 | 9.844 | 9.836 | -0.806 | 0.38 | 71. | 322 | 341. | 2.533 | V |
| 42081 | IC3583 | 13.311 | / | 13.311 | -1.341 | 0.42 | 68. | 100 | 108. | 2.033 | V |
| 42396 | NGC4595 | 12.495 | / | 12.495 | -1.095 | 0.70 | 47. | 131 | 180. | 2.255 | V |
| 42544 | NGC4607 | 11.929 | / | 11.929 | -0.499 | 0.20 | 90. | 170 | 170. | 2.230 | V |
| 42741 | NGC4639 | 11.243 | 11.247 | 11.245 | -1.095 | 0.55 | 58. | 274 | 321. | 2.507 | V |
| 42857 | NGC4654 | 10.103 | 10.097 | 10.100 | -0.850 | 0.56 | 58. | 282 | 334. | 2.523 | V |
| 43001 | IC3742 | 13.985 | / | 13.985 | -1.395 | 0.40 | 69. | 161 | 172. | 2.236 | V |
| 43254 | NGC4698 | 10.069 | / | 10.069 | -1.159 | 0.44 | 66. | 419 | 457. | 2.660 | V |
| 11856 | ESO357-007 | 14.728 | 14.580 | 14.654 | -1.494 | 0.24 | 82. | 125 | 126. | 2.101 | F |
| 12181 | ESO357-012 | 13.471 | 13.519 | 13.495 | -0.975 | 0.66 | 50. | 123 | 160. | 2.205 | F |
| 12404 | IC1913 | 14.106 | 14.115 | 14.111 | -1.211 | 0.22 | 85. | 157 | 158. | 2.198 | F |
| 12952 | NGC1351A | 12.808 | 12.839 | 12.823 | -0.933 | 0.21 | 86. | 200 | 200. | 2.302 | F |
| 13059 | NGC1350 | 9.804 | 9.797 | 9.801 | -1.081 | 0.47 | 64. | 390 | 433. | 2.636 | F |
| 13089 | ESO418-008 | 13.770 | 13.796 | 13.783 | -1.093 | 0.70 | 47. | 121 | 166. | 2.220 | F |
| 13179 | NGC1365 | 8.814 | 8.808 | 8.811 | -0.721 | 0.61 | 54. | 371 | 459. | 2.662 | F |
| 13458 | NGC1406 | 10.774 | 10.753 | 10.763 | -0.723 | 0.22 | 85. | 322 | 323. | 2.510 | F |
| 13571 | ESO358-051 | 13.522 | 13.555 | 13.539 | -1.079 | 0.50 | 62. | 118 | 134. | 2.125 | F |
| 13602 | NGC1425 | 10.686 | 10.693 | 10.690 | -1.190 | 0.46 | 65. | 354 | 391. | 2.592 | F |
| 13687 | NGC1436 | 11.301 | 11.382 | 11.341 | -0.911 | 0.63 | 52. | 201 | 254. | 2.404 | F |
| 13809 | ESO358-063 | 11.245 | 11.198 | 11.222 | -1.032 | 0.24 | 82. | 285 | 288. | 2.459 | F |
| 13854 | ESO302-009 | / | 14.513 | 14.513 | -1.533 | 0.21 | 86. | 142 | 142. | 2.153 | F |
| 13998 | ESO359-003 | 13.901 | 13.861 | 13.881 | -1.261 | 0.42 | 68. | 112 | 121. | 2.082 | F |
| 14071 | NGC1484 | / | 13.172 | 13.172 | -1.222 | 0.24 | 82. | 162 | 164. | 2.214 | F |
| 34971 | UGC06399 | 14.126 | / | 14.126 | -1.546 | 0.28 | 78. | 167 | 170. | 2.232 | U |
| 35202 | UGC06446 | 14.406 | 14.047 | 14.227 | -1.867 | 0.63 | 52. | 125 | 158. | 2.198 | U |
| 35676 | NGC3726 | 10.318 | 10.259 | 10.288 | -1.038 | 0.58 | 56. | 263 | 316. | 2.500 | U |
| 36343 | UGC06667 | 13.553 | 13.563 | 13.558 | -1.468 | 0.14 | 90. | 173 | 173. | 2.238 | U |
| 36699 | NGC3877 | 10.187 | 10.172 | 10.180 | -0.980 | 0.24 | 82. | 347 | 350. | 2.544 | U |
| 36825 | UGC06773 | 14.704 | / | 14.704 | -1.784 | 0.44 | 66. | 89 | 97. | 1.987 | U |
| 36875 | NGC3893 | 10.348 | 10.281 | 10.314 | -0.834 | 0.66 | 50. | 283 | 369. | 2.567 | U |
| 37036 | NGC3917 | 11.477 | 11.461 | 11.469 | -1.219 | 0.24 | 82. | 273 | 276. | 2.440 | U |
| 37038 | UGC06818 | 14.340 | / | 14.340 | -1.400 | 0.35 | 73. | 141 | 147. | 2.169 | U |
| 37290 | NGC3949 | 10.921 | 10.949 | 10.935 | -0.965 | 0.63 | 52. | 252 | 318. | 2.502 | U |
| 37306 | NGC3953 | 9.531 | 9.531 | 9.531 | -0.931 | 0.50 | 62. | 404 | 457. | 2.660 | U |
| 37418 | UGC06894 | 14.934 | / | 14.934 | -1.144 | 0.16 | 90. | 121 | 121. | 2.083 | U |
| 37466 | NGC3972 | 11.940 | 11.961 | 11.950 | -1.050 | 0.29 | 78. | 258 | 264. | 2.422 | U |
| 37525 | UGC06917 | 12.959 | 12.781 | 12.870 | -1.450 | 0.59 | 55. | 178 | 216. | 2.334 | U |
| 37542 | NGC3985 | 12.604 | / | 12.604 | -0.994 | 0.62 | 53. | 150 | 187. | 2.273 | U |
| 37553 | UGC06923 | 13.650 | 13.665 | 13.657 | -1.397 | 0.42 | 68. | 139 | 150. | 2.176 | U |
| 37617 | NGC3992 | 9.749 | 9.555 | 9.652 | -1.152 | 0.55 | 58. | 459 | 538. | 2.731 | U |
| 37691 | NGC4013 | 10.017 | 9.993 | 10.005 | -0.695 | 0.22 | 85. | 388 | 390. | 2.591 | U |
| 37697 | NGC4010 | / | 11.781 | 11.781 | -0.891 | 0.17 | 90. | 248 | 248. | 2.394 | U |
| 37700 | UGC06969 | 15.150 | / | 15.150 | -1.300 | 0.31 | 76. | 125 | 129. | 2.110 | U |
| 37735 | UGC06983 | 13.338 | 12.996 | 13.167 | -1.397 | 0.66 | 50. | 171 | 223. | 2.348 | U |
| 38283 | NGC4085 | 11.478 | 11.472 | 11.475 | -0.775 | 0.24 | 82. | 268 | 270. | 2.432 | U |
| 38302 | NGC4088 | 9.788 | 9.779 | 9.783 | -0.793 | 0.39 | 70. | 331 | 352. | 2.547 | U |
| 38356 | UGC07089 | 13.413 | / | 13.413 | -1.313 | 0.22 | 85. | 137 | 138. | 2.139 | U |

| PGC | Name | $[3.6]_{ext}^{b,i,k,a}$ | $[3.6]_{CHP}^{b,i,k,a}$ | $[3.6]_{ave}^{b,i,k,a}$ | Diff | b/a | Inc | W_{mx} | W_{mx}^i | W_{mxl}^i | S |
|-------|------------|-------------------------|-------------------------|-------------------------|--------|------|-----|----------|------------|-------------|----|
| 38370 | NGC4100 | 10.441 | 10.402 | 10.421 | -1.021 | 0.31 | 76. | 374 | 385. | 2.586 | U |
| 38392 | NGC4102 | 10.224 | 10.640 | 10.432 | -0.782 | 0.57 | 57. | 298 | 355. | 2.551 | U |
| 38795 | NGC4157 | 9.723 | 9.726 | 9.724 | -0.644 | 0.19 | 90. | 387 | 387. | 2.588 | U |
| 38951 | UGC07218 | 14.874 | / | 14.874 | -1.384 | 0.53 | 60. | 89 | 103. | 2.012 | U |
| 38988 | NGC4183 | 12.317 | 12.246 | 12.281 | -1.351 | 0.17 | 90. | 227 | 227. | 2.356 | U |
| 39241 | NGC4217 | / | 9.889 | 9.889 | -0.639 | 0.27 | 79. | 383 | 390. | 2.591 | U |
| 39344 | UGC07301 | 15.093 | 15.087 | 15.090 | -1.370 | 0.16 | 90. | 139 | 139. | 2.143 | U |
| 40537 | NGC4389 | 11.587 | / | 11.587 | -0.847 | 0.66 | 50. | 154 | 201. | 2.303 | U |
| 29727 | IC2556 | 13.642 | 13.577 | 13.610 | -1.330 | 0.55 | 58. | 214 | 251. | 2.400 | An |
| 29898 | IC2559 | 12.885 | 13.057 | 12.971 | -1.001 | 0.41 | 69. | 256 | 275. | 2.439 | An |
| 30308 | NGC3223 | 10.180 | 10.190 | 10.185 | -0.875 | 0.69 | 48. | 415 | 562. | 2.750 | An |
| 30716 | ESO375-026 | 12.335 | 12.230 | 12.283 | -0.743 | 0.20 | 90. | 332 | 332. | 2.521 | An |
| 31493 | ESO437-014 | 11.660 | 11.685 | 11.673 | -0.873 | 0.31 | 76. | 364 | 375. | 2.574 | An |
| 31761 | NGC3347A | 11.996 | 11.980 | 11.988 | -0.948 | 0.34 | 74. | 322 | 335. | 2.526 | An |
| 31995 | ESO318-004 | 11.715 | 11.678 | 11.697 | -1.037 | 0.23 | 83. | 382 | 385. | 2.585 | An |
| 29993 | IC2560 | 11.129 | 11.093 | 11.111 | -1.031 | 0.46 | 65. | 376 | 415. | 2.618 | An |
| 31875 | NGC3347B | 12.579 | 12.508 | 12.543 | -1.323 | 0.26 | 80. | 327 | 332. | 2.521 | An |
| 31926 | NGC3347 | 10.838 | 10.879 | 10.858 | -1.138 | 0.36 | 72. | 401 | 421. | 2.624 | An |
| 32039 | ESO437-056 | 12.921 | 12.975 | 12.948 | -1.088 | 0.64 | 52. | 239 | 305. | 2.484 | An |
| 41010 | ESO322-017 | 15.041 | 15.198 | 15.119 | -1.539 | 0.40 | 69. | 147 | 157. | 2.196 | Ce |
| 42181 | NGC4575 | 11.555 | 11.565 | 11.560 | -0.680 | 0.62 | 53. | 263 | 328. | 2.516 | Ce |
| 42271 | ESO322-042 | / | 13.357 | 13.357 | -1.257 | 0.31 | 76. | 226 | 233. | 2.367 | Ce |
| 42369 | NGC4603A | 12.485 | 12.450 | 12.468 | -0.868 | 0.39 | 70. | 270 | 287. | 2.458 | Ce |
| 42510 | NGC4603 | 10.679 | 10.660 | 10.669 | -0.909 | 0.64 | 52. | 353 | 450. | 2.653 | Ce |
| 42880 | ESO381-014 | 14.529 | 14.423 | 14.476 | -1.226 | 0.21 | 86. | 213 | 213. | 2.329 | Ce |
| 43073 | NGC4672 | 12.034 | 11.962 | 11.998 | -0.958 | 0.24 | 82. | 353 | 356. | 2.552 | Ce |
| 43282 | ESO268-044 | 12.938 | 13.074 | 13.006 | -0.776 | 0.47 | 64. | 247 | 274. | 2.438 | Ce |
| 43717 | ESO323-027 | 12.167 | 12.148 | 12.158 | -0.958 | 0.53 | 60. | 335 | 387. | 2.588 | Ce |
| 44695 | ESO269-028 | 14.444 | 14.510 | 14.477 | -1.177 | 0.38 | 71. | 225 | 238. | 2.377 | Ce |
| 45573 | ESO269-052 | 15.456 | 15.581 | 15.519 | -1.659 | 0.17 | 90. | 213 | 213. | 2.328 | Ce |
| 70702 | IC1474 | 13.054 | 13.053 | 13.053 | -0.433 | 0.49 | 63. | 255 | 287. | 2.457 | Pe |
| 70803 | UGC12451 | / | 15.007 | 15.007 | -1.477 | 0.24 | 82. | 172 | 174. | 2.240 | Pe |
| 70880 | NGC7562A | 14.667 | 15.082 | 14.875 | -1.825 | 0.25 | 81. | 199 | 201. | 2.304 | Pe |
| 70927 | PGC070927 | 14.497 | 16.548 | 14.497 | -1.237 | 0.64 | 52. | 180 | 230. | 2.361 | Pe |
| 70981 | NGC7593 | 13.365 | 13.352 | 13.359 | -0.829 | 0.63 | 52. | 239 | 302. | 2.479 | Pe |
| 71034 | UGC12494 | 14.670 | 14.655 | 14.662 | -1.372 | 0.31 | 76. | 208 | 214. | 2.331 | Pe |
| 71051 | IC5309 | 13.142 | 13.120 | 13.131 | -1.011 | 0.49 | 63. | 270 | 303. | 2.482 | Pe |
| 71087 | NGC7610 | 13.337 | 13.287 | 13.312 | -1.052 | 0.61 | 54. | 241 | 298. | 2.474 | Pe |
| 71159 | PGC071159 | 14.605 | 14.621 | 14.613 | -1.203 | 0.43 | 67. | 148 | 161. | 2.206 | Pe |
| 71181 | NGC7631 | 12.470 | 12.479 | 12.475 | -1.105 | 0.42 | 68. | 366 | 395. | 2.597 | Pe |
| 71260 | UGC12562 | 15.723 | 15.715 | 15.719 | -1.449 | 0.27 | 79. | 153 | 156. | 2.192 | Pe |
| 71262 | UGC12561 | 15.287 | 15.285 | 15.286 | -1.436 | 0.32 | 75. | 184 | 190. | 2.279 | Pe |
| 31154 | ESO436-034 | 11.730 | 11.653 | 11.692 | -0.662 | 0.23 | 83. | 533 | 537. | 2.730 | H |
| 31242 | ESO436-039 | 12.499 | 12.487 | 12.493 | -0.593 | 0.20 | 90. | 412 | 412. | 2.615 | H |
| 31360 | ESO437-004 | 12.606 | 12.629 | 12.617 | -0.867 | 0.50 | 62. | 322 | 364. | 2.561 | H |
| 31590 | ESO437-018 | 13.602 | 13.591 | 13.596 | -0.826 | 0.33 | 74. | 300 | 311. | 2.493 | H |
| 31626 | ESO437-022 | 14.177 | 14.156 | 14.166 | -1.246 | 0.27 | 79. | 284 | 289. | 2.461 | H |
| 31642 | ESO437-025 | 13.218 | 13.193 | 13.205 | -0.915 | 0.37 | 71. | 245 | 258. | 2.412 | H |
| 31677 | ESO437-030 | 11.759 | 11.755 | 11.757 | -0.997 | 0.22 | 85. | 428 | 430. | 2.633 | H |
| 31683 | ESO501-068 | 13.065 | 13.051 | 13.058 | -1.168 | 0.32 | 75. | 323 | 334. | 2.524 | H |
| 31690 | ESO437-031 | 14.422 | 14.431 | 14.427 | -1.297 | 0.62 | 53. | 203 | 254. | 2.404 | H |
| 31732 | ESO437-034 | 16.163 | 16.081 | 16.122 | -1.932 | 0.39 | 70. | 170 | 181. | 2.257 | H |
| 31738 | ESO437-035 | 13.270 | 13.262 | 13.266 | -0.956 | 0.37 | 71. | 236 | 249. | 2.396 | H |

| PGC | Name | $[3.6]_{ext}^{b,i,k,a}$ | $[3.6]_{CHP}^{b,i,k,a}$ | $[3.6]_{ave}^{b,i,k,a}$ | Diff | b/a | Inc | W_{mx} | W_{mx}^i | W_{mxt}^i | S |
|--------|------------|-------------------------|-------------------------|-------------------------|--------|------|-----|----------|------------|-------------|----|
| 31805 | ESO501-075 | 12.361 | 12.345 | 12.353 | -1.023 | 0.50 | 62. | 322 | 364. | 2.561 | H |
| 31951 | ESO501-082 | 12.819 | 12.861 | 12.840 | -0.970 | 0.42 | 68. | 383 | 414. | 2.616 | H |
| 31981 | ESO437-054 | 13.674 | 13.620 | 13.647 | -0.477 | 0.21 | 86. | 275 | 276. | 2.440 | H |
| 3664 | UGC00633 | 13.448 | 13.437 | 13.443 | -1.133 | 0.27 | 79. | 392 | 399. | 2.601 | Pi |
| 3773 | UGC00646 | 12.970 | 12.951 | 12.961 | -1.201 | 0.38 | 71. | 367 | 389. | 2.590 | Pi |
| 3866 | UGC00669 | 13.385 | 13.381 | 13.383 | -0.543 | 0.25 | 81. | 264 | 267. | 2.427 | Pi |
| 3950 | UGC00679 | 15.810 | 15.793 | 15.802 | -1.312 | 0.23 | 83. | 174 | 175. | 2.243 | Pi |
| 4110 | UGC00714 | 13.430 | 13.454 | 13.442 | -0.922 | 0.71 | 46. | 216 | 301. | 2.478 | Pi |
| 4210 | UGC00732 | 13.540 | 13.558 | 13.549 | -1.069 | 0.60 | 55. | 260 | 318. | 2.503 | Pi |
| 4561 | NGC0444 | 14.052 | 14.051 | 14.051 | -1.301 | 0.25 | 81. | 253 | 256. | 2.408 | Pi |
| 4596 | NGC0452 | 11.984 | 11.988 | 11.986 | -1.126 | 0.29 | 78. | 457 | 468. | 2.670 | Pi |
| 4735 | UGC00841 | 14.045 | 14.066 | 14.056 | -1.076 | 0.23 | 83. | 282 | 284. | 2.453 | Pi |
| 5061 | NGC0496 | 13.200 | 13.187 | 13.194 | -0.984 | 0.55 | 58. | 285 | 334. | 2.524 | Pi |
| 5132 | NGC0512 | 12.321 | 12.316 | 12.318 | -1.058 | 0.28 | 78. | 521 | 532. | 2.726 | Pi |
| 5284 | UGC00987 | 12.497 | 12.499 | 12.498 | -1.018 | 0.32 | 75. | 383 | 396. | 2.598 | Pi |
| 5344 | NGC0536 | 11.708 | 11.722 | 11.715 | -1.255 | 0.36 | 72. | 513 | 539. | 2.731 | Pi |
| 5563 | UGC01066 | 16.788 | 16.712 | 16.750 | -1.800 | 0.28 | 78. | 158 | 161. | 2.208 | Pi |
| 6502 | NGC0668 | 12.669 | 12.650 | 12.660 | -0.890 | 0.69 | 48. | 279 | 378. | 2.577 | Pi |
| 6607 | UGC01257 | 13.819 | 13.835 | 13.827 | -1.107 | 0.44 | 66. | 324 | 354. | 2.548 | Pi |
| 6799 | NGC0688 | 12.437 | 12.405 | 12.421 | -0.981 | 0.68 | 48. | 337 | 450. | 2.654 | Pi |
| 6851 | UGC01316 | 15.702 | 15.673 | 15.687 | -1.537 | 0.47 | 64. | 205 | 228. | 2.357 | Pi |
| 6865 | UGC01319 | 13.222 | 13.223 | 13.222 | -0.712 | 0.71 | 46. | 241 | 335. | 2.525 | Pi |
| 7066 | UGC01366 | 12.885 | 12.861 | 12.873 | -1.203 | 0.29 | 78. | 412 | 422. | 2.625 | Pi |
| 7254 | UGC01405 | 15.148 | 15.130 | 15.139 | -1.229 | 0.16 | 90. | 247 | 247. | 2.393 | Pi |
| 7387 | NGC0753 | 11.703 | 11.653 | 11.678 | -0.798 | 0.71 | 46. | 314 | 437. | 2.640 | Pi |
| 7504 | UGC01459 | 13.122 | 13.228 | 13.175 | -0.925 | 0.16 | 90. | 362 | 362. | 2.559 | Pi |
| 23146 | PGC023146 | 14.336 | 14.282 | 14.309 | -0.919 | 0.19 | 90. | 267 | 267. | 2.427 | Ca |
| 23169 | UGC04299 | 12.460 | 12.480 | 12.470 | -0.820 | 0.18 | 90. | 389 | 389. | 2.590 | Ca |
| 23338 | PGC023338 | 15.151 | 15.180 | 15.165 | -1.385 | 0.68 | 48. | 185 | 247. | 2.393 | Ca |
| 23347 | PGC023347 | 14.693 | 14.685 | 14.689 | -0.889 | 0.72 | 45. | 162 | 229. | 2.359 | Ca |
| 23374 | PGC023374 | 15.620 | 15.647 | 15.633 | -1.373 | 0.35 | 73. | 232 | 243. | 2.385 | Ca |
| 23420 | PGC023420 | 13.863 | 13.828 | 13.845 | -1.045 | 0.66 | 50. | 215 | 280. | 2.448 | Ca |
| 23567 | UGC04386 | 12.106 | 12.115 | 12.110 | -1.100 | 0.23 | 83. | 480 | 483. | 2.684 | Ca |
| 23661 | UGC04400 | 15.790 | 15.715 | 15.753 | -1.453 | 0.20 | 90. | 214 | 214. | 2.330 | Ca |
| 23662 | UGC04399 | 14.570 | 14.558 | 14.564 | -1.214 | 0.36 | 72. | 232 | 244. | 2.387 | Ca |
| 23748 | UGC04424 | 15.854 | 15.742 | 15.798 | -1.548 | 0.27 | 79. | 203 | 207. | 2.315 | Ca |
| 142820 | PGC142820 | 15.892 | 15.852 | 15.872 | -1.402 | 0.28 | 78. | 190 | 194. | 2.288 | Ca |
| 42765 | UGC07890 | 14.429 | 14.422 | 14.425 | -0.945 | 0.67 | 49. | 233 | 308. | 2.488 | Co |
| 43142 | UGC07955 | 13.809 | 13.849 | 13.829 | -1.059 | 0.18 | 90. | 361 | 361. | 2.558 | Co |
| 43278 | PGC043278 | 13.685 | 13.669 | 13.677 | -0.637 | 0.26 | 80. | 311 | 316. | 2.499 | Co |
| 43686 | UGC08013 | 14.531 | 14.511 | 14.521 | -1.371 | 0.29 | 78. | 365 | 374. | 2.573 | Co |
| 43726 | UGC08017 | 12.664 | 12.618 | 12.641 | -0.601 | 0.37 | 71. | 521 | 549. | 2.740 | Co |
| 43840 | PGC043840 | 14.672 | 14.658 | 14.665 | -0.885 | 0.43 | 67. | 286 | 310. | 2.492 | Co |
| 43863 | UGC08025 | 12.705 | 12.735 | 12.720 | -1.100 | 0.19 | 90. | 505 | 505. | 2.703 | Co |
| 44795 | IC0842 | 13.524 | 13.540 | 13.532 | -1.032 | 0.49 | 63. | 368 | 414. | 2.617 | Co |
| 44921 | IC4088 | 13.302 | 13.311 | 13.306 | -1.116 | 0.30 | 77. | 467 | 480. | 2.681 | Co |
| 45097 | UGC08161 | 13.581 | 13.547 | 13.564 | -0.794 | 0.43 | 67. | 355 | 385. | 2.586 | Co |
| 45366 | UGC08195 | 15.258 | 15.266 | 15.262 | -1.262 | 0.17 | 90. | 233 | 233. | 2.367 | Co |
| 45549 | IC4202 | 12.925 | 12.918 | 12.922 | -1.162 | 0.18 | 90. | 524 | 524. | 2.719 | Co |
| 45580 | UGC08229 | 13.203 | 13.075 | 13.139 | -0.799 | 0.53 | 60. | 342 | 395. | 2.597 | Co |
| 45366 | UGC08195 | 15.258 | 15.266 | 15.262 | -1.262 | 0.17 | 90. | 233 | 233. | 2.367 | Co |
| 45549 | IC4202 | 12.925 | 12.918 | 12.922 | -1.162 | 0.18 | 90. | 524 | 524. | 2.719 | Co |
| 45580 | UGC08229 | 13.203 | 13.075 | 13.139 | -0.799 | 0.53 | 60. | 342 | 395. | 2.597 | Co |

| PGC | Name | $[3.6]_{ext}^{b,i,k,a}$ | $[3.6]_{CHP}^{b,i,k,a}$ | $[3.6]_{ave}^{b,i,k,a}$ | Diff | b/a | Inc | W_{mx} | W_{mx}^i | W_{mxl}^i | S |
|--------|-----------|-------------------------|-------------------------|-------------------------|--------|------|-----|----------|------------|-------------|----|
| 45668 | UGC08244 | 15.219 | 15.193 | 15.206 | -1.356 | 0.38 | 71. | 238 | 252. | 2.402 | Co |
| 45742 | IC4210 | 14.375 | 14.352 | 14.363 | -0.963 | 0.64 | 52. | 227 | 289. | 2.462 | Co |
| 45757 | NGC5004A | 13.196 | 13.228 | 13.212 | -0.742 | 0.43 | 67. | 336 | 365. | 2.562 | Co |
| 10913 | UGC02364 | 13.933 | 13.917 | 13.925 | -1.205 | 0.35 | 73. | 323 | 338. | 2.529 | A4 |
| 10943 | UGC02375 | 13.320 | 13.339 | 13.329 | -1.219 | 0.30 | 77. | 440 | 452. | 2.655 | A4 |
| 11074 | UGC02405 | 13.494 | 13.472 | 13.483 | -1.203 | 0.37 | 71. | 400 | 422. | 2.625 | A4 |
| 11102 | UGC02415 | 14.145 | 14.118 | 14.131 | -0.861 | 0.35 | 73. | 323 | 338. | 2.529 | A4 |
| 11136 | UGC02423 | 13.399 | 13.411 | 13.405 | -0.945 | 0.33 | 74. | 382 | 396. | 2.598 | A4 |
| 11255 | UGC02444 | 13.050 | 13.049 | 13.050 | -0.620 | 0.62 | 53. | 361 | 451. | 2.654 | A4 |
| 11306 | UGC02454 | 14.048 | 14.048 | 14.048 | -1.188 | 0.22 | 85. | 359 | 361. | 2.557 | A4 |
| 35347 | NGC3697 | 12.581 | 12.577 | 12.579 | -1.239 | 0.32 | 75. | 504 | 521. | 2.717 | A1 |
| 35622 | PGC035622 | 14.679 | 14.667 | 14.673 | -0.983 | 0.58 | 56. | 243 | 292. | 2.466 | A1 |
| 35942 | UGC06583 | 13.415 | 13.434 | 13.424 | -0.644 | 0.59 | 55. | 319 | 387. | 2.588 | A1 |
| 35978 | PGC035978 | 14.669 | 14.658 | 14.664 | -1.134 | 0.49 | 63. | 261 | 293. | 2.467 | A1 |
| 36132 | PGC036132 | 14.317 | 14.284 | 14.300 | -0.980 | 0.62 | 53. | 247 | 308. | 2.489 | A1 |
| 36349 | PGC036349 | 13.205 | 13.199 | 13.202 | -0.512 | 0.56 | 58. | 327 | 387. | 2.587 | A1 |
| 36431 | UGC06686 | 13.118 | 13.165 | 13.142 | -1.312 | 0.16 | 90. | 398 | 398. | 2.600 | A1 |
| 36466 | UGC06697 | 12.989 | 13.011 | 13.000 | -1.160 | 0.20 | 90. | 557 | 557. | 2.746 | A1 |
| 36604 | NGC3861 | 12.290 | 12.323 | 12.307 | -1.077 | 0.57 | 57. | 459 | 547. | 2.738 | A1 |
| 36683 | PGC036683 | 14.112 | 14.088 | 14.100 | -0.850 | 0.39 | 70. | 265 | 282. | 2.450 | A1 |
| 36706 | NGC3884 | 12.084 | 12.081 | 12.083 | -0.923 | 0.72 | 45. | 462 | 652. | 2.814 | A1 |
| 36778 | PGC036778 | 14.798 | 14.815 | 14.806 | -1.226 | 0.23 | 83. | 357 | 359. | 2.556 | A1 |
| 36779 | PGC036779 | 13.987 | 13.994 | 13.991 | -1.181 | 0.37 | 71. | 379 | 400. | 2.602 | A1 |
| 36856 | PGC036856 | 13.757 | 13.779 | 13.768 | -0.858 | 0.27 | 79. | 366 | 372. | 2.571 | A1 |
| 37143 | UGC06837 | 14.555 | 14.580 | 14.567 | -0.737 | 0.18 | 90. | 331 | 331. | 2.520 | A1 |
| 37264 | NGC3947 | 12.642 | 12.649 | 12.645 | -0.905 | 0.57 | 57. | 386 | 460. | 2.663 | A1 |
| 37288 | NGC3951 | 12.949 | 12.944 | 12.947 | -0.807 | 0.49 | 63. | 371 | 417. | 2.620 | A1 |
| 37409 | UGC06891 | 13.822 | 13.849 | 13.835 | -1.135 | 0.26 | 80. | 344 | 349. | 2.543 | A1 |
| 37463 | PGC037463 | 14.625 | 14.624 | 14.624 | -1.174 | 0.37 | 71. | 293 | 309. | 2.490 | A1 |
| 71597 | UGC12631 | 13.460 | 13.487 | 13.473 | -1.023 | 0.32 | 75. | 459 | 475. | 2.676 | A2 |
| 71795 | UGC12678 | 13.669 | 13.668 | 13.668 | -1.238 | 0.22 | 85. | 505 | 507. | 2.705 | A2 |
| 71880 | UGC12701 | 14.286 | 14.275 | 14.281 | -0.651 | 0.26 | 80. | 348 | 353. | 2.548 | A2 |
| 72024 | UGC12721 | 13.384 | 13.391 | 13.387 | -1.047 | 0.44 | 66. | 394 | 430. | 2.633 | A2 |
| 72115 | PGC072115 | 12.759 | 12.749 | 12.754 | -0.134 | 0.51 | 61. | 425 | 484. | 2.685 | A2 |
| 72169 | PGC072169 | 13.654 | 13.679 | 13.666 | -0.696 | 0.24 | 82. | 377 | 381. | 2.580 | A2 |
| 72188 | UGC12746 | 12.883 | 12.884 | 12.883 | -0.733 | 0.19 | 90. | 451 | 451. | 2.654 | A2 |
| 72233 | UGC12755 | 13.011 | 13.016 | 13.014 | -1.164 | 0.53 | 60. | 503 | 581. | 2.764 | A2 |
| 72328 | NGC7747 | 12.677 | 12.681 | 12.679 | -1.109 | 0.40 | 69. | 531 | 568. | 2.754 | A2 |
| 72411 | PGC072411 | 13.700 | 13.631 | 13.665 | -0.965 | 0.45 | 66. | 367 | 403. | 2.605 | A2 |
| 72438 | PGC072438 | 13.688 | 13.658 | 13.673 | -0.683 | 0.32 | 75. | 398 | 412. | 2.614 | A2 |
| 72665 | PGC072665 | 14.178 | 14.155 | 14.167 | -0.747 | 0.48 | 64. | 302 | 337. | 2.528 | A2 |
| 72751 | PGC072751 | 14.199 | 14.186 | 14.193 | -0.803 | 0.59 | 55. | 262 | 318. | 2.502 | A2 |
| 72784 | PGC072784 | 14.413 | 14.388 | 14.401 | -1.021 | 0.48 | 64. | 344 | 384. | 2.585 | A2 |
| 72968 | PGC072968 | 14.850 | 14.854 | 14.859 | -1.189 | 0.27 | 79. | 321 | 327. | 2.514 | A2 |
| 85512 | PGC085512 | 15.880 | 15.848 | 15.864 | -0.954 | 0.55 | 58. | 234 | 275. | 2.439 | A2 |
| 91814 | PGC091814 | 14.898 | 14.859 | 14.878 | -1.118 | 0.20 | 90. | 239 | 239. | 2.378 | A2 |
| 169662 | PGC169662 | 14.842 | 14.794 | 14.818 | -1.058 | 0.26 | 80. | 346 | 351. | 2.545 | A2 |

TABLE B.1: Calibrator parameters for the Tully-Fisher relation: (1) PGC number, (2) Common Name, (3) CFS corrected magnitude, mag, (4) CHP corrected magnitude, mag, (5) CFS and CHP averaged corrected magnitude, mag, (6) Color term ($I^{b,i,k} - [3.6]_{ave}^{b,i,k,a}$), mag, (7) Axial Ratio, (8) Inclination, degrees, (9) linewidth not corrected for inclination, km s^{-1} , (10) linewidth corrected for inclination, km s^{-1} , (11) Logarithm of the inclination corrected linewidth, (12) Sample ZP Zeropoint Calibrators, V Virgo, F Fornax, U Ursa Major, An Antlia, Ce Centaurus30, Pe Pegasus, H Hydra, Pi Pisces, Ca Cancer, Co Coma, A4 Abell 400, A1 Abell 1367 and A2 Abell 2634 and 2666

Table B.2

| PGC | Name | $I_{ext}^{b,i,k}$ | $[3.6]_{ave}^{b,i,k,a}$ | $C_{[3.6]_{ave}}^{b,i,k,a}$ | b/a | Inc | W_{mx} | W_{mx}^i | W_{mxl}^i | S |
|-------|---------|-------------------|-------------------------|-----------------------------|------|-----|----------|------------|-------------|----|
| 2758 | NGC0247 | 7.79 | 9.10 | 8.98 | 0.31 | 76. | 190 | 196 | 2.292 | ZP |
| 3238 | NGC0300 | 7.28 | 8.40 | 8.38 | 0.71 | 46. | 140 | 195 | 2.290 | ZP |
| 9332 | NGC0925 | 8.96 | 10.25 | 10.14 | 0.57 | 57. | 194 | 231. | 2.364 | ZP |
| 13179 | NGC1365 | 8.09 | 8.77 | 8.97 | 0.61 | 54. | 371 | 459. | 2.662 | ZP |
| 13602 | NGC1425 | 9.50 | 10.72 | 10.64 | 0.46 | 65. | 354 | 391. | 2.592 | ZP |
| 17819 | NGC2090 | 9.33 | 10.38 | 10.39 | 0.43 | 67. | 277 | 301. | 2.478 | ZP |
| 21396 | NGC2403 | 7.11 | 8.46 | 8.32 | 0.53 | 60. | 226 | 261. | 2.417 | ZP |
| 23110 | NGC2541 | 10.76 | 12.06 | 11.94 | 0.49 | 63. | 188 | 211. | 2.325 | ZP |
| 26512 | NGC2841 | 7.53 | 8.65 | 8.63 | 0.45 | 66. | 592 | 650. | 2.813 | ZP |
| 28120 | NGC2976 | 8.98 | 9.89 | 9.97 | 0.53 | 60. | 129 | 149. | 2.173 | ZP |
| 28630 | NGC3031 | 5.20 | 6.29 | 6.28 | 0.54 | 59. | 416 | 485 | 2.686 | ZP |
| 30197 | NGC3198 | 9.17 | 10.33 | 10.28 | 0.39 | 70. | 296 | 315. | 2.498 | ZP |
| 30819 | IC2574 | 10.12 | 11.12 | 11.16 | 0.40 | 69. | 106 | 113 | 2.054 | ZP |
| 31671 | NGC3319 | 10.55 | 11.82 | 11.72 | 0.54 | 59. | 195 | 227. | 2.356 | ZP |
| 32007 | NGC3351 | 8.33 | 9.20 | 9.31 | 0.70 | 47. | 262 | 312. | 2.556 | ZP |
| 32192 | NGC3368 | 7.88 | 8.80 | 8.88 | 0.64 | 52. | 329 | 418. | 2.621 | ZP |
| 34554 | NGC3621 | 8.01 | 9.01 | 9.05 | 0.45 | 66. | 266 | 292. | 2.465 | ZP |
| 34695 | NGC3627 | 7.39 | 8.28 | 8.38 | 0.53 | 60. | 333 | 385 | 2.585 | ZP |
| 39422 | NGC4244 | 8.92 | 10.25 | 10.12 | 0.20 | 90. | 192 | 192. | 2.283 | ZP |
| 39600 | NGC4258 | 6.84 | 7.98 | 7.95 | 0.40 | 69. | 414 | 444. | 2.647 | ZP |
| 40596 | NGC4395 | 9.08 | 11.21 | 10.66 | 0.73 | 44. | 112 | 161 | 2.206 | ZP |
| 40692 | NGC4414 | 8.73 | 9.38 | 9.60 | 0.60 | 55. | 378 | 463. | 2.666 | ZP |
| 41812 | NGC4535 | 8.95 | 9.75 | 9.89 | 0.72 | 45. | 265 | 374 | 2.573 | ZP |
| 41823 | NGC4536 | 9.03 | 9.85 | 9.98 | 0.38 | 71. | 322 | 341. | 2.533 | ZP |
| 42408 | NGC4605 | 9.19 | 10.17 | 10.22 | 0.41 | 69. | 154 | 165. | 2.219 | ZP |
| 42510 | NGC4603 | 9.76 | 10.67 | 10.75 | 0.64 | 52. | 353 | 450. | 2.653 | ZP |
| 42741 | NGC4639 | 10.18 | 11.27 | 11.26 | 0.60 | 55. | 274 | 336. | 2.526 | ZP |
| 43451 | NGC4725 | 7.84 | 8.87 | 8.89 | 0.56 | 58. | 397 | 470. | 2.672 | ZP |
| 47368 | NGC5204 | / | 11.93 | / | 0.50 | 62. | 186 | 267. | 2.095 | ZP |
| 60921 | NGC6503 | 8.67 | 9.78 | 9.76 | 0.32 | 75. | 223 | 231. | 2.363 | ZP |
| 69327 | NGC7331 | 7.52 | 8.39 | 8.50 | 0.44 | 66. | 501 | 547. | 2.738 | ZP |
| 73049 | NGC7793 | 8.25 | 9.27 | 9.30 | 0.62 | 53. | 162 | 202. | 2.306 | ZP |
| 40095 | NGC4312 | 10.23 | 11.32 | 11.31 | 0.27 | 79. | 217 | 221. | 2.344 | V |
| 40105 | NGC4313 | 9.97 | 11.04 | 11.04 | 0.22 | 85. | 257 | 258. | 2.412 | V |
| 40201 | NGC4330 | 10.81 | 11.97 | 11.92 | 0.17 | 90. | 251 | 251. | 2.400 | V |
| 40507 | NGC4380 | 9.82 | 11.11 | 11.00 | 0.52 | 61. | 265 | 304. | 2.483 | V |
| 40516 | NGC4383 | 10.87 | 11.69 | 11.82 | 0.58 | 56. | 199 | 239. | 2.379 | V |
| 40530 | IC3311 | 12.81 | 13.94 | 13.91 | 0.21 | 86. | 160 | 160. | 2.205 | V |
| 40581 | NGC4388 | 9.32 | 10.32 | 10.36 | 0.26 | 80. | 364 | 369. | 2.567 | V |
| 40622 | NGC4396 | 12.67 | 12.40 | 13.10 | 0.35 | 73. | 181 | 189. | 2.277 | V |
| 40644 | NGC4402 | 10.17 | 10.79 | 11.03 | 0.34 | 74. | 267 | 278. | 2.444 | V |
| 40811 | IC3365 | 13.06 | 14.40 | 14.26 | 0.42 | 68. | 122 | 132. | 2.120 | V |
| 41024 | NGC4450 | 8.63 | 9.67 | 9.69 | 0.67 | 49. | 304 | 401. | 2.603 | V |
| 41061 | IC3392 | 10.92 | 11.79 | 11.90 | 0.42 | 68. | 178 | 192. | 2.284 | V |
| 41472 | NGC4498 | 11.00 | 12.21 | 12.14 | 0.48 | 64. | 182 | 203. | 2.308 | V |
| 41504 | IC0797 | 12.01 | 13.06 | 13.07 | 0.69 | 48. | 118 | 160. | 2.203 | V |
| 41517 | NGC4501 | 7.88 | 8.82 | 8.89 | 0.48 | 64. | 507 | 566. | 2.573 | V |
| 41608 | IC3476 | 11.97 | 12.90 | 12.97 | 0.64 | 52. | 126 | 161. | 2.206 | V |
| 41729 | NGC4522 | 10.95 | 12.01 | 12.02 | 0.25 | 81. | 209 | 211. | 2.325 | V |
| 41763 | IC0800 | 12.07 | 13.16 | 13.15 | 0.68 | 48. | 115 | 154. | 2.187 | V |
| 41812 | NGC4535 | 8.96 | 9.74 | 9.89 | 0.72 | 45. | 265 | 374. | 2.573 | V |

| PGC | Name | $I_{ext}^{b,i,k}$ | $[3.6]_{ave}^{b,i,k,a}$ | $C_{[3.6]_{ave}}^{b,i,k,a}$ | b/a | Inc | W_{mx} | W_{mx}^i | W_{mxl}^i | S |
|-------|------------|-------------------|-------------------------|-----------------------------|------|-----|----------|------------|-------------|---|
| 41823 | NGC4536 | 9.04 | 9.85 | 9.99 | 0.38 | 71. | 322 | 341. | 2.533 | V |
| 42160 | PGC042160 | 13.55 | 14.56 | 14.59 | 0.62 | 53. | 85 | 106. | 2.024 | V |
| 42230 | UGC07802 | 13.05 | 14.35 | 14.23 | 0.18 | 90. | 150 | 150. | 2.176 | V |
| 42348 | IC3617 | 13.36 | 14.82 | 14.62 | 0.52 | 61. | 103 | 118. | 2.072 | V |
| 42396 | NGC4595 | 11.42 | 12.50 | 12.50 | 0.70 | 47. | 131 | 180. | 2.255 | V |
| 42544 | NGC4607 | 11.45 | 11.93 | 12.24 | 0.20 | 90. | 170 | 170. | 2.230 | V |
| 42741 | NGC4639 | 10.16 | 11.27 | 11.25 | 0.55 | 58. | 274 | 321. | 2.507 | V |
| 42833 | NGC4651 | 9.43 | 10.37 | 10.44 | 0.64 | 52. | 364 | 466. | 2.669 | V |
| 42857 | NGC4654 | 9.26 | 10.11 | 10.23 | 0.56 | 58. | 282 | 334. | 2.523 | V |
| 43001 | IC3742 | 12.61 | 13.99 | 13.83 | 0.40 | 69. | 161 | 172. | 2.236 | V |
| 43254 | NGC4698 | 8.92 | 10.10 | 10.04 | 0.44 | 66. | 419 | 457. | 2.660 | V |
| 11856 | ESO357-007 | 13.17 | 14.72 | 14.47 | 0.24 | 82. | 125 | 126. | 2.101 | F |
| 12181 | ESO357-012 | 12.53 | 13.62 | 13.61 | 0.66 | 50. | 123 | 160. | 2.205 | F |
| 12404 | IC1913 | 12.91 | 14.13 | 14.05 | 0.22 | 85. | 157 | 158. | 2.198 | F |
| 12952 | NGC1351A | 11.90 | 12.86 | 12.92 | 0.21 | 86. | 200 | 200. | 2.302 | F |
| 13059 | NGC1350 | 8.72 | 9.84 | 9.82 | 0.47 | 64. | 390 | 433. | 2.636 | F |
| 13089 | ESO418-008 | 12.70 | 13.80 | 13.79 | 0.70 | 47. | 121 | 166. | 2.220 | F |
| 13179 | NGC1365 | 8.10 | 8.77 | 8.98 | 0.61 | 54. | 371 | 459. | 2.662 | F |
| 13458 | NGC1406 | 10.05 | 10.78 | 10.96 | 0.22 | 85. | 322 | 323. | 2.510 | F |
| 13571 | ESO358-051 | 12.46 | 13.59 | 13.56 | 0.50 | 62. | 118 | 134. | 2.125 | F |
| 13602 | NGC1425 | 9.51 | 10.69 | 10.63 | 0.46 | 65. | 354 | 391. | 2.592 | F |
| 13687 | NGC1436 | 10.44 | 11.37 | 11.44 | 0.63 | 52. | 201 | 254. | 2.404 | F |
| 13809 | ESO358-063 | 10.19 | 11.23 | 11.25 | 0.24 | 82. | 285 | 288. | 2.459 | F |
| 13854 | ESO302-009 | 12.98 | 14.60 | 14.32 | 0.21 | 86. | 142 | 142. | 2.153 | F |
| 13998 | ESO359-003 | 12.63 | 14.14 | 13.91 | 0.42 | 68. | 112 | 121. | 2.082 | F |
| 14071 | NGC1484 | 11.95 | 13.19 | 13.10 | 0.24 | 82. | 162 | 164. | 2.214 | F |
| 34971 | UGC06399 | 12.59 | 14.09 | 13.87 | 0.28 | 78. | 167 | 170. | 2.232 | U |
| 35202 | UGC06446 | 12.37 | 14.16 | 13.79 | 0.63 | 52. | 125 | 158. | 2.198 | U |
| 35676 | NGC3726 | 9.26 | 10.27 | 10.30 | 0.58 | 56. | 263 | 316. | 2.500 | U |
| 36343 | UGC06667 | 12.10 | 13.55 | 13.35 | 0.14 | 90. | 173 | 173. | 2.238 | U |
| 36699 | NGC3877 | 9.21 | 10.17 | 10.23 | 0.24 | 82. | 347 | 350. | 2.544 | U |
| 36825 | UGC06773 | 12.93 | 14.70 | 14.34 | 0.44 | 66. | 89 | 97. | 1.987 | U |
| 36875 | NGC3893 | 9.49 | 10.31 | 10.44 | 0.66 | 50. | 283 | 369. | 2.567 | U |
| 36930 | UGC06792 | / | 14.10 | / | 0.21 | 86. | 163 | 163. | 2.213 | U |
| 37036 | NGC3917 | 10.26 | 11.49 | 11.41 | 0.24 | 82. | 273 | 276. | 2.440 | U |
| 37038 | UGC06818 | 12.95 | 14.40 | 14.20 | 0.35 | 73. | 141 | 147. | 2.169 | U |
| 37290 | NGC3949 | 9.98 | 10.93 | 10.99 | 0.63 | 52. | 252 | 318. | 2.502 | U |
| 37306 | NGC3953 | 8.61 | 9.53 | 9.61 | 0.50 | 62. | 404 | 457. | 2.660 | U |
| 37418 | UGC06894 | 13.80 | 14.96 | 14.91 | 0.16 | 90. | 121 | 121. | 2.083 | U |
| 37466 | NGC3972 | 10.91 | 11.97 | 11.98 | 0.29 | 78. | 258 | 264. | 2.422 | U |
| 37525 | UGC06917 | 11.43 | 12.90 | 12.69 | 0.59 | 55. | 178 | 216. | 2.334 | U |
| 37542 | NGC3985 | 11.62 | 12.60 | 12.65 | 0.62 | 53. | 150 | 187. | 2.273 | U |
| 37553 | UGC06923 | 12.27 | 13.66 | 13.50 | 0.42 | 68. | 139 | 150. | 2.176 | U |
| 37617 | NGC3992 | 8.51 | 9.55 | 9.57 | 0.55 | 58. | 459 | 538. | 2.731 | U |
| 37691 | NGC4013 | 9.32 | 10.00 | 10.20 | 0.22 | 85. | 388 | 390. | 2.591 | U |
| 37697 | NGC4010 | 10.90 | 11.78 | 11.88 | 0.17 | 90. | 248 | 248. | 2.394 | U |
| 37735 | UGC06983 | 11.78 | 13.06 | 12.95 | 0.66 | 50. | 171 | 223. | 2.348 | U |
| 37832 | UGC06992 | 12.79 | 13.97 | 13.91 | 0.45 | 66. | 128 | 140. | 2.147 | U |
| 38283 | NGC4085 | 10.71 | 11.48 | 11.64 | 0.24 | 82. | 268 | 270. | 2.432 | U |
| 38302 | NGC4088 | 9.00 | 9.79 | 9.94 | 0.39 | 70. | 331 | 352. | 2.547 | U |
| 38356 | UGC07089 | 12.10 | 13.45 | 13.31 | 0.22 | 85. | 137 | 138. | 2.139 | U |
| 38370 | NGC4100 | 9.41 | 10.42 | 10.45 | 0.31 | 76. | 374 | 385. | 2.586 | U |
| 38375 | UGC07094 | 13.21 | 14.35 | 14.32 | 0.36 | 72. | 80 | 84. | 1.924 | U |

| PGC | Name | $I_{ext}^{b,i,k}$ | $[3.6]_{ave}^{b,i,k,a}$ | $C_{[3.6]_{ave}}^{b,i,k,a}$ | b/a | Inc | W_{mx} | W_{mx}^i | W_{mxl}^i | S |
|-------|------------|-------------------|-------------------------|-----------------------------|------|-----|----------|------------|-------------|----|
| 38392 | NGC4102 | 9.66 | 10.36 | 10.55 | 0.57 | 57. | 298 | 355. | 2.551 | U |
| 38795 | NGC4157 | 9.09 | 9.72 | 9.95 | 0.19 | 90. | 387 | 387. | 2.588 | U |
| 38951 | UGC07218 | 13.50 | 14.72 | 14.64 | 0.53 | 60. | 89 | 103. | 2.012 | U |
| 38988 | NGC4183 | 10.93 | 12.30 | 12.15 | 0.17 | 90. | 227 | 227. | 2.356 | U |
| 39237 | NGC4218 | 12.34 | 13.41 | 13.41 | 0.61 | 54. | 116 | 143. | 2.157 | U |
| 39241 | NGC4217 | 9.26 | 9.92 | 10.13 | 0.27 | 79. | 383 | 390. | 2.591 | U |
| 39344 | UGC07301 | 13.73 | 15.16 | 14.97 | 0.16 | 90. | 139 | 139. | 2.143 | U |
| 40537 | NGC4389 | 10.74 | 11.58 | 11.70 | 0.66 | 50. | 154 | 201. | 2.303 | U |
| 29727 | IC2556 | 12.33 | 13.58 | 13.49 | 0.55 | 58. | 214 | 251. | 2.400 | An |
| 29895 | IC2558 | / | 13.52 | / | 0.61 | 54. | 154 | 190. | 2.280 | An |
| 29898 | IC2559 | 12.01 | 12.97 | 13.03 | 0.41 | 69. | 256 | 275. | 2.439 | An |
| 29993 | IC2560 | 10.12 | 11.11 | 11.15 | 0.46 | 65. | 376 | 415. | 2.618 | An |
| 30308 | NGC3223 | 9.36 | 10.06 | 10.25 | 0.69 | 48. | 415 | 562. | 2.750 | An |
| 30534 | ESO317-023 | 11.12 | 11.70 | 11.96 | 0.47 | 64. | 363 | 403. | 2.605 | An |
| 30716 | ESO375-026 | 11.57 | 12.29 | 12.47 | 0.20 | 90. | 332 | 332. | 2.521 | An |
| 30774 | NGC3250C | / | 12.14 | / | 0.37 | 71. | 348 | 367. | 2.565 | An |
| 31053 | NGC3258C | / | 13.20 | / | 0.67 | 49. | 194 | 256. | 2.408 | An |
| 31058 | ESO436-032 | / | 13.77 | / | 0.51 | 61. | 253 | 288. | 2.459 | An |
| 31094 | NGC3258D | / | 12.34 | / | 0.42 | 68. | 219 | 236. | 2.374 | An |
| 31273 | NGC3281D | 11.92 | 12.94 | 12.97 | 0.22 | 85. | 255 | 256. | 2.408 | An |
| 31493 | ESO437-014 | 10.83 | 11.67 | 11.79 | 0.31 | 76. | 364 | 375. | 2.574 | An |
| 31761 | NGC3347A | 11.07 | 11.99 | 12.07 | 0.34 | 74. | 322 | 335. | 2.526 | An |
| 31875 | NGC3347B | 11.25 | 12.55 | 12.43 | 0.26 | 80. | 327 | 332. | 2.521 | An |
| 31926 | NGC3347 | 9.74 | 10.86 | 10.84 | 0.36 | 72. | 401 | 421. | 2.624 | An |
| 31995 | ESO318-004 | 10.69 | 11.70 | 11.73 | 0.23 | 83. | 382 | 385. | 2.585 | An |
| 32039 | ESO437-056 | 11.89 | 12.95 | 12.96 | 0.64 | 52. | 239 | 305. | 2.484 | An |
| 41010 | ESO322-017 | 13.62 | 15.11 | 14.89 | 0.40 | 69. | 147 | 157. | 2.196 | Ce |
| 42181 | NGC4575 | 10.93 | 11.56 | 11.79 | 0.62 | 53. | 263 | 328. | 2.516 | Ce |
| 42245 | ESO322-040 | / | 12.82 | / | 0.68 | 48. | 248 | 332. | 2.521 | Ce |
| 42271 | ESO322-042 | 12.15 | 13.36 | 13.29 | 0.31 | 76. | 226 | 233. | 2.367 | Ce |
| 42369 | NGC4603A | 11.66 | 12.47 | 12.61 | 0.39 | 70. | 270 | 287. | 2.458 | Ce |
| 42510 | NGC4603 | 9.84 | 10.67 | 10.80 | 0.64 | 52. | 353 | 450. | 2.653 | Ce |
| 42640 | NGC4603D | 11.62 | 12.56 | 12.63 | 0.62 | 53. | 235 | 293. | 2.467 | Ce |
| 42880 | ESO381-014 | 13.28 | 14.48 | 14.41 | 0.21 | 86. | 213 | 213. | 2.329 | Ce |
| 43073 | NGC4672 | 11.10 | 12.00 | 12.09 | 0.24 | 82. | 353 | 356. | 2.552 | Ce |
| 43282 | ESO268-044 | 12.27 | 13.01 | 13.18 | 0.47 | 64. | 247 | 274. | 2.438 | Ce |
| 43717 | ESO323-027 | 11.25 | 12.16 | 12.24 | 0.53 | 60. | 335 | 387. | 2.588 | Ce |
| 43893 | ESO323-038 | / | 12.19 | / | 0.49 | 63. | 263 | 295. | 2.469 | Ce |
| 44695 | ESO269-028 | 13.34 | 14.47 | 14.44 | 0.38 | 71. | 225 | 238. | 2.377 | Ce |
| 45573 | ESO269-052 | 13.93 | 15.52 | 15.25 | 0.17 | 90. | 213 | 213. | 2.328 | Ce |
| 70702 | IC1474 | 12.67 | 13.06 | 13.42 | 0.49 | 63. | 255 | 287. | 2.457 | Pe |
| 70803 | UGC12451 | 13.57 | 15.03 | 14.83 | 0.24 | 82. | 172 | 174. | 2.240 | Pe |
| 70880 | NGC7562A | 13.09 | 14.88 | 14.51 | 0.25 | 81. | 199 | 201. | 2.304 | Pe |
| 70927 | PGC070927 | 13.31 | 15.52 | 14.93 | 0.64 | 52. | 180 | 230. | 2.361 | Pe |
| 70981 | NGC7593 | 12.55 | 13.36 | 13.50 | 0.63 | 52. | 239 | 302. | 2.479 | Pe |
| 71034 | UGC12494 | 13.33 | 14.67 | 14.53 | 0.31 | 76. | 208 | 214. | 2.331 | Pe |
| 71049 | UGC12501 | 13.13 | 14.15 | 14.18 | 0.21 | 86. | 258 | 259. | 2.413 | Pe |
| 71051 | IC5309 | 12.16 | 13.13 | 13.18 | 0.49 | 63. | 270 | 303. | 2.482 | Pe |
| 71055 | NGC7608 | 12.24 | 13.22 | 13.27 | 0.27 | 79. | 279 | 284. | 2.453 | Pe |
| 71087 | NGC7610 | 12.28 | 13.31 | 13.33 | 0.61 | 54. | 241 | 298. | 2.474 | Pe |
| 71155 | UGC12535 | 13.47 | 14.27 | 14.41 | 0.23 | 83. | 187 | 188. | 2.275 | Pe |
| 71159 | PGC071159 | 13.45 | 14.61 | 14.56 | 0.43 | 67. | 148 | 161. | 2.206 | Pe |
| 71181 | NGC7631 | 11.40 | 12.48 | 12.48 | 0.42 | 68. | 366 | 395. | 2.597 | Pe |

| PGC | Name | $I_{ext}^{b,i,k}$ | $[3.6]_{ave}^{b,i,k,a}$ | $C_{[3.6]_{ave}}^{b,i,k,a}$ | b/a | Inc | W_{mx} | W_{mx}^i | W_{mxl}^i | S |
|-------|------------|-------------------|-------------------------|-----------------------------|------|-----|----------|------------|-------------|----|
| 71260 | UGC12562 | 14.30 | 15.72 | 15.54 | 0.27 | 79. | 153 | 156. | 2.192 | Pe |
| 71262 | UGC12561 | 13.87 | 15.29 | 15.11 | 0.32 | 75. | 184 | 190. | 2.279 | Pe |
| 93031 | PGC093031 | 15.15 | 16.47 | 16.34 | 0.21 | 86. | 139 | 139. | 2.144 | Pe |
| 31001 | ESO501-002 | 12.28 | 13.54 | 13.44 | 0.20 | 90. | 420 | 420. | 2.623 | H |
| 31154 | ESO436-034 | 11.06 | 11.70 | 11.93 | 0.23 | 83. | 533 | 537. | 2.730 | H |
| 31217 | NGC3285 | 10.18 | 11.17 | 11.21 | 0.51 | 61. | 545 | 621. | 2.793 | H |
| 31238 | ESO436-038 | / | 15.13 | / | 0.57 | 57. | 190 | 227. | 2.355 | H |
| 31242 | ESO436-039 | 11.92 | 12.50 | 12.76 | 0.20 | 90. | 412 | 412. | 2.615 | H |
| 31293 | NGC3285B | / | 12.90 | / | 0.63 | 52. | 241 | 304. | 2.483 | H |
| 31355 | ESO501-022 | / | 15.99 | / | 0.23 | 83. | 170 | 171. | 2.233 | H |
| 31360 | ESO437-004 | 11.78 | 12.62 | 12.74 | 0.50 | 62. | 322 | 364. | 2.561 | H |
| 31513 | NGC3312 | 9.52 | 11.20 | 10.88 | 0.34 | 74. | 584 | 608. | 2.784 | H |
| 31557 | ESO501-051 | 10.46 | 11.62 | 11.57 | 0.59 | 55. | 501 | 608. | 2.784 | H |
| 31590 | ESO437-018 | 12.80 | 13.60 | 13.74 | 0.33 | 74. | 300 | 311. | 2.493 | H |
| 31593 | ESO437-019 | 12.00 | 12.87 | 12.98 | 0.70 | 47. | 288 | 395. | 2.597 | H |
| 31626 | ESO437-022 | 12.94 | 14.17 | 14.09 | 0.27 | 79. | 284 | 289. | 2.461 | H |
| 31642 | ESO437-025 | 12.32 | 13.21 | 13.31 | 0.37 | 71. | 245 | 258. | 2.412 | H |
| 31677 | ESO437-030 | 10.79 | 11.76 | 11.81 | 0.22 | 85. | 428 | 430. | 2.633 | H |
| 31683 | ESO501-068 | 11.92 | 13.06 | 13.03 | 0.32 | 75. | 323 | 334. | 2.524 | H |
| 31690 | ESO437-031 | 13.15 | 14.43 | 14.32 | 0.62 | 53. | 203 | 254. | 2.404 | H |
| 31730 | ESO437-033 | / | 12.30 | / | 0.68 | 48. | 252 | 337. | 2.527 | H |
| 31732 | ESO437-034 | 14.21 | 16.12 | 15.68 | 0.39 | 70. | 170 | 181. | 2.257 | H |
| 31738 | ESO437-035 | 12.34 | 13.27 | 13.34 | 0.37 | 71. | 236 | 249. | 2.396 | H |
| 31805 | ESO501-075 | 11.36 | 12.36 | 12.40 | 0.50 | 62. | 322 | 364. | 2.561 | H |
| 31822 | ESO437-040 | / | 14.16 | / | 0.19 | 90. | 172 | 172. | 2.236 | H |
| 31829 | ESO501-078 | / | 14.11 | / | 0.22 | 85. | 253 | 254. | 2.405 | H |
| 31951 | ESO501-082 | 11.90 | 12.84 | 12.91 | 0.42 | 68. | 383 | 414. | 2.616 | H |
| 31981 | ESO437-054 | 13.20 | 13.62 | 13.96 | 0.21 | 86. | 275 | 276. | 2.440 | H |
| 2747 | UGC00485 | 12.00 | 13.20 | 13.13 | 0.11 | 90. | 344 | 344. | 2.537 | Pi |
| 2865 | UGC00501 | 12.21 | 13.09 | 13.19 | 0.17 | 90. | 375 | 375. | 2.574 | Pi |
| 2899 | UGC00509 | 13.88 | 15.27 | 15.11 | 0.45 | 66. | 210 | 230. | 2.362 | Pi |
| 2928 | UGC00511 | 13.42 | 14.80 | 14.64 | 0.22 | 85. | 269 | 270. | 2.432 | Pi |
| 3020 | UGC00525 | 12.96 | 14.21 | 14.12 | 0.50 | 62. | 199 | 225. | 2.352 | Pi |
| 3081 | UGC00536 | 13.63 | 15.20 | 14.94 | 0.50 | 62. | 219 | 248. | 2.394 | Pi |
| 3133 | UGC00542 | 11.60 | 12.70 | 12.69 | 0.24 | 82. | 366 | 369. | 2.568 | Pi |
| 3184 | PGC003184 | 13.24 | 14.56 | 14.43 | 0.39 | 70. | 281 | 299. | 2.476 | Pi |
| 3222 | UGC00557 | 13.24 | 14.72 | 14.51 | 0.43 | 67. | 258 | 280. | 2.447 | Pi |
| 3235 | UGC00556 | 12.57 | 12.44 | 13.07 | 0.53 | 60. | 366 | 423. | 2.626 | Pi |
| 3274 | UGC00565 | 13.36 | 14.44 | 14.44 | 0.30 | 77. | 222 | 228. | 2.358 | Pi |
| 3285 | PGC003285 | 14.08 | 15.39 | 15.27 | 0.54 | 59. | 218 | 254. | 2.404 | Pi |
| 3332 | UGC00575 | 13.22 | 14.22 | 14.26 | 0.20 | 90. | 276 | 276. | 2.441 | Pi |
| 3466 | PGC003466 | 13.73 | 14.92 | 14.86 | 0.61 | 54. | 179 | 221. | 2.345 | Pi |
| 3606 | IC0066 | 12.48 | 13.33 | 13.45 | 0.44 | 66. | 359 | 392. | 2.593 | Pi |
| 3611 | NGC0338 | 10.82 | 11.66 | 11.78 | 0.40 | 69. | 529 | 566. | 2.752 | Pi |
| 3664 | UGC00633 | 12.34 | 13.45 | 13.43 | 0.27 | 79. | 392 | 399. | 2.601 | Pi |
| 3773 | UGC00646 | 11.79 | 12.97 | 12.91 | 0.38 | 71. | 367 | 389. | 2.590 | Pi |
| 3866 | UGC00669 | 12.87 | 13.39 | 13.68 | 0.25 | 81. | 264 | 267. | 2.427 | Pi |
| 3903 | UGC00673 | 13.58 | 14.98 | 14.81 | 0.36 | 72. | 279 | 293. | 2.467 | Pi |
| 3950 | UGC00679 | 14.52 | 15.81 | 15.70 | 0.23 | 83. | 174 | 175. | 2.243 | Pi |
| 4110 | UGC00714 | 12.55 | 13.44 | 13.54 | 0.71 | 46. | 216 | 301. | 2.478 | Pi |
| 4210 | UGC00732 | 12.50 | 13.55 | 13.56 | 0.60 | 55. | 260 | 318. | 2.503 | Pi |
| 4561 | NGC0444 | 12.78 | 14.06 | 13.95 | 0.25 | 81. | 253 | 256. | 2.408 | Pi |
| 4563 | UGC00809 | 12.95 | 13.96 | 13.99 | 0.21 | 86. | 300 | 301. | 2.478 | Pi |

| PGC | Name | $I_{ext}^{b,i,k}$ | $[3.6]_{ave}^{b,i,k,a}$ | $C_{[3.6]_{ave}}^{b,i,k,a}$ | b/a | Inc | W_{mx} | W_{mx}^i | W_{mxl}^i | S |
|-------|------------|-------------------|-------------------------|-----------------------------|------|-----|----------|------------|-------------|----|
| 4596 | NGC0452 | 10.89 | 11.99 | 11.98 | 0.29 | 78. | 457 | 468. | 2.670 | Pi |
| 4735 | UGC00841 | 13.01 | 14.06 | 14.07 | 0.23 | 83. | 282 | 284. | 2.453 | Pi |
| 4971 | UGC00909 | 12.82 | 13.92 | 13.91 | 0.69 | 48. | 238 | 322. | 2.508 | Pi |
| 5061 | NGC0496 | 12.24 | 13.20 | 13.26 | 0.55 | 58. | 285 | 334. | 2.524 | Pi |
| 5132 | NGC0512 | 11.29 | 12.31 | 12.34 | 0.28 | 78. | 521 | 532. | 2.726 | Pi |
| 5284 | UGC00987 | 11.51 | 12.51 | 12.55 | 0.32 | 75. | 383 | 396. | 2.598 | Pi |
| 5344 | NGC0536 | 10.48 | 11.72 | 11.63 | 0.36 | 72. | 513 | 539. | 2.731 | Pi |
| 5440 | UGC01033 | 11.99 | 13.30 | 13.18 | 0.19 | 90. | 337 | 337. | 2.528 | Pi |
| 5450 | NGC0551 | 11.62 | 12.73 | 12.71 | 0.43 | 67. | 372 | 404. | 2.606 | Pi |
| 5702 | NGC0582 | 11.23 | 12.30 | 12.30 | 0.27 | 79. | 438 | 446. | 2.649 | Pi |
| 6045 | UGC01160 | 12.90 | 13.79 | 13.89 | 0.17 | 90. | 319 | 319. | 2.504 | Pi |
| 6189 | UGC01178 | 12.10 | 12.68 | 12.94 | 0.20 | 90. | 366 | 366. | 2.563 | Pi |
| 6473 | UGC01234 | 13.36 | 14.52 | 14.47 | 0.59 | 55. | 265 | 322. | 2.507 | Pi |
| 6502 | NGC0668 | 11.79 | 12.66 | 12.77 | 0.69 | 48. | 279 | 378. | 2.577 | Pi |
| 6607 | UGC01257 | 12.74 | 13.83 | 13.82 | 0.44 | 66. | 324 | 354. | 2.548 | Pi |
| 6799 | NGC0688 | 11.46 | 12.42 | 12.48 | 0.68 | 48. | 337 | 450. | 2.654 | Pi |
| 6851 | UGC01316 | 14.17 | 15.69 | 15.46 | 0.47 | 64. | 205 | 228. | 2.357 | Pi |
| 6865 | UGC01319 | 12.54 | 13.22 | 13.42 | 0.71 | 46. | 241 | 335. | 2.525 | Pi |
| 7066 | UGC01366 | 11.71 | 12.88 | 12.83 | 0.29 | 78. | 412 | 422. | 2.625 | Pi |
| 7097 | NGC0721 | 12.10 | 13.16 | 13.17 | 0.60 | 55. | 275 | 337. | 2.527 | Pi |
| 7254 | UGC01405 | 13.94 | 15.13 | 15.07 | 0.16 | 90. | 247 | 247. | 2.393 | Pi |
| 7300 | UGC01416 | 12.72 | 13.76 | 13.78 | 0.52 | 61. | 368 | 423. | 2.627 | Pi |
| 7387 | NGC0753 | 10.92 | 11.68 | 11.84 | 0.71 | 46. | 314 | 437. | 2.640 | Pi |
| 7504 | UGC01459 | 12.29 | 13.18 | 13.28 | 0.16 | 90. | 362 | 362. | 2.559 | Pi |
| 7646 | UGC01493 | 11.64 | 12.45 | 12.59 | 0.37 | 71. | 346 | 365. | 2.562 | Pi |
| 7847 | NGC0801 | 10.72 | 11.90 | 11.84 | 0.25 | 81. | 459 | 464. | 2.667 | Pi |
| 8185 | NGC0818 | 10.85 | 11.78 | 11.85 | 0.41 | 69. | 448 | 481. | 2.682 | Pi |
| 23146 | PGC023146 | 13.40 | 14.32 | 14.40 | 0.19 | 90. | 267 | 267. | 2.427 | Ca |
| 23169 | UGC04299 | 11.67 | 12.48 | 12.62 | 0.18 | 90. | 389 | 389. | 2.590 | Ca |
| 23289 | UGC04324 | 12.41 | 13.22 | 13.36 | 0.39 | 70. | 308 | 328. | 2.515 | Ca |
| 23338 | PGC023338 | 13.80 | 15.17 | 15.02 | 0.68 | 48. | 185 | 247. | 2.393 | Ca |
| 23347 | PGC023347 | 13.82 | 14.69 | 14.80 | 0.72 | 45. | 162 | 229. | 2.359 | Ca |
| 23374 | PGC023374 | 14.28 | 15.64 | 15.49 | 0.35 | 73. | 232 | 243. | 2.385 | Ca |
| 23420 | PGC023420 | 12.82 | 13.85 | 13.87 | 0.66 | 50. | 215 | 280. | 2.448 | Ca |
| 23567 | UGC04386 | 11.03 | 12.12 | 12.11 | 0.23 | 83. | 480 | 483. | 2.684 | Ca |
| 23661 | UGC04400 | 14.32 | 15.76 | 15.57 | 0.20 | 90. | 214 | 214. | 2.330 | Ca |
| 23662 | UGC04399 | 13.37 | 14.57 | 14.50 | 0.36 | 72. | 232 | 244. | 2.387 | Ca |
| 23748 | UGC04424 | 14.27 | 15.80 | 15.56 | 0.27 | 79. | 203 | 207. | 2.315 | Ca |
| 42820 | ESO574-023 | 14.49 | 15.88 | 15.72 | 0.28 | 78. | 190 | 194. | 2.288 | Ca |
| 42726 | UGC07877 | 13.37 | 14.48 | 14.46 | 0.28 | 78. | 321 | 328. | 2.515 | Co |
| 42765 | UGC07890 | 13.49 | 14.43 | 14.50 | 0.67 | 49. | 233 | 308. | 2.488 | Co |
| 43142 | UGC07955 | 12.78 | 13.84 | 13.85 | 0.18 | 90. | 361 | 361. | 2.558 | Co |
| 43278 | PGC043278 | 13.05 | 13.68 | 13.91 | 0.26 | 80. | 311 | 316. | 2.499 | Co |
| 43359 | UGC07978 | 12.98 | 13.98 | 14.02 | 0.63 | 52. | 295 | 372. | 2.571 | Co |
| 43575 | UGC08004 | 13.23 | 14.48 | 14.39 | 0.39 | 70. | 285 | 303. | 2.482 | Co |
| 43686 | UGC08013 | 13.15 | 14.53 | 14.37 | 0.29 | 78. | 365 | 374. | 2.573 | Co |
| 43726 | UGC08017 | 12.05 | 12.63 | 12.89 | 0.37 | 71. | 521 | 549. | 2.740 | Co |
| 43840 | PGC043840 | 13.78 | 14.67 | 14.77 | 0.43 | 67. | 286 | 310. | 2.492 | Co |
| 43863 | UGC08025 | 11.63 | 12.73 | 12.72 | 0.19 | 90. | 505 | 505. | 2.703 | Co |
| 44416 | PGC044416 | 13.19 | 14.06 | 14.17 | 0.32 | 75. | 260 | 269. | 2.430 | Co |
| 44795 | IC0842 | 12.51 | 13.53 | 13.56 | 0.49 | 63. | 368 | 414. | 2.617 | Co |
| 44921 | IC4088 | 12.19 | 13.31 | 13.29 | 0.30 | 77. | 467 | 480. | 2.681 | Co |
| 45097 | UGC08161 | 12.77 | 13.57 | 13.71 | 0.43 | 67. | 355 | 385. | 2.586 | Co |

| PGC | Name | $I_{ext}^{b,i,k}$ | $[3.6]_{ave}^{b,i,k,a}$ | $C_{[3.6]_{ave}}^{b,i,k,a}$ | b/a | Inc | W_{mx} | W_{mx}^i | W_{mxl}^i | S |
|-------|-----------|-------------------|-------------------------|-----------------------------|------|-----|----------|------------|-------------|----|
| 45366 | UGC08195 | 14.00 | 15.27 | 15.17 | 0.17 | 90. | 233 | 233. | 2.367 | Co |
| 45549 | IC4202 | 11.77 | 12.93 | 12.88 | 0.18 | 90. | 524 | 524. | 2.719 | Co |
| 45580 | UGC08229 | 12.35 | 13.14 | 13.29 | 0.53 | 60. | 342 | 395. | 2.597 | Co |
| 45668 | UGC08244 | 13.86 | 15.22 | 15.07 | 0.38 | 71. | 238 | 252. | 2.402 | Co |
| 45742 | IC4210 | 13.40 | 14.36 | 14.42 | 0.64 | 52. | 227 | 289. | 2.462 | Co |
| 45757 | NGC5004A | 12.48 | 13.22 | 13.39 | 0.43 | 67. | 336 | 365. | 2.562 | Co |
| 45905 | UGC08294 | 13.75 | 15.04 | 14.93 | 0.66 | 50. | 195 | 254. | 2.405 | Co |
| 46028 | UGC08317 | 13.09 | 14.24 | 14.20 | 0.43 | 67. | 276 | 300. | 2.476 | Co |
| 46427 | NGC5081 | 11.46 | 12.72 | 12.62 | 0.38 | 71. | 530 | 561. | 2.749 | Co |
| 10913 | UGC02364 | 12.82 | 13.93 | 13.91 | 0.35 | 73. | 323 | 338. | 2.529 | A4 |
| 10943 | UGC02375 | 12.20 | 13.33 | 13.30 | 0.30 | 77. | 440 | 452. | 2.655 | A4 |
| 11074 | UGC02405 | 12.36 | 13.49 | 13.46 | 0.37 | 71. | 400 | 422. | 2.625 | A4 |
| 11102 | UGC02415 | 13.34 | 14.13 | 14.28 | 0.35 | 73. | 323 | 338. | 2.529 | A4 |
| 11136 | UGC02423 | 12.53 | 13.42 | 13.52 | 0.33 | 74. | 382 | 396. | 2.598 | A4 |
| 11255 | UGC02444 | 12.51 | 13.05 | 13.33 | 0.62 | 53. | 361 | 451. | 2.654 | A4 |
| 11306 | UGC02454 | 12.95 | 14.05 | 14.04 | 0.22 | 85. | 359 | 361. | 2.557 | A4 |
| 35347 | NGC3697 | 11.36 | 12.58 | 12.50 | 0.32 | 75. | 504 | 521. | 2.717 | A1 |
| 35622 | PGC035622 | 13.70 | 14.67 | 14.72 | 0.58 | 56. | 243 | 292. | 2.466 | A1 |
| 35942 | UGC06583 | 12.79 | 13.43 | 13.66 | 0.59 | 55. | 319 | 387. | 2.588 | A1 |
| 35978 | PGC035978 | 13.54 | 14.67 | 14.64 | 0.49 | 63. | 261 | 293. | 2.467 | A1 |
| 36132 | PGC036132 | 13.33 | 14.30 | 14.35 | 0.62 | 53. | 247 | 308. | 2.489 | A1 |
| 36349 | PGC036349 | 12.70 | 13.20 | 13.50 | 0.56 | 58. | 327 | 387. | 2.587 | A1 |
| 36371 | PGC036371 | 12.75 | 13.73 | 13.78 | 0.46 | 65. | 292 | 323. | 2.509 | A1 |
| 36431 | UGC06686 | 11.85 | 13.15 | 13.03 | 0.16 | 90. | 398 | 398. | 2.600 | A1 |
| 36466 | UGC06697 | 11.85 | 13.01 | 12.96 | 0.20 | 90. | 557 | 557. | 2.746 | A1 |
| 36604 | NGC3861 | 11.24 | 12.34 | 12.33 | 0.57 | 57. | 459 | 547. | 2.738 | A1 |
| 36683 | PGC036683 | 13.26 | 14.10 | 14.22 | 0.39 | 70. | 265 | 282. | 2.450 | A1 |
| 36706 | NGC3884 | 11.17 | 12.08 | 12.16 | 0.72 | 45. | 462 | 652. | 2.814 | A1 |
| 36778 | PGC036778 | 13.59 | 14.82 | 14.74 | 0.23 | 83. | 357 | 359. | 2.556 | A1 |
| 36779 | PGC036779 | 12.83 | 13.99 | 13.94 | 0.37 | 71. | 379 | 400. | 2.602 | A1 |
| 36856 | PGC036856 | 12.93 | 13.77 | 13.89 | 0.27 | 79. | 366 | 372. | 2.571 | A1 |
| 37143 | UGC06837 | 13.84 | 14.57 | 14.75 | 0.18 | 90. | 331 | 331. | 2.520 | A1 |
| 37264 | NGC3947 | 11.76 | 12.65 | 12.75 | 0.57 | 57. | 386 | 460. | 2.663 | A1 |
| 37288 | NGC3951 | 12.15 | 12.95 | 13.09 | 0.49 | 63. | 371 | 417. | 2.620 | A1 |
| 37409 | UGC06891 | 12.73 | 13.84 | 13.82 | 0.26 | 80. | 344 | 349. | 2.543 | A1 |
| 37463 | PGC037463 | 13.47 | 14.63 | 14.58 | 0.37 | 71. | 293 | 309. | 2.490 | A1 |
| 71597 | UGC12631 | 12.48 | 13.48 | 13.52 | 0.32 | 75. | 459 | 475. | 2.676 | A2 |
| 71795 | UGC12678 | 12.46 | 13.67 | 13.60 | 0.22 | 85. | 505 | 507. | 2.705 | A2 |
| 71880 | UGC12701 | 13.67 | 14.29 | 14.53 | 0.26 | 80. | 348 | 353. | 2.548 | A2 |
| 72024 | UGC12721 | 12.38 | 13.39 | 13.42 | 0.44 | 66. | 394 | 430. | 2.633 | A2 |
| 72115 | PGC072115 | 12.64 | 12.76 | 13.26 | 0.51 | 61. | 425 | 484. | 2.685 | A2 |
| 72169 | PGC072169 | 13.00 | 13.63 | 13.86 | 0.24 | 82. | 377 | 381. | 2.580 | A2 |
| 72188 | UGC12746 | 12.18 | 12.84 | 13.05 | 0.19 | 90. | 451 | 451. | 2.654 | A2 |
| 72233 | UGC12755 | 11.90 | 13.02 | 13.00 | 0.53 | 60. | 503 | 581. | 2.764 | A2 |
| 72328 | NGC7747 | 11.61 | 12.64 | 12.66 | 0.40 | 69. | 531 | 568. | 2.754 | A2 |
| 72411 | PGC072411 | 12.73 | 13.67 | 13.74 | 0.45 | 66. | 367 | 403. | 2.605 | A2 |
| 72438 | PGC072438 | 13.01 | 13.68 | 13.89 | 0.32 | 75. | 398 | 412. | 2.614 | A2 |
| 72665 | PGC072665 | 13.44 | 14.10 | 14.31 | 0.48 | 64. | 302 | 337. | 2.528 | A2 |
| 72751 | PGC072751 | 13.41 | 14.13 | 14.31 | 0.59 | 55. | 262 | 318. | 2.502 | A2 |
| 72784 | PGC072784 | 13.40 | 14.29 | 14.39 | 0.48 | 64. | 344 | 384. | 2.585 | A2 |
| 72968 | PGC072968 | 13.69 | 14.81 | 14.79 | 0.27 | 79. | 321 | 327. | 2.514 | A2 |
| 85512 | PGC085512 | 14.93 | 15.87 | 15.94 | 0.55 | 58. | 234 | 275. | 2.439 | A2 |
| 85551 | PGC085551 | 14.02 | 14.47 | 14.79 | 0.47 | 64. | 338 | 375. | 2.574 | A2 |

| PGC | Name | $I_{ext}^{b,i,k}$ | $[3.6]_{ave}^{b,i,k,a}$ | $C_{[3.6]_{ave}}^{b,i,k,a}$ | b/a | Inc | W_{mx} | W_{mx}^i | W_{mxl}^i | S |
|---------|------------|-------------------|-------------------------|-----------------------------|------|-----|----------|------------|-------------|----|
| 91814 | PGC091814 | 13.81 | 14.85 | 14.87 | 0.20 | 90. | 239 | 239. | 2.378 | A2 |
| 169662 | PGC169662 | 13.78 | 14.77 | 14.81 | 0.26 | 80. | 346 | 351. | 2.545 | A2 |
| 1809186 | PGC1809186 | 13.90 | 14.91 | 14.94 | 0.36 | 72. | 281 | 295. | 2.470 | A2 |

TABLE B.2: Calibrator parameters for the control Tully-Fisher relation: (1) PGC number, (2) Common Name, (3) I band corrected magnitude, mag, (4) [3.6] averaged corrected magnitude, mag, (5) Pseudo [3.6] magnitude, mag, (6) Axial Ratio, (7) Inclination, degrees, (8) linewidth not corrected for inclination, km s⁻¹, (9) linewidth corrected for inclination, km s⁻¹, (10) Logarithm of the inclination corrected linewidth, (11) Sample ZP Zeropoint Calibrators, V Virgo, F Fornax, U Ursa Major, An Antlia, Ce Centaurus30, Pe Pegasus, H Hydra, Pi Pisces, Ca Cancer, Co Coma, A4 Abell 400, A1 Abell 1367 and A2 Abell 2634 and 2666

Appendix C

Distance Estimates

| PGC Name | l | b | sgl | sgb | v_{hel} | v_{mod} | t | b/a | w_{max} | $\log w_{max}^2$ | I | $I^{b,i,k}$ | [3.6] | [3.6]* | $C_{[3.6]}$ | M_C | $M_{[3.6]}$ | μ_C | dC | $\mu_{[3.6]}$ | $d_{[3.6]}$ |
|----------------|----------|----------|----------|----------|-----------|-----------|-----|------|-----------|------------------|-------|-------------|-------|--------|-------------|--------|-------------|---------|------|---------------|-------------|
| 218 NGC07814 | 106.4089 | -45.1745 | 309.0614 | 16.4026 | 1051 | 695 | 2.0 | 0.20 | 455 | 2.658 | 9.18 | 8.63 | 9.61 | 9.57 | 9.46 | -21.75 | -21.85 | 31.20 | 17.4 | 31.42 | 19.2 |
| 255 UGC00017 | 106.2149 | -46.0989 | 308.1422 | 16.0958 | 878 | 521 | 9.1 | 0.63 | 98 | 2.092 | 13.85 | 14.07 | 14.78 | 14.87 | 14.83 | -16.60 | -16.33 | 31.43 | 19.3 | 31.20 | 17.4 |
| 279 NGC007817 | 108.2283 | -40.7605 | 313.8141 | 17.1420 | 2311 | 1970 | 4.1 | 0.26 | 411 | 2.620 | 10.62 | 10.22 | 10.84 | 10.87 | 10.91 | -21.40 | -21.48 | 32.31 | 29.0 | 32.36 | 29.7 |
| 527 UGC000054 | 114.0896 | -20.3652 | 335.8192 | 19.2667 | 4249 | 3993 | 6.0 | 0.20 | 192 | 2.283 | / | / | 15.96 | 16.04 | / | -18.19 | / | / | / | 34.32 | 73.1 |
| 627 AGC020097 | 13.9928 | -80.1378 | 264.5900 | 1.9316 | 1497 | 1214 | 4.8 | 0.21 | 158 | 2.200 | 12.91 | 12.94 | 13.92 | 14.00 | 13.82 | -17.58 | -17.37 | 31.40 | 19.0 | 31.38 | 18.8 |
| 698 NGC00023 | 111.3675 | -36.0132 | 319.3855 | 16.7229 | 4568 | 4275 | 1.2 | 0.68 | 367 | 2.692 | 10.83 | 10.90 | 11.20 | 11.31 | 11.47 | -22.06 | -22.19 | 33.56 | 51.6 | 33.54 | 51.1 |
| 701 AGC020114 | 43.6860 | -80.4343 | 269.3872 | 3.2262 | 554 | 250 | 5.1 | 0.30 | 202 | 2.317 | 10.40 | 10.38 | 11.43 | 11.44 | 11.27 | -18.64 | -18.52 | 29.91 | 9.6 | 29.96 | 9.8 |
| 767 NGC00021 | 113.2524 | -28.7536 | 327.1050 | 17.6437 | 4770 | 4500 | 4.0 | 0.47 | 382 | 2.627 | 12.27 | 12.17 | 12.78 | 12.86 | 12.88 | -21.47 | -21.55 | 34.41 | 76.3 | 34.52 | 80.2 |
| 924 UGC00132 | 108.9883 | -48.8920 | 306.4453 | 13.1609 | 1696 | 1345 | 7.9 | 0.32 | 140 | 2.161 | / | / | 14.48 | 14.56 | / | / | -17.00 | / | / | 31.56 | 20.5 |
| 963 UGC00139 | 102.8519 | -62.1619 | 292.9641 | 9.5361 | 3971 | 3652 | 5.1 | 0.43 | 287 | 2.493 | 12.89 | 12.83 | 13.44 | 13.52 | 13.54 | -20.25 | -20.25 | 33.83 | 58.3 | 33.83 | 58.4 |
| 1315 UGC00196 | 117.5333 | -15.1136 | 341.9918 | 17.2721 | 5150 | 4942 | 5.3 | 0.65 | 256 | 2.519 | / | / | 13.09 | 13.19 | / | -20.49 | / | / | / | 33.74 | 56.0 |
| 1525 UGC00231 | 113.4792 | -45.8820 | 310.5250 | 11.6066 | 843 | 495 | 5.9 | 0.20 | 204 | 2.310 | 12.19 | 12.02 | 12.90 | 12.95 | 12.84 | -18.58 | -18.45 | 31.42 | 19.2 | 31.40 | 19.1 |
| 1651 AGC020302 | 340.4905 | -81.5678 | 262.2390 | -2.9613 | 1831 | 1572 | 3.9 | 0.35 | 207 | 2.335 | 12.58 | 12.60 | 13.65 | 13.73 | 13.52 | -18.81 | -18.70 | 32.34 | 29.4 | 32.45 | 30.9 |
| 1658 UGC000256 | 118.9045 | -12.6493 | 344.7872 | 16.4431 | 5173 | 4978 | 4.0 | 0.20 | 331 | 2.520 | 13.02 | 12.45 | 12.70 | 12.74 | 12.96 | -20.49 | -20.50 | 33.49 | 49.8 | 33.28 | 45.3 |
| 1665 UGC00260 | 113.4479 | -50.8383 | 305.8528 | 9.7393 | 2134 | 1792 | 5.8 | 0.23 | 254 | 2.408 | 12.35 | 12.09 | 12.67 | 12.71 | 12.76 | -19.47 | -19.41 | 32.24 | 28.0 | 32.13 | 26.7 |
| 1713 UGC00272 | 109.6294 | -63.4603 | 293.4407 | 6.2135 | 3917 | 3604 | 6.4 | 0.40 | 236 | 2.402 | 13.58 | 13.58 | 14.65 | 14.74 | 14.51 | -19.42 | -19.35 | 33.98 | 62.5 | 34.17 | 68.4 |
| 1851 NGC000134 | 338.3093 | -82.3778 | 262.8701 | -3.5542 | 1583 | 1322 | 4.0 | 0.28 | 455 | 2.666 | 9.20 | 8.85 | 9.29 | 9.32 | 9.45 | -21.82 | -21.93 | 31.27 | 18.0 | 31.26 | 17.9 |
| 1921 UGC00312 | 114.4661 | -54.0753 | 303.0705 | 7.9214 | 4371 | 4065 | 8.0 | 0.42 | 285 | 2.488 | 12.71 | 12.65 | 13.44 | 13.53 | 13.45 | -20.20 | -20.19 | 33.69 | 54.6 | 33.78 | 57.1 |
| 1970 UGC00320 | 113.4616 | -59.9491 | 297.4139 | 6.1096 | 2394 | 2058 | 6.1 | 0.20 | 149 | 2.173 | 14.77 | 14.81 | 15.85 | 15.94 | 15.72 | -17.34 | -17.12 | 33.08 | 41.3 | 33.08 | 41.4 |
| 1977 IC0001553 | 51.7638 | -85.5297 | 270.3423 | -1.8628 | 2929 | 2655 | 7.0 | 0.22 | 256 | 2.410 | 12.82 | 12.63 | 12.87 | 12.93 | 13.15 | -19.49 | -19.43 | 32.65 | 33.9 | 32.38 | 29.9 |
| 2052 AGC020385 | 21.8940 | -86.1300 | 268.3344 | -2.8241 | 1580 | 1301 | 3.4 | 0.47 | 317 | 2.548 | 10.43 | 10.42 | 10.82 | 10.89 | 11.02 | -20.74 | -20.78 | 31.77 | 22.6 | 31.67 | 21.6 |
| 2071 IC0001555 | 354.0143 | -85.2990 | 266.2225 | -3.5025 | 1530 | 1258 | 7.0 | 0.57 | 115 | 2.137 | 13.16 | 13.40 | 14.34 | 14.44 | 14.27 | -17.01 | -16.76 | 31.28 | 18.0 | 31.20 | 17.4 |
| 2142 IC0001558 | 58.6007 | -86.0752 | 270.7645 | -2.4699 | 1551 | 1264 | 9.0 | 0.52 | 110 | 2.103 | 12.01 | 12.25 | 13.24 | 13.34 | 13.15 | -16.69 | -16.43 | 29.84 | 9.3 | 29.77 | 9.0 |
| 2437 AGC400333 | 111.5732 | -76.5046 | 282.1291 | -0.3496 | 1638 | 1322 | 3.1 | 0.61 | 273 | 2.528 | 9.99 | 10.09 | 10.69 | 10.78 | 10.79 | -20.57 | -20.59 | 31.36 | 18.7 | 31.37 | 18.8 |
| 2445 ES079-005 | 304.9496 | -53.6455 | 233.6427 | -12.4376 | 1712 | 1607 | 7.0 | 0.41 | 148 | 2.202 | 12.72 | 12.86 | 13.77 | 13.86 | 13.71 | -17.60 | -17.40 | 31.32 | 18.3 | 31.26 | 17.9 |
| 2479 UGC00438 | 120.1021 | -37.3172 | 320.3882 | 9.6661 | 4555 | 4276 | 5.0 | 0.70 | 346 | 2.675 | 11.13 | 11.23 | 11.63 | 11.74 | 11.85 | -21.90 | -22.02 | 33.79 | 57.4 | 33.82 | 58.1 |
| 2492 PG0002492 | 110.1297 | -79.4921 | 279.3344 | -1.4478 | 1552 | 1243 | 2.0 | 0.68 | 134 | 2.253 | / | / | 14.05 | 14.15 | / | -17.90 | / | / | / | 32.06 | 25.8 |
| 2526 AGC020471 | 109.1648 | -80.7868 | 278.1159 | -1.9168 | 1554 | 1249 | 6.0 | 0.20 | 187 | 2.272 | 13.06 | 12.99 | 14.45 | 14.52 | 14.09 | -18.23 | -18.08 | 32.34 | 29.3 | 32.62 | 33.4 |
| 2699 UGC00477 | 121.2400 | -43.3647 | 314.7419 | 7.1900 | 2650 | 2331 | 7.9 | 0.20 | 223 | 2.348 | 13.20 | 13.01 | 14.23 | 14.29 | 14.00 | -18.93 | -18.83 | 32.95 | 38.9 | 33.15 | 42.7 |
| 2747 UGC00485 | 121.8318 | -32.5215 | 325.4576 | 9.5158 | 5248 | 4999 | 6.1 | 0.20 | 344 | 2.537 | 13.04 | 12.59 | 13.18 | 13.23 | 13.27 | -20.64 | -20.67 | 33.96 | 62.0 | 33.96 | 62.1 |
| 2805 PG0002805 | 119.9027 | -72.7498 | 286.4339 | -0.9546 | 1342 | 1021 | 6.7 | 0.20 | 135 | 2.130 | 13.30 | 13.37 | 14.52 | 14.61 | 14.34 | -16.95 | -16.70 | 31.28 | 18.1 | 31.31 | 18.2 |
| 2865 UGC00501 | 122.2883 | -34.6508 | 323.4566 | 8.6359 | 5103 | 4846 | 5.8 | 0.20 | 375 | 2.574 | 13.10 | 12.62 | 13.06 | 13.10 | 13.23 | -20.98 | -21.03 | 34.27 | 71.4 | 34.22 | 69.8 |
| 2899 UGC00509 | 122.5147 | -31.2692 | 326.8292 | 9.2455 | 5157 | 4910 | 5.9 | 0.46 | 210 | 2.366 | 14.23 | 14.24 | 15.17 | 15.27 | 15.11 | -19.09 | -19.00 | 34.25 | 70.9 | 34.36 | 74.4 |
| 2928 UGC00511 | 122.6152 | -31.1398 | 326.9768 | 9.1915 | 4602 | 4342 | 5.9 | 0.22 | 269 | 2.432 | 14.05 | 13.76 | 14.74 | 14.80 | 14.64 | -19.69 | -19.64 | 34.39 | 75.4 | 34.55 | 81.3 |
| 2964 P0002964 | 122.7750 | -34.1707 | 324.0245 | 8.3598 | 4992 | 4735 | 2.8 | 0.35 | 186 | 2.289 | / | / | 14.82 | 14.91 | / | -18.25 | / | / | / | 33.20 | 43.6 |
| 2992 UGC00521 | 122.8400 | -50.8471 | 307.7917 | 4.1335 | 682 | 346 | 9.9 | 0.68 | 109 | 2.163 | / | / | 15.47 | 15.55 | / | -17.02 | / | / | / | 32.59 | 33.0 |

| PGC Name | l | b | sgl | sgb | v_{hel} | v_{mod} | t | b/a | w _{max} | log w _{max} | I | I* | [3.6] | [3.6]* | C _[3.6] | M _C | M _[3.6] | μ_C | d _C | $\mu_{[3.6]}$ | d _[3.6] | |
|----------------|----------|----------|----------|----------|-----------|-----------|-----|------|------------------|----------------------|-------|-------|-------|--------|--------------------|----------------|--------------------|---------|----------------|---------------|--------------------|------|
| 3020 UGC00525 | 122.9675 | -33.1553 | 325.0605 | 8.4396 | 4941 | 4685 | 3.5 | 0.42 | 199 | 2.331 | 13.25 | 13.25 | 14.11 | 14.21 | 14.08 | -18.78 | -18.66 | 32.88 | 37.6 | 32.89 | 37.9 | |
| 3062 PGC003062 | 123.4703 | -66.8380 | 292.4467 | -0.4180 | 1409 | 1082 | 6.8 | 0.33 | 144 | 2.175 | / | / | 15.19 | 15.27 | / | / | -17.13 | / | / | / | 32.41 | 30.4 |
| 3081 UGC00536 | 123.2326 | -33.6638 | 324.6116 | 8.1076 | 4862 | 4604 | 3.0 | 0.51 | 219 | 2.398 | 13.94 | 13.98 | 15.10 | 15.20 | 14.94 | -19.38 | -19.31 | 34.38 | 75.2 | 34.62 | 84.0 | |
| 3089 NGC000289 | 299.1260 | -85.9130 | 266.0845 | -7.5839 | 1628 | 1371 | 4.0 | 0.68 | 271 | 2.556 | 10.26 | 10.40 | 10.42 | 10.51 | 10.83 | -20.82 | -20.86 | 31.65 | 21.4 | 31.37 | 18.8 | |
| 3133 UGC00542 | 123.4573 | -33.5994 | 324.7178 | 7.9401 | 4516 | 4250 | 3.4 | 0.23 | 366 | 2.567 | 12.33 | 11.94 | 12.65 | 12.70 | 12.68 | -20.92 | -20.96 | 33.63 | 53.3 | 33.72 | 55.5 | |
| 3183 P0003183 | 123.1261 | 10.2141 | 8.9127 | 15.0819 | 4775 | 4692 | 1.0 | 0.58 | 311 | 2.573 | / | / | 12.06 | 12.04 | / | / | -21.02 | / | / | / | 33.09 | 41.6 |
| 3184 P0003184 | 123.6086 | -32.5226 | 325.8063 | 8.0579 | 6783 | 6584 | 4.4 | 0.41 | 281 | 2.479 | 13.71 | 13.60 | 14.47 | 14.57 | 14.44 | -20.12 | -20.10 | 34.63 | 84.3 | 34.79 | 90.7 | |
| 3218 UGC00549 | 123.6591 | -26.1022 | 332.1612 | 9.3882 | 6061 | 5856 | 5.9 | 0.23 | 220 | 2.346 | 14.69 | 14.52 | 15.31 | 15.40 | 15.32 | -18.91 | -18.80 | 34.29 | 72.0 | 34.29 | 72.2 | |
| 3222 UGC00557 | 123.7695 | -31.5005 | 326.8437 | 8.1498 | 4513 | 4253 | 3.5 | 0.46 | 258 | 2.454 | 13.64 | 13.59 | 14.63 | 14.72 | 14.51 | -19.89 | -19.86 | 34.46 | 78.1 | 34.69 | 86.6 | |
| 3235 UGC00556 | 123.8226 | -33.6193 | 324.7672 | 7.6391 | 4633 | 4371 | 1.5 | 0.53 | 366 | 2.626 | 12.96 | 12.90 | 12.35 | 12.44 | 13.05 | -21.46 | -21.54 | 34.58 | 82.5 | 34.05 | 64.6 | |
| 3250 NGC000298 | 125.5672 | -70.1866 | 289.3897 | -1.9859 | 1753 | 1435 | 5.9 | 0.33 | 193 | 2.302 | / | / | 13.74 | 13.80 | / | / | -18.37 | / | / | / | 32.18 | 27.3 |
| 3260 NGC00296 | 123.8518 | -31.3229 | 327.0342 | 8.1199 | 5464 | 5228 | 3.1 | 0.36 | 455 | 2.679 | 11.35 | 11.05 | 11.53 | 11.60 | 11.69 | -21.94 | -22.06 | 33.67 | 54.1 | 33.72 | 55.5 | |
| 3274 UGC00565 | 123.9073 | -31.1875 | 327.1782 | 8.1028 | 5645 | 5415 | 5.8 | 0.31 | 222 | 2.360 | 13.82 | 13.71 | 14.35 | 14.44 | 14.44 | -19.03 | -18.94 | 33.50 | 50.2 | 33.43 | 48.5 | |
| 3285 P0003285 | 123.9815 | -32.4652 | 325.9327 | 7.7637 | 6678 | 6477 | 3.0 | 0.52 | 218 | 2.400 | 14.39 | 14.42 | 15.28 | 15.39 | 15.26 | -19.40 | -19.33 | 34.73 | 88.5 | 34.84 | 93.0 | |
| 3332 UGC00575 | 124.1204 | -31.7869 | 326.6268 | 7.7961 | 4658 | 4401 | 4.0 | 0.23 | 276 | 2.444 | 13.90 | 13.62 | 14.16 | 14.22 | 14.28 | -19.80 | -19.76 | 34.13 | 67.1 | 34.06 | 64.8 | |
| 3466 P0003466 | 124.6031 | -32.1453 | 326.3619 | 7.3194 | 4722 | 4467 | 3.4 | 0.64 | 179 | 2.361 | 13.98 | 14.09 | 14.81 | 14.92 | 14.86 | -19.04 | -18.95 | 33.95 | 61.6 | 33.93 | 61.2 | |
| 3526 AGC020704 | 134.9897 | -81.4377 | 278.6006 | -5.8952 | 2000 | 1711 | 4.2 | 0.44 | 271 | 2.471 | 11.47 | 11.46 | 12.32 | 12.40 | 12.28 | -20.04 | -20.03 | 32.34 | 29.3 | 32.43 | 30.7 | |
| 3543 ES541-005 | 138.6985 | -83.2087 | 276.8327 | -6.4326 | 1955 | 1671 | 8.0 | 0.46 | 152 | 2.225 | / | / | 15.36 | 15.46 | / | / | -17.62 | / | / | / | 33.11 | 41.8 |
| 3572 AGC400534 | 129.1303 | -70.3488 | 289.4716 | -3.1969 | 1649 | 1334 | 6.7 | 0.62 | 225 | 2.449 | 10.78 | 10.78 | 11.44 | 11.46 | 11.49 | -19.84 | -19.81 | 31.33 | 18.4 | 31.27 | 18.0 | |
| 3603 UGC00622 | 124.4947 | -14.8491 | 343.5389 | 10.7117 | 2717 | 2480 | 5.8 | 0.60 | 247 | 2.482 | 12.24 | 12.16 | 12.52 | 12.58 | 12.74 | -20.15 | -20.13 | 32.90 | 38.0 | 32.74 | 35.3 | |
| 3606 IC000066 | 125.2381 | -32.0339 | 326.5847 | 6.8165 | 4827 | 4577 | 1.0 | 0.40 | 359 | 2.584 | 12.96 | 12.79 | 13.24 | 13.32 | 13.42 | -21.08 | -21.13 | 34.56 | 81.8 | 34.56 | 81.5 | |
| 3611 UGC00624 | 125.2612 | -32.1615 | 326.4630 | 6.7711 | 4797 | 4546 | 2.0 | 0.39 | 529 | 2.750 | 11.44 | 11.15 | 11.60 | 11.66 | 11.77 | -22.59 | -22.76 | 34.42 | 76.6 | 34.52 | 80.2 | |
| 3635 UGC00625 | 124.5858 | -15.1592 | 343.2426 | 10.5735 | 2619 | 2380 | 4.0 | 0.32 | 332 | 2.536 | 11.44 | 11.07 | 11.77 | 11.80 | 11.80 | -20.64 | -20.66 | 32.44 | 30.8 | 32.48 | 31.3 | |
| 3639 UGC00628 | 125.9881 | -43.3399 | 315.6107 | 3.8478 | 5471 | 5217 | 8.7 | 0.54 | 219 | 2.406 | / | / | 15.05 | 15.16 | / | / | -19.40 | / | / | / | 34.66 | 85.7 |
| 3664 UGC00633 | 125.4057 | -31.3165 | 327.3214 | 6.8233 | 5596 | 5368 | 3.0 | 0.27 | 392 | 2.601 | 13.06 | 12.69 | 13.40 | 13.46 | 13.43 | -21.23 | -21.30 | 34.74 | 88.9 | 34.88 | 94.8 | |
| 3667 UGC00634 | 127.2641 | -55.1618 | 304.2234 | 0.5316 | 2214 | 1893 | 8.8 | 0.49 | 133 | 2.175 | 13.75 | 13.89 | 14.91 | 15.00 | 14.80 | -17.35 | -17.13 | 32.15 | 27.0 | 32.14 | 26.8 | |
| 3743 NGC000360 | 301.0396 | -51.4762 | 231.7545 | -15.0811 | 2310 | 2230 | 4.4 | 0.20 | 361 | 2.558 | 11.27 | 10.87 | 11.60 | 11.64 | 11.61 | -20.83 | -20.87 | 32.46 | 31.0 | 32.52 | 32.0 | |
| 3773 UGC00646 | 125.8793 | -30.5657 | 328.1438 | 6.5752 | 5298 | 5065 | 2.5 | 0.37 | 367 | 2.588 | 12.36 | 12.13 | 12.90 | 12.98 | 12.91 | -21.11 | -21.17 | 34.08 | 65.3 | 34.23 | 70.3 | |
| 3853 P0003853 | 132.3600 | -68.8341 | 291.1376 | -4.0895 | 1095 | 779 | 7.0 | 0.69 | 164 | 2.346 | 10.55 | 10.58 | 11.46 | 11.53 | 11.41 | -18.91 | -18.81 | 30.32 | 11.6 | 30.34 | 11.7 | |
| 3855 PGC003855 | 132.4295 | -68.8980 | 291.0770 | -4.1221 | 2417 | 2111 | 8.8 | 0.25 | 148 | 2.175 | / | / | 15.34 | 15.41 | / | / | -17.14 | / | / | / | 32.56 | 32.5 |
| 3866 UGC00669 | 126.3799 | -31.0968 | 327.7041 | 6.0500 | 5859 | 5641 | 5.8 | 0.25 | 264 | 2.426 | 13.47 | 13.21 | 13.32 | 13.39 | 13.67 | -19.64 | -19.59 | 33.34 | 46.6 | 33.01 | 40.1 | |
| 3903 UGC00673 | 126.6109 | -31.3607 | 327.4819 | 5.8053 | 6272 | 6067 | 5.3 | 0.35 | 279 | 2.466 | 14.07 | 13.92 | 14.89 | 14.98 | 14.81 | -20.00 | -19.98 | 34.89 | 95.2 | 35.10 | 104.9 | |
| 3950 UGC00679 | 126.7540 | -30.3663 | 328.4867 | 5.8737 | 5125 | 4890 | 7.8 | 0.23 | 174 | 2.243 | 14.93 | 14.86 | 15.72 | 15.82 | 15.69 | -17.98 | -17.80 | 33.71 | 55.1 | 33.68 | 54.4 | |
| 3980 NGC000406 | 300.9117 | -47.1880 | 227.3663 | -15.7908 | 1508 | 1445 | 4.9 | 0.42 | 228 | 2.392 | 11.58 | 11.61 | 12.36 | 12.44 | 12.38 | -19.33 | -19.25 | 31.71 | 22.0 | 31.70 | 21.9 | |
| 4063 UGC00711 | 131.7944 | -60.9341 | 298.9539 | -2.8260 | 1964 | 1648 | 6.5 | 0.20 | 164 | 2.215 | 13.04 | 13.02 | 14.23 | 14.31 | 14.02 | -17.72 | -17.52 | 31.73 | 22.2 | 31.84 | 23.3 | |
| 4110 UGC00714 | 127.3065 | -30.5692 | 328.3756 | 5.3681 | 4638 | 4392 | 5.2 | 0.70 | 216 | 2.475 | 12.77 | 12.88 | 13.32 | 13.43 | 13.52 | -20.08 | -20.06 | 33.64 | 53.4 | 33.54 | 51.2 | |

| PGC Name | l | b | sgl | sgb | v_{hel} | v_{mod} | t | b/a | w_{max} | $\log w_{max}^2$ | I | I* | [3.6] | [3.6]* | $C_{[3.6]}$ | Mc | $M_{[3.6]}$ | μC | dC | $\mu_{[3.6]}$ | $d_{[3.6]}$ |
|-----------------|----------|----------|----------|----------|-----------|-----------|-----|------|-----------|------------------|-------|-------|-------|--------|-------------|--------|-------------|---------|------|---------------|-------------|
| 4143 PGC0004143 | 133.6758 | -64.7570 | 295.2575 | -4.1438 | 1863 | 1551 | 9.8 | 0.48 | 142 | 2.200 | / | / | 14.94 | 15.03 | / | / | -17.38 | / | / | 32.43 | 30.6 |
| 4210 UGC000732 | 127.5350 | -29.1407 | 329.8227 | 5.4329 | 5461 | 5240 | 6.4 | 0.55 | 260 | 2.485 | 12.79 | 12.81 | 13.44 | 13.54 | 13.54 | -20.18 | -20.17 | 33.75 | 56.3 | 33.77 | 56.7 |
| 4286 UGC000748 | 127.5954 | -27.4118 | 331.5416 | 5.6882 | 4855 | 4624 | 3.3 | 0.46 | 298 | 2.517 | / | / | 13.80 | 13.89 | / | / | -20.48 | / | / | 34.46 | 78.0 |
| 4367 UGC000763 | 134.2162 | -61.4184 | 298.6121 | -4.0430 | 1155 | 838 | 8.6 | 0.67 | 148 | 2.290 | 10.74 | 10.94 | 11.71 | 11.76 | 11.70 | -18.40 | -18.26 | 30.10 | 10.5 | 30.01 | 10.1 |
| 4387 UGC000764 | 127.9680 | -27.6928 | 331.3216 | 5.3138 | 4739 | 4505 | 6.0 | 0.20 | 199 | 2.299 | 15.41 | 15.27 | 16.17 | 16.25 | 16.12 | -18.48 | -18.35 | 34.68 | 86.1 | 34.72 | 87.8 |
| 4540 UGC000806 | 136.3298 | -63.1049 | 297.0089 | -5.1643 | 1762 | 1452 | 5.8 | 0.64 | 166 | 2.324 | 11.43 | 11.59 | 12.41 | 12.50 | 12.40 | -18.71 | -18.59 | 31.11 | 16.7 | 31.10 | 16.6 |
| 4561 UGC000810 | 129.0567 | -31.5013 | 327.7210 | 3.7274 | 4851 | 4612 | 6.4 | 0.24 | 253 | 2.407 | 13.34 | 13.10 | 13.99 | 14.06 | 13.94 | -19.46 | -19.40 | 33.43 | 48.5 | 33.51 | 50.3 |
| 4563 UGC000809 | 128.7201 | -28.7863 | 330.3543 | 4.4736 | 4210 | 3963 | 5.9 | 0.21 | 300 | 2.478 | 13.62 | 13.26 | 13.91 | 13.96 | 13.97 | -20.11 | -20.09 | 34.13 | 67.1 | 34.13 | 67.1 |
| 4596 NGC00452 | 129.1678 | -31.5374 | 327.7014 | 3.6280 | 4964 | 4728 | 2.0 | 0.27 | 457 | 2.667 | 11.64 | 11.20 | 11.94 | 11.99 | 11.95 | -21.83 | -21.95 | 33.83 | 58.3 | 34.01 | 63.3 |
| 4650 UGC000825 | 127.3451 | -13.6375 | 345.1930 | 8.1744 | 5337 | 5165 | 7.6 | 0.20 | 290 | 2.462 | / | / | 14.44 | 14.49 | / | / | -19.94 | / | / | 34.53 | 80.6 |
| 4735 UGC000841 | 129.6072 | -29.4815 | 329.7957 | 3.5943 | 5600 | 5388 | 4.0 | 0.23 | 282 | 2.453 | 13.65 | 13.35 | 13.98 | 14.06 | 14.06 | -19.88 | -19.85 | 34.00 | 63.0 | 33.98 | 62.5 |
| 4777 UGC000858 | 136.6290 | -58.7070 | 301.4240 | -5.0135 | 2375 | 2072 | 3.1 | 0.55 | 364 | 2.629 | 10.85 | 10.84 | 11.28 | 11.31 | 11.44 | -21.48 | -21.57 | 32.94 | 38.8 | 32.91 | 38.1 |
| 4805 UGC000866 | 138.4573 | -62.2097 | 297.9566 | -6.0950 | 1739 | 1432 | 7.8 | 0.29 | 125 | 2.107 | 14.14 | 14.28 | 15.24 | 15.34 | 15.16 | -16.73 | -16.47 | 31.90 | 24.0 | 31.81 | 23.0 |
| 4921 UGC000895 | 136.0246 | -55.0884 | 305.0194 | -4.4113 | 2290 | 1986 | 6.0 | 0.33 | 235 | 2.388 | 12.53 | 12.43 | 13.13 | 13.20 | 13.17 | -19.29 | -19.21 | 32.47 | 31.2 | 32.43 | 30.6 |
| 4948 UGC000903 | 133.1302 | -44.6773 | 315.1826 | -1.4411 | 2551 | 2254 | 4.0 | 0.25 | 363 | 2.565 | 12.19 | 11.76 | 11.60 | 11.63 | 12.07 | -20.90 | -20.94 | 32.99 | 39.6 | 32.59 | 33.0 |
| 4957 NGC00489 | 135.4633 | -52.9225 | 307.1537 | -3.8926 | 2514 | 2213 | 5.0 | 0.25 | 382 | 2.587 | 11.59 | 11.23 | 12.15 | 12.19 | 12.06 | -21.10 | -21.16 | 33.19 | 43.5 | 33.40 | 47.8 |
| 4971 UGC00909 | 129.6341 | -25.0719 | 334.1629 | 4.2745 | 5096 | 4883 | 6.4 | 0.73 | 238 | 2.533 | 13.06 | 13.18 | 13.81 | 13.92 | 13.91 | -20.61 | -20.63 | 34.59 | 82.9 | 34.66 | 85.7 |
| 4979 UGC00914 | 138.9115 | -60.9695 | 299.2104 | -6.2707 | 2342 | 2042 | 5.9 | 0.24 | 257 | 2.414 | 11.60 | 11.41 | 12.28 | 12.34 | 12.23 | -22.75 | -22.93 | 35.14 | 22.5 | 31.81 | 23.1 |
| 4992 UGC00915 | 140.0142 | -62.7157 | 297.4637 | -6.8259 | 8142 | 7994 | 4.0 | 0.43 | 541 | 2.768 | 11.78 | 11.54 | 12.23 | 12.33 | 12.29 | -20.36 | -20.36 | 33.63 | 53.2 | 33.62 | 52.9 |
| 5061 NGC00496 | 130.4870 | -28.8766 | 330.5157 | 2.9316 | 6015 | 5819 | 4.0 | 0.49 | 285 | 2.506 | 12.60 | 12.54 | 13.10 | 13.20 | 13.23 | -22.36 | -22.52 | 34.77 | 89.9 | 34.95 | 97.8 |
| 5132 UGC00944 | 130.6143 | -28.4778 | 330.9274 | 2.8823 | 4859 | 4633 | 2.0 | 0.28 | 521 | 2.726 | 12.10 | 11.62 | 12.26 | 12.30 | 12.32 | -22.36 | -22.36 | 32.04 | 25.6 | 32.10 | 26.3 |
| 5139 UGC00947 | 135.1454 | -49.1791 | 310.8672 | -3.3299 | 2472 | 2173 | 5.2 | 0.68 | 242 | 2.507 | 10.77 | 10.90 | 11.67 | 11.72 | 11.67 | -20.37 | -20.38 | 32.04 | 25.6 | 32.10 | 26.3 |
| 5147 UGC00949 | 136.1146 | -52.1021 | 308.0082 | -4.2145 | 2422 | 2122 | 3.0 | 0.50 | 183 | 2.316 | 13.27 | 13.32 | 14.07 | 14.16 | 14.09 | -18.64 | -18.51 | 32.74 | 35.4 | 32.69 | 34.5 |
| 5194 UGC00958 | 134.3164 | -45.6011 | 314.3678 | -2.3847 | 2446 | 2150 | 5.7 | 0.21 | 152 | 2.183 | 14.35 | 14.28 | 15.43 | 15.50 | 15.24 | -17.42 | -17.21 | 32.68 | 34.3 | 32.74 | 35.3 |
| 5198 UGC00964 | 137.0769 | -54.2377 | 305.9166 | -4.9539 | 2740 | 2444 | 3.0 | 0.27 | 204 | 2.317 | 14.10 | 14.02 | 14.40 | 14.47 | 14.61 | -18.65 | -18.52 | 33.28 | 45.4 | 33.03 | 40.3 |
| 5218 NGC00522 | 136.3365 | -52.0081 | 308.1136 | -4.3425 | 2720 | 2424 | 4.1 | 0.20 | 379 | 2.579 | 11.61 | 11.09 | 11.88 | 11.90 | 11.85 | -21.03 | -21.08 | 32.90 | 38.0 | 33.01 | 39.9 |
| 5264 NGC00532 | 136.7979 | -52.6939 | 307.4499 | -4.6774 | 2370 | 2070 | 1.9 | 0.34 | 384 | 2.603 | 11.01 | 10.70 | 11.37 | 11.41 | 11.42 | -21.24 | -21.31 | 32.67 | 34.3 | 32.74 | 35.4 |
| 5284 UGC00987 | 131.2785 | -30.1826 | 329.3277 | 2.0533 | 4669 | 4435 | 1.0 | 0.30 | 383 | 2.595 | 12.13 | 11.82 | 12.45 | 12.51 | 12.53 | -21.18 | -21.24 | 33.74 | 56.0 | 33.81 | 57.9 |
| 5329 AGC410199 | 144.0363 | -65.4290 | 294.6840 | -8.5163 | 1997 | 1701 | 8.0 | 0.35 | 135 | 2.150 | / | / | 15.02 | 15.11 | / | / | -16.89 | / | / | 32.01 | 25.2 |
| 5341 AGC410203 | 145.9709 | -67.3957 | 292.6390 | -9.1348 | 1959 | 1666 | 5.6 | 0.20 | 236 | 2.373 | 12.16 | 11.93 | 12.90 | 12.90 | 12.77 | -19.15 | -19.07 | 31.93 | 24.3 | 31.97 | 24.8 |
| 5344 UGC01013 | 131.0287 | -27.6190 | 331.8325 | 2.6501 | 5183 | 4969 | 3.1 | 0.36 | 513 | 2.731 | 11.15 | 10.83 | 11.65 | 11.72 | 11.63 | -22.42 | -22.57 | 34.10 | 66.1 | 34.38 | 75.2 |
| 5375 ES476-010 | 201.9959 | -81.8875 | 273.5676 | -13.6334 | 1604 | 1351 | 8.8 | 0.33 | 117 | 2.084 | 13.98 | 14.18 | 15.37 | 15.47 | 15.17 | -16.53 | -16.25 | 31.70 | 21.9 | 31.72 | 22.1 |
| 5382 UGC01020 | 134.8436 | -44.7894 | 315.2169 | -2.6629 | 2592 | 2300 | 2.1 | 0.37 | 231 | 2.387 | / | / | 13.71 | 13.76 | / | / | -19.20 | / | / | 32.99 | 39.7 |
| 5440 UGC01033 | 131.8850 | -30.6879 | 328.9038 | 1.4632 | 4058 | 3812 | 5.8 | 0.20 | 337 | 2.528 | 12.77 | 12.35 | 13.26 | 13.30 | 13.18 | -20.56 | -20.58 | 33.78 | 57.1 | 33.95 | 61.7 |
| 5450 NGC00551 | 130.8970 | -25.1277 | 334.2820 | 3.1357 | 5188 | 4981 | 4.0 | 0.42 | 372 | 2.603 | 12.10 | 11.94 | 12.65 | 12.73 | 12.69 | -21.25 | -21.32 | 33.99 | 62.8 | 34.12 | 66.8 |
| 5518 UGC01054 | 131.6553 | -27.8922 | 331.6432 | 2.0617 | 2668 | 2406 | 6.2 | 0.20 | 167 | 2.223 | / | / | 16.51 | 16.59 | / | / | -17.60 | / | / | 34.27 | 71.5 |

| PGC Name | l | b | sgl | sgb | v_{hel} | v_{mod} | t | b/a | w_{max} | $\log w_{max}^*$ | I | I* | [3.6] | [3.6]* | $C_{[3.6]}$ | M_C | $M_{[3.6]}$ | μ_C | d_C | $\mu_{[3.6]}$ | $d_{[3.6]}$ |
|----------------|----------|----------|----------|----------|-----------|-----------|-----|------|-----------|------------------|-------|-------|-------|--------|-------------|--------|-------------|---------|-------|---------------|-------------|
| 5563 UGC01066 | 132.2157 | -30.1230 | 329.5036 | 1.2600 | 5073 | 4852 | 6.0 | 0.33 | 158 | 2.214 | 15.28 | 15.33 | 16.79 | 16.89 | 16.46 | -17.71 | -17.52 | 34.22 | 69.9 | 34.51 | 79.9 |
| 5619 AGC021148 | 188.3085 | -80.0921 | 276.4149 | -13.9592 | 1628 | 1371 | 5.0 | 0.56 | 256 | 2.481 | 10.40 | 10.49 | 11.08 | 11.17 | 11.19 | -20.14 | -20.13 | 31.33 | 18.4 | 31.29 | 18.1 |
| 5643 UGC01082 | 136.2435 | -44.6603 | 315.4457 | -3.6394 | 2809 | 2523 | 3.0 | 0.28 | 385 | 2.594 | 11.90 | 11.49 | 11.89 | 11.93 | 12.07 | -21.16 | -21.23 | 33.26 | 45.0 | 33.19 | 43.5 |
| 5702 UGC001094 | 132.5565 | -28.6366 | 331.0171 | 1.1714 | 4363 | 4131 | 3.1 | 0.26 | 438 | 2.647 | 11.98 | 11.55 | 12.25 | 12.29 | 12.28 | -21.65 | -21.75 | 33.98 | 62.6 | 34.12 | 66.8 |
| 5794 UGC01110 | 138.3333 | -48.2838 | 311.9330 | -5.3528 | 2768 | 2481 | 5.9 | 0.21 | 204 | 2.311 | 13.49 | 13.33 | 14.28 | 14.35 | 14.19 | -18.59 | -18.46 | 32.80 | 36.2 | 32.83 | 36.9 |
| 5799 UGC01112 | 143.0448 | -58.1566 | 302.0494 | -8.3585 | 1705 | 1408 | 5.8 | 0.39 | 147 | 2.195 | 13.45 | 13.59 | 14.51 | 14.60 | 14.45 | -17.53 | -17.33 | 31.98 | 24.9 | 31.93 | 24.4 |
| 5897 AGC410271 | 152.5473 | -67.6663 | 291.9850 | -11.5782 | 1842 | 1558 | 3.0 | 0.38 | 369 | 2.593 | 10.62 | 10.47 | 11.10 | 11.16 | 11.17 | -21.15 | -21.21 | 32.33 | 29.3 | 32.39 | 30.0 |
| 6045 UGC01160 | 134.2055 | -29.3550 | 330.4919 | -0.3519 | 5469 | 5266 | 6.1 | 0.20 | 319 | 2.504 | 13.67 | 13.29 | 13.73 | 13.79 | 13.91 | -20.34 | -20.35 | 34.31 | 72.8 | 34.23 | 70.0 |
| 6189 UGC01178 | 134.2559 | -27.1659 | 332.6699 | -0.1273 | 5525 | 5331 | 5.9 | 0.21 | 366 | 2.564 | 12.88 | 12.45 | 12.62 | 12.68 | 12.94 | -20.89 | -20.94 | 33.87 | 59.5 | 33.67 | 54.2 |
| 6190 AGC410313 | 153.4888 | -65.4413 | 294.1314 | -12.4045 | 2125 | 1846 | 6.8 | 0.25 | 170 | 2.236 | 13.61 | 13.60 | 14.68 | 14.76 | 14.53 | -17.91 | -17.73 | 32.45 | 30.9 | 32.51 | 31.8 |
| 6228 AGC410316 | 153.8899 | -65.4092 | 294.1271 | -12.5743 | 1493 | 1210 | 8.7 | 0.40 | 163 | 2.241 | 12.50 | 12.59 | 13.59 | 13.67 | 13.48 | -17.95 | -17.78 | 31.44 | 19.4 | 31.46 | 19.5 |
| 6249 NGC002573 | 302.7687 | -27.7776 | 207.1277 | -15.8422 | 2416 | 2474 | 5.8 | 0.39 | 217 | 2.363 | / | / | 12.98 | 13.04 | / | -18.98 | / | / | / | 32.02 | 25.4 |
| 6275 NGC00658 | 141.7591 | -48.4069 | 311.8980 | -7.6327 | 2992 | 2716 | 3.0 | 0.62 | 298 | 2.571 | 11.56 | 11.62 | 12.12 | 12.21 | 12.28 | -20.95 | -21.00 | 33.26 | 44.8 | 33.25 | 44.7 |
| 6294 UGC01197 | 139.5913 | -42.9065 | 317.3784 | -5.9212 | 2795 | 2521 | 9.8 | 0.26 | 175 | 2.249 | 13.82 | 13.75 | 14.88 | 14.96 | 14.71 | -18.03 | -17.86 | 32.75 | 35.5 | 32.84 | 37.1 |
| 6309 UGC01200 | 141.7395 | -47.8312 | 312.4785 | -7.6097 | 824 | 531 | 9.9 | 0.56 | 117 | 2.139 | 12.60 | 12.79 | 13.78 | 13.87 | 13.68 | -17.03 | -16.79 | 30.71 | 13.9 | 30.66 | 13.5 |
| 6473 UGC01234 | 135.3436 | -26.4456 | 333.5001 | -1.0060 | 5654 | 5469 | 5.3 | 0.56 | 265 | 2.497 | 13.65 | 13.68 | 14.41 | 14.52 | 14.46 | -20.28 | -20.28 | 34.83 | 92.4 | 34.93 | 97.0 |
| 6500 UGC01240 | 147.9122 | -55.9217 | 304.1548 | -11.1321 | 1815 | 1531 | 7.9 | 0.32 | 123 | 2.104 | / | / | 15.31 | 15.41 | / | -16.45 | / | / | 31.86 | 23.5 | 23.5 |
| 6502 UGC01238 | 135.1064 | -25.1094 | 334.8029 | -0.6397 | 4499 | 4288 | 3.1 | 0.68 | 279 | 2.572 | 12.03 | 12.12 | 12.57 | 12.67 | 12.76 | -20.96 | -21.01 | 33.76 | 56.5 | 33.74 | 56.0 |
| 6607 UGC01257 | 135.4834 | -25.0333 | 334.9178 | -0.9703 | 4661 | 4455 | 2.0 | 0.42 | 324 | 2.544 | 13.16 | 13.05 | 13.74 | 13.82 | 13.80 | -20.71 | -20.74 | 34.58 | 82.6 | 34.68 | 86.3 |
| 6624 UGC01259 | 144.4573 | -48.9559 | 311.3392 | -9.4129 | 5181 | 4955 | 5.3 | 0.71 | 315 | 2.640 | 11.59 | 11.63 | 11.99 | 12.09 | 12.23 | -21.58 | -21.68 | 33.85 | 59.0 | 33.83 | 58.4 |
| 6671 AGC410359 | 164.8344 | -68.4628 | 289.7771 | -15.7044 | 1756 | 1490 | 2.0 | 0.68 | 372 | 2.696 | 10.56 | 10.64 | 11.02 | 11.10 | 11.24 | -22.10 | -22.23 | 33.36 | 47.1 | 33.38 | 47.3 |
| 6675 UGC01276 | 140.7178 | -40.1556 | 320.1853 | -6.6238 | 2748 | 2482 | 7.8 | 0.45 | 212 | 2.367 | 12.15 | 12.12 | 12.82 | 12.90 | 12.87 | -19.10 | -19.01 | 31.97 | 24.8 | 31.91 | 24.1 |
| 6703 PG0006703 | 170.8881 | -70.8033 | 286.6153 | -16.5246 | 1439 | 1177 | 3.1 | 0.28 | 164 | 2.224 | / | / | 14.46 | 14.54 | / | -17.61 | / | / | 32.16 | 27.0 | 27.0 |
| 6793 UGC01305 | 140.7382 | -39.0542 | 321.2935 | -6.5866 | 2669 | 2404 | 4.0 | 0.69 | 317 | 2.631 | 10.59 | 10.63 | 11.30 | 11.39 | 11.37 | -21.50 | -21.59 | 32.89 | 37.8 | 33.00 | 39.9 |
| 6799 NGC00688 | 136.3732 | -26.0348 | 334.0105 | -1.8785 | 4148 | 3931 | 3.1 | 0.60 | 337 | 2.614 | 11.74 | 11.75 | 12.34 | 12.44 | 12.45 | -21.35 | -21.43 | 33.85 | 58.8 | 33.93 | 61.1 |
| 6826 AGC410368 | 164.6580 | -67.6051 | 290.6224 | -15.9850 | 1830 | 1565 | 5.0 | 0.48 | 247 | 2.440 | 11.09 | 11.13 | 11.47 | 11.55 | 11.71 | -19.76 | -19.72 | 31.47 | 19.7 | 31.28 | 18.0 |
| 6833 UGC01313 | 140.8080 | -38.8775 | 321.4738 | -6.6322 | 2938 | 2677 | 5.0 | 0.56 | 148 | 2.243 | 12.73 | 12.84 | 13.45 | 13.55 | 13.55 | -17.97 | -17.80 | 31.53 | 20.2 | 31.35 | 18.6 |
| 6851 UGC01316 | 136.6195 | -26.4271 | 333.6435 | -2.1396 | 4688 | 4482 | 3.1 | 0.44 | 205 | 2.351 | 14.48 | 14.50 | 15.60 | 15.70 | 15.45 | -18.95 | -18.85 | 34.47 | 78.5 | 34.67 | 85.8 |
| 6864 AGC410377 | 160.3276 | -64.9344 | 293.8563 | -15.3050 | 2130 | 1863 | 6.9 | 0.26 | 175 | 2.250 | 14.05 | 14.06 | 15.35 | 15.43 | 15.09 | -18.03 | -17.87 | 33.15 | 42.6 | 33.34 | 46.5 |
| 6865 UGC01319 | 136.3163 | -25.2403 | 334.7954 | -1.7425 | 5312 | 5125 | 3.6 | 0.68 | 241 | 2.510 | 12.80 | 12.87 | 13.11 | 13.22 | 13.41 | -20.40 | -20.40 | 33.85 | 59.0 | 33.68 | 54.5 |
| 6898 PG0006898 | 159.2347 | -64.0262 | 294.9014 | -15.1338 | 1643 | 1371 | 7.9 | 0.35 | 146 | 2.184 | / | / | 15.46 | 15.55 | / | -17.22 | / | / | 32.79 | 36.1 | 36.1 |
| 6966 PG0006966 | 157.3565 | -62.1438 | 297.0171 | -14.8365 | 5008 | 4789 | 5.0 | 0.20 | 517 | 2.713 | 11.98 | 11.39 | 11.60 | 11.64 | 11.88 | -22.25 | -22.40 | 34.19 | 68.9 | 34.11 | 66.3 |
| 6972 NGC00710 | 136.6248 | -25.1793 | 334.8858 | -2.0136 | 6112 | 5949 | 5.9 | 0.65 | 210 | 2.433 | / | / | 12.98 | 13.09 | / | -19.65 | / | / | 32.76 | 35.7 | 35.7 |
| 7066 UGC01366 | 136.7641 | -24.5469 | 335.5283 | -2.0729 | 5107 | 4918 | 5.8 | 0.28 | 412 | 2.624 | 12.43 | 12.03 | 12.85 | 12.90 | 12.82 | -21.44 | -21.52 | 34.32 | 73.1 | 34.52 | 80.3 |
| 7097 NGC00721 | 136.0634 | -21.8682 | 338.1232 | -1.1442 | 5597 | 5428 | 3.8 | 0.59 | 275 | 2.523 | 12.39 | 12.43 | 13.06 | 13.16 | 13.16 | -20.52 | -20.54 | 33.72 | 55.4 | 33.76 | 56.5 |
| 7247 UGC01378 | 127.6272 | 11.0054 | 10.0498 | 10.7264 | 2933 | 2831 | 1.2 | 0.47 | 496 | 2.741 | / | / | 10.68 | 10.66 | / | -22.66 | / | / | 33.36 | 47.0 | 47.0 |

| PGC Name | l | b | sgl | sgb | v_{hel} | v_{mod} | t | b/a | w_{mz} | $\log w_{mz}^2$ | I | I* | [3.6] | [3.6]* | $C_{[3.6]}$ | MC | $M_{[3.6]}$ | μC | dC | $\mu_{[3.6]}$ | $d_{[3.6]}$ |
|-----------------|----------|----------|----------|----------|-----------|-----------|-----|------|----------|-----------------|-------|-------|-------|--------|-------------|--------|-------------|---------|-------|---------------|-------------|
| 7262 AGC410401 | 166.3108 | -66.2983 | 291.5958 | -17.1055 | 1639 | 1377 | 3.4 | 0.33 | 221 | 2.361 | 11.77 | 11.74 | 12.48 | 12.56 | 12.51 | -19.04 | -18.95 | 31.55 | 20.4 | 31.51 | 20.0 |
| 7300 UGC01416 | 137.2041 | -24.1681 | 335.9468 | -2.4325 | 5471 | 5294 | 3.1 | 0.52 | 368 | 2.626 | 13.16 | 13.06 | 13.68 | 13.76 | 13.77 | -21.46 | -21.54 | 35.34 | 117.1 | 35.48 | 124.9 |
| 7324 PGC0007324 | 171.1763 | -68.2714 | 288.8580 | -17.8778 | 1856 | 1601 | 8.0 | 0.20 | 152 | 2.182 | 13.96 | 13.99 | 15.10 | 15.19 | 14.94 | -17.41 | -17.20 | 32.36 | 29.7 | 32.40 | 30.2 |
| 7504 UGC01459 | 137.9543 | -24.8267 | 335.3581 | -3.1769 | 5466 | 5289 | 5.8 | 0.20 | 362 | 2.559 | 13.26 | 12.74 | 13.10 | 13.15 | 13.31 | -20.84 | -20.88 | 34.21 | 69.4 | 34.11 | 66.3 |
| 7537 NGC000769 | 139.7614 | -29.7245 | 330.6038 | -5.1979 | 4427 | 4215 | 5.5 | 0.54 | 300 | 2.543 | 12.25 | 12.25 | 12.59 | 12.68 | 12.83 | -20.70 | -20.73 | 33.57 | 51.7 | 33.46 | 49.2 |
| 7544 NGC000779 | 163.4911 | -63.3247 | 294.9503 | -17.1465 | 1393 | 1129 | 3.0 | 0.37 | 351 | 2.568 | 10.01 | 9.86 | 10.60 | 10.66 | 10.62 | -20.93 | -20.97 | 31.55 | 20.4 | 31.64 | 21.2 |
| 7545 UGC01470 | 139.3867 | -28.5992 | 331.7043 | -4.7842 | 5186 | 4994 | 7.7 | 0.20 | 232 | 2.365 | / | / | 15.16 | 15.23 | / | / | -19.00 | / | / | 34.32 | 73.1 |
| 7646 UGC01493 | 137.6587 | -22.6661 | 337.4846 | -2.6964 | 4147 | 3945 | 2.0 | 0.36 | 346 | 2.561 | 12.16 | 11.97 | 12.38 | 12.45 | 12.57 | -20.86 | -20.90 | 33.47 | 49.4 | 33.40 | 47.8 |
| 7663 UGC01500 | 144.6302 | -40.2388 | 320.1767 | -9.6131 | 2433 | 2174 | 5.9 | 0.24 | 154 | 2.192 | 14.35 | 14.27 | 14.90 | 14.97 | 14.98 | -17.50 | -17.30 | 32.49 | 31.5 | 32.28 | 28.5 |
| 7847 UGC01550 | 138.2191 | -22.4567 | 337.7441 | -3.1908 | 5772 | 5613 | 5.3 | 0.24 | 459 | 2.666 | 11.52 | 11.04 | 11.85 | 11.90 | 11.83 | -21.82 | -21.93 | 33.68 | 54.4 | 33.89 | 60.1 |
| 7849 UGC01554 | 147.1705 | -43.4117 | 316.9179 | -11.4523 | 2099 | 1836 | 5.3 | 0.37 | 247 | 2.416 | 11.40 | 11.32 | 12.20 | 12.22 | 12.13 | -19.55 | -19.49 | 31.68 | 21.7 | 31.72 | 22.1 |
| 7933 UGC001567 | 136.8995 | -17.7147 | 342.3387 | -1.4739 | 9015 | 8992 | 6.3 | 0.20 | 543 | 2.735 | 13.69 | 13.00 | 13.21 | 13.26 | 13.50 | -22.45 | -22.60 | 36.10 | 166.2 | 36.09 | 165.1 |
| 7957 AGC120016 | 139.7027 | -25.6666 | 334.6605 | -4.8267 | 4416 | 4216 | 3.0 | 0.25 | 341 | 2.538 | 13.63 | 13.25 | 13.71 | 13.77 | 13.87 | -20.66 | -20.69 | 34.60 | 83.3 | 34.56 | 81.5 |
| 7972 UGC01581 | 139.7304 | -25.5612 | 334.7680 | -4.8430 | 4421 | 4222 | 7.2 | 0.48 | 330 | 2.567 | 12.62 | 12.49 | 12.69 | 12.77 | 13.00 | -20.92 | -20.96 | 33.96 | 62.1 | 33.79 | 57.4 |
| 8066 UGC01598 | 136.8078 | -16.2584 | 343.7774 | -1.2295 | 5161 | 5004 | 5.9 | 0.24 | 435 | 2.643 | 11.76 | 11.27 | 12.02 | 12.06 | 12.02 | -21.61 | -21.70 | 33.67 | 54.1 | 33.83 | 58.2 |
| 8165 UGC01629 | 149.5327 | -44.5098 | 315.7026 | -13.0914 | 4418 | 4196 | 2.9 | 0.64 | 342 | 2.640 | 11.80 | 11.82 | 12.20 | 12.30 | 12.42 | -21.58 | -21.67 | 34.05 | 64.6 | 34.04 | 64.4 |
| 8173 UGC01636 | 154.8946 | -51.6986 | 307.8914 | -15.7764 | 3415 | 3174 | 1.1 | 0.47 | 459 | 2.707 | 11.88 | 11.72 | 12.28 | 12.35 | 12.39 | -22.20 | -22.33 | 34.67 | 85.7 | 34.80 | 91.2 |
| 8185 UGC01633 | 139.0493 | -21.6629 | 338.6083 | -3.8822 | 4265 | 4074 | 4.4 | 0.38 | 448 | 2.677 | 11.40 | 11.16 | 11.71 | 11.78 | 11.83 | -21.92 | -22.04 | 33.79 | 57.3 | 33.88 | 59.7 |
| 8232 AGC420030 | 173.1555 | -64.6386 | 291.7582 | -20.3904 | 1938 | 1694 | 4.1 | 0.23 | 268 | 2.431 | 11.65 | 11.43 | 11.66 | 11.71 | 11.94 | -19.68 | -19.63 | 31.62 | 21.1 | 31.35 | 18.6 |
| 8237 UGC01650 | 139.7161 | -23.0580 | 337.2698 | -4.6203 | 4594 | 4407 | 6.2 | 0.20 | 221 | 2.344 | / | / | 15.45 | 15.53 | / | / | -18.79 | / | / | 34.41 | 76.3 |
| 8295 AGC420037 | 173.5220 | -64.5231 | 291.7780 | -20.5847 | 2017 | 1774 | 5.0 | 0.23 | 152 | 2.185 | 13.08 | 13.12 | 14.07 | 14.15 | 13.99 | -17.44 | -17.23 | 31.44 | 19.4 | 31.39 | 18.9 |
| 8372 NGC00841 | 140.0078 | -22.7125 | 337.6382 | -4.8587 | 4545 | 4359 | 2.0 | 0.50 | 394 | 2.648 | 11.39 | 11.30 | 11.90 | 11.99 | 12.00 | -21.65 | -21.75 | 33.70 | 54.8 | 33.80 | 57.7 |
| 8396 UGC01685 | 141.3489 | -25.9428 | 334.4964 | -6.3254 | 6181 | 6033 | 2.0 | 0.29 | 427 | 2.641 | 12.94 | 12.51 | 12.94 | 12.99 | 13.12 | -21.59 | -21.68 | 34.79 | 90.7 | 34.80 | 91.1 |
| 8480 E544-027 | 194.5725 | -69.7525 | 281.7597 | -23.1051 | 2463 | 2246 | 3.5 | 0.24 | 250 | 2.402 | 13.38 | 13.20 | 13.56 | 13.63 | 13.78 | -19.41 | -19.35 | 33.22 | 44.1 | 33.00 | 39.9 |
| 8599 UGC01726 | 143.0661 | -28.1197 | 332.3995 | -7.9835 | 5295 | 5120 | 4.0 | 0.26 | 339 | 2.537 | 13.16 | 12.82 | 13.38 | 13.44 | 13.49 | -20.65 | -20.67 | 34.19 | 68.9 | 34.19 | 69.0 |
| 8673 IC000217 | 179.6527 | -64.9809 | 289.7948 | -22.4923 | 1890 | 1656 | 5.7 | 0.20 | 208 | 2.318 | 12.30 | 12.17 | 12.96 | 13.02 | 12.95 | -18.65 | -18.53 | 31.61 | 21.0 | 31.55 | 20.5 |
| 8678 UGC01747 | 144.5999 | -30.6787 | 329.8687 | -9.4244 | 3002 | 2776 | 4.0 | 0.29 | 271 | 2.444 | 12.28 | 12.04 | 12.55 | 12.61 | 12.69 | -19.80 | -19.76 | 32.49 | 31.5 | 32.38 | 29.9 |
| 8691 UGC01753 | 144.8395 | -31.0215 | 329.5274 | -9.6401 | 3006 | 2780 | 9.9 | 0.39 | 142 | 2.179 | / | / | 15.00 | 15.09 | / | / | -17.18 | / | / | 32.27 | 28.5 |
| 8778 AGC120150 | 143.6047 | -27.4914 | 333.0574 | -8.4281 | 6063 | 5914 | 3.3 | 0.53 | 290 | 2.525 | 13.76 | 13.72 | 13.81 | 13.91 | 14.18 | -20.54 | -20.56 | 34.80 | 91.4 | 34.57 | 82.0 |
| 8851 ES545-002 | 195.4614 | -68.2407 | 282.4370 | -24.5204 | 1607 | 1388 | 8.9 | 0.40 | 135 | 2.160 | 13.28 | 13.42 | 14.50 | 14.59 | 14.35 | -17.22 | -16.99 | 31.57 | 20.6 | 31.58 | 20.7 |
| 8862 ES545-003 | 201.8624 | -69.1763 | 279.7204 | -24.9473 | 1597 | 1384 | 4.0 | 0.22 | 129 | 2.112 | 14.05 | 14.16 | 15.17 | 15.26 | 15.07 | -16.78 | -16.52 | 31.85 | 23.5 | 31.79 | 22.8 |
| 8896 AGC021790 | 197.7003 | -68.4062 | 281.5810 | -24.8463 | 2337 | 2128 | 7.6 | 0.25 | 251 | 2.404 | 12.35 | 12.18 | 12.85 | 12.91 | 12.91 | -19.44 | -19.37 | 32.35 | 29.6 | 32.30 | 28.8 |
| 8974 NGC00895 | 171.7744 | -59.5474 | 296.8710 | -22.3044 | 2290 | 2057 | 6.0 | 0.65 | 254 | 2.515 | 10.96 | 11.08 | 11.63 | 11.67 | 11.74 | -20.45 | -20.46 | 32.20 | 27.5 | 32.14 | 26.8 |
| 8984 UGC01820 | 143.9513 | -26.1371 | 334.4405 | -8.6710 | 3980 | 3784 | 5.9 | 0.22 | 227 | 2.358 | 13.59 | 13.35 | 14.05 | 14.12 | 14.09 | -19.02 | -18.92 | 33.13 | 42.3 | 33.07 | 41.2 |
| 9028 UGC01839 | 166.2158 | -55.6410 | 302.0195 | -21.1926 | 1541 | 1298 | 7.1 | 0.23 | 142 | 2.155 | / | / | 15.14 | 15.23 | / | / | -16.94 | / | / | 32.18 | 27.3 |
| 9054 AGC021830 | 200.8171 | -68.1433 | 280.6403 | -25.6684 | 1655 | 1445 | 7.6 | 0.36 | 262 | 2.440 | 11.66 | 11.59 | 12.24 | 12.31 | 12.31 | -19.77 | -19.72 | 32.08 | 26.1 | 32.04 | 25.6 |

| PGC Name | l | b | sgl | sgb | v_{hel} | v_{mod} | t | b/a | w _{max} | log w _{max} | I | I* | [3.6] | [3.6]* | C _[3.6] | M _C | M _[3.6] | μ_C | d _C | $\mu_{[3.6]}$ | d _[3.6] | |
|-----------------|----------|----------|----------|----------|-----------|-----------|-----|------|------------------|----------------------|-------|-------|-------|--------|--------------------|----------------|--------------------|---------|----------------|---------------|--------------------|------|
| 9057 AGC021831 | 202.1393 | -68.3224 | 280.0677 | -25.7477 | 1508 | 1298 | 5.1 | 0.43 | 377 | 2.612 | 9.31 | 9.20 | 9.68 | 9.75 | 9.84 | -21.33 | -21.40 | 31.17 | 17.1 | 31.15 | 17.0 | |
| 9115 UGC01845 | 138.5622 | -12.0690 | 348.1254 | -2.4782 | 4642 | 4496 | 2.0 | 0.32 | 235 | 2.386 | / | / | 12.04 | 12.09 | / | / | -19.19 | / | / | / | 31.28 | 18.1 |
| 9186 UGC01867 | 139.6823 | -14.3469 | 345.9651 | -3.7916 | 5193 | 5055 | 5.9 | 0.20 | 279 | 2.446 | 13.57 | 13.19 | 13.99 | 14.05 | 13.98 | -19.81 | -19.78 | 33.84 | 58.5 | 33.90 | 60.2 | |
| 9236 UGC01888 | 152.1608 | -38.9581 | 321.2656 | -15.4574 | 1509 | 1267 | 5.2 | 0.55 | 241 | 2.451 | 10.93 | 10.52 | 11.22 | 11.24 | 11.24 | -19.87 | -19.83 | 31.11 | 16.6 | 31.07 | 16.4 | |
| 9253 UGC01887 | 141.0989 | -17.3646 | 343.0756 | -5.4253 | 5359 | 5399 | 5.3 | 0.61 | 339 | 2.620 | 12.32 | 12.32 | 12.64 | 12.74 | 12.89 | -21.40 | -21.49 | 34.36 | 74.5 | 34.31 | 72.9 | |
| 9272 P0009272 | 179.7598 | -61.7257 | 292.6072 | -24.4788 | 2106 | 1883 | 8.0 | 0.32 | 180 | 2.271 | 13.43 | 13.46 | 14.44 | 14.52 | 14.35 | -18.22 | -18.07 | 32.58 | 32.8 | 32.61 | 33.3 | |
| 9273 ES479-004 | 210.6892 | -68.4633 | 276.7837 | -26.8662 | 1510 | 1311 | 8.5 | 0.47 | 182 | 2.305 | 11.63 | 11.75 | 12.63 | 12.71 | 12.58 | -18.54 | -18.41 | 31.12 | 16.8 | 31.12 | 16.8 | |
| 9332 NGC00925 | 144.8853 | -25.1743 | 335.4545 | -9.4668 | 553 | 326 | 7.0 | 0.51 | 194 | 2.346 | 9.27 | 9.31 | 10.20 | 10.27 | 10.14 | -18.91 | -18.80 | 29.05 | 6.5 | 29.07 | 6.5 | |
| 9354 AGC420105 | 180.6853 | -61.7130 | 292.3301 | -24.8380 | 2099 | 1878 | 5.1 | 0.33 | 144 | 2.174 | 13.07 | 13.19 | 14.09 | 14.18 | 14.04 | -17.34 | -17.13 | 31.38 | 18.9 | 31.30 | 18.2 | |
| 9399 UGC01935 | 146.1145 | -27.1661 | 333.4748 | -10.6434 | 4999 | 4830 | 3.6 | 0.27 | 422 | 2.633 | 11.51 | 11.06 | 10.94 | 10.99 | 11.40 | -21.52 | -21.61 | 32.94 | 38.8 | 32.62 | 33.4 | |
| 9510 UGC01970 | 149.4600 | -32.4938 | 328.0429 | -13.5752 | 1924 | 1696 | 5.8 | 0.20 | 218 | 2.338 | 13.15 | 12.86 | 13.60 | 13.64 | 13.61 | -18.84 | -18.73 | 32.46 | 31.0 | 32.38 | 30.0 | |
| 9549 UGC01986 | 169.5002 | -54.7581 | 302.1332 | -23.2617 | 1485 | 1252 | 2.0 | 0.30 | 328 | 2.527 | 10.82 | 10.60 | 11.32 | 11.37 | 11.34 | -20.56 | -20.58 | 31.90 | 24.0 | 31.95 | 24.5 | |
| 9550 UGC01980 | 146.2173 | -26.1749 | 334.4859 | -10.7048 | 4777 | 4606 | 2.9 | 0.44 | 418 | 2.659 | 12.13 | 11.92 | 12.08 | 12.15 | 12.41 | -21.76 | -21.86 | 34.22 | 69.9 | 34.09 | 65.8 | |
| 9560 NGC0958 | 171.6769 | -56.1096 | 300.2291 | -23.8128 | 5739 | 5583 | 4.9 | 0.34 | 570 | 2.774 | 11.08 | 10.73 | 11.13 | 11.19 | 11.33 | -22.80 | -22.98 | 34.18 | 68.6 | 34.26 | 71.2 | |
| 9590 UGC01988 | 142.7485 | -18.6099 | 341.9544 | -7.0897 | 5779 | 5651 | 2.0 | 0.36 | 324 | 2.532 | 12.91 | 12.73 | 13.11 | 13.19 | 13.33 | -20.60 | -20.62 | 33.98 | 62.4 | 33.88 | 59.7 | |
| 9617 UGC01998 | 168.3519 | -53.4934 | 303.6854 | -23.1328 | 6345 | 6206 | 6.0 | 0.56 | 183 | 2.334 | 14.39 | 14.52 | 15.23 | 15.35 | 15.29 | -18.80 | -18.69 | 34.15 | 67.6 | 34.12 | 66.7 | |
| 9618 UGC01993 | 143.2545 | -19.5054 | 341.0890 | -7.6319 | 8025 | 7974 | 3.2 | 0.22 | 483 | 2.686 | 12.77 | 12.22 | 13.07 | 13.13 | 13.03 | -22.00 | -22.13 | 35.13 | 106.2 | 35.43 | 121.7 | |
| 9638 UGC01999 | 153.3749 | -37.7108 | 322.4792 | -16.5070 | 975 | 738 | 5.7 | 0.25 | 143 | 2.161 | 13.52 | 13.48 | 14.71 | 14.78 | 14.48 | -17.22 | -17.00 | 31.70 | 21.9 | 31.78 | 22.7 | |
| 9665 UGC02002 | 145.0888 | -22.9959 | 337.6697 | -9.5490 | 596 | 378 | 7.9 | 0.60 | 134 | 2.213 | 11.58 | 11.71 | 12.37 | 12.45 | 12.44 | -17.70 | -17.51 | 30.14 | 10.7 | 29.96 | 9.8 | |
| 9773 UGC02035 | 141.5935 | -14.7801 | 345.7040 | -5.6736 | 5078 | 4942 | 3.2 | 0.61 | 301 | 2.571 | 12.55 | 12.53 | 12.84 | 12.94 | 13.10 | -20.95 | -21.00 | 34.11 | 66.3 | 34.01 | 63.4 | |
| 9788 UGC02045 | 148.3956 | -28.4293 | 332.2225 | -12.6837 | 1541 | 1319 | 2.1 | 0.47 | 300 | 2.522 | 9.89 | 9.76 | 10.04 | 10.09 | 10.29 | -20.51 | -20.53 | 30.81 | 14.5 | 30.62 | 13.3 | |
| 9795 UGC02048 | 146.8659 | -25.5398 | 335.1507 | -11.2688 | 4865 | 4701 | 3.3 | 0.20 | 583 | 2.766 | 11.43 | 10.67 | 11.01 | 11.02 | 11.22 | -22.73 | -22.91 | 33.99 | 62.8 | 34.00 | 63.1 | |
| 9800 P0009800 | 183.9828 | -60.8244 | 292.0001 | -26.6304 | 4766 | 4600 | 3.9 | 0.42 | 371 | 2.603 | 12.27 | 12.16 | 12.44 | 12.53 | 12.71 | -21.25 | -21.32 | 34.01 | 63.5 | 33.92 | 60.8 | |
| 9816 AGC120356 | 145.8200 | -23.3754 | 337.3169 | -10.2382 | 3762 | 3578 | 4.2 | 0.35 | 222 | 2.366 | 13.25 | 13.17 | 13.10 | 13.18 | 13.55 | -19.09 | -19.00 | 32.65 | 34.0 | 32.19 | 27.4 | |
| 9869 UGC02081 | 169.5892 | -52.7085 | 304.1669 | -24.1194 | 2622 | 2405 | 5.8 | 0.60 | 181 | 2.344 | 13.06 | 13.21 | 14.16 | 14.26 | 14.09 | -18.89 | -18.78 | 33.00 | 39.7 | 33.07 | 41.1 | |
| 9888 UGC02082 | 150.8871 | -31.6959 | 328.8352 | -14.8034 | 707 | 479 | 5.8 | 0.22 | 191 | 2.283 | 11.85 | 11.56 | 12.61 | 12.64 | 12.45 | -18.33 | -18.19 | 30.79 | 14.4 | 30.82 | 14.6 | |
| 9938 NGC00992 | 153.6278 | -35.3758 | 324.8925 | -16.8948 | 4136 | 3946 | 5.1 | 0.66 | 295 | 2.585 | 12.17 | 12.09 | 11.79 | 11.87 | 12.36 | -21.08 | -21.14 | 33.48 | 49.6 | 33.04 | 40.6 | |
| 10029 UGC02134 | 150.1867 | -29.2784 | 331.3448 | -14.2501 | 4585 | 4413 | 3.1 | 0.40 | 321 | 2.536 | 12.07 | 11.76 | 12.31 | 12.37 | 12.43 | -20.64 | -20.66 | 33.09 | 41.4 | 33.06 | 40.9 | |
| 10052 NGC01003 | 144.0041 | -17.5449 | 343.1141 | -8.2023 | 624 | 423 | 6.0 | 0.27 | 204 | 2.317 | 10.82 | 10.70 | 11.70 | 11.76 | 11.58 | -18.64 | -18.52 | 30.23 | 11.1 | 30.28 | 11.4 | |
| 10065 NGC01035 | 181.3687 | -58.1509 | 295.2754 | -27.2472 | 1242 | 1026 | 5.2 | 0.28 | 241 | 2.390 | 11.01 | 10.90 | 11.44 | 11.50 | 11.56 | -19.31 | -19.24 | 30.87 | 14.9 | 30.74 | 14.0 | |
| 10126 UGC02159 | 149.3736 | -27.1344 | 333.5565 | -13.5424 | 5191 | 5038 | 6.6 | 0.20 | 164 | 2.215 | 15.23 | 15.01 | 15.78 | 15.85 | 15.79 | -17.72 | -17.52 | 33.54 | 50.9 | 33.42 | 48.3 | |
| 10172 NGC001051 | 180.1341 | -57.0790 | 296.6892 | -27.3340 | 1295 | 1080 | 8.8 | 0.58 | 175 | 2.323 | / | / | 12.97 | 13.06 | / | / | -18.58 | / | / | / | 31.65 | 21.4 |
| 10208 NGC01055 | 171.3298 | -51.7502 | 304.6675 | -25.4789 | 992 | 769 | 3.1 | 0.47 | 386 | 2.631 | 9.38 | 9.30 | 9.39 | 9.45 | 9.74 | -21.50 | -21.59 | 31.24 | 17.7 | 31.03 | 16.1 | |
| 10218 UGC02171 | 148.6610 | -25.2057 | 335.5307 | -12.8825 | 4571 | 4407 | 6.5 | 0.20 | 211 | 2.325 | 14.73 | 14.37 | 15.18 | 15.23 | 15.16 | -18.72 | -18.60 | 33.92 | 60.8 | 33.89 | 60.1 | |
| 10272 UGC02183 | 150.6761 | -28.2305 | 332.4218 | -14.6916 | 1557 | 1344 | 1.0 | 0.70 | 266 | 2.565 | 10.89 | 10.84 | 11.38 | 11.45 | 11.51 | -20.90 | -20.95 | 32.42 | 30.5 | 32.41 | 30.3 | |
| 10312 UGC02194 | 144.5054 | -16.7256 | 343.9746 | -8.6221 | 5482 | 5359 | 3.0 | 0.38 | 302 | 2.505 | / | / | 13.26 | 13.34 | / | / | -20.36 | / | / | / | 33.76 | 56.5 |

| PGC Name | l | b | sgl | sgb | v_{hel} | v_{mod} | t | b/a | w_{max} | $\log w_{max}^2$ | I | I* | [3.6] | [3.6]* | $C_{[3.6]}$ | M_C | $M_{[3.6]}$ | μ_C | dC | $\mu_{[3.6]}$ | $d_{[3.6]}$ |
|-----------------|----------|----------|----------|----------|-----------|-----------|-----|------|-----------|------------------|-------|-------|-------|--------|-------------|--------|-------------|---------|-------|---------------|-------------|
| 10331 UGC002201 | 148.8314 | -24.6673 | 336.0858 | -13.0276 | 4148 | 3978 | 6.4 | 0.25 | 321 | 2.511 | 13.56 | 13.05 | 13.35 | 13.38 | 13.58 | -20.41 | -20.42 | 34.05 | 64.5 | 33.87 | 59.3 |
| 10448 AGC120493 | 169.6596 | -48.9801 | 307.9549 | -25.5647 | 6806 | 6699 | 4.0 | 0.36 | 294 | 2.490 | 13.35 | 13.23 | 13.57 | 13.67 | 13.82 | -20.22 | -20.21 | 34.08 | 65.6 | 33.95 | 61.7 |
| 10464 AGC420244 | 182.4810 | -56.5545 | 296.3188 | -28.6822 | 1406 | 1199 | 4.9 | 0.65 | 296 | 2.583 | 9.69 | 9.80 | 10.12 | 10.21 | 10.37 | -21.07 | -21.12 | 31.43 | 19.4 | 31.33 | 18.4 |
| 10488 NGC001097 | 226.9150 | -64.6804 | 270.2285 | -31.6387 | 1271 | 1108 | 3.3 | 0.64 | 384 | 2.692 | 8.19 | 8.25 | 8.70 | 8.73 | 8.85 | -22.06 | -22.19 | 30.91 | 15.2 | 30.91 | 15.2 |
| 10496 NGC001087 | 173.7451 | -51.6513 | 304.0589 | -26.8760 | 1518 | 1304 | 5.2 | 0.61 | 309 | 2.412 | 10.27 | 10.39 | 10.75 | 10.83 | 10.98 | -19.51 | -19.45 | 30.49 | 12.5 | 30.29 | 11.4 |
| 10507 NGC001090 | 173.5090 | -51.4438 | 304.3402 | -26.8353 | 2757 | 2556 | 3.8 | 0.43 | 310 | 2.527 | 11.07 | 11.01 | 11.60 | 11.68 | 11.70 | -20.55 | -20.57 | 32.27 | 28.4 | 32.26 | 28.4 |
| 10673 NGC001110 | 183.7298 | -56.1064 | 296.2441 | -29.5043 | 1332 | 1129 | 8.9 | 0.20 | 159 | 2.201 | 13.09 | 13.06 | 14.05 | 14.13 | 13.95 | -17.59 | -17.39 | 31.54 | 20.3 | 31.52 | 20.1 |
| 10913 UGC02364 | 168.6322 | -45.2409 | 312.1253 | -26.1904 | 5429 | 5288 | 3.0 | 0.36 | 323 | 2.531 | 13.59 | 13.16 | 13.89 | 13.94 | 13.91 | -20.59 | -20.61 | 34.57 | 82.1 | 34.67 | 85.7 |
| 10943 UGC02375 | 169.0791 | -45.3447 | 311.9017 | -26.4540 | 7610 | 7542 | 2.0 | 0.29 | 440 | 2.654 | 13.17 | 12.58 | 13.28 | 13.33 | 13.31 | -21.71 | -21.82 | 35.12 | 105.9 | 35.30 | 114.9 |
| 10965 AGC022202 | 202.7802 | -60.4866 | 284.1077 | -32.7535 | 2064 | 1891 | 5.2 | 0.20 | 320 | 2.506 | 11.48 | 11.13 | 11.75 | 11.79 | 11.82 | -20.36 | -20.36 | 32.18 | 27.3 | 32.16 | 27.0 |
| 10966 AGC420295 | 188.3252 | -56.3400 | 294.1172 | -31.2973 | 1500 | 1308 | 9.2 | 0.50 | 177 | 2.302 | 11.85 | 11.95 | 12.68 | 12.71 | 12.69 | -18.50 | -18.37 | 31.20 | 17.3 | 31.09 | 16.5 |
| 11004 P0011004 | 134.8772 | 6.4415 | 6.1374 | 3.1705 | 3485 | 3391 | 4.8 | 0.50 | 371 | 2.623 | 12.82 | 11.27 | 11.81 | 11.69 | 11.85 | -21.43 | -21.51 | 33.30 | 45.8 | 33.24 | 44.5 |
| 11016 ES356-018 | 239.9914 | -62.2675 | 263.0136 | -33.2831 | 1438 | 1302 | 5.0 | 0.22 | 117 | 2.070 | 13.78 | 13.95 | 14.93 | 15.02 | 14.84 | -16.40 | -16.11 | 31.24 | 17.7 | 31.13 | 16.9 |
| 11067 UGC02404 | 174.6762 | -48.8857 | 306.5732 | -28.6231 | 5032 | 4887 | 6.1 | 0.20 | 276 | 2.441 | 14.43 | 14.05 | 14.47 | 14.52 | 14.65 | -19.77 | -19.73 | 34.49 | 79.2 | 34.35 | 74.0 |
| 11074 UGC02405 | 169.3718 | -44.8582 | 312.3397 | -26.8090 | 7696 | 7634 | 5.7 | 0.36 | 400 | 2.624 | 13.14 | 12.72 | 13.43 | 13.50 | 13.47 | -21.44 | -21.52 | 35.00 | 99.9 | 35.16 | 107.9 |
| 11102 UGC02415 | 169.7958 | -45.0483 | 312.0267 | -27.0288 | 7773 | 7715 | 4.0 | 0.33 | 323 | 2.525 | 14.09 | 13.71 | 14.07 | 14.15 | 14.30 | -20.54 | -20.55 | 34.92 | 96.4 | 34.82 | 92.1 |
| 11153 UGC02429 | 174.7747 | -48.4748 | 306.9634 | -28.8599 | 1772 | 1573 | 9.0 | 0.28 | 144 | 2.167 | / | / | 15.28 | 15.35 | / | / | -17.06 | / | / | 32.42 | 30.5 |
| 11202 IC0001870 | 179.0608 | -50.8918 | 303.0100 | -30.1597 | 1542 | 1345 | 9.0 | 0.47 | 181 | 2.304 | 11.81 | 11.85 | 12.88 | 12.96 | 12.76 | -18.53 | -18.40 | 31.29 | 18.1 | 31.36 | 18.7 |
| 11245 UGC02443 | 178.8314 | -50.6000 | 303.3860 | -30.1837 | 2515 | 2328 | 5.8 | 0.50 | 204 | 2.365 | 12.79 | 12.78 | 13.44 | 13.52 | 13.51 | -19.08 | -18.99 | 32.60 | 33.2 | 32.53 | 32.0 |
| 11248 AGC420325 | 181.5474 | -52.0827 | 300.8808 | -30.8298 | 2374 | 2188 | 6.4 | 0.42 | 193 | 2.319 | / | / | 13.31 | 13.39 | / | -18.54 | / | / | / | 31.93 | 24.4 |
| 11255 UGC02444 | 170.2165 | -44.5892 | 312.3998 | -27.4645 | 6714 | 6619 | 3.5 | 0.61 | 361 | 2.651 | 13.06 | 12.86 | 12.97 | 13.05 | 13.33 | -21.68 | -21.78 | 35.11 | 105.2 | 34.97 | 98.6 |
| 11282 UGC02411 | 130.6540 | 14.8188 | 14.1337 | 8.0783 | 2538 | 2460 | 8.2 | 0.20 | 306 | 2.486 | 13.02 | 11.93 | 12.65 | 12.60 | 12.62 | -20.18 | -20.17 | 32.82 | 36.6 | 32.79 | 36.1 |
| 11306 UGC02454 | 169.5079 | -43.7079 | 313.5255 | -27.2753 | 7623 | 7562 | 6.3 | 0.23 | 359 | 2.558 | 13.93 | 13.31 | 14.02 | 14.06 | 14.04 | -20.84 | -20.88 | 34.97 | 98.7 | 35.08 | 103.7 |
| 11350 AGC120852 | 171.2062 | -44.7602 | 311.9436 | -28.0659 | 8406 | 8379 | 4.1 | 0.70 | 188 | 2.412 | 14.20 | 14.25 | 14.67 | 14.79 | 14.89 | -19.50 | -19.45 | 34.46 | 77.9 | 34.33 | 73.4 |
| 11359 AGC420340 | 201.1734 | -58.6301 | 286.0800 | -33.9344 | 2286 | 2120 | 4.1 | 0.21 | 293 | 2.468 | 12.51 | 12.21 | 12.68 | 12.73 | 12.83 | -20.01 | -19.99 | 32.86 | 37.4 | 32.75 | 35.4 |
| 11365 PG0011365 | 191.8464 | -55.8838 | 292.8698 | -33.0140 | 8972 | 8988 | 1.3 | 0.62 | 416 | 2.716 | / | / | 12.80 | 12.93 | / | -22.42 | / | / | / | 35.52 | 127.1 |
| 11368 UGC02459 | 143.6729 | -8.5556 | 352.1271 | -7.1391 | 2469 | 2318 | 7.9 | 0.20 | 318 | 2.502 | 13.03 | 12.06 | 12.33 | 12.29 | 12.55 | -20.33 | -20.33 | 32.90 | 38.0 | 32.65 | 33.8 |
| 11403 UGC02475 | 145.7781 | -12.0822 | 348.7565 | -9.5064 | 2529 | 2371 | 5.9 | 0.45 | 252 | 2.442 | 11.80 | 11.51 | 12.18 | 12.22 | 12.22 | -19.78 | -19.74 | 32.01 | 25.2 | 31.97 | 24.8 |
| 11479 NGC001187 | 212.0911 | -60.0562 | 279.2434 | -35.0275 | 1389 | 1229 | 5.0 | 0.71 | 263 | 2.567 | 9.90 | 10.06 | 10.44 | 10.53 | 10.66 | -20.92 | -20.96 | 31.57 | 20.7 | 31.49 | 19.9 |
| 11521 UGC02503 | 145.4277 | -10.6334 | 350.1915 | -9.0467 | 2386 | 2231 | 2.6 | 0.62 | 450 | 2.751 | 9.87 | 9.61 | 10.28 | 10.33 | 10.33 | -22.59 | -22.76 | 32.94 | 38.8 | 33.12 | 42.1 |
| 11538 AGC022291 | 216.9322 | -60.3273 | 276.3183 | -35.4182 | 1723 | 1572 | 8.8 | 0.58 | 104 | 2.097 | / | / | 14.96 | 15.07 | / | -16.37 | / | / | / | 31.44 | 19.4 |
| 11574 UGC002511 | 144.5979 | -8.9313 | 351.8343 | -8.0840 | 3860 | 3733 | 2.2 | 0.29 | 381 | 2.591 | / | / | 12.48 | 12.46 | / | -21.20 | / | / | / | 33.71 | 55.3 |
| 11606 E300-009 | 245.6969 | -59.6393 | 258.8290 | -34.8810 | 6075 | 6048 | 3.7 | 0.34 | 307 | 2.506 | 13.99 | 13.86 | 14.68 | 14.77 | 14.68 | -20.36 | -20.37 | 35.14 | 106.5 | 35.30 | 114.7 |
| 11617 NGC1186 | 147.5468 | -13.5375 | 347.4084 | -11.3324 | 2742 | 2587 | 4.5 | 0.40 | 421 | 2.653 | 10.60 | 10.27 | 11.03 | 11.08 | 11.03 | -21.70 | -21.81 | 32.75 | 35.5 | 32.91 | 38.2 |
| 11679 UGC02540 | 151.3839 | -19.1049 | 341.8737 | -15.2754 | 3926 | 3782 | 2.1 | 0.55 | 411 | 2.688 | / | / | 12.81 | 12.86 | / | -22.10 | / | / | / | 35.10 | 104.7 |
| 11744 PG0011744 | 197.3573 | -55.4794 | 290.3340 | -35.3404 | 1573 | 1405 | 1.0 | 0.47 | 107 | 2.075 | / | / | 13.73 | 13.83 | / | -16.16 | / | / | / | 29.98 | 9.9 |

| PGC Name | l | b | sgl | sgb | v_{hel} | v_{mod} | t | b/a | w_{max} | $\log w_{max}^2$ | I | I* | [3.6] | [3.6]* | $C_{[3.6]}$ | M_C | $M_{[3.6]}$ | μ_C | dC | $\mu_{[3.6]}$ | $d_{[3.6]}$ |
|-----------------|----------|----------|----------|----------|-----------|-----------|-----|------|-----------|------------------|-------|-------|-------|--------|-------------|--------|-------------|---------|------|---------------|-------------|
| 11750 IC0001892 | 213.1263 | -58.8086 | 279.1064 | -36.3769 | 2883 | 2746 | 7.7 | 0.67 | 173 | 2.360 | 12.85 | 13.03 | 13.81 | 13.91 | 13.83 | -19.04 | -18.94 | 32.88 | 37.7 | 32.88 | 37.7 |
| 11767 PGC011767 | 187.6387 | -51.7392 | 298.5327 | -34.0399 | 8712 | 8722 | 1.1 | 0.30 | 412 | 2.627 | / | / | 13.26 | 13.35 | / | / | -21.55 | / | / | 35.03 | 101.3 |
| 11782 AGC430066 | 192.1568 | -53.4905 | 294.7149 | -34.8627 | 3119 | 2965 | 1.1 | 0.40 | 291 | 2.493 | / | / | 13.40 | 13.46 | / | / | -20.24 | / | / | 33.76 | 56.6 |
| 11793 AGC02519 | 128.8162 | 18.8736 | 18.1103 | 10.1075 | 2344 | 2281 | 5.9 | 0.61 | 228 | 2.448 | 11.93 | 11.69 | 12.19 | 12.24 | 12.33 | -19.84 | -19.80 | 32.17 | 27.2 | 32.05 | 25.7 |
| 11809 UGC022360 | 203.9821 | -56.8758 | 285.5948 | -36.2068 | 2015 | 1859 | 7.9 | 0.20 | 123 | 2.000 | / | / | 16.69 | 16.78 | / | / | -16.30 | / | / | 33.12 | 42.0 |
| 11812 ES300-014 | 248.0576 | -58.4621 | 256.8871 | -35.6434 | 956 | 846 | 8.9 | 0.48 | 124 | 2.142 | 11.83 | 12.04 | 12.93 | 13.02 | 12.88 | -17.05 | -16.81 | 29.94 | 9.7 | 29.83 | 9.3 |
| 11836 NGC001249 | 268.2131 | -53.4145 | 242.4896 | -32.4487 | 1072 | 999 | 6.0 | 0.40 | 217 | 2.365 | 10.97 | 11.00 | 11.90 | 11.97 | 11.84 | -19.09 | -19.00 | 30.93 | 15.3 | 30.97 | 15.6 |
| 11846 UGC02567 | 149.4207 | -14.8608 | 346.1701 | -13.2265 | 2992 | 2842 | 7.4 | 0.45 | 276 | 2.481 | 12.35 | 12.14 | 12.54 | 12.60 | 12.73 | -20.14 | -20.13 | 32.89 | 37.8 | 32.75 | 35.4 |
| 11851 AGC022377 | 212.1415 | -58.2222 | 279.9442 | -36.7716 | 1324 | 1172 | 5.7 | 0.20 | 246 | 2.391 | 11.66 | 11.45 | 12.22 | 12.27 | 12.22 | -19.32 | -19.24 | 31.54 | 20.3 | 31.52 | 20.1 |
| 11856 ES357-007 | 232.8664 | -59.5019 | 266.5262 | -36.6523 | 1117 | 988 | 9.0 | 0.30 | 125 | 2.109 | 13.35 | 13.52 | 14.75 | 14.79 | 14.50 | -16.75 | -16.49 | 31.25 | 17.8 | 31.28 | 18.0 |
| 11941 NGC001233 | 150.6084 | -15.8521 | 345.2094 | -14.4198 | 4389 | 4266 | 3.0 | 0.41 | 419 | 2.652 | 12.05 | 11.70 | 12.11 | 12.16 | 12.30 | -21.70 | -21.80 | 34.04 | 64.3 | 34.03 | 64.0 |
| 12007 NGC001255 | 218.6023 | -58.2626 | 275.8095 | -37.6142 | 1685 | 1547 | 4.0 | 0.61 | 221 | 2.438 | 9.99 | 10.14 | 11.06 | 11.15 | 11.00 | -19.74 | -19.70 | 30.74 | 14.1 | 30.86 | 14.8 |
| 12011 ES481-014 | 217.6176 | -58.1286 | 276.4854 | -37.6406 | 1733 | 1594 | 8.9 | 0.20 | 158 | 2.199 | 12.83 | 12.85 | 14.17 | 14.25 | 13.90 | -17.57 | -17.37 | 31.46 | 19.6 | 31.62 | 21.1 |
| 12041 NGC01253 | 183.6907 | -48.1171 | 303.8730 | -34.1838 | 1709 | 1536 | 5.9 | 0.37 | 293 | 2.491 | 10.77 | 10.58 | 11.53 | 11.53 | 11.41 | -20.22 | -20.22 | 31.64 | 21.3 | 31.75 | 22.4 |
| 12080 UGC02609 | 151.8399 | -16.8011 | 344.2766 | -15.6387 | 4951 | 4842 | 3.1 | 0.65 | 337 | 2.638 | 12.56 | 12.24 | 12.55 | 12.60 | 12.79 | -21.57 | -21.66 | 34.42 | 76.6 | 34.35 | 74.1 |
| 12130 P0012130 | 187.3351 | -49.3849 | 300.9017 | -35.3770 | 2314 | 2153 | 2.3 | 0.28 | 273 | 2.444 | 12.18 | 11.95 | 12.79 | 12.84 | 12.75 | -19.80 | -19.77 | 32.57 | 32.6 | 32.63 | 33.6 |
| 12132 UGC02617 | 150.3132 | -14.1749 | 346.9230 | -14.0520 | 4698 | 4588 | 6.3 | 0.40 | 278 | 2.473 | 12.48 | 12.22 | 13.02 | 13.09 | 13.01 | -20.06 | -20.05 | 33.10 | 41.6 | 33.17 | 43.1 |
| 12181 AGC022447 | 237.3039 | -58.0192 | 263.3664 | -37.7268 | 1568 | 1456 | 7.0 | 0.71 | 123 | 2.231 | 12.65 | 12.88 | 13.63 | 13.68 | 13.64 | -17.87 | -17.69 | 31.51 | 20.0 | 31.36 | 18.7 |
| 12227 UGC02637 | 152.1862 | -16.4105 | 344.6944 | -15.9567 | 5146 | 5045 | 6.1 | 0.20 | 274 | 2.438 | 13.99 | 13.18 | 13.49 | 13.50 | 13.71 | -19.74 | -19.70 | 33.48 | 49.7 | 33.23 | 44.3 |
| 12285 AGC022455 | 222.4210 | -57.5238 | 273.4004 | -38.6501 | 1367 | 1237 | 5.0 | 0.41 | 227 | 2.388 | 11.28 | 11.31 | 12.02 | 12.01 | 12.06 | -19.29 | -19.22 | 31.36 | 18.7 | 31.32 | 18.3 |
| 12333 UGC02655 | 149.4392 | -11.9223 | 349.1833 | -13.0664 | 6190 | 6128 | 6.3 | 0.38 | 295 | 2.495 | 12.81 | 12.48 | 13.18 | 13.25 | 13.22 | -20.26 | -20.26 | 33.52 | 50.5 | 33.56 | 51.4 |
| 12390 IC0001914 | 261.4893 | -53.8953 | 246.1978 | -35.0162 | 1028 | 952 | 6.9 | 0.58 | 192 | 2.362 | 11.89 | 12.03 | 13.10 | 13.19 | 12.96 | -19.06 | -18.97 | 32.02 | 25.4 | 32.16 | 27.0 |
| 12404 AGC022474 | 231.4916 | -57.5849 | 267.1729 | -38.6340 | 1449 | 1331 | 3.4 | 0.21 | 157 | 2.197 | 13.21 | 13.24 | 14.10 | 14.13 | 14.04 | -17.55 | -17.35 | 31.60 | 20.9 | 31.48 | 19.8 |
| 12466 NGC001299 | 189.2036 | -48.9898 | 300.3253 | -36.5728 | 2335 | 2181 | 3.0 | 0.51 | 218 | 2.395 | 12.01 | 12.06 | 12.52 | 12.61 | 12.70 | -19.35 | -19.28 | 32.06 | 25.8 | 31.90 | 24.0 |
| 12484 AGC022479 | 220.4563 | -56.8997 | 274.8611 | -39.1281 | 1749 | 1622 | 6.9 | 0.33 | 115 | 2.076 | 14.31 | 14.52 | 15.30 | 15.40 | 15.32 | -16.46 | -16.17 | 31.77 | 22.6 | 31.58 | 20.7 |
| 12608 PG0012608 | 202.6316 | -53.3409 | 288.7123 | -38.8491 | 2003 | 1860 | 9.0 | 0.50 | 123 | 2.144 | / | / | 15.28 | 15.37 | / | / | -16.83 | / | / | 32.21 | 27.7 |
| 12737 AGC022540 | 212.3081 | -54.8415 | 281.2632 | -39.9917 | 1588 | 1455 | 4.0 | 0.33 | 334 | 2.540 | 10.51 | 10.34 | 11.27 | 11.32 | 11.19 | -20.68 | -20.70 | 31.87 | 23.6 | 32.04 | 25.5 |
| 12798 AGC430249 | 204.0059 | -52.7750 | 288.1856 | -39.7636 | 1874 | 1736 | 7.6 | 0.20 | 215 | 2.332 | 12.73 | 12.55 | 13.39 | 13.45 | 13.36 | -18.79 | -18.67 | 32.15 | 26.9 | 32.13 | 26.7 |
| 12807 IC0001933 | 265.5352 | -51.6332 | 242.1384 | -34.8446 | 1061 | 1000 | 6.2 | 0.51 | 172 | 2.291 | 11.76 | 11.90 | 12.70 | 12.79 | 12.70 | -18.41 | -18.27 | 31.11 | 16.7 | 31.06 | 16.3 |
| 12816 UGC002730 | 151.9878 | -13.2516 | 347.9655 | -15.6280 | 3767 | 3647 | 3.1 | 0.20 | 451 | 2.654 | 12.78 | 11.99 | 12.46 | 12.46 | 12.59 | -21.71 | -21.82 | 34.37 | 74.7 | 34.37 | 74.8 |
| 12889 AGC022597 | 212.1621 | -54.0443 | 281.7242 | -40.7123 | 1683 | 1555 | 7.7 | 0.20 | 167 | 2.223 | 13.19 | 13.16 | 14.05 | 14.13 | 14.00 | -17.79 | -17.60 | 31.79 | 22.8 | 31.73 | 22.2 |
| 12916 AGC430266 | 193.5410 | -48.5182 | 298.3286 | -39.0035 | 1239 | 1089 | 6.0 | 0.25 | 244 | 2.393 | 10.81 | 10.60 | 11.68 | 11.73 | 11.52 | -19.33 | -19.26 | 30.85 | 14.8 | 30.99 | 15.8 |
| 12952 NGC1351A | 236.3571 | -55.6165 | 263.3691 | -40.1847 | 1352 | 1251 | 4.2 | 0.23 | 200 | 2.304 | 12.31 | 12.24 | 12.82 | 12.89 | 12.93 | -18.52 | -18.39 | 31.45 | 19.5 | 31.28 | 18.0 |
| 13059 NGC1350 | 233.6122 | -55.1679 | 265.2873 | -40.8965 | 1903 | 1806 | 1.9 | 0.47 | 390 | 2.636 | 9.11 | 9.06 | 9.84 | 9.86 | 9.82 | -21.55 | -21.64 | 31.37 | 18.8 | 31.50 | 20.0 |
| 13089 ES418-008 | 227.6614 | -54.9310 | 269.7768 | -41.3884 | 1191 | 1082 | 7.7 | 0.71 | 121 | 2.226 | 12.79 | 13.04 | 13.76 | 13.81 | 13.78 | -17.82 | -17.64 | 31.60 | 20.9 | 31.44 | 19.4 |
| 13090 IC0001954 | 263.6451 | -51.2013 | 242.7240 | -36.0058 | 1063 | 1005 | 3.2 | 0.53 | 213 | 2.392 | 10.52 | 10.64 | 11.18 | 11.26 | 11.31 | -19.33 | -19.26 | 30.64 | 13.4 | 30.52 | 12.7 |

| PGC Name | l | b | sgl | sgb | v_{hel} | v_{mod} | t | b/a | w_{max} | $\log w_{max}^i$ | I | I* | [3.6] | [3.6]* | $C_{[3.6]}$ | M_C | $M_{[3.6]}$ | μ_C | dC | $\mu_{[3.6]}$ | d _[3.6] |
|-----------------|----------|----------|----------|----------|-----------|-----------|-----|------|-----------|------------------|-------|-------|-------|--------|-------------|--------|-------------|---------|------|---------------|--------------------|
| 13108 NGC01353 | 212.0339 | -52.9290 | 282.3354 | -41.7313 | 1535 | 1411 | 3.2 | 0.41 | 378 | 2.609 | 10.16 | 10.03 | 10.66 | 10.72 | 10.74 | -21.30 | -21.38 | 32.04 | 25.6 | 32.10 | 26.4 |
| 13154 ES482-005 | 217.4728 | -53.6064 | 277.8917 | -42.0330 | 1916 | 1802 | 7.7 | 0.20 | 155 | 2.190 | / | / | 15.11 | 15.19 | / | / | -17.28 | / | / | 32.49 | 31.5 |
| 13163 IC0001959 | 261.2809 | -51.5385 | 244.3128 | -36.8163 | 639 | 577 | 8.5 | 0.26 | 119 | 2.082 | 12.10 | 12.29 | 13.33 | 13.37 | 13.18 | -16.50 | -16.22 | 29.68 | 8.6 | 29.59 | 8.3 |
| 13171 IC0001952 | 216.8244 | -53.4151 | 278.4576 | -42.1272 | 1814 | 1699 | 4.0 | 0.37 | 239 | 2.402 | 11.68 | 11.65 | 12.34 | 12.41 | 12.39 | -19.41 | -19.35 | 31.81 | 23.0 | 31.76 | 22.5 |
| 13255 NGC001367 | 218.9543 | -53.3471 | 276.8028 | -42.4746 | 1462 | 1349 | 1.1 | 0.64 | 382 | 2.688 | 9.49 | 9.55 | 10.25 | 10.33 | 10.30 | -22.02 | -22.14 | 32.33 | 29.2 | 32.49 | 31.5 |
| 13283 AGC022735 | 213.1896 | -52.2760 | 281.7463 | -42.5848 | 1809 | 1693 | 7.8 | 0.22 | 149 | 2.175 | 13.40 | 13.45 | 14.62 | 14.70 | 14.42 | -17.35 | -17.14 | 31.78 | 22.7 | 31.84 | 23.4 |
| 13304 ES482-011 | 220.1531 | -53.2082 | 275.8801 | -42.7428 | 1593 | 1484 | 4.6 | 0.31 | 124 | 2.106 | / | / | 14.24 | 14.33 | / | / | -16.47 | / | / | 30.80 | 14.4 |
| 13368 NGC001385 | 218.4606 | -52.7084 | 277.3761 | -43.0394 | 1501 | 1390 | 5.9 | 0.63 | 173 | 2.339 | 10.05 | 10.23 | 10.65 | 10.75 | 10.85 | -18.84 | -18.74 | 29.70 | 8.7 | 29.48 | 7.9 |
| 13400 UGC02798 | 153.7726 | -11.6961 | 349.6803 | -17.2869 | 4942 | 4863 | 3.8 | 0.37 | 411 | 2.638 | 12.11 | 11.61 | 12.34 | 12.38 | 12.35 | -21.56 | -21.65 | 33.96 | 62.0 | 34.11 | 66.3 |
| 13410 UGC02801 | 153.6067 | -11.4309 | 349.9483 | -17.1102 | 6012 | 5963 | 5.7 | 0.21 | 390 | 2.592 | 13.65 | 12.86 | 13.14 | 13.15 | 13.38 | -21.15 | -21.21 | 34.59 | 82.9 | 34.46 | 77.8 |
| 13458 NGC001406 | 229.7850 | -53.3358 | 268.0303 | -42.9429 | 1067 | 969 | 4.4 | 0.22 | 322 | 2.510 | 10.67 | 10.38 | 10.81 | 10.80 | 10.95 | -20.40 | -20.41 | 31.35 | 18.7 | 31.20 | 17.4 |
| 13561 ES482-035 | 217.7425 | -51.7159 | 278.2693 | -43.9103 | 1880 | 1777 | 2.2 | 0.63 | 185 | 2.370 | 11.97 | 12.14 | 12.91 | 13.00 | 12.93 | -19.13 | -19.04 | 32.06 | 25.9 | 32.05 | 25.8 |
| 13569 AGC022861 | 214.4370 | -51.0788 | 281.2658 | -43.9664 | 1639 | 1530 | 2.3 | 0.25 | 143 | 2.160 | 12.44 | 12.52 | 13.08 | 13.16 | 13.20 | -17.22 | -16.99 | 30.42 | 12.2 | 30.16 | 10.7 |
| 13602 AGC022873 | 227.5201 | -52.5993 | 269.8739 | -43.7205 | 1512 | 1418 | 3.2 | 0.46 | 354 | 2.592 | 9.87 | 9.83 | 10.71 | 10.73 | 10.64 | -21.15 | -21.21 | 31.79 | 22.8 | 31.95 | 24.5 |
| 13620 NGC001421 | 202.8026 | -47.8797 | 292.5941 | -43.4656 | 2078 | 1962 | 4.1 | 0.27 | 344 | 2.544 | 10.42 | 10.09 | 10.74 | 10.78 | 10.80 | -20.71 | -20.74 | 31.51 | 20.0 | 31.52 | 20.1 |
| 13631 AGC022880 | 208.4120 | -49.4385 | 287.0836 | -44.0179 | 1722 | 1609 | 4.2 | 0.51 | 143 | 2.212 | / | / | 15.44 | 15.52 | / | / | -17.50 | / | / | 33.04 | 40.6 |
| 13646 AGC430438 | 202.1100 | -47.5314 | 293.3955 | -43.4811 | 2163 | 2048 | 4.8 | 0.20 | 358 | 2.554 | 11.85 | 11.38 | 11.78 | 11.80 | 11.96 | -20.80 | -20.84 | 32.77 | 35.9 | 32.66 | 34.0 |
| 13684 PG0013684 | 206.4259 | -48.6805 | 289.1776 | -44.0720 | 1214 | 1096 | 8.1 | 0.50 | 175 | 2.297 | / | / | 13.80 | 13.88 | / | / | -18.32 | / | / | 32.22 | 27.8 |
| 13687 NGC01436 | 237.3503 | -52.5847 | 261.7197 | -43.0149 | 1393 | 1312 | 2.0 | 0.66 | 201 | 2.419 | 10.61 | 10.79 | 11.32 | 11.37 | 11.44 | -19.57 | -19.51 | 31.01 | 15.9 | 30.88 | 15.0 |
| 13695 ES015-001 | 294.7818 | -34.1184 | 214.3548 | -22.1978 | 1648 | 1676 | 9.8 | 0.37 | 120 | 2.102 | 13.35 | 13.45 | 14.66 | 14.75 | 14.45 | -16.69 | -16.42 | 31.14 | 16.9 | 31.17 | 17.2 |
| 13716 AGC430459 | 204.2133 | -47.9153 | 291.4794 | -43.9621 | 1580 | 1463 | 4.0 | 0.31 | 289 | 2.474 | 11.72 | 11.52 | 12.22 | 12.27 | 12.25 | -20.07 | -20.05 | 32.33 | 29.3 | 32.33 | 29.3 |
| 13727 NGC1448 | 251.5220 | -51.3942 | 250.3258 | -40.6853 | 1169 | 1106 | 6.0 | 0.20 | 388 | 2.589 | 9.76 | 9.33 | 10.03 | 10.00 | 10.03 | -21.12 | -21.18 | 31.15 | 17.0 | 31.18 | 17.2 |
| 13794 NGC1437B | 238.1588 | -52.1100 | 260.9031 | -43.3538 | 1506 | 1429 | 8.9 | 0.32 | 111 | 2.060 | 12.24 | 12.46 | 12.97 | 13.07 | 13.13 | -16.31 | -16.01 | 29.43 | 7.7 | 29.08 | 6.5 |
| 13809 AGC022940 | 235.8582 | -52.0392 | 262.7796 | -43.7472 | 1927 | 1852 | 7.7 | 0.26 | 285 | 2.461 | 10.72 | 10.54 | 11.21 | 11.27 | 11.27 | -19.95 | -19.93 | 31.22 | 17.5 | 31.20 | 17.4 |
| 13821 P0013821 | 207.5967 | -48.2141 | 288.5422 | -44.8562 | 1253 | 1141 | 8.9 | 0.44 | 140 | 2.184 | 11.65 | 11.76 | 12.09 | 12.17 | 12.33 | -17.43 | -17.22 | 29.77 | 9.0 | 29.40 | 7.6 |
| 13871 ES549-018 | 214.8391 | -49.5248 | 281.5966 | -45.5239 | 1587 | 1487 | 4.8 | 0.57 | 223 | 2.424 | 11.69 | 11.74 | 12.49 | 12.57 | 12.51 | -19.62 | -19.56 | 32.13 | 26.7 | 32.14 | 26.8 |
| 13884 UGC02868 | 159.1528 | -14.9806 | 346.3732 | -22.6285 | 5426 | 5367 | 4.0 | 0.22 | 386 | 2.588 | 13.57 | 12.85 | 13.34 | 13.36 | 13.47 | -21.12 | -21.17 | 34.66 | 85.4 | 34.64 | 84.8 |
| 13912 IC0002000 | 257.6482 | -49.6042 | 244.8306 | -39.7989 | 980 | 931 | 6.2 | 0.20 | 255 | 2.407 | 11.30 | 11.09 | 12.08 | 12.13 | 11.96 | -19.46 | -19.40 | 31.42 | 19.2 | 31.52 | 20.2 |
| 13926 AGC022986 | 223.3077 | -50.5292 | 273.6943 | -45.6605 | 1526 | 1437 | 5.1 | 0.20 | 215 | 2.332 | 12.34 | 12.21 | 13.03 | 13.09 | 13.00 | -18.79 | -18.67 | 31.79 | 22.8 | 31.77 | 22.5 |
| 13931 ES054-021 | 286.3376 | -39.2291 | 221.3728 | -27.8091 | 1430 | 1438 | 7.9 | 0.52 | 193 | 2.344 | 11.14 | 11.21 | 12.34 | 12.42 | 12.17 | -18.89 | -18.79 | 31.06 | 16.3 | 31.21 | 17.5 |
| 13998 E359-003 | 233.5517 | -50.8150 | 264.4584 | -45.2073 | 1577 | 1503 | 1.4 | 0.38 | 112 | 2.074 | 12.73 | 12.95 | 14.31 | 14.42 | 14.03 | -16.43 | -16.14 | 30.46 | 12.4 | 30.56 | 13.0 |
| 13999 IC0002051 | 297.8127 | -31.3858 | 211.1477 | -19.9599 | 1716 | 1755 | 4.1 | 0.56 | 341 | 2.607 | 10.35 | 10.24 | 10.65 | 10.72 | 10.84 | -21.28 | -21.35 | 32.13 | 26.7 | 32.07 | 26.0 |
| 14071 NGC001484 | 239.0863 | -50.4155 | 259.4875 | -44.8284 | 1041 | 973 | 3.2 | 0.25 | 162 | 2.214 | 12.24 | 12.28 | 13.13 | 13.21 | 13.10 | -17.71 | -17.52 | 30.81 | 14.5 | 30.73 | 14.0 |
| 14099 AGC023045 | 214.0012 | -47.6735 | 283.2209 | -47.0974 | 1821 | 1731 | 6.0 | 0.71 | 115 | 2.204 | / | / | 15.41 | 15.51 | / | / | -17.42 | / | / | 32.95 | 39.0 |
| 14169 NGC001494 | 257.1704 | -48.2279 | 243.9611 | -41.0458 | 1130 | 1090 | 7.0 | 0.57 | 156 | 2.268 | 11.20 | 11.40 | 12.08 | 12.17 | 12.15 | -18.20 | -18.05 | 30.35 | 11.7 | 30.22 | 11.1 |
| 14236 NGC001511 | 281.3718 | -40.7246 | 224.3524 | -30.9673 | 1327 | 1330 | 1.8 | 0.34 | 273 | 2.455 | 10.45 | 10.31 | 10.55 | 10.60 | 10.83 | -19.90 | -19.87 | 30.73 | 14.0 | 30.47 | 12.4 |

| PGC Name | l | b | sgl | sgb | v_{hel} | v_{mod} | t | b/a | w_{mz} | $\log w_{mz}^i$ | I | I* | [3.6] | [3.6]* | $C_{[3.6]}$ | M_C | $M_{[3.6]}$ | μ_C | dC | $\mu_{[3.6]}$ | $d_{[3.6]}$ |
|-----------------|----------|----------|----------|----------|-----------|-----------|-----|------|----------|-----------------|-------|-------|-------|--------|-------------|--------|-------------|---------|------|---------------|-------------|
| 14246 UGC02915 | 162.7252 | -15.3291 | 346.0000 | -26.0774 | 5304 | 5255 | 6.1 | 0.21 | 287 | 2.459 | 14.52 | 13.91 | 14.38 | 14.41 | 14.52 | -19.93 | -19.90 | 34.52 | 80.3 | 34.41 | 76.0 |
| 14276 UGC02920 | 161.1948 | -13.4309 | 348.0934 | -24.5870 | 4184 | 4110 | 6.0 | 0.20 | 364 | 2.561 | 13.12 | 12.43 | 13.22 | 13.23 | 13.19 | -20.87 | -20.91 | 34.11 | 66.3 | 34.22 | 69.9 |
| 14286 UGC02906 | 135.0444 | 15.8601 | 15.5434 | 3.9497 | 2492 | 2433 | 3.0 | 0.59 | 445 | 2.732 | 11.25 | 10.92 | 11.47 | 11.51 | 11.58 | -22.42 | -22.58 | 34.05 | 64.6 | 34.17 | 68.2 |
| 14370 AGC130364 | 136.8383 | 14.2434 | 14.1059 | 2.0645 | 4512 | 4487 | 5.0 | 0.28 | 311 | 2.502 | / | / | 13.90 | 13.93 | / | / | -20.33 | / | / | 34.35 | 74.0 |
| 14391 NGC001512 | 248.6680 | -48.1658 | 250.1794 | -44.4003 | 900 | 854 | 1.1 | 0.67 | 234 | 2.487 | 9.26 | 9.42 | 9.98 | 10.02 | 10.08 | -20.19 | -20.18 | 30.28 | 11.4 | 30.21 | 11.0 |
| 14397 NGC001515 | 264.0947 | -45.8511 | 237.4179 | -39.3364 | 1182 | 1159 | 4.0 | 0.25 | 368 | 2.571 | 9.79 | 9.49 | 10.32 | 10.36 | 10.28 | -20.96 | -21.00 | 31.24 | 17.7 | 31.36 | 18.7 |
| 14409 UGC02947 | 193.0645 | -37.5576 | 309.9312 | -45.8863 | 865 | 761 | 8.5 | 0.24 | 172 | 2.240 | 11.52 | 11.31 | 12.15 | 12.20 | 12.11 | -17.94 | -17.77 | 30.05 | 10.2 | 29.96 | 9.8 |
| 14468 UGC02956 | 164.7201 | -15.3449 | 345.9567 | -28.0009 | 4542 | 4482 | 5.9 | 0.32 | 329 | 2.532 | 13.26 | 12.56 | 13.06 | 13.06 | 13.17 | -20.60 | -20.62 | 33.81 | 57.9 | 33.74 | 56.0 |
| 14475 AGC023188 | 216.3313 | -45.3069 | 282.0549 | -49.8497 | 923 | 845 | 8.2 | 0.34 | 157 | 2.213 | 10.98 | 11.04 | 11.80 | 11.88 | 11.82 | -17.70 | -17.50 | 29.51 | 8.0 | 29.38 | 7.5 |
| 14514 AGC023201 | 211.2105 | -43.6814 | 288.2610 | -50.0339 | 1833 | 1758 | 3.0 | 0.33 | 186 | 2.286 | 12.04 | 12.07 | 12.81 | 12.89 | 12.84 | -18.36 | -18.22 | 31.20 | 17.4 | 31.11 | 16.7 |
| 14600 AGC440044 | 199.4885 | -38.8377 | 303.6357 | -48.8818 | 2930 | 2860 | 6.8 | 0.20 | 200 | 2.301 | / | / | 14.06 | 14.12 | / | / | -18.37 | / | / | 32.50 | 31.6 |
| 14626 AGC440053 | 210.3742 | -42.6127 | 289.8634 | -50.7197 | 1877 | 1806 | 8.8 | 0.24 | 178 | 2.254 | / | / | 14.95 | 15.02 | / | / | -17.91 | / | / | 32.96 | 39.1 |
| 14638 NGC001532 | 233.1684 | -46.5841 | 263.8717 | -49.4270 | 1201 | 1149 | 3.1 | 0.31 | 518 | 2.728 | 8.75 | 8.42 | 8.98 | 9.01 | 9.08 | -22.39 | -22.54 | 31.47 | 19.6 | 31.55 | 20.5 |
| 14651 UGC02982 | 186.7401 | -31.5021 | 321.0918 | -44.4808 | 5318 | 5291 | 2.0 | 0.51 | 368 | 2.622 | / | / | 11.78 | 11.81 | / | / | -21.51 | / | / | 33.35 | 46.8 |
| 14693 UGC02988 | 170.1788 | -18.3173 | 342.2281 | -33.0830 | 3822 | 3755 | 3.0 | 0.20 | 446 | 2.649 | / | / | 11.95 | 11.89 | / | / | -21.77 | / | / | 33.71 | 55.2 |
| 14768 AGC440077 | 211.6162 | -41.7213 | 289.1860 | -51.9291 | 1953 | 1890 | 7.6 | 0.35 | 168 | 2.245 | / | / | 14.28 | 14.36 | / | / | -17.82 | / | / | 32.19 | 27.4 |
| 14780 PG0014780 | 206.3935 | -39.8955 | 296.1810 | -51.5012 | 8914 | 9043 | 3.1 | 0.37 | 414 | 2.640 | / | / | 13.31 | 13.41 | / | / | -21.68 | / | / | 35.24 | 111.9 |
| 14814 NGC001559 | 274.5105 | -41.1983 | 227.3292 | -35.5354 | 1302 | 1307 | 5.9 | 0.51 | 242 | 2.442 | 9.78 | 9.84 | 10.18 | 10.21 | 10.39 | -19.78 | -19.74 | 30.17 | 10.8 | 29.95 | 9.8 |
| 14853 UGC03009 | 170.5286 | -16.9461 | 343.8363 | -33.5122 | 3750 | 3690 | 5.7 | 0.22 | 248 | 2.396 | 13.52 | 12.88 | 13.85 | 13.86 | 13.73 | -19.37 | -19.30 | 33.12 | 42.0 | 33.20 | 43.6 |
| 14897 NGC001566 | 264.3102 | -43.3932 | 234.7922 | -40.7595 | 1504 | 1499 | 4.0 | 0.65 | 196 | 2.403 | 8.67 | 8.85 | 9.30 | 9.35 | 9.46 | -19.42 | -19.36 | 28.89 | 6.0 | 28.70 | 5.5 |
| 14936 ES550-024 | 218.6140 | -42.3113 | 280.8271 | -53.1817 | 898 | 841 | 6.7 | 0.38 | 168 | 2.250 | 11.23 | 11.32 | 12.56 | 12.64 | 12.33 | -18.03 | -17.86 | 30.36 | 11.8 | 30.51 | 12.6 |
| 15018 UGC03013 | 135.2231 | 17.7646 | 17.4601 | 3.9592 | 2459 | 2411 | 3.0 | 0.55 | 316 | 2.568 | 10.15 | 9.99 | 10.46 | 10.52 | 10.62 | -20.93 | -20.97 | 31.55 | 20.4 | 31.49 | 19.9 |
| 15047 UGC03028 | 165.5878 | -10.8111 | 351.1148 | -28.8329 | 5482 | 5471 | 4.4 | 0.40 | 417 | 2.649 | / | / | 11.81 | 11.82 | / | / | -21.77 | / | / | 33.64 | 53.6 |
| 15263 UGC03048 | 139.3218 | 14.8583 | 14.9810 | -0.2574 | 3050 | 3008 | 4.0 | 0.68 | 257 | 2.536 | / | / | 12.24 | 12.29 | / | / | -20.66 | / | / | 32.98 | 39.5 |
| 15355 UGC03066 | 189.8455 | -27.7449 | 324.4350 | -48.4944 | 4642 | 4628 | 6.5 | 0.67 | 314 | 2.617 | 12.43 | 12.10 | 12.45 | 12.50 | 12.67 | -21.38 | -21.46 | 34.10 | 66.0 | 34.03 | 64.0 |
| 15356 UGC03070 | 197.1546 | -31.8377 | 313.9503 | -51.9743 | 2518 | 2470 | 3.1 | 0.51 | 156 | 2.251 | 13.14 | 13.25 | 14.36 | 14.45 | 14.20 | -18.05 | -17.88 | 32.25 | 28.2 | 32.34 | 29.4 |
| 15455 ES202-035 | 256.7618 | -42.5516 | 238.9908 | -45.4297 | 1877 | 1880 | 3.5 | 0.20 | 275 | 2.439 | 11.84 | 11.58 | 12.51 | 12.56 | 12.43 | -19.76 | -19.72 | 32.19 | 27.4 | 32.29 | 28.7 |
| 15461 UGC03078 | 167.1959 | -10.0659 | 352.0157 | -30.3961 | 5419 | 5417 | 4.0 | 0.30 | 417 | 2.631 | 13.05 | 11.96 | 12.38 | 12.35 | 12.52 | -21.51 | -21.59 | 34.08 | 65.4 | 34.01 | 63.4 |
| 15481 UGC03084 | 185.7442 | -24.5550 | 330.7620 | -46.1794 | 4062 | 4034 | 5.8 | 0.20 | 322 | 2.508 | 13.05 | 12.22 | 12.91 | 12.90 | 12.92 | -20.38 | -20.39 | 33.33 | 46.3 | 33.33 | 46.3 |
| 15533 UGC03089 | 180.3154 | -20.3791 | 338.1026 | -42.3075 | 4603 | 4586 | 3.9 | 0.60 | 308 | 2.577 | / | / | 12.66 | 12.70 | / | / | -21.06 | / | / | 33.82 | 57.9 |
| 15638 UGC03103 | 196.1557 | -29.6695 | 317.6689 | -52.4746 | 3514 | 3489 | 4.5 | 0.30 | 427 | 2.642 | 10.95 | 10.60 | 11.39 | 11.43 | 11.37 | -21.60 | -21.69 | 32.99 | 39.7 | 33.16 | 42.9 |
| 15693 UGC003092 | 138.3285 | 16.6023 | 16.6060 | 0.8893 | 4784 | 4784 | 6.4 | 0.20 | 307 | 2.487 | 14.10 | 13.57 | 13.86 | 13.89 | 14.10 | -20.19 | -20.18 | 34.36 | 74.3 | 34.16 | 67.9 |
| 15793 UGC03114 | 142.9674 | 13.1636 | 13.7317 | -3.9752 | 3697 | 3697 | 5.8 | 0.39 | 361 | 2.584 | 12.47 | 11.92 | 12.54 | 12.56 | 12.60 | -21.08 | -21.14 | 33.72 | 55.5 | 33.75 | 56.3 |
| 15810 UGC03110 | 137.3263 | 17.6309 | 17.5260 | -1.9522 | 4487 | 4482 | 5.9 | 0.40 | 409 | 2.641 | 11.72 | 11.36 | 11.99 | 12.04 | 12.06 | -21.59 | -21.68 | 33.69 | 54.6 | 33.79 | 57.2 |
| 15869 P0015869 | 205.1376 | -32.1864 | 305.8485 | -56.8538 | 2524 | 2501 | 8.0 | 0.62 | 188 | 2.371 | / | / | 13.99 | 14.08 | / | / | -19.05 | / | / | 33.16 | 42.8 |
| 15924 UGC03148 | 180.6151 | -17.2412 | 342.2598 | -43.0774 | 4733 | 4735 | 3.5 | 0.51 | 347 | 2.597 | / | / | 12.87 | 12.87 | / | / | -21.26 | / | / | 34.21 | 69.4 |

| PGC Name | l | b | sgl | sgb | v_{hel} | v_{mod} | t | b/a | w_{max} | $\log w_{max}^*$ | I | I^* | [3.6] | [3.6]* | $C_{[3.6]}$ | M_C | $M_{[3.6]}$ | μ_C | d_C | $\mu_{[3.6]}$ | $d_{[3.6]}$ |
|-----------------|----------|----------|----------|----------|-----------|-----------|-----|------|-----------|------------------|-------|-------|-------|--------|-------------|--------|-------------|---------|-------|---------------|-------------|
| 15967 UGC03137 | 135.2257 | 19.5512 | 19.2437 | 4.1222 | 993 | 942 | 4.4 | 0.22 | 225 | 2.354 | 12.33 | 12.01 | 12.93 | 12.96 | 12.84 | -18.98 | -18.88 | 31.82 | 23.1 | 31.84 | 23.4 |
| 15982 UGC03161 | 196.8935 | -27.1371 | 320.7385 | -54.3422 | 8786 | 8946 | 5.9 | 0.20 | 499 | 2.698 | / | / | 13.91 | 13.96 | / | / | -22.25 | / | / | 36.47 | 196.7 |
| 15986 UGC03143 | 140.5232 | 15.7830 | 16.0359 | -1.2989 | 4560 | 4557 | 6.0 | 0.20 | 329 | 2.517 | 13.77 | 13.19 | 13.52 | 13.55 | 13.73 | -20.47 | -20.48 | 34.26 | 71.0 | 34.10 | 66.1 |
| 16027 UGC03147 | 138.3092 | 17.5194 | 17.5157 | 1.0086 | 2884 | 2851 | 4.0 | 0.49 | 247 | 2.443 | / | / | 13.07 | 13.12 | / | / | -19.76 | / | / | 32.91 | 38.1 |
| 16033 UGC03172 | 189.6003 | -22.4681 | 332.1194 | -50.1841 | 4732 | 4745 | 6.7 | 0.20 | 343 | 2.535 | / | / | 13.41 | 13.44 | / | / | -20.65 | / | / | 34.17 | 68.4 |
| 16084 ES421-019 | 230.0780 | -38.1368 | 265.9689 | -58.0884 | 1477 | 1473 | 9.0 | 0.72 | 131 | 2.267 | / | / | 13.12 | 13.22 | / | / | -18.03 | / | / | 31.25 | 17.8 |
| 16092 UGC03167 | 145.7298 | 12.1850 | 13.1215 | -6.7775 | 4736 | 4737 | 4.0 | 0.35 | 437 | 2.660 | 13.27 | 12.35 | 12.05 | 12.03 | 12.57 | -21.77 | -21.87 | 34.40 | 75.9 | 33.97 | 62.4 |
| 16118 AGC440373 | 208.8478 | -31.8257 | 301.7928 | -59.1819 | 4479 | 4505 | 4.0 | 0.51 | 218 | 2.394 | 13.57 | 13.58 | 14.27 | 14.36 | 14.33 | -19.35 | -19.28 | 33.72 | 55.4 | 33.69 | 54.8 |
| 16120 AGC023772 | 233.5623 | -38.5519 | 261.0207 | -57.2841 | 1052 | 1049 | 9.4 | 0.68 | 129 | 2.236 | 10.94 | 11.17 | 11.77 | 11.82 | 11.85 | -17.91 | -17.74 | 29.77 | 9.0 | 29.56 | 8.1 |
| 16144 IC002098 | 203.4248 | -29.2359 | 311.6897 | -57.8257 | 2820 | 2811 | 5.8 | 0.20 | 323 | 2.509 | 12.70 | 12.31 | 12.50 | 12.54 | 12.80 | -20.39 | -20.40 | 33.22 | 44.0 | 32.97 | 39.3 |
| 16191 UGC03186 | 194.7613 | -24.4437 | 326.3258 | -53.8775 | 4578 | 4597 | 6.1 | 0.20 | 240 | 2.380 | 14.40 | 14.14 | 14.79 | 14.86 | 14.86 | -19.22 | -19.14 | 34.13 | 67.1 | 34.08 | 65.3 |
| 16199 ES361-015 | 235.1864 | -38.3533 | 258.6478 | -57.1928 | 1169 | 1170 | 6.7 | 0.24 | 181 | 2.261 | 12.01 | 11.98 | 13.05 | 13.12 | 12.90 | -18.14 | -17.98 | 31.04 | 16.1 | 31.10 | 16.6 |
| 16299 ES085-014 | 272.8853 | -37.1483 | 223.4515 | -38.4335 | 1407 | 1440 | 9.0 | 0.38 | 173 | 2.263 | / | / | 13.24 | 13.32 | / | / | -17.99 | / | / | 31.31 | 18.3 |
| 16317 AGC023849 | 240.5241 | -38.3956 | 251.5081 | -55.7826 | 2317 | 2337 | 1.1 | 0.35 | 111 | 2.065 | / | / | 14.07 | 14.18 | / | / | -16.06 | / | / | 30.24 | 11.2 |
| 16322 P0016322 | 202.6879 | -27.6629 | 314.7681 | -58.3198 | 3850 | 3865 | 3.6 | 0.20 | 374 | 2.573 | 12.29 | 11.84 | 12.37 | 12.41 | 12.49 | -20.97 | -21.02 | 33.50 | 50.0 | 33.48 | 49.7 |
| 16359 UGC03207 | 196.8060 | -24.3019 | 325.1537 | -55.6186 | 4563 | 4590 | 3.1 | 0.36 | 497 | 2.718 | 11.71 | 11.37 | 12.09 | 12.15 | 12.11 | -22.30 | -22.44 | 34.48 | 78.6 | 34.70 | 87.1 |
| 16360 UGC03205 | 172.9608 | -8.2063 | 354.4323 | -36.0326 | 3588 | 3577 | 2.0 | 0.41 | 417 | 2.651 | / | / | 12.02 | 11.99 | / | / | -21.79 | / | / | 33.85 | 58.8 |
| 16420 UGC03214 | 199.2164 | -25.0833 | 322.0349 | -57.1772 | 4910 | 4951 | 3.0 | 0.28 | 547 | 2.746 | 11.45 | 10.91 | 11.47 | 11.51 | 11.57 | -22.55 | -22.72 | 34.18 | 68.6 | 34.31 | 72.9 |
| 16423 UGC03203 | 142.6457 | 15.5197 | 16.0318 | -3.3596 | 882 | 834 | 5.0 | 0.59 | 216 | 2.418 | 10.57 | 10.49 | 11.03 | 11.09 | 11.15 | -19.57 | -19.51 | 30.72 | 13.9 | 30.60 | 13.2 |
| 16502 AGC023914 | 223.1000 | -34.1251 | 277.5231 | -61.9157 | 1764 | 1771 | 8.9 | 0.42 | 142 | 2.186 | / | / | 15.45 | 15.55 | / | / | -17.24 | / | / | 32.81 | 36.4 |
| 16517 AGC023923 | 226.9930 | -35.0221 | 270.6428 | -61.2957 | 741 | 745 | 6.7 | 0.41 | 187 | 2.302 | 10.53 | 10.58 | 11.67 | 11.74 | 11.51 | -18.51 | -18.38 | 30.02 | 10.1 | 30.12 | 10.6 |
| 16537 UGC03218 | 147.8877 | 12.1810 | 13.4227 | -8.8657 | 5228 | 5251 | 3.1 | 0.59 | 495 | 2.779 | / | / | 11.47 | 11.49 | / | / | -23.03 | / | / | 34.63 | 84.4 |
| 16600 NGC01752 | 207.7621 | -28.0084 | 308.2969 | -61.4405 | 3577 | 3601 | 4.9 | 0.30 | 437 | 2.652 | 11.25 | 10.76 | 11.48 | 11.51 | 11.50 | -21.69 | -21.80 | 33.22 | 44.0 | 33.35 | 46.8 |
| 16646 UGC03237 | 199.2310 | -23.4962 | 324.6111 | -57.9587 | 4194 | 4226 | 5.8 | 0.23 | 290 | 2.465 | 13.44 | 13.06 | 13.48 | 13.54 | 13.67 | -19.99 | -19.97 | 33.69 | 54.8 | 33.55 | 51.4 |
| 16654 NGC01762 | 198.3946 | -23.0014 | 326.0921 | -57.5004 | 4753 | 4798 | 5.1 | 0.70 | 420 | 2.764 | 11.60 | 11.60 | 11.98 | 12.08 | 12.21 | -22.71 | -22.89 | 35.01 | 100.3 | 35.11 | 105.1 |
| 16709 AGC024019 | 241.6956 | -36.4527 | 248.4812 | -57.1408 | 1208 | 1231 | 4.0 | 0.48 | 296 | 2.519 | 9.05 | 9.05 | 9.34 | 9.41 | 9.60 | -20.49 | -20.50 | 30.08 | 10.4 | 29.91 | 9.6 |
| 16716 AGC450011 | 211.8854 | -28.8405 | 301.1765 | -63.1435 | 2316 | 2329 | 4.8 | 0.59 | 324 | 2.593 | 10.40 | 10.29 | 10.72 | 10.78 | 10.90 | -21.16 | -21.22 | 32.07 | 25.9 | 32.01 | 25.2 |
| 16761 NGC001824 | 268.7876 | -36.2523 | 224.3315 | -41.7715 | 1248 | 1287 | 8.9 | 0.29 | 146 | 2.175 | 11.97 | 12.05 | 13.04 | 13.12 | 12.94 | -17.35 | -17.13 | 30.29 | 11.4 | 30.25 | 11.2 |
| 16779 NGC1808 | 241.2119 | -35.9016 | 248.6686 | -57.8086 | 996 | 1021 | 1.2 | 0.51 | 271 | 2.490 | 8.80 | 8.83 | 8.88 | 8.95 | 9.26 | -20.21 | -20.21 | 29.47 | 7.8 | 29.16 | 6.8 |
| 16790 ES305-009 | 242.2024 | -35.9414 | 247.3729 | -57.4047 | 1021 | 1047 | 8.0 | 0.64 | 105 | 2.129 | 12.76 | 12.99 | 13.72 | 13.81 | 13.76 | -16.94 | -16.69 | 30.70 | 13.8 | 30.50 | 12.6 |
| 16858 UGC03250 | 147.7788 | 13.6298 | 14.8560 | -8.5443 | 4529 | 4541 | 3.1 | 0.66 | 431 | 2.750 | / | / | 11.94 | 11.99 | / | / | -22.75 | / | / | 34.87 | 94.0 |
| 16878 AGC024102 | 220.7268 | -30.5405 | 283.6307 | -64.9889 | 1968 | 1992 | 5.0 | 0.26 | 146 | 2.171 | 14.26 | 14.32 | 15.83 | 15.92 | 15.46 | -17.32 | -17.10 | 32.79 | 36.2 | 33.05 | 40.7 |
| 16911 NGC001853 | 265.8320 | -35.8171 | 225.4160 | -44.0674 | 1411 | 1455 | 7.1 | 0.54 | 192 | 2.348 | 12.21 | 12.34 | 12.82 | 12.91 | 12.99 | -18.93 | -18.83 | 31.92 | 24.2 | 31.74 | 22.3 |
| 16957 AGC150027 | 148.5212 | 13.6572 | 14.9948 | -9.2531 | 112 | 74 | 9.9 | 0.42 | 114 | 2.090 | / | / | 11.67 | 11.70 | / | / | -16.31 | / | / | 28.01 | 4.0 |
| 16976 ES305-017 | 246.1697 | -35.0449 | 241.4746 | -56.4626 | 1071 | 1108 | 9.9 | 0.42 | 146 | 2.198 | / | / | 14.56 | 14.64 | / | / | -17.36 | / | / | 32.00 | 25.2 |
| 16983 ES423-002 | 233.2987 | -32.9519 | 259.0682 | -62.8035 | 1468 | 1501 | 6.5 | 0.27 | 223 | 2.356 | 11.83 | 11.75 | 12.63 | 12.69 | 12.58 | -19.00 | -18.91 | 31.58 | 20.7 | 31.60 | 20.9 |

| PGC Name | l | b | sgl | sgb | v_{hel} | v_{mod} | t | b/a | w _{max} | log w _{max} | I | I* | [3.6] | [3.6]* | C _[3.6] | M _C | M _[3.6] | μ _C | d _C | μ _[3.6] | d _[3.6] |
|-----------------|----------|----------|----------|----------|-----------|-----------|-----|------|------------------|----------------------|-------|-------|-------|--------|--------------------|----------------|--------------------|----------------|----------------|--------------------|--------------------|
| 17027 ES362-011 | 241.0785 | -34.0774 | 247.2601 | -59.4828 | 1344 | 1382 | 4.3 | 0.21 | 269 | 2.431 | 11.02 | 10.74 | 11.57 | 11.62 | 11.54 | -19.68 | -19.64 | 31.22 | 17.5 | 31.25 | 17.8 |
| 17031 UGC03275 | 195.5694 | -17.5949 | 337.1888 | -56.9799 | 7965 | 8135 | 4.0 | 0.22 | 498 | 2.699 | 13.26 | 12.51 | 13.36 | 13.39 | 13.31 | -22.12 | -22.25 | 35.55 | 128.7 | 35.85 | 148.0 |
| 17042 NGC001892 | 274.9174 | -34.3164 | 219.3098 | -38.0364 | 1359 | 1409 | 5.6 | 0.34 | 203 | 2.326 | 11.42 | 11.35 | 12.11 | 12.18 | 12.12 | -18.73 | -18.61 | 30.85 | 14.8 | 30.79 | 14.4 |
| 17056 AGC450046 | 217.0388 | -27.5833 | 293.5767 | -66.5837 | 2823 | 2865 | 5.0 | 0.25 | 349 | 2.548 | 12.11 | 11.73 | 12.38 | 12.41 | 12.43 | -20.75 | -20.78 | 33.20 | 43.7 | 33.23 | 44.2 |
| 17058 UGC03283 | 202.8723 | -21.2899 | 325.2982 | -61.9689 | 4494 | 4558 | 5.9 | 0.20 | 338 | 2.529 | 13.82 | 13.22 | 13.39 | 13.41 | 13.68 | -20.57 | -20.59 | 34.32 | 73.0 | 34.08 | 65.5 |
| 17104 UGC03253 | 128.9602 | 24.6827 | 24.0121 | 10.2562 | 4121 | 4121 | 3.0 | 0.54 | 335 | 2.589 | 12.16 | 12.11 | 12.69 | 12.77 | 12.80 | -21.12 | -21.18 | 33.97 | 62.3 | 34.03 | 64.0 |
| 17157 E362-019 | 241.1012 | -33.1857 | 246.3925 | -60.2611 | 1287 | 1330 | 8.9 | 0.24 | 132 | 2.125 | 13.12 | 13.21 | 14.55 | 14.63 | 14.27 | -16.90 | -16.65 | 31.16 | 17.1 | 31.28 | 18.0 |
| 17170 UGC03257 | 128.5560 | 24.9122 | 24.2310 | 10.6317 | 2193 | 2162 | 1.1 | 0.45 | 158 | 2.239 | / | / | 13.16 | 13.24 | / | -17.76 | / | / | / | 31.00 | 15.9 |
| 17174 NGC01886 | 226.2527 | -29.6357 | 272.4519 | -66.6606 | 1754 | 1795 | 3.7 | 0.20 | 335 | 2.525 | 11.57 | 11.21 | 11.68 | 11.72 | 11.83 | -20.54 | -20.55 | 32.37 | 29.8 | 32.28 | 28.6 |
| 17229 AGC450056 | 219.4871 | -26.8687 | 289.1691 | -68.1245 | 3187 | 3246 | 4.8 | 0.47 | 269 | 2.475 | 12.70 | 12.67 | 13.30 | 13.38 | 13.39 | -20.08 | -20.07 | 33.50 | 50.1 | 33.50 | 50.1 |
| 17395 P0017395 | 213.4005 | -22.3857 | 308.5865 | -69.0295 | 2719 | 2778 | 2.1 | 0.29 | 266 | 2.435 | 12.47 | 12.07 | 12.51 | 12.54 | 12.67 | -19.72 | -19.68 | 32.40 | 30.1 | 32.22 | 27.8 |
| 17402 IC0002130 | 226.4029 | -27.2417 | 272.4063 | -69.0581 | 1827 | 1883 | 7.6 | 0.48 | 154 | 2.236 | 12.34 | 12.46 | 13.15 | 13.24 | 13.21 | -17.90 | -17.73 | 31.11 | 16.7 | 30.97 | 15.6 |
| 17433 AGC024358 | 241.0485 | -30.6880 | 243.9095 | -62.4580 | 1322 | 1381 | 5.9 | 0.20 | 226 | 2.354 | 11.34 | 11.15 | 11.77 | 11.83 | 11.85 | -18.98 | -18.88 | 30.83 | 14.7 | 30.71 | 13.9 |
| 17436 AGC024354 | 225.2750 | -26.5018 | 275.4160 | -69.7197 | 1660 | 1716 | 3.3 | 0.41 | 409 | 2.642 | 9.70 | 9.54 | 10.12 | 10.17 | 10.22 | -21.60 | -21.70 | 31.82 | 23.1 | 31.87 | 23.7 |
| 17456 UGC03319 | 142.7316 | 19.2279 | 19.7236 | -2.9485 | 4216 | 4232 | 5.8 | 0.20 | 332 | 2.521 | 14.11 | 13.63 | 13.30 | 13.34 | 13.86 | -20.50 | -20.52 | 34.43 | 76.9 | 33.92 | 60.8 |
| 17475 AGC450071 | 213.4101 | -21.4986 | 310.2808 | -69.6855 | 7039 | 7215 | 5.1 | 0.20 | 305 | 2.484 | 14.59 | 13.94 | 14.77 | 14.81 | 14.73 | -20.17 | -20.16 | 34.99 | 99.6 | 35.11 | 105.1 |
| 17509 UGC03329 | 189.4015 | -8.2302 | 354.7087 | -52.3022 | 5265 | 5364 | 4.1 | 0.42 | 484 | 2.718 | 12.08 | 11.09 | 12.23 | 12.20 | 12.00 | -22.29 | -22.44 | 34.35 | 74.2 | 34.76 | 89.4 |
| 17513 AGC024404 | 222.1464 | -24.5441 | 284.8134 | -71.1000 | 2861 | 2935 | 5.4 | 0.20 | 195 | 2.290 | 14.16 | 14.00 | 15.04 | 15.10 | 14.90 | -18.40 | -18.26 | 33.33 | 46.3 | 33.40 | 48.0 |
| 17554 UGC03332 | 190.6391 | -8.2703 | 354.6271 | -53.5265 | 5821 | 5941 | 3.8 | 0.22 | 440 | 2.645 | / | / | 12.54 | 12.50 | / | -21.73 | / | / | / | 34.32 | 73.2 |
| 17561 UGC03326 | 136.0141 | -22.6185 | 22.3729 | 3.6721 | 4089 | 4098 | 5.9 | 0.20 | 543 | 2.735 | 12.36 | 11.60 | 11.86 | 11.87 | 12.10 | -22.45 | -22.60 | 34.62 | 84.1 | 34.58 | 82.3 |
| 17657 NGC02049 | 234.7006 | -27.0190 | 252.2106 | -68.1579 | 2988 | 3079 | 1.0 | 0.49 | 418 | 2.671 | 11.44 | 11.36 | 12.15 | 12.23 | 12.15 | -21.86 | -21.98 | 34.06 | 65.0 | 34.29 | 72.2 |
| 17776 UGC03351 | 153.9928 | 15.0111 | 17.2765 | -14.2478 | 4471 | 4513 | 2.0 | 0.20 | 451 | 2.654 | / | / | 11.60 | 11.58 | / | -21.82 | / | / | / | 33.44 | 48.8 |
| 17810 IC2143 | 223.2536 | -22.3771 | 283.4824 | -73.4588 | 3051 | 3144 | 3.5 | 0.45 | 324 | 2.551 | 11.62 | 11.48 | 12.06 | 12.12 | 12.16 | -20.77 | -20.81 | 32.96 | 39.0 | 32.96 | 39.0 |
| 17819 AGC024538 | 239.4557 | -27.4295 | 242.8462 | -65.9712 | 921 | 995 | 4.6 | 0.45 | 277 | 2.483 | 9.75 | 9.73 | 10.42 | 10.48 | 10.46 | -20.16 | -20.15 | 30.62 | 13.3 | 30.63 | 13.4 |
| 17831 UGC03354 | 156.4512 | 13.9734 | 16.6877 | -16.7817 | 3088 | 3107 | 2.0 | 0.33 | 396 | 2.614 | 12.07 | 11.57 | 11.64 | 11.66 | 11.99 | -21.35 | -21.42 | 33.36 | 47.1 | 33.12 | 42.1 |
| 17969 AGC024602 | 224.5973 | -21.9770 | 279.4332 | -74.1155 | 2369 | 2458 | 4.3 | 0.20 | 320 | 2.505 | 12.54 | 12.14 | 12.47 | 12.50 | 12.69 | -20.36 | -20.36 | 33.07 | 41.1 | 32.89 | 37.8 |
| 18000 IC002150 | 244.1417 | -27.6348 | 235.1869 | -63.3984 | 3117 | 3221 | 4.9 | 0.27 | 352 | 2.554 | 11.73 | 11.42 | 12.31 | 12.36 | 12.25 | -20.80 | -20.84 | 33.07 | 41.1 | 33.24 | 44.4 |
| 18047 AGC450098 | 223.0130 | -20.7080 | 285.9415 | -75.0050 | 3123 | 3226 | 5.0 | 0.64 | 298 | 2.581 | 11.19 | 11.22 | 11.75 | 11.84 | 11.89 | -21.05 | -21.10 | 32.96 | 39.1 | 32.97 | 39.2 |
| 18089 UGC03375 | 160.8445 | 13.0631 | 16.6589 | -21.1489 | 5791 | 5887 | 5.2 | 0.44 | 490 | 2.728 | 11.52 | 11.07 | 11.81 | 11.86 | 11.82 | -22.39 | -22.54 | 34.27 | 71.4 | 34.49 | 79.2 |
| 18109 AGC150194 | 163.9581 | 11.6121 | 15.8276 | -24.4306 | 5798 | 5900 | 5.0 | 0.65 | 295 | 2.580 | / | / | 13.02 | 13.09 | / | -21.09 | / | / | / | 34.27 | 71.4 |
| 18147 AGC024702 | 225.6643 | -20.4985 | 276.4926 | -75.7253 | 2963 | 3072 | 3.1 | 0.29 | 424 | 2.638 | 11.34 | 10.97 | 11.84 | 11.88 | 11.78 | -21.57 | -21.66 | 33.38 | 47.3 | 33.59 | 52.2 |
| 18148 IC0002152 | 228.7453 | -21.6483 | 265.1770 | -74.6141 | 1866 | 1961 | 1.1 | 0.71 | 194 | 2.431 | 11.64 | 11.80 | 12.37 | 12.46 | 12.49 | -19.68 | -19.64 | 32.18 | 27.3 | 32.11 | 26.4 |
| 18161 UGC03379 | 145.3504 | 20.4404 | 21.2804 | -5.2129 | 4114 | 4144 | 3.1 | 0.46 | 369 | 2.610 | / | / | 12.15 | 12.22 | / | -21.38 | / | / | / | 33.66 | 53.9 |
| 18181 UGC03373 | 135.1949 | 23.9997 | 23.6849 | 4.5447 | 4758 | 4788 | 5.2 | 0.62 | 267 | 2.523 | 12.77 | 12.75 | 13.17 | 13.26 | 13.37 | -20.52 | -20.53 | 33.94 | 61.3 | 33.86 | 59.2 |
| 18369 AGC024782 | 226.5589 | -19.1747 | 273.4389 | -77.1211 | 2893 | 3011 | 6.6 | 0.20 | 270 | 2.431 | 13.25 | 12.92 | 13.76 | 13.81 | 13.72 | -19.69 | -19.64 | 33.44 | 48.7 | 33.50 | 50.1 |
| 18373 PG0018373 | 219.1517 | -16.0231 | 309.0060 | -77.3914 | 2216 | 2322 | 3.0 | 0.20 | 240 | 2.380 | / | / | 12.69 | 12.69 | / | -19.14 | / | / | / | 31.84 | 23.3 |

| PGC Name | l | b | sgl | sgb | v_{hel} | v_{mod} | t | b/a | w_{max} | $\log w_{max}^*$ | I | I* | [3.6] | [3.6]* | $C_{[3.6]}$ | M_C | $M_{[3.6]}$ | μ_C | d_C | $\mu_{[3.6]}$ | $d_{[3.6]}$ |
|-----------------|----------|----------|----------|----------|-----------|-----------|-----|------|-----------|------------------|-------|-------|-------|--------|-------------|--------|-------------|---------|-------|---------------|-------------|
| 18394 ES005-004 | 299.2013 | -27.7466 | 207.2105 | -18.9980 | 1870 | 1930 | 2.8 | 0.20 | 413 | 2.616 | 10.92 | 10.29 | 10.47 | 10.47 | 10.75 | -21.37 | -21.45 | 32.12 | 26.6 | 31.92 | 24.2 |
| 18437 ES121-006 | 270.9720 | -28.8167 | 214.1086 | -43.1318 | 1211 | 1297 | 5.2 | 0.20 | 281 | 2.449 | 11.42 | 11.10 | 11.12 | 11.16 | 11.50 | -19.84 | -19.81 | 31.35 | 18.6 | 30.97 | 15.6 |
| 18445 ES489-006 | 229.9393 | -19.6576 | 259.6346 | -76.4307 | 2223 | 2337 | 7.2 | 0.57 | 192 | 2.359 | 12.07 | 12.19 | 12.80 | 12.89 | 12.90 | -19.02 | -18.93 | 31.93 | 24.3 | 31.82 | 23.2 |
| 18487 ES425-011 | 235.6975 | -21.4350 | 242.7573 | -72.8721 | 3202 | 3332 | 5.9 | 0.20 | 220 | 2.342 | / | / | 14.91 | 14.98 | / | / | -18.77 | / | / | 33.82 | 58.0 |
| 18556 UGC003406 | 147.0045 | 21.0828 | 22.1635 | -6.6389 | 5200 | 5266 | 6.7 | 0.20 | 237 | 2.375 | / | / | 14.97 | 15.02 | / | / | -19.09 | / | / | 34.19 | 68.8 |
| 18557 UGC003403 | 142.8045 | 22.4412 | 22.9200 | -2.5781 | 1264 | 1255 | 5.8 | 0.28 | 226 | 2.362 | 11.77 | 11.38 | 12.18 | 12.20 | 12.15 | -19.06 | -18.96 | 31.21 | 17.4 | 31.17 | 17.1 |
| 18581 P0018581 | 222.5529 | -15.7797 | 296.1313 | -79.4274 | 2064 | 2179 | 3.9 | 0.60 | 209 | 2.408 | 12.15 | 11.98 | 12.58 | 12.63 | 12.67 | -19.47 | -19.41 | 32.15 | 26.9 | 32.05 | 25.7 |
| 18747 UGC03432 | 157.3379 | 17.9731 | 20.9592 | -16.7913 | 4998 | 5082 | 5.9 | 0.29 | 285 | 2.466 | 13.65 | 13.37 | 14.01 | 14.08 | 14.09 | -20.00 | -19.98 | 34.14 | 67.3 | 34.13 | 67.1 |
| 18764 UGC03413 | 132.6454 | 25.4691 | 24.9825 | 6.9641 | 4213 | 4231 | 4.7 | 0.71 | 264 | 2.563 | 11.70 | 11.74 | 12.15 | 12.24 | 12.35 | -20.89 | -20.93 | 33.27 | 45.0 | 33.20 | 43.7 |
| 18765 AGC024981 | 234.6077 | -19.1343 | 241.8687 | -75.3779 | 1702 | 1823 | 4.1 | 0.25 | 315 | 2.504 | 11.49 | 11.22 | 11.72 | 11.76 | 11.86 | -20.34 | -20.35 | 32.21 | 27.6 | 32.12 | 26.5 |
| 18778 UGC03423 | 135.1437 | 24.9631 | 24.6439 | 4.6726 | 4272 | 4296 | 7.9 | 0.29 | 211 | 2.334 | / | / | 15.15 | 15.23 | / | / | -18.69 | / | / | 33.99 | 62.8 |
| 18813 P0018813 | 192.9611 | 1.5220 | 11.7197 | -54.7656 | 5477 | 5646 | 7.8 | 0.60 | 387 | 2.676 | / | / | 12.30 | 12.24 | / | / | -22.03 | / | / | 34.36 | 74.5 |
| 18855 P0018855 | 217.1108 | -10.6141 | 336.3651 | -78.9840 | 732 | 848 | 5.9 | 0.41 | 274 | 2.469 | 10.90 | 9.65 | 10.22 | 10.12 | 10.25 | -20.03 | -20.01 | 30.28 | 11.4 | 30.13 | 10.6 |
| 18989 P0018989 | 149.0407 | 21.9200 | 23.3227 | -8.3620 | 4300 | 4355 | 3.7 | 0.69 | 143 | 2.287 | / | / | 14.08 | 14.18 | / | / | -18.23 | / | / | 32.42 | 30.4 |
| 19024 AGC025099 | 235.9490 | -17.5471 | 234.0149 | -75.9915 | 7056 | 7316 | 4.2 | 0.20 | 370 | 2.568 | 13.77 | 13.32 | 13.97 | 14.04 | 14.04 | -20.93 | -20.98 | 35.07 | 103.1 | 35.16 | 107.6 |
| 19064 IC002166 | 155.8723 | 20.0212 | 22.7217 | -14.9908 | 2685 | 2726 | 4.7 | 0.49 | 310 | 2.542 | 11.17 | 11.05 | 11.69 | 11.75 | 11.76 | -20.69 | -20.72 | 32.47 | 31.1 | 32.49 | 31.5 |
| 19121 ES490-005 | 235.5905 | -16.6403 | 232.7620 | -76.9154 | 7110 | 7377 | 4.5 | 0.20 | 400 | 2.602 | / | / | 13.85 | 13.91 | / | / | -21.31 | / | / | 35.38 | 119.0 |
| 19222 UGC03474 | 143.1462 | 24.1731 | 24.6806 | -2.6470 | 3634 | 3666 | 5.9 | 0.20 | 357 | 2.553 | / | / | 12.45 | 12.46 | / | / | -20.82 | / | / | 33.32 | 46.2 |
| 19249 UGC03489 | 192.1760 | 5.6786 | 18.1370 | -52.8788 | 5458 | 5643 | 4.0 | 0.20 | 467 | 2.669 | / | / | 12.51 | 12.50 | / | / | -21.96 | / | / | 34.56 | 81.8 |
| 19255 E490-014 | 233.7712 | -14.7697 | 233.8569 | -79.4681 | 2709 | 2866 | 3.9 | 0.51 | 225 | 2.410 | 12.34 | 12.35 | 13.03 | 13.11 | 13.09 | -19.49 | -19.43 | 32.59 | 32.9 | 32.56 | 32.4 |
| 19261 UGC003484 | 156.4107 | 20.8165 | 23.6413 | -15.3058 | 7422 | 7597 | 4.1 | 0.20 | 406 | 2.609 | / | / | 13.51 | 13.57 | / | / | -21.37 | / | / | 35.08 | 103.7 |
| 19281 ES557-005 | 228.7150 | -12.2349 | 257.4540 | -83.9381 | 11126 | 11597 | 4.8 | 0.20 | 592 | 2.772 | / | / | 13.22 | 13.25 | / | / | -22.97 | / | / | 36.49 | 198.3 |
| 19292 UGC03498 | 197.7802 | 3.2970 | 17.2137 | -58.9299 | 3797 | 3952 | 3.8 | 0.20 | 341 | 2.533 | / | / | 12.74 | 12.69 | / | / | -20.63 | / | / | 33.36 | 47.0 |
| 19343 PG0019343 | 224.9290 | -9.7039 | 305.3764 | -85.8417 | 749 | 893 | 8.1 | 0.36 | 188 | 2.295 | / | / | 12.23 | 12.24 | / | / | -18.31 | / | / | 30.55 | 12.9 |
| 19355 NGC02263 | 234.0883 | -13.7243 | 228.7530 | -80.0741 | 2741 | 2905 | 2.2 | 0.39 | 316 | 2.527 | 11.08 | 10.90 | 11.53 | 11.59 | 11.60 | -20.55 | -20.57 | 32.16 | 27.1 | 32.17 | 27.1 |
| 19413 ES122-001 | 268.0416 | -24.2435 | 209.1910 | -47.1019 | 2615 | 2746 | 3.0 | 0.49 | 293 | 2.518 | 11.46 | 11.35 | 11.59 | 11.66 | 11.87 | -20.47 | -20.48 | 32.35 | 29.5 | 32.15 | 26.9 |
| 19512 UGC03524 | 201.0396 | 4.0005 | 20.7644 | -61.7577 | 3923 | 4097 | 1.6 | 0.31 | 404 | 2.619 | / | / | 11.65 | 11.63 | / | / | -21.48 | / | / | 33.14 | 42.5 |
| 19531 AGC025325 | 237.3052 | -13.5501 | 217.2312 | -77.8387 | 1897 | 2058 | 5.9 | 0.46 | 384 | 2.626 | 10.19 | 9.99 | 10.51 | 10.56 | 10.64 | -21.46 | -21.54 | 32.10 | 26.3 | 32.11 | 26.4 |
| 19627 UGC03500 | 129.4798 | 26.8867 | 26.2671 | 9.8735 | 4385 | 4406 | 4.9 | 0.28 | 236 | 2.382 | / | / | 14.05 | 14.13 | / | / | -19.15 | / | / | 33.32 | 46.2 |
| 19652 UGC03539 | 149.1696 | 24.4210 | 25.8289 | -8.0218 | 3307 | 3356 | 4.3 | 0.21 | 310 | 2.492 | 13.22 | 12.81 | 12.95 | 12.99 | 13.27 | -20.24 | -20.23 | 33.54 | 51.1 | 33.26 | 44.9 |
| 19732 UGC03561 | 166.3564 | 20.3932 | 25.7992 | -24.4003 | 5688 | 5841 | 3.1 | 0.57 | 349 | 2.619 | 12.70 | 12.61 | 12.97 | 13.06 | 13.20 | -21.40 | -21.48 | 34.67 | 86.0 | 34.65 | 85.0 |
| 19788 UGC03576 | 166.3008 | 20.7116 | 26.1156 | -24.2556 | 5962 | 6124 | 3.0 | 0.50 | 356 | 2.607 | 12.54 | 12.42 | 13.00 | 13.09 | 13.12 | -21.28 | -21.35 | 34.47 | 78.2 | 34.55 | 81.2 |
| 19792 UGC03584 | 188.6303 | 12.3372 | 25.8545 | -47.2087 | 4439 | 4613 | 4.1 | 0.20 | 284 | 2.453 | / | / | 13.85 | 13.91 | / | / | -19.85 | / | / | 33.82 | 58.2 |
| 19838 UGC03575 | 144.4078 | 25.7768 | 26.4374 | -3.5427 | 3890 | 3940 | 6.1 | 0.20 | 266 | 2.425 | / | / | 14.20 | 14.24 | / | / | -19.58 | / | / | 33.88 | 59.8 |
| 19861 ES491-009 | 237.3407 | -10.9760 | 205.9734 | -79.1013 | 2056 | 2233 | 7.7 | 0.28 | 268 | 2.437 | / | / | 12.93 | 12.95 | / | / | -19.69 | / | / | 32.67 | 34.1 |
| 19877 UGC03605 | 200.9853 | 7.2539 | 26.8662 | -60.3844 | 7967 | 8286 | 6.0 | 0.20 | 456 | 2.659 | / | / | 13.67 | 13.71 | / | / | -21.86 | / | / | 35.77 | 142.6 |

| PGC Name | l | b | sgl | sgb | v_{hel} | v_{mod} | t | b/a | w_{max} | $\log w_{max}^2$ | I | I* | [3.6] | [3.6]* | $C_{[3.6]}$ | M_C | $M_{[3.6]}$ | μ_C | dC | $\mu_{[3.6]}$ | $d_{[3.6]}$ |
|-----------------|----------|----------|----------|----------|-----------|-----------|-----|------|-----------|------------------|-------|-------|-------|--------|-------------|--------|-------------|---------|-------|---------------|-------------|
| 19920 E491-012 | 235.8059 | -9.7685 | 202.9855 | -80.9646 | 2578 | 2765 | 5.0 | 0.20 | 343 | 2.535 | / | / | 12.45 | 12.45 | / | / | -20.65 | / | / | 33.14 | 42.4 |
| 19975 P0019975 | 156.6790 | 24.1410 | 27.0478 | -14.7669 | 3296 | 3371 | 3.9 | 0.58 | 193 | 2.366 | / | / | 13.86 | 13.95 | / | / | -19.00 | / | / | 32.98 | 39.5 |
| 19996 E491-015 | 238.5516 | -10.2331 | 200.2231 | -78.2658 | 2678 | 2870 | 5.1 | 0.20 | 356 | 2.551 | 11.81 | 11.19 | 12.02 | 12.03 | 11.96 | -20.78 | -20.81 | 32.76 | 35.6 | 32.87 | 37.4 |
| 20007 UGC03627 | 165.4279 | 22.2805 | 27.4813 | -23.0083 | 6284 | 6461 | 6.4 | 0.66 | 255 | 2.522 | 13.16 | 13.22 | 13.60 | 13.71 | 13.83 | -20.51 | -20.52 | 34.40 | 75.9 | 34.33 | 73.3 |
| 20027 UGC03637 | 209.7273 | 4.5473 | 31.2553 | -69.3033 | 3548 | 3750 | 8.0 | 0.37 | 222 | 2.369 | / | / | 13.60 | 13.63 | / | / | -19.03 | / | / | 32.68 | 34.4 |
| 20214 UGC03691 | 201.1257 | 10.4563 | 32.5415 | -58.9463 | 2205 | 2380 | 6.1 | 0.52 | 229 | 2.421 | 11.88 | 11.86 | 12.52 | 12.60 | 12.59 | -19.59 | -19.54 | 32.18 | 27.3 | 32.14 | 26.8 |
| 20222 UGC03693 | 197.8349 | 12.0576 | 32.0043 | -55.3553 | 2254 | 2424 | 4.0 | 0.68 | 316 | 2.624 | 10.60 | 10.62 | 10.85 | 10.93 | 11.14 | -21.44 | -21.52 | 32.59 | 33.0 | 32.46 | 31.1 |
| 20274 PG0020274 | 219.8332 | 1.5421 | 46.0134 | -79.1176 | 1717 | 1911 | 9.8 | 0.55 | 266 | 2.494 | 12.20 | 11.61 | 12.11 | 12.10 | 12.22 | -20.26 | -20.25 | 32.49 | 31.5 | 32.37 | 29.8 |
| 20293 UGC003675 | 139.9367 | 27.3482 | 27.4524 | 0.6323 | 3781 | 3823 | 5.7 | 0.20 | 334 | 2.524 | 13.23 | 12.82 | 13.25 | 13.30 | 13.43 | -20.53 | -20.54 | 34.00 | 63.1 | 33.91 | 60.5 |
| 20361 UGC03731 | 188.3036 | 16.8965 | 31.5779 | -44.9419 | 4901 | 5106 | 7.9 | 0.29 | 405 | 2.618 | / | / | 12.55 | 12.61 | / | / | -21.46 | / | / | 34.15 | 67.6 |
| 20418 UGC03717 | 141.1268 | 27.4839 | 27.7170 | -0.3994 | 4187 | 4242 | 4.0 | 0.38 | 366 | 2.589 | 11.93 | 11.77 | 12.32 | 12.40 | 12.44 | -21.12 | -21.18 | 33.60 | 52.5 | 33.63 | 53.3 |
| 20458 UGC03653 | 129.2391 | 27.5465 | 26.9290 | 10.1106 | 2230 | 2216 | 4.0 | 0.51 | 365 | 2.619 | 10.38 | 10.30 | 10.85 | 10.91 | 10.97 | -21.40 | -21.48 | 32.37 | 29.8 | 32.40 | 30.2 |
| 20486 UGC003757 | 168.7182 | 23.7892 | 30.1179 | -25.3876 | 5529 | 5703 | 5.9 | 0.20 | 365 | 2.562 | 14.28 | 13.77 | 14.01 | 14.06 | 14.28 | -20.88 | -20.92 | 35.26 | 112.9 | 35.12 | 105.6 |
| 20487 UGC03763 | 183.0264 | 19.5888 | 31.7439 | -39.2546 | 7150 | 7419 | 6.1 | 0.20 | 322 | 2.508 | 14.65 | 14.25 | 14.95 | 15.02 | 14.99 | -20.38 | -20.39 | 35.49 | 125.5 | 35.59 | 131.4 |
| 20504 E428-009 | 241.7135 | -8.1912 | 188.3635 | -75.6501 | 2251 | 2453 | 5.2 | 0.29 | 260 | 2.425 | 12.95 | 12.58 | 13.12 | 13.15 | 13.23 | -19.63 | -19.58 | 32.87 | 37.6 | 32.75 | 35.5 |
| 20513 UGC03770 | 194.1676 | 15.4759 | 33.8514 | -50.5455 | 6378 | 6646 | 9.8 | 0.44 | 314 | 2.536 | 12.94 | 12.83 | 13.51 | 13.61 | 13.58 | -20.64 | -20.66 | 34.28 | 71.6 | 34.36 | 74.6 |
| 20526 UGC03749 | 147.7263 | 27.2756 | 28.4165 | -6.2210 | 1154 | 1187 | 5.8 | 0.20 | 172 | 2.236 | 13.55 | 13.48 | 14.35 | 14.42 | 14.30 | -17.90 | -17.73 | 32.21 | 27.7 | 32.15 | 26.9 |
| 20539 UGC03759 | 151.3841 | 26.9402 | 28.7269 | -9.4796 | 4425 | 4518 | 3.1 | 0.65 | 431 | 2.747 | 11.51 | 11.48 | 11.83 | 11.92 | 12.07 | -22.56 | -22.73 | 34.70 | 87.2 | 34.77 | 89.8 |
| 20556 NGC002369 | 273.3130 | -21.0122 | 203.0121 | -43.2090 | 3237 | 3395 | 1.2 | 0.25 | 442 | 2.651 | 10.87 | 10.34 | 10.77 | 10.80 | 10.93 | -21.68 | -21.78 | 32.62 | 33.5 | 32.60 | 33.0 |
| 20559 UGC03776 | 183.9755 | 19.6281 | 32.3086 | -40.0369 | 3881 | 4056 | 3.0 | 0.23 | 294 | 2.471 | 12.68 | 12.39 | 13.09 | 13.15 | 13.13 | -20.05 | -20.03 | 33.20 | 43.7 | 33.22 | 44.0 |
| 20562 UGC03777 | 188.0661 | 18.1769 | 33.0105 | -44.1369 | 3211 | 3384 | 5.9 | 0.20 | 268 | 2.428 | 12.68 | 12.37 | 13.16 | 13.21 | 13.15 | -19.66 | -19.61 | 32.82 | 36.6 | 32.84 | 37.0 |
| 20577 E428-017 | 241.5801 | -7.6434 | 186.2010 | -75.8342 | 2388 | 2595 | 5.0 | 0.28 | 245 | 2.398 | / | / | 13.33 | 13.36 | / | / | -19.31 | / | / | 32.69 | 34.5 |
| 20592 UGC03782 | 194.4409 | 15.9107 | 34.6513 | -50.5434 | 2277 | 2451 | 5.8 | 0.20 | 315 | 2.498 | 11.94 | 11.54 | 11.96 | 11.99 | 12.13 | -20.29 | -20.29 | 32.43 | 30.7 | 32.30 | 28.8 |
| 20603 UGC03783 | 193.1183 | 16.4999 | 34.4016 | -49.1525 | 6183 | 6445 | 6.1 | 0.20 | 360 | 2.556 | 13.99 | 13.53 | 14.04 | 14.10 | 14.18 | -20.82 | -20.86 | 35.10 | 104.5 | 35.10 | 104.6 |
| 20608 UGC03784 | 191.3003 | 17.2425 | 34.0219 | -47.2780 | 2591 | 2763 | 5.9 | 0.24 | 192 | 2.287 | / | / | 15.70 | 15.76 | / | / | -18.23 | / | / | 34.07 | 65.2 |
| 20766 NGC002397 | 280.2981 | -22.5951 | 203.5207 | -36.5454 | 1357 | 1475 | 3.0 | 0.46 | 307 | 2.529 | 10.61 | 10.31 | 10.73 | 10.77 | 10.91 | -20.58 | -20.59 | 31.48 | 19.8 | 31.36 | 18.7 |
| 20830 P0020830 | 199.1243 | 15.0863 | 37.6338 | -54.7603 | 5135 | 5382 | 2.3 | 0.34 | 356 | 2.569 | 13.74 | 13.49 | 13.44 | 13.51 | 13.88 | -20.94 | -20.99 | 34.90 | 95.7 | 34.61 | 83.5 |
| 20835 UGC03820 | 200.6522 | 14.4606 | 38.2665 | -56.3242 | 2530 | 2725 | 5.7 | 0.21 | 299 | 2.477 | 12.85 | 12.49 | 12.74 | 12.78 | 13.01 | -20.10 | -20.08 | 33.12 | 42.2 | 32.89 | 37.9 |
| 20844 UGC03804 | 143.6939 | 28.0814 | 28.6229 | -2.5662 | 2869 | 2911 | 5.8 | 0.58 | 294 | 2.550 | 11.52 | 11.59 | 12.21 | 12.30 | 12.31 | -20.77 | -20.80 | 33.10 | 41.6 | 33.14 | 42.4 |
| 20865 E5123-009 | 273.2518 | -20.2245 | 201.9651 | -43.4172 | 3212 | 3375 | 4.9 | 0.37 | 274 | 2.461 | 12.61 | 12.31 | 12.67 | 12.72 | 12.88 | -19.96 | -19.93 | 32.86 | 37.3 | 32.67 | 34.2 |
| 20903 AGC025665 | 243.2391 | -6.9178 | 183.0783 | -74.2261 | 2242 | 2453 | 5.5 | 0.20 | 369 | 2.567 | 11.87 | 11.15 | 11.32 | 11.31 | 11.60 | -20.92 | -20.96 | 32.53 | 32.1 | 32.29 | 28.7 |
| 21020 UGC03845 | 171.0001 | 25.2699 | 32.4858 | -26.7948 | 3030 | 3162 | 3.7 | 0.67 | 195 | 2.408 | 12.58 | 12.69 | 13.32 | 13.41 | 13.41 | -19.47 | -19.41 | 32.90 | 38.0 | 32.85 | 37.1 |
| 21033 NGC2336 | 133.9581 | 28.2168 | 27.8204 | 5.9793 | 2201 | 2204 | 4.0 | 0.57 | 439 | 2.719 | 9.60 | 9.57 | 10.26 | 10.33 | 10.31 | -22.30 | -22.45 | 32.63 | 33.5 | 32.81 | 36.4 |
| 21136 UGC003879 | 185.2416 | 22.0920 | 35.8717 | -39.9124 | 4794 | 5007 | 7.6 | 0.24 | 248 | 2.398 | 13.71 | 13.50 | 14.46 | 14.54 | 14.37 | -19.39 | -19.32 | 33.80 | 57.5 | 33.92 | 60.9 |
| 21154 NGC002393 | 184.9207 | 22.2676 | 35.8796 | -39.5673 | 4884 | 5099 | 5.3 | 0.58 | 265 | 2.505 | 12.84 | 12.88 | 13.48 | 13.58 | 13.59 | -20.36 | -20.36 | 34.00 | 63.1 | 34.01 | 63.5 |
| 21164 UGC03834 | 134.2929 | 28.3785 | 28.0035 | 5.6967 | 2033 | 2036 | 5.2 | 0.42 | 286 | 2.490 | 11.62 | 11.58 | 12.33 | 12.41 | 12.35 | -20.22 | -20.21 | 32.58 | 32.8 | 32.63 | 33.6 |

| PGC Name | l | b | sgl | sgb | v_{hel} | v_{mod} | t | b/a | w_{max} | $\log w_{max}$ | I | Γ^* | [3.6] | [3.6]* | $C_{[3.6]}$ | M _C | M _[3.6] | μ_C | d _C | $\mu_{[3.6]}$ | d _[3.6] | |
|-----------------|----------|----------|----------|----------|-----------|-----------|-----|------|-----------|----------------|-------|------------|-------|--------|-------------|----------------|--------------------|---------|----------------|---------------|--------------------|-------|
| 21167 ES123-016 | 273.3508 | -19.3078 | 200.6397 | -43.4900 | 3254 | 3423 | 7.6 | 0.22 | 257 | 2.412 | 13.23 | 12.79 | 12.86 | 12.89 | 13.21 | -19.51 | -19.45 | 32.74 | 35.3 | 32.35 | 29.6 | |
| 21328 IC002199 | 188.0918 | 22.3468 | 37.9538 | -42.0471 | 4674 | 4896 | 3.9 | 0.59 | 307 | 2.571 | 12.36 | 12.38 | 12.62 | 12.72 | 12.92 | -20.96 | -21.01 | 33.92 | 61.0 | 33.79 | 57.3 | |
| 21338 ES257-019 | 259.5336 | -12.5881 | 193.5977 | -57.6883 | 2871 | 3076 | 6.1 | 0.20 | 321 | 2.507 | 12.38 | 11.74 | 12.40 | 12.41 | 12.43 | -20.37 | -20.38 | 32.82 | 36.7 | 32.81 | 36.4 | |
| 21375 NGC002427 | 260.2869 | -12.6993 | 193.6100 | -56.9450 | 973 | 1156 | 7.8 | 0.41 | 236 | 2.403 | 10.23 | 9.95 | 10.55 | 10.58 | 10.63 | -19.43 | -19.36 | 30.06 | 10.3 | 29.94 | 9.7 | |
| 21380 UGC03922 | 162.5765 | 28.2911 | 32.7447 | -18.6967 | 8790 | 9085 | 5.8 | 0.28 | 465 | 2.676 | 13.60 | 13.16 | 13.37 | 13.45 | 13.67 | -21.91 | -22.03 | 35.72 | 139.1 | 35.66 | 135.7 | |
| 21397 UGC03919 | 151.7715 | 29.1699 | 31.0086 | -9.3346 | 4866 | 4983 | 5.9 | 0.20 | 287 | 2.458 | 14.16 | 13.84 | 13.11 | 13.17 | 13.89 | -19.93 | -19.90 | 33.86 | 59.2 | 33.10 | 41.7 | |
| 21425 UGC03937 | 183.7982 | 24.2175 | 37.3908 | -37.7038 | 3994 | 4191 | 3.7 | 0.38 | 319 | 2.530 | 12.18 | 12.05 | 12.43 | 12.51 | 12.64 | -20.58 | -20.60 | 33.25 | 44.6 | 33.14 | 42.5 | |
| 21451 UGC003921 | 144.5518 | 29.3345 | 29.9780 | -3.1182 | 2486 | 2532 | 6.1 | 0.35 | 177 | 2.267 | / | / | 15.66 | 15.75 | / | / | -18.04 | / | / | / | 33.85 | 58.9 |
| 21488 E560-004 | 237.8397 | -0.0664 | 149.4866 | -77.8233 | 2177 | 2413 | 4.1 | 0.22 | 406 | 2.610 | / | / | 11.58 | 11.46 | / | / | -21.39 | / | / | / | 32.87 | 37.6 |
| 21503 UGC003955 | 210.3235 | 14.6727 | 51.2680 | -63.0477 | 5108 | 5394 | 6.9 | 0.20 | 325 | 2.512 | / | / | 13.08 | 13.14 | / | / | -20.43 | / | / | / | 33.62 | 52.9 |
| 21549 AGC170347 | 193.7645 | 21.7701 | 41.4391 | -46.7139 | 8388 | 8761 | 5.4 | 0.22 | 382 | 2.584 | / | / | 14.59 | 14.67 | / | / | -21.13 | / | / | / | 36.02 | 159.7 |
| 21558 UGC03959 | 180.1364 | 25.8048 | 37.1056 | -34.0328 | 3355 | 3531 | 3.3 | 0.23 | 431 | 2.637 | 11.49 | 11.02 | 11.81 | 11.84 | 11.79 | -21.56 | -21.65 | 33.38 | 47.3 | 33.54 | 51.0 | |
| 21660 ES163-014 | 269.2490 | -15.7290 | 196.5175 | -47.9160 | 2861 | 3047 | 2.3 | 0.29 | 318 | 2.512 | 12.27 | 11.83 | 12.38 | 12.41 | 12.48 | -20.42 | -20.43 | 32.92 | 38.4 | 32.86 | 37.4 | |
| 21684 UGC03979 | 148.6564 | 29.9672 | 31.2306 | -6.5190 | 4063 | 4154 | 4.0 | 0.20 | 373 | 2.572 | 12.88 | 12.41 | 12.91 | 12.95 | 13.04 | -20.96 | -21.01 | 34.05 | 64.7 | 34.03 | 64.0 | |
| 21697 PG0021697 | 158.2229 | 29.7761 | 33.0427 | -14.6211 | 5174 | 5326 | 7.9 | 0.27 | 176 | 2.253 | / | / | 16.48 | 16.58 | / | / | -17.90 | / | / | / | 34.58 | 82.5 |
| 21759 ES560-012 | 235.6632 | 3.1791 | 131.3083 | -77.3985 | 3305 | 3570 | 6.2 | 0.25 | 364 | 2.566 | / | / | 12.33 | 12.30 | / | / | -20.96 | / | / | / | 33.29 | 45.5 |
| 21822 E560-013 | 236.0096 | 3.3738 | 131.8991 | -77.0237 | 3239 | 3505 | 4.0 | 0.20 | 503 | 2.702 | / | / | 11.28 | 11.23 | / | / | -22.28 | / | / | / | 33.56 | 51.6 |
| 21831 AGC170349 | 192.0543 | 24.0986 | 42.7514 | -44.0581 | 4723 | 4969 | 6.7 | 0.20 | 190 | 2.279 | / | / | 15.58 | 15.67 | / | / | -18.15 | / | / | / | 33.88 | 59.7 |
| 21854 UGC04024 | 154.5187 | 30.3802 | 32.7713 | -11.3702 | 1716 | 1793 | 5.8 | 0.29 | 204 | 2.319 | 13.22 | 13.13 | 14.00 | 14.07 | 13.95 | -18.67 | -18.55 | 32.63 | 33.6 | 32.63 | 33.6 | |
| 21857 UGC04032 | 190.2754 | 24.7689 | 42.1749 | -42.3564 | 8126 | 8486 | 5.9 | 0.20 | 357 | 2.553 | 14.37 | 13.93 | 14.36 | 14.43 | 14.54 | -20.79 | -20.82 | 35.45 | 123.0 | 35.43 | 121.7 | |
| 21918 UGC04040 | 186.3366 | 26.1571 | 41.0248 | -38.6405 | 4798 | 5032 | 5.8 | 0.20 | 451 | 2.654 | 12.94 | 12.38 | 12.36 | 12.40 | 12.76 | -21.71 | -21.82 | 34.55 | 81.2 | 34.30 | 72.5 | |
| 22002 UGC04060 | 206.7735 | 19.5086 | 52.3014 | -57.1632 | 4677 | 4958 | 2.0 | 0.35 | 399 | 2.621 | 12.12 | 11.90 | 12.62 | 12.70 | 12.66 | -21.41 | -21.50 | 34.12 | 66.8 | 34.28 | 71.7 | |
| 22174 ES035-018 | 288.7558 | -22.7003 | 202.4683 | -28.7905 | 1765 | 1875 | 5.0 | 0.25 | 296 | 2.476 | 11.76 | 11.30 | 12.24 | 12.26 | 12.13 | -20.10 | -20.08 | 32.24 | 28.0 | 32.35 | 29.5 | |
| 22188 IC0000480 | 194.3672 | 25.0931 | 45.6798 | -45.0880 | 4626 | 4882 | 4.0 | 0.21 | 318 | 2.503 | 13.09 | 12.73 | 12.89 | 12.95 | 13.21 | -20.34 | -20.34 | 33.59 | 52.1 | 33.33 | 46.4 | |
| 22297 UGC04113 | 189.5059 | 26.9484 | 43.9747 | -40.5100 | 5271 | 5533 | 6.1 | 0.20 | 197 | 2.294 | / | / | 16.44 | 16.53 | / | / | -18.30 | / | / | / | 34.96 | 98.1 |
| 22306 E561-003 | 237.5929 | 5.0724 | 132.0800 | -74.7050 | 3515 | 3797 | 6.1 | 0.20 | 331 | 2.520 | / | / | 12.59 | 12.60 | / | / | -20.50 | / | / | / | 33.14 | 42.4 |
| 22338 ES209-009 | 264.0140 | -10.5807 | 189.2625 | -53.5270 | 1117 | 1314 | 6.2 | 0.20 | 303 | 2.481 | 10.68 | 10.01 | 10.28 | 10.27 | 10.51 | -20.14 | -20.13 | 30.65 | 13.5 | 30.40 | 12.0 | |
| 22381 UGC04132 | 188.0734 | 27.7444 | 43.8305 | -39.0132 | 5215 | 5473 | 4.0 | 0.31 | 515 | 2.725 | 12.01 | 11.59 | 11.91 | 11.97 | 12.14 | -22.35 | -22.50 | 34.57 | 82.0 | 34.58 | 82.3 | |
| 22401 AGC170378 | 194.9108 | 25.9329 | 47.0334 | -44.9152 | 7403 | 7755 | 5.9 | 0.20 | 375 | 2.574 | 13.90 | 13.45 | 13.98 | 14.05 | 14.11 | -20.98 | -21.03 | 35.20 | 109.5 | 35.23 | 111.4 | |
| 22446 UGC04148 | 177.8142 | 30.1110 | 40.4056 | -30.1677 | 731 | 886 | 7.2 | 0.21 | 127 | 2.105 | 14.25 | 14.34 | 15.82 | 15.90 | 15.47 | -16.71 | -16.45 | 32.18 | 27.3 | 32.36 | 29.7 | |
| 22561 UGC04169 | 155.4741 | 32.0348 | 34.6170 | -11.7379 | 1585 | 1672 | 5.8 | 0.49 | 206 | 2.365 | 12.55 | 12.58 | 13.39 | 13.46 | 13.38 | -19.08 | -18.99 | 32.46 | 31.1 | 32.46 | 31.1 | |
| 22565 UGC04180 | 194.2084 | 26.8382 | 47.4092 | -43.8459 | 5226 | 5504 | 5.2 | 0.50 | 332 | 2.575 | 12.49 | 12.45 | 12.89 | 12.98 | 13.08 | -20.99 | -21.04 | 34.13 | 66.9 | 34.10 | 66.1 | |
| 22596 UGC04191 | 198.5116 | 25.6207 | 49.8950 | -47.5021 | 4714 | 4990 | 3.0 | 0.61 | 337 | 2.620 | 11.93 | 11.95 | 12.18 | 12.28 | 12.48 | -21.40 | -21.48 | 33.93 | 61.0 | 33.82 | 58.0 | |
| 22640 UGC04078 | 128.7347 | 28.6863 | 28.0739 | -10.5886 | 1862 | 1850 | 4.0 | 0.20 | 208 | 2.318 | 13.16 | 12.98 | 13.42 | 13.47 | 13.59 | -18.65 | -18.53 | 32.25 | 28.2 | 32.01 | 25.3 | |
| 22695 UGC04195 | 149.1019 | 31.9996 | 33.3119 | -6.4915 | 4880 | 5003 | 3.0 | 0.57 | 361 | 2.636 | 12.32 | 12.30 | 12.89 | 12.99 | 13.00 | -21.55 | -21.64 | 34.62 | 84.1 | 34.74 | 88.7 | |
| 22712 ES494-021 | 241.7260 | 4.7404 | 142.6737 | -71.8962 | 1584 | 1843 | 6.7 | 0.21 | 149 | 2.174 | / | / | 15.63 | 15.67 | / | / | -17.13 | / | / | / | 32.82 | 36.6 |

| PGC Name | l | b | sgl | sgb | v_{hel} | v_{mod} | t | b/a | w_{mz} | $\log w_{mz}^2$ | I | I* | [3.6] | [3.6]* | $C_{[3.6]}$ | MC | $M_{[3.6]}$ | μC | dC | $\mu_{[3.6]}$ | $d_{[3.6]}$ | |
|-----------------|----------|---------|----------|----------|-----------|-----------|-----|------|----------|-----------------|-------|-------|-------|--------|-------------|--------|-------------|---------|-------|---------------|-------------|------|
| 22873 UGC004247 | 205.9739 | 24.4629 | 56.6668 | -52.8219 | 2839 | 3097 | 6.8 | 0.20 | 188 | 2.274 | 15.20 | 15.09 | 16.39 | 16.46 | 16.12 | -18.25 | -18.10 | 34.44 | 77.3 | 34.67 | 86.1 | |
| 22921 UGC04257 | 197.5306 | 27.6393 | 51.0691 | -45.4551 | 4160 | 4426 | 6.0 | 0.20 | 240 | 2.380 | 13.97 | 13.73 | 14.65 | 14.72 | 14.58 | -19.22 | -19.14 | 33.84 | 58.6 | 33.93 | 61.0 | |
| 22969 UGC04238 | 137.8402 | 30.9877 | 30.8727 | -2.8478 | 1544 | 1568 | 6.6 | 0.41 | 169 | 2.259 | 12.05 | 12.12 | 13.47 | 13.56 | 13.19 | -18.12 | -17.96 | 31.30 | 18.2 | 31.51 | 20.1 | |
| 23028 NGC02543 | 185.1493 | 31.3061 | 45.5904 | -34.8684 | 2475 | 2678 | 3.0 | 0.51 | 299 | 2.534 | 11.35 | 11.31 | 11.85 | 11.87 | 11.95 | -20.62 | -20.64 | 32.58 | 32.8 | 32.53 | 32.0 | |
| 23071 UGC04278 | 174.1234 | 33.0572 | 41.6555 | -26.0029 | 557 | 709 | 6.5 | 0.20 | 169 | 2.228 | 12.01 | 11.94 | 13.16 | 13.17 | 12.90 | -17.83 | -17.65 | 30.74 | 14.0 | 30.82 | 14.6 | |
| 23110 UGC04284 | 170.1834 | 33.4780 | 40.4670 | -22.8632 | 559 | 699 | 6.0 | 0.51 | 188 | 2.330 | 11.07 | 11.15 | 12.09 | 12.17 | 12.01 | -18.76 | -18.64 | 30.77 | 14.3 | 30.81 | 14.5 | |
| 23146 AGC180141 | 201.5263 | 27.6394 | 54.8697 | -47.8484 | 4263 | 4545 | 5.2 | 0.20 | 267 | 2.427 | 14.02 | 13.74 | 14.29 | 14.36 | 14.41 | -19.64 | -19.59 | 34.11 | 66.2 | 34.02 | 63.7 | |
| 23147 UGC04296 | 214.9532 | 22.4522 | 67.4657 | -58.7657 | 9014 | 9495 | 6.1 | 0.20 | 299 | 2.476 | 14.73 | 14.42 | 15.17 | 15.27 | 15.20 | -20.09 | -20.07 | 35.41 | 120.5 | 35.52 | 126.9 | |
| 23169 UGC04299 | 199.8340 | 28.3335 | 53.8808 | -46.3445 | 4284 | 4563 | 4.1 | 0.20 | 389 | 2.590 | 12.56 | 12.07 | 12.45 | 12.49 | 12.65 | -21.13 | -21.19 | 33.82 | 58.0 | 33.74 | 55.9 | |
| 23239 UGC04306 | 186.3149 | 32.0520 | 47.0415 | -35.2278 | 2415 | 2624 | 1.3 | 0.50 | 207 | 2.370 | 12.54 | 12.56 | 12.45 | 12.53 | 12.92 | -19.13 | -19.04 | 32.06 | 25.8 | 31.57 | 20.7 | |
| 23289 UGC004324 | 202.6592 | 28.0469 | 56.4137 | -48.1689 | 4816 | 5118 | 2.2 | 0.39 | 308 | 2.515 | 12.88 | 12.76 | 13.14 | 13.22 | 13.36 | -20.45 | -20.46 | 33.85 | 58.9 | 33.74 | 56.0 | |
| 23338 AGC180197 | 202.7306 | 28.2044 | 56.6342 | -48.0847 | 5029 | 5337 | 3.0 | 0.68 | 185 | 2.393 | 14.04 | 14.18 | 15.04 | 15.15 | 15.02 | -19.34 | -19.27 | 34.42 | 76.6 | 34.52 | 80.2 | |
| 23340 NGC002552 | 169.0971 | 34.2908 | 40.8569 | -21.7040 | 521 | 660 | 9.0 | 0.57 | 126 | 2.177 | 11.64 | 11.82 | 12.73 | 12.76 | 12.64 | -17.37 | -17.15 | 30.01 | 10.1 | 29.91 | 9.6 | |
| 23347 AGC180199 | 202.4205 | 28.3343 | 56.4357 | -47.8131 | 4856 | 5159 | 5.0 | 0.71 | 162 | 2.353 | 14.03 | 14.19 | 14.58 | 14.69 | 14.81 | -18.97 | -18.87 | 33.82 | 58.2 | 33.62 | 53.0 | |
| 23355 UGC04332 | 202.3889 | 28.4192 | 56.4822 | -47.7293 | 5484 | 5805 | 2.5 | 0.59 | 471 | 2.757 | 12.36 | 12.31 | 12.56 | 12.66 | 12.85 | -22.65 | -22.82 | 35.63 | 133.6 | 35.67 | 135.8 | |
| 23362 UGC04334 | 201.4237 | 28.7719 | 55.8398 | -46.9213 | 3581 | 3852 | 3.7 | 0.47 | 403 | 2.650 | 11.40 | 11.28 | 11.94 | 12.02 | 12.01 | -21.68 | -21.78 | 33.72 | 55.6 | 33.86 | 59.1 | |
| 23374 P0023374 | 202.4726 | 28.4791 | 56.6233 | -47.7284 | 4235 | 4523 | 5.1 | 0.35 | 232 | 2.385 | 14.74 | 14.67 | 15.54 | 15.63 | 15.50 | -19.26 | -19.18 | 34.85 | 93.2 | 34.94 | 97.2 | |
| 23420 AGC180218 | 200.8395 | 29.2037 | 55.6698 | -46.2626 | 4143 | 4426 | 3.2 | 0.66 | 215 | 2.448 | 13.05 | 13.16 | 13.76 | 13.87 | 13.87 | -19.83 | -19.80 | 33.75 | 56.2 | 33.72 | 55.5 | |
| 23447 IC002327 | 220.6540 | 21.4306 | 76.8215 | -61.4780 | 2677 | 2968 | 1.1 | 0.37 | 286 | 2.479 | 12.74 | 12.66 | 13.36 | 13.43 | 13.40 | -20.12 | -20.11 | 33.56 | 51.5 | 33.59 | 52.2 | |
| 23465 UGC04361 | 200.9524 | 29.4338 | 55.9919 | -46.1488 | 3742 | 4017 | 5.8 | 0.32 | 174 | 2.255 | 14.27 | 14.27 | 15.18 | 15.27 | 15.12 | -18.08 | -17.91 | 33.23 | 44.2 | 33.22 | 44.1 | |
| 23519 UGC04381 | 224.6617 | 19.8797 | 84.2512 | -63.6652 | 4617 | 4954 | 4.3 | 0.26 | 335 | 2.531 | 12.71 | 12.42 | 12.88 | 12.94 | 13.04 | -20.60 | -20.62 | 33.68 | 54.3 | 33.61 | 52.8 | |
| 23522 UGC04375 | 201.0401 | 29.7208 | 56.3399 | -45.9759 | 2061 | 2309 | 5.3 | 0.68 | 277 | 2.566 | 11.29 | 11.39 | 12.10 | 12.19 | 12.15 | -20.91 | -20.95 | 33.08 | 41.2 | 33.17 | 43.1 | |
| 23567 UGC04386 | 202.8871 | 29.3516 | 57.8405 | -47.2630 | 4642 | 4944 | 3.0 | 0.23 | 480 | 2.684 | 11.84 | 11.33 | 12.08 | 12.12 | 12.08 | -21.98 | -22.11 | 34.12 | 66.7 | 34.31 | 72.9 | |
| 23574 PG0023574 | 236.9677 | 13.0248 | 116.2255 | -68.4329 | 4722 | 5065 | 7.4 | 0.20 | 204 | 2.310 | / | / | 15.32 | 15.40 | / | -18.45 | / | / | / | / | 33.92 | 60.8 |
| 23589 AGC180254 | 203.4473 | 29.2486 | 58.3253 | -47.6396 | 5969 | 6312 | 2.0 | 0.52 | 293 | 2.526 | 13.78 | 13.79 | 14.41 | 14.52 | 14.51 | -20.54 | -20.56 | 35.15 | 107.4 | 35.23 | 111.2 | |
| 23604 NGC02550 | 140.3606 | 32.3597 | 32.4723 | 0.8661 | 2262 | 2308 | 3.1 | 0.43 | 221 | 2.380 | 12.26 | 12.29 | 12.78 | 12.87 | 12.94 | -19.22 | -19.14 | 32.17 | 27.1 | 32.01 | 25.2 | |
| 23616 UGC04392 | 224.6446 | 20.4087 | 84.3400 | -63.1373 | 4995 | 5344 | 3.6 | 0.27 | 472 | 2.682 | 11.76 | 11.33 | 11.87 | 11.92 | 11.99 | -21.96 | -22.08 | 34.00 | 63.0 | 34.08 | 65.3 | |
| 23660 UGC04393 | 174.0886 | 35.1743 | 43.7103 | -24.9817 | 2125 | 2298 | 3.5 | 0.57 | 108 | 2.111 | 12.45 | 12.66 | 13.29 | 13.40 | 13.39 | -16.77 | -16.51 | 30.16 | 10.7 | 29.90 | 9.6 | |
| 23661 UGC04400 | 202.3828 | 30.0220 | 57.9283 | -46.4644 | 4390 | 4686 | 5.9 | 0.20 | 214 | 2.330 | 14.85 | 14.67 | 15.72 | 15.80 | 15.59 | -18.77 | -18.65 | 34.42 | 76.5 | 34.56 | 81.5 | |
| 23662 UGC04399 | 202.6148 | 29.9575 | 58.1033 | -46.6378 | 4476 | 4775 | 7.7 | 0.35 | 232 | 2.386 | 13.77 | 13.71 | 14.49 | 14.58 | 14.50 | -19.27 | -19.19 | 33.81 | 57.8 | 33.83 | 58.4 | |
| 23709 AGC180284 | 200.8424 | 30.8057 | 57.1280 | -45.0267 | 5289 | 5607 | 3.8 | 0.26 | 305 | 2.490 | 14.12 | 13.88 | 14.53 | 14.60 | 14.60 | -20.22 | -20.21 | 34.91 | 95.8 | 34.95 | 97.7 | |
| 23748 UGC04424 | 204.0952 | 29.9862 | 59.6425 | -47.3753 | 4438 | 4741 | 3.0 | 0.26 | 203 | 2.314 | 14.73 | 14.66 | 15.77 | 15.86 | 15.61 | -18.62 | -18.49 | 34.28 | 71.9 | 34.45 | 77.6 | |
| 23757 AGC180599 | 202.1779 | 30.6213 | 58.2523 | -45.8812 | 6450 | 6809 | 4.0 | 0.22 | 194 | 2.290 | 15.25 | 15.14 | 16.01 | 16.11 | 15.98 | -18.40 | -18.26 | 34.45 | 77.6 | 34.47 | 78.4 | |
| 23840 UGC004413 | 140.4252 | 32.7536 | 32.8700 | 0.8597 | 2292 | 2341 | 6.0 | 0.21 | 144 | 2.159 | / | / | 15.48 | 15.57 | / | -16.98 | / | / | / | / | 32.57 | 32.7 |
| 23878 UGC04446 | 203.9676 | 30.6634 | 60.0852 | -46.7591 | 6012 | 6362 | 5.9 | 0.20 | 328 | 2.516 | 14.06 | 13.69 | 13.92 | 13.99 | 14.21 | -20.45 | -20.47 | 34.74 | 88.7 | 34.56 | 81.5 | |
| 23997 NGC002613 | 245.3603 | 10.0554 | 137.7094 | -65.7257 | 1675 | 1964 | 3.1 | 0.27 | 599 | 2.785 | 9.22 | 8.64 | 9.38 | 9.38 | 9.37 | -22.90 | -23.09 | 32.28 | 28.6 | 32.49 | 31.5 | |

| PGC Name | l | b | sgl | sgb | v_{hel} | v_{mod} | t | b/a | w_{max} | $\log w_{max}^2$ | I | I* | [3.6] | [3.6]* | $C_{[3.6]}$ | MC | $M_{[3.6]}$ | μC | dC | $\mu_{[3.6]}$ | $d_{[3.6]}$ | |
|-----------------|----------|---------|----------|----------|-----------|-----------|-----|------|-----------|------------------|-------|-------|-------|--------|-------------|--------|-------------|---------|-------|---------------|-------------|------|
| 24034 ES562-018 | 244.1069 | 11.0699 | 133.8406 | -65.9192 | 4729 | 5076 | 6.4 | 0.20 | 214 | 2.330 | / | / | 15.98 | 16.05 | / | / | -18.65 | / | / | / | 34.83 | 92.3 |
| 24111 NGC02608 | 195.4559 | 34.0479 | 55.3560 | -39.5995 | 2156 | 2400 | 3.3 | 0.54 | 207 | 2.383 | 11.26 | 11.34 | 11.81 | 11.85 | 11.96 | -19.25 | -19.17 | 31.21 | 17.5 | 31.02 | 16.0 | |
| 24189 AGC480047 | 236.3402 | 16.9767 | 110.7215 | -65.0727 | 5915 | 6306 | 6.8 | 0.20 | 317 | 2.501 | / | / | 13.97 | 14.03 | / | / | -20.32 | / | / | / | 34.44 | 77.4 |
| 24219 AGC026102 | 245.2795 | 11.9001 | 135.5780 | -65.0149 | 1653 | 1946 | 5.2 | 0.20 | 160 | 2.204 | / | / | 14.38 | 14.44 | / | / | -17.42 | / | / | / | 31.86 | 23.6 |
| 24231 UGC04472 | 135.5645 | 31.9001 | 31.6124 | 4.8620 | 1333 | 1353 | 5.9 | 0.21 | 258 | 2.413 | 11.48 | 11.27 | 11.82 | 11.87 | 11.93 | -19.52 | -19.46 | 31.45 | 19.5 | 31.33 | 18.4 | |
| 24242 UGC004499 | 167.0911 | 37.1956 | 42.9662 | -19.0248 | 691 | 836 | 8.0 | 0.44 | 110 | 2.079 | / | / | 13.81 | 13.91 | / | / | -16.20 | / | / | / | 30.11 | 10.5 |
| 24351 UGC04514 | 164.8069 | 37.3956 | 42.4034 | -17.2767 | 694 | 832 | 5.9 | 0.33 | 149 | 2.189 | 12.71 | 12.80 | 13.76 | 13.84 | 13.67 | -17.48 | -17.28 | 31.16 | 17.0 | 31.11 | 16.7 | |
| 24374 UGC04524 | 220.6558 | 26.7191 | 79.1434 | -56.3265 | 1940 | 2238 | 6.7 | 0.24 | 146 | 2.169 | 14.44 | 14.49 | 15.40 | 15.48 | 15.34 | -17.29 | -17.07 | 32.65 | 33.8 | 32.57 | 32.6 | |
| 24479 E563-014 | 244.2604 | 13.5677 | 130.0864 | -63.9854 | 1709 | 2010 | 6.6 | 0.22 | 306 | 2.488 | 11.85 | 11.38 | 11.70 | 11.72 | 11.92 | -20.20 | -20.19 | 32.13 | 26.7 | 31.92 | 24.3 | |
| 24490 UGC004550 | 213.3793 | 30.6398 | 70.8332 | -50.6864 | 2068 | 2358 | 3.4 | 0.25 | 268 | 2.433 | 12.73 | 12.50 | 13.13 | 13.19 | 13.20 | -19.70 | -19.65 | 32.92 | 38.3 | 32.86 | 37.4 | |
| 24530 UGC04559 | 194.0782 | 36.3179 | 56.2857 | -37.1726 | 2084 | 2330 | 2.1 | 0.26 | 341 | 2.539 | 12.19 | 11.86 | 12.44 | 12.48 | 12.54 | -20.67 | -20.69 | 33.23 | 44.2 | 33.21 | 43.9 | |
| 24548 UGC04565 | 217.2268 | 29.3885 | 75.2339 | -52.9835 | 4066 | 4399 | 6.0 | 0.20 | 224 | 2.350 | 15.23 | 15.00 | 15.67 | 15.74 | 15.73 | -18.95 | -18.85 | 34.75 | 89.2 | 34.70 | 87.0 | |
| 24558 E563-017 | 244.7318 | 13.6881 | 130.6826 | -63.5916 | 3460 | 3789 | 1.4 | 0.63 | 389 | 2.690 | 11.38 | 11.25 | 11.68 | 11.75 | 11.86 | -22.03 | -22.16 | 33.94 | 61.5 | 33.98 | 62.6 | |
| 24602 IC000499 | 127.2179 | 29.0932 | 28.4639 | 11.9238 | 1958 | 1945 | 1.0 | 0.48 | 384 | 2.632 | / | / | 11.90 | 11.97 | / | / | -21.60 | / | / | / | 33.62 | 53.0 |
| 24685 ES563-021 | 244.8672 | 14.3975 | 129.8566 | -62.9731 | 4582 | 4940 | 4.3 | 0.20 | 664 | 2.823 | 11.53 | 10.57 | 11.30 | 11.28 | 11.28 | -23.25 | -23.46 | 34.60 | 83.3 | 34.87 | 94.2 | |
| 24711 UGC04576 | 140.3156 | 34.0600 | 34.1561 | 1.1081 | 2383 | 2440 | 3.0 | 0.28 | 179 | 2.261 | 12.98 | 12.99 | 13.61 | 13.69 | 13.70 | -18.14 | -17.98 | 31.84 | 23.4 | 31.68 | 21.6 | |
| 24723 UGC04574 | 139.6800 | 33.8725 | 33.9082 | 1.6098 | 2170 | 2221 | 3.0 | 0.65 | 256 | 2.521 | 10.99 | 11.12 | 11.26 | 11.30 | 11.58 | -20.50 | -20.52 | 32.09 | 26.2 | 31.82 | 23.1 | |
| 24778 P0024778 | 234.6008 | 21.7527 | 103.9741 | -61.0461 | 2907 | 3236 | 4.0 | 0.61 | 228 | 2.450 | 12.30 | 12.39 | 12.92 | 13.01 | 13.06 | -19.86 | -19.82 | 32.94 | 38.7 | 32.86 | 37.3 | |
| 24784 UGC04605 | 156.1243 | 37.8086 | 40.4251 | -10.6604 | 1358 | 1473 | 2.0 | 0.28 | 422 | 2.634 | 10.66 | 10.27 | 11.03 | 11.06 | 11.03 | -21.53 | -21.62 | 32.56 | 32.6 | 32.70 | 34.6 | |
| 24829 UGC04621 | 188.2576 | 38.5206 | 54.2594 | -32.3312 | 2299 | 2535 | 1.0 | 0.50 | 239 | 2.431 | 12.37 | 12.41 | 12.81 | 12.90 | 13.02 | -19.68 | -19.63 | 32.71 | 34.8 | 32.54 | 32.3 | |
| 24830 UGC04625 | 224.1102 | 27.9139 | 84.8945 | -55.6216 | 8476 | 8975 | 6.1 | 0.20 | 422 | 2.625 | 13.90 | 13.38 | 13.88 | 13.95 | 14.03 | -21.45 | -21.53 | 35.61 | 132.3 | 35.68 | 136.5 | |
| 24840 AGC026184 | 244.9032 | 15.2928 | 128.6476 | -62.2705 | 3404 | 3738 | 6.4 | 0.20 | 170 | 2.230 | / | / | 15.26 | 15.32 | / | / | -17.68 | / | / | / | 33.02 | 40.3 |
| 24854 ES563-028 | 246.9590 | 13.8885 | 133.8122 | -61.9573 | 2578 | 2895 | 1.5 | 0.26 | 402 | 2.611 | 11.79 | 11.22 | 11.50 | 11.51 | 11.73 | -21.32 | -21.39 | 33.07 | 41.1 | 32.93 | 38.5 | |
| 24870 P0024870 | 243.3633 | 16.5960 | 124.4232 | -62.1543 | 2001 | 2315 | 6.5 | 0.29 | 306 | 2.497 | 12.08 | 11.70 | 12.69 | 12.72 | 12.56 | -20.28 | -20.28 | 32.86 | 37.3 | 33.03 | 40.3 | |
| 24893 UGC04640 | 229.7552 | 25.3844 | 94.0929 | -58.2109 | 3307 | 3644 | 5.3 | 0.34 | 324 | 2.528 | 12.06 | 11.91 | 12.79 | 12.86 | 12.74 | -20.56 | -20.58 | 33.33 | 46.4 | 33.49 | 49.9 | |
| 24930 UGC04641 | 190.4556 | 38.7603 | 55.8670 | -33.4183 | 411 | 639 | 3.0 | 0.27 | 426 | 2.637 | 8.43 | 8.07 | 8.84 | 8.82 | 8.80 | -21.55 | -21.64 | 30.36 | 11.8 | 30.46 | 12.4 | |
| 24947 UGC04623 | 136.8775 | 33.2791 | 33.0820 | 3.8730 | 2885 | 2934 | 5.8 | 0.29 | 365 | 2.573 | 11.48 | 11.23 | 12.25 | 12.31 | 12.12 | -20.97 | -21.02 | 33.11 | 42.0 | 33.37 | 47.1 | |
| 24960 UGC04655 | 223.2717 | 29.2423 | 83.8773 | -54.2198 | 6188 | 6597 | 6.1 | 0.20 | 265 | 2.423 | 14.82 | 14.54 | 15.06 | 15.13 | 15.20 | -19.61 | -19.56 | 34.90 | 95.4 | 34.82 | 91.9 | |
| 25012 UGC04659 | 172.7888 | 40.1148 | 47.8775 | -21.6904 | 1749 | 1933 | 8.0 | 0.31 | 174 | 2.254 | 13.70 | 13.74 | 14.89 | 14.97 | 14.70 | -18.07 | -17.90 | 32.79 | 36.1 | 32.90 | 38.1 | |
| 25102 NGC02706 | 230.8139 | 26.1086 | 95.7460 | -57.3996 | 1629 | 1946 | 3.8 | 0.27 | 304 | 2.490 | 11.94 | 11.74 | 11.69 | 11.74 | 12.12 | -20.22 | -20.22 | 32.35 | 29.5 | 31.96 | 24.7 | |
| 25161 UGC04691 | 225.6620 | 29.1655 | 87.4327 | -54.4764 | 3916 | 4267 | 2.5 | 0.43 | 629 | 2.835 | 10.36 | 10.11 | 10.79 | 10.85 | 10.84 | -23.36 | -23.58 | 34.26 | 71.0 | 34.54 | 80.8 | |
| 25166 UGC04601 | 128.0340 | 29.7421 | 29.1361 | 11.2219 | 1789 | 1780 | 2.5 | 0.31 | 271 | 2.446 | 12.34 | 12.16 | 12.45 | 12.51 | 12.70 | -19.82 | -19.78 | 32.53 | 32.1 | 32.30 | 28.9 | |
| 25221 AGC480085 | 232.2737 | 26.0358 | 98.1726 | -57.2960 | 2761 | 3096 | 4.2 | 0.52 | 250 | 2.458 | 12.09 | 12.16 | 12.58 | 12.67 | 12.78 | -19.92 | -19.90 | 32.72 | 35.0 | 32.58 | 32.8 | |
| 25237 UGC04695 | 164.0128 | 40.2326 | 44.8858 | -15.6144 | 2328 | 2490 | 5.2 | 0.68 | 239 | 2.504 | 11.43 | 11.59 | 12.13 | 12.23 | 12.27 | -20.35 | -20.35 | 32.63 | 33.6 | 32.60 | 33.1 | |
| 25248 UGC04708 | 175.6469 | 41.0028 | 49.9009 | -23.1058 | 1821 | 2018 | 3.1 | 0.54 | 303 | 2.546 | 11.06 | 11.10 | 11.63 | 11.66 | 11.74 | -20.73 | -20.76 | 32.48 | 31.3 | 32.43 | 30.6 | |
| 25258 NGC02710 | 161.4935 | 40.0254 | 43.9477 | -13.9025 | 2523 | 2678 | 3.1 | 0.50 | 265 | 2.477 | 12.18 | 12.22 | 12.91 | 12.99 | 12.97 | -20.10 | -20.08 | 33.09 | 41.4 | 33.11 | 41.9 | |

| PGC Name | l | b | sgl | sgb | v_{hel} | v_{mod} | t | b/a | w_{max} | $\log w_{max}^{\dagger}$ | I | I* | [3.6] | [3.6]* | $C_{[3.6]}$ | M_C | $M_{[3.6]}$ | μ_C | d_C | $\mu_{[3.6]}$ | $d_{[3.6]}$ |
|-----------------|----------|----------|----------|----------|-----------|-----------|-----|------|-----------|--------------------------|-------|-------|-------|--------|-------------|--------|-------------|---------|-------|---------------|-------------|
| 25318 UGC004725 | 192.6666 | 40.2190 | 58.5531 | -33.5630 | 1998 | 2250 | 6.1 | 0.20 | 131 | 2.117 | 15.31 | 15.40 | 16.42 | 16.52 | 16.31 | -16.83 | -16.57 | 33.16 | 42.8 | 33.12 | 42.0 |
| 25371 UGC004701 | 134.6963 | 32.9573 | 32.6180 | 5.6694 | 1406 | 1430 | 7.0 | 0.52 | 175 | 2.303 | / | / | 14.55 | 14.64 | / | / | -18.38 | / | / | 33.05 | 40.7 |
| 25373 ES090-015 | 281.5159 | -12.0762 | 190.3598 | -36.3212 | 1678 | 1860 | 3.2 | 0.35 | 264 | 2.441 | 12.34 | 12.03 | 12.37 | 12.41 | 12.58 | -19.77 | -19.73 | 32.37 | 29.7 | 32.15 | 26.9 |
| 25376 NGC02731 | 220.7996 | 32.7712 | 81.3164 | -50.4126 | 2585 | 2908 | 4.2 | 0.61 | 174 | 2.333 | 12.38 | 12.48 | 12.76 | 12.80 | 13.01 | -18.79 | -18.68 | 31.80 | 22.9 | 31.48 | 19.8 |
| 25412 ES564-012 | 245.5412 | 18.5625 | 125.4288 | -59.3372 | 3542 | 3891 | 6.2 | 0.21 | 179 | 2.254 | / | / | 16.46 | 16.52 | / | / | -17.90 | / | / | 34.53 | 80.5 |
| 25450 UGC004754 | 229.5995 | 29.0710 | 93.3604 | -54.5440 | 5679 | 6086 | 4.0 | 0.22 | 318 | 2.504 | / | / | 13.87 | 13.94 | / | / | -20.35 | / | / | 34.39 | 75.4 |
| 25472 UGC004753 | 175.1135 | 41.8854 | 50.4840 | -22.2998 | 1836 | 2035 | 6.7 | 0.20 | 156 | 2.193 | / | / | 14.88 | 14.96 | / | / | -17.31 | / | / | 32.28 | 28.6 |
| 25498 NGC02726 | 155.9198 | 39.7864 | 42.3022 | -9.9351 | 1517 | 1642 | 1.0 | 0.43 | 374 | 2.608 | 11.80 | 11.68 | 12.34 | 12.40 | 12.40 | -21.29 | -21.36 | 33.73 | 55.7 | 33.83 | 58.3 |
| 25525 UGC04769 | 201.3295 | 39.8292 | 64.6796 | -37.9735 | 2674 | 2961 | 5.3 | 0.66 | 134 | 2.242 | 11.48 | 11.68 | 11.84 | 11.94 | 12.18 | -17.97 | -17.79 | 30.14 | 10.7 | 29.74 | 8.9 |
| 25562 UGC04777 | 189.4672 | 41.8045 | 57.8037 | -30.7455 | 2052 | 2299 | 9.2 | 0.22 | 171 | 2.235 | 13.73 | 13.71 | 14.62 | 14.70 | 14.56 | -17.90 | -17.72 | 32.47 | 31.1 | 32.43 | 30.7 |
| 25563 PG0025563 | 236.1279 | 26.0799 | 104.3474 | -56.5036 | 3758 | 4120 | 6.9 | 0.20 | 302 | 2.480 | / | / | 13.93 | 13.98 | / | / | -20.11 | / | / | 34.18 | 68.5 |
| 25640 UGC04779 | 155.1216 | 39.9563 | 42.2890 | -9.2994 | 1294 | 1415 | 5.3 | 0.51 | 285 | 2.511 | 10.50 | 10.51 | 11.18 | 11.20 | 11.21 | -20.41 | -20.42 | 31.63 | 21.2 | 31.62 | 21.1 |
| 25676 UGC04759 | 134.7283 | 33.3225 | 32.9860 | 5.6673 | 1323 | 1349 | 5.2 | 0.35 | 277 | 2.461 | 10.53 | 10.44 | 11.08 | 11.15 | 11.15 | -19.96 | -19.93 | 31.11 | 16.7 | 31.08 | 16.4 |
| 25694 ES564-023 | 250.0125 | 16.7483 | 133.8536 | -57.8525 | 7741 | 8221 | 5.5 | 0.22 | 311 | 2.494 | 14.68 | 14.16 | 14.76 | 14.82 | 14.85 | -20.26 | -20.26 | 35.21 | 110.3 | 35.23 | 111.0 |
| 25732 ES314-005 | 262.4599 | 6.1828 | 161.0173 | -52.8153 | 4867 | 5212 | 3.3 | 0.30 | 460 | 2.674 | / | / | 12.03 | 12.03 | / | / | -22.01 | / | / | 34.12 | 66.7 |
| 25761 NGC002788 | 284.3412 | -13.5124 | 192.0418 | -33.5369 | 1640 | 1809 | 2.2 | 0.28 | 218 | 2.348 | 12.39 | 12.21 | 12.03 | 12.08 | 12.52 | -18.93 | -18.82 | 31.45 | 19.5 | 30.91 | 15.2 |
| 25781 UGC04800 | 162.1887 | 41.5056 | 45.5652 | -13.8561 | 2433 | 2596 | 5.9 | 0.31 | 231 | 2.376 | 13.22 | 13.16 | 14.03 | 14.10 | 13.99 | -19.18 | -19.10 | 33.19 | 43.5 | 33.24 | 44.5 |
| 25806 UGC04806 | 191.5700 | 42.1967 | 59.4331 | -31.5525 | 1952 | 2205 | 5.3 | 0.25 | 318 | 2.508 | 11.12 | 10.86 | 11.82 | 11.87 | 11.72 | -20.38 | -20.38 | 32.11 | 26.4 | 32.27 | 28.4 |
| 25867 ES497-018 | 251.1365 | 16.4665 | 135.6094 | -57.2588 | 5116 | 5503 | 1.2 | 0.21 | 442 | 2.646 | 13.17 | 12.46 | 13.09 | 13.11 | 13.14 | -21.64 | -21.74 | 34.87 | 94.2 | 34.98 | 99.0 |
| 25886 PG0025886 | 238.9033 | 25.5894 | 108.9039 | -56.1794 | 1839 | 2172 | 3.3 | 0.20 | 518 | 2.714 | 10.06 | 9.44 | 10.11 | 10.11 | 10.14 | -22.26 | -22.40 | 32.41 | 30.3 | 32.53 | 32.1 |
| 25910 UGC04824 | 166.9523 | 42.4830 | 47.9623 | -16.7092 | 2182 | 2361 | 6.4 | 0.23 | 244 | 2.391 | 12.63 | 12.47 | 13.59 | 13.65 | 13.41 | -19.31 | -19.24 | 32.74 | 35.3 | 32.92 | 38.4 |
| 25926 AGC026338 | 248.6566 | 18.9000 | 129.3426 | -57.1957 | 2177 | 2508 | 6.3 | 0.20 | 328 | 2.516 | 12.21 | 11.66 | 12.22 | 12.24 | 12.31 | -20.45 | -20.47 | 32.78 | 36.0 | 32.72 | 35.0 |
| 25932 E497-022 | 254.0016 | 14.5580 | 141.5027 | -56.3335 | 2423 | 2748 | 2.9 | 0.50 | 212 | 2.380 | 12.74 | 12.65 | 13.04 | 13.11 | 13.24 | -19.22 | -19.14 | 32.47 | 31.2 | 32.25 | 28.2 |
| 25956 UGC04845 | 220.3923 | 35.7837 | 81.6301 | -47.3885 | 2120 | 2442 | 6.9 | 0.35 | 207 | 2.336 | 13.13 | 13.05 | 14.07 | 14.14 | 13.95 | -18.82 | -18.71 | 32.78 | 36.0 | 32.88 | 37.6 |
| 26003 ES091-003 | 281.3722 | -10.3006 | 188.1550 | -36.4735 | 1901 | 2095 | 2.3 | 0.66 | 333 | 2.638 | / | / | 11.14 | 11.19 | / | / | -21.66 | / | / | 32.87 | 37.5 |
| 26018 NGC02748 | 136.2549 | 34.3615 | 34.1199 | 4.4793 | 1473 | 1510 | 4.0 | 0.36 | 279 | 2.467 | 10.81 | 10.72 | 11.06 | 11.12 | 11.29 | -20.01 | -19.99 | 31.30 | 18.2 | 31.11 | 16.7 |
| 26057 E564-031 | 248.6268 | 19.7502 | 128.2767 | -56.5755 | 5150 | 5547 | 4.4 | 0.32 | 345 | 2.552 | 12.76 | 12.44 | 13.01 | 13.07 | 13.12 | -20.79 | -20.82 | 33.95 | 61.7 | 33.96 | 62.0 |
| 26068 UGC04867 | 181.0932 | 43.8081 | 54.9317 | -24.8068 | 2493 | 2726 | 7.0 | 0.63 | 191 | 2.382 | 13.03 | 13.19 | 14.40 | 14.50 | 14.19 | -19.24 | -19.16 | 33.46 | 49.2 | 33.71 | 55.3 |
| 26093 AGC026360 | 255.5757 | 14.1138 | 143.7211 | -55.3476 | 2122 | 2442 | 4.9 | 0.65 | 244 | 2.499 | 11.85 | 11.77 | 12.36 | 12.43 | 12.46 | -20.30 | -20.30 | 32.78 | 35.9 | 32.75 | 35.5 |
| 26135 ES564-033 | 248.3372 | 20.3999 | 127.1416 | -56.2563 | 5168 | 5567 | 7.9 | 0.20 | 240 | 2.380 | / | / | 15.49 | 15.56 | / | / | -19.14 | / | / | 34.82 | 92.1 |
| 26157 AGC026375 | 252.1723 | 17.3983 | 135.5597 | -55.8989 | 2543 | 2878 | 2.9 | 0.31 | 545 | 2.749 | 10.51 | 9.97 | 10.77 | 10.79 | 10.74 | -22.57 | -22.74 | 33.34 | 46.5 | 33.58 | 51.9 |
| 26192 AGC026380 | 254.7273 | 15.3651 | 141.0931 | -55.2895 | 2436 | 2764 | 4.0 | 0.33 | 385 | 2.602 | 11.89 | 11.52 | 11.86 | 11.89 | 12.07 | -21.23 | -21.30 | 33.34 | 46.5 | 33.23 | 44.3 |
| 26295 UGC04888 | 138.9917 | 35.9307 | 35.8931 | -2.3968 | 2255 | 2316 | 5.2 | 0.44 | 289 | 2.499 | 11.28 | 11.26 | 11.99 | 12.06 | 12.02 | -20.30 | -20.30 | 32.33 | 29.2 | 32.37 | 29.9 |
| 26304 UGC004922 | 171.3351 | 44.0859 | 51.0003 | -18.8007 | 1992 | 2188 | 8.9 | 0.41 | 226 | 2.385 | 12.56 | 12.58 | 13.63 | 13.71 | 13.50 | -19.27 | -19.19 | 32.78 | 36.0 | 32.92 | 38.4 |
| 26383 ES061-008 | 285.7751 | -13.4240 | 191.9037 | -32.1445 | 3372 | 3564 | 5.0 | 0.30 | 306 | 2.498 | 12.51 | 12.19 | 12.85 | 12.90 | 12.91 | -20.29 | -20.29 | 33.22 | 44.1 | 33.23 | 44.2 |
| 26390 IC002461 | 186.2841 | 44.7179 | 58.3738 | -27.0567 | 2261 | 2509 | 3.3 | 0.27 | 367 | 2.572 | 12.45 | 12.18 | 12.36 | 12.41 | 12.66 | -20.97 | -21.02 | 33.67 | 54.2 | 33.47 | 49.5 |

| PGC Name | l | b | sgl | sgb | v_{hel} | v_{mod} | t | b/a | w_{max} | $\log w_{max}^*$ | I | I* | [3.6] | [3.6]* | $C_{[3.6]}$ | M_C | $M_{[3.6]}$ | μ_C | d_C | $\mu_{[3.6]}$ | $d_{[3.6]}$ |
|----------|-----------|----------|---------|----------|-----------|-----------|------|-----|-----------|------------------|-------|-------|-------|--------|-------------|--------|-------------|---------|-------|---------------|-------------|
| 26411 | PG0026411 | 239.5536 | 28.0911 | 108.3008 | 53.6348 | 3437 | 3803 | 3.0 | 0.51 | 359 | 2.612 | / | 12.46 | 12.54 | / | -21.40 | / | / | 34.01 | 63.5 | |
| 26455 | AGC026407 | 260.1700 | 11.6930 | 151.1652 | -52.7319 | 2427 | 2744 | 3.1 | 0.21 | 375 | 2.575 | 12.18 | 11.47 | 11.53 | 11.52 | 11.87 | -20.99 | -21.04 | 32.87 | 37.6 | 32.58 |
| 26495 | UGC04970 | 183.0050 | 45.1429 | 57.0212 | -25.0337 | 2409 | 2650 | 5.7 | 0.20 | 227 | 2.356 | 13.98 | 13.81 | 14.40 | 14.47 | 14.50 | -19.00 | -18.90 | 33.53 | 50.9 | 33.41 |
| 26501 | UGC04971 | 182.1172 | 45.1525 | 56.5907 | -24.5444 | 1480 | 1708 | 1.0 | 0.55 | 314 | 2.566 | 11.54 | 11.59 | 12.35 | 12.37 | 12.34 | -20.91 | -20.96 | 33.28 | 45.2 | 33.37 |
| 26512 | UGC04966 | 166.9418 | 44.1508 | 49.5245 | -15.9782 | 633 | 805 | 3.0 | 0.44 | 592 | 2.809 | 8.05 | 7.86 | 8.65 | 8.65 | 8.61 | -23.13 | -23.33 | 31.74 | 23.3 | 31.99 |
| 26561 | IC002469 | 259.9222 | 12.5112 | 149.7861 | -52.5645 | 1666 | 1977 | 2.1 | 0.21 | 495 | 2.696 | 9.71 | 9.00 | 9.90 | 9.89 | 9.80 | -22.09 | -22.22 | 31.89 | 23.9 | 32.12 |
| 26563 | UGC04982 | 175.8602 | 45.1956 | 53.7949 | -20.9661 | 2659 | 2882 | 7.9 | 0.32 | 269 | 2.445 | 12.69 | 12.59 | 13.23 | 13.30 | 13.31 | -19.81 | -19.77 | 33.14 | 42.5 | 33.11 |
| 26608 | E498-003 | 255.8444 | 16.4402 | 140.7128 | -53.7858 | 2368 | 2700 | 3.2 | 0.31 | 296 | 2.485 | 12.15 | 11.89 | 12.18 | 12.23 | 12.43 | -20.17 | -20.16 | 32.61 | 33.3 | 32.41 |
| 26752 | UGC05020 | 190.0005 | 45.7656 | 61.2937 | -28.1749 | 1623 | 1878 | 5.8 | 0.24 | 194 | 2.292 | 13.34 | 13.29 | 14.33 | 14.40 | 14.20 | -18.42 | -18.28 | 32.63 | 33.5 | 32.70 |
| 26932 | UGC05056 | 225.3261 | 38.4920 | 87.7316 | -45.1478 | 2136 | 2475 | 1.0 | 0.61 | 395 | 2.687 | 11.05 | 11.03 | 11.69 | 11.76 | 11.75 | -22.01 | -22.13 | 33.81 | 57.7 | 33.96 |
| 27045 | ES434-011 | 259.6745 | 15.3218 | 145.6415 | -51.3647 | 2559 | 2891 | 6.8 | 0.46 | 192 | 2.326 | 12.58 | 12.54 | 13.05 | 13.12 | 13.19 | -18.73 | -18.61 | 31.92 | 24.2 | 31.73 |
| 27054 | PG0027054 | 248.6046 | 25.1192 | 122.4963 | -52.3816 | 4366 | 4757 | 6.1 | 0.20 | 323 | 2.509 | / | 13.58 | 13.63 | / | -20.40 | / | / | 34.10 | 66.2 | |
| 27074 | UGC05081 | 224.9035 | 39.4032 | 87.3405 | -44.2199 | 2144 | 2484 | 5.9 | 0.55 | 348 | 2.611 | 11.20 | 11.19 | 11.69 | 11.71 | 11.81 | -21.32 | -21.39 | 33.16 | 42.8 | 33.14 |
| 27077 | UGC05079 | 208.7108 | 44.5403 | 73.5331 | -36.4398 | 554 | 850 | 4.0 | 0.49 | 368 | 2.617 | 7.82 | 7.77 | 8.37 | 8.38 | 8.43 | -21.37 | -21.45 | 29.81 | 9.1 | 29.83 |
| 27130 | PG0027130 | 249.4789 | 24.9205 | 123.7260 | -52.0660 | 2117 | 2466 | 3.0 | 0.68 | 231 | 2.490 | 11.43 | 11.53 | 12.06 | 12.14 | 12.20 | -20.21 | -20.21 | 32.42 | 30.5 | 32.36 |
| 27158 | AGC490097 | 244.9380 | 28.5586 | 115.0466 | -51.2284 | 2666 | 3027 | 4.0 | 0.28 | 309 | 2.499 | 12.10 | 11.86 | 12.51 | 12.56 | 12.57 | -20.30 | -20.30 | 32.89 | 37.8 | 32.89 |
| 27214 | NGC002921 | 253.0443 | 22.3385 | 130.4802 | -51.8809 | 2967 | 3325 | 1.1 | 0.32 | 430 | 2.648 | / | 11.63 | 11.68 | / | -21.76 | / | / | 33.48 | 49.7 | |
| 27232 | UGC05102 | 223.1747 | 40.8472 | 85.6832 | -42.6756 | 2431 | 2773 | 3.7 | 0.35 | 314 | 2.516 | 12.02 | 11.88 | 12.48 | 12.55 | 12.57 | -20.46 | -20.47 | 33.05 | 40.7 | 33.05 |
| 27248 | UGC05107 | 229.0911 | 38.4134 | 91.9152 | -45.2380 | 2010 | 2355 | 6.4 | 0.23 | 166 | 2.223 | 13.93 | 13.91 | 15.09 | 15.16 | 14.89 | -17.79 | -17.61 | 32.69 | 34.6 | 32.79 |
| 27458 | ES091-016 | 283.2489 | -8.2646 | 185.6993 | -34.5808 | 1999 | 2203 | 3.0 | 0.31 | 218 | 2.352 | 12.01 | 11.66 | 11.93 | 11.96 | 12.18 | -18.96 | -18.86 | 31.14 | 16.9 | 30.82 |
| 27473 | UGC05115 | 135.4790 | 35.6745 | 35.3858 | 5.2119 | 2286 | 2336 | 5.8 | 0.56 | 198 | 2.370 | 13.03 | 13.15 | 13.93 | 14.02 | 13.94 | -19.12 | -19.04 | 33.09 | 41.4 | 33.09 |
| 27606 | E373-019 | 262.9033 | 14.8055 | 148.7772 | -48.9249 | 2808 | 3143 | 1.1 | 0.31 | 361 | 2.571 | / | 11.80 | 11.83 | / | -21.00 | / | / | 32.86 | 37.3 | |
| 27690 | E434-023 | 259.7780 | 18.3750 | 141.7115 | -49.6087 | 2527 | 2869 | 6.8 | 0.57 | 245 | 2.467 | 12.30 | 12.26 | 12.84 | 12.91 | 12.95 | -20.01 | -19.98 | 32.97 | 39.3 | 32.92 |
| 27747 | AGC490130 | 241.9207 | 33.4170 | 108.2400 | -47.9344 | 1851 | 2207 | 6.1 | 0.21 | 198 | 2.298 | 13.48 | 13.38 | 14.21 | 14.27 | 14.18 | -18.47 | -18.34 | 32.67 | 34.1 | 32.63 |
| 27810 | PG0027810 | 245.4679 | 31.2454 | 113.7003 | -48.6439 | 2701 | 3069 | 6.8 | 0.37 | 304 | 2.505 | 12.40 | 12.24 | 13.14 | 13.20 | 13.08 | -20.36 | -20.36 | 33.46 | 49.3 | 33.61 |
| 28087 | UGC05238 | 236.0706 | 38.3695 | 99.5857 | -44.5845 | 1792 | 2147 | 7.0 | 0.35 | 181 | 2.278 | 13.37 | 13.19 | 14.20 | 14.25 | 14.07 | -18.29 | -18.14 | 32.37 | 29.8 | 32.40 |
| 28098 | UGC05203 | 131.7712 | 33.9114 | 33.4483 | 8.1572 | 1540 | 1563 | 6.4 | 0.20 | 166 | 2.220 | 13.70 | 13.69 | 14.87 | 14.94 | 14.66 | -17.76 | -17.58 | 32.43 | 30.7 | 32.53 |
| 28117 | AGC026634 | 258.2653 | 21.6507 | 136.3982 | -48.7732 | 4299 | 4686 | 5.0 | 0.24 | 365 | 2.566 | 12.06 | 11.65 | 12.53 | 12.58 | 12.47 | -20.91 | -20.95 | 33.41 | 48.1 | 33.59 |
| 28136 | UGC05245 | 238.7928 | 37.0161 | 103.0076 | -45.3670 | 1420 | 1773 | 8.0 | 0.20 | 145 | 2.161 | 13.77 | 13.79 | 15.02 | 15.10 | 14.79 | -17.23 | -17.00 | 32.02 | 25.4 | 32.11 |
| 28147 | IC002510 | 264.0697 | 15.8345 | 148.2264 | -47.4451 | 2805 | 3144 | 2.8 | 0.54 | 250 | 2.462 | 12.02 | 11.93 | 12.36 | 12.43 | 12.54 | -19.97 | -19.94 | 32.52 | 31.9 | 32.38 |
| 28148 | UGC05249 | 233.9745 | 39.7453 | 97.0065 | -43.5325 | 1878 | 2232 | 6.7 | 0.22 | 201 | 2.306 | 12.90 | 12.76 | 13.95 | 14.02 | 13.74 | -18.54 | -18.41 | 32.29 | 28.7 | 32.44 |
| 28186 | UGC05251 | 192.3425 | 50.3406 | 65.9984 | -25.7664 | 1481 | 1751 | 4.3 | 0.24 | 270 | 2.435 | 11.12 | 10.94 | 11.77 | 11.83 | 11.74 | -19.72 | -19.68 | 31.46 | 19.6 | 31.50 |
| 28196 | UGC05250 | 175.7182 | 49.8103 | 57.7896 | -18.2918 | 4772 | 5054 | 5.2 | 0.48 | 374 | 2.622 | 11.74 | 11.70 | 12.21 | 12.31 | 12.37 | -21.42 | -21.50 | 33.83 | 58.3 | 33.87 |
| 28224 | AGC026650 | 255.2264 | 25.1800 | 129.6104 | -48.4528 | 4701 | 5107 | 4.0 | 0.25 | 268 | 2.434 | 13.65 | 13.45 | 13.81 | 13.89 | 14.03 | -19.71 | -19.66 | 33.78 | 57.1 | 33.60 |
| 28246 | IC002511 | 264.3443 | 16.0681 | 148.1101 | -47.1015 | 2888 | 3229 | 1.7 | 0.20 | 414 | 2.617 | 11.30 | 10.68 | 11.48 | 11.49 | 11.44 | -21.37 | -21.45 | 32.83 | 36.9 | 32.97 |
| 28283 | IC002513 | 264.4737 | 16.1189 | 148.1319 | -46.9681 | 2868 | 3209 | 2.1 | 0.20 | 438 | 2.641 | / | 10.98 | 10.98 | / | -21.69 | / | / | 32.70 | 34.6 | |

| PGC Name | l | b | sgl | sgb | v_{hel} | v_{mod} | t | b/a | w_{max} | $\log w_{max}^i$ | I | I* | [3.6] | [3.6]* | $C_{[3.6]}$ | M_C | $M_{[3.6]}$ | μ_C | d_C | $\mu_{[3.6]}$ | $d_{[3.6]}$ | |
|-----------------|----------|---------|----------|----------|-----------|-----------|-----|------|-----------|------------------|-------|-------|-------|--------|-------------|--------|-------------|---------|-------|---------------|-------------|------|
| 28296 UGC05271 | 222.3635 | 45.3333 | 85.5255 | -38.1522 | 1442 | 1777 | 5.9 | 0.43 | 202 | 2.340 | 11.96 | 12.00 | 12.82 | 12.90 | 12.81 | -18.85 | -18.74 | 31.66 | 21.5 | 31.65 | 21.3 | |
| 28313 E499-009 | 257.4631 | 23.4501 | 133.6079 | -48.1694 | 2086 | 2437 | 2.6 | 0.43 | 290 | 2.498 | / | / | 12.39 | 12.46 | / | / | -20.29 | / | / | / | 32.77 | 35.8 |
| 28357 UGC05280 | 192.1783 | 50.8387 | 66.2587 | -25.3149 | 1537 | 1809 | 4.0 | 0.56 | 254 | 2.476 | 11.15 | 11.24 | 11.63 | 11.67 | 11.82 | -20.09 | -20.07 | 31.91 | 24.1 | 31.75 | 22.3 | |
| 28376 AGC026671 | 264.5895 | 16.3890 | 147.8629 | -46.7411 | 2790 | 3131 | 2.8 | 0.60 | 397 | 2.687 | 10.44 | 10.31 | 10.85 | 10.92 | 10.98 | -22.01 | -22.14 | 33.01 | 39.9 | 33.08 | 41.3 | |
| 28380 PGC028380 | 249.3412 | 30.9492 | 118.1888 | -47.2135 | 2526 | 2895 | 5.7 | 0.62 | 178 | 2.347 | / | / | 14.17 | 14.27 | / | / | -18.81 | / | / | / | 33.11 | 42.0 |
| 28416 AGC026676 | 264.9242 | 16.2426 | 148.2734 | -46.5286 | 2928 | 3270 | 5.6 | 0.34 | 249 | 2.414 | 12.09 | 11.91 | 12.98 | 13.04 | 12.82 | -19.53 | -19.47 | 32.36 | 29.6 | 32.52 | 32.0 | |
| 28485 UGC05303 | 217.6683 | 47.5708 | 81.9789 | -35.4319 | 1411 | 1738 | 5.4 | 0.64 | 265 | 2.530 | 10.57 | 10.67 | 11.27 | 11.35 | 11.37 | -20.59 | -20.61 | 31.96 | 24.7 | 31.96 | 24.7 | |
| 28492 NGC03045 | 254.6520 | 27.0856 | 127.0972 | -47.4220 | 2256 | 2617 | 2.9 | 0.45 | 237 | 2.415 | 12.39 | 12.39 | 12.79 | 12.87 | 13.00 | -19.54 | -19.48 | 32.54 | 32.3 | 32.36 | 29.7 | |
| 28517 UGC05311 | 236.1971 | 40.3741 | 99.1389 | -42.6038 | 1289 | 1642 | 5.6 | 0.20 | 317 | 2.501 | 10.99 | 10.65 | 11.26 | 11.29 | 11.33 | -20.32 | -20.32 | 31.65 | 21.4 | 31.62 | 21.1 | |
| 28590 NGC03049 | 227.5655 | 44.7228 | 90.1786 | -38.9569 | 1495 | 1840 | 2.5 | 0.47 | 199 | 2.343 | 11.68 | 11.74 | 12.38 | 12.41 | 12.44 | -18.88 | -18.78 | 31.32 | 18.3 | 31.18 | 17.2 | |
| 28607 IC0002523 | 265.5477 | 16.5744 | 148.2595 | -45.8448 | 2615 | 2953 | 4.0 | 0.51 | 179 | 2.311 | 12.05 | 12.07 | 12.47 | 12.56 | 12.68 | -18.59 | -18.46 | 31.27 | 17.9 | 31.02 | 16.0 | |
| 28617 NGC03055 | 233.5392 | 42.2223 | 96.0653 | -41.1326 | 1821 | 2177 | 5.3 | 0.53 | 255 | 2.469 | 11.34 | 11.36 | 11.87 | 11.90 | 11.99 | -20.02 | -20.00 | 32.02 | 25.4 | 31.90 | 24.0 | |
| 28636 NGC03027 | 138.7809 | 39.0524 | 38.9841 | 2.8860 | 1059 | 1126 | 6.4 | 0.37 | 206 | 2.336 | 11.44 | 11.45 | 12.48 | 12.55 | 12.35 | -18.82 | -18.71 | 31.18 | 17.2 | 31.27 | 17.9 | |
| 28741 UGC05347 | 233.6153 | 42.7746 | 96.0350 | -40.5780 | 2154 | 2515 | 6.5 | 0.20 | 207 | 2.316 | 13.76 | 13.58 | 14.40 | 14.46 | 14.37 | -18.64 | -18.51 | 33.03 | 40.4 | 33.00 | 39.8 | |
| 28778 AGC026733 | 262.7822 | 20.5211 | 141.4499 | -46.0594 | 2662 | 3014 | 5.0 | 0.20 | 286 | 2.456 | 12.65 | 12.25 | 12.93 | 12.97 | 12.97 | -19.91 | -19.88 | 32.90 | 38.0 | 32.87 | 37.6 | |
| 28795 UGC05349 | 186.1655 | 52.3051 | 64.3044 | -21.7240 | 1376 | 1633 | 7.8 | 0.27 | 182 | 2.268 | / | / | 14.05 | 14.12 | / | / | -18.04 | / | / | / | 32.17 | 27.1 |
| 28801 E499-025 | 260.4019 | 23.1918 | 136.4541 | -46.2684 | 2403 | 2758 | 5.0 | 0.20 | 200 | 2.301 | / | / | 13.64 | 13.70 | / | / | -18.37 | / | / | / | 32.07 | 26.0 |
| 28821 UGC05358 | 225.5657 | 46.5872 | 88.4460 | -37.0684 | 2914 | 3276 | 3.1 | 0.32 | 194 | 2.302 | / | / | 14.63 | 14.72 | / | / | -18.38 | / | / | / | 33.13 | 42.2 |
| 28830 UGC05354 | 169.5310 | 50.7355 | 56.4062 | -14.4549 | 1169 | 1376 | 4.3 | 0.60 | 161 | 2.295 | 12.80 | 12.99 | 14.31 | 14.40 | 14.04 | -18.44 | -18.31 | 32.49 | 31.5 | 32.73 | 35.1 | |
| 28840 AGC026748 | 264.2141 | 19.3758 | 143.8767 | -45.5480 | 2810 | 3161 | 5.0 | 0.22 | 264 | 2.423 | 12.15 | 11.85 | 12.37 | 12.42 | 12.50 | -19.61 | -19.56 | 32.12 | 26.5 | 31.99 | 25.0 | |
| 28909 AGC026767 | 263.9258 | 19.9758 | 142.9456 | -45.4596 | 2472 | 2819 | 5.0 | 0.20 | 469 | 2.671 | 10.93 | 10.31 | 10.89 | 10.90 | 10.96 | -21.87 | -21.98 | 32.85 | 37.1 | 32.90 | 38.1 | |
| 28939 UGC05376 | 235.5206 | 42.7874 | 97.8452 | -40.3364 | 2050 | 2412 | 7.8 | 0.32 | 363 | 2.575 | / | / | 11.94 | 12.00 | / | / | -21.04 | / | / | / | 33.06 | 41.0 |
| 29022 ES567-006 | 257.5796 | 27.1628 | 129.7438 | -45.5576 | 3725 | 4114 | 6.5 | 0.20 | 227 | 2.356 | 14.64 | 14.43 | 15.46 | 15.53 | 15.33 | -19.00 | -18.90 | 34.39 | 75.7 | 34.53 | 80.6 | |
| 29036 UGC005393 | 193.0179 | 53.0624 | 68.2288 | -23.8993 | 1458 | 1735 | 8.0 | 0.52 | 145 | 2.221 | / | / | 14.46 | 14.55 | / | / | -17.58 | / | / | / | 32.15 | 26.9 |
| 29086 PGC029086 | 245.6432 | 37.4316 | 109.9182 | -43.0428 | 662 | 1019 | 7.2 | 0.20 | 117 | 2.068 | / | / | 14.73 | 14.77 | / | / | -16.09 | / | / | / | 30.86 | 14.9 |
| 29157 IC0002536 | 267.4413 | 17.1054 | 148.7839 | -43.9930 | 2732 | 3074 | 4.9 | 0.25 | 250 | 2.403 | 12.58 | 12.30 | 12.79 | 12.84 | 12.93 | -19.43 | -19.36 | 32.37 | 29.8 | 32.21 | 27.7 | |
| 29203 IC0002539 | 265.8710 | 19.2249 | 145.1947 | -44.2841 | 2833 | 3184 | 4.0 | 0.37 | 275 | 2.462 | 12.10 | 11.96 | 12.40 | 12.47 | 12.58 | -19.96 | -19.93 | 32.55 | 32.4 | 32.42 | 30.4 | |
| 29278 NGC003120 | 267.9365 | 17.1349 | 149.0454 | -43.5581 | 2791 | 3134 | 4.2 | 0.62 | 205 | 2.410 | 11.62 | 11.64 | 12.04 | 12.12 | 12.24 | -19.50 | -19.44 | 31.74 | 22.3 | 31.56 | 20.5 | |
| 29296 NGC003057 | 130.6924 | 34.1952 | 33.7061 | 9.0597 | 1524 | 1545 | 7.9 | 0.63 | 133 | 2.225 | / | / | 13.44 | 13.54 | / | / | -17.62 | / | / | / | 31.16 | 17.0 |
| 29427 UGC005451 | 170.0032 | 52.3109 | 57.9646 | -13.9205 | 635 | 845 | 9.9 | 0.41 | 114 | 2.088 | 12.49 | 12.72 | 13.54 | 13.63 | 13.53 | -16.56 | -16.28 | 30.09 | 10.4 | 29.92 | 9.6 | |
| 29466 PGC029466 | 224.6404 | 49.4175 | 87.8530 | -34.2117 | 2756 | 3116 | 6.2 | 0.20 | 156 | 2.193 | 15.30 | 15.29 | 16.45 | 16.53 | 16.26 | -17.52 | -17.31 | 33.82 | 58.1 | 33.91 | 60.6 | |
| 29472 UGC005459 | 160.8352 | 50.2756 | 53.5070 | -9.6872 | 1109 | 1290 | 5.2 | 0.20 | 261 | 2.417 | / | / | 12.12 | 12.12 | / | / | -19.50 | / | / | / | 31.61 | 21.0 |
| 29487 ES435-044 | 266.3669 | 20.0667 | 144.5144 | -43.4557 | 2200 | 2544 | 6.4 | 0.20 | 130 | 2.114 | / | / | 16.64 | 16.72 | / | / | -16.54 | / | / | / | 33.29 | 45.6 |
| 29530 NGC003137 | 265.2097 | 21.6742 | 141.8458 | -43.5336 | 1104 | 1441 | 5.9 | 0.45 | 244 | 2.427 | 10.73 | 10.69 | 11.42 | 11.48 | 11.44 | -19.65 | -19.60 | 31.09 | 16.5 | 31.08 | 16.4 | |
| 29641 ES435-050 | 266.4260 | 20.8360 | 143.6461 | -43.0143 | 2716 | 3070 | 5.4 | 0.20 | 182 | 2.260 | 14.55 | 14.40 | 15.25 | 15.32 | 15.22 | -18.13 | -17.97 | 33.37 | 47.2 | 33.33 | 46.3 | |
| 29691 NGC003157 | 267.3776 | 19.9847 | 145.2628 | -42.6750 | 2840 | 3193 | 5.0 | 0.25 | 302 | 2.486 | 11.95 | 11.60 | 12.16 | 12.21 | 12.27 | -20.18 | -20.17 | 32.46 | 31.0 | 32.39 | 30.1 | |

| PGC Name | l | b | sgl | sgb | v_{hel} | v_{mod} | t | b/a | w_{max} | $\log w_{max}^{\dagger}$ | I | I* | [3.6] | [3.6]* | $C_{[3.6]}$ | M_C | $M_{[3.6]}$ | μ_C | d_C | $\mu_{[3.6]}$ | $d_{[3.6]}$ | |
|-----------------|----------|---------|----------|----------|-----------|-----------|-----|------|-----------|--------------------------|-------|-------|-------|--------|-------------|--------|-------------|---------|-------|---------------|-------------|------|
| 29727 IC2556 | 269.5032 | 17.6367 | 149.3442 | -41.9963 | 2503 | 2842 | 6.9 | 0.52 | 214 | 2.390 | 12.72 | 12.67 | 13.53 | 13.60 | 13.49 | -19.31 | -19.24 | 32.82 | 36.6 | 32.86 | 37.4 | |
| 29743 ES436-001 | 265.0721 | 23.1348 | 140.0772 | -42.8360 | 2614 | 2973 | 4.5 | 0.23 | 346 | 2.542 | 12.03 | 11.64 | 12.05 | 12.09 | 12.23 | -20.69 | -20.72 | 32.94 | 38.7 | 32.83 | 36.9 | |
| 29835 UGC05522 | 233.8863 | 47.6186 | 95.4089 | -35.7552 | 1220 | 1575 | 6.4 | 0.50 | 209 | 2.374 | 13.03 | 13.11 | 14.02 | 14.10 | 13.96 | -19.16 | -19.08 | 33.15 | 42.6 | 33.22 | 44.0 | |
| 29892 AGC026974 | 266.1194 | 22.5773 | 141.4303 | -42.3364 | 1090 | 1430 | 1.9 | 0.31 | 324 | 2.523 | 9.98 | 9.72 | 10.15 | 10.19 | 10.32 | -20.52 | -20.54 | 30.84 | 14.7 | 30.73 | 14.0 | |
| 29898 IC0002559 | 269.4558 | 18.4367 | 148.3566 | -41.6791 | 2990 | 3340 | 3.1 | 0.39 | 256 | 2.435 | 12.46 | 12.32 | 12.82 | 12.89 | 12.97 | -19.71 | -19.67 | 32.70 | 34.6 | 32.58 | 32.8 | |
| 29993 IC0002560 | 269.4218 | 19.0267 | 147.6352 | -41.4387 | 2924 | 3275 | 3.4 | 0.46 | 376 | 2.617 | 10.63 | 10.45 | 11.07 | 11.14 | 11.15 | -21.38 | -21.45 | 32.54 | 32.2 | 32.61 | 33.2 | |
| 30022 ES213-011 | 278.5252 | 6.5295 | 166.7910 | -37.3613 | 2745 | 3038 | 5.0 | 0.51 | 360 | 2.613 | 10.58 | 10.28 | 10.81 | 10.85 | 10.92 | -21.34 | -21.41 | 32.27 | 28.4 | 32.27 | 28.5 | |
| 30041 AGC500062 | 246.3249 | 41.8189 | 108.1073 | -38.8410 | 1308 | 1675 | 7.8 | 0.54 | 168 | 2.291 | / | / | 13.55 | 13.63 | / | / | -18.27 | / | / | / | 31.91 | 24.1 |
| 30059 UGC05554 | 213.2224 | 54.7039 | 80.8097 | -27.8414 | 1248 | 1570 | 1.2 | 0.56 | 263 | 2.491 | 11.09 | 11.16 | 11.68 | 11.76 | 11.82 | -20.23 | -20.22 | 32.06 | 25.8 | 31.99 | 25.0 | |
| 30064 NGC03155 | 135.3688 | 38.8398 | 38.5518 | 5.5130 | 2945 | 3022 | 3.5 | 0.54 | 248 | 2.460 | 12.72 | 12.78 | 13.35 | 13.44 | 13.47 | -19.95 | -19.92 | 33.45 | 49.1 | 33.41 | 48.0 | |
| 30182 UGC05574 | 212.1751 | 55.3780 | 80.3767 | -27.0249 | 1468 | 1791 | 5.9 | 0.28 | 128 | 2.115 | 13.88 | 14.01 | 15.00 | 15.09 | 14.90 | -16.81 | -16.55 | 31.72 | 22.0 | 31.65 | 21.4 | |
| 30197 NGC03198 | 171.2186 | 54.8288 | 60.5646 | -13.2329 | 660 | 881 | 5.2 | 0.34 | 296 | 2.490 | 9.57 | 9.47 | 10.33 | 10.33 | 10.26 | -20.22 | -20.21 | 30.48 | 12.5 | 30.54 | 12.9 | |
| 30308 AGC027067 | 270.7960 | 19.0907 | 148.3370 | -40.2516 | 2896 | 3246 | 3.4 | 0.70 | 415 | 2.754 | 9.73 | 9.70 | 9.85 | 9.92 | 10.18 | -22.62 | -22.79 | 32.82 | 36.6 | 32.73 | 35.2 | |
| 30322 UGC05589 | 154.0945 | 50.1613 | 51.9360 | -5.6647 | 1162 | 1325 | 6.0 | 0.59 | 164 | 2.300 | 11.76 | 11.94 | 12.79 | 12.88 | 12.77 | -18.49 | -18.35 | 31.26 | 17.8 | 31.23 | 17.7 | |
| 30492 E436-014 | 267.9710 | 23.7697 | 141.3029 | -40.2604 | 3887 | 4271 | 4.4 | 0.51 | 176 | 2.302 | / | / | 14.78 | 14.88 | / | / | -18.38 | / | / | / | 33.29 | 45.5 |
| 30534 E317-023 | 274.3014 | 15.2733 | 154.6194 | -38.7375 | 2751 | 3083 | 1.0 | 0.44 | 363 | 2.597 | 11.63 | 11.43 | 11.65 | 11.70 | 11.93 | -21.19 | -21.25 | 33.14 | 42.6 | 32.98 | 39.5 | |
| 30569 UGC05631 | 152.1236 | 49.8645 | 51.2959 | -4.5310 | 2121 | 2287 | 5.8 | 0.54 | 254 | 2.471 | 12.41 | 12.50 | 13.08 | 13.17 | 13.20 | -20.04 | -20.03 | 33.27 | 45.0 | 33.23 | 44.4 | |
| 30604 UGC05642 | 229.9612 | 52.5435 | 91.8400 | -31.0951 | 2359 | 2722 | 4.1 | 0.20 | 242 | 2.384 | 13.36 | 13.14 | 13.80 | 13.86 | 13.86 | -19.25 | -19.17 | 33.13 | 42.4 | 33.07 | 41.0 | |
| 30670 IC000610 | 216.7851 | 56.2218 | 83.4268 | -26.8527 | 1165 | 1494 | 3.8 | 0.20 | 303 | 2.481 | / | / | 12.15 | 12.19 | / | / | -20.13 | / | / | / | 32.33 | 29.2 |
| 30688 ES568-012 | 263.7881 | 29.7971 | 132.0692 | -39.7448 | 5699 | 6148 | 5.5 | 0.20 | 300 | 2.477 | 14.39 | 13.98 | 14.11 | 14.17 | 14.45 | -20.10 | -20.09 | 34.62 | 84.0 | 34.34 | 73.9 | |
| 30714 NGC3245A | 201.6435 | 58.1720 | 75.6799 | -22.2519 | 1326 | 1628 | 3.4 | 0.20 | 179 | 2.253 | 13.32 | 13.26 | 14.11 | 14.17 | 14.07 | -18.06 | -17.90 | 32.14 | 26.8 | 32.08 | 26.0 | |
| 30716 E375-026 | 272.9316 | 18.0953 | 150.6288 | -38.8496 | 3128 | 3477 | 4.3 | 0.20 | 332 | 2.521 | 12.35 | 11.91 | 12.31 | 12.35 | 12.50 | -20.50 | -20.52 | 33.02 | 40.1 | 32.89 | 37.8 | |
| 30774 NGC3250C | 275.1965 | 15.0046 | 155.3359 | -38.0280 | 2593 | 2921 | 1.9 | 0.37 | 348 | 2.565 | / | / | 12.09 | 12.14 | / | / | -20.94 | / | / | / | 33.12 | 42.0 |
| 30867 NGC03256B | 277.8233 | 11.4154 | 160.6510 | -36.7648 | 2714 | 3028 | 3.9 | 0.31 | 326 | 2.526 | 11.79 | 11.45 | 11.85 | 11.89 | 12.04 | -20.55 | -20.57 | 32.60 | 33.1 | 32.47 | 31.3 | |
| 30895 NGC03254 | 200.1086 | 58.7545 | 75.2197 | -21.3568 | 1359 | 1659 | 4.0 | 0.32 | 393 | 2.610 | 10.69 | 10.46 | 11.42 | 11.47 | 11.32 | -21.31 | -21.38 | 32.64 | 33.7 | 32.87 | 37.6 | |
| 30915 AGC027187 | 265.9322 | 28.3868 | 135.0079 | -39.1532 | 3805 | 4199 | 6.7 | 0.52 | 245 | 2.449 | 13.01 | 13.00 | 13.89 | 13.97 | 13.84 | -19.84 | -19.81 | 33.72 | 55.5 | 33.85 | 58.8 | |
| 31011 UGC005689 | 134.9406 | 39.7920 | 39.4866 | 5.9018 | 2827 | 2906 | 6.4 | 0.32 | 254 | 2.419 | / | / | 13.72 | 13.79 | / | / | -19.52 | / | / | / | 33.35 | 46.8 |
| 31037 UGC05708 | 240.7977 | 49.6307 | 100.3128 | -32.8408 | 1177 | 1541 | 6.6 | 0.20 | 167 | 2.223 | 12.92 | 12.87 | 14.22 | 14.29 | 13.93 | -17.79 | -17.60 | 31.72 | 22.1 | 31.90 | 24.0 | |
| 31053 NGC3258C | 273.1328 | 19.4229 | 149.1903 | -38.1210 | 2561 | 2905 | 1.2 | 0.66 | 194 | 2.403 | / | / | 13.12 | 13.20 | / | / | -19.36 | / | / | / | 32.58 | 32.9 |
| 31059 UGC05711 | 209.0458 | 58.5747 | 79.7070 | -23.4536 | 6258 | 6682 | 3.1 | 0.30 | 512 | 2.721 | 11.81 | 11.45 | 12.07 | 12.14 | 12.16 | -22.32 | -22.47 | 34.54 | 81.0 | 34.72 | 87.8 | |
| 31075 UGC005713 | 206.9519 | 58.8192 | 78.6978 | -22.8354 | 6294 | 6715 | 4.0 | 0.26 | 477 | 2.685 | 12.61 | 12.21 | 12.80 | 12.86 | 12.90 | -22.00 | -22.12 | 34.99 | 99.4 | 35.13 | 106.1 | |
| 31094 NGC3258D | 273.3369 | 19.3215 | 149.4105 | -37.9894 | 2480 | 2822 | 3.1 | 0.43 | 219 | 2.376 | / | / | 12.28 | 12.35 | / | / | -19.10 | / | / | / | 31.45 | 19.5 |
| 31125 NGC003264 | 153.9364 | 51.8400 | 53.5196 | -5.0797 | 935 | 1103 | 7.9 | 0.30 | 132 | 2.132 | / | / | 13.76 | 13.85 | / | / | -16.72 | / | / | / | 30.57 | 13.0 |
| 31126 IC0002589 | 266.4586 | 28.8109 | 134.9283 | -38.5289 | 3703 | 4096 | 3.2 | 0.48 | 212 | 2.374 | / | / | 12.88 | 12.97 | / | / | -19.08 | / | / | / | 32.06 | 25.8 |
| 31145 UGC05717 | 143.2583 | 46.2282 | 46.5150 | 0.5129 | 1675 | 1796 | 3.7 | 0.60 | 233 | 2.454 | 11.91 | 12.04 | 12.51 | 12.60 | 12.69 | -19.89 | -19.86 | 32.59 | 33.0 | 32.48 | 31.3 | |
| 31154 ES436-034 | 269.4599 | 25.1006 | 140.7687 | -38.4062 | 3611 | 3992 | 3.1 | 0.22 | 533 | 2.729 | 11.98 | 11.38 | 11.72 | 11.74 | 11.93 | -22.39 | -22.55 | 34.39 | 75.4 | 34.38 | 75.2 | |

| PGC Name | l | b | sgl | sgb | v_{hel} | v_{mod} | t | b/a | w_{max} | $\log w_{max}^i$ | I | I* | [3.6] | [3.6]* | C _[3.6] | M _C | M _[3.6] | μ_C | d _C | $\mu_{[3.6]}$ | d _[3.6] |
|-----------------|----------|----------|----------|----------|-----------|-----------|-----|------|-----------|------------------|-------|-------|-------|--------|--------------------|----------------|--------------------|---------|----------------|---------------|--------------------|
| 31186 ES501-011 | 266.9654 | 28.5063 | 135.5784 | -38.3522 | 3769 | 4163 | 6.0 | 0.20 | 293 | 2.467 | 13.55 | 13.19 | 13.69 | 13.74 | 13.83 | -20.01 | -19.99 | 33.88 | 59.7 | 33.78 | 57.1 |
| 31217 NGC03285 | 268.9156 | 26.1640 | 139.2887 | -38.2518 | 3394 | 3774 | 1.2 | 0.50 | 545 | 2.791 | 10.71 | 10.52 | 11.10 | 11.17 | 11.20 | -22.96 | -23.15 | 34.22 | 69.7 | 34.41 | 76.3 |
| 31238 E436-038 | 269.2104 | 25.8902 | 139.7642 | -38.1769 | 2748 | 3116 | 4.2 | 0.58 | 190 | 2.359 | / | / | 15.04 | 15.13 | / | -18.93 | / | / | / | 34.14 | 67.3 |
| 31242 E436-039 | 270.6575 | 23.9547 | 142.7328 | -38.0600 | 3493 | 3808 | 3.9 | 0.20 | 412 | 2.615 | 12.79 | 12.27 | 12.48 | 12.51 | 12.76 | -21.36 | -21.43 | 34.17 | 68.2 | 34.02 | 63.6 |
| 31265 IC0002596 | 293.3305 | -12.9807 | 191.4074 | -24.7885 | 3380 | 3561 | 2.2 | 0.62 | 121 | 2.179 | / | / | 12.18 | 12.26 | / | -17.18 | / | / | / | 29.44 | 7.7 |
| 31273 NGC3281D | 273.2013 | 20.4334 | 148.0698 | -37.6280 | 2643 | 2992 | 6.5 | 0.22 | 255 | 2.408 | 12.55 | 12.26 | 12.90 | 12.95 | 12.96 | -19.48 | -19.42 | 32.45 | 30.9 | 32.38 | 29.9 |
| 31276 E436-040 | 271.9263 | 22.3077 | 145.2771 | -37.8387 | 4435 | 4827 | 2.1 | 0.31 | 281 | 2.462 | / | / | 13.19 | 13.25 | / | -19.94 | / | / | / | 33.23 | 44.2 |
| 31293 NGC3285B | 269.2476 | 26.1255 | 139.5349 | -38.0220 | 3027 | 3400 | 3.2 | 0.63 | 241 | 2.483 | / | / | 12.82 | 12.90 | / | -20.14 | / | / | / | 33.08 | 41.3 |
| 31302 UGC05741 | 232.6218 | 54.1729 | 93.5239 | -29.3465 | 1392 | 1748 | 6.4 | 0.20 | 347 | 2.540 | 11.69 | 11.29 | 11.75 | 11.78 | 11.90 | -20.68 | -20.70 | 32.59 | 32.9 | 32.50 | 31.6 |
| 31307 UGC005740 | 161.1693 | 54.9767 | 57.9721 | -8.0500 | 656 | 853 | 8.8 | 0.59 | 127 | 2.188 | / | / | 14.69 | 14.78 | / | -17.26 | / | / | / | 32.05 | 25.7 |
| 31311 NGC03287 | 215.3858 | 58.5059 | 83.1558 | -24.4598 | 1305 | 1633 | 7.6 | 0.41 | 188 | 2.305 | 11.42 | 11.49 | 12.18 | 12.26 | 12.24 | -18.54 | -18.41 | 30.77 | 14.3 | 30.67 | 13.6 |
| 31355 E501-022 | 269.4271 | 26.1818 | 139.5848 | -37.8560 | 2900 | 3271 | 4.2 | 0.23 | 170 | 2.233 | / | / | 15.91 | 15.99 | / | -17.71 | / | / | / | 33.75 | 56.3 |
| 31360 E437-004 | 269.8131 | 25.6701 | 140.3674 | -37.8348 | 3298 | 3675 | 4.0 | 0.47 | 317 | 2.546 | 12.18 | 12.07 | 12.53 | 12.61 | 12.71 | -20.73 | -20.76 | 33.46 | 49.2 | 33.41 | 48.0 |
| 31428 UGC05753 | 184.6183 | 59.8424 | 69.2473 | -15.7521 | 1573 | 1844 | 5.1 | 0.47 | 386 | 2.631 | 10.23 | 10.17 | 10.78 | 10.80 | 10.84 | -21.51 | -21.59 | 32.36 | 29.6 | 32.40 | 30.3 |
| 31482 E501-037 | 268.1889 | 28.3739 | 136.5081 | -37.5537 | 3669 | 4060 | 2.7 | 0.72 | 127 | 2.254 | / | / | 14.98 | 15.09 | / | -17.90 | / | / | / | 33.02 | 40.3 |
| 31487 E437-012 | 271.4937 | 23.9027 | 143.2692 | -37.4220 | 3566 | 3942 | 3.8 | 0.46 | 122 | 2.129 | / | / | 16.20 | 16.30 | / | -16.69 | / | / | / | 33.02 | 40.2 |
| 31493 ES437-014 | 272.5083 | 22.4567 | 145.4278 | -37.2933 | 2859 | 3218 | 2.2 | 0.39 | 364 | 2.588 | 11.44 | 11.24 | 11.62 | 11.68 | 11.83 | -21.11 | -21.17 | 32.96 | 39.0 | 32.88 | 37.6 |
| 31494 E501-041 | 269.3441 | 26.9046 | 138.7660 | -37.5271 | 3551 | 3936 | 3.8 | 0.60 | 188 | 2.362 | / | / | 14.76 | 14.86 | / | -18.96 | / | / | / | 33.89 | 59.8 |
| 31528 UGC05774 | 230.9791 | 55.4311 | 92.3222 | -28.1762 | 2890 | 3263 | 7.8 | 0.49 | 259 | 2.463 | 12.48 | 12.52 | 12.65 | 12.73 | 13.00 | -19.98 | -19.95 | 32.99 | 39.7 | 32.71 | 34.8 |
| 31533 NGC03318 | 277.6690 | 14.5693 | 156.8701 | -35.9297 | 2773 | 3100 | 3.6 | 0.54 | 330 | 2.585 | 11.02 | 10.95 | 11.37 | 11.44 | 11.56 | -21.08 | -21.14 | 32.65 | 34.0 | 32.59 | 33.0 |
| 31560 UGC005765 | 138.9931 | 43.8966 | 43.8268 | 3.2125 | 1826 | 1925 | 4.0 | 0.23 | 200 | 2.304 | / | / | 14.47 | 14.54 | / | -18.39 | / | / | / | 32.96 | 39.1 |
| 31590 ES437-018 | 271.7240 | 23.9883 | 143.3049 | -37.1966 | 3369 | 3742 | 3.5 | 0.29 | 300 | 2.488 | 13.34 | 13.11 | 13.54 | 13.60 | 13.72 | -20.20 | -20.19 | 33.97 | 62.1 | 33.86 | 59.1 |
| 31593 E437-019 | 270.6922 | 25.4799 | 141.0939 | -37.2576 | 4382 | 4782 | 1.7 | 0.68 | 288 | 2.584 | 12.27 | 12.34 | 12.77 | 12.87 | 12.97 | -21.07 | -21.13 | 34.09 | 65.8 | 34.07 | 65.2 |
| 31600 ES019-003 | 297.7498 | -19.5998 | 198.5975 | -20.5688 | 2004 | 2117 | 5.2 | 0.56 | 200 | 2.376 | 12.23 | 12.24 | 12.77 | 12.84 | 12.90 | -19.18 | -19.10 | 32.09 | 26.1 | 31.94 | 24.5 |
| 31626 AGC027386 | 270.7527 | 25.5408 | 141.0637 | -37.1793 | 4387 | 4787 | 4.0 | 0.26 | 284 | 2.459 | 13.53 | 13.27 | 14.12 | 14.18 | 14.09 | -19.94 | -19.91 | 34.08 | 65.3 | 34.18 | 68.4 |
| 31638 AGC027392 | 270.1115 | 26.5358 | 139.6214 | -37.1485 | 4413 | 4816 | 6.5 | 0.57 | 148 | 2.248 | 12.60 | 12.72 | 13.18 | 13.29 | 13.37 | -18.02 | -17.85 | 31.39 | 18.9 | 31.14 | 16.9 |
| 31642 E437-025 | 270.6385 | 25.8514 | 140.6635 | -37.1067 | 3463 | 3843 | 3.4 | 0.37 | 245 | 2.412 | 12.76 | 12.66 | 13.15 | 13.22 | 13.31 | -19.51 | -19.45 | 32.83 | 36.9 | 32.70 | 34.6 |
| 31653 AGC500163 | 258.8818 | 39.6227 | 119.6890 | -35.6251 | 2487 | 2875 | 5.1 | 0.48 | 265 | 2.472 | 12.12 | 12.10 | 12.91 | 12.99 | 12.90 | -20.06 | -20.04 | 32.98 | 39.4 | 33.06 | 40.9 |
| 31671 UGC05789 | 175.9803 | 59.3417 | 65.8825 | -12.8012 | 739 | 984 | 6.0 | 0.49 | 195 | 2.342 | 10.76 | 10.87 | 11.74 | 11.82 | 11.70 | -18.87 | -18.76 | 30.57 | 13.0 | 30.59 | 13.1 |
| 31677 ES437-030 | 271.7820 | 24.4610 | 142.8216 | -36.9184 | 3762 | 4144 | 4.2 | 0.22 | 428 | 2.634 | 11.63 | 11.13 | 11.74 | 11.77 | 11.81 | -21.53 | -21.62 | 33.37 | 47.2 | 33.43 | 48.6 |
| 31683 AGC027404 | 269.7188 | 27.3787 | 138.4952 | -36.9890 | 3080 | 3457 | 4.0 | 0.34 | 323 | 2.528 | 12.50 | 12.29 | 13.02 | 13.08 | 13.04 | -20.56 | -20.58 | 33.64 | 53.5 | 33.72 | 55.4 |
| 31690 E437-031 | 271.3867 | 25.0775 | 141.9292 | -36.9224 | 3881 | 4267 | 7.2 | 0.62 | 203 | 2.403 | 13.40 | 13.50 | 14.32 | 14.43 | 14.32 | -19.43 | -19.36 | 33.79 | 57.3 | 33.85 | 58.9 |
| 31697 UGC05791 | 164.9637 | 56.9874 | 60.7228 | -9.1210 | 852 | 1066 | 3.0 | 0.34 | 143 | 2.173 | 13.53 | 13.67 | 15.09 | 15.18 | 14.77 | -17.34 | -17.12 | 32.11 | 26.4 | 32.31 | 28.9 |
| 31708 UGC05794 | 165.8441 | 57.2593 | 61.1895 | -9.4212 | 2315 | 2545 | 5.8 | 0.44 | 277 | 2.481 | 11.84 | 11.83 | 12.41 | 12.49 | 12.52 | -20.14 | -20.12 | 32.67 | 34.2 | 32.63 | 33.6 |
| 31720 UGC05798 | 164.9406 | 57.0442 | 60.7683 | -9.0841 | 1529 | 1748 | 6.4 | 0.34 | 169 | 2.247 | 13.46 | 13.54 | 14.73 | 14.82 | 14.53 | -18.00 | -17.83 | 32.54 | 32.3 | 32.67 | 34.2 |
| 31732 E437-034 | 271.4134 | 25.2959 | 141.7087 | -36.7913 | 3767 | 4151 | 3.8 | 0.38 | 170 | 2.255 | 14.50 | 14.54 | 16.07 | 16.17 | 15.70 | -18.08 | -17.92 | 33.82 | 58.0 | 34.16 | 68.0 |

| PGC Name | l | b | sgl | sgb | v_{hel} | v_{mod} | t | b/a | w_{max} | $\log w_{max}^i$ | I | I* | [3.6] | [3.6]* | $C_{[3.6]}$ | M_C | $M_{[3.6]}$ | μ_C | dC | $\mu_{[3.6]}$ | $d_{[3.6]}$ |
|-----------------|----------|---------|----------|----------|-----------|-----------|-----|------|-----------|------------------|-------|-------|-------|--------|-------------|--------|-------------|---------|-------|---------------|-------------|
| 31738 E437-035 | 271.9301 | 24.5815 | 142.7734 | -36.7417 | 3392 | 3767 | 3.9 | 0.37 | 236 | 2.396 | 12.76 | 12.67 | 13.20 | 13.28 | 13.34 | -19.36 | -19.29 | 32.71 | 34.9 | 32.59 | 32.9 |
| 31761 NGC3347A | 275.4308 | 19.3642 | 150.3814 | -36.1713 | 2785 | 3131 | 5.6 | 0.28 | 322 | 2.516 | 11.62 | 11.32 | 11.95 | 12.00 | 12.02 | -20.46 | -20.47 | 32.49 | 31.4 | 32.48 | 31.3 |
| 31797 NGC03347C | 275.4655 | 19.5267 | 150.2134 | -36.0760 | 2656 | 3000 | 6.9 | 0.69 | 113 | 2.185 | / | / | 14.50 | 14.60 | / | / | -17.23 | / | / | 31.83 | 23.3 |
| 31805 AGC027441 | 270.2220 | 27.3772 | 138.7994 | -36.6144 | 4743 | 5157 | 5.0 | 0.50 | 322 | 2.562 | 11.76 | 11.69 | 12.27 | 12.36 | 12.39 | -20.87 | -20.92 | 33.29 | 45.5 | 33.32 | 46.1 |
| 31809 E437-039 | 271.2232 | 25.9825 | 140.8632 | -36.5887 | 3744 | 4130 | 2.9 | 0.56 | 152 | 2.255 | / | / | 14.94 | 15.04 | / | / | -17.91 | / | / | 32.99 | 39.6 |
| 31829 E501-078 | 269.7246 | 28.1857 | 137.6568 | -36.5417 | 4440 | 4848 | 3.0 | 0.21 | 253 | 2.404 | / | / | 14.04 | 14.10 | / | -19.37 | / | / | 33.53 | 50.7 | |
| 31875 NGC03347B | 276.0162 | 19.0813 | 150.9734 | -35.7764 | 3187 | 3538 | 7.2 | 0.24 | 327 | 2.519 | 11.90 | 11.54 | 12.55 | 12.59 | 12.42 | -20.48 | -20.49 | 32.92 | 38.3 | 33.12 | 42.0 |
| 31883 NGC03338 | 230.3314 | 57.0195 | 91.8026 | -26.6142 | 1298 | 1649 | 5.1 | 0.52 | 331 | 2.578 | 10.10 | 10.09 | 10.75 | 10.77 | 10.79 | -21.02 | -21.08 | 31.82 | 23.1 | 31.86 | 23.5 |
| 31919 ES501-080 | 268.6224 | 30.2208 | 134.8984 | -36.1768 | 1043 | 1400 | 4.9 | 0.25 | 132 | 2.126 | 12.70 | 12.76 | 13.67 | 13.75 | 13.61 | -16.91 | -16.66 | 30.52 | 12.7 | 30.41 | 12.1 |
| 31951 ES501-082 | 270.1841 | 28.3456 | 137.7675 | -36.1158 | 4520 | 4930 | 4.0 | 0.43 | 383 | 2.619 | 12.40 | 12.23 | 12.75 | 12.83 | 12.89 | -21.39 | -21.47 | 34.34 | 73.8 | 34.39 | 75.5 |
| 31987 AGC027491 | 269.1495 | 30.0021 | 135.4457 | -35.9320 | 3728 | 4124 | 4.2 | 0.46 | 335 | 2.567 | 12.17 | 12.06 | 12.74 | 12.82 | 12.80 | -20.92 | -20.97 | 33.76 | 56.6 | 33.85 | 59.0 |
| 31995 E318-004 | 277.0489 | 18.1126 | 152.5331 | -35.2431 | 2935 | 3278 | 5.1 | 0.21 | 382 | 2.583 | 11.47 | 11.00 | 11.69 | 11.72 | 11.72 | -21.07 | -21.12 | 32.80 | 36.3 | 32.87 | 37.5 |
| 31996 UGC05844 | 203.3727 | 61.8234 | 78.2546 | -19.3731 | 1465 | 1774 | 6.6 | 0.22 | 129 | 2.112 | / | / | 15.59 | 15.68 | / | / | -16.52 | / | / | 32.21 | 27.7 |
| 32039 E437-056 | 273.9027 | 23.4053 | 145.1189 | -35.7162 | 2929 | 3291 | 3.9 | 0.64 | 239 | 2.485 | 12.17 | 12.22 | 12.84 | 12.92 | 12.93 | -20.17 | -20.16 | 33.13 | 42.2 | 33.12 | 42.1 |
| 32044 AGC500190 | 259.9342 | 40.8317 | 119.4917 | -34.1825 | 1915 | 2296 | 5.0 | 0.35 | 249 | 2.416 | 11.90 | 11.84 | 12.56 | 12.63 | 12.59 | -19.55 | -19.49 | 32.14 | 26.8 | 32.13 | 26.6 |
| 32059 NGC003329 | 131.6928 | 38.0794 | 37.6557 | 8.3539 | 1890 | 1939 | 2.9 | 0.62 | 322 | 2.604 | 11.08 | 11.16 | 11.81 | 11.90 | 11.89 | -21.26 | -21.33 | 33.17 | 43.1 | 33.27 | 45.0 |
| 32153 NGC03365 | 247.7518 | 50.7552 | 104.7812 | -30.2763 | 988 | 1357 | 5.9 | 0.20 | 217 | 2.336 | 11.76 | 11.58 | 12.55 | 12.60 | 12.44 | -18.82 | -18.71 | 31.26 | 17.9 | 31.31 | 18.3 |
| 32183 NGC03359 | 143.5967 | 48.5922 | 48.8864 | 0.6452 | 1014 | 1142 | 5.2 | 0.72 | 237 | 2.527 | 10.08 | 10.27 | 10.86 | 10.96 | 10.97 | -20.55 | -20.57 | 31.53 | 20.2 | 31.53 | 20.2 |
| 32192 UGC05882 | 234.4355 | 57.0102 | 94.2884 | -26.4066 | 892 | 1245 | 2.2 | 0.64 | 328 | 2.621 | 8.12 | 8.21 | 8.77 | 8.80 | 8.87 | -21.42 | -21.42 | 30.28 | 11.4 | 30.30 | 11.5 |
| 32207 UGC05887 | 225.3509 | 59.6722 | 88.8842 | -23.9883 | 1283 | 1626 | 5.1 | 0.55 | 264 | 2.492 | 11.15 | 11.21 | 11.70 | 11.73 | 11.83 | -20.24 | -20.23 | 32.08 | 26.0 | 31.97 | 24.8 |
| 32251 UGC05897 | 235.8052 | 56.7996 | 95.1495 | -26.5029 | 2716 | 3092 | 5.2 | 0.32 | 283 | 2.466 | 12.09 | 11.96 | 12.83 | 12.90 | 12.78 | -20.00 | -19.98 | 32.80 | 36.3 | 32.90 | 38.1 |
| 32287 UGC05906 | 202.5714 | 62.7982 | 78.3470 | -18.3333 | 1603 | 1913 | 1.0 | 0.56 | 111 | 2.118 | 11.68 | 11.91 | 12.33 | 12.43 | 12.53 | -16.84 | -16.58 | 29.37 | 7.5 | 29.01 | 6.3 |
| 32306 UGC05914 | 233.7198 | 57.7405 | 93.7573 | -25.7323 | 1306 | 1661 | 5.3 | 0.44 | 247 | 2.430 | 11.12 | 11.13 | 11.77 | 11.84 | 11.85 | -19.67 | -19.63 | 31.52 | 20.1 | 31.47 | 19.7 |
| 32532 UGC05958 | 204.3580 | 63.4053 | 79.3887 | -18.1263 | 1182 | 1491 | 4.0 | 0.24 | 166 | 2.224 | 13.44 | 13.45 | 14.04 | 14.11 | 14.14 | -17.80 | -17.61 | 31.94 | 24.5 | 31.73 | 22.2 |
| 32550 AGC027566 | 268.0294 | 34.7199 | 130.1552 | -33.8512 | 2054 | 2430 | 6.4 | 0.20 | 253 | 2.403 | 12.16 | 11.91 | 12.89 | 12.94 | 12.78 | -19.43 | -19.36 | 32.21 | 27.7 | 32.31 | 29.0 |
| 32565 ES376-023 | 277.0431 | 21.2993 | 148.9633 | -34.0070 | 4756 | 5149 | 4.9 | 0.21 | 337 | 2.528 | 13.62 | 13.18 | 13.59 | 13.64 | 13.77 | -20.57 | -20.59 | 34.40 | 76.0 | 34.31 | 72.9 |
| 32614 UGC05982 | 192.9020 | 63.6382 | 74.8923 | -15.3803 | 1585 | 1878 | 5.1 | 0.50 | 337 | 2.580 | 10.68 | 10.67 | 11.23 | 11.31 | 11.35 | -21.04 | -21.10 | 32.40 | 30.2 | 32.41 | 30.4 |
| 32625 ES437-067 | 275.7238 | 23.8293 | 145.5754 | -34.0359 | 3186 | 3552 | 2.0 | 0.52 | 121 | 2.142 | / | / | 12.08 | 12.18 | / | / | -16.82 | / | / | 29.00 | 6.3 |
| 32648 UGC05995 | 215.1816 | 62.8195 | 84.1004 | -20.2343 | 1276 | 1603 | 5.3 | 0.36 | 300 | 2.499 | 10.99 | 10.90 | 11.22 | 11.23 | 11.43 | -20.30 | -20.30 | 31.74 | 22.2 | 31.54 | 20.3 |
| 32666 AGC027580 | 275.9842 | 23.6679 | 145.8770 | -33.8932 | 3277 | 3644 | 2.1 | 0.38 | 503 | 2.727 | 10.72 | 10.40 | 11.10 | 11.15 | 11.13 | -22.37 | -22.52 | 33.54 | 51.0 | 33.73 | 55.7 |
| 32671 UGC06000 | 225.9867 | 61.0847 | 89.2757 | -22.5866 | 1133 | 1475 | 6.6 | 0.49 | 169 | 2.277 | 12.80 | 12.91 | 13.92 | 14.01 | 13.81 | -18.28 | -18.13 | 32.10 | 26.3 | 32.15 | 26.9 |
| 32714 UGC06009 | 149.5546 | 53.5012 | 54.4235 | -2.0795 | 1908 | 2081 | 3.0 | 0.35 | 222 | 2.366 | 12.99 | 12.99 | 13.94 | 14.02 | 13.86 | -19.09 | -19.00 | 32.97 | 39.3 | 33.05 | 40.8 |
| 32719 NGC03403 | 133.4429 | 40.9516 | 40.5967 | 7.0977 | 1261 | 1325 | 4.0 | 0.34 | 282 | 2.467 | 11.60 | 11.38 | 12.06 | 12.10 | 12.10 | -20.01 | -19.99 | 32.12 | 26.5 | 32.10 | 26.3 |
| 32754 UGC06023 | 205.8873 | 64.0213 | 80.2988 | -17.8286 | 1333 | 1646 | 6.6 | 0.47 | 227 | 2.400 | 11.99 | 12.05 | 12.80 | 12.88 | 12.82 | -19.40 | -19.33 | 32.23 | 27.9 | 32.22 | 27.8 |
| 32813 NGC003463 | 272.7617 | 29.8362 | 137.7192 | -33.4152 | 3948 | 4346 | 3.0 | 0.45 | 390 | 2.631 | 12.05 | 11.88 | 12.42 | 12.50 | 12.55 | -21.51 | -21.59 | 34.11 | 66.3 | 34.17 | 68.2 |
| 32869 AGC027604 | 276.1459 | 24.8730 | 144.6596 | -33.2261 | 3334 | 3705 | 6.0 | 0.21 | 359 | 2.556 | 12.72 | 12.21 | 12.88 | 12.91 | 12.92 | -20.82 | -20.86 | 33.78 | 57.0 | 33.83 | 58.2 |

| PGC Name | l | b | sgl | sgb | v_{hel} | v_{mod} | t | b/a | w_{max} | $\log w_{max}^*$ | I | I* | [3.6] | [3.6]* | $C_{[3.6]}$ | M_C | $M_{[3.6]}$ | μ_C | d_C | $\mu_{[3.6]}$ | $d_{[3.6]}$ |
|-----------------|----------|---------|----------|----------|-----------|-----------|-----|------|-----------|------------------|-------|-------|-------|--------|-------------|--------|-------------|---------|-------|---------------|-------------|
| 33163 UGC06083 | 229.2797 | 62.2933 | 90.9533 | -21.3709 | 946 | 1290 | 4.1 | 0.20 | 167 | 2.223 | 13.89 | 13.87 | 14.82 | 14.89 | 14.73 | -17.79 | -17.60 | 32.53 | 32.0 | 32.50 | 31.6 |
| 33188 UGC06080 | 143.7345 | 51.0985 | 51.3767 | 0.9441 | 2180 | 2331 | 6.5 | 0.20 | 169 | 2.228 | 13.99 | 13.98 | 15.07 | 15.15 | 14.92 | -17.83 | -17.65 | 32.77 | 35.7 | 32.83 | 36.8 |
| 33234 UGC06098 | 249.8872 | 54.7261 | 104.2600 | -26.1261 | 1126 | 1496 | 6.4 | 0.23 | 297 | 2.475 | 10.79 | 10.50 | 11.28 | 11.27 | 11.24 | -20.09 | -20.07 | 31.33 | 18.4 | 31.34 | 18.5 |
| 33242 UGC06096 | 147.6777 | 53.8409 | 54.5085 | -0.9201 | 2994 | 3179 | 5.2 | 0.60 | 232 | 2.452 | 12.13 | 12.26 | 12.94 | 13.04 | 13.01 | -19.87 | -19.84 | 32.89 | 37.9 | 32.90 | 38.0 |
| 33276 UGC06104 | 229.7863 | 62.5643 | 91.1930 | -21.0907 | 2946 | 3314 | 4.0 | 0.29 | 229 | 2.371 | 13.49 | 13.42 | 14.40 | 14.48 | 14.31 | -19.13 | -19.05 | 33.47 | 49.4 | 33.58 | 52.0 |
| 33343 UGC06116 | 227.2718 | 63.3743 | 89.9531 | -20.3057 | 1129 | 1471 | 5.9 | 0.20 | 291 | 2.464 | 11.51 | 11.21 | 11.67 | 11.71 | 11.82 | -19.98 | -19.96 | 31.81 | 23.0 | 31.67 | 21.5 |
| 33385 NGC003511 | 272.9003 | 33.4089 | 134.2440 | -31.3733 | 1105 | 1467 | 5.1 | 0.31 | 279 | 2.459 | 10.01 | 9.82 | 10.45 | 10.50 | 10.52 | -19.93 | -19.91 | 30.45 | 12.3 | 30.41 | 12.1 |
| 33408 UGC06126 | 202.3635 | 66.2108 | 79.8214 | -15.2250 | 706 | 1009 | 8.6 | 0.26 | 177 | 2.254 | 12.21 | 12.20 | 13.24 | 13.26 | 13.08 | -18.07 | -17.91 | 31.16 | 17.0 | 31.17 | 17.1 |
| 33474 ES377-004 | 280.6291 | 20.5574 | 151.3071 | -31.2013 | 3155 | 3506 | 5.9 | 0.20 | 165 | 2.217 | / | / | 15.51 | 15.58 | / | -17.55 | / | / | / | 33.16 | 42.9 |
| 33550 UGC06150 | 255.5318 | 52.8293 | 108.5325 | -26.2132 | 802 | 1174 | 4.0 | 0.58 | 441 | 2.725 | 7.73 | 7.68 | 8.19 | 8.20 | 8.30 | -22.35 | -22.50 | 30.66 | 13.5 | 30.70 | 13.8 |
| 33601 E377-010 | 280.9668 | 20.7036 | 151.2823 | -30.8537 | 2875 | 3221 | 3.1 | 0.31 | 394 | 2.609 | 11.24 | 10.85 | 11.59 | 11.63 | 11.60 | -21.30 | -21.38 | 32.92 | 38.3 | 33.04 | 40.5 |
| 33633 UGC06162 | 155.1956 | 58.8719 | 60.4544 | -3.6153 | 2207 | 2418 | 6.4 | 0.49 | 215 | 2.383 | 12.25 | 12.33 | 13.33 | 13.42 | 13.23 | -19.25 | -19.17 | 32.49 | 31.4 | 32.60 | 33.2 |
| 33635 UGC06167 | 246.9673 | 58.1859 | 101.1237 | -23.5823 | 1420 | 1788 | 5.2 | 0.21 | 190 | 2.280 | 12.36 | 12.27 | 13.15 | 13.22 | 13.10 | -18.31 | -18.16 | 31.41 | 19.1 | 31.38 | 18.9 |
| 33647 NGC03533 | 280.8657 | 21.1893 | 150.7157 | -30.7640 | 3122 | 3474 | 2.8 | 0.27 | 392 | 2.601 | 11.48 | 11.04 | 11.76 | 11.79 | 11.77 | -21.23 | -21.30 | 33.02 | 40.2 | 33.12 | 42.0 |
| 33705 ES265-007 | 284.9839 | 12.7032 | 161.4720 | -29.6783 | 1068 | 1359 | 6.1 | 0.29 | 232 | 2.376 | 10.15 | 9.90 | 10.63 | 10.67 | 10.65 | -19.19 | -19.10 | 29.83 | 9.2 | 29.77 | 9.0 |
| 33813 ES502-020 | 274.2361 | 34.2463 | 134.1436 | -29.9858 | 1380 | 1745 | 5.0 | 0.71 | 115 | 2.204 | / | / | 13.80 | 13.89 | / | -17.42 | / | / | / | 31.31 | 18.3 |
| 33866 NGC03547 | 242.5353 | 61.0332 | 97.8323 | -21.6099 | 1589 | 1952 | 3.1 | 0.49 | 185 | 2.317 | 12.05 | 12.15 | 12.77 | 12.86 | 12.87 | -18.64 | -18.52 | 31.51 | 20.0 | 31.38 | 18.9 |
| 33952 NGC003568 | 281.7033 | 21.2411 | 150.9898 | -30.0181 | 2442 | 2782 | 5.0 | 0.32 | 264 | 2.436 | 11.38 | 11.15 | 11.49 | 11.54 | 11.71 | -19.73 | -19.69 | 31.44 | 19.4 | 31.23 | 17.6 |
| 33962 ES377-021 | 281.0862 | 22.5891 | 149.2986 | -30.0517 | 2762 | 3112 | 3.1 | 0.40 | 272 | 2.463 | 12.29 | 12.15 | 12.86 | 12.92 | 12.90 | -19.97 | -19.94 | 32.88 | 37.7 | 32.89 | 37.9 |
| 33964 UGC06215 | 151.3384 | 57.8426 | 58.8811 | -1.9772 | 2851 | 3059 | 5.1 | 0.34 | 406 | 2.627 | 11.08 | 10.88 | 11.61 | 11.67 | 11.63 | -21.46 | -21.55 | 33.11 | 42.0 | 33.25 | 44.7 |
| 34030 UGC06225 | 148.3145 | 56.2518 | 56.9420 | -0.7622 | 699 | 871 | 6.0 | 0.35 | 300 | 2.498 | 9.03 | 8.93 | 9.38 | 9.44 | 9.55 | -20.29 | -20.29 | 29.84 | 9.3 | 29.72 | 8.8 |
| 34248 UGC06267 | 231.6630 | 65.5381 | 91.8685 | -18.0722 | 1297 | 1642 | 5.3 | 0.23 | 188 | 2.278 | 12.64 | 12.61 | 13.22 | 13.29 | 13.31 | -18.29 | -18.14 | 31.60 | 20.9 | 31.43 | 19.3 |
| 34260 UGC06271 | 198.6375 | 68.5774 | 79.6408 | -12.4654 | 1996 | 2305 | 1.0 | 0.38 | 217 | 2.361 | / | / | 13.44 | 13.52 | / | -18.96 | / | / | / | 32.50 | 31.6 |
| 34292 E438-015 | 278.4675 | 29.8605 | 140.5773 | -29.1112 | 3369 | 3751 | 4.2 | 0.40 | 306 | 2.514 | 11.97 | 11.81 | 12.48 | 12.55 | 12.54 | -20.44 | -20.45 | 33.00 | 39.8 | 33.03 | 40.3 |
| 34308 UGC06275 | 142.1439 | 52.6901 | 52.8110 | 2.1444 | 1969 | 2122 | 7.0 | 0.51 | 147 | 2.224 | 12.97 | 13.15 | 14.31 | 14.41 | 14.13 | -17.80 | -17.61 | 31.93 | 24.3 | 32.03 | 25.4 |
| 34362 ES377-031 | 281.2380 | 24.8524 | 146.9617 | -29.0469 | 3017 | 3377 | 4.0 | 0.49 | 273 | 2.487 | 12.20 | 12.15 | 12.96 | 13.04 | 12.95 | -20.19 | -20.18 | 33.16 | 42.9 | 33.26 | 44.8 |
| 34508 UGC06309 | 152.5338 | 59.9290 | 61.0581 | -2.0063 | 2873 | 3092 | 4.5 | 0.70 | 211 | 2.460 | 12.10 | 12.27 | 12.63 | 12.74 | 12.87 | -19.94 | -19.92 | 32.83 | 36.8 | 32.67 | 34.2 |
| 34519 ES319-011 | 284.3566 | 18.8799 | 154.5046 | -28.4746 | 3096 | 3436 | 5.8 | 0.68 | 273 | 2.562 | 11.73 | 11.70 | 12.65 | 12.72 | 12.56 | -20.87 | -20.92 | 33.47 | 49.4 | 33.70 | 54.9 |
| 34554 NGC003621 | 281.2141 | 26.0988 | 145.6488 | -28.5667 | 731 | 1068 | 6.9 | 0.44 | 266 | 2.462 | 8.46 | 8.37 | 8.93 | 8.98 | 9.04 | -19.96 | -19.93 | 29.00 | 6.3 | 28.92 | 6.1 |
| 34561 UGC06318 | 161.5459 | 63.7840 | 66.1502 | -4.6495 | 2328 | 2570 | 5.2 | 0.61 | 285 | 2.548 | 11.12 | 11.23 | 12.10 | 12.19 | 12.06 | -20.75 | -20.78 | 32.83 | 36.8 | 33.00 | 39.8 |
| 34612 UGC06328 | 241.3297 | 64.2218 | 96.3585 | -18.6843 | 807 | 1159 | 1.0 | 0.29 | 483 | 2.695 | 8.11 | 7.75 | 8.63 | 8.61 | 8.54 | -22.08 | -22.21 | 30.62 | 13.3 | 30.82 | 14.6 |
| 34691 ES570-019 | 276.2199 | 36.6241 | 132.8674 | -27.3378 | 1339 | 1706 | 4.5 | 0.54 | 154 | 2.254 | / | / | 14.01 | 14.10 | / | -17.90 | / | / | / | 32.01 | 25.2 |
| 34692 UGC06339 | 135.7685 | 47.5488 | 47.3050 | 5.7376 | 1316 | 1422 | 6.0 | 0.68 | 149 | 2.299 | 12.24 | 12.46 | 13.09 | 13.13 | 13.16 | -18.48 | -18.35 | 31.64 | 21.3 | 31.48 | 19.8 |
| 34695 UGC06346 | 241.9619 | 64.4182 | 96.5841 | -18.4237 | 728 | 1079 | 3.1 | 0.55 | 333 | 2.593 | 7.75 | 7.77 | 8.27 | 8.29 | 8.39 | -21.15 | -21.22 | 29.55 | 8.1 | 29.51 | 8.0 |
| 34697 NGC03628 | 240.8527 | 64.7802 | 96.0025 | -18.1944 | 845 | 1196 | 3.1 | 0.22 | 451 | 2.656 | 8.09 | 7.62 | 8.46 | 8.42 | 8.38 | -21.73 | -21.83 | 30.11 | 10.5 | 30.26 | 11.3 |
| 34718 UGC06348 | 144.2185 | 55.4288 | 55.6993 | -1.3404 | 1946 | 2116 | 3.1 | 0.32 | 238 | 2.392 | 12.70 | 12.65 | 13.45 | 13.52 | 13.45 | -19.32 | -19.25 | 32.78 | 36.1 | 32.80 | 36.3 |

| PGC Name | l | b | sgl | sgb | v_{hel} | v_{mod} | t | b/a | w_{max} | $\log w_{max}$ | I | I* | [3.6] | [3.6]* | $C_{[3.6]}$ | M_C | $M_{[3.6]}$ | μ_C | d_C | $\mu_{[3.6]}$ | $d_{[3.6]}$ |
|-----------------|----------|---------|----------|----------|-----------|-----------|-----|------|-----------|----------------|-------|-------|-------|--------|-------------|--------|-------------|---------|-------|---------------|-------------|
| 34719 NGC03629 | 208.1715 | 69.7855 | 83.3094 | -12.7698 | 1507 | 1823 | 5.9 | 0.71 | 190 | 2.422 | 11.93 | 12.13 | 13.02 | 13.12 | 12.98 | -19.60 | -19.55 | 32.59 | 33.0 | 32.69 | 34.5 |
| 34733 UGC06355 | 195.8197 | 69.8056 | 79.4003 | -10.8989 | 2182 | 2490 | 6.4 | 0.20 | 178 | 2.250 | 13.62 | 13.57 | 14.65 | 14.73 | 14.50 | -18.04 | -17.87 | 32.55 | 32.4 | 32.62 | 33.4 |
| 34836 UGC06376 | 226.8524 | 68.3466 | 89.8020 | -15.3325 | 4246 | 4631 | 4.6 | 0.50 | 508 | 2.759 | 10.38 | 10.27 | 10.90 | 10.98 | 10.99 | -22.67 | -22.85 | 33.70 | 54.9 | 33.89 | 59.9 |
| 34869 UGC06378 | 133.8169 | 45.5629 | 45.2500 | 6.9917 | 1308 | 1399 | 6.5 | 0.20 | 146 | 2.164 | 13.48 | 13.53 | 14.41 | 14.49 | 14.37 | -17.26 | -17.03 | 31.62 | 21.1 | 31.52 | 20.2 |
| 34874 ES319-016 | 284.1764 | 21.5319 | 151.6025 | -27.7598 | 2884 | 3229 | 5.3 | 0.45 | 360 | 2.596 | 13.04 | 12.84 | 13.58 | 13.64 | 13.60 | -21.18 | -21.25 | 34.87 | 94.0 | 35.02 | 101.2 |
| 34917 NGC03652 | 177.6527 | 68.5406 | 73.6458 | -7.6228 | 1995 | 2272 | 5.7 | 0.40 | 225 | 2.381 | 11.86 | 11.88 | 12.67 | 12.70 | 12.65 | -19.22 | -19.14 | 31.87 | 23.7 | 31.85 | 23.5 |
| 34929 UGC06390 | 137.9454 | 50.3962 | 50.2519 | 4.4996 | 1013 | 1137 | 6.4 | 0.20 | 150 | 2.177 | 13.86 | 13.92 | 15.00 | 15.08 | 14.85 | -17.37 | -17.15 | 32.22 | 27.9 | 32.24 | 28.1 |
| 34935 UGC06396 | 235.5865 | 66.9685 | 93.3426 | -16.4729 | 1501 | 1850 | 5.0 | 0.73 | 285 | 2.611 | 10.78 | 10.94 | 11.11 | 11.15 | 11.41 | -21.32 | -21.40 | 32.75 | 35.5 | 32.56 | 32.5 |
| 34971 UGC06399 | 152.0791 | 60.9605 | 61.9874 | -1.5048 | 792 | 992 | 8.8 | 0.28 | 167 | 2.231 | 12.87 | 12.92 | 14.07 | 14.09 | 13.86 | -17.86 | -17.68 | 31.72 | 22.1 | 31.78 | 22.7 |
| 34995 NGC03659 | 233.0786 | 67.7547 | 92.2430 | -15.8142 | 1285 | 1628 | 7.7 | 0.51 | 206 | 2.370 | 11.90 | 12.00 | 12.48 | 12.51 | 12.62 | -19.12 | -19.04 | 31.75 | 22.3 | 31.55 | 20.4 |
| 35006 AGC510055 | 271.8302 | 45.2298 | 122.9527 | -24.9265 | 5016 | 5462 | 3.9 | 0.72 | 314 | 2.647 | / | / | 12.42 | 12.53 | / | -21.74 | / | / | / | 34.36 | 74.5 |
| 35025 NGC03654 | 133.7425 | 45.8403 | 45.5276 | 7.0527 | 1574 | 1668 | 4.0 | 0.55 | 195 | 2.358 | 12.26 | 12.40 | 13.02 | 13.11 | 13.11 | -19.02 | -18.92 | 32.13 | 26.7 | 32.04 | 25.5 |
| 35043 UGC06420 | 246.4031 | 64.1789 | 98.5928 | -18.0688 | 1059 | 1416 | 5.2 | 0.33 | 257 | 2.427 | 11.04 | 10.95 | 11.55 | 11.56 | 11.62 | -19.64 | -19.59 | 31.26 | 17.9 | 31.16 | 17.0 |
| 35088 AGC510059 | 270.4229 | 47.5490 | 120.3273 | -24.1412 | 1866 | 2249 | 5.0 | 0.44 | 377 | 2.615 | 10.20 | 10.09 | 10.62 | 10.63 | 10.72 | -21.36 | -21.44 | 32.09 | 26.2 | 32.08 | 26.0 |
| 35097 AGC027880 | 280.0942 | 32.2830 | 138.8824 | -26.7517 | 1939 | 2302 | 3.2 | 0.42 | 312 | 2.527 | 10.20 | 10.09 | 10.98 | 11.04 | 10.92 | -20.56 | -20.58 | 31.48 | 19.8 | 31.62 | 21.1 |
| 35113 NGC003669 | 143.3449 | 55.8673 | 56.0569 | 1.8949 | 1846 | 2015 | 6.8 | 0.20 | 224 | 2.350 | 12.07 | 11.91 | 13.00 | 13.06 | 12.84 | -18.95 | -18.85 | 31.79 | 22.8 | 31.91 | 24.1 |
| 35164 UGC06439 | 163.6604 | 66.1897 | 68.7137 | -4.4169 | 768 | 1006 | 3.0 | 0.57 | 405 | 2.684 | 8.75 | 8.77 | 9.24 | 9.31 | 9.40 | -21.98 | -22.11 | 31.39 | 18.9 | 31.42 | 19.2 |
| 35249 UGC06458 | 143.8159 | 56.7179 | 56.9377 | 1.7466 | 1709 | 1881 | 5.0 | 0.41 | 354 | 2.581 | 11.05 | 10.96 | 10.86 | 10.87 | 11.29 | -21.04 | -21.10 | 32.34 | 29.4 | 31.98 | 24.8 |
| 35288 ES378-003 | 284.7874 | 23.3743 | 149.8790 | -26.5926 | 3019 | 3371 | 5.4 | 0.51 | 257 | 2.466 | 12.12 | 12.03 | 12.94 | 13.01 | 12.87 | -20.00 | -19.97 | 32.89 | 37.8 | 33.01 | 40.0 |
| 35294 UGC06467 | 212.7145 | 71.3200 | 85.2523 | -11.7532 | 2738 | 3074 | 5.3 | 0.61 | 327 | 2.607 | 11.24 | 11.31 | 11.63 | 11.72 | 11.88 | -21.28 | -21.35 | 33.19 | 43.4 | 33.11 | 41.8 |
| 35314 NGC03692 | 251.1340 | 63.5797 | 100.8564 | -17.8285 | 1718 | 2084 | 3.1 | 0.22 | 404 | 2.608 | 11.29 | 10.85 | 11.71 | 11.74 | 11.65 | -21.29 | -21.37 | 32.96 | 39.1 | 33.13 | 42.4 |
| 35347 NGC3697 | 227.0504 | 70.1264 | 89.8882 | -13.5533 | 6265 | 6707 | 3.4 | 0.30 | 504 | 2.715 | 12.02 | 11.66 | 12.52 | 12.59 | 12.48 | -22.26 | -22.41 | 34.83 | 92.4 | 35.14 | 106.7 |
| 35405 UGC06493 | 217.6929 | 71.2985 | 86.8399 | -12.1156 | 2804 | 3147 | 4.0 | 0.50 | 249 | 2.451 | 12.19 | 12.25 | 12.97 | 13.06 | 13.01 | -19.86 | -19.83 | 32.89 | 37.9 | 32.91 | 38.2 |
| 35440 UGC06498 | 252.0215 | 63.7858 | 101.1371 | -17.4738 | 1018 | 1378 | 2.4 | 0.45 | 345 | 2.577 | 9.81 | 9.72 | 10.46 | 10.47 | 10.45 | -21.01 | -21.07 | 31.46 | 19.6 | 31.53 | 20.3 |
| 35521 UGC06509 | 221.0056 | 71.4608 | 87.9342 | -12.1051 | 2914 | 3261 | 6.6 | 0.20 | 177 | 2.248 | 14.26 | 14.22 | 15.43 | 15.51 | 15.21 | -18.02 | -17.85 | 33.26 | 44.8 | 33.40 | 47.9 |
| 35539 NGC003717 | 283.1292 | 29.4730 | 142.9687 | -25.6401 | 1733 | 2084 | 3.1 | 0.28 | 406 | 2.617 | 9.72 | 9.34 | 9.89 | 9.92 | 9.99 | -21.37 | -21.45 | 31.37 | 18.8 | 31.37 | 18.8 |
| 35540 AGC510082 | 275.3620 | 44.3214 | 125.4324 | -23.5138 | 2120 | 2503 | 3.8 | 0.65 | 262 | 2.529 | 11.63 | 11.74 | 11.94 | 12.03 | 12.25 | -20.57 | -20.59 | 32.84 | 37.0 | 32.64 | 33.7 |
| 35608 NGC03752 | 129.7859 | 41.4339 | 41.0361 | 9.8573 | 1918 | 1982 | 2.0 | 0.44 | 212 | 2.363 | 12.42 | 12.44 | 12.85 | 12.93 | 13.05 | -19.07 | -18.98 | 32.12 | 26.5 | 31.91 | 24.1 |
| 35622 AGC210432 | 230.2292 | 70.6642 | 90.9712 | -12.9917 | 6130 | 6569 | 5.3 | 0.56 | 243 | 2.458 | 13.95 | 14.04 | 14.56 | 14.68 | 14.72 | -19.93 | -19.90 | 34.73 | 88.4 | 34.70 | 87.0 |
| 35675 UGC06534 | 136.9535 | 51.6699 | 51.4828 | 5.2116 | 1271 | 1401 | 6.4 | 0.23 | 162 | 2.213 | 12.51 | 12.52 | 13.50 | 13.58 | 13.41 | -17.70 | -17.50 | 31.10 | 16.6 | 31.08 | 16.5 |
| 35676 UGC06537 | 155.3789 | 64.8789 | 66.1762 | -1.7641 | 865 | 1085 | 5.1 | 0.57 | 263 | 2.497 | 9.48 | 9.57 | 10.25 | 10.28 | 10.29 | -20.28 | -20.28 | 30.57 | 13.0 | 30.56 | 13.0 |
| 35705 PG0035705 | 268.4146 | 54.1452 | 114.2404 | -20.4784 | 1610 | 1989 | 7.9 | 0.62 | 129 | 2.207 | / | / | 14.85 | 14.95 | / | -17.45 | / | / | / | 32.41 | 30.4 |
| 35797 UGC06554 | 144.3775 | 58.9812 | 59.2209 | 1.8253 | 1185 | 1364 | 5.6 | 0.32 | 227 | 2.371 | / | / | 12.61 | 12.68 | / | -19.05 | / | / | / | 31.73 | 22.2 |
| 35869 UGC06567 | 131.7423 | 45.2795 | 44.9334 | 8.4416 | 2694 | 2794 | 5.3 | 0.24 | 486 | 2.691 | 10.72 | 10.27 | 10.85 | 10.84 | 10.92 | -22.04 | -22.17 | 32.98 | 39.4 | 33.04 | 40.6 |
| 35900 UGC06575 | 140.6991 | 56.2751 | 56.2718 | 3.4117 | 1216 | 1376 | 5.8 | 0.30 | 206 | 2.325 | 13.11 | 13.09 | 14.02 | 14.09 | 13.95 | -18.72 | -18.60 | 32.68 | 34.4 | 32.72 | 34.9 |
| 35913 UGC06577 | 177.9547 | 71.6251 | 76.0784 | -5.7027 | 1571 | 1848 | 5.2 | 0.40 | 262 | 2.446 | 11.98 | 11.94 | 12.88 | 12.95 | 12.80 | -19.82 | -19.79 | 32.63 | 33.6 | 32.75 | 35.5 |

| PGC Name | l | b | sgl | sgb | v_{hel} | v_{mod} | t | b/a | w_{mz} | $\log w_{mz}^2$ | I | I* | [3.6] | [3.6]* | $C_{[3.6]}$ | M_C | $M_{[3.6]}$ | μ_C | dC | $\mu_{[3.6]}$ | $d_{[3.6]}$ |
|-----------------|----------|---------|----------|----------|-----------|-----------|-----|------|----------|-----------------|-------|-------|-------|--------|-------------|--------|-------------|---------|-------|---------------|-------------|
| 35931 UGC06579 | 144.5763 | 59.5866 | 59.8350 | 1.8232 | 1290 | 1473 | 4.0 | 0.52 | 284 | 2.514 | 10.41 | 10.47 | 11.17 | 11.24 | 11.21 | -20.43 | -20.44 | 31.65 | 21.4 | 31.69 | 21.8 |
| 35942 UGC06583 | 231.7145 | 71.5073 | 91.4082 | -12.1196 | 6209 | 6651 | 8.4 | 0.58 | 319 | 2.586 | 13.10 | 13.15 | 13.30 | 13.42 | 13.65 | -21.09 | -21.15 | 34.83 | 92.3 | 34.68 | 86.2 |
| 35952 UGC06586 | 242.9320 | 69.2180 | 95.6227 | -13.6983 | 3959 | 4348 | 4.0 | 0.66 | 252 | 2.516 | 12.89 | 12.99 | 13.55 | 13.65 | 13.68 | -20.45 | -20.46 | 34.19 | 68.9 | 34.20 | 69.1 |
| 35978 P0035978 | 224.6306 | 72.5835 | 89.1648 | -11.0767 | 6861 | 7318 | 4.0 | 0.50 | 261 | 2.469 | 13.85 | 13.88 | 14.56 | 14.67 | 14.64 | -20.03 | -20.01 | 34.74 | 88.8 | 34.80 | 91.2 |
| 35991 UGC06594 | 240.8811 | 69.9097 | 94.7286 | -13.2135 | 1040 | 1383 | 6.4 | 0.20 | 155 | 2.190 | 13.25 | 13.26 | 14.30 | 14.37 | 14.17 | -17.49 | -17.28 | 31.66 | 21.5 | 31.66 | 21.5 |
| 36029 UGC06603 | 181.1447 | 72.3836 | 77.3085 | -5.9226 | 1628 | 1911 | 5.9 | 0.21 | 169 | 2.229 | 13.26 | 13.25 | 14.26 | 14.34 | 14.15 | -17.84 | -17.66 | 31.99 | 25.0 | 32.00 | 25.2 |
| 36079 UGC06610 | 185.3909 | 73.0025 | 78.6538 | -6.3569 | 1852 | 2143 | 5.9 | 0.22 | 197 | 2.297 | 13.28 | 13.21 | 14.19 | 14.26 | 14.09 | -18.46 | -18.33 | 32.56 | 32.5 | 32.61 | 33.2 |
| 36132 AGC210570 | 233.8045 | 71.8316 | 92.0453 | -11.7341 | 6777 | 7240 | 3.0 | 0.61 | 247 | 2.485 | 13.59 | 13.70 | 14.19 | 14.32 | 14.37 | -20.17 | -20.16 | 34.62 | 83.8 | 34.59 | 82.7 |
| 36174 AGC06626 | 256.7705 | 65.1163 | 102.3681 | -15.3370 | 1987 | 2356 | 9.8 | 0.50 | 148 | 2.224 | / | / | 14.02 | 14.11 | / | / | -17.61 | / | / | 31.72 | 22.1 |
| 36192 UGC06629 | 139.5696 | 56.1514 | 56.0848 | 4.0241 | 1213 | 1370 | 3.7 | 0.25 | 218 | 2.344 | 12.35 | 12.27 | 13.06 | 13.13 | 13.06 | -18.89 | -18.79 | 31.95 | 24.6 | 31.92 | 24.2 |
| 36238 UGC06640 | 141.6319 | 58.2912 | 58.3359 | 3.1429 | 1383 | 1555 | 6.3 | 0.57 | 168 | 2.301 | 12.21 | 12.38 | 13.25 | 13.34 | 13.22 | -18.50 | -18.36 | 31.71 | 22.0 | 31.70 | 21.9 |
| 36243 UGC06644 | 252.9407 | 67.2202 | 99.9276 | -14.2202 | 994 | 1348 | 5.2 | 0.69 | 242 | 2.516 | 9.74 | 9.86 | 10.23 | 10.31 | 10.45 | -20.46 | -20.47 | 30.91 | 15.2 | 30.78 | 14.3 |
| 36266 UGC06651 | 176.1902 | 72.4223 | 76.3429 | -4.7739 | 1466 | 1741 | 3.3 | 0.49 | 278 | 2.496 | 10.72 | 10.75 | 11.12 | 11.20 | 11.34 | -20.27 | -20.27 | 31.61 | 21.0 | 31.47 | 19.7 |
| 36330 AGC210622 | 233.5460 | 72.6274 | 91.8750 | -10.9521 | 7806 | 8308 | 8.7 | 0.47 | 226 | 2.400 | 14.27 | 14.33 | 14.81 | 14.94 | 15.00 | -19.40 | -19.34 | 34.47 | 78.2 | 34.37 | 74.7 |
| 36343 UGC06667 | 146.2692 | 62.2902 | 62.6419 | 1.4876 | 974 | 1169 | 5.9 | 0.21 | 173 | 2.239 | 12.54 | 12.52 | 13.54 | 13.56 | 13.39 | -17.93 | -17.76 | 31.33 | 18.4 | 31.32 | 18.3 |
| 36349 AGC210629 | 233.1791 | 72.7280 | 91.7535 | -10.8636 | 5971 | 6403 | 4.5 | 0.54 | 327 | 2.581 | 13.00 | 13.02 | 13.10 | 13.21 | 13.49 | -21.05 | -21.10 | 34.61 | 83.5 | 34.41 | 76.1 |
| 36371 AGC210634 | 233.5649 | 72.7599 | 91.8659 | -10.8198 | 6330 | 6774 | 2.8 | 0.46 | 292 | 2.509 | 13.10 | 13.09 | 13.62 | 13.73 | 13.77 | -20.39 | -20.39 | 34.22 | 69.7 | 34.21 | 69.4 |
| 36381 UGC06679 | 164.3613 | 70.3546 | 72.5470 | -2.7504 | 5163 | 5487 | 6.6 | 0.20 | 307 | 2.487 | / | / | 14.02 | 14.09 | / | -20.18 | / | / | 34.36 | 74.6 | 74.6 |
| 36386 UGC06675 | 127.6987 | 39.1133 | 38.6952 | -11.4786 | 1709 | 1753 | 6.0 | 0.49 | 191 | 2.332 | / | / | 13.80 | 13.88 | / | -18.67 | / | / | 32.57 | 32.6 | 32.6 |
| 36431 UGC06686 | 243.4729 | 70.9867 | 95.2995 | -11.9482 | 6543 | 7005 | 3.3 | 0.20 | 398 | 2.600 | 12.76 | 12.29 | 13.09 | 13.14 | 13.08 | -21.22 | -21.29 | 34.36 | 74.4 | 34.53 | 80.6 |
| 36475 NGC03839 | 255.5048 | 67.2069 | 100.8412 | -13.7725 | 5913 | 6366 | 7.4 | 0.52 | 310 | 2.551 | 12.52 | 12.50 | 12.75 | 12.85 | 13.04 | -20.77 | -20.81 | 33.86 | 59.2 | 33.72 | 55.4 |
| 36493 UGC06703 | 137.5267 | 55.0588 | 54.9005 | 5.0878 | 2456 | 2616 | 2.0 | 0.31 | 400 | 2.615 | 11.57 | 11.32 | 12.10 | 12.16 | 12.10 | -21.36 | -21.44 | 33.49 | 49.9 | 33.65 | 53.7 |
| 36604 UGC06724 | 234.6125 | 73.2121 | 92.1212 | -10.3345 | 5087 | 5492 | 3.1 | 0.56 | 459 | 2.735 | 11.61 | 11.57 | 12.26 | 12.35 | 12.32 | -22.45 | -22.60 | 34.85 | 93.5 | 35.10 | 104.7 |
| 36643 PG0036643 | 277.4439 | 49.4747 | 121.8727 | -19.3187 | 1715 | 2093 | 6.3 | 0.34 | 185 | 2.284 | 12.66 | 12.68 | 13.47 | 13.55 | 13.47 | -18.35 | -18.20 | 31.82 | 23.1 | 31.76 | 22.5 |
| 36660 NGC003850 | 140.8461 | 58.8923 | 58.8870 | 3.6187 | 1154 | 1326 | 5.3 | 0.44 | 167 | 2.262 | 12.30 | 12.43 | 13.54 | 13.63 | 13.38 | -18.14 | -17.98 | 31.52 | 20.1 | 31.61 | 21.0 |
| 36664 AGC028071 | 285.8011 | 32.3089 | 141.1533 | -22.3923 | 1843 | 2198 | 7.9 | 0.55 | 166 | 2.289 | 13.40 | 13.46 | 14.26 | 14.34 | 14.26 | -18.39 | -18.25 | 32.67 | 34.1 | 32.61 | 33.3 |
| 36683 P0036683 | 232.8581 | 73.6702 | 91.5644 | -9.9352 | 7088 | 7537 | 9.5 | 0.38 | 265 | 2.449 | 13.64 | 13.60 | 14.01 | 14.12 | 14.22 | -19.85 | -19.81 | 34.12 | 66.7 | 34.00 | 63.1 |
| 36699 UGC06745 | 150.7194 | 65.9565 | 66.6448 | 0.4029 | 889 | 1105 | 5.1 | 0.23 | 347 | 2.543 | 9.86 | 9.53 | 10.20 | 10.19 | 10.22 | -20.70 | -20.73 | 30.92 | 15.3 | 30.92 | 15.2 |
| 36743 NGC003879 | 131.1442 | 46.7009 | 46.3701 | 8.8609 | 1430 | 1522 | 8.0 | 0.25 | 196 | 2.297 | / | / | 13.84 | 13.91 | / | -18.33 | / | / | 32.25 | 28.1 | 28.1 |
| 36779 AGC210791 | 235.7485 | 73.7291 | 92.3743 | -9.7781 | 6167 | 6605 | 3.5 | 0.37 | 379 | 2.602 | 13.36 | 13.18 | 13.91 | 14.00 | 13.94 | -21.24 | -21.30 | 35.29 | 114.1 | 35.47 | 124.2 |
| 36836 UGC06774 | 141.0678 | 59.8534 | 59.8566 | 3.6120 | 2419 | 2608 | 5.9 | 0.24 | 230 | 2.365 | 13.86 | 13.74 | 14.77 | 14.84 | 14.64 | -19.09 | -19.00 | 33.77 | 56.8 | 33.90 | 60.3 |
| 36856 AGC210803 | 232.1232 | 74.4574 | 91.2887 | -9.1694 | 6821 | 7279 | 3.0 | 0.26 | 366 | 2.570 | 13.58 | 13.27 | 13.69 | 13.77 | 13.88 | -20.95 | -21.00 | 34.92 | 96.5 | 34.89 | 95.1 |
| 36882 ES440-011 | 286.5396 | 32.5755 | 141.1573 | -21.7144 | 1939 | 2294 | 6.9 | 0.62 | 92 | 2.060 | / | / | 12.33 | 12.42 | / | -16.01 | / | / | 28.44 | 4.9 | 4.9 |
| 36887 UGC06780 | 273.1136 | 57.1704 | 113.8857 | -16.4720 | 1729 | 2105 | 6.4 | 0.41 | 210 | 2.354 | 13.00 | 13.04 | 14.18 | 14.26 | 14.00 | -18.98 | -18.88 | 33.00 | 39.9 | 33.18 | 43.3 |
| 36930 UGC06792 | 164.5166 | 71.9587 | 73.9926 | -2.0504 | 851 | 1105 | 5.9 | 0.20 | 163 | 2.212 | 13.05 | 13.05 | 14.11 | 14.14 | 13.94 | -17.69 | -17.50 | 31.64 | 21.3 | 31.64 | 21.3 |
| 36932 UGC06791 | 210.9953 | 76.1749 | 86.1086 | -6.9488 | 1855 | 2172 | 6.5 | 0.21 | 208 | 2.319 | 13.16 | 13.04 | 13.86 | 13.93 | 13.84 | -18.66 | -18.54 | 32.51 | 31.8 | 32.48 | 31.4 |

| PGC Name | l | b | sgl | sgb | v_{hel} | v_{mod} | t | b/a | w_{mz} | $\log w_{mz}^2$ | I | I* | [3.6] | [3.6]* | $C_{[3.6]}$ | MC | $M_{[3.6]}$ | μC | dC | $\mu_{[3.6]}$ | $d_{[3.6]}$ |
|-----------------|----------|---------|----------|----------|-----------|-----------|-----|------|----------|-----------------|-------|-------|-------|--------|-------------|--------|-------------|---------|-------|---------------|-------------|
| 37036 NGC03917 | 143.6499 | 62.7941 | 62.9366 | 2.7625 | 962 | 1154 | 5.9 | 0.23 | 273 | 2.439 | 10.81 | 10.60 | 11.51 | 11.41 | 11.41 | -19.76 | -19.72 | 31.17 | 17.1 | 31.23 | 17.6 |
| 37040 AGC210829 | 233.0171 | 74.9700 | 91.4790 | -8.6375 | 7681 | 8172 | 3.7 | 0.54 | 252 | 2.468 | 13.53 | 13.57 | 13.98 | 14.10 | 14.20 | -20.02 | -20.00 | 34.28 | 71.9 | 34.18 | 68.7 |
| 37132 UGC06833 | 168.1942 | 73.4093 | 75.7948 | -2.2879 | 918 | 1180 | 5.2 | 0.64 | 145 | 2.268 | 11.23 | 11.43 | 12.49 | 12.58 | 12.36 | -18.20 | -18.05 | 30.56 | 13.0 | 30.63 | 13.4 |
| 37143 UGC06837 | 241.8715 | 73.8357 | 94.0511 | -9.3321 | 5974 | 6408 | 6.1 | 0.20 | 331 | 2.520 | 14.60 | 14.23 | 14.51 | 14.57 | 14.77 | -20.49 | -20.50 | 35.37 | 118.5 | 35.23 | 111.1 |
| 37153 P0037153 | 233.6818 | 75.1761 | 91.6294 | -8.4146 | 6639 | 7089 | 4.9 | 0.70 | 193 | 2.421 | 13.08 | 13.22 | 13.64 | 13.77 | 13.86 | -19.59 | -19.54 | 33.48 | 49.7 | 33.35 | 46.8 |
| 37178 AGC028144 | 286.9872 | 34.1297 | 139.7863 | -20.7541 | 2021 | 2380 | 4.4 | 0.20 | 292 | 2.466 | 11.03 | 10.66 | 11.44 | 11.48 | 11.43 | -20.00 | -19.98 | 31.43 | 19.3 | 31.46 | 19.6 |
| 37243 AGC028152 | 290.0645 | 24.7699 | 150.1888 | -21.5848 | 2952 | 3298 | 5.1 | 0.20 | 350 | 2.544 | 11.99 | 11.52 | 12.08 | 12.11 | 12.18 | -20.71 | -20.74 | 32.91 | 38.1 | 32.88 | 37.6 |
| 37259 UGC06862 | 258.7178 | 69.3445 | 100.7869 | -11.3277 | 2737 | 3108 | 6.7 | 0.20 | 181 | 2.258 | 14.88 | 14.81 | 16.17 | 16.25 | 15.88 | -18.10 | -17.94 | 34.03 | 64.0 | 34.28 | 71.8 |
| 37264 NGC03947 | 235.4931 | 75.2878 | 92.0780 | -8.2455 | 6199 | 6634 | 3.0 | 0.56 | 386 | 2.661 | 12.10 | 12.08 | 12.54 | 12.65 | 12.72 | -21.77 | -21.88 | 34.57 | 82.0 | 34.64 | 84.6 |
| 37271 ES440-027 | 287.7884 | 32.6063 | 141.5653 | -20.7329 | 1707 | 2058 | 6.6 | 0.23 | 263 | 2.423 | 11.51 | 11.22 | 11.81 | 11.85 | 11.90 | -19.61 | -19.55 | 31.50 | 20.0 | 31.40 | 19.1 |
| 37280 ES504-024 | 287.3512 | 34.1212 | 139.9225 | -20.4809 | 1893 | 2249 | 9.0 | 0.72 | 90 | 2.104 | / | / | 15.30 | 15.39 | / | / | -16.44 | / | / | 31.84 | 23.3 |
| 37288 UGC06867 | 225.7614 | 76.4254 | 89.6194 | -7.2493 | 6457 | 6893 | 2.0 | 0.48 | 371 | 2.618 | 12.54 | 12.48 | 12.85 | 12.96 | 13.08 | -21.39 | -21.46 | 34.54 | 80.9 | 34.52 | 80.2 |
| 37290 UGC06869 | 147.6336 | 66.4057 | 66.7945 | 1.7189 | 803 | 1015 | 4.0 | 0.63 | 252 | 2.501 | 10.19 | 10.32 | 10.90 | 10.93 | 10.99 | -20.32 | -20.32 | 31.31 | 18.3 | 31.26 | 17.8 |
| 37306 UGC06870 | 142.2177 | 62.5906 | 62.6451 | 3.3857 | 1050 | 1240 | 4.0 | 0.50 | 404 | 2.659 | 9.01 | 8.95 | 9.53 | 9.54 | 9.61 | -21.75 | -21.86 | 31.36 | 18.7 | 31.40 | 19.0 |
| 37325 NGC003956 | 285.2049 | 40.3195 | 133.1796 | -19.4025 | 1657 | 2023 | 5.1 | 0.30 | 254 | 2.416 | 11.49 | 11.36 | 12.23 | 12.29 | 12.18 | -19.55 | -19.49 | 31.73 | 22.2 | 31.78 | 22.7 |
| 37352 UGC06879 | 275.6767 | 57.5033 | 114.5655 | -15.2085 | 2388 | 2772 | 7.1 | 0.30 | 229 | 2.371 | / | / | 13.44 | 13.46 | / | / | -19.05 | / | / | 32.53 | 32.1 |
| 37409 UGC06891 | 246.6603 | 73.8467 | 95.3383 | -8.9317 | 6783 | 7248 | 2.0 | 0.26 | 344 | 2.543 | 13.41 | 13.07 | 13.76 | 13.83 | 13.81 | -20.70 | -20.73 | 34.58 | 82.6 | 34.67 | 86.0 |
| 37418 UGC06894 | 139.5226 | 60.6289 | 60.5541 | 4.4518 | 850 | 1025 | 5.9 | 0.20 | 121 | 2.083 | 14.00 | 14.15 | 14.93 | 14.97 | 14.92 | -16.51 | -16.23 | 31.43 | 19.3 | 31.20 | 17.4 |
| 37463 P0037463 | 245.7762 | 74.1837 | 94.9945 | -8.6922 | 6350 | 6798 | 6.7 | 0.36 | 293 | 2.489 | 13.92 | 13.80 | 14.53 | 14.63 | 14.57 | -20.21 | -20.20 | 34.86 | 93.9 | 34.96 | 98.3 |
| 37466 NGC3972 | 138.8481 | 60.0535 | 59.9513 | 4.7373 | 846 | 1017 | 4.0 | 0.28 | 258 | 2.420 | 11.29 | 11.17 | 11.96 | 11.97 | 11.93 | -19.58 | -19.53 | 31.51 | 20.1 | 31.50 | 20.0 |
| 37483 UGC06906 | 267.5344 | 65.7333 | 105.7376 | -12.2284 | 2496 | 2871 | 3.2 | 0.31 | 424 | 2.640 | 10.67 | 10.40 | 11.14 | 11.14 | 11.13 | -21.58 | -21.67 | 32.73 | 35.1 | 32.84 | 37.0 |
| 37496 AGC028198 | 285.5782 | 41.1043 | 132.5739 | -18.7956 | 1720 | 2087 | 4.1 | 0.40 | 284 | 2.481 | 10.64 | 10.56 | 10.81 | 10.87 | 11.08 | -20.14 | -20.13 | 31.22 | 17.6 | 31.00 | 15.9 |
| 37525 UGC06917 | 143.4703 | 64.4518 | 64.5674 | 3.0820 | 911 | 1110 | 8.8 | 0.59 | 178 | 2.334 | 11.62 | 11.77 | 12.92 | 13.01 | 12.74 | -18.80 | -18.69 | 31.55 | 20.4 | 31.71 | 21.9 |
| 37542 UGC06921 | 145.9417 | 66.2760 | 66.5359 | 2.3599 | 938 | 1148 | 8.8 | 0.64 | 150 | 2.284 | 11.75 | 11.94 | 12.56 | 12.61 | 12.64 | -18.34 | -18.20 | 30.98 | 15.7 | 30.81 | 14.5 |
| 37549 AGC028206 | 291.2557 | 23.4368 | 151.9061 | -20.9536 | 2997 | 3338 | 5.0 | 0.67 | 209 | 2.439 | 12.16 | 12.12 | 12.73 | 12.80 | 12.82 | -19.76 | -19.71 | 32.59 | 33.0 | 32.53 | 32.1 |
| 37553 UGC06923 | 140.5150 | 62.0639 | 62.0313 | 4.1120 | 1067 | 1252 | 9.8 | 0.53 | 139 | 2.205 | 12.45 | 12.63 | 13.56 | 13.66 | 13.50 | -17.62 | -17.43 | 31.12 | 16.8 | 31.08 | 16.5 |
| 37566 ES572-024 | 285.8721 | 41.0745 | 132.7071 | -18.6112 | 1847 | 2215 | 7.0 | 0.23 | 146 | 2.167 | / | / | 15.02 | 15.10 | / | / | -17.06 | / | / | 32.17 | 27.1 |
| 37598 UGC06931 | 136.3730 | 57.7665 | 57.5812 | 5.8740 | 1192 | 1350 | 9.0 | 0.65 | 105 | 2.132 | / | / | 14.39 | 14.49 | / | / | -16.71 | / | / | 31.20 | 17.3 |
| 37617 NGC3992 | 140.0920 | 61.9234 | 61.8719 | 4.2962 | 1048 | 1231 | 4.0 | 0.60 | 459 | 2.749 | 8.88 | 8.88 | 9.54 | 9.56 | 9.58 | -22.57 | -22.74 | 32.16 | 27.0 | 32.31 | 29.0 |
| 37681 ES572-030 | 287.1540 | 38.8021 | 135.3181 | -18.7134 | 1795 | 2158 | 9.1 | 0.41 | 133 | 2.154 | 12.88 | 13.00 | 14.01 | 14.10 | 13.90 | -17.16 | -16.93 | 31.06 | 16.3 | 31.03 | 16.1 |
| 37689 UGC06955 | 165.0320 | 74.4068 | 76.2244 | -1.0317 | 904 | 1164 | 9.8 | 0.38 | 144 | 2.183 | 12.93 | 13.08 | 13.65 | 13.74 | 13.77 | -17.43 | -17.22 | 31.20 | 17.4 | 30.96 | 15.5 |
| 37691 UGC06963 | 151.8655 | 70.0890 | 70.7448 | 1.0758 | 832 | 1063 | 3.1 | 0.26 | 388 | 2.595 | 10.04 | 9.73 | 10.03 | 10.02 | 10.24 | -21.18 | -21.24 | 31.42 | 19.2 | 31.26 | 17.8 |
| 37697 UGC06964 | 146.6732 | 67.3589 | 67.6543 | 2.2778 | 903 | 1118 | 6.8 | 0.20 | 248 | 2.394 | 11.51 | 11.29 | 11.80 | 11.79 | 11.90 | -19.35 | -19.28 | 31.25 | 17.8 | 31.07 | 16.4 |
| 37723 UGC06971 | 193.8957 | 78.0456 | 83.4262 | -3.6713 | 761 | 1052 | 6.9 | 0.45 | 152 | 2.222 | 11.78 | 11.93 | 12.72 | 12.76 | 12.70 | -17.78 | -17.60 | 30.49 | 12.5 | 30.35 | 11.8 |
| 37832 UGC06992 | 141.9766 | 64.5432 | 64.5735 | 3.7316 | 755 | 951 | 7.9 | 0.46 | 128 | 2.149 | 12.93 | 13.12 | 13.88 | 13.97 | 13.90 | -17.11 | -16.88 | 31.02 | 16.0 | 30.85 | 14.8 |
| 37906 ES505-003 | 288.5910 | 36.8982 | 137.6404 | -18.4557 | 1790 | 2148 | 7.7 | 0.21 | 196 | 2.293 | 12.52 | 12.37 | 13.29 | 13.35 | 13.22 | -18.43 | -18.29 | 31.65 | 21.4 | 31.65 | 21.4 |

| PGC Name | l | b | sgl | sgb | v_{hel} | v_{mod} | t | b/a | w_{max} | $\log w_{max}$ | I | I* | [3.6] | [3.6]* | $C_{[3.6]}$ | M_C | μ_C | d_C | $\mu_{[3.6]}$ | $d_{[3.6]}$ | | |
|-----------------|----------|---------|----------|----------|-----------|-----------|-----|------|-----------|----------------|-------|-------|-------|--------|-------------|--------|---------|-------|---------------|-------------|-------|-------|
| 37935 NGC004034 | 129.3797 | 47.1742 | 46.8681 | 10.0585 | 2370 | 2471 | 6.0 | 0.61 | 201 | 2.393 | 12.89 | 13.04 | 13.70 | 13.80 | 13.78 | -19.34 | -19.27 | 33.14 | 42.4 | 33.10 | 41.6 | |
| 38012 AGC007016 | 257.5760 | 73.2326 | 98.4320 | -8.1868 | 7276 | 7765 | 2.1 | 0.26 | 535 | 2.735 | / | / | 12.46 | 12.52 | / | / | -22.60 | / | / | / | 35.28 | 113.7 |
| 38014 UGC07019 | 132.4956 | 53.7924 | 53.5357 | 7.9733 | 1517 | 1651 | 9.9 | 0.40 | 112 | 2.078 | / | / | 14.93 | 15.03 | / | / | -16.19 | / | / | / | 31.22 | 17.6 |
| 38031 NGC4045 | 275.9771 | 62.2705 | 110.9097 | -12.0260 | 1976 | 2348 | 1.3 | 0.65 | 308 | 2.601 | 10.60 | 10.71 | 11.14 | 11.23 | 11.33 | -21.23 | -21.30 | 32.57 | 32.7 | 32.54 | 32.2 | |
| 38049 NGC004050 | 286.3799 | 44.9325 | 129.2759 | -16.5318 | 1761 | 2130 | 2.2 | 0.54 | 340 | 2.597 | 10.29 | 10.26 | 11.14 | 11.21 | 11.09 | -21.20 | -21.26 | 32.29 | 28.8 | 32.49 | 31.5 | |
| 38068 NGC4051 | 148.8827 | 70.0854 | 70.4894 | 2.0591 | 704 | 931 | 4.0 | 0.59 | 233 | 2.451 | 9.43 | 9.56 | 9.86 | 9.89 | 10.09 | -19.87 | -19.84 | 29.96 | 9.8 | 29.73 | 8.8 | |
| 38087 AGC028292 | 287.6531 | 41.9196 | 132.5243 | -17.0417 | 1660 | 2024 | 5.8 | 0.22 | 170 | 2.232 | 13.43 | 13.37 | 14.58 | 14.65 | 14.36 | -17.87 | -17.69 | 32.24 | 28.1 | 32.36 | 29.6 | |
| 38126 ES505-009 | 290.1859 | 34.0885 | 140.8991 | -18.3219 | 2140 | 2495 | 5.0 | 0.34 | 149 | 2.191 | / | / | 15.28 | 15.36 | / | / | -17.29 | / | / | / | 32.67 | 34.2 |
| 38150 UGC07045 | 185.2649 | 78.6533 | 82.4144 | -2.1291 | 766 | 1050 | 5.3 | 0.37 | 291 | 2.488 | 9.95 | 9.87 | 10.57 | 10.63 | 10.61 | -20.20 | -20.19 | 30.81 | 14.5 | 30.82 | 14.6 | |
| 38167 UGC07054 | 249.0753 | 76.0849 | 95.1368 | -6.6165 | 933 | 1263 | 1.4 | 0.40 | 185 | 2.296 | 10.34 | 10.42 | 11.10 | 11.13 | 11.13 | -18.45 | -18.31 | 29.59 | 8.3 | 29.45 | 7.7 | |
| 38168 UGC07048 | 266.3384 | 70.2924 | 102.4000 | -9.0304 | 2414 | 2778 | 3.1 | 0.71 | 243 | 2.529 | 11.74 | 11.90 | 12.39 | 12.49 | 12.56 | -20.57 | -20.59 | 33.15 | 42.8 | 33.12 | 42.0 | |
| 38212 NGC04081 | 131.1055 | 51.9406 | 51.6729 | 8.8319 | 1455 | 1576 | 1.1 | 0.38 | 206 | 2.340 | 11.94 | 11.97 | 12.37 | 12.45 | 12.57 | -18.85 | -18.75 | 31.43 | 19.3 | 31.19 | 17.3 | |
| 38222 ES440-046 | 290.5408 | 33.6280 | 141.4634 | -18.2133 | 1751 | 2100 | 8.7 | 0.63 | 97 | 2.088 | 12.43 | 12.61 | 13.42 | 13.52 | 13.42 | -16.56 | -16.28 | 29.98 | 9.9 | 29.80 | 9.1 | |
| 38244 NGC004080 | 211.0236 | 79.6339 | 87.0913 | -3.6309 | 571 | 872 | 9.5 | 0.48 | 155 | 2.238 | / | / | 13.27 | 13.30 | / | / | -17.75 | / | / | / | 31.06 | 16.3 |
| 38283 UGC07075 | 140.5868 | 65.1672 | 65.1312 | 4.3862 | 744 | 940 | 5.2 | 0.25 | 268 | 2.434 | 11.27 | 11.10 | 11.49 | 11.49 | 11.66 | -19.71 | -19.66 | 31.37 | 18.8 | 31.15 | 17.0 | |
| 38302 UGC07081 | 140.3368 | 65.0104 | 64.9646 | 4.4761 | 746 | 941 | 4.7 | 0.38 | 331 | 2.544 | 9.44 | 9.33 | 9.79 | 9.79 | 9.93 | -20.71 | -20.74 | 30.64 | 13.4 | 30.53 | 12.8 | |
| 38346 AGC520004 | 286.6908 | 46.9043 | 127.5585 | -15.4322 | 1440 | 1807 | 5.4 | 0.35 | 247 | 2.412 | / | / | 11.62 | 11.68 | / | / | -19.45 | / | / | / | 31.14 | 16.9 |
| 38347 UGC07086 | 126.0950 | 39.3424 | 38.9671 | 12.7134 | 2013 | 2058 | 3.1 | 0.25 | 271 | 2.438 | 12.18 | 11.90 | 12.52 | 12.57 | 12.60 | -19.74 | -19.70 | 32.34 | 29.4 | 32.28 | 28.6 | |
| 38356 UGC07089 | 149.9189 | 71.5220 | 71.9668 | 2.0609 | 772 | 1005 | 7.9 | 0.22 | 137 | 2.139 | 12.34 | 12.44 | 13.42 | 13.45 | 13.30 | -17.02 | -16.78 | 30.32 | 11.6 | 30.23 | 11.1 | |
| 38361 UGC07090 | 143.5441 | 67.7911 | 67.8826 | 3.5264 | 571 | 781 | 5.3 | 0.25 | 301 | 2.483 | 9.75 | 9.52 | 10.27 | 10.27 | 10.25 | -20.16 | -20.15 | 30.41 | 12.1 | 30.41 | 12.1 | |
| 38370 NGC04100 | 141.1097 | 65.9164 | 65.9006 | 4.2463 | 1074 | 1276 | 4.1 | 0.29 | 374 | 2.583 | 9.98 | 9.73 | 10.44 | 10.44 | 10.44 | -21.07 | -21.13 | 31.51 | 20.1 | 31.56 | 20.5 | |
| 38392 NGC04102 | 138.0768 | 63.0727 | 62.9493 | 5.3129 | 837 | 1021 | 3.1 | 0.58 | 298 | 2.554 | 9.96 | 10.03 | 10.20 | 10.23 | 10.50 | -20.81 | -20.84 | 31.30 | 18.2 | 31.07 | 16.4 | |
| 38464 AGC028345 | 291.6621 | 31.8781 | 143.5341 | -17.9378 | 1723 | 2066 | 5.6 | 0.23 | 262 | 2.422 | 12.14 | 11.88 | 12.21 | 12.26 | 12.43 | -19.60 | -19.54 | 32.03 | 25.5 | 31.80 | 23.0 | |
| 38536 AGC028356 | 292.3679 | 29.9756 | 145.6322 | -17.9925 | 2220 | 2564 | 4.1 | 0.21 | 157 | 2.197 | 13.48 | 13.43 | 14.32 | 14.39 | 14.26 | -17.55 | -17.35 | 31.82 | 23.1 | 31.74 | 22.3 | |
| 38550 UGC07122 | 126.1209 | 40.0569 | 39.6981 | 12.6648 | 1815 | 1862 | 5.1 | 0.56 | 248 | 2.466 | 11.84 | 11.82 | 12.35 | 12.42 | 12.48 | -20.00 | -19.98 | 32.49 | 31.5 | 32.41 | 30.4 | |
| 38553 NGC004120 | 128.4194 | 47.1235 | 46.8385 | 10.7130 | 2246 | 2343 | 5.5 | 0.24 | 208 | 2.322 | / | / | 13.66 | 13.74 | / | / | -18.57 | / | / | / | 32.32 | 29.1 |
| 38567 UGC07125 | 163.3362 | 76.7619 | 78.1186 | 0.4298 | 1071 | 1335 | 8.8 | 0.42 | 139 | 2.176 | / | / | 13.98 | 14.07 | / | / | -17.15 | / | / | / | 31.22 | 17.5 |
| 38580 AGC520011 | 285.5494 | 52.3934 | 122.2179 | -13.4496 | 1175 | 1541 | 2.3 | 0.30 | 247 | 2.404 | 11.59 | 11.42 | 11.75 | 11.80 | 11.98 | -19.44 | -19.38 | 31.42 | 19.2 | 31.18 | 17.2 | |
| 38582 UGC07129 | 151.0006 | 72.9908 | 73.4723 | 2.1060 | 936 | 1176 | 2.0 | 0.68 | 97 | 2.113 | 12.19 | 12.46 | 12.93 | 13.03 | 13.11 | -16.79 | -16.53 | 29.89 | 9.5 | 29.56 | 8.1 | |
| 38628 ES441-011 | 291.9287 | 33.1710 | 142.3382 | -17.2874 | 2144 | 2495 | 5.7 | 0.24 | 140 | 2.150 | 14.15 | 14.19 | 15.34 | 15.43 | 15.16 | -17.13 | -16.89 | 32.29 | 28.7 | 32.33 | 29.3 | |
| 38645 NGC004142 | 136.8009 | 62.8801 | 62.7262 | 5.8819 | 1165 | 1348 | 6.5 | 0.52 | 168 | 2.286 | 12.77 | 12.91 | 13.85 | 13.94 | 13.78 | -18.37 | -18.22 | 32.15 | 27.0 | 32.17 | 27.2 | |
| 38652 AGC028378 | 290.6492 | 38.4600 | 136.7936 | -16.3487 | 1676 | 2032 | 9.0 | 0.32 | 128 | 2.122 | / | / | 15.57 | 15.66 | / | / | -16.62 | / | / | / | 32.28 | 28.6 |
| 38669 UGC07147 | 132.9420 | 57.4624 | 57.2391 | 7.7052 | 1900 | 2057 | 6.0 | 0.65 | 155 | 2.301 | / | / | 14.39 | 14.49 | / | / | -18.36 | / | / | / | 32.87 | 37.5 |
| 38680 UGC07153 | 131.1965 | 54.1863 | 53.9437 | 8.7319 | 2608 | 2754 | 5.9 | 0.20 | 229 | 2.360 | 13.60 | 13.43 | 14.33 | 14.40 | 14.27 | -19.03 | -18.94 | 33.33 | 46.3 | 33.38 | 47.4 | |
| 38688 UGC07151 | 143.1747 | 69.0075 | 69.0714 | 3.8281 | 265 | 478 | 5.9 | 0.22 | 150 | 2.178 | 10.78 | 10.84 | 11.76 | 11.83 | 11.69 | -17.38 | -17.16 | 29.07 | 6.5 | 28.99 | 6.3 | |
| 38711 AGC028383 | 292.3490 | 32.2873 | 143.3343 | -17.2523 | 2135 | 2483 | 5.0 | 0.27 | 274 | 2.445 | 11.33 | 11.11 | 12.12 | 12.18 | 11.99 | -19.81 | -19.78 | 31.81 | 23.0 | 31.96 | 24.6 | |

| PGC Name | l | b | sgl | sgb | v_{hel} | v_{mod} | t | b/a | w_{max} | $\log w_{max}^*$ | I | I* | [3.6] | [3.6]* | $C_{[3.6]}$ | M_C | $M_{[3.6]}$ | μ_C | dC | $\mu_{[3.6]}$ | $d_{[3.6]}$ | |
|----------|-----------|----------|---------|----------|-----------|-----------|------|-----|-----------|------------------|-------|-------|-------|--------|-------------|-------|-------------|---------|-------|---------------|-------------|------|
| 38712 | AGC028382 | 292.4243 | 31.9513 | 143.6884 | -17.3034 | 2164 | 2512 | 4.2 | 0.29 | 225 | 2.362 | 13.50 | 13.37 | 14.38 | 14.45 | 14.26 | -19.06 | -18.97 | 33.35 | 46.7 | 33.46 | 49.2 |
| 38777 | NGC004159 | 126.1253 | 40.7501 | 40.4076 | 12.6318 | 1755 | 1805 | 6.5 | 0.41 | 164 | 2.246 | / | / | 13.35 | 13.43 | / | / | -17.83 | / | / | 31.26 | 17.8 |
| 38795 | UGC07183 | 138.4712 | 65.4081 | 65.3009 | 5.2871 | 764 | 958 | 3.3 | 0.20 | 387 | 2.588 | 9.88 | 9.44 | 9.70 | 9.72 | 9.95 | -21.11 | -21.17 | 31.06 | 16.3 | 30.89 | 15.1 |
| 38803 | AGC007181 | 266.1524 | 73.5126 | 100.3080 | -6.5653 | 266 | 602 | 7.6 | 0.40 | 111 | 2.073 | 13.38 | 13.58 | 15.11 | 15.19 | 14.73 | -16.43 | -16.14 | 31.16 | 17.0 | 31.34 | 18.5 |
| 38815 | UGC07184 | 280.6944 | 62.6197 | 112.0026 | -10.0943 | 2112 | 2478 | 6.4 | 0.43 | 175 | 2.279 | 13.31 | 13.40 | 14.37 | 14.46 | 14.29 | -18.29 | -18.15 | 32.59 | 33.0 | 32.63 | 33.5 |
| 38841 | ES321-010 | 294.4607 | 23.6689 | 152.5488 | -18.0694 | 3140 | 3483 | 1.0 | 0.20 | 315 | 2.498 | 12.55 | 12.12 | 12.49 | 12.53 | 12.69 | -20.29 | -20.29 | 33.00 | 39.9 | 32.84 | 37.0 |
| 38851 | UGC07193 | 229.3622 | 80.5932 | 90.3260 | -3.0812 | 2573 | 2901 | 4.0 | 0.64 | 310 | 2.599 | 11.23 | 11.30 | 11.72 | 11.81 | 11.92 | -21.21 | -21.28 | 33.16 | 42.8 | 33.12 | 42.1 |
| 38897 | NGC04173 | 197.0748 | 81.1405 | 85.5428 | -1.3411 | 1120 | 1414 | 7.2 | 0.21 | 141 | 2.150 | 12.41 | 12.48 | 13.73 | 13.81 | 13.50 | -17.13 | -16.89 | 30.62 | 13.3 | 30.71 | 13.8 |
| 38916 | UGC07209 | 269.7444 | 72.4399 | 101.8141 | -6.6948 | 2209 | 2564 | 4.0 | 0.61 | 240 | 2.472 | 11.77 | 11.88 | 12.91 | 13.00 | 12.79 | -20.06 | -20.04 | 32.86 | 37.4 | 33.07 | 41.1 |
| 38943 | UGC07215 | 271.8619 | 71.3662 | 103.0389 | -7.0209 | 374 | 716 | 7.0 | 0.28 | 244 | 2.396 | 10.57 | 10.45 | 11.29 | 11.29 | 11.23 | -19.37 | -19.30 | 30.60 | 13.2 | 30.59 | 13.1 |
| 38988 | UGC07222 | 145.3974 | 71.7271 | 71.8774 | 3.4978 | 929 | 1158 | 5.8 | 0.20 | 227 | 2.356 | 11.48 | 11.32 | 12.33 | 12.34 | 12.18 | -19.00 | -18.90 | 31.18 | 17.3 | 31.24 | 17.7 |
| 39025 | AGC007235 | 268.3712 | 73.7152 | 100.6604 | -6.0084 | 2110 | 2461 | 6.0 | 0.60 | 248 | 2.482 | 10.85 | 10.95 | 11.40 | 11.49 | 11.58 | -20.15 | -20.14 | 31.73 | 22.2 | 31.63 | 21.2 |
| 39040 | UGC07234 | 268.9091 | 73.5125 | 100.9095 | -6.0608 | 2472 | 2828 | 4.1 | 0.46 | 336 | 2.568 | 11.30 | 11.24 | 11.88 | 11.95 | 11.95 | -20.93 | -20.97 | 32.90 | 38.0 | 32.95 | 38.9 |
| 39113 | UGC07249 | 270.0804 | 73.2903 | 101.3089 | -6.0014 | 622 | 960 | 9.5 | 0.30 | 122 | 2.098 | 14.38 | 14.53 | 15.62 | 15.70 | 15.47 | -16.65 | -16.38 | 32.13 | 26.6 | 32.09 | 26.2 |
| 39114 | NGC004197 | 278.9660 | 66.9492 | 108.0537 | -8.0744 | 2062 | 2426 | 6.7 | 0.23 | 258 | 2.414 | 12.02 | 11.83 | 12.48 | 12.54 | 12.54 | -19.53 | -19.47 | 32.08 | 26.1 | 32.02 | 25.3 |
| 39143 | NGC004205 | 129.5993 | 52.8703 | 52.6419 | 9.7229 | 1439 | 1562 | 4.0 | 0.40 | 176 | 2.275 | 12.03 | 12.12 | 12.61 | 12.70 | 12.77 | -18.26 | -18.11 | 31.03 | 16.1 | 30.81 | 14.5 |
| 39152 | UGC07255 | 268.1971 | 74.3936 | 100.1780 | -5.5267 | 2316 | 2667 | 5.2 | 0.20 | 289 | 2.461 | 12.62 | 12.31 | 13.14 | 13.19 | 13.11 | -19.96 | -19.93 | 33.08 | 41.4 | 33.15 | 42.7 |
| 39183 | UGC07260 | 270.2035 | 73.5535 | 101.1553 | -5.7842 | 706 | 1044 | 4.0 | 0.20 | 268 | 2.428 | 11.24 | 10.97 | 11.90 | 11.94 | 11.81 | -19.66 | -19.61 | 31.47 | 19.7 | 31.55 | 20.4 |
| 39201 | E321-016 | 295.1826 | 24.1856 | 152.2118 | -17.2953 | 3180 | 3519 | 5.6 | 0.29 | 229 | 2.370 | 12.45 | 12.27 | 12.90 | 12.96 | 12.98 | -19.13 | -19.04 | 32.11 | 26.4 | 32.01 | 25.2 |
| 39206 | AGC007268 | 275.4459 | 70.5146 | 104.4729 | -6.7617 | 600 | 944 | 9.3 | 0.49 | 182 | 2.309 | 11.61 | 11.73 | 11.83 | 11.86 | 12.17 | -18.58 | -18.45 | 30.74 | 14.1 | 30.31 | 11.5 |
| 39212 | E380-006 | 294.7815 | 26.6737 | 149.6040 | -16.9615 | 2944 | 3286 | 3.1 | 0.45 | 435 | 2.679 | 10.19 | 9.99 | 10.76 | 10.82 | 10.76 | -21.94 | -22.06 | 32.71 | 34.9 | 32.90 | 38.0 |
| 39224 | UGC07275 | 268.8899 | 74.3576 | 100.3430 | -5.4312 | -85 | 248 | 4.9 | 0.63 | 245 | 2.491 | 10.09 | 10.20 | 10.67 | 10.74 | 10.83 | -20.23 | -20.22 | 31.06 | 16.3 | 30.96 | 15.6 |
| 39237 | NGC4218 | 138.8760 | 67.8782 | 67.7867 | 5.2868 | 722 | 927 | 1.0 | 0.62 | 116 | 2.160 | 12.43 | 12.67 | 13.33 | 13.42 | 13.41 | -17.21 | -16.98 | 30.62 | 13.3 | 30.41 | 12.1 |
| 39241 | UGC07282 | 139.8975 | 68.8468 | 68.7844 | 4.9822 | 1031 | 1243 | 3.1 | 0.28 | 383 | 2.592 | 9.89 | 9.62 | 9.91 | 9.95 | 10.15 | -21.15 | -21.21 | 31.30 | 18.2 | 31.16 | 17.1 |
| 39308 | UGC07291 | 270.5353 | 73.9315 | 100.9650 | -5.4442 | 231 | 566 | 6.6 | 0.20 | 216 | 2.334 | 12.14 | 11.98 | 12.46 | 12.51 | 12.61 | -18.80 | -18.69 | 31.41 | 19.2 | 31.20 | 17.4 |
| 39315 | NGC004219 | 296.2099 | 19.0904 | 157.6343 | -17.6407 | 1989 | 2291 | 4.0 | 0.34 | 358 | 2.573 | 10.45 | 10.11 | 10.47 | 10.50 | 10.67 | -20.97 | -21.02 | 31.65 | 21.3 | 31.52 | 20.2 |
| 39328 | UGC07292 | 278.5306 | 68.6655 | 106.5940 | -7.1367 | 2593 | 2961 | 1.0 | 0.40 | 519 | 2.744 | 10.51 | 10.29 | 11.16 | 11.22 | 11.11 | -22.53 | -22.70 | 33.68 | 54.4 | 33.99 | 62.7 |
| 39344 | UGC07301 | 140.6210 | 69.8380 | 69.7975 | 4.8132 | 706 | 921 | 6.6 | 0.20 | 139 | 2.143 | 14.01 | 14.09 | 15.17 | 15.20 | 15.00 | -17.06 | -16.82 | 32.07 | 25.9 | 32.03 | 25.5 |
| 39366 | UGC07308 | 129.3801 | 53.2843 | 53.0674 | 9.8365 | 2765 | 2905 | 6.5 | 0.31 | 230 | 2.376 | 12.86 | 12.80 | 13.71 | 13.78 | 13.65 | -19.18 | -19.09 | 32.84 | 37.0 | 32.90 | 38.1 |
| 39390 | AGC007313 | 272.5630 | 73.2707 | 101.8399 | -5.5204 | 2132 | 2484 | 6.1 | 0.20 | 206 | 2.314 | 13.28 | 13.14 | 14.15 | 14.22 | 14.03 | -18.62 | -18.49 | 32.66 | 34.1 | 32.73 | 35.2 |
| 39393 | UGC07315 | 267.2113 | 75.7628 | 99.0956 | -4.6454 | 864 | 1197 | 4.0 | 0.62 | 235 | 2.468 | 10.57 | 10.69 | 11.14 | 11.17 | 11.29 | -20.01 | -19.99 | 31.31 | 18.3 | 31.16 | 17.1 |
| 39422 | NGC04244 | 154.5696 | 77.1568 | 77.7293 | 2.4070 | 245 | 497 | 6.0 | 0.42 | 192 | 2.317 | 9.39 | 9.46 | 10.25 | 10.27 | 10.22 | -18.65 | -18.52 | 28.87 | 5.9 | 28.79 | 5.7 |
| 39423 | UGC07323 | 140.7708 | 70.3158 | 70.2796 | 4.8064 | 514 | 730 | 7.9 | 0.63 | 116 | 2.166 | 10.25 | 10.50 | 11.48 | 11.53 | 11.37 | -17.27 | -17.05 | 28.64 | 5.3 | 28.58 | 5.2 |
| 39432 | UGC07321 | 241.9342 | 81.0535 | 92.2430 | -2.3416 | 408 | 718 | 6.5 | 0.20 | 216 | 2.334 | 12.41 | 12.26 | 13.12 | 13.12 | 13.05 | -18.80 | -18.69 | 31.85 | 23.5 | 31.82 | 23.1 |
| 39483 | UGC07333 | 280.2165 | 68.0386 | 107.4774 | -7.0307 | 735 | 1084 | 5.5 | 0.69 | 115 | 2.195 | 12.32 | 12.56 | 13.51 | 13.61 | 13.44 | -17.54 | -17.33 | 30.97 | 15.7 | 30.94 | 15.4 |
| 39600 | NGC004258 | 138.3199 | 68.8423 | 68.7409 | 5.5499 | 456 | 663 | 4.0 | 0.41 | 372 | 2.602 | 7.32 | 7.22 | 7.93 | 7.99 | 7.96 | -21.23 | -21.30 | 29.19 | 6.9 | 29.29 | 7.2 |

| PGC Name | l | b | sgl | sgb | v_{hel} | v_{mod} | t | b/a | w_{max} | $\log w_{max}^*$ | I | I* | [3.6] | [3.6]* | $C_{[3.6]}$ | M_C | $M_{[3.6]}$ | μ_C | d_C | $\mu_{[3.6]}$ | $d_{[3.6]}$ |
|-----------------|----------|---------|----------|----------|-----------|-----------|-----|------|-----------|------------------|-------|-------|-------|--------|-------------|--------|-------------|---------|-------|---------------|-------------|
| 39613 UGC07352 | 278.6909 | 70.1882 | 105.4333 | -6.1404 | 2467 | 2829 | 7.9 | 0.56 | 154 | 2.259 | 13.39 | 13.56 | 14.36 | 14.46 | 14.37 | -18.11 | -17.95 | 32.49 | 31.5 | 32.42 | 30.5 |
| 39738 UGC07380 | 282.5303 | 66.9594 | 108.8810 | -6.9459 | 2374 | 2740 | 5.2 | 0.70 | 261 | 2.552 | 10.89 | 11.05 | 11.28 | 11.33 | 11.56 | -20.79 | -20.82 | 32.35 | 29.5 | 32.16 | 27.0 |
| 39775 UGC07393 | 130.8417 | 58.5532 | 58.3662 | 8.7931 | 4204 | 4402 | 4.0 | 0.43 | 350 | 2.580 | 12.34 | 12.27 | 13.02 | 13.10 | 13.04 | -21.04 | -21.09 | 34.14 | 67.3 | 34.28 | 71.9 |
| 39794 UGC07387 | 283.6083 | 65.8979 | 110.0100 | -7.1854 | 4969 | 5392 | 6.7 | 0.20 | 252 | 2.401 | 13.09 | 12.86 | 13.43 | 13.51 | 13.54 | -19.41 | -19.35 | 32.98 | 39.4 | 32.88 | 37.6 |
| 39819 UGC07394 | 285.4936 | 63.2879 | 112.6675 | -7.9092 | 1593 | 1954 | 6.6 | 0.20 | 171 | 2.233 | 13.68 | 13.65 | 14.68 | 14.75 | 14.55 | -17.88 | -17.70 | 32.44 | 30.8 | 32.47 | 31.2 |
| 39860 NGC004287 | 282.8270 | 67.3082 | 108.6579 | -6.6529 | 2149 | 2511 | 3.4 | 0.32 | 193 | 2.300 | / | / | 13.83 | 13.91 | / | -18.36 | / | / | / | 32.28 | 28.5 |
| 39886 UGC07403 | 284.3796 | 65.4929 | 110.5267 | -7.1417 | 2539 | 2909 | 5.7 | 0.20 | 353 | 2.548 | 12.35 | 11.96 | 12.29 | 12.33 | 12.51 | -20.74 | -20.78 | 33.28 | 45.3 | 33.14 | 42.4 |
| 39925 UGC07407 | 277.0941 | 72.8524 | 103.0466 | -4.8332 | 347 | 684 | 5.8 | 0.39 | 210 | 2.349 | 11.33 | 11.34 | 12.13 | 12.19 | 12.13 | -18.94 | -18.84 | 31.06 | 16.3 | 31.03 | 16.1 |
| 40023 E380-019 | 296.2617 | 26.6979 | 149.9595 | -15.6836 | 2935 | 3274 | 5.8 | 0.20 | 455 | 2.658 | 10.99 | 10.39 | 11.21 | 11.23 | 11.16 | -21.75 | -21.85 | 32.93 | 38.6 | 33.11 | 41.9 |
| 40033 NGC04307 | 280.5837 | 70.6313 | 105.4725 | -5.3674 | 1054 | 1399 | 3.2 | 0.25 | 311 | 2.497 | 10.74 | 10.49 | 11.13 | 11.17 | 11.19 | -20.29 | -20.28 | 31.48 | 19.8 | 31.46 | 19.6 |
| 40085 NGC004331 | 125.2041 | 40.8286 | 40.5237 | 13.3244 | 1564 | 1611 | 9.9 | 0.23 | 158 | 2.202 | / | / | 14.12 | 14.19 | / | -17.39 | / | / | / | 31.59 | 20.8 |
| 40095 AGC007442 | 271.3783 | 76.6043 | 99.2786 | -3.3555 | 144 | 471 | 2.0 | 0.27 | 217 | 2.344 | 10.65 | 10.57 | 11.31 | 11.32 | 11.30 | -18.89 | -18.79 | 30.20 | 10.9 | 30.10 | 10.5 |
| 40105 NGC04313 | 277.7436 | 73.2484 | 102.8654 | -4.4331 | 1445 | 1788 | 2.1 | 0.24 | 257 | 2.414 | 10.53 | 10.33 | 11.04 | 11.04 | 11.05 | -19.53 | -19.47 | 30.57 | 13.0 | 30.51 | 12.7 |
| 40119 UGC07447 | 280.7138 | 70.9543 | 105.2388 | -5.1394 | 1252 | 1598 | 5.6 | 0.24 | 303 | 2.485 | 11.60 | 11.35 | 11.66 | 11.71 | 11.90 | -20.18 | -20.17 | 32.08 | 26.1 | 31.88 | 23.8 |
| 40201 AGC007456 | 278.8069 | 72.9069 | 103.3270 | -4.4100 | 1563 | 1907 | 6.1 | 0.20 | 251 | 2.400 | 11.43 | 11.20 | 11.99 | 11.99 | 11.96 | -19.40 | -19.33 | 31.35 | 18.7 | 31.32 | 18.4 |
| 40205 UGC07459 | 195.4608 | 83.5305 | 86.5853 | 0.8201 | 569 | 856 | 6.5 | 0.20 | 149 | 2.173 | 13.64 | 13.67 | 14.36 | 14.43 | 14.41 | -17.34 | -17.12 | 31.75 | 22.4 | 31.55 | 20.4 |
| 40208 ES380-023 | 296.7670 | 25.1525 | 151.6322 | -15.6524 | 2748 | 3079 | 5.9 | 0.20 | 286 | 2.457 | 13.25 | 12.86 | 13.73 | 13.77 | 13.67 | -19.92 | -19.89 | 33.62 | 53.0 | 33.71 | 55.3 |
| 40273 UGC07469 | 283.4767 | 69.0079 | 107.3820 | -5.4964 | 1422 | 1772 | 7.9 | 0.47 | 154 | 2.232 | 12.43 | 12.57 | 13.32 | 13.41 | 13.35 | -17.87 | -17.69 | 31.22 | 17.5 | 31.10 | 16.6 |
| 40284 AGC520051 | 289.6105 | 58.7148 | 117.6800 | -8.4140 | 2017 | 2384 | 4.1 | 0.25 | 382 | 2.587 | 11.20 | 10.84 | 11.33 | 11.37 | 11.47 | -21.10 | -21.16 | 32.58 | 32.8 | 32.54 | 32.3 |
| 40342 NGC004356 | 282.5830 | 70.3258 | 106.1146 | -5.0059 | 1133 | 1478 | 5.8 | 0.24 | 218 | 2.342 | 11.54 | 11.43 | 12.13 | 12.19 | 12.17 | -18.88 | -18.77 | 31.04 | 16.2 | 30.96 | 15.5 |
| 40475 NGC04384 | 131.1093 | 62.2036 | 62.0496 | 8.5067 | 2528 | 2714 | 1.0 | 0.66 | 142 | 2.268 | 12.33 | 12.54 | 12.90 | 13.01 | 13.14 | -18.20 | -18.04 | 31.34 | 18.5 | 31.05 | 16.2 |
| 40507 AGC007503 | 281.9420 | 71.8180 | 104.7726 | -4.3126 | 963 | 1304 | 2.3 | 0.51 | 265 | 2.481 | 10.10 | 10.15 | 11.08 | 11.11 | 10.98 | -20.14 | -20.13 | 31.12 | 16.8 | 31.23 | 17.6 |
| 40530 UGC07510 | 279.4687 | 73.9411 | 102.6335 | -3.6185 | -139 | 193 | 7.4 | 0.21 | 160 | 2.205 | 13.14 | 13.15 | 13.89 | 13.95 | 13.91 | -17.63 | -17.43 | 31.54 | 20.3 | 31.38 | 18.9 |
| 40537 NGC04389 | 136.7308 | 70.7441 | 70.6285 | 6.1758 | 716 | 930 | 4.1 | 0.51 | 154 | 2.243 | 10.87 | 11.04 | 11.54 | 11.58 | 11.67 | -17.97 | -17.80 | 29.65 | 8.5 | 29.38 | 7.5 |
| 40566 UGC07513 | 284.7173 | 69.1735 | 107.4882 | -5.0356 | 991 | 1337 | 6.0 | 0.20 | 281 | 2.449 | 11.80 | 11.52 | 12.01 | 12.05 | 12.15 | -19.84 | -19.81 | 32.00 | 25.1 | 31.86 | 23.6 |
| 40581 AGC007520 | 279.1221 | 74.3354 | 102.2648 | -3.4480 | 2513 | 2865 | 2.8 | 0.25 | 364 | 2.566 | 9.97 | 9.64 | 10.32 | 10.32 | 10.34 | -20.91 | -20.95 | 31.25 | 17.8 | 31.27 | 18.0 |
| 40607 UGC07518 | 284.5764 | 69.5112 | 107.1765 | -4.8938 | 1194 | 1541 | 6.3 | 0.25 | 195 | 2.296 | 12.40 | 12.35 | 12.98 | 13.05 | 13.06 | -18.45 | -18.31 | 31.51 | 20.1 | 31.37 | 18.8 |
| 40621 UGC07522 | 287.4337 | 65.5321 | 111.1572 | -6.0411 | 1427 | 1781 | 5.8 | 0.20 | 308 | 2.489 | 12.23 | 11.90 | 12.38 | 12.42 | 12.53 | -20.21 | -20.20 | 32.75 | 35.4 | 32.64 | 33.7 |
| 40644 UGC07528 | 278.7876 | 74.7856 | 101.8572 | -3.2358 | 239 | 570 | 3.3 | 0.29 | 267 | 2.436 | 10.65 | 10.51 | 10.80 | 10.80 | 11.02 | -19.73 | -19.69 | 30.75 | 14.2 | 30.49 | 12.5 |
| 40649 ES322-009 | 297.5904 | 23.4857 | 153.5019 | -15.3440 | 3571 | 3910 | 3.2 | 0.40 | 202 | 2.333 | 12.38 | 12.32 | 13.03 | 13.11 | 13.08 | -18.79 | -18.68 | 31.87 | 23.7 | 31.80 | 22.9 |
| 40692 NGC04414 | 174.5410 | 83.1818 | 84.5678 | 2.1783 | 714 | 992 | 5.2 | 0.58 | 378 | 2.658 | 9.00 | 9.04 | 9.36 | 9.38 | 9.58 | -21.75 | -21.86 | 31.33 | 18.4 | 31.24 | 17.7 |
| 40775 UGC07549 | 288.5211 | 64.6796 | 112.1300 | -6.0615 | 1693 | 2050 | 4.7 | 0.50 | 177 | 2.301 | 11.37 | 11.50 | 12.01 | 12.05 | 12.14 | -18.50 | -18.36 | 30.63 | 13.4 | 30.41 | 12.1 |
| 40811 AGC007563 | 275.0949 | 77.4389 | 99.2670 | -2.1756 | 2340 | 2682 | 9.9 | 0.53 | 122 | 2.149 | 13.22 | 13.41 | 14.31 | 14.41 | 14.27 | -17.12 | -16.88 | 31.38 | 18.9 | 31.29 | 18.1 |
| 40839 UGC07565 | 282.5832 | 72.7806 | 104.0994 | -3.5959 | 925 | 1263 | 6.0 | 0.20 | 148 | 2.170 | 14.07 | 14.10 | 15.38 | 15.46 | 15.12 | -17.31 | -17.09 | 32.44 | 30.8 | 32.56 | 32.5 |
| 40860 NGC004428 | 292.7510 | 54.2295 | 122.5280 | -8.7842 | 2976 | 3357 | 5.0 | 0.43 | 332 | 2.557 | 11.68 | 11.60 | 11.87 | 11.95 | 12.14 | -20.83 | -20.87 | 32.99 | 39.7 | 32.84 | 37.0 |
| 40987 NGC04445 | 284.6621 | 71.4813 | 105.5357 | -3.7958 | 363 | 700 | 2.1 | 0.20 | 234 | 2.369 | / | / | 12.26 | 12.30 | / | -19.03 | / | / | / | 31.34 | 18.5 |

| PGC Name | l | b | sgl | sgb | v_{hel} | v_{mod} | t | b/a | w_{max} | $\log w_{max}^*$ | I | I* | [3.6] | [3.6]* | $C_{[3.6]}$ | M_C | $M_{[3.6]}$ | μ_C | d_C | $\mu_{[3.6]}$ | $d_{[3.6]}$ |
|-----------------|----------|---------|----------|----------|-----------|-----------|-----|------|-----------|------------------|-------|-------|-------|--------|-------------|--------|-------------|---------|-------|---------------|-------------|
| 40988 NGC04448 | 195.3514 | 84.6652 | 87.1730 | 1.7909 | 663 | 949 | 1.8 | 0.45 | 382 | 2.622 | 9.78 | 9.70 | 10.43 | 10.43 | 10.43 | -21.42 | -21.51 | 31.85 | 23.5 | 31.94 | 24.5 |
| 40993 UGC07590 | 285.3044 | 70.8054 | 106.2181 | -3.9866 | 1119 | 1462 | 4.1 | 0.48 | 162 | 2.258 | 13.20 | 13.34 | 14.12 | 14.21 | 14.13 | -18.10 | -17.94 | 32.24 | 28.1 | 32.15 | 27.0 |
| 41010 E322-017 | 297.9973 | 24.1637 | 152.9148 | -14.8178 | 3405 | 3742 | 5.0 | 0.48 | 147 | 2.215 | 13.90 | 13.97 | 14.95 | 15.05 | 14.86 | -17.71 | -17.52 | 32.59 | 33.0 | 32.59 | 32.9 |
| 41024 NGC004450 | 273.9121 | 78.6422 | 98.2216 | -1.5304 | 1954 | 2287 | 2.4 | 0.67 | 304 | 2.601 | 8.86 | 8.97 | 9.63 | 9.67 | 9.68 | -21.23 | -21.29 | 30.90 | 15.2 | 30.96 | 15.6 |
| 41050 UGC07600 | 285.1224 | 71.3392 | 105.7351 | -3.7495 | 862 | 1202 | 2.4 | 0.63 | 204 | 2.411 | 11.58 | 11.74 | 12.29 | 12.37 | 12.42 | -19.50 | -19.44 | 31.92 | 24.2 | 31.81 | 23.0 |
| 41061 UGC07602 | 278.2452 | 76.7696 | 100.2339 | -2.0849 | 1680 | 2015 | 2.4 | 0.41 | 178 | 2.282 | 11.19 | 11.25 | 11.77 | 11.80 | 11.89 | -18.32 | -18.18 | 30.21 | 11.0 | 29.98 | 9.9 |
| 41150 NGC004462 | 296.3564 | 39.4231 | 137.4610 | -11.8537 | 1792 | 2141 | 2.1 | 0.37 | 378 | 2.601 | / | / | 11.08 | 11.12 | / | / | -21.29 | / | / | 32.43 | 30.6 |
| 41189 UGC07627 | 286.9447 | 70.0158 | 107.1811 | -3.9317 | 2341 | 2698 | 1.4 | 0.69 | 131 | 2.247 | 11.68 | 11.90 | 12.37 | 12.48 | 12.55 | -18.01 | -17.84 | 30.56 | 12.9 | 30.32 | 11.6 |
| 41399 NGC004487 | 294.2353 | 54.4737 | 122.6468 | -7.8931 | 1036 | 1391 | 6.0 | 0.55 | 189 | 2.346 | / | / | 11.36 | 11.44 | / | / | -18.80 | / | / | 30.25 | 11.2 |
| 41472 UGC07669 | 277.9024 | 78.7520 | 98.6615 | -0.8747 | 1508 | 1835 | 6.4 | 0.49 | 182 | 2.310 | 11.25 | 11.35 | 12.17 | 12.21 | 12.14 | -18.58 | -18.45 | 30.72 | 13.9 | 30.66 | 13.6 |
| 41504 AGC007676 | 281.2301 | 77.1653 | 100.3372 | -1.3111 | 2097 | 2435 | 6.0 | 0.69 | 118 | 2.203 | 12.12 | 12.34 | 12.96 | 13.07 | 13.06 | -17.61 | -17.41 | 30.68 | 13.6 | 30.48 | 12.5 |
| 41517 NGC4501 | 282.3310 | 76.5077 | 101.0167 | -1.4954 | 2280 | 2622 | 3.3 | 0.48 | 508 | 2.754 | 8.34 | 8.20 | 8.80 | 8.81 | 8.87 | -22.62 | -22.79 | 31.49 | 19.9 | 31.61 | 20.9 |
| 41555 AGC520071 | 294.6400 | 54.9999 | 122.2468 | -7.4756 | 997 | 1351 | 6.0 | 0.58 | 223 | 2.430 | 10.56 | 10.68 | 11.56 | 11.64 | 11.51 | -19.68 | -19.63 | 31.19 | 17.3 | 31.27 | 18.0 |
| 41599 IC0003474 | 291.6961 | 65.1210 | 112.3603 | -4.6631 | 1734 | 2089 | 6.8 | 0.20 | 136 | 2.134 | 13.37 | 13.45 | 14.47 | 14.56 | 14.36 | -16.98 | -16.73 | 31.34 | 18.5 | 31.29 | 18.1 |
| 41608 UGC07695 | 283.5155 | 76.2110 | 101.4200 | -1.4362 | 168 | 156 | 9.6 | 0.65 | 126 | 2.211 | 12.10 | 12.31 | 12.87 | 12.91 | 12.97 | -17.68 | -17.48 | 30.65 | 13.5 | 30.39 | 12.0 |
| 41618 UGC07694 | 292.7362 | 62.6160 | 114.8285 | -5.3250 | 1125 | 1476 | 6.0 | 0.22 | 298 | 2.476 | 9.45 | 9.17 | 9.81 | 9.85 | 9.87 | -20.09 | -20.07 | 29.96 | 9.8 | 29.92 | 9.6 |
| 41620 UGC007699 | 142.2705 | 78.7971 | 78.7909 | 5.2492 | 498 | 746 | 6.1 | 0.28 | 186 | 2.278 | / | / | 13.16 | 13.18 | / | / | -18.14 | / | / | 31.32 | 18.4 |
| 41639 UGC07697 | 270.4787 | 81.8582 | 95.5541 | -0.3556 | 2534 | 2864 | 5.9 | 0.21 | 217 | 2.338 | 13.84 | 13.69 | 14.67 | 14.73 | 14.56 | -18.83 | -18.72 | 33.43 | 48.5 | 33.50 | 50.2 |
| 41725 AGC520073 | 294.6036 | 57.6984 | 119.7284 | -6.4587 | 1289 | 1644 | 8.8 | 0.20 | 123 | 2.090 | / | / | 15.00 | 15.09 | / | / | -16.30 | / | / | 31.39 | 19.0 |
| 41729 UGC07711 | 288.9356 | 71.5620 | 106.1652 | -2.5935 | 2326 | 2678 | 6.0 | 0.25 | 209 | 2.326 | 11.35 | 11.28 | 12.00 | 12.02 | 12.01 | -18.73 | -18.61 | 30.73 | 14.0 | 30.63 | 13.4 |
| 41755 UGC07714 | 172.6553 | 85.0221 | 85.9310 | 3.4311 | 1175 | 1456 | 5.9 | 0.50 | 140 | 2.201 | 11.70 | 11.88 | 12.59 | 12.68 | 12.64 | -17.59 | -17.39 | 30.23 | 11.1 | 30.07 | 10.3 |
| 41763 UGC07716 | 282.9990 | 77.5442 | 100.2559 | -0.7756 | 2344 | 2684 | 5.2 | 0.68 | 115 | 2.187 | 12.19 | 12.40 | 13.07 | 13.17 | 13.15 | -17.46 | -17.25 | 30.61 | 13.2 | 30.42 | 12.1 |
| 41789 NGC4527 | 292.5933 | 65.1772 | 112.4727 | -4.2987 | 1737 | 2091 | 4.0 | 0.29 | 352 | 2.557 | 9.27 | 9.03 | 9.36 | 9.36 | 9.36 | -20.83 | -20.86 | 30.39 | 12.0 | 30.22 | 11.1 |
| 41811 UGC07726 | 291.0253 | 68.9427 | 108.8133 | -3.1958 | 2005 | 2357 | 9.7 | 0.41 | 181 | 2.290 | 11.05 | 11.13 | 11.80 | 11.89 | 11.87 | -18.40 | -18.26 | 30.27 | 11.3 | 30.15 | 10.7 |
| 41823 NGC4536 | 292.9499 | 64.7299 | 112.9433 | -4.3509 | 1806 | 2161 | 4.3 | 0.37 | 322 | 2.531 | 9.46 | 9.35 | 9.84 | 9.85 | 9.97 | -20.59 | -20.61 | 30.56 | 12.9 | 30.46 | 12.4 |
| 41838 UGC07747 | 126.0913 | 53.4997 | 53.4242 | 11.7779 | 2738 | 2873 | 5.6 | 0.58 | 248 | 2.474 | 11.73 | 11.84 | 12.48 | 12.58 | 12.57 | -20.07 | -20.05 | 32.65 | 33.9 | 32.65 | 33.8 |
| 41955 UGC07758 | 231.8529 | 86.2280 | 90.2949 | 2.5595 | 1352 | 1649 | 7.1 | 0.32 | 118 | 2.086 | 12.51 | 12.71 | 13.57 | 13.67 | 13.54 | -16.55 | -16.27 | 30.09 | 10.4 | 29.94 | 9.7 |
| 41958 UGC07756 | 293.3257 | 65.6106 | 112.2070 | -3.8398 | 1151 | 1498 | 1.5 | 0.36 | 184 | 2.286 | 11.96 | 12.02 | 12.50 | 12.58 | 12.66 | -18.36 | -18.21 | 31.02 | 16.0 | 30.79 | 14.4 |
| 41965 PG0041965 | 296.1325 | 54.7863 | 122.7672 | -6.7575 | 986 | 1338 | 8.0 | 0.40 | 156 | 2.222 | / | / | 13.21 | 13.29 | / | / | -17.60 | / | / | 30.88 | 15.0 |
| 41978 AGC220825 | 286.0865 | 76.7670 | 101.2822 | -0.6295 | 9172 | 9731 | 3.0 | 0.43 | 340 | 2.567 | 14.09 | 13.98 | 9.61 | 9.73 | 12.31 | -20.92 | -20.96 | 33.26 | 44.8 | 30.69 | 13.7 |
| 42002 NGC04559 | 198.4192 | 86.4704 | 88.2896 | 3.2291 | 814 | 1100 | 6.0 | 0.38 | 231 | 2.389 | 9.22 | 9.23 | 10.08 | 10.10 | 10.02 | -19.30 | -19.23 | 29.32 | 7.3 | 29.32 | 7.3 |
| 42038 UGC07772 | 230.7637 | 86.4377 | 90.2110 | 2.7640 | 1226 | 1521 | 3.3 | 0.20 | 500 | 2.699 | 8.25 | 7.70 | 8.42 | 8.43 | 8.42 | -22.12 | -22.25 | 30.54 | 12.8 | 30.68 | 13.7 |
| 42045 UGC07774 | 135.6087 | 76.7501 | 76.6677 | 6.5547 | 523 | 759 | 6.3 | 0.20 | 186 | 2.270 | 13.22 | 13.16 | 14.14 | 14.15 | 14.01 | -18.21 | -18.06 | 32.23 | 27.9 | 32.22 | 27.8 |
| 42081 AGC007784 | 288.2785 | 75.7108 | 102.4564 | -0.7219 | 1120 | 1449 | 9.6 | 0.56 | 100 | 2.073 | 12.11 | 12.33 | 13.38 | 13.42 | 13.23 | -16.42 | -16.14 | 29.65 | 8.5 | 29.56 | 8.2 |
| 42123 ES442-013 | 299.1525 | 34.2747 | 143.1543 | -11.2315 | 1521 | 1853 | 5.9 | 0.38 | 192 | 2.308 | 12.51 | 12.49 | 13.66 | 13.73 | 13.46 | -18.57 | -18.44 | 32.03 | 25.5 | 32.18 | 27.3 |
| 42166 AGC028657 | 299.7928 | 27.2705 | 150.2167 | -12.4950 | 2954 | 3287 | 4.8 | 0.61 | 239 | 2.471 | 12.02 | 12.06 | 12.65 | 12.73 | 12.76 | -20.04 | -20.02 | 32.82 | 36.6 | 32.78 | 35.9 |

| PGC Name | l | b | sgl | sgb | v_{hel} | v_{mod} | t | b/a | w_{mz} | $\log w_{mz}^2$ | I | I* | [3.6] | [3.6]* | $C_{[3.6]}$ | Mc | $M_{[3.6]}$ | μC | dC | $\mu_{[3.6]}$ | $d_{[3.6]}$ |
|-----------------|----------|---------|----------|----------|-----------|-----------|-----|------|----------|-----------------|-------|-------|-------|--------|-------------|--------|-------------|---------|-------|---------------|-------------|
| 42230 UGC07802 | 293.1725 | 70.5149 | 107.7228 | -1.8403 | 1786 | 2131 | 6.1 | 0.20 | 150 | 2.176 | 13.39 | 13.41 | 14.28 | 14.36 | 14.24 | -17.36 | -17.15 | 31.60 | 20.9 | 31.50 | 20.0 |
| 42245 E322-040 | 300.2599 | 22.4367 | 155.1416 | -13.1953 | 3348 | 3673 | 3.8 | 0.68 | 248 | 2.520 | / | / | 12.74 | 12.82 | / | / | -20.51 | / | / | 33.37 | 47.3 |
| 42336 UGC07819 | 296.4247 | 62.1865 | 115.8991 | -3.9232 | 1070 | 1418 | 8.0 | 0.29 | 191 | 2.292 | 11.06 | 11.06 | 12.03 | 12.05 | 11.91 | -18.42 | -18.28 | 30.33 | 11.6 | 30.33 | 11.6 |
| 42348 AGC007822 | 293.9222 | 70.6255 | 107.7258 | -1.5675 | 2072 | 2420 | 9.9 | 0.47 | 103 | 2.059 | 13.47 | 13.70 | 14.72 | 14.83 | 14.61 | -16.30 | -16.01 | 30.92 | 15.2 | 30.83 | 14.7 |
| 42369 NGC4603A | 300.5155 | 22.0765 | 155.5554 | -13.0427 | 3672 | 4002 | 5.1 | 0.40 | 270 | 2.460 | 12.23 | 12.01 | 12.43 | 12.49 | 12.62 | -19.95 | -19.92 | 32.58 | 32.8 | 32.43 | 30.6 |
| 42396 UGC07826 | 289.5386 | 77.8674 | 100.7120 | 0.5784 | 631 | 951 | 3.8 | 0.68 | 131 | 2.242 | 11.55 | 11.75 | 12.46 | 12.50 | 12.49 | -17.96 | -17.78 | 30.45 | 12.3 | 30.29 | 11.4 |
| 42407 NGC004594 | 298.4607 | 51.1493 | 126.6907 | -6.6799 | 1095 | 1444 | 1.1 | 0.44 | 733 | 2.903 | 6.61 | 6.31 | 7.44 | 7.43 | 7.22 | -23.98 | -24.25 | 31.20 | 17.4 | 31.68 | 21.7 |
| 42475 UGC007844 | 123.9542 | 43.3883 | 43.2170 | 14.0757 | 1825 | 1887 | 6.1 | 0.20 | 125 | 2.097 | / | / | 15.43 | 15.53 | / | / | -16.37 | / | / | 31.90 | 24.0 |
| 42476 NGC004602 | 297.8936 | 57.6333 | 120.4318 | -4.8431 | 2536 | 2902 | 4.2 | 0.43 | 404 | 2.643 | 10.72 | 10.60 | 10.97 | 11.04 | 11.19 | -21.61 | -21.70 | 32.81 | 36.4 | 32.76 | 35.7 |
| 42510 NGC04603 | 300.7932 | 21.8518 | 155.8373 | -12.8394 | 2594 | 2903 | 5.0 | 0.65 | 353 | 2.658 | 10.31 | 10.18 | 10.62 | 10.68 | 10.79 | -21.75 | -21.85 | 32.55 | 32.4 | 32.56 | 32.4 |
| 42520 UGC07848 | 124.8992 | 53.5686 | 53.5678 | 12.4758 | 2499 | 2629 | 5.9 | 0.41 | 264 | 2.453 | 12.77 | 12.76 | 13.70 | 13.78 | 13.63 | -19.88 | -19.85 | 33.54 | 51.0 | 33.69 | 54.6 |
| 42544 AGC007843 | 293.4839 | 74.5700 | 104.0798 | -0.0553 | 2270 | 2612 | 4.0 | 0.20 | 170 | 2.230 | 11.82 | 11.78 | 11.91 | 11.93 | 12.23 | -17.86 | -17.68 | 30.08 | 10.4 | 29.61 | 8.4 |
| 42640 NGC4603D | 301.0337 | 22.0167 | 155.7207 | -12.5864 | 2712 | 3023 | 6.9 | 0.62 | 235 | 2.469 | 12.05 | 11.96 | 12.50 | 12.57 | 12.63 | -20.03 | -20.01 | 32.67 | 34.1 | 32.59 | 33.0 |
| 42689 NGC04632 | 298.0748 | 62.7052 | 115.6844 | -3.0256 | 1724 | 2075 | 5.1 | 0.39 | 216 | 2.361 | 10.90 | 10.92 | 11.43 | 11.51 | 11.58 | -19.05 | -18.96 | 30.62 | 13.3 | 30.46 | 12.4 |
| 42692 NGC004629 | 298.2786 | 61.4409 | 116.9075 | -3.3667 | 1110 | 1456 | 9.2 | 0.69 | 149 | 2.305 | / | / | 14.08 | 14.17 | / | / | -18.40 | / | / | 32.59 | 32.9 |
| 42726 UGC07877 | 208.1721 | 89.3639 | 89.3639 | 4.4980 | 5913 | 6296 | 3.0 | 0.28 | 321 | 2.515 | 13.99 | 13.78 | 14.40 | 14.48 | 14.49 | -20.45 | -20.46 | 35.03 | 101.4 | 35.08 | 103.8 |
| 42765 UGC07890 | 194.9128 | 88.0570 | 88.9539 | 4.6796 | 7523 | 7963 | 4.0 | 0.71 | 233 | 2.513 | 13.65 | 13.82 | 14.30 | 14.43 | 14.49 | -20.43 | -20.43 | 35.01 | 100.3 | 35.00 | 100.1 |
| 42791 UGC07893 | 298.5717 | 62.1589 | 116.2772 | -2.9944 | 2644 | 3008 | 3.9 | 0.31 | 295 | 2.482 | 12.30 | 12.14 | 12.90 | 12.97 | 12.91 | -20.15 | -20.14 | 33.08 | 41.4 | 33.14 | 42.4 |
| 42818 UGC07908 | 123.6905 | 43.5036 | 43.3518 | 14.2570 | 1667 | 1727 | 5.9 | 0.24 | 131 | 2.121 | / | / | 14.44 | 14.53 | / | / | -16.61 | / | / | 31.14 | 16.9 |
| 42833 UGC07901 | 293.0690 | 79.1168 | 99.9134 | 1.7692 | 801 | 1117 | 5.2 | 0.64 | 364 | 2.668 | 9.69 | 9.77 | 10.35 | 10.37 | 10.43 | -21.84 | -21.95 | 32.28 | 28.5 | 32.33 | 29.3 |
| 42857 UGC07902 | 295.4274 | 75.8890 | 103.0717 | 0.9288 | 1042 | 1367 | 5.9 | 0.54 | 282 | 2.515 | 9.55 | 9.60 | 10.10 | 10.12 | 10.22 | -20.45 | -20.46 | 30.67 | 13.6 | 30.58 | 13.1 |
| 42863 NGC004656 | 140.3366 | 84.7033 | 84.6810 | 6.0192 | 648 | 913 | 9.0 | 0.20 | 135 | 2.130 | 10.48 | 10.58 | 11.75 | 11.83 | 11.56 | -16.95 | -16.70 | 28.50 | 5.0 | 28.53 | 5.1 |
| 42880 E381-014 | 301.3000 | 26.3377 | 151.4644 | -11.4043 | 3303 | 3637 | 4.2 | 0.22 | 213 | 2.330 | 13.83 | 13.63 | 14.47 | 14.54 | 14.44 | -18.76 | -18.65 | 33.23 | 44.2 | 33.22 | 44.1 |
| 42929 AGC520135 | 300.1626 | 52.7521 | 125.4891 | -5.1832 | 2396 | 2757 | 4.0 | 0.50 | 254 | 2.460 | 11.58 | 11.60 | 12.08 | 12.16 | 12.24 | -19.95 | -19.92 | 32.19 | 27.5 | 32.08 | 26.1 |
| 42975 UGC07926 | 299.5378 | 62.3684 | 116.2267 | -2.5009 | 1517 | 1865 | 5.1 | 0.30 | 379 | 2.590 | 9.46 | 9.21 | 9.30 | 9.35 | 9.65 | -21.13 | -21.19 | 30.78 | 14.3 | 30.54 | 12.8 |
| 42999 UGC07931 | 299.7549 | 62.3002 | 116.3236 | -2.4272 | 1616 | 1965 | 7.4 | 0.55 | 147 | 2.236 | 12.28 | 12.46 | 13.21 | 13.30 | 13.24 | -17.90 | -17.73 | 31.14 | 16.9 | 31.03 | 16.1 |
| 43001 UGC07932 | 296.9244 | 76.1345 | 102.9800 | 1.3563 | 965 | 1288 | 5.0 | 0.38 | 161 | 2.231 | 12.84 | 12.93 | 13.96 | 13.99 | 13.81 | -17.86 | -17.68 | 31.68 | 21.7 | 31.68 | 21.6 |
| 43020 PG0043020 | 300.3234 | 56.7701 | 121.6767 | -3.8755 | 1476 | 1826 | 8.9 | 0.71 | 143 | 2.299 | / | / | 12.69 | 12.78 | / | / | -18.34 | / | / | 31.13 | 16.8 |
| 43052 UGC07941 | 123.8893 | 52.5489 | 52.6005 | 13.1961 | 2300 | 2420 | 7.0 | 0.24 | 224 | 2.354 | 13.43 | 13.31 | 14.85 | 14.92 | 14.46 | -18.98 | -18.89 | 33.47 | 49.5 | 33.87 | 59.4 |
| 43073 NGC04672 | 301.8959 | 21.1553 | 156.7532 | -11.9806 | 3254 | 3569 | 1.1 | 0.56 | 353 | 2.621 | 11.94 | 11.78 | 12.02 | 12.08 | 12.30 | -21.41 | -21.49 | 33.75 | 56.2 | 33.62 | 53.0 |
| 43118 NGC04680 | 301.1626 | 51.2195 | 127.1416 | -5.0454 | 2429 | 2789 | 1.0 | 0.63 | 186 | 2.370 | 11.57 | 11.70 | 12.12 | 12.17 | 12.30 | -19.13 | -19.04 | 31.43 | 19.3 | 31.21 | 17.5 |
| 43142 UGC07955 | 236.3811 | 88.9671 | 90.1625 | 5.2998 | 6759 | 7171 | 5.8 | 0.20 | 361 | 2.558 | 13.60 | 13.20 | 13.76 | 13.83 | 13.88 | -20.83 | -20.87 | 34.79 | 90.8 | 34.82 | 92.0 |
| 43164 AGC221022 | 192.2078 | 89.0593 | 89.4557 | 5.5507 | 6615 | 7018 | 1.8 | 0.54 | 224 | 2.417 | 13.06 | 13.17 | 13.15 | 13.28 | 13.60 | -19.56 | -19.50 | 33.18 | 43.2 | 32.80 | 36.3 |
| 43170 NGC04679 | 302.1066 | 23.2947 | 154.6565 | -11.3496 | 4646 | 4999 | 4.8 | 0.40 | 398 | 2.630 | 11.49 | 11.24 | 11.78 | 11.85 | 11.91 | -21.49 | -21.58 | 33.43 | 48.5 | 33.47 | 49.5 |
| 43254 UGC07970 | 300.5688 | 71.3452 | 107.8325 | 0.7106 | 1010 | 1341 | 1.7 | 0.58 | 419 | 2.702 | 9.37 | 9.38 | 10.10 | 10.12 | 10.11 | -22.15 | -22.29 | 32.27 | 28.4 | 32.42 | 30.5 |
| 43278 AGC221033 | 262.1075 | 89.0628 | 90.5366 | 5.5496 | 6889 | 7306 | 5.0 | 0.28 | 311 | 2.502 | 13.62 | 13.43 | 13.60 | 13.70 | 13.93 | -20.32 | -20.33 | 34.32 | 73.0 | 34.10 | 66.1 |

| PGC Name | l | b | sgl | sgb | v_{hel} | v_{mod} | t | b/a | w_{max} | $\log w_{max}^2$ | I | I* | [3.6] | [3.6]* | $C_{[3.6]}$ | MC | $M_{[3.6]}$ | μ_C | dC | $\mu_{[3.6]}$ | $d_{[3.6]}$ | |
|-----------------|----------|---------|----------|----------|-----------|-----------|-----|------|-----------|------------------|-------|-------|-------|--------|-------------|--------|-------------|---------|-------|---------------|-------------|------|
| 43330 NGC004700 | 302.0221 | 51.4560 | 127.0650 | -4.4636 | 1410 | 1756 | 4.9 | 0.20 | 124 | 2.093 | 11.35 | 11.44 | 12.18 | 12.26 | 12.21 | -16.61 | -16.34 | 28.82 | 5.8 | 28.60 | 5.3 | |
| 43341 PG0043341 | 301.9036 | 58.8511 | 119.9333 | -2.4583 | 1507 | 1854 | / | 0.49 | 127 | 2.155 | / | / | 14.46 | 14.56 | / | / | -16.94 | / | / | / | 31.49 | 19.9 |
| 43345 PG0043345 | 302.1003 | 52.7486 | 125.8323 | -4.0614 | 1310 | 1655 | 9.0 | 0.47 | 124 | 2.139 | / | / | 12.51 | 12.61 | / | / | -16.78 | / | / | / | 29.39 | 7.5 |
| 43359 UGC007978 | 128.9457 | 86.2615 | 86.2753 | 6.8541 | 8078 | 8526 | 5.9 | 0.63 | 295 | 2.571 | 13.24 | 13.34 | 13.85 | 13.98 | 14.02 | -20.95 | -21.00 | 35.07 | 103.5 | 35.13 | 106.2 | |
| 43397 UGC007982 | 301.9600 | 65.7208 | 113.3542 | -0.4728 | 1157 | 1495 | 4.7 | 0.20 | 217 | 2.336 | 12.02 | 11.85 | 12.57 | 12.63 | 12.60 | -18.82 | -18.71 | 31.42 | 19.2 | 31.34 | 18.5 | |
| 43413 UGC007985 | 301.9451 | 68.1802 | 110.9960 | 0.2255 | 652 | 984 | 6.8 | 0.72 | 159 | 2.351 | 11.05 | 11.25 | 11.79 | 11.83 | 11.90 | -18.96 | -18.86 | 30.86 | 14.8 | 30.68 | 13.7 | |
| 43451 UGC07989 | 295.0800 | 88.3574 | 91.5273 | 5.6948 | 1206 | 1495 | 2.2 | 0.54 | 397 | 2.665 | 8.19 | 8.20 | 8.83 | 8.85 | 8.89 | -21.81 | -21.92 | 30.70 | 13.8 | 30.77 | 14.3 | |
| 43458 PG0043458 | 302.5536 | 52.0166 | 126.6138 | -3.9943 | 2391 | 2748 | 9.0 | 0.34 | 253 | 2.420 | 12.16 | 12.06 | 13.03 | 13.10 | 12.93 | -19.59 | -19.53 | 32.53 | 32.0 | 32.65 | 33.8 | |
| 43470 UGC07991 | 302.4770 | 64.3356 | 114.7448 | -0.6541 | 1270 | 1610 | 6.6 | 0.20 | 177 | 2.248 | 12.85 | 12.80 | 13.57 | 13.64 | 13.57 | -18.02 | -17.85 | 31.59 | 20.8 | 31.48 | 19.8 | |
| 43507 AGC520188 | 302.7447 | 56.4779 | 122.3406 | -2.6838 | 1492 | 1838 | 5.9 | 0.40 | 211 | 2.352 | 10.76 | 10.78 | 11.53 | 11.61 | 11.55 | -18.97 | -18.87 | 30.52 | 12.7 | 30.47 | 12.4 | |
| 43527 UGC08006 | 122.9586 | 45.4916 | 45.4459 | 14.5908 | 1746 | 1817 | 3.0 | 0.25 | 333 | 2.528 | 11.99 | 11.73 | 11.73 | 11.77 | 12.12 | -20.56 | -20.58 | 32.70 | 34.6 | 32.36 | 29.7 | |
| 43575 UGC08004 | 122.3685 | 85.7753 | 85.8852 | 7.3965 | 6187 | 6559 | 6.4 | 0.40 | 285 | 2.483 | 13.63 | 13.58 | 14.38 | 14.48 | 14.39 | -20.16 | -20.14 | 34.62 | 83.9 | 34.74 | 88.9 | |
| 43601 UGC08007 | 303.3862 | 74.9543 | 104.6041 | 2.5195 | 1780 | 2109 | 3.1 | 0.28 | 323 | 2.518 | 11.63 | 11.39 | 11.68 | 11.73 | 11.93 | -20.47 | -20.49 | 32.41 | 30.4 | 32.23 | 27.9 | |
| 43686 UGC08013 | 337.4762 | 89.5410 | 90.4338 | 6.4776 | 7884 | 8337 | 3.0 | 0.28 | 365 | 2.571 | 13.75 | 13.49 | 14.44 | 14.54 | 14.37 | -20.96 | -21.00 | 35.44 | 122.4 | 35.74 | 140.4 | |
| 43707 UGC08014 | 304.5304 | 78.7142 | 101.0234 | 3.7112 | 1243 | 1558 | 9.1 | 0.20 | 178 | 2.250 | 11.75 | 11.69 | 12.43 | 12.50 | 12.46 | -18.04 | -17.87 | 30.49 | 12.6 | 30.37 | 11.9 | |
| 43717 E323-027 | 303.2208 | 22.4194 | 155.7418 | -10.5222 | 3846 | 4174 | 5.0 | 0.52 | 322 | 2.569 | 11.70 | 11.59 | 12.10 | 12.17 | 12.24 | -20.94 | -20.98 | 33.20 | 43.7 | 33.19 | 43.5 | |
| 43726 UGC08017 | 108.4940 | 88.7162 | 88.8676 | 6.9387 | 7065 | 7479 | 2.2 | 0.36 | 521 | 2.738 | 12.61 | 12.35 | 12.55 | 12.63 | 12.86 | -22.48 | -22.64 | 35.46 | 123.3 | 35.44 | 122.4 | |
| 43744 NGC4767A | 303.2629 | 23.0354 | 155.1357 | -10.3618 | 2913 | 3225 | 6.0 | 0.46 | 224 | 2.393 | / | / | 13.91 | 13.98 | / | / | -19.26 | / | / | / | 33.28 | 45.3 |
| 43840 P0043840 | 106.9820 | 88.0735 | 88.3247 | 7.2917 | 7938 | 8385 | 6.0 | 0.43 | 286 | 2.491 | 14.15 | 14.13 | 14.56 | 14.68 | 14.76 | -20.23 | -20.22 | 35.09 | 104.3 | 35.04 | 101.8 | |
| 43863 UGC08025 | 110.0590 | 87.4592 | 87.7232 | 7.4805 | 6317 | 6698 | 3.2 | 0.20 | 505 | 2.703 | 12.56 | 11.99 | 12.68 | 12.72 | 12.72 | -22.16 | -22.30 | 34.97 | 98.5 | 35.17 | 108.0 | |
| 43902 NGC004781 | 304.1218 | 52.3279 | 126.5615 | -2.9849 | 1260 | 1602 | 7.0 | 0.45 | 226 | 2.395 | 10.46 | 10.47 | 10.96 | 11.03 | 11.11 | -19.36 | -19.29 | 30.47 | 12.4 | 30.32 | 11.6 | |
| 43931 NGC04800 | 121.2803 | 70.5870 | 70.9961 | 11.2668 | 889 | 1088 | 3.0 | 0.71 | 291 | 2.607 | / | / | 10.85 | 10.94 | / | / | -21.36 | / | / | / | 32.31 | 29.0 |
| 43939 NGC004793 | 101.5728 | 88.0546 | 88.4087 | 7.4554 | 2484 | 2773 | 5.1 | 0.52 | 315 | 2.557 | 10.85 | 10.88 | 11.08 | 11.16 | 11.39 | -20.83 | -20.87 | 32.22 | 27.8 | 32.03 | 25.5 | |
| 43961 UGC08036 | 308.6706 | 82.0116 | 97.9269 | 5.0555 | 920 | 1223 | 5.8 | 0.37 | 203 | 2.331 | 12.70 | 12.73 | 13.65 | 13.72 | 13.58 | -18.77 | -18.65 | 32.36 | 29.6 | 32.39 | 30.1 | |
| 43970 PG0043970 | 304.2574 | 50.9704 | 127.8999 | -3.2378 | 2469 | 2824 | 7.9 | 0.20 | 172 | 2.236 | / | / | 14.58 | 14.65 | / | / | -17.73 | / | / | / | 32.39 | 30.0 |
| 43975 UGC08052 | 122.5857 | 43.9477 | 43.8851 | 15.0110 | 1543 | 1603 | 4.7 | 0.24 | 221 | 2.348 | / | / | 13.41 | 13.48 | / | / | -18.83 | / | / | / | 32.32 | 29.0 |
| 43994 AGC28979 | 303.6608 | 21.8960 | 156.3445 | -10.2248 | 4202 | 4535 | 4.2 | 0.33 | 279 | 2.461 | 12.23 | 11.99 | 12.57 | 12.64 | 12.67 | -19.96 | -19.93 | 32.64 | 33.8 | 32.59 | 32.9 | |
| 44014 UGC08041 | 305.0081 | 62.9732 | 116.3512 | 0.0784 | 1324 | 1663 | 6.9 | 0.47 | 179 | 2.299 | 11.30 | 11.42 | 12.52 | 12.56 | 12.34 | -18.48 | -18.35 | 30.82 | 14.6 | 30.91 | 15.2 | |
| 44025 UGC08051 | 121.9379 | 58.7766 | 59.0957 | 13.3699 | 2507 | 2661 | 3.1 | 0.62 | 338 | 2.628 | 10.84 | 10.93 | 11.50 | 11.59 | 11.62 | -21.47 | -21.56 | 33.12 | 42.0 | 33.18 | 43.3 | |
| 44086 UGC08054 | 305.7439 | 67.1520 | 112.3602 | 1.3563 | 760 | 1090 | 5.9 | 0.38 | 251 | 2.425 | 10.97 | 10.92 | 11.34 | 11.40 | 11.52 | -19.62 | -19.57 | 31.15 | 17.0 | 30.97 | 15.6 | |
| 44147 AGC221130 | 41.5015 | 88.8682 | 90.1167 | 7.4459 | 7526 | 7960 | 6.6 | 0.69 | 181 | 2.387 | 13.97 | 14.17 | 14.67 | 14.81 | 14.85 | -19.29 | -19.21 | 34.19 | 68.9 | 34.10 | 65.9 | |
| 44182 UGC08062 | 315.6839 | 84.4222 | 95.6076 | 6.1261 | 410 | 702 | 2.3 | 0.53 | 305 | 2.547 | 7.31 | 7.31 | 7.91 | 7.93 | 7.98 | -20.74 | -20.77 | 28.72 | 5.6 | 28.70 | 5.5 | |
| 44191 NGC04818 | 305.2119 | 54.3227 | 124.7811 | -1.8719 | 1064 | 1403 | 2.0 | 0.35 | 253 | 2.423 | 10.05 | 9.98 | 10.47 | 10.54 | 10.62 | -19.61 | -19.56 | 30.23 | 11.1 | 30.10 | 10.4 | |
| 44254 UGC08067 | 305.9166 | 61.1316 | 118.2413 | 0.0638 | 2843 | 3201 | 3.7 | 0.27 | 293 | 2.475 | 12.54 | 12.36 | 12.92 | 12.98 | 13.03 | -20.08 | -20.06 | 33.13 | 42.3 | 33.08 | 41.2 | |
| 44278 PG0044278 | 305.6306 | 57.4951 | 121.7489 | -0.9072 | 1257 | 1597 | 7.9 | 0.66 | 136 | 2.249 | / | / | 13.89 | 13.99 | / | / | -17.86 | / | / | / | 31.85 | 23.4 |
| 44358 PG0044358 | 305.5424 | 53.2059 | 125.9134 | -1.9407 | 1482 | 1823 | 6.7 | 0.20 | 240 | 2.380 | / | / | 12.50 | 12.55 | / | / | -19.14 | / | / | / | 31.69 | 21.8 |

| PGC Name | l | b | sgl | sgb | v_{hel} | v_{mod} | t | b/a | w_{mz} | $\log w_{mz}^2$ | I | I* | [3.6] | [3.6]* | $C_{[3.6]}$ | MC | $M_{[3.6]}$ | μC | dC | $\mu_{[3.6]}$ | $d_{[3.6]}$ |
|-----------------|----------|---------|----------|----------|-----------|-----------|-----|------|----------|-----------------|-------|-------|-------|--------|-------------|--------|-------------|---------|-------|---------------|-------------|
| 44392 UGC08078 | 306.7409 | 64.3989 | 115.1364 | 1.1493 | 1098 | 1432 | 2.3 | 0.25 | 375 | 2.579 | 9.83 | 9.51 | 10.27 | 10.31 | 10.27 | -21.03 | -21.08 | 31.30 | 18.2 | 31.39 | 19.0 |
| 44416 AGC221206 | 80.1192 | 87.8320 | 88.8155 | 8.1419 | 7619 | 8050 | 4.2 | 0.31 | 260 | 2.428 | 13.62 | 13.53 | 13.95 | 14.06 | 14.16 | -19.66 | -19.61 | 33.86 | 59.1 | 33.73 | 55.6 |
| 44432 UGC08085 | 310.5090 | 77.3277 | 102.6226 | 4.6663 | 2041 | 2363 | 5.8 | 0.20 | 220 | 2.342 | 12.81 | 12.64 | 13.57 | 13.63 | 13.49 | -18.88 | -18.77 | 32.37 | 29.8 | 32.41 | 30.3 |
| 44506 PG0044506 | 306.2724 | 56.7117 | 122.5907 | -0.7438 | 1600 | 1947 | 7.9 | 0.21 | 138 | 2.141 | / | / | 14.45 | 14.54 | / | -16.80 | / | / | / | 31.34 | 18.5 |
| 44663 AGC029082 | 305.0960 | 33.2366 | 145.3750 | -6.6841 | 2813 | 3147 | 5.7 | 0.28 | 327 | 2.523 | 12.76 | 12.43 | 12.53 | 12.58 | 12.87 | -20.52 | -20.53 | 33.42 | 48.4 | 33.14 | 42.5 |
| 44795 UGC08118 | 76.3778 | 87.2226 | 88.6377 | 8.7470 | 7289 | 7704 | 4.2 | 0.47 | 368 | 2.611 | 12.89 | 12.84 | 13.41 | 13.53 | 13.55 | -21.32 | -21.39 | 34.95 | 97.8 | 35.06 | 102.7 |
| 44846 UGC08121 | 308.1459 | 62.7476 | 116.8804 | 1.4272 | 1173 | 1506 | 5.8 | 0.66 | 179 | 2.367 | 11.06 | 11.24 | 11.78 | 11.88 | 11.92 | -19.10 | -19.01 | 31.02 | 16.0 | 30.88 | 15.0 |
| 44921 UGC08140 | 73.7197 | 87.0307 | 88.6662 | 8.9789 | 7091 | 7498 | 2.0 | 0.29 | 467 | 2.680 | 12.88 | 12.54 | 13.23 | 13.31 | 13.28 | -21.95 | -22.07 | 35.34 | 116.9 | 35.56 | 129.2 |
| 44961 UGC08146 | 120.2832 | 58.3731 | 58.8520 | 14.2924 | 666 | 799 | 6.4 | 0.20 | 158 | 2.199 | 13.07 | 13.10 | 14.25 | 14.32 | 14.06 | -17.57 | -17.37 | 31.63 | 21.2 | 31.69 | 21.8 |
| 44966 ES381-051 | 305.5078 | 29.6977 | 148.9368 | -7.0616 | 5021 | 5394 | 3.7 | 0.22 | 430 | 2.635 | 12.43 | 11.90 | 12.13 | 12.17 | 12.40 | -21.54 | -21.63 | 33.99 | 62.9 | 33.86 | 59.3 |
| 44982 PG0044982 | 306.6163 | 45.5567 | 133.5362 | -2.9385 | 750 | 1078 | 9.7 | 0.62 | 104 | 2.114 | / | / | 14.91 | 14.94 | / | -16.53 | / | / | / | 31.47 | 19.7 |
| 44992 ES219-021 | 304.7155 | 12.5000 | 165.9342 | -10.8800 | 1375 | 1625 | 6.8 | 0.27 | 233 | 2.375 | 11.34 | 10.98 | 11.83 | 11.86 | 11.77 | -19.17 | -19.09 | 30.95 | 15.5 | 30.95 | 15.5 |
| 45097 UGC08161 | 21.4753 | 87.2513 | 91.2143 | 8.7911 | 6675 | 7073 | 2.3 | 0.43 | 355 | 2.586 | 13.19 | 13.11 | 13.48 | 13.59 | 13.72 | -21.09 | -21.15 | 34.89 | 95.2 | 34.86 | 93.7 |
| 45098 ES443-042 | 306.0491 | 32.9700 | 145.8018 | -5.9571 | 2909 | 3241 | 3.0 | 0.20 | 365 | 2.562 | 11.81 | 11.30 | 12.04 | 12.07 | 12.05 | -20.88 | -20.92 | 32.94 | 38.7 | 33.02 | 40.2 |
| 45137 UGC08166 | 313.7901 | 73.5813 | 106.4515 | 5.0514 | 2942 | 3281 | 6.0 | 0.20 | 159 | 2.201 | 15.12 | 15.13 | 16.22 | 16.30 | 16.06 | -17.59 | -17.39 | 33.70 | 54.8 | 33.75 | 56.3 |
| 45170 AGC530010 | 308.0967 | 52.4039 | 127.0241 | -0.6013 | 3110 | 3469 | 4.0 | 0.54 | 444 | 2.713 | 10.21 | 10.15 | 10.70 | 10.78 | 10.82 | -22.25 | -22.39 | 33.10 | 41.6 | 33.21 | 43.8 |
| 45190 AGC230051 | 37.1607 | 87.1034 | 90.5198 | 9.1705 | 5499 | 5855 | 4.3 | 0.60 | 156 | 2.281 | 14.43 | 14.63 | 15.28 | 15.40 | 15.37 | -18.32 | -18.17 | 33.73 | 55.8 | 33.63 | 53.2 |
| 45224 NGC004948 | 308.7311 | 54.7720 | 124.7705 | 0.2180 | 1353 | 1688 | 7.3 | 0.34 | 139 | 2.162 | 12.05 | 12.14 | 12.80 | 12.88 | 12.87 | -17.23 | -17.00 | 30.10 | 10.5 | 29.88 | 9.5 |
| 45241 AGC029208 | 307.0734 | 40.3781 | 138.6822 | -3.6708 | 2542 | 2881 | 3.3 | 0.33 | 214 | 2.346 | 13.10 | 12.94 | 13.53 | 13.59 | 13.63 | -18.91 | -18.81 | 32.55 | 32.3 | 32.41 | 30.3 |
| 45311 UGC08185 | 44.5195 | 86.7578 | 90.1634 | 9.5582 | 2533 | 2819 | 5.6 | 0.66 | 209 | 2.437 | 12.36 | 12.54 | 13.13 | 13.23 | 13.25 | -19.74 | -19.69 | 33.00 | 39.8 | 32.96 | 39.0 |
| 45484 UGC08209 | 1.4776 | 85.6699 | 93.1494 | 9.3229 | 6343 | 6732 | 3.0 | 0.64 | 227 | 2.460 | 12.84 | 12.98 | 13.33 | 13.46 | 13.58 | -19.95 | -19.92 | 33.56 | 51.6 | 33.42 | 48.3 |
| 45487 ES508-011 | 307.8284 | 39.8588 | 139.3051 | -3.2057 | 2610 | 2947 | 6.6 | 0.20 | 230 | 2.362 | 12.61 | 12.28 | 13.26 | 13.31 | 13.15 | -19.05 | -18.96 | 32.21 | 27.6 | 32.28 | 28.5 |
| 45524 ES575-061 | 308.1916 | 41.6984 | 137.5486 | -2.5877 | 1649 | 1976 | 7.0 | 0.20 | 153 | 2.185 | 14.56 | 14.45 | 14.41 | 14.47 | 14.84 | -17.44 | -17.23 | 32.29 | 28.7 | 31.71 | 21.9 |
| 45549 UGC08220 | 1.5964 | 85.4555 | 93.3000 | 9.4777 | 7131 | 7549 | 4.1 | 0.20 | 524 | 2.719 | 12.78 | 12.19 | 12.90 | 12.95 | 12.93 | -22.31 | -22.45 | 35.35 | 117.3 | 35.58 | 130.7 |
| 45552 UGC08219 | 336.5859 | 82.7741 | 96.9002 | 8.6474 | 2618 | 2924 | 3.8 | 0.41 | 235 | 2.403 | 13.01 | 13.01 | 13.73 | 13.82 | 13.77 | -19.43 | -19.36 | 33.22 | 44.1 | 33.22 | 44.0 |
| 45563 AGC029277 | 306.3902 | 21.2947 | 157.4132 | -7.8398 | 3126 | 3427 | 4.9 | 0.55 | 114 | 2.126 | 12.85 | 12.93 | 13.52 | 13.61 | 13.63 | -16.91 | -16.66 | 30.54 | 12.8 | 30.27 | 11.3 |
| 45574 NGC4981 | 310.6281 | 55.8344 | 123.9097 | 1.4644 | 1678 | 2013 | 4.0 | 0.69 | 244 | 2.521 | 10.40 | 10.53 | 11.04 | 11.13 | 11.19 | -20.50 | -20.51 | 31.69 | 21.8 | 31.64 | 21.3 |
| 45580 UGC08229 | 49.2052 | 85.9914 | 89.8696 | 10.3266 | 5989 | 6354 | 3.1 | 0.52 | 342 | 2.595 | 12.65 | 12.67 | 13.09 | 13.20 | 13.30 | -21.18 | -21.24 | 34.54 | 81.0 | 34.54 | 81.0 |
| 45596 NGC004980 | 307.6288 | 34.0684 | 144.9747 | -4.4530 | 1428 | 1739 | 1.1 | 0.47 | 158 | 2.243 | 12.26 | 12.33 | 13.27 | 13.35 | 13.19 | -17.97 | -17.80 | 31.16 | 17.1 | 31.15 | 17.0 |
| 45643 NGC04995 | 310.7774 | 54.7604 | 124.9840 | 1.3791 | 1743 | 2078 | 3.1 | 0.71 | 284 | 2.595 | 10.17 | 10.28 | 10.70 | 10.79 | 10.90 | -21.17 | -21.24 | 32.08 | 26.0 | 32.03 | 25.5 |
| 45666 ES508-019 | 308.2950 | 38.4399 | 140.7689 | -3.1158 | 2929 | 3268 | 8.8 | 0.33 | 235 | 2.387 | 12.95 | 12.74 | 13.84 | 13.89 | 13.67 | -19.28 | -19.21 | 32.97 | 39.3 | 33.14 | 42.4 |
| 45668 UGC08244 | 51.0924 | 85.7342 | 89.7185 | 10.5768 | 7101 | 7505 | 6.4 | 0.37 | 238 | 2.400 | 14.23 | 14.23 | 15.13 | 15.25 | 15.09 | -19.40 | -19.33 | 34.57 | 81.9 | 34.70 | 86.9 |
| 45683 ES269-057 | 306.2755 | 16.3137 | 162.3579 | -8.7798 | 3107 | 3390 | 1.7 | 0.58 | 322 | 2.588 | / | / | 10.98 | 11.06 | / | -21.17 | / | / | / | 32.24 | 28.0 |
| 45684 UGC08246 | 94.4777 | 81.8903 | 83.9393 | 11.7951 | 808 | 1051 | 5.9 | 0.20 | 128 | 2.107 | 13.12 | 13.25 | 14.28 | 14.37 | 14.16 | -16.74 | -16.47 | 30.90 | 15.1 | 30.84 | 14.7 |
| 45721 AGC029327 | 308.8209 | 40.9044 | 138.4167 | -2.2690 | 2959 | 3301 | 6.7 | 0.37 | 218 | 2.362 | 12.68 | 12.56 | 13.47 | 13.54 | 13.40 | -19.05 | -18.96 | 32.46 | 31.1 | 32.51 | 31.7 |
| 45728 NGC05002 | 100.9613 | 79.6612 | 81.4966 | 12.3668 | 1081 | 1315 | 9.0 | 0.51 | 104 | 2.074 | / | / | 14.18 | 14.28 | / | -16.14 | / | / | / | 30.42 | 12.2 |

| PGC Name | l | b | sgl | sgb | v_{hel} | v_{mod} | t | b/a | w_{max} | $\log w_{max}^i$ | I | I* | [3.6] | [3.6]* | C _[3.6] | MC | M _[3.6] | μ_C | d _C | $\mu_{[3.6]}$ | d _[3.6] | |
|-----------------|----------|---------|----------|---------|-----------|-----------|-----|------|-----------|------------------|-------|-------|-------|--------|--------------------|--------|--------------------|---------|----------------|---------------|--------------------|------|
| 45742 AGC230139 | 65.3082 | 85.0233 | 88.4400 | 11.0519 | 6367 | 6738 | 3.3 | 0.65 | 227 | 2.466 | 13.60 | 13.76 | 14.25 | 14.38 | 14.43 | -20.00 | -19.98 | 34.50 | 79.6 | 34.46 | 77.9 | |
| 45749 NGC5005 | 101.6137 | 79.2490 | 81.0799 | 12.5029 | 940 | 1172 | 4.0 | 0.43 | 535 | 2.764 | 8.52 | 8.35 | 9.03 | 9.02 | 9.05 | -22.71 | -22.89 | 31.76 | 22.5 | 31.92 | 24.2 | |
| 45757 NGC5004A | 63.6929 | 85.0430 | 88.5820 | 11.0748 | 7267 | 7672 | 2.3 | 0.42 | 336 | 2.560 | 12.78 | 12.72 | 13.09 | 13.20 | 13.32 | -20.85 | -20.89 | 34.23 | 70.2 | 34.17 | 68.4 | |
| 45772 ES576-005 | 309.3080 | 42.7953 | 136.6195 | -1.5757 | 2733 | 3073 | 8.0 | 0.23 | 270 | 2.434 | / | / | 14.33 | 14.38 | / | / | / | / | / | / | 34.12 | 66.8 |
| 45787 UGC08271 | 99.2032 | 79.9030 | 81.8844 | 12.4774 | 1142 | 1378 | 1.4 | 0.31 | 116 | 2.077 | 11.97 | 12.18 | 12.51 | 12.60 | 12.75 | -16.46 | -16.18 | 29.21 | 7.0 | 28.78 | 5.7 | |
| 45795 UGC08270 | 351.3629 | 83.7849 | 95.2257 | 9.7642 | 2609 | 2908 | 5.1 | 0.53 | 393 | 2.657 | 10.72 | 10.71 | 11.26 | 11.30 | 11.37 | -21.74 | -21.85 | 33.13 | 42.2 | 33.18 | 43.2 | |
| 45807 UGC08282 | 118.3175 | 56.6977 | 57.3830 | 15.6730 | 2064 | 2196 | 5.9 | 0.36 | 191 | 2.302 | 14.07 | 14.13 | 15.02 | 15.11 | 14.98 | -18.51 | -18.38 | 33.52 | 50.6 | 33.53 | 50.9 | |
| 45847 NGC5011A | 306.9268 | 19.4032 | 159.3805 | -7.6636 | 3177 | 3471 | 4.8 | 0.53 | 237 | 2.437 | 12.30 | 12.21 | 12.63 | 12.71 | 12.82 | -19.74 | -19.70 | 32.57 | 32.7 | 32.42 | 30.5 | |
| 45848 UGC08280 | 96.8515 | 80.3831 | 82.5258 | 12.4984 | 813 | 1049 | 5.8 | 0.20 | 180 | 2.255 | 12.59 | 12.55 | 13.59 | 13.65 | 13.45 | -18.08 | -17.92 | 31.54 | 20.3 | 31.58 | 20.7 | |
| 45849 UGC08286 | 110.3867 | 72.5811 | 74.0498 | 13.8886 | 408 | 607 | 5.9 | 0.20 | 170 | 2.230 | 11.41 | 11.39 | 12.43 | 12.45 | 12.27 | -17.86 | -17.68 | 30.13 | 10.6 | 30.12 | 10.6 | |
| 45877 P0045877 | 310.0752 | 45.0357 | 134.5065 | -0.6472 | 2760 | 3102 | 4.9 | 0.28 | 363 | 2.569 | 11.16 | 10.82 | 11.23 | 11.27 | 11.41 | -20.94 | -20.99 | 32.36 | 29.6 | 32.27 | 28.4 | |
| 45901 ES443-083 | 308.1518 | 29.9600 | 149.1089 | -4.7594 | 2376 | 2687 | 6.9 | 0.23 | 231 | 2.366 | 11.83 | 11.61 | 12.53 | 12.59 | 12.45 | -19.09 | -19.00 | 31.55 | 20.4 | 31.59 | 20.8 | |
| 45905 UGC08294 | 75.5314 | 83.7453 | 86.9887 | 11.8233 | 6073 | 6427 | 5.8 | 0.66 | 195 | 2.404 | 13.97 | 14.15 | 14.91 | 15.04 | 14.95 | -19.44 | -19.38 | 34.46 | 77.9 | 34.52 | 80.2 | |
| 45911 ES576-011 | 309.8485 | 42.6041 | 136.8764 | -1.2174 | 2757 | 3096 | 5.8 | 0.20 | 294 | 2.468 | 12.23 | 11.83 | 12.60 | 12.64 | 12.59 | -20.02 | -20.00 | 32.62 | 33.5 | 32.66 | 34.0 | |
| 45947 NGC05032 | 42.0547 | 85.0715 | 90.4649 | 11.2270 | 6413 | 6791 | 3.0 | 0.58 | 524 | 2.800 | 11.66 | 11.64 | 12.24 | 12.34 | 12.35 | -23.04 | -23.24 | 35.52 | 126.8 | 35.79 | 143.7 | |
| 45948 UGC08307 | 98.0588 | 79.4480 | 81.6415 | 12.9165 | 873 | 1104 | 5.1 | 0.48 | 422 | 2.674 | 8.92 | 8.86 | 9.40 | 9.41 | 9.50 | -21.89 | -22.01 | 31.40 | 19.0 | 31.43 | 19.3 | |
| 45952 NGC05022 | 310.0525 | 43.0197 | 136.4917 | -0.9999 | 3004 | 3348 | 3.7 | 0.21 | 372 | 2.572 | 11.69 | 11.18 | 11.99 | 11.97 | 11.93 | -20.96 | -21.01 | 32.92 | 38.3 | 33.01 | 40.0 | |
| 46028 UGC08317 | 68.0063 | 83.9560 | 87.8261 | 11.9704 | 6039 | 6394 | 4.2 | 0.43 | 276 | 2.477 | 13.45 | 13.44 | 14.14 | 14.25 | 14.20 | -20.10 | -20.09 | 34.37 | 74.7 | 34.43 | 76.8 | |
| 46124 UGC08328 | 36.1838 | 84.6646 | 91.0550 | 11.5527 | 6482 | 6862 | 5.9 | 0.28 | 248 | 2.403 | 14.86 | 14.76 | 15.75 | 15.85 | 15.66 | -19.43 | -19.37 | 35.19 | 109.2 | 35.38 | 119.3 | |
| 46126 AGC029403 | 309.9705 | 38.5590 | 140.8812 | -1.8039 | 1390 | 1705 | 5.0 | 0.54 | 222 | 2.411 | 10.56 | 10.42 | 11.35 | 11.41 | 11.27 | -19.50 | -19.44 | 30.76 | 14.2 | 30.84 | 14.7 | |
| 46153 UGC08334 | 105.9971 | 74.2878 | 76.1990 | 14.2465 | 500 | 706 | 4.0 | 0.52 | 375 | 2.634 | 7.55 | 7.55 | 7.95 | 7.96 | 8.12 | -21.53 | -21.62 | 29.65 | 8.5 | 29.58 | 8.2 | |
| 46159 UGC08333 | 17.1492 | 84.2624 | 92.9411 | 11.2676 | 941 | 1211 | 9.7 | 0.25 | 119 | 2.081 | 14.13 | 14.31 | 15.29 | 15.38 | 15.20 | -16.50 | -16.22 | 31.70 | 21.9 | 31.60 | 20.9 | |
| 46246 ES508-034 | 310.1730 | 37.1752 | 142.2732 | -1.8739 | 1909 | 2226 | 8.1 | 0.44 | 147 | 2.205 | 13.50 | 13.54 | 14.39 | 14.47 | 14.36 | -17.63 | -17.43 | 31.99 | 25.0 | 31.90 | 24.0 | |
| 46247 NGC5054 | 311.7225 | 45.8007 | 133.9326 | 0.6148 | 1740 | 2066 | 4.2 | 0.58 | 319 | 2.586 | 9.55 | 9.52 | 10.01 | 10.08 | 10.16 | -21.09 | -21.15 | 31.25 | 17.8 | 31.23 | 17.6 | |
| 46252 IC0004216 | 313.0829 | 51.5966 | 128.3128 | 2.2989 | 2839 | 3183 | 5.8 | 0.38 | 240 | 2.405 | / | / | 13.27 | 13.35 | / | / | / | / | / | / | 32.75 | 35.5 |
| 46261 AGC530085 | 311.8446 | 46.1750 | 133.5748 | 0.7535 | 2631 | 2969 | 5.2 | 0.20 | 274 | 2.438 | 12.75 | 12.39 | 13.20 | 13.25 | 13.17 | -19.74 | -19.70 | 32.93 | 38.6 | 32.98 | 39.4 | |
| 46304 IC004214 | 309.3850 | 30.4407 | 148.8159 | -3.6273 | 2314 | 2622 | 1.4 | 0.63 | 370 | 2.669 | 10.08 | 10.09 | 10.64 | 10.72 | 10.77 | -21.85 | -21.96 | 32.63 | 33.6 | 32.71 | 34.8 | |
| 46373 AGC029453 | 311.3352 | 41.1290 | 138.5099 | -0.3610 | 1949 | 2271 | 6.8 | 0.20 | 145 | 2.161 | 13.78 | 13.65 | 14.48 | 14.54 | 14.45 | -17.23 | -17.00 | 31.68 | 21.7 | 31.55 | 20.4 | |
| 46386 UGC08365 | 104.0291 | 74.1611 | 76.3607 | 14.7736 | 1265 | 1474 | 6.4 | 0.30 | 127 | 2.115 | 13.40 | 13.57 | 14.42 | 14.51 | 14.40 | -16.81 | -16.55 | 31.20 | 17.4 | 31.06 | 16.3 | |
| 46409 NGC005064 | 307.7010 | 14.7076 | 164.1769 | -7.6728 | 2984 | 3255 | 2.7 | 0.53 | 493 | 2.756 | 10.31 | 10.04 | 10.40 | 10.45 | 10.61 | -22.64 | -22.81 | 33.27 | 45.1 | 33.29 | 45.6 | |
| 46427 UGC08366 | 47.2193 | 83.7233 | 90.0169 | 12.5966 | 6658 | 7038 | 2.9 | 0.39 | 530 | 2.751 | 12.07 | 11.83 | 12.64 | 12.72 | 12.63 | -22.59 | -22.76 | 35.33 | 116.5 | 35.67 | 136.3 | |
| 46441 AGC530097 | 312.9370 | 47.4843 | 132.3810 | 1.6746 | 2745 | 3084 | 5.1 | 0.20 | 367 | 2.565 | 11.31 | 10.84 | 11.49 | 11.53 | 11.55 | -20.90 | -20.94 | 32.45 | 30.9 | 32.48 | 31.4 | |
| 46452 ES382-041 | 309.3907 | 27.4183 | 151.8054 | -4.1163 | 1749 | 2042 | 5.7 | 0.20 | 147 | 2.167 | 14.05 | 14.03 | 14.90 | 14.97 | 14.86 | -17.28 | -17.06 | 32.14 | 26.8 | 32.04 | 25.6 | |
| 46491 ES576-032 | 311.5422 | 40.1172 | 139.5339 | -0.3579 | 1628 | 1944 | 5.8 | 0.71 | 135 | 2.272 | 11.48 | 11.58 | 12.10 | 12.18 | 12.24 | -18.23 | -18.08 | 30.48 | 12.5 | 30.27 | 11.3 | |
| 46502 ES269-085 | 307.9444 | 15.3120 | 163.6099 | -7.3497 | 2845 | 3115 | 5.0 | 0.54 | 308 | 2.555 | 10.90 | 10.76 | 11.28 | 11.35 | 11.42 | -20.81 | -20.84 | 32.23 | 27.9 | 32.20 | 27.5 | |
| 46535 AGC530112 | 313.8689 | 49.6853 | 130.2724 | 2.5601 | 1431 | 1753 | 4.2 | 0.30 | 224 | 2.362 | 11.64 | 11.54 | 12.45 | 12.51 | 12.38 | -19.05 | -18.96 | 31.43 | 19.3 | 31.47 | 19.7 | |

| PGC Name | l | b | sgl | sgb | v_{hel} | v_{mod} | t | b/a | w_{max} | $\log w_{max}^i$ | I | I* | [3.6] | [3.6]* | C _[3.6] | M _C | M _[3.6] | μ_C | d _C | $\mu_{[3.6]}$ | d _[3.6] |
|-----------------|----------|----------|----------|----------|-----------|-----------|-----|------|-----------|------------------|-------|-------|-------|--------|--------------------|----------------|--------------------|---------|----------------|---------------|--------------------|
| 46574 AGC029511 | 311.8447 | 40.3133 | 139.3741 | -0.1005 | 2085 | 2406 | 6.7 | 0.22 | 169 | 2.230 | 12.95 | 12.81 | 13.81 | 13.83 | 13.67 | -17.86 | -17.68 | 31.53 | 20.2 | 31.50 | 20.0 |
| 46633 NGC05104 | 319.1905 | 62.2651 | 117.9109 | 6.4380 | 5561 | 5963 | 1.2 | 0.43 | 436 | 2.674 | 12.08 | 11.94 | 12.05 | 12.13 | 12.41 | -21.90 | -22.01 | 34.36 | 74.6 | 34.23 | 70.2 |
| 46664 AGC530120 | 314.2422 | 48.9967 | 130.9853 | 2.9122 | 2903 | 3243 | 5.0 | 0.62 | 205 | 2.408 | 12.15 | 12.26 | 12.97 | 13.02 | 13.02 | -19.47 | -19.41 | 32.51 | 31.7 | 32.50 | 31.6 |
| 46671 UGC08403 | 96.0655 | 76.7585 | 79.7426 | 14.9174 | 969 | 1187 | 5.8 | 0.60 | 187 | 2.360 | 10.96 | 11.13 | 12.01 | 12.05 | 11.95 | -19.03 | -18.94 | 30.98 | 15.7 | 30.99 | 15.8 |
| 46710 PGC046710 | 313.5144 | 45.5280 | 134.3731 | 1.8184 | 6855 | 7301 | 3.0 | 0.30 | 390 | 2.603 | / | / | 11.86 | 11.94 | / | / | -21.31 | / | / | 33.29 | 45.5 |
| 46744 UGC08410 | 33.5212 | 82.9888 | 91.7192 | 13.1236 | 2389 | 3171 | 4.9 | 0.37 | 328 | 2.538 | 11.87 | 11.74 | 12.38 | 12.45 | 12.46 | -20.66 | -20.68 | 33.14 | 42.4 | 33.17 | 43.1 |
| 46746 UGC08411 | 44.4227 | 82.9292 | 90.3728 | 13.3813 | 2892 | 2662 | 5.7 | 0.43 | 214 | 2.365 | 12.95 | 13.00 | 13.41 | 13.50 | 13.62 | -19.09 | -19.00 | 32.72 | 34.9 | 32.51 | 31.8 |
| 46768 AGC029560 | 311.7481 | 36.0279 | 143.6025 | -0.8020 | 2263 | 2578 | 4.1 | 0.23 | 236 | 2.376 | 12.47 | 12.25 | 13.06 | 13.12 | 13.04 | -19.18 | -19.10 | 32.23 | 27.9 | 32.22 | 27.9 |
| 46878 AGC029585 | 313.1919 | 41.0745 | 138.7614 | 1.0163 | 2667 | 2994 | 3.5 | 0.67 | 311 | 2.613 | 11.30 | 11.32 | 11.88 | 11.96 | 12.00 | -21.34 | -21.42 | 33.37 | 47.2 | 33.42 | 48.3 |
| 46889 ES576-050 | 313.5714 | 42.4878 | 137.3957 | 1.4782 | 1969 | 2288 | 5.1 | 0.42 | 172 | 2.269 | 11.76 | 11.77 | 12.65 | 12.72 | 12.60 | -18.21 | -18.05 | 30.81 | 14.5 | 30.77 | 14.3 |
| 47102 ES444-037 | 312.0258 | 32.1664 | 147.4573 | -1.1321 | 1897 | 2197 | 7.5 | 0.60 | 133 | 2.212 | 13.84 | 13.99 | 15.05 | 15.14 | 14.92 | -17.69 | -17.50 | 32.62 | 33.4 | 32.65 | 34.0 |
| 47270 UGC08470 | 105.1227 | 68.8969 | 71.4245 | 17.0762 | 2704 | 2901 | 6.6 | 0.23 | 211 | 2.328 | 13.40 | 13.30 | 14.48 | 14.55 | 14.27 | -18.74 | -18.63 | 33.04 | 40.5 | 33.22 | 44.0 |
| 47321 AGC029708 | 311.9737 | 29.0336 | 150.5528 | -1.6218 | 2389 | 2687 | 5.4 | 0.32 | 333 | 2.537 | 10.45 | 10.22 | 11.10 | 11.15 | 11.04 | -20.65 | -20.67 | 31.69 | 21.8 | 31.83 | 23.2 |
| 47345 ES383-005 | 311.8031 | 27.9458 | 151.6088 | -1.9247 | 3609 | 3926 | 3.8 | 0.22 | 428 | 2.633 | 12.17 | 11.67 | 11.71 | 11.75 | 12.08 | -21.52 | -21.61 | 33.64 | 53.5 | 33.40 | 47.9 |
| 47368 UGC08490 | 113.5013 | 58.0047 | 59.4010 | 17.8457 | 200 | 321 | 8.9 | 0.62 | 110 | 2.138 | 10.54 | 10.79 | 11.88 | 11.93 | 11.71 | -17.01 | -16.77 | 28.73 | 5.6 | 28.70 | 5.5 |
| 47394 AGC029724 | 315.6540 | 43.9553 | 136.1081 | 3.1517 | 1502 | 1813 | 4.9 | 0.20 | 509 | 2.707 | 9.90 | 9.24 | 10.13 | 10.13 | 10.04 | -22.19 | -22.33 | 32.24 | 28.0 | 32.47 | 31.2 |
| 47425 UGC08501 | 115.3553 | 54.0450 | 55.1013 | 17.9304 | 1765 | 1874 | 3.5 | 0.61 | 252 | 2.492 | 11.73 | 11.84 | 12.53 | 12.62 | 12.59 | -20.24 | -20.23 | 32.84 | 37.0 | 32.87 | 37.5 |
| 47514 AGC530277 | 316.9465 | 46.6892 | 133.4623 | 4.3047 | 4232 | 4590 | 4.9 | 0.22 | 284 | 2.456 | 13.33 | 13.02 | 14.01 | 14.07 | 13.90 | -19.91 | -19.88 | 33.84 | 58.7 | 34.02 | 63.6 |
| 47549 NGC005188 | 312.1788 | 27.3576 | 152.2383 | -1.6781 | 2429 | 2722 | 3.0 | 0.48 | 317 | 2.549 | 10.71 | 10.65 | 10.80 | 10.87 | 11.13 | -20.76 | -20.79 | 31.89 | 23.9 | 31.67 | 21.5 |
| 47788 UGC08550 | 103.9490 | 67.6120 | 70.4638 | 18.0767 | 359 | 527 | 6.8 | 0.28 | 121 | 2.092 | / | / | 13.78 | 13.82 | / | / | -16.32 | / | / | 30.14 | 10.7 |
| 47847 ES270-017 | 310.8305 | 16.6587 | 162.6733 | -4.4097 | 828 | 1073 | 8.8 | 0.22 | 129 | 2.112 | 10.44 | 10.42 | 11.12 | 11.19 | 11.17 | -16.78 | -16.52 | 27.94 | 3.9 | 27.71 | 3.5 |
| 47903 ES040-012 | 305.3457 | -14.9752 | 193.9486 | -13.2072 | 2657 | 2785 | 3.9 | 0.22 | 412 | 2.617 | 11.65 | 10.97 | 11.39 | 11.39 | 11.55 | -21.38 | -21.45 | 32.94 | 38.8 | 32.87 | 37.5 |
| 47948 AGC029872 | 315.7240 | 37.6964 | 142.3473 | 2.5632 | 2589 | 2902 | 4.7 | 0.27 | 334 | 2.532 | 11.78 | 11.43 | 12.02 | 12.06 | 12.11 | -20.60 | -20.62 | 32.72 | 34.9 | 32.70 | 34.7 |
| 47971 UGC08587 | 77.4220 | 77.2987 | 83.3795 | 17.2500 | 2233 | 2465 | 5.8 | 0.67 | 240 | 2.498 | 11.92 | 12.07 | 12.75 | 12.84 | 12.82 | -20.29 | -20.29 | 33.13 | 42.3 | 33.17 | 43.0 |
| 47985 UGC08593 | 105.3973 | 65.6224 | 68.3313 | 18.5115 | 1611 | 1776 | 3.0 | 0.23 | 253 | 2.406 | 12.31 | 12.15 | 12.67 | 12.73 | 12.80 | -19.46 | -19.39 | 32.27 | 28.4 | 32.13 | 26.7 |
| 48093 NGC005219 | 311.4726 | 16.2307 | 163.1826 | -3.8581 | 2517 | 2775 | 3.5 | 0.67 | 203 | 2.428 | 11.76 | 11.80 | 12.25 | 12.33 | 12.43 | -19.65 | -19.61 | 32.09 | 26.2 | 31.95 | 24.5 |
| 48130 UGC08616 | 335.9299 | 68.7502 | 110.6092 | 12.5480 | 1151 | 1442 | 4.0 | 0.60 | 267 | 2.515 | 9.27 | 9.36 | 9.69 | 9.72 | 9.91 | -20.44 | -20.45 | 30.35 | 11.8 | 30.17 | 10.8 |
| 48161 ES444-086 | 314.5561 | 30.8881 | 149.0069 | 0.8387 | 4079 | 4406 | 3.5 | 0.23 | 433 | 2.639 | 12.22 | 11.74 | 12.18 | 12.22 | 12.34 | -21.58 | -21.67 | 33.97 | 62.2 | 33.96 | 61.9 |
| 48175 ES324-044 | 312.5828 | 22.1555 | 157.4445 | -2.0235 | 2530 | 2807 | 5.9 | 0.54 | 206 | 2.379 | 12.48 | 12.51 | 13.06 | 13.15 | 13.19 | -19.21 | -19.13 | 32.41 | 30.3 | 32.28 | 28.6 |
| 48206 UGC08630 | 66.3163 | 78.2197 | 86.0159 | 17.4388 | 2427 | 2669 | 5.7 | 0.25 | 212 | 2.331 | / | / | 13.56 | 13.64 | / | / | -18.66 | / | / | 32.31 | 29.0 |
| 48291 UGC08642 | 99.3224 | 68.8482 | 72.5224 | 18.8871 | 2428 | 2618 | 6.8 | 0.20 | 131 | 2.117 | 14.73 | 14.84 | 15.90 | 16.00 | 15.77 | -16.83 | -16.57 | 32.61 | 33.2 | 32.59 | 32.9 |
| 48307 AGC530342 | 321.3477 | 49.6469 | 130.6426 | 7.3848 | 2312 | 2628 | 5.0 | 0.43 | 332 | 2.556 | 10.97 | 10.82 | 11.52 | 11.58 | 11.56 | -20.82 | -20.86 | 32.39 | 30.0 | 32.45 | 30.9 |
| 48392 UGC08658 | 107.9154 | 61.3369 | 63.7292 | 19.3308 | 2022 | 2169 | 5.0 | 0.54 | 228 | 2.424 | 12.19 | 12.30 | 13.06 | 13.15 | 13.08 | -19.62 | -19.57 | 32.71 | 34.9 | 32.74 | 35.3 |
| 48441 UGC08662 | 67.7236 | 77.3830 | 85.4151 | 18.1179 | 2033 | 2265 | 5.9 | 0.20 | 165 | 2.217 | / | / | 15.09 | 15.17 | / | / | -17.55 | / | / | 32.75 | 35.4 |
| 48533 ES445-015 | 315.5725 | 30.5846 | 149.4090 | 1.6716 | 4379 | 4710 | 3.9 | 0.35 | 377 | 2.596 | 12.48 | 12.25 | 13.06 | 13.12 | 13.04 | -21.19 | -21.25 | 34.29 | 72.0 | 34.47 | 78.4 |
| 48534 UGC08684 | 112.0676 | 55.2663 | 56.8948 | 19.4206 | 2193 | 2310 | 5.9 | 0.30 | 207 | 2.327 | 12.48 | 12.46 | 13.19 | 13.26 | 13.22 | -18.74 | -18.62 | 31.96 | 24.7 | 31.89 | 23.9 |

| PGC Name | l | b | sgl | sgb | v_{hel} | v_{mod} | t | b/a | w_{max} | $\log w_{max}^{\dagger}$ | I | I* | [3.6] | [3.6]* | $C_{[3.6]}$ | M_C | $M_{[3.6]}$ | μ_C | d_C | $\mu_{[3.6]}$ | $d_{[3.6]}$ |
|-----------------|----------|---------|----------|---------|-----------|-----------|-----|------|-----------|--------------------------|-------|-------|-------|--------|-------------|--------|-------------|---------|-------|---------------|-------------|
| 48629 ES383-067 | 315.4115 | 28.6857 | 151.2809 | 1.3203 | 4096 | 4415 | 5.4 | 0.20 | 226 | 2.354 | 13.90 | 13.68 | 14.15 | 14.22 | 14.31 | -18.98 | -18.88 | 33.32 | 46.1 | 33.13 | 42.3 |
| 48690 UGC08693 | 71.6437 | 76.1020 | 84.0079 | 18.9345 | 2439 | 2668 | 4.2 | 0.45 | 235 | 2.411 | 12.91 | 12.96 | 13.44 | 13.53 | 13.61 | -19.50 | -19.44 | 33.13 | 42.3 | 33.00 | 39.8 |
| 48749 UGC005289 | 88.9097 | 71.8923 | 77.3605 | 19.6243 | 2526 | 2732 | 2.0 | 0.31 | 376 | 2.588 | 11.66 | 11.44 | 12.24 | 12.29 | 12.23 | -21.11 | -21.17 | 33.37 | 47.2 | 33.52 | 50.5 |
| 48767 UGC08700 | 89.2755 | 71.7142 | 77.1413 | 19.6709 | 2583 | 2789 | 4.0 | 0.20 | 456 | 2.659 | 10.73 | 10.24 | 10.88 | 10.91 | 10.93 | -21.76 | -21.86 | 32.70 | 34.7 | 32.79 | 36.2 |
| 48816 UGC08711 | 96.7005 | 68.1210 | 72.4846 | 20.0920 | 1507 | 1681 | 4.7 | 0.24 | 299 | 2.480 | 10.95 | 10.72 | 11.35 | 11.39 | 11.42 | -20.13 | -20.11 | 31.55 | 20.4 | 31.51 | 20.0 |
| 48925 UGC08726 | 85.4342 | 72.2812 | 78.4769 | 20.0610 | 2330 | 2535 | 6.4 | 0.20 | 169 | 2.228 | 13.59 | 13.59 | 14.74 | 14.82 | 14.56 | -17.84 | -17.66 | 32.40 | 30.3 | 32.49 | 31.5 |
| 48953 UGC08737 | 115.0370 | 48.1627 | 49.1138 | 19.5077 | 1784 | 1858 | 4.0 | 0.20 | 338 | 2.529 | 12.06 | 11.70 | 12.03 | 12.07 | 12.25 | -20.57 | -20.59 | 32.84 | 37.0 | 32.68 | 34.4 |
| 48959 UGC08727 | 335.7500 | 63.1426 | 116.2066 | 13.8743 | 1170 | 1458 | 5.2 | 0.66 | 200 | 2.415 | 10.81 | 10.97 | 11.64 | 11.73 | 11.71 | -19.54 | -19.48 | 31.25 | 17.8 | 31.21 | 17.5 |
| 48989 UGC08733 | 91.2397 | 70.0253 | 75.3717 | 20.3792 | 2333 | 2526 | 5.9 | 0.52 | 180 | 2.314 | 12.86 | 13.00 | 13.79 | 13.89 | 13.80 | -18.61 | -18.49 | 32.42 | 30.5 | 32.39 | 30.1 |
| 49063 ES383-088 | 316.7389 | 28.2397 | 151.8502 | 2.4325 | 4237 | 4554 | 3.9 | 0.34 | 329 | 2.536 | 12.31 | 12.10 | 12.93 | 13.00 | 12.90 | -20.63 | -20.66 | 33.57 | 51.8 | 33.71 | 55.2 |
| 49069 NGC05313 | 83.4129 | 72.3611 | 79.0348 | 20.3913 | 2562 | 2771 | 3.1 | 0.53 | 404 | 2.669 | 10.94 | 10.94 | 11.25 | 11.33 | 11.50 | -21.85 | -21.96 | 33.38 | 47.4 | 33.33 | 46.4 |
| 49112 UGC08749 | 86.3660 | 71.3241 | 77.5700 | 20.5877 | 2609 | 2813 | 5.2 | 0.50 | 299 | 2.529 | 11.39 | 11.43 | 12.14 | 12.23 | 12.19 | -20.57 | -20.59 | 32.77 | 35.8 | 32.84 | 37.0 |
| 49138 UGC008756 | 88.7462 | 70.4430 | 76.3183 | 20.6949 | 1342 | 1527 | 1.2 | 0.26 | 253 | 2.409 | / | / | 12.92 | 12.98 | / | -19.43 | / | / | / | 32.42 | 30.5 |
| 49301 UGC08795 | 75.4909 | 73.4403 | 81.7370 | 20.8154 | 2301 | 2513 | 6.0 | 0.33 | 192 | 2.300 | 13.52 | 13.54 | 14.46 | 14.54 | 14.40 | -18.49 | -18.36 | 32.90 | 38.1 | 32.92 | 38.4 |
| 49322 UGC08804 | 81.0518 | 72.1482 | 79.5078 | 20.9974 | 2507 | 2714 | 5.8 | 0.46 | 215 | 2.376 | 12.69 | 12.77 | 13.70 | 13.80 | 13.64 | -19.18 | -19.10 | 32.83 | 36.8 | 32.92 | 38.3 |
| 49347 UGC08810 | 82.8376 | 71.5926 | 78.6737 | 21.1041 | 2326 | 2527 | 3.6 | 0.65 | 292 | 2.574 | 10.23 | 10.35 | 11.22 | 11.31 | 11.19 | -20.99 | -21.04 | 32.18 | 27.3 | 32.36 | 29.7 |
| 49411 NGC005348 | 340.0273 | 63.4849 | 115.3281 | 15.6304 | 1452 | 1735 | 3.8 | 0.20 | 180 | 2.255 | 12.24 | 12.17 | 13.02 | 13.09 | 12.99 | -18.08 | -17.92 | 31.07 | 16.4 | 31.01 | 15.9 |
| 49464 UGC08835 | 84.4319 | 70.7438 | 77.6705 | 21.4380 | 2169 | 2363 | 3.4 | 0.40 | 253 | 2.431 | 11.78 | 11.79 | 12.45 | 12.53 | 12.52 | -19.68 | -19.64 | 32.21 | 27.6 | 32.17 | 27.2 |
| 49489 NGC05376 | 108.5593 | 55.8049 | 58.1370 | 21.1155 | 2076 | 2191 | 2.3 | 0.61 | 291 | 2.556 | 11.13 | 11.23 | 11.67 | 11.76 | 11.86 | -20.82 | -20.86 | 32.69 | 34.6 | 32.63 | 33.6 |
| 49563 UGC08863 | 94.9057 | 66.2096 | 71.3064 | 21.8029 | 1798 | 1964 | 1.0 | 0.41 | 375 | 2.606 | 10.10 | 9.99 | 10.80 | 10.81 | 10.76 | -21.27 | -21.34 | 32.03 | 25.5 | 32.16 | 27.1 |
| 49573 ES384-015 | 318.3183 | 27.8526 | 152.3701 | 3.7828 | 3545 | 3840 | 7.6 | 0.20 | 187 | 2.272 | / | / | 14.67 | 14.74 | / | -18.08 | / | / | / | 32.85 | 37.1 |
| 49580 AGC030236 | 318.4857 | 28.2670 | 151.9696 | 3.9668 | 4372 | 4687 | 4.1 | 0.43 | 464 | 2.701 | 12.19 | 11.97 | 12.35 | 12.42 | 12.56 | -22.14 | -22.28 | 34.78 | 90.5 | 34.82 | 92.0 |
| 49656 AGC030254 | 321.1048 | 34.7352 | 145.6510 | 6.6571 | 2363 | 2650 | 9.0 | 0.59 | 121 | 2.167 | / | / | 14.60 | 14.69 | / | -17.05 | / | / | / | 31.75 | 22.4 |
| 49676 IC0004351 | 319.9088 | 31.3557 | 148.9793 | 5.4443 | 2672 | 2958 | 3.3 | 0.20 | 481 | 2.682 | 10.59 | 10.00 | 10.51 | 10.53 | 10.63 | -21.97 | -22.09 | 32.61 | 33.2 | 32.64 | 33.7 |
| 49728 ES445-085 | 319.2009 | 28.9693 | 151.3211 | 4.6518 | 4286 | 4599 | 5.7 | 0.20 | 250 | 2.398 | 14.67 | 14.37 | 14.84 | 14.90 | 15.00 | -19.38 | -19.31 | 34.45 | 77.5 | 34.30 | 72.6 |
| 49763 UGC08899 | 18.0753 | 73.8340 | 98.3524 | 20.3081 | 2854 | 3117 | 4.0 | 0.30 | 177 | 2.260 | 14.40 | 14.43 | 15.36 | 15.45 | 15.29 | -18.12 | -17.96 | 33.45 | 48.9 | 33.46 | 49.2 |
| 49881 NGC05430 | 107.3095 | 55.6474 | 58.2573 | 21.8280 | 2961 | 3086 | 3.1 | 0.67 | 321 | 2.629 | 10.96 | 11.08 | 11.32 | 11.42 | 11.62 | -21.48 | -21.57 | 33.12 | 42.0 | 33.01 | 40.0 |
| 49889 NGC05425 | 95.2751 | 64.7915 | 69.9897 | 22.5430 | 2072 | 2232 | 6.5 | 0.27 | 228 | 2.366 | 12.69 | 12.61 | 13.48 | 13.55 | 13.44 | -19.09 | -19.00 | 32.54 | 32.2 | 32.57 | 32.7 |
| 49993 NGC05443 | 103.7985 | 58.6077 | 62.0138 | 22.3498 | 1803 | 1928 | 3.0 | 0.33 | 355 | 2.566 | 10.88 | 10.71 | 11.57 | 11.62 | 11.52 | -20.91 | -20.96 | 32.44 | 30.8 | 32.60 | 33.1 |
| 50031 UGC08969 | 95.7173 | 64.0122 | 69.1884 | 22.8550 | 2020 | 2175 | 1.4 | 0.38 | 388 | 2.615 | 10.61 | 10.47 | 11.22 | 11.23 | 11.21 | -21.35 | -21.43 | 32.58 | 32.8 | 32.68 | 34.4 |
| 50069 UGC008988 | 108.1705 | 54.0293 | 56.4386 | 21.9563 | 2077 | 2181 | 5.9 | 0.22 | 189 | 2.278 | 13.61 | 13.56 | 14.37 | 14.44 | 14.36 | -18.29 | -18.14 | 32.66 | 34.1 | 32.60 | 33.1 |
| 50166 ES384-043 | 319.9659 | 26.9277 | 153.4177 | 5.1629 | 4407 | 4713 | 6.8 | 0.20 | 232 | 2.365 | / | / | 15.32 | 15.39 | / | -19.00 | / | / | / | 34.48 | 78.8 |
| 50194 UGC08995 | 349.7711 | 64.7710 | 112.3806 | 19.0619 | 1234 | 1498 | 7.4 | 0.37 | 150 | 2.199 | 13.12 | 13.24 | 14.03 | 14.11 | 14.03 | -17.57 | -17.37 | 31.61 | 21.0 | 31.49 | 19.8 |
| 50317 NGC005470 | 346.5493 | 62.3595 | 115.3335 | 18.8037 | 1023 | 1288 | 3.1 | 0.20 | 242 | 2.384 | / | / | 12.31 | 12.36 | / | -19.17 | / | / | / | 31.54 | 20.3 |
| 50334 UGC09024 | 20.5490 | 72.1870 | 98.5672 | 22.0952 | 2322 | 2569 | 3.0 | 0.62 | 108 | 2.130 | 13.53 | 13.76 | 15.43 | 15.54 | 14.99 | -16.94 | -16.69 | 31.93 | 24.4 | 32.24 | 28.1 |
| 50404 ES325-055 | 319.0483 | 22.3072 | 157.9652 | 3.9402 | 4030 | 4315 | 4.4 | 0.20 | 244 | 2.387 | / | / | 14.70 | 14.76 | / | -19.21 | / | / | / | 34.05 | 64.5 |

| PGC Name | l | b | sgl | sgb | v_{hel} | v_{mod} | t | b/a | w_{max} | $\log w_{max}^{\dagger}$ | I | I* | [3.6] | [3.6]* | $C_{[3.6]}$ | MC | $M_{[3.6]}$ | μ_C | dC | $\mu_{[3.6]}$ | $d_{[3.6]}$ |
|-----------------|----------|----------|----------|----------|-----------|-----------|-----|------|-----------|--------------------------|-------|-------|-------|--------|-------------|--------|-------------|---------|-------|---------------|-------------|
| 50509 UGC09056 | 93.6748 | 63.4282 | 69.2780 | 23.9283 | 2015 | 2166 | 3.1 | 0.37 | 170 | 2.253 | 13.22 | 13.28 | 13.99 | 14.08 | 14.04 | -18.06 | -17.89 | 32.10 | 26.3 | 31.97 | 24.8 |
| 50581 UGC09071 | 100.2673 | 59.3141 | 63.6259 | 23.6189 | 1827 | 1954 | 5.9 | 0.23 | 190 | 2.281 | 13.39 | 13.34 | 14.16 | 14.23 | 14.14 | -18.32 | -18.18 | 32.47 | 31.2 | 32.42 | 30.5 |
| 50587 UGC09057 | 338.6108 | 54.7446 | 124.3029 | 17.3220 | 1563 | 1836 | 7.0 | 0.25 | 212 | 2.331 | 12.80 | 12.66 | 13.69 | 13.75 | 13.56 | -18.77 | -18.66 | 32.34 | 29.4 | 32.42 | 30.5 |
| 50620 AGC240147 | 0.6200 | 67.0533 | 107.7738 | 21.5235 | 4900 | 5214 | 1.3 | 0.58 | 165 | 2.298 | 13.27 | 13.43 | 13.34 | 13.46 | 13.82 | -18.47 | -18.33 | 32.29 | 28.8 | 31.79 | 22.8 |
| 50675 AGC030464 | 322.7568 | 29.3653 | 151.1296 | 7.7760 | 6925 | 7309 | 4.5 | 0.20 | 466 | 2.668 | 13.23 | 12.62 | 13.30 | 13.35 | 13.35 | -21.84 | -21.96 | 35.30 | 114.6 | 35.48 | 124.5 |
| 50676 UGC09079 | 340.4566 | 55.7559 | 122.9929 | 18.0781 | 1541 | 1811 | 6.5 | 0.20 | 239 | 2.378 | 11.84 | 11.59 | 12.80 | 12.84 | 12.57 | -19.20 | -19.12 | 31.77 | 22.6 | 31.97 | 24.8 |
| 50728 NGC005520 | 94.7666 | 62.1219 | 67.8084 | 24.3245 | 1876 | 2018 | 3.1 | 0.56 | 276 | 2.514 | 11.84 | 11.91 | 12.26 | 12.29 | 12.47 | -20.44 | -20.44 | 32.92 | 38.4 | 32.76 | 35.6 |
| 50798 ES271-022 | 317.6944 | 15.0929 | 165.0277 | 1.9540 | 2995 | 3236 | 5.9 | 0.20 | 364 | 2.561 | 11.95 | 11.39 | 12.16 | 12.18 | 12.15 | -20.87 | -20.91 | 33.03 | 40.4 | 33.12 | 42.1 |
| 50832 UGC09115 | 103.2617 | 56.0957 | 59.7040 | 23.7195 | 2046 | 2158 | 4.1 | 0.22 | 249 | 2.398 | 12.53 | 12.36 | 12.62 | 12.63 | 12.86 | -19.39 | -19.32 | 32.26 | 28.3 | 31.95 | 24.6 |
| 50895 UGC09119 | 32.1154 | 71.2225 | 95.3356 | 24.3864 | 1045 | 1262 | 5.8 | 0.28 | 261 | 2.426 | 11.34 | 11.22 | 12.17 | 12.23 | 12.08 | -19.63 | -19.58 | 31.71 | 22.0 | 31.82 | 23.1 |
| 50973 UGC09133 | 62.6258 | 70.1750 | 84.3311 | 25.3892 | 3848 | 4073 | 2.4 | 0.56 | 418 | 2.695 | 10.51 | 10.52 | 11.11 | 11.21 | 11.22 | -22.08 | -22.21 | 33.33 | 46.4 | 33.46 | 49.3 |
| 51015 IC004390 | 318.4441 | 15.3023 | 164.8940 | 2.6952 | 2113 | 2339 | 4.2 | 0.32 | 246 | 2.406 | / | / | 12.08 | 12.13 | / | / | -19.39 | / | / | 31.52 | 20.1 |
| 51061 AGC030549 | 323.7852 | 28.0011 | 152.5502 | 8.6116 | 2757 | 3021 | 5.8 | 0.20 | 315 | 2.498 | 12.76 | 12.35 | 12.63 | 12.66 | 12.88 | -20.29 | -20.29 | 33.19 | 43.5 | 32.99 | 39.5 |
| 51106 NGC005530 | 319.2639 | 16.7057 | 163.5733 | 3.6181 | 1193 | 1413 | 4.2 | 0.45 | 251 | 2.440 | 10.06 | 9.94 | 10.38 | 10.44 | 10.56 | -19.76 | -19.72 | 30.32 | 11.6 | 30.16 | 10.8 |
| 51143 AGC030573 | 322.6199 | 24.6476 | 155.8743 | 7.3868 | 3749 | 4024 | 6.1 | 0.20 | 271 | 2.433 | 13.75 | 13.42 | 13.96 | 14.01 | 14.08 | -19.70 | -19.66 | 33.82 | 58.1 | 33.73 | 55.6 |
| 51210 NGC05585 | 100.9968 | 56.4747 | 60.7022 | 24.6654 | 305 | 406 | 6.9 | 0.62 | 141 | 2.244 | 10.42 | 10.63 | 11.61 | 11.65 | 11.49 | -17.98 | -17.80 | 29.47 | 7.8 | 29.46 | 7.8 |
| 51265 AGC030592 | 325.5013 | 29.8996 | 150.6815 | 10.1802 | 7231 | 7619 | 5.4 | 0.20 | 313 | 2.496 | 14.31 | 13.89 | 14.71 | 14.78 | 14.69 | -20.27 | -20.27 | 35.06 | 102.6 | 35.20 | 109.6 |
| 51291 PG0051291 | 341.4880 | 52.2491 | 126.3850 | 19.6143 | 2733 | 3009 | 2.0 | 0.45 | 160 | 2.244 | / | / | 14.75 | 14.85 | / | / | -17.81 | / | / | 32.68 | 34.3 |
| 51344 NGC005584 | 345.1143 | 54.8559 | 123.0419 | 20.8767 | 1637 | 1895 | 6.0 | 0.71 | 186 | 2.416 | 10.81 | 10.98 | 11.75 | 11.79 | 11.74 | -19.55 | -19.49 | 31.29 | 18.1 | 31.28 | 18.0 |
| 51351 UGC09206 | 7.9019 | 65.6591 | 106.7493 | 24.6167 | 2283 | 2528 | 3.8 | 0.48 | 128 | 2.155 | / | / | 13.97 | 14.07 | / | / | -16.94 | / | / | 31.01 | 16.0 |
| 51400 UGC09215 | 347.7775 | 56.3647 | 120.9489 | 21.7344 | 1391 | 1644 | 6.3 | 0.49 | 209 | 2.372 | 11.99 | 12.06 | 12.87 | 12.95 | 12.86 | -19.14 | -19.06 | 32.01 | 25.2 | 32.01 | 25.3 |
| 51404 IC0004407 | 340.2832 | 50.0841 | 128.8103 | 19.4349 | 2722 | 2996 | 8.8 | 0.47 | 194 | 2.333 | / | / | 14.56 | 14.65 | / | / | -18.68 | / | / | 33.37 | 47.2 |
| 51445 AGC540081 | 332.7749 | 40.7109 | 139.4108 | 15.7793 | 2702 | 2974 | 4.9 | 0.53 | 298 | 2.536 | 11.26 | 11.20 | 11.43 | 11.51 | 11.72 | -20.64 | -20.66 | 32.37 | 29.8 | 32.18 | 27.2 |
| 51471 AGC540084 | 343.1160 | 52.2281 | 126.1081 | 20.5769 | 2746 | 3018 | 1.3 | 0.59 | 311 | 2.577 | 11.74 | 11.73 | 12.03 | 12.11 | 12.29 | -21.01 | -21.06 | 33.32 | 46.2 | 33.21 | 43.8 |
| 51503 UGC09242 | 71.3915 | 66.8982 | 79.6523 | 27.2234 | 1441 | 1608 | 6.6 | 0.20 | 187 | 2.272 | 13.14 | 13.08 | 13.99 | 14.06 | 13.93 | -18.23 | -18.08 | 32.17 | 27.1 | 32.15 | 26.9 |
| 51509 UGC09245 | 99.4362 | 56.3098 | 61.0053 | 25.5008 | 1894 | 2003 | 6.4 | 0.36 | 125 | 2.118 | 13.41 | 13.59 | 14.37 | 14.47 | 14.39 | -16.83 | -16.57 | 31.22 | 17.5 | 31.04 | 16.2 |
| 51523 PG0051523 | 341.4781 | 50.2757 | 128.4108 | 20.1284 | 1697 | 1955 | 9.0 | 0.50 | 121 | 2.136 | / | / | 13.94 | 14.03 | / | / | -16.76 | / | / | 30.79 | 14.4 |
| 51549 IC4423 | 35.9687 | 68.8250 | 94.5982 | 27.0383 | 9078 | 9503 | 4.2 | 0.49 | 413 | 2.667 | 13.35 | 13.28 | 13.75 | 13.88 | 13.94 | -21.83 | -21.94 | 35.91 | 152.4 | 36.04 | 161.4 |
| 51613 ES001-006 | 303.9313 | -25.0891 | 204.3302 | -14.8255 | 2254 | 2323 | 5.6 | 0.25 | 305 | 2.489 | 11.85 | 11.46 | 12.17 | 12.20 | 12.19 | -20.21 | -20.21 | 32.41 | 30.4 | 32.42 | 30.5 |
| 51635 NGC005630 | 74.7326 | 65.7414 | 77.6987 | 27.5829 | 2653 | 2826 | 7.9 | 0.36 | 228 | 2.379 | 12.38 | 12.38 | 13.14 | 13.23 | 13.16 | -19.21 | -19.13 | 32.38 | 29.9 | 32.37 | 29.8 |
| 51641 NGC005671 | 111.3449 | 45.2068 | 46.6775 | 22.6668 | 8981 | 9237 | 3.1 | 0.72 | 358 | 2.704 | / | / | 12.62 | 12.76 | / | / | -22.30 | / | / | 35.21 | 110.3 |
| 51665 UGC09279 | 56.6880 | 68.1862 | 86.0993 | 27.8176 | 4090 | 4314 | 6.0 | 0.37 | 165 | 2.241 | / | / | 16.04 | 16.15 | / | / | -17.78 | / | / | 33.99 | 62.9 |
| 51713 UGC09291 | 69.4888 | 66.5436 | 80.2386 | 27.8721 | 2888 | 3071 | 6.4 | 0.47 | 250 | 2.444 | 12.06 | 12.10 | 13.15 | 13.24 | 13.02 | -19.80 | -19.76 | 32.84 | 37.0 | 33.04 | 40.5 |
| 51745 UGC09303 | 54.1834 | 68.1334 | 87.1311 | 28.0168 | 4274 | 4504 | 3.4 | 0.43 | 209 | 2.356 | 14.71 | 14.78 | 15.52 | 15.62 | 15.56 | -19.00 | -18.90 | 34.63 | 84.3 | 34.63 | 84.3 |
| 51776 ES385-031 | 324.8917 | 24.0301 | 156.6134 | 9.4192 | 3113 | 3365 | 6.2 | 0.20 | 128 | 2.107 | / | / | 16.25 | 16.34 | / | / | -16.47 | / | / | 32.84 | 37.0 |
| 51780 UGC09299 | 347.9424 | 54.0458 | 123.2279 | 22.7014 | 1543 | 1791 | 6.4 | 0.41 | 173 | 2.269 | 13.19 | 13.25 | 14.24 | 14.27 | 14.12 | -18.21 | -18.05 | 32.33 | 29.3 | 32.34 | 29.3 |

| PGC Name | l | b | sgl | sgb | v_{hel} | v_{mod} | t | b/a | w_{mr} | $\log w_{mr}^*$ | I | I* | [3.6] | [3.6]* | $C_{[3.6]}$ | M_C | $M_{[3.6]}$ | μ_C | d_C | $\mu_{[3.6]}$ | $d_{[3.6]}$ |
|-----------------|----------|---------|----------|---------|-----------|-----------|-----|------|----------|-----------------|-------|-------|-------|--------|-------------|--------|-------------|---------|-------|---------------|-------------|
| 51820 AGC030669 | 324.0044 | 21.8333 | 158.7891 | 8.4840 | 2840 | 3083 | 4.6 | 0.67 | 264 | 2.541 | 11.55 | 11.61 | 12.14 | 12.23 | 12.28 | -20.68 | -20.71 | 32.98 | 39.5 | 32.96 | 39.1 |
| 51831 NGC05656 | 60.2821 | 67.3849 | 84.3993 | 28.3043 | 3159 | 3357 | 2.0 | 0.69 | 357 | 2.681 | 11.33 | 11.45 | 11.64 | 11.73 | 11.96 | -21.96 | -22.08 | 33.97 | 62.1 | 33.88 | 59.7 |
| 51846 UGC09328 | 357.3365 | 59.2178 | 115.6259 | 24.9173 | 1366 | 1604 | 6.6 | 0.55 | 179 | 2.322 | 11.25 | 11.39 | 12.20 | 12.29 | 12.19 | -18.69 | -18.57 | 30.88 | 15.0 | 30.85 | 14.8 |
| 51854 AGC240420 | 9.3396 | 63.6417 | 107.7971 | 26.5020 | 12158 | 12779 | 1.5 | 0.58 | 360 | 2.638 | 13.73 | 13.75 | 16.23 | 16.39 | 15.39 | -21.57 | -21.66 | 37.21 | 276.1 | 38.58 | 521.2 |
| 51901 UGC09347 | 89.7159 | 60.2190 | 67.8587 | 27.4135 | 2080 | 2211 | 5.2 | 0.22 | 256 | 2.411 | 12.60 | 12.40 | 13.48 | 13.53 | 13.32 | -19.50 | -19.44 | 32.83 | 36.8 | 33.00 | 39.8 |
| 51909 UGC09345 | 356.1366 | 58.2527 | 116.8922 | 24.9023 | 2340 | 2588 | 6.4 | 0.20 | 211 | 2.324 | / | / | 15.37 | 15.43 | / | -18.59 | / | / | / | 34.10 | 66.2 |
| 51932 UGC09358 | 100.0446 | 54.5048 | 59.0665 | 26.0750 | 1906 | 2004 | 3.4 | 0.58 | 383 | 2.662 | 10.26 | 10.30 | 10.64 | 10.72 | 10.88 | -21.79 | -21.90 | 32.68 | 34.3 | 32.64 | 33.7 |
| 51948 E447-019 | 328.4452 | 29.4447 | 151.1818 | 12.7314 | 3863 | 4137 | 2.2 | 0.24 | 333 | 2.526 | 12.35 | 11.94 | 12.55 | 12.59 | 12.63 | -20.55 | -20.57 | 33.20 | 43.7 | 33.20 | 43.6 |
| 51953 UGC09352 | 359.0798 | 59.4358 | 114.8791 | 25.5353 | 2237 | 2481 | 5.0 | 0.59 | 194 | 2.373 | 11.20 | 11.34 | 11.70 | 11.80 | 11.93 | -19.15 | -19.07 | 31.09 | 16.5 | 30.87 | 14.9 |
| 51955 IC0001029 | 89.4360 | 60.1392 | 67.8943 | 27.5708 | 2378 | 2512 | 3.1 | 0.38 | 444 | 2.672 | 11.15 | 10.95 | 11.51 | 11.57 | 11.62 | -21.87 | -21.99 | 33.53 | 50.7 | 33.61 | 52.6 |
| 51973 UGC09353 | 1.9339 | 60.5564 | 112.9378 | 26.0210 | 1368 | 1599 | 6.0 | 0.60 | 182 | 2.348 | 11.00 | 11.15 | 11.94 | 11.97 | 11.92 | -18.93 | -18.83 | 30.85 | 14.8 | 30.80 | 14.5 |
| 51978 UGC09366 | 88.6767 | 60.3857 | 68.3849 | 27.6876 | 2106 | 2238 | 4.7 | 0.47 | 443 | 2.693 | 10.03 | 9.93 | 10.33 | 10.40 | 10.53 | -22.07 | -22.20 | 32.61 | 33.3 | 32.61 | 33.3 |
| 52090 AGC030724 | 329.1422 | 29.5742 | 151.0481 | 13.3378 | 3776 | 4046 | 5.8 | 0.51 | 302 | 2.537 | 12.28 | 12.19 | 12.77 | 12.84 | 12.88 | -20.64 | -20.67 | 33.55 | 51.4 | 33.56 | 51.6 |
| 52159 UGC09389 | 7.8096 | 61.8081 | 109.7960 | 27.3244 | 1830 | 2058 | 3.2 | 0.28 | 222 | 2.355 | 12.61 | 12.53 | 13.89 | 13.96 | 13.59 | -18.99 | -18.89 | 32.59 | 32.9 | 32.88 | 37.6 |
| 52167 UGC09394 | 8.3025 | 61.9322 | 109.5124 | 27.4016 | 1801 | 2028 | 5.9 | 0.24 | 169 | 2.232 | 13.48 | 13.49 | 14.44 | 14.52 | 14.36 | -17.87 | -17.69 | 32.24 | 28.0 | 32.22 | 27.8 |
| 52251 NGC05698 | 66.7605 | 65.1705 | 80.7755 | 29.5774 | 3676 | 3867 | 3.1 | 0.43 | 295 | 2.505 | / | / | 12.49 | 12.58 | / | -20.36 | / | / | / | 32.97 | 39.2 |
| 52266 NGC05707 | 90.8888 | 58.4551 | 65.8985 | 28.0916 | 2215 | 2337 | 2.0 | 0.25 | 405 | 2.613 | 11.24 | 10.89 | 11.93 | 11.97 | 11.78 | -21.33 | -21.41 | 33.14 | 42.5 | 33.42 | 48.4 |
| 52273 UGC09416 | 353.1551 | 54.4535 | 121.4444 | 25.3059 | 1749 | 1987 | 5.4 | 0.30 | 293 | 2.478 | 10.81 | 10.63 | 11.17 | 11.23 | 11.29 | -20.11 | -20.10 | 31.41 | 19.1 | 31.33 | 18.5 |
| 52307 UGC09431 | 82.9175 | 61.3401 | 71.4136 | 28.9764 | 2240 | 2379 | 5.8 | 0.20 | 333 | 2.522 | 12.01 | 11.66 | 12.31 | 12.35 | 12.36 | -20.51 | -20.53 | 32.89 | 37.9 | 32.90 | 38.1 |
| 52315 NGC05708 | 70.9697 | 64.2652 | 78.4622 | 29.6458 | 2723 | 2890 | 7.8 | 0.38 | 236 | 2.399 | 12.33 | 12.34 | 12.94 | 13.03 | 13.04 | -19.39 | -19.32 | 32.44 | 30.8 | 32.36 | 29.7 |
| 52324 IC004468 | 333.1314 | 34.1535 | 146.1952 | 16.5720 | 2455 | 2703 | 4.7 | 0.32 | 269 | 2.444 | 11.91 | 11.70 | 12.30 | 12.36 | 12.39 | -19.80 | -19.77 | 32.20 | 27.5 | 32.13 | 26.7 |
| 52328 UGC09439 | 89.5876 | 58.8089 | 66.6995 | 28.3847 | 7784 | 8058 | 3.0 | 0.60 | 409 | 2.700 | 12.38 | 12.42 | 12.94 | 13.07 | 13.10 | -22.13 | -22.26 | 35.34 | 117.0 | 35.50 | 126.1 |
| 52361 UGC09437 | 19.8750 | 63.8697 | 103.4630 | 29.1519 | 14401 | 15161 | 3.3 | 0.47 | 404 | 2.652 | / | / | 14.65 | 14.81 | / | -21.79 | / | / | / | 36.92 | 241.9 |
| 52381 NGC005688 | 322.2500 | 13.7579 | 166.7839 | 6.2177 | 2798 | 3014 | 5.0 | 0.46 | 438 | 2.684 | 10.59 | 10.29 | 10.59 | 10.64 | 10.83 | -21.99 | -22.11 | 32.83 | 36.9 | 32.77 | 35.8 |
| 52455 UGC09462 | 351.2195 | 51.9783 | 124.4676 | 25.3237 | 1741 | 1977 | 2.4 | 0.40 | 375 | 2.604 | 10.48 | 10.34 | 10.63 | 10.69 | 10.88 | -21.25 | -21.32 | 32.14 | 26.8 | 32.01 | 25.3 |
| 52460 PG0052460 | 343.1914 | 45.2523 | 133.3137 | 22.5166 | 1877 | 2118 | 1.4 | 0.66 | 173 | 2.353 | / | / | 13.46 | 13.55 | / | -18.88 | / | / | / | 32.44 | 30.7 |
| 52521 AGC540121 | 337.3245 | 38.0986 | 141.7229 | 19.5637 | 2784 | 3035 | 1.2 | 0.47 | 393 | 2.640 | 10.18 | 9.99 | 10.54 | 10.55 | 10.63 | -21.58 | -21.68 | 32.22 | 27.8 | 32.23 | 27.9 |
| 52558 UGC009482 | 352.8509 | 52.3932 | 123.5830 | 26.0565 | 1803 | 2037 | 6.6 | 0.20 | 164 | 2.215 | / | / | 15.35 | 15.42 | / | -17.52 | / | / | / | 32.97 | 39.3 |
| 52620 ES386-016 | 327.0872 | 21.3994 | 159.3776 | 11.3241 | 7285 | 7639 | 4.1 | 0.20 | 363 | 2.560 | / | / | 14.41 | 14.47 | / | -20.90 | / | / | / | 35.54 | 128.2 |
| 52665 NGC5746 | 354.9659 | 52.9555 | 122.3756 | 26.9472 | 1723 | 1952 | 3.0 | 0.22 | 634 | 2.804 | 9.33 | 8.68 | 9.40 | 9.40 | 9.40 | -23.08 | -23.28 | 32.49 | 31.5 | 32.70 | 34.7 |
| 52730 AGC030834 | 337.7491 | 36.9814 | 142.8542 | 20.0419 | 2224 | 2462 | 7.7 | 0.69 | 145 | 2.293 | / | / | 13.32 | 13.41 | / | -18.29 | / | / | / | 31.69 | 21.8 |
| 52809 AGC540131 | 338.4701 | 37.2971 | 142.4391 | 20.5695 | 2200 | 2436 | 5.8 | 0.20 | 224 | 2.350 | 11.90 | 11.62 | 11.93 | 11.97 | 12.17 | -18.95 | -18.85 | 31.11 | 16.7 | 30.82 | 14.6 |
| 52811 AGC540133 | 341.1316 | 40.3987 | 138.7902 | 22.1068 | 2909 | 3157 | 3.1 | 0.34 | 382 | 2.599 | 11.37 | 11.07 | 11.90 | 11.95 | 11.87 | -21.21 | -21.28 | 33.10 | 41.7 | 33.27 | 45.0 |
| 52824 AGC030851 | 336.9681 | 35.3196 | 144.6877 | 19.6128 | 2591 | 2832 | 5.0 | 0.20 | 328 | 2.516 | 12.10 | 11.64 | 12.09 | 12.12 | 12.24 | -20.45 | -20.47 | 32.71 | 34.8 | 32.60 | 33.1 |
| 52825 AGC540134 | 340.3317 | 39.4402 | 139.9260 | 21.6775 | 2148 | 2384 | 3.9 | 0.40 | 291 | 2.493 | 11.24 | 11.08 | 11.55 | 11.61 | 11.71 | -20.25 | -20.24 | 31.96 | 24.6 | 31.86 | 23.5 |
| 52832 UGC09530 | 5.9764 | 57.4982 | 114.1107 | 29.5699 | 8603 | 9014 | 4.1 | 0.68 | 234 | 2.495 | / | / | 14.10 | 14.25 | / | -20.26 | / | / | / | 34.62 | 83.9 |

| PGC Name | l | b | sgl | sgb | v_{hel} | v_{mod} | t | b/a | w_{max} | $\log w_{max}^i$ | I | I* | [3.6] | [3.6]* | $C_{[3.6]}$ | M_C | $M_{[3.6]}$ | μ_C | dC | $\mu_{[3.6]}$ | $d_{[3.6]}$ |
|-----------------|----------|----------|----------|---------|-----------|-----------|-----|------|-----------|------------------|-------|-------|-------|--------|-------------|--------|-------------|---------|------|---------------|-------------|
| 52853 AGC540136 | 340.8435 | 39.8610 | 139.4044 | 21.9904 | 2045 | 2280 | 6.0 | 0.69 | 198 | 2.431 | 12.05 | 12.13 | 13.19 | 13.27 | 13.06 | -19.68 | -19.64 | 32.75 | 35.5 | 32.94 | 38.6 |
| 52991 ES580-041 | 338.7881 | 36.2902 | 143.4687 | 20.9593 | 2945 | 3188 | 4.1 | 0.20 | 229 | 2.360 | 12.78 | 12.49 | 13.32 | 13.37 | 13.29 | -19.03 | -18.94 | 32.33 | 29.2 | 32.32 | 29.1 |
| 53043 UGC09568 | 98.2108 | 52.0106 | 57.1991 | 28.2344 | 2141 | 2225 | 3.2 | 0.20 | 413 | 2.616 | 11.53 | 11.08 | 11.68 | 11.71 | 11.75 | -21.37 | -21.44 | 33.14 | 42.5 | 33.19 | 43.4 |
| 53093 P0053093 | 344.6989 | 42.1341 | 136.3117 | 24.3454 | 2583 | 2820 | 2.9 | 0.52 | 292 | 2.525 | / | / | 12.52 | 12.60 | / | / | -20.55 | / | / | / | 43.4 |
| 53134 AGC540146 | 351.2431 | 47.6220 | 128.9272 | 27.0458 | 1952 | 2177 | 8.0 | 0.35 | 149 | 2.193 | / | / | 13.52 | 13.59 | / | / | -17.31 | / | / | / | 15.1 |
| 53183 AGC030906 | 338.3335 | 34.6369 | 145.2742 | 20.8023 | 3978 | 4237 | 4.2 | 0.24 | 259 | 2.418 | 13.54 | 13.26 | 13.98 | 14.04 | 14.01 | -19.56 | -19.51 | 33.60 | 52.5 | 33.59 | 52.3 |
| 53217 UGC09586 | 88.8193 | 56.1987 | 64.7275 | 30.3925 | 2337 | 2446 | 5.2 | 0.63 | 242 | 2.483 | 11.94 | 12.04 | 12.84 | 12.94 | 12.84 | -20.16 | -20.15 | 33.02 | 40.2 | 33.12 | 42.0 |
| 53247 UGC09579 | 359.4314 | 52.4229 | 121.3652 | 29.5578 | 1681 | 1896 | 5.2 | 0.20 | 392 | 2.593 | 10.10 | 9.63 | 9.95 | 9.98 | 10.17 | -21.16 | -21.22 | 31.33 | 18.4 | 31.20 | 17.4 |
| 53469 UGC09649 | 110.1038 | 42.1571 | 43.7002 | 24.2948 | 447 | 469 | 3.3 | 0.42 | 153 | 2.218 | / | / | 12.31 | 12.34 | / | / | -17.55 | / | / | / | 9.5 |
| 53499 UGC09631 | 355.3529 | 48.4268 | 126.8211 | 29.2258 | 1922 | 2138 | 3.0 | 0.39 | 422 | 2.652 | 9.92 | 9.70 | 10.24 | 10.29 | 10.35 | -21.70 | -21.80 | 32.05 | 25.8 | 32.09 | 26.2 |
| 53578 UGC09645 | 359.0910 | 50.1942 | 123.6937 | 30.5323 | 1360 | 1565 | 3.2 | 0.54 | 340 | 2.598 | 10.33 | 10.30 | 10.83 | 10.90 | 10.96 | -21.20 | -21.27 | 32.17 | 27.2 | 32.18 | 27.3 |
| 53634 AGC540178 | 343.5080 | 37.3400 | 141.6694 | 24.5122 | 2928 | 3158 | 7.0 | 0.23 | 199 | 2.302 | 13.70 | 13.51 | 14.61 | 14.67 | 14.44 | -18.51 | -18.37 | 32.96 | 39.1 | 33.07 | 41.2 |
| 53657 UGC09665 | 81.7757 | 57.0928 | 68.6443 | 32.5430 | 2558 | 2675 | 4.0 | 0.23 | 291 | 2.467 | 12.49 | 12.25 | 12.56 | 12.62 | 12.80 | -20.01 | -19.99 | 32.82 | 36.7 | 32.62 | 33.5 |
| 53764 PG0053764 | 347.7391 | 40.3240 | 137.5950 | 27.0222 | 2438 | 2657 | 5.5 | 0.20 | 190 | 2.279 | / | / | 14.76 | 14.82 | / | / | -18.15 | / | / | / | 39.7 |
| 53779 PG0053779 | 350.8528 | 42.9607 | 133.9616 | 28.4441 | 1874 | 2084 | 3.0 | 0.71 | 145 | 2.305 | / | / | 13.09 | 13.18 | / | / | -18.40 | / | / | / | 20.8 |
| 53796 AGC550006 | 344.8625 | 37.3759 | 141.3885 | 25.5590 | 2932 | 3158 | 6.2 | 0.20 | 216 | 2.334 | / | / | 14.59 | 14.64 | / | / | -18.69 | / | / | / | 47.3 |
| 53802 UGC09682 | 357.2093 | 47.5010 | 127.1293 | 30.7525 | 1821 | 2027 | 8.6 | 0.25 | 190 | 2.284 | / | / | 14.65 | 14.72 | / | / | -18.20 | / | / | / | 38.8 |
| 53861 UGC09703 | 78.3349 | 57.2845 | 70.4992 | 33.5899 | 2498 | 2616 | 3.0 | 0.30 | 214 | 2.342 | / | / | 13.43 | 13.51 | / | / | -18.77 | / | / | / | 28.6 |
| 54097 NGC5861 | 348.5268 | 39.0531 | 138.7895 | 27.9495 | 1852 | 2056 | 5.0 | 0.51 | 321 | 2.562 | 10.54 | 10.42 | 10.89 | 10.95 | 11.05 | -20.88 | -20.92 | 31.93 | 24.3 | 31.87 | 23.7 |
| 54117 UGC09753 | 93.2294 | 51.3966 | 58.4384 | 31.1916 | 770 | 836 | 3.6 | 0.39 | 269 | 2.457 | 10.52 | 10.49 | 11.15 | 11.16 | 11.19 | -19.92 | -19.89 | 31.11 | 16.6 | 31.05 | 16.2 |
| 54134 UGC09746 | 1.7370 | 48.2945 | 124.5460 | 32.9953 | 1739 | 1934 | 4.0 | 0.29 | 195 | 2.300 | 13.12 | 13.07 | 13.73 | 13.80 | 13.79 | -18.49 | -18.36 | 32.29 | 28.7 | 32.16 | 27.1 |
| 54234 NGC5894 | 96.5168 | 49.5064 | 55.2909 | 30.3909 | 2476 | 2547 | 7.8 | 0.20 | 440 | 2.643 | 11.21 | 10.73 | 11.46 | 11.49 | 11.46 | -21.62 | -21.71 | 33.10 | 41.7 | 33.23 | 44.3 |
| 54250 NGC005833 | 312.9424 | -12.7776 | 192.2738 | -5.6918 | 3031 | 3154 | 4.2 | 0.37 | 407 | 2.633 | 10.72 | 10.36 | 10.74 | 10.78 | 10.93 | -21.52 | -21.61 | 32.46 | 31.1 | 32.40 | 30.2 |
| 54262 UGC09760 | 1.8951 | 47.8067 | 124.9730 | 33.3437 | 2023 | 2219 | 6.6 | 0.20 | 135 | 2.130 | 14.19 | 14.23 | 15.42 | 15.50 | 15.22 | -16.95 | -16.70 | 32.17 | 27.1 | 32.21 | 27.7 |
| 54324 IC0004536 | 344.1234 | 33.1573 | 146.1108 | 25.7707 | 2282 | 2486 | 7.4 | 0.68 | 165 | 2.343 | / | / | 12.83 | 12.92 | / | / | -18.78 | / | / | / | 21.9 |
| 54348 ES581-025 | 342.3440 | 31.1134 | 148.5962 | 24.5921 | 2269 | 2471 | 6.9 | 0.21 | 333 | 2.523 | 11.53 | 11.00 | 11.47 | 11.48 | 11.61 | -20.52 | -20.54 | 32.13 | 26.7 | 32.03 | 25.4 |
| 54364 AGC550029 | 347.1860 | 36.0927 | 142.3300 | 27.6578 | 1992 | 2192 | 3.2 | 0.35 | 444 | 2.667 | 10.38 | 9.96 | 10.79 | 10.81 | 10.74 | -21.83 | -21.94 | 32.58 | 32.8 | 32.78 | 35.9 |
| 54392 ES274-001 | 326.8056 | 9.3372 | 171.6166 | 10.2908 | 522 | 680 | 6.7 | 0.20 | 156 | 2.193 | 10.20 | 9.87 | 10.61 | 10.63 | 10.61 | -17.52 | -17.31 | 28.13 | 4.2 | 27.94 | 3.9 |
| 54428 UGC09789 | 69.3982 | 57.2155 | 75.4121 | 36.2598 | 2589 | 2712 | 5.3 | 0.37 | 472 | 2.697 | 10.69 | 10.44 | 10.96 | 11.02 | 11.09 | -22.10 | -22.23 | 33.22 | 44.0 | 33.29 | 45.5 |
| 54431 UGC09790 | 69.6795 | 57.1671 | 75.2169 | 36.2318 | 2463 | 2583 | 3.0 | 0.34 | 412 | 2.633 | 12.06 | 11.83 | 11.63 | 11.68 | 12.13 | -21.52 | -21.61 | 33.69 | 54.7 | 33.33 | 46.3 |
| 54470 UGC09801 | 91.5844 | 51.0871 | 58.8190 | 32.2170 | 667 | 730 | 5.3 | 0.20 | 469 | 2.671 | 9.10 | 8.59 | 9.15 | 9.12 | 9.22 | -21.87 | -21.98 | 31.08 | 16.5 | 31.10 | 16.6 |
| 54754 AGC031140 | 345.6075 | 31.8797 | 147.2768 | 27.2231 | 2215 | 2408 | 5.0 | 0.35 | 202 | 2.325 | 13.10 | 12.93 | 14.28 | 14.33 | 13.98 | -18.72 | -18.60 | 32.71 | 34.8 | 32.96 | 39.1 |
| 54755 ES387-026 | 333.3838 | 16.9557 | 164.1629 | 17.1202 | 4374 | 4593 | 4.7 | 0.40 | 455 | 2.687 | 11.25 | 10.92 | 11.61 | 11.67 | 11.65 | -22.01 | -22.14 | 33.70 | 55.0 | 33.87 | 59.4 |
| 54761 NGC05913 | 359.3860 | 43.3194 | 130.7062 | 34.0236 | 2008 | 2194 | 1.0 | 0.44 | 345 | 2.576 | 11.57 | 11.21 | 11.59 | 11.62 | 11.78 | -21.00 | -21.05 | 32.80 | 36.3 | 32.69 | 34.6 |
| 54944 PG0054944 | 358.3587 | 41.8138 | 132.7390 | 34.0061 | 1999 | 2183 | 1.8 | 0.63 | 174 | 2.341 | 12.05 | 12.09 | 12.54 | 12.62 | 12.72 | -18.87 | -18.76 | 31.59 | 20.8 | 31.38 | 18.9 |
| 54969 AGC031164 | 341.1593 | 25.8829 | 154.4285 | 24.1269 | 3694 | 3904 | 5.4 | 0.20 | 189 | 2.276 | 15.54 | 15.23 | 15.96 | 16.01 | 15.98 | -18.28 | -18.13 | 34.32 | 73.0 | 34.22 | 69.8 |

| PGC Name | l | b | sgl | sgb | v_{hel} | v_{mod} | t | b/a | w_{mz} | $\log w_{mz}^2$ | I | I* | [3.6] | [3.6]* | $C_{[3.6]}$ | MC | $M_{[3.6]}$ | μC | dC | $\mu_{[3.6]}$ | $d_{[3.6]}$ |
|-----------------|----------|----------|----------|---------|-----------|-----------|-----|------|----------|-----------------|-------|-------|-------|--------|-------------|--------|-------------|---------|-------|---------------|-------------|
| 55078 UGC09845 | 14.2016 | 49.3689 | 117.1636 | 38.7054 | 1892 | 2058 | 5.8 | 0.20 | 163 | 2.212 | 14.01 | 13.99 | 15.83 | 15.91 | 15.28 | -17.69 | -17.50 | 33.00 | 39.8 | 33.46 | 49.1 |
| 55081 AGC031181 | 343.8596 | 28.0372 | 151.7849 | 26.2980 | 2318 | 2503 | 5.0 | 0.55 | 274 | 2.506 | 11.02 | 10.91 | 11.44 | 11.51 | 11.57 | -20.37 | -20.37 | 31.94 | 24.4 | 31.88 | 23.8 |
| 55097 UGC09856 | 67.1648 | 55.3149 | 75.7416 | 38.5140 | 2491 | 2602 | 6.3 | 0.20 | 197 | 2.294 | 13.71 | 13.60 | 14.67 | 14.75 | 14.53 | -18.44 | -18.30 | 32.99 | 39.5 | 33.08 | 41.3 |
| 55104 UGC09858 | 65.9010 | 55.4207 | 76.6333 | 38.7178 | 2618 | 2732 | 4.0 | 0.24 | 356 | 2.556 | 11.69 | 11.38 | 12.29 | 12.34 | 12.22 | -20.82 | -20.86 | 33.05 | 40.8 | 33.23 | 44.2 |
| 55165 UGC09866 | 100.5709 | 44.9717 | 49.1797 | 29.9338 | 425 | 454 | 4.0 | 0.46 | 177 | 2.291 | 11.07 | 11.19 | 11.79 | 11.82 | 11.86 | -18.41 | -18.27 | 30.28 | 11.4 | 30.09 | 10.4 |
| 55256 ES329-007 | 333.9285 | 14.4874 | 166.7650 | 17.5654 | 4654 | 4867 | 3.0 | 0.43 | 472 | 2.709 | 11.58 | 11.17 | 11.52 | 11.57 | 11.74 | -22.22 | -22.36 | 34.00 | 63.1 | 34.00 | 63.0 |
| 55281 NGC005937 | 1.3269 | 41.3073 | 132.0889 | 36.2211 | 2809 | 2992 | 3.2 | 0.61 | 333 | 2.615 | 11.24 | 11.07 | 11.24 | 11.30 | 11.56 | -21.35 | -21.43 | 32.93 | 38.5 | 32.75 | 35.6 |
| 55305 NGC005950 | 65.3923 | 54.5412 | 76.5220 | 39.6403 | 2599 | 2708 | 3.1 | 0.50 | 208 | 2.372 | / | / | 13.27 | 13.37 | / | / | -19.06 | / | / | 32.44 | 30.7 |
| 55328 AGC031212 | 343.2559 | 25.2639 | 154.9227 | 26.0658 | 4435 | 4651 | 5.2 | 0.20 | 278 | 2.444 | 14.14 | 13.60 | 14.25 | 14.28 | 14.30 | -19.80 | -19.76 | 34.16 | 67.8 | 34.12 | 66.8 |
| 55388 UGC09888 | 3.0523 | 41.6346 | 130.9623 | 37.2023 | 2797 | 2975 | 7.3 | 0.58 | 197 | 2.376 | 12.58 | 12.52 | 13.08 | 13.15 | 13.20 | -19.18 | -19.10 | 32.39 | 30.0 | 32.26 | 28.3 |
| 55435 UGC09895 | 23.5230 | 50.4494 | 110.1321 | 41.5856 | 1778 | 1924 | 5.2 | 0.23 | 261 | 2.419 | 11.88 | 11.63 | 12.58 | 12.63 | 12.49 | -19.58 | -19.52 | 32.07 | 25.9 | 32.16 | 27.1 |
| 55588 UGC09926 | 26.2516 | 50.4729 | 108.1070 | 42.4540 | 1957 | 2099 | 5.1 | 0.67 | 338 | 2.647 | 10.38 | 10.44 | 10.77 | 10.85 | 11.01 | -21.65 | -21.74 | 32.67 | 34.2 | 32.61 | 33.3 |
| 55620 UGC09940 | 69.8233 | 52.9624 | 72.5557 | 39.8787 | 5712 | 5877 | 5.7 | 0.70 | 304 | 2.620 | 11.95 | 12.07 | 12.27 | 12.39 | 12.60 | -21.40 | -21.48 | 34.05 | 64.6 | 33.94 | 61.4 |
| 55647 NGC05981 | 93.2156 | 46.9911 | 54.0367 | 33.5568 | 2594 | 2648 | 4.2 | 0.20 | 449 | 2.652 | 11.63 | 11.11 | 11.80 | 11.78 | 11.81 | -21.70 | -21.80 | 33.53 | 50.9 | 33.63 | 53.2 |
| 55665 UGC09943 | 20.4118 | 48.1692 | 114.1240 | 42.2893 | 1956 | 2101 | 5.0 | 0.60 | 306 | 2.574 | 10.50 | 10.55 | 11.16 | 11.24 | 11.25 | -20.98 | -21.03 | 32.24 | 28.1 | 32.28 | 28.6 |
| 55725 UGC09969 | 92.9788 | 46.8301 | 53.9721 | 33.7787 | 2520 | 2572 | 3.0 | 0.52 | 534 | 2.788 | 10.22 | 10.15 | 10.66 | 10.74 | 10.80 | -22.93 | -23.12 | 33.78 | 56.9 | 33.93 | 61.1 |
| 55739 UGC09963 | 33.9474 | 51.3629 | 101.5455 | 43.6004 | 4389 | 4560 | 3.5 | 0.46 | 358 | 2.597 | 12.24 | 12.12 | 12.28 | 12.36 | 12.61 | -21.19 | -21.25 | 33.84 | 58.6 | 33.67 | 54.1 |
| 55800 NGC05980 | 25.8081 | 49.0518 | 109.4086 | 43.5474 | 4088 | 4259 | 4.4 | 0.32 | 416 | 2.634 | / | / | 11.78 | 11.84 | / | -21.62 | / | / | / | 33.50 | 50.2 |
| 55821 UGC09977 | 7.3441 | 41.3253 | 129.1607 | 40.1099 | 1913 | 2065 | 5.3 | 0.20 | 246 | 2.391 | 12.47 | 12.12 | 12.92 | 12.96 | 12.90 | -19.32 | -19.24 | 32.22 | 27.8 | 32.21 | 27.7 |
| 55853 UGC09987 | 23.8676 | 48.1099 | 111.6008 | 43.6729 | 1107 | 1235 | 6.4 | 0.27 | 222 | 2.354 | 11.74 | 11.63 | 12.42 | 12.48 | 12.41 | -18.98 | -18.88 | 31.39 | 19.0 | 31.37 | 18.8 |
| 55867 UGC09991 | 24.2237 | 48.0837 | 111.3445 | 43.8244 | 1951 | 2086 | 5.9 | 0.23 | 199 | 2.302 | 13.49 | 13.40 | 14.72 | 14.79 | 14.44 | -18.51 | -18.38 | 32.97 | 39.3 | 33.21 | 43.8 |
| 56077 IC0004555 | 311.5891 | -18.3975 | 197.8034 | -7.4545 | 2662 | 2753 | 5.8 | 0.22 | 238 | 2.379 | 12.37 | 12.09 | 12.86 | 12.91 | 12.86 | -19.21 | -19.13 | 32.07 | 25.9 | 32.04 | 25.6 |
| 56078 NGC005967 | 313.2985 | -16.4948 | 196.0253 | -5.6770 | 2905 | 3005 | 5.7 | 0.63 | 301 | 2.581 | 11.06 | 11.04 | 11.40 | 11.47 | 11.62 | -21.05 | -21.10 | 32.68 | 34.4 | 32.59 | 33.0 |
| 56094 UGC10043 | 35.4684 | 49.5387 | 101.0340 | 45.6334 | 2175 | 2294 | 4.2 | 0.20 | 319 | 2.504 | 13.05 | 12.66 | 12.59 | 12.63 | 13.02 | -20.34 | -20.35 | 33.39 | 47.7 | 33.00 | 39.9 |
| 56111 UGC10041 | 13.6324 | 42.4191 | 124.2193 | 43.1908 | 2167 | 2307 | 7.9 | 0.54 | 192 | 2.349 | 12.51 | 12.56 | 13.56 | 13.65 | 13.46 | -18.94 | -18.84 | 32.41 | 30.3 | 32.50 | 31.6 |
| 56157 ES515-010 | 347.4886 | 23.3955 | 156.5741 | 30.0959 | 5736 | 5963 | 2.5 | 0.40 | 377 | 2.605 | / | / | 12.92 | 12.96 | / | / | -21.34 | / | / | 34.39 | 75.6 |
| 56219 UGC10075 | 95.6924 | 44.1246 | 50.0219 | 33.4392 | 833 | 854 | 5.9 | 0.48 | 295 | 2.518 | 10.16 | 10.18 | 10.83 | 10.90 | 10.90 | -20.47 | -20.48 | 31.37 | 18.8 | 31.39 | 18.9 |
| 56500 AGC031339 | 349.7512 | 22.9873 | 156.7584 | 32.2095 | 7403 | 7678 | 5.0 | 0.20 | 500 | 2.699 | / | / | 13.19 | 13.21 | / | / | -22.25 | / | / | 35.65 | 135.1 |
| 56537 UGC10113 | 30.3645 | 45.9035 | 107.6261 | 47.7703 | 2170 | 2281 | 5.1 | 0.40 | 226 | 2.383 | 12.10 | 12.09 | 12.86 | 12.89 | 12.85 | -19.24 | -19.16 | 32.10 | 26.3 | 32.06 | 25.8 |
| 56723 UGC10133 | 12.0558 | 37.8952 | 130.2105 | 45.0425 | 1926 | 2047 | 5.1 | 0.51 | 235 | 2.427 | 11.93 | 11.86 | 12.58 | 12.64 | 12.61 | -19.64 | -19.59 | 32.26 | 28.3 | 32.25 | 28.1 |
| 56917 UGC010194 | 96.4842 | 42.2036 | 47.6465 | 33.7707 | 871 | 880 | 6.8 | 0.20 | 127 | 2.104 | / | / | 15.88 | 15.96 | / | / | -16.44 | / | / | 32.42 | 30.4 |
| 57140 E451-008 | 346.1372 | 16.8122 | 164.2430 | 29.3223 | 4718 | 4893 | 3.0 | 0.20 | 471 | 2.673 | / | / | 12.47 | 12.47 | / | / | -22.00 | / | / | 34.58 | 82.3 |
| 57173 UGC10205 | 48.9182 | 47.3726 | 88.4042 | 48.9260 | 6562 | 6745 | 1.0 | 0.59 | 541 | 2.817 | / | / | 12.15 | 12.26 | / | / | -23.41 | / | / | 35.87 | 149.6 |
| 57205 UGC10210 | 19.8851 | 39.9538 | 122.1259 | 48.2998 | 2848 | 2966 | 5.9 | 0.55 | 265 | 2.493 | 12.23 | 12.27 | 13.02 | 13.06 | 13.02 | -20.24 | -20.24 | 33.29 | 45.5 | 33.34 | 46.5 |
| 57261 UGC10219 | 19.5517 | 39.5082 | 122.8694 | 48.4394 | 1369 | 1469 | 6.0 | 0.20 | 199 | 2.299 | 12.65 | 12.51 | 13.19 | 13.25 | 13.24 | -18.48 | -18.35 | 31.72 | 22.1 | 31.60 | 20.9 |
| 57271 ES516-008 | 349.6882 | 19.4659 | 160.9115 | 32.5260 | 7124 | 7373 | 4.0 | 0.25 | 337 | 2.532 | 14.23 | 13.74 | 14.14 | 14.20 | 14.33 | -20.60 | -20.62 | 35.03 | 101.3 | 34.95 | 97.8 |

| PGC Name | l | b | sgl | sgb | v_{hel} | v_{mod} | t | b/a | w_{mz} | $\log w_{mz}^2$ | I | I* | [3.6] | [3.6]* | $C_{[3.6]}$ | MC | $M_{[3.6]}$ | μC | dC | $\mu_{[3.6]}$ | $d_{[3.6]}$ | |
|-----------------|----------|----------|----------|---------|-----------|-----------|-----|------|----------|-----------------|-------|-------|-------|--------|-------------|--------|-------------|---------|-------|---------------|-------------|-------|
| 57345 NGC06070 | 12.4700 | 35.5919 | 132.6515 | 46.6312 | 2005 | 2115 | 6.0 | 0.52 | 373 | 2.631 | / | / | 10.84 | 10.89 | / | / | -21.59 | / | / | / | 32.49 | 31.5 |
| 57582 UGC10288 | 12.2858 | 34.1609 | 134.5246 | 47.2918 | 2044 | 2148 | 5.3 | 0.20 | 359 | 2.555 | 11.85 | 11.28 | 11.83 | 11.84 | 11.92 | -20.81 | -20.85 | 32.75 | 35.5 | 32.71 | 34.8 | |
| 57627 UGC10297 | 34.2512 | 42.6480 | 105.6850 | 51.8651 | 2312 | 2398 | 5.1 | 0.21 | 223 | 2.349 | 13.35 | 13.15 | 13.95 | 14.01 | 13.94 | -18.94 | -18.84 | 32.89 | 37.9 | 32.87 | 37.5 | |
| 57665 IC0004596 | 352.7858 | 19.8666 | 160.0793 | 35.3883 | 7623 | 7880 | 2.1 | 0.23 | 577 | 2.764 | / | / | 12.72 | 12.74 | / | / | -22.89 | / | / | / | 35.83 | 146.7 |
| 57799 UGC10439 | 21.0100 | 37.1671 | 124.1368 | 50.9125 | 1447 | 1531 | 5.3 | 0.58 | 227 | 2.437 | 11.35 | 11.40 | 12.02 | 12.10 | 12.11 | -19.74 | -19.70 | 31.85 | 23.4 | 31.80 | 22.9 | |
| 57876 IC0004595 | 319.0275 | -14.1288 | 194.2236 | 0.0578 | 3391 | 3493 | 5.1 | 0.20 | 434 | 2.637 | 11.60 | 10.98 | 11.04 | 11.05 | 11.39 | -21.56 | -21.65 | 32.97 | 39.3 | 32.73 | 35.1 | |
| 57924 NGC006118 | 11.4579 | 31.4696 | 138.4855 | 48.0786 | 1570 | 1659 | 6.0 | 0.39 | 338 | 2.555 | 10.38 | 10.07 | 10.70 | 10.74 | 10.76 | -20.81 | -20.85 | 31.58 | 20.7 | 31.59 | 20.8 | |
| 58115 NGC006155 | 75.1553 | 43.7138 | 61.3403 | 45.3692 | 2419 | 2450 | 5.2 | 0.68 | 193 | 2.410 | 11.73 | 11.92 | 12.31 | 12.42 | 12.53 | -19.49 | -19.43 | 32.03 | 25.4 | 31.85 | 23.4 | |
| 58336 UGC10413 | 38.7444 | 40.3357 | 101.5307 | 55.1163 | 2996 | 3068 | 5.7 | 0.37 | 240 | 2.404 | 13.12 | 13.07 | 13.98 | 14.06 | 13.92 | -19.44 | -19.37 | 33.38 | 47.5 | 33.48 | 49.6 | |
| 58423 UGC10434 | 37.5054 | 39.5486 | 103.5239 | 55.6047 | 2529 | 2592 | 8.0 | 0.24 | 257 | 2.414 | 12.52 | 12.28 | 12.84 | 12.90 | 12.95 | -19.53 | -19.47 | 32.49 | 31.5 | 32.38 | 29.9 | |
| 58470 UGC10439 | 37.1664 | 39.2081 | 104.1526 | 55.8481 | 2373 | 2433 | 5.2 | 0.50 | 362 | 2.613 | 10.69 | 10.60 | 10.96 | 11.03 | 11.18 | -21.34 | -21.42 | 32.53 | 32.1 | 32.46 | 31.1 | |
| 58596 UGC10469 | 62.3114 | 42.1427 | 71.9903 | 51.8054 | 9021 | 9252 | 3.1 | 0.54 | 517 | 2.779 | 12.09 | 12.03 | 12.58 | 12.70 | 12.72 | -22.85 | -23.04 | 35.71 | 138.7 | 35.96 | 155.3 | |
| 58792 ES517-013 | 354.9984 | 13.8799 | 167.3062 | 37.9893 | 8286 | 8533 | 6.2 | 0.20 | 302 | 2.480 | / | / | 15.44 | 15.45 | / | / | -20.11 | / | / | / | 35.76 | 141.7 |
| 58798 AGC560012 | 12.0476 | 25.7437 | 146.0357 | 51.1030 | 1566 | 1625 | 4.0 | 0.43 | 278 | 2.480 | 11.61 | 10.93 | 11.48 | 11.46 | 11.56 | -20.13 | -20.12 | 31.69 | 21.8 | 31.58 | 20.7 | |
| 58827 UGC10521 | 59.5360 | 40.6793 | 74.2386 | 53.9580 | 852 | 864 | 5.0 | 0.51 | 215 | 2.390 | 10.80 | 10.91 | 11.46 | 11.49 | 11.56 | -19.31 | -19.23 | 30.87 | 14.9 | 30.73 | 14.0 | |
| 58864 UGC10564 | 102.1899 | 35.7836 | 38.6217 | 31.9323 | 1130 | 1105 | 6.4 | 0.58 | 148 | 2.250 | 12.80 | 12.96 | 13.84 | 13.93 | 13.80 | -18.04 | -17.87 | 31.84 | 23.4 | 31.81 | 23.0 | |
| 58891 UGC10546 | 102.7407 | 35.7736 | 38.4602 | 31.5069 | 1277 | 1253 | 5.9 | 0.62 | 178 | 2.346 | 11.99 | 12.14 | 13.06 | 13.15 | 13.00 | -18.90 | -18.80 | 31.91 | 24.0 | 31.95 | 24.6 | |
| 59083 UGC10577 | 67.3831 | 39.7641 | 64.6882 | 52.0259 | 938 | 936 | 3.3 | 0.46 | 237 | 2.418 | 11.58 | 11.63 | 12.32 | 12.40 | 12.37 | -19.56 | -19.50 | 31.94 | 24.4 | 31.91 | 24.1 | |
| 59175 NGC006221 | 329.7378 | -9.5727 | 191.0752 | 11.0470 | 1489 | 1550 | 4.9 | 0.59 | 279 | 2.530 | 9.31 | 9.18 | 9.35 | 9.40 | 9.66 | -20.58 | -20.60 | 30.24 | 11.2 | 30.00 | 10.0 | |
| 59244 UGC10606 | 59.4852 | 38.3040 | 72.7863 | 56.1835 | 920 | 918 | 5.9 | 0.34 | 174 | 2.259 | 12.14 | 12.22 | 13.46 | 13.54 | 13.23 | -18.12 | -17.95 | 31.34 | 18.6 | 31.49 | 19.9 | |
| 59551 UGC10713 | 104.0294 | 33.7405 | 35.8386 | 31.0245 | 1071 | 1034 | 3.0 | 0.50 | 228 | 2.412 | 12.73 | 12.77 | 12.82 | 12.89 | 13.20 | -19.51 | -19.45 | 32.72 | 35.0 | 32.35 | 29.5 | |
| 59635 ES138-014 | 328.4569 | -12.6830 | 194.0095 | 9.3403 | 1509 | 1559 | 6.7 | 0.20 | 223 | 2.348 | 12.91 | 12.56 | 12.68 | 12.71 | 13.01 | -18.93 | -18.83 | 31.94 | 24.5 | 31.54 | 20.3 | |
| 59676 UGC10721 | 47.0604 | 33.0522 | 90.5769 | 63.2662 | 2919 | 2927 | 5.8 | 0.58 | 264 | 2.502 | / | / | 12.83 | 12.92 | / | / | -20.33 | / | / | / | 33.29 | 45.4 |
| 59735 UGC10757 | 103.8439 | 33.3411 | 35.4308 | 31.2727 | 1168 | 1129 | 6.0 | 0.56 | 208 | 2.392 | 13.19 | 13.27 | 14.17 | 14.25 | 14.11 | -19.33 | -19.25 | 33.47 | 49.5 | 33.56 | 51.4 | |
| 59769 UGC10738 | 26.4998 | 24.9516 | 134.7327 | 62.6813 | 6712 | 6828 | 4.1 | 0.22 | 585 | 2.769 | 12.88 | 12.08 | 12.56 | 12.58 | 12.70 | -22.76 | -22.94 | 35.58 | 130.7 | 35.71 | 139.0 | |
| 59782 UGC10743 | 28.6680 | 25.8255 | 130.3999 | 63.5561 | 2571 | 2583 | 1.0 | 0.37 | 215 | 2.356 | 12.50 | 12.30 | 12.69 | 12.74 | 12.89 | -19.00 | -18.90 | 31.89 | 23.8 | 31.64 | 21.3 | |
| 59884 IC0004633 | 315.1226 | -21.4595 | 201.1407 | -4.3901 | 2945 | 3012 | 6.0 | 0.61 | 318 | 2.593 | 10.86 | 10.63 | 10.92 | 10.97 | 11.17 | -21.16 | -21.22 | 32.34 | 29.3 | 32.20 | 27.6 | |
| 59908 UGC10791 | 103.7266 | 33.0213 | 35.0957 | 31.4461 | 1327 | 1287 | 8.8 | 0.67 | 152 | 2.302 | 13.13 | 13.29 | 14.27 | 14.36 | 14.18 | -18.51 | -18.38 | 32.71 | 34.8 | 32.76 | 35.7 | |
| 59995 UGC10780 | 28.6232 | 24.4053 | 132.8274 | 64.4990 | 6743 | 6850 | 5.9 | 0.20 | 353 | 2.548 | 14.36 | 13.74 | 13.95 | 13.99 | 14.23 | -20.74 | -20.78 | 35.07 | 103.5 | 34.90 | 95.4 | |
| 60001 NGC006300 | 328.4916 | -14.0515 | 195.3850 | 9.1637 | 1109 | 1149 | 3.1 | 0.62 | 291 | 2.560 | 9.03 | 9.01 | 9.27 | 9.34 | 9.54 | -20.86 | -20.90 | 30.40 | 12.0 | 30.24 | 11.2 | |
| 60003 UGC10790 | 65.5716 | 34.5812 | 61.7201 | 57.1245 | 2108 | 2084 | 6.3 | 0.60 | 211 | 2.412 | 11.68 | 11.80 | 12.45 | 12.54 | 12.53 | -19.50 | -19.45 | 32.04 | 25.6 | 31.99 | 25.0 | |
| 60124 IC0004660 | 107.5313 | 31.6775 | 32.7779 | 28.5984 | 1250 | 1206 | 3.3 | 0.26 | 116 | 2.071 | / | / | 13.84 | 13.93 | / | / | -16.12 | / | / | / | 30.04 | 10.2 |
| 60241 UGC10854 | 86.6798 | 34.1030 | 42.8584 | 44.3069 | 2817 | 2788 | 6.0 | 0.43 | 167 | 2.258 | 14.32 | 14.41 | 15.40 | 15.49 | 15.31 | -18.11 | -17.95 | 33.45 | 48.9 | 33.49 | 49.8 | |
| 60271 UGC10858 | 88.1677 | 33.9255 | 41.8486 | 43.2962 | 5459 | 5459 | 5.8 | 0.22 | 201 | 2.305 | 15.34 | 15.23 | 16.17 | 16.27 | 16.10 | -18.53 | -18.40 | 34.71 | 87.7 | 34.79 | 90.7 | |
| 60277 UGC10887 | 109.5556 | 30.9617 | 31.6382 | 27.0215 | 1838 | 1798 | 5.9 | 0.21 | 145 | 2.162 | / | / | 15.71 | 15.79 | / | / | -17.01 | / | / | / | 32.82 | 36.7 |
| 60286 UGC10852 | 33.7045 | 23.9746 | 125.1903 | 68.0015 | 2778 | 2767 | 7.6 | 0.20 | 140 | 2.146 | / | / | 15.62 | 15.69 | / | / | -16.85 | / | / | / | 32.56 | 32.5 |

| PGC Name | l | b | sgl | sgb | v_{hel} | v_{mod} | t | b/a | w_{mz} | $\log w_{mz}^*$ | I | I* | [3.6] | [3.6]* | C _[3.6] | Mc | M _[3.6] | μ_C | dC | $\mu_{[3.6]}$ | d _[3.6] |
|-----------------|----------|----------|----------|---------|-----------|-----------|-----|------|----------|-----------------|-------|-------|-------|--------|--------------------|--------|--------------------|---------|-------|---------------|--------------------|
| 60291 UGC10876 | 101.9750 | 32.3980 | 34.8185 | 33.0290 | 1162 | 1115 | 5.8 | 0.30 | 199 | 2.310 | 12.07 | 12.03 | 13.09 | 13.16 | 12.95 | -18.58 | -18.45 | 31.53 | 20.2 | 31.61 | 21.0 |
| 60315 UGC10856 | 34.0312 | 23.8672 | 124.7429 | 68.2715 | 2765 | 2752 | 3.1 | 0.25 | 408 | 2.616 | 11.08 | 10.52 | 11.42 | 11.44 | 11.34 | -21.36 | -21.44 | 32.71 | 34.9 | 32.90 | 38.1 |
| 60330 NGC06372 | 49.6253 | 29.2405 | 84.9624 | 66.9809 | 4753 | 4769 | 3.8 | 0.62 | 259 | 2.508 | 12.02 | 12.09 | 12.49 | 12.59 | 12.71 | -20.38 | -20.38 | 33.11 | 41.8 | 33.01 | 39.9 |
| 60370 UGC10874 | 52.8424 | 29.7699 | 78.2615 | 65.9902 | 6799 | 6874 | 5.9 | 0.20 | 238 | 2.377 | 15.39 | 15.15 | 16.30 | 16.39 | 16.12 | -19.19 | -19.10 | 35.42 | 121.6 | 35.69 | 137.2 |
| 60376 AGC270324 | 31.5737 | 22.3069 | 132.0449 | 67.9107 | 8759 | 8926 | 4.8 | 0.26 | 374 | 2.579 | / | / | 14.10 | 14.17 | / | / | -21.08 | / | / | 35.42 | 121.5 |
| 60459 UGC10891 | 30.2599 | 20.7710 | 137.2703 | 68.0072 | 1665 | 1634 | 3.6 | 0.54 | 362 | 2.625 | 10.36 | 10.21 | 9.99 | 10.05 | 10.51 | -21.44 | -21.53 | 31.96 | 24.6 | 31.58 | 20.7 |
| 60568 UGC10917 | 67.7044 | 31.1538 | 55.0729 | 58.7070 | 2161 | 2113 | 2.0 | 0.38 | 253 | 2.428 | 12.65 | 12.60 | 13.27 | 13.34 | 13.33 | -19.66 | -19.61 | 33.01 | 39.9 | 32.98 | 39.4 |
| 60573 UGC10934 | 102.9648 | 31.4290 | 33.4558 | 32.4534 | 2488 | 2449 | 4.0 | 0.43 | 315 | 2.533 | 11.76 | 11.69 | 12.42 | 12.49 | 12.45 | -20.61 | -20.63 | 33.08 | 41.3 | 33.15 | 42.7 |
| 60925 UGC10997 | 45.5483 | 22.5698 | 95.9875 | 73.6555 | 3364 | 3321 | 5.8 | 0.56 | 278 | 2.515 | 12.15 | 12.12 | 12.65 | 12.73 | 12.79 | -20.45 | -20.46 | 33.26 | 44.8 | 33.23 | 44.2 |
| 60957 UGC11001 | 39.2206 | 19.8844 | 119.5032 | 74.2950 | 4216 | 4191 | 8.1 | 0.46 | 298 | 2.517 | / | / | 13.17 | 13.25 | / | / | -20.48 | / | / | 33.78 | 57.1 |
| 60972 UGC11004 | 42.4475 | 21.0874 | 107.4129 | 74.4824 | 3039 | 2990 | 2.3 | 0.54 | 269 | 2.496 | / | / | 12.88 | 12.96 | / | / | -20.27 | / | / | 33.26 | 44.9 |
| 60975 UGC11003 | 39.7895 | 19.9999 | 117.5722 | 74.4656 | 4064 | 4035 | 5.7 | 0.23 | 277 | 2.445 | / | / | 13.28 | 13.34 | / | / | -19.78 | / | / | 33.15 | 42.7 |
| 61008 UGC11010 | 49.5238 | 23.4175 | 83.3113 | 72.7774 | 3112 | 3060 | 3.0 | 0.52 | 360 | 2.616 | / | / | 11.91 | 11.99 | / | / | -21.44 | / | / | 33.48 | 49.6 |
| 61036 UGC11021 | 54.3206 | 24.7604 | 70.8841 | 70.3937 | 5186 | 5176 | 3.1 | 0.23 | 380 | 2.582 | 13.51 | 13.08 | 13.23 | 13.28 | 13.55 | -21.06 | -21.12 | 34.69 | 86.7 | 34.50 | 79.4 |
| 61092 UGC11041 | 60.5155 | 26.0216 | 58.9691 | 66.6435 | 4876 | 4855 | 2.0 | 0.60 | 364 | 2.649 | 12.23 | 12.25 | 12.12 | 12.22 | 12.61 | -21.67 | -21.77 | 34.34 | 73.8 | 34.06 | 64.8 |
| 61120 UGC11050 | 60.3680 | 25.7996 | 58.9247 | 66.9016 | 4861 | 4838 | 4.1 | 0.22 | 285 | 2.457 | 13.76 | 13.47 | 14.27 | 14.34 | 14.26 | -19.92 | -19.89 | 34.24 | 70.4 | 34.32 | 73.0 |
| 61161 UGC11055 | 37.9837 | 17.5198 | 128.4833 | 75.5270 | 2948 | 2890 | 3.3 | 0.71 | 216 | 2.478 | / | / | 12.73 | 12.81 | / | / | -20.09 | / | / | 32.93 | 38.5 |
| 61164 UGC11060 | 53.5374 | 23.4645 | 71.5487 | 71.8579 | 4662 | 4633 | 1.0 | 0.28 | 440 | 2.653 | 12.21 | 11.83 | 12.15 | 12.20 | 12.38 | -21.70 | -21.80 | 34.14 | 67.3 | 34.08 | 65.6 |
| 61300 UGC11093 | 33.5717 | 14.1779 | 148.8449 | 74.3230 | 1963 | 1888 | 6.0 | 0.21 | 306 | 2.486 | 11.45 | 10.89 | 11.51 | 11.51 | 11.56 | -20.19 | -20.18 | 31.75 | 22.4 | 31.69 | 21.8 |
| 61353 P0061353 | 33.9102 | 13.6765 | 149.9232 | 74.8496 | 1798 | 1718 | 2.0 | 0.49 | 194 | 2.339 | / | / | 13.41 | 13.45 | / | / | -18.73 | / | / | 32.19 | 27.5 |
| 61469 UGC11132 | 65.6767 | 24.3370 | 47.6869 | 64.8410 | 2836 | 2756 | 3.1 | 0.22 | 318 | 2.504 | 13.00 | 12.68 | 12.98 | 13.02 | 13.22 | -20.35 | -20.35 | 33.60 | 52.5 | 33.42 | 48.3 |
| 61526 UGC11142 | 52.4288 | 19.6355 | 70.2026 | 75.8058 | 4508 | 4454 | 5.8 | 0.23 | 355 | 2.553 | 13.27 | 12.71 | 13.17 | 13.20 | 13.32 | -20.79 | -20.83 | 34.17 | 68.3 | 34.11 | 66.4 |
| 61553 UGC11159 | 66.7327 | 24.0263 | 45.6548 | 64.3270 | 2827 | 2744 | 4.0 | 0.22 | 285 | 2.457 | 12.20 | 11.94 | 12.45 | 12.51 | 12.59 | -19.92 | -19.89 | 32.52 | 31.9 | 32.42 | 30.4 |
| 61600 NGC06586 | 48.1522 | 17.4820 | 86.1519 | 78.8118 | 3138 | 3055 | 2.0 | 0.51 | 257 | 2.466 | / | / | 12.75 | 12.83 | / | / | -19.98 | / | / | 32.84 | 36.9 |
| 61637 UGC011182 | 85.1137 | 27.2901 | 34.8186 | 48.4990 | 4266 | 4220 | 4.1 | 0.31 | 248 | 2.408 | / | / | 14.44 | 14.53 | / | / | -19.41 | / | / | 34.00 | 63.2 |
| 61658 P0061658 | 41.4553 | 13.9976 | 126.6953 | 80.3675 | 2998 | 2911 | 5.0 | 0.45 | 131 | 2.158 | / | / | 13.51 | 13.59 | / | / | -16.96 | / | / | 30.55 | 12.9 |
| 61690 UGC11188 | 46.4338 | 15.7819 | 95.4631 | 80.4937 | 5284 | 5242 | 6.6 | 0.25 | 293 | 2.472 | / | / | 13.56 | 13.61 | / | / | -20.04 | / | / | 33.70 | 55.0 |
| 61698 UGC11194 | 54.0612 | 18.7242 | 62.8860 | 75.9879 | 4742 | 4685 | 4.0 | 0.53 | 357 | 2.615 | 12.05 | 11.89 | 12.47 | 12.55 | 12.58 | -21.36 | -21.44 | 33.99 | 62.7 | 34.06 | 64.9 |
| 61712 ES182-010 | 339.7518 | -17.3658 | 200.8808 | 19.1690 | 3546 | 3555 | 5.1 | 0.56 | 182 | 2.333 | / | / | 12.92 | 13.00 | / | / | -18.68 | / | / | 31.68 | 21.7 |
| 61742 UGC11218 | 105.5357 | 28.1747 | 29.1741 | 30.9384 | 1483 | 1416 | 5.2 | 0.51 | 326 | 2.570 | 10.02 | 9.97 | 10.40 | 10.47 | 10.59 | -20.94 | -20.99 | 31.53 | 20.2 | 31.46 | 19.6 |
| 61836 UGC11236 | 102.1882 | 27.7638 | 29.3610 | 33.9191 | 5761 | 5767 | 4.4 | 0.51 | 360 | 2.613 | 12.30 | 12.22 | 12.56 | 12.65 | 12.80 | -21.34 | -21.41 | 34.19 | 69.0 | 34.14 | 67.4 |
| 61936 UGC11255 | 80.2797 | 24.3105 | 33.2768 | 53.6831 | 9724 | 9857 | 5.9 | 0.20 | 432 | 2.635 | 13.57 | 13.05 | 13.53 | 13.61 | 13.69 | -21.54 | -21.63 | 35.35 | 117.4 | 35.41 | 121.0 |
| 61942 UGC11254 | 58.6627 | 17.6778 | 46.8408 | 74.1715 | 4987 | 4921 | 5.9 | 0.20 | 237 | 2.375 | 14.32 | 13.98 | 14.50 | 14.56 | 14.63 | -19.17 | -19.09 | 33.85 | 58.8 | 33.71 | 55.1 |
| 61972 UGC11269 | 98.1801 | 26.9325 | 29.3255 | 37.5746 | 2572 | 2500 | 2.0 | 0.52 | 360 | 2.617 | 11.20 | 11.14 | 11.60 | 11.68 | 11.77 | -21.38 | -21.46 | 33.17 | 43.1 | 33.17 | 43.0 |
| 62017 UGC011295 | 106.5032 | 27.3325 | 28.0437 | 30.2346 | 2366 | 2304 | 7.9 | 0.20 | 173 | 2.238 | / | / | 15.24 | 15.30 | / | / | -17.75 | / | / | 33.08 | 41.4 |
| 62037 UGC11275 | 60.6489 | 17.5163 | 41.9643 | 72.8675 | 5453 | 5395 | 5.9 | 0.20 | 389 | 2.590 | 13.73 | 13.19 | 13.93 | 13.97 | 13.94 | -21.13 | -21.19 | 35.17 | 108.2 | 35.32 | 115.9 |

| PGC Name | l | b | sgl | sgb | v_{hel} | v_{mod} | t | b/a | w_{max} | $\log w_{max}^2$ | I | I* | [3.6] | [3.6]* | $C_{[3.6]}$ | MC | $M_{[3.6]}$ | μ_C | dC | $\mu_{[3.6]}$ | $d_{[3.6]}$ | |
|-----------------|----------|----------|----------|---------|-----------|-----------|-----|------|-----------|------------------|-------|-------|-------|--------|-------------|--------|-------------|---------|-------|---------------|-------------|-------|
| 62059 UGC11280 | 60.6186 | 17.3850 | 41.6790 | 72.9726 | 5480 | 5422 | 2.0 | 0.31 | 468 | 2.683 | / | / | 12.50 | 12.55 | / | / | -22.10 | / | / | / | 34.77 | 90.0 |
| 62066 IC0004721 | 336.7975 | -20.7476 | 203.6569 | 15.6736 | 2234 | 2218 | 5.9 | 0.28 | 310 | 2.501 | 10.69 | 10.41 | 11.12 | 11.17 | 11.15 | -20.32 | -20.32 | 31.47 | 19.7 | 31.49 | 19.9 | 19.9 |
| 62077 UGC11300 | 101.0521 | 26.8315 | 28.5040 | 35.0979 | 489 | 403 | 6.4 | 0.29 | 204 | 2.319 | 11.23 | 11.13 | 12.06 | 12.11 | 11.97 | -18.67 | -18.55 | 30.64 | 13.4 | 30.66 | 13.5 | 13.5 |
| 62097 UGC11289 | 51.5965 | 13.3197 | 59.5834 | 81.8565 | 3991 | 3891 | 4.5 | 0.62 | 283 | 2.548 | / | / | 12.65 | 12.73 | / | / | -20.78 | / | / | / | 33.56 | 51.4 |
| 62149 UGC11305 | 68.7550 | 19.5743 | 34.5331 | 65.3519 | 2495 | 2378 | 4.0 | 0.72 | 255 | 2.554 | 11.34 | 11.42 | 11.94 | 12.03 | 12.09 | -20.81 | -20.84 | 32.91 | 38.2 | 32.90 | 38.0 | 38.0 |
| 62164 UGC11301 | 47.2230 | 10.8038 | 91.8460 | 85.5138 | 4502 | 4410 | 5.4 | 0.20 | 485 | 2.686 | / | / | 12.10 | 12.08 | / | / | -22.12 | / | / | / | 34.30 | 72.3 |
| 62178 UGC11308 | 54.5923 | 13.9192 | 47.4831 | 79.5973 | 3429 | 3316 | 3.0 | 0.58 | 431 | 2.715 | 10.81 | 10.69 | 11.23 | 11.30 | 11.35 | -22.26 | -22.41 | 33.65 | 53.8 | 33.76 | 56.6 | 56.6 |
| 62204 UGC011334 | 104.7731 | 26.7980 | 27.7217 | 31.8417 | 4562 | 4534 | 5.6 | 0.33 | 264 | 2.438 | / | / | 15.10 | 15.17 | / | / | -19.70 | / | / | / | 35.01 | 100.5 |
| 62231 UGC11320 | 53.2175 | 12.7667 | 48.6333 | 81.3528 | 4813 | 4725 | 4.1 | 0.20 | 456 | 2.659 | 12.60 | 11.92 | 12.41 | 12.43 | 12.54 | -21.76 | -21.86 | 34.36 | 74.4 | 34.38 | 75.3 | 75.3 |
| 62248 UGC011328 | 66.9542 | 18.2525 | 33.7635 | 67.4860 | 5660 | 5603 | 5.9 | 0.20 | 291 | 2.464 | 14.38 | 13.99 | 14.69 | 14.76 | 14.73 | -19.98 | -19.96 | 34.80 | 91.0 | 34.84 | 92.7 | 92.7 |
| 62296 NGC06695 | 69.4235 | 18.7322 | 32.0438 | 65.1972 | 5496 | 5435 | 3.1 | 0.56 | 421 | 2.697 | / | / | 12.79 | 12.88 | / | / | -22.24 | / | / | / | 35.28 | 113.5 |
| 62338 UGC11344 | 53.9788 | 12.2362 | 42.6999 | 81.1965 | 3834 | 3720 | 2.0 | 0.41 | 394 | 2.627 | 11.64 | 11.36 | 12.32 | 12.37 | 12.22 | -21.46 | -21.55 | 33.72 | 55.5 | 33.99 | 62.8 | 62.8 |
| 62380 UGC11350 | 52.7598 | 11.1764 | 42.7345 | 82.7927 | 4702 | 4604 | 5.9 | 0.63 | 319 | 2.605 | / | / | 12.66 | 12.72 | / | / | -21.33 | / | / | / | 34.13 | 67.0 |
| 62509 UGC11371 | 56.8968 | 11.6334 | 30.1314 | 79.1968 | 3750 | 3625 | 4.4 | 0.33 | 358 | 2.570 | 12.35 | 11.85 | 12.35 | 12.37 | 12.47 | -20.95 | -20.99 | 33.45 | 49.0 | 33.41 | 48.1 | 48.1 |
| 62518 UGC11377 | 104.1962 | 25.8123 | 26.6745 | 32.5153 | 7458 | 7513 | 6.0 | 0.20 | 362 | 2.559 | / | / | 13.87 | 13.93 | / | / | -20.88 | / | / | / | 34.95 | 97.6 |
| 62550 ES396-007 | 1.6139 | -15.5674 | 206.2774 | 39.6795 | 5867 | 5850 | 4.8 | 0.34 | 448 | 2.670 | 11.84 | 11.45 | 12.03 | 12.09 | 12.13 | -21.86 | -21.97 | 34.04 | 64.2 | 34.14 | 67.3 | 67.3 |
| 62585 E281-038 | 353.4223 | -19.0110 | 206.7345 | 31.1435 | 4958 | 4934 | 1.8 | 0.32 | 381 | 2.596 | 12.40 | 12.09 | 12.33 | 12.39 | 12.61 | -21.19 | -21.25 | 33.84 | 58.6 | 33.70 | 54.9 | 54.9 |
| 62595 UGC11380 | 66.8526 | 14.7827 | 25.4194 | 69.0810 | 2878 | 2740 | 2.0 | 0.25 | 285 | 2.460 | / | / | 12.21 | 12.26 | / | / | -19.92 | / | / | / | 32.19 | 27.4 |
| 62651 UGC011385 | 51.2131 | 6.9932 | 10.2214 | 86.1239 | 3118 | 2969 | 8.1 | 0.68 | 256 | 2.534 | / | / | 12.47 | 12.47 | / | / | -20.64 | / | / | / | 33.15 | 42.6 |
| 62671 NGC06750 | 89.4248 | -21.9195 | 25.4103 | 46.5300 | 3696 | 3605 | 5.0 | 0.65 | 243 | 2.496 | / | / | 12.62 | 12.72 | / | / | -20.27 | / | / | / | 33.02 | 40.1 |
| 62706 IC0004810 | 340.3709 | -23.8107 | 207.6187 | 18.1118 | 3182 | 3150 | 6.6 | 0.20 | 283 | 2.452 | 12.44 | 12.03 | 12.83 | 12.87 | 12.80 | -19.87 | -19.84 | 32.69 | 34.5 | 32.73 | 35.1 | 35.1 |
| 62717 UGC11394 | 59.0505 | 9.7556 | 17.3075 | 77.9369 | 4227 | 4097 | 6.0 | 0.20 | 377 | 2.576 | / | / | 12.93 | 12.93 | / | / | -21.06 | / | / | / | 34.06 | 64.8 |
| 62781 UGC11404 | 60.6648 | 9.6764 | 15.1680 | 76.4159 | 3916 | 3776 | 3.6 | 0.55 | 405 | 2.677 | / | / | 11.12 | 11.17 | / | / | -22.04 | / | / | / | 33.24 | 44.5 |
| 62806 UGC11407 | 81.4985 | 18.2322 | 22.8378 | 54.6751 | 2414 | 2280 | 3.6 | 0.52 | 261 | 2.478 | 11.01 | 11.00 | 11.52 | 11.60 | 11.67 | -20.11 | -20.09 | 31.78 | 22.6 | 31.70 | 21.9 | 21.9 |
| 62836 NGC006744 | 332.2237 | -26.1460 | 208.1009 | 10.3822 | 841 | 804 | 4.0 | 0.58 | 315 | 2.578 | 7.62 | 7.65 | 8.30 | 8.37 | 8.37 | -21.02 | -21.08 | 29.40 | 7.6 | 29.45 | 7.8 | 7.8 |
| 62861 E282-018 | 353.2539 | -21.7950 | 209.6909 | 30.0044 | 5603 | 5584 | 5.9 | 0.36 | 352 | 2.568 | 12.59 | 12.31 | 12.88 | 12.95 | 12.99 | -20.93 | -20.97 | 33.96 | 62.0 | 33.99 | 62.8 | 62.8 |
| 62882 ES593-003 | 15.9507 | -13.7816 | 212.9380 | 52.8964 | 8226 | 8243 | 5.9 | 0.20 | 401 | 2.603 | 13.89 | 13.26 | 13.58 | 13.63 | 13.81 | -21.25 | -21.32 | 35.16 | 107.7 | 35.09 | 104.4 | 104.4 |
| 62889 E459-006 | 5.4649 | -18.0893 | 211.3312 | 41.9889 | 5750 | 5701 | 4.2 | 0.32 | 453 | 2.671 | 12.15 | 11.72 | 12.44 | 12.49 | 12.47 | -21.86 | -21.98 | 34.39 | 75.6 | 34.58 | 82.2 | 82.2 |
| 62982 UGC11422 | 74.7981 | 14.1855 | 18.4328 | 61.9176 | 4655 | 4540 | 5.9 | 0.20 | 295 | 2.470 | / | / | 12.49 | 12.55 | / | / | -20.02 | / | / | / | 32.58 | 32.8 |
| 63040 UGC11426 | 67.0507 | 10.0707 | 12.2090 | 70.1681 | 4453 | 4317 | 2.0 | 0.68 | 277 | 2.568 | / | / | 12.20 | 12.29 | / | / | -20.98 | / | / | / | 33.30 | 45.8 |
| 63096 UGC11429 | 74.9129 | 13.1986 | 16.3312 | 62.0225 | 4638 | 4517 | 3.1 | 0.51 | 518 | 2.771 | 11.04 | 10.83 | 11.49 | 11.56 | 11.55 | -22.77 | -22.96 | 34.39 | 75.6 | 34.62 | 84.1 | 84.1 |
| 63121 NGC006796 | 92.3106 | 20.0703 | 21.9879 | 44.3140 | 2191 | 2068 | 4.0 | 0.24 | 391 | 2.596 | 11.43 | 11.00 | 11.56 | 11.59 | 11.66 | -21.19 | -21.25 | 32.86 | 37.3 | 32.86 | 37.4 | 37.4 |
| 63165 UGC11433 | 67.5205 | 9.0466 | 9.0563 | 69.8489 | 4437 | 4295 | 6.7 | 0.20 | 283 | 2.452 | / | / | 13.65 | 13.69 | / | / | -19.84 | / | / | / | 33.58 | 51.9 |
| 63166 UGC11435 | 87.3373 | 17.9270 | 20.2659 | 49.3457 | 3748 | 3633 | 5.8 | 0.20 | 299 | 2.476 | 12.52 | 12.10 | 12.66 | 12.70 | 12.76 | -20.09 | -20.07 | 32.87 | 37.4 | 32.79 | 36.2 | 36.2 |
| 63173 ES397-018 | 3.3248 | -21.4870 | 214.0819 | 38.6418 | 5410 | 5345 | 5.0 | 0.20 | 353 | 2.548 | 13.36 | 12.77 | 13.14 | 13.17 | 13.34 | -20.75 | -20.78 | 34.14 | 67.3 | 34.03 | 63.9 | 63.9 |
| 63229 UGC11443 | 85.9940 | 16.8090 | 18.9442 | 50.8202 | 4364 | 4255 | 5.8 | 0.51 | 288 | 2.515 | 12.23 | 12.09 | 12.65 | 12.72 | 12.77 | -20.45 | -20.46 | 33.24 | 44.4 | 33.21 | 43.9 | 43.9 |

| PGC Name | l | b | sgl | sgb | v_{hel} | v_{mod} | t | b/a | w_{max} | $\log w_{max}^*$ | I | I* | [3.6] | [3.6]* | $C_{[3.6]}$ | M_C | $M_{[3.6]}$ | μ_C | dC | $\mu_{[3.6]}$ | d _[3.6] |
|-----------------|----------|----------|----------|---------|-----------|-----------|-----|------|-----------|------------------|-------|-------|-------|--------|-------------|--------|-------------|---------|------|---------------|--------------------|
| 63286 UGC11455 | 103.7484 | 22.8450 | 23.2507 | 33.3607 | 5392 | 5359 | 5.8 | 0.20 | 608 | 2.784 | 12.05 | 11.12 | 11.59 | 11.59 | 11.72 | -22.89 | -23.08 | 34.69 | 86.5 | 34.79 | 90.7 |
| 63395 IC0004871 | 339.7605 | -28.4500 | 212.1205 | 16.2863 | 1925 | 1856 | 6.6 | 0.20 | 249 | 2.396 | 12.28 | 11.98 | 13.01 | 13.05 | 12.87 | -19.37 | -19.30 | 32.24 | 28.1 | 32.36 | 29.7 |
| 63424 UGC11459 | 74.0834 | 9.3839 | 8.3431 | 63.3681 | 3119 | 2947 | 6.3 | 0.56 | 359 | 2.627 | 11.48 | 11.24 | 11.84 | 11.89 | 11.93 | -21.46 | -21.55 | 33.42 | 48.3 | 33.49 | 49.8 |
| 63540 AGC590024 | 24.0528 | -18.2660 | 227.3132 | 56.3308 | 5996 | 5881 | 5.0 | 0.20 | 462 | 2.665 | 12.56 | 11.82 | 12.52 | 12.54 | 12.54 | -21.81 | -21.92 | 34.41 | 76.2 | 34.56 | 81.8 |
| 63552 UGC11466 | 78.6905 | 10.6319 | 10.0942 | 58.7392 | 821 | 631 | 5.0 | 0.56 | 185 | 2.342 | 11.42 | 11.34 | 11.63 | 11.69 | 11.88 | -18.87 | -18.76 | 30.75 | 14.1 | 30.45 | 12.3 |
| 63592 AGC032742 | 12.7868 | -22.9989 | 222.0797 | 45.2548 | 5802 | 5705 | 4.8 | 0.20 | 480 | 2.682 | 12.56 | 11.74 | 12.50 | 12.51 | 12.48 | -21.96 | -22.08 | 34.51 | 79.9 | 34.71 | 87.3 |
| 63622 E398-029 | 5.2020 | -25.4737 | 219.5876 | 38.1493 | 5758 | 5679 | 4.4 | 0.20 | 361 | 2.558 | / | / | 13.45 | 13.47 | / | / | -20.87 | / | / | 34.44 | 77.2 |
| 63664 UGC11477 | 89.5853 | 15.3917 | 15.9541 | 47.6411 | 3715 | 3585 | 6.5 | 0.27 | 265 | 2.431 | / | / | 13.15 | 13.21 | / | / | -19.63 | / | / | 32.87 | 37.4 |
| 63751 ES461-006 | 8.5922 | -26.0040 | 222.3390 | 40.4013 | 5953 | 5864 | 4.9 | 0.20 | 366 | 2.563 | / | / | 13.39 | 13.42 | / | / | -20.93 | / | / | 34.44 | 77.4 |
| 63766 UGC11492 | 90.4527 | 14.9530 | 15.1583 | 46.8656 | 3563 | 3428 | 4.1 | 0.50 | 294 | 2.522 | 11.91 | 11.80 | 12.44 | 12.52 | 12.52 | -20.51 | -20.52 | 33.05 | 40.7 | 33.07 | 41.2 |
| 63776 AGC032834 | 15.8142 | -24.0398 | 225.7469 | 46.7730 | 5854 | 5743 | 6.2 | 0.20 | 283 | 2.452 | 14.38 | 13.96 | 14.65 | 14.71 | 14.69 | -19.87 | -19.84 | 34.64 | 84.7 | 34.66 | 85.5 |
| 63840 E339-008 | 2.2294 | -28.5379 | 221.0906 | 34.2851 | 5679 | 5597 | 1.0 | 0.35 | 381 | 2.600 | 12.64 | 12.34 | 12.70 | 12.77 | 12.92 | -21.22 | -21.29 | 34.20 | 69.2 | 34.14 | 67.4 |
| 64060 AGC033027 | 23.0763 | -24.3266 | 233.1856 | 51.2724 | 2231 | 2019 | 7.5 | 0.38 | 221 | 2.370 | 12.77 | 12.58 | 13.22 | 13.27 | 13.29 | -19.13 | -19.04 | 32.42 | 30.5 | 32.33 | 29.2 |
| 64070 UGC11515 | 96.0902 | 16.0988 | 15.9116 | 41.3409 | 3255 | 3125 | 6.6 | 0.66 | 118 | 2.187 | / | / | 13.02 | 13.10 | / | / | -17.25 | / | / | 30.35 | 11.8 |
| 64318 UGC11527 | 41.5935 | -18.8160 | 257.3434 | 64.2271 | 5487 | 5298 | 2.2 | 0.26 | 451 | 2.661 | 12.31 | 11.69 | 12.40 | 12.43 | 12.42 | -21.77 | -21.88 | 34.24 | 70.6 | 34.40 | 75.8 |
| 64373 PG0064373 | 29.7524 | -24.7185 | 241.7151 | 54.5355 | 5681 | 5513 | 8.0 | 0.35 | 451 | 2.674 | / | / | 12.69 | 12.75 | / | / | -22.01 | / | / | 34.89 | 94.9 |
| 64429 ES340-009 | 2.5576 | -32.6376 | 225.3982 | 32.3032 | 2587 | 2423 | 7.1 | 0.20 | 168 | 2.225 | 13.60 | 13.53 | 14.53 | 14.60 | 14.42 | -17.81 | -17.63 | 32.23 | 28.0 | 32.24 | 28.0 |
| 64458 UGC11537 | 43.1279 | -19.3719 | 260.8499 | 63.9707 | 5418 | 5221 | 5.3 | 0.28 | 499 | 2.707 | 11.73 | 11.17 | 12.02 | 12.06 | 11.97 | -22.20 | -22.34 | 34.22 | 70.0 | 34.49 | 79.2 |
| 64485 UGC11540 | 100.4582 | 16.6713 | 16.1498 | 37.1155 | 2485 | 2352 | 3.0 | 0.53 | 349 | 2.606 | 11.53 | 10.75 | 11.21 | 11.19 | 11.34 | -21.27 | -21.34 | 32.62 | 33.4 | 32.55 | 32.3 |
| 64488 ES340-017 | 1.9316 | -33.1951 | 225.5979 | 31.5560 | 2614 | 2450 | 8.0 | 0.58 | 209 | 2.400 | / | / | 13.53 | 13.62 | / | / | -19.34 | / | / | 32.98 | 39.5 |
| 64506 E527-019 | 19.2381 | -29.6703 | 234.5938 | 44.9990 | 3118 | 2912 | 4.2 | 0.62 | 234 | 2.466 | 12.27 | 12.31 | 12.86 | 12.95 | 12.99 | -20.00 | -19.97 | 33.01 | 39.9 | 32.95 | 38.9 |
| 64534 AGC600053 | 33.5750 | -24.7824 | 247.1474 | 56.1209 | 5660 | 5479 | 7.0 | 0.20 | 426 | 2.629 | / | / | 12.69 | 12.73 | / | / | -21.57 | / | / | 34.40 | 75.8 |
| 64540 UGC011545 | 88.1963 | 8.7749 | 6.1221 | 49.4718 | 2951 | 2770 | 5.4 | 0.22 | 187 | 2.274 | / | / | 13.06 | 13.10 | / | / | -18.10 | / | / | 31.20 | 17.4 |
| 64552 NGC06901 | 49.6190 | -16.8973 | 275.4420 | 66.6764 | 4791 | 4570 | 2.4 | 0.40 | 371 | 2.598 | / | / | 12.90 | 12.96 | / | / | -21.27 | / | / | 34.32 | 73.1 |
| 64601 NGC06906 | 49.7926 | -17.1472 | 275.7928 | 66.4109 | 4859 | 4638 | 3.8 | 0.43 | 436 | 2.675 | / | / | 11.97 | 12.03 | / | / | -22.02 | / | / | 34.13 | 66.9 |
| 64637 UGC11552 | 55.2298 | -14.2029 | 290.7679 | 68.0454 | 4527 | 4297 | 2.0 | 0.37 | 466 | 2.691 | 12.29 | 11.89 | 12.03 | 12.08 | 12.36 | -22.05 | -22.18 | 34.47 | 78.3 | 34.35 | 74.0 |
| 64638 UGC11551 | 50.3514 | -17.1270 | 277.1229 | 66.3685 | 4881 | 4659 | 4.0 | 0.22 | 397 | 2.601 | 12.35 | 11.79 | 12.33 | 12.36 | 12.44 | -21.23 | -21.29 | 33.70 | 55.0 | 33.71 | 55.3 |
| 64724 ES400-025 | 9.7421 | -33.5305 | 230.6957 | 36.5397 | 2175 | 1977 | 7.8 | 0.47 | 158 | 2.245 | 13.39 | 13.46 | 14.65 | 14.74 | 14.45 | -17.99 | -17.82 | 32.45 | 30.9 | 32.58 | 32.8 |
| 64759 UGC11568 | 54.2614 | -15.8771 | 287.0197 | 66.7779 | 4225 | 3984 | 5.8 | 0.31 | 435 | 2.652 | 11.84 | 11.38 | 11.82 | 11.86 | 11.99 | -21.69 | -21.79 | 33.71 | 55.3 | 33.71 | 55.1 |
| 64812 P0064812 | 42.8051 | -22.7263 | 261.3964 | 60.6124 | 5648 | 5446 | 2.5 | 0.35 | 297 | 2.492 | / | / | 13.49 | 13.55 | / | / | -20.23 | / | / | 33.85 | 59.0 |
| 64862 UGC11579 | 44.2560 | -22.2993 | 264.0080 | 61.2187 | 5901 | 5704 | 5.8 | 0.20 | 407 | 2.610 | 13.40 | 12.67 | 13.44 | 13.46 | 13.43 | -21.31 | -21.38 | 34.82 | 91.9 | 34.98 | 98.9 |
| 64891 UGC11584 | 46.4321 | -21.4119 | 268.1243 | 62.2528 | 5348 | 5133 | 5.8 | 0.20 | 437 | 2.641 | 13.47 | 12.71 | 12.84 | 12.85 | 13.15 | -21.59 | -21.69 | 34.83 | 92.3 | 34.64 | 84.9 |
| 64909 ES234-043 | 350.9954 | -36.3410 | 223.5718 | 22.2168 | 2444 | 2305 | 8.9 | 0.52 | 122 | 2.146 | 13.22 | 13.40 | 14.30 | 14.50 | 14.30 | -17.09 | -16.85 | 31.39 | 19.0 | 31.35 | 18.6 |
| 64980 AGC033592 | 11.2713 | -34.6938 | 232.8284 | 36.7018 | 2789 | 2589 | 4.0 | 0.29 | 506 | 2.714 | 9.69 | 9.26 | 10.51 | 10.55 | 10.25 | -22.26 | -22.40 | 32.52 | 31.9 | 32.97 | 39.4 |
| 65003 ES340-042 | 0.8291 | -36.2752 | 227.9649 | 29.0794 | 2656 | 2485 | 7.8 | 0.54 | 132 | 2.187 | / | / | 14.28 | 14.38 | / | / | -17.25 | / | / | 31.63 | 21.2 |
| 65007 UGC11595 | 47.2381 | -21.9151 | 269.7413 | 61.7646 | 4013 | 3763 | 4.1 | 0.20 | 328 | 2.516 | 13.10 | 12.64 | 13.00 | 13.04 | 13.20 | -20.45 | -20.47 | 33.70 | 54.9 | 33.55 | 51.4 |

| PGC Name | l | b | sgl | sgb | v_{hel} | v_{mod} | t | b/a | w_{mz} | $\log w_{mz}^*$ | I | I* | [3.6] | [3.6]* | $C_{[3.6]}$ | MC | $M_{[3.6]}$ | μC | dC | $\mu_{[3.6]}$ | $d_{[3.6]}$ |
|------------------|----------|----------|----------|---------|-----------|-----------|-----|------|----------|-----------------|-------|-------|-------|--------|-------------|--------|-------------|---------|-------|---------------|-------------|
| 65022 AGC600084 | 39.4332 | -25.9308 | 256.8774 | 56.8412 | 5797 | 5599 | 5.2 | 0.20 | 515 | 2.712 | 12.73 | 12.11 | 12.48 | 12.51 | 12.68 | -22.24 | -22.38 | 35.01 | 100.3 | 35.03 | 101.2 |
| 65052 UGC11603 | 98.8248 | 13.5966 | 12.3887 | 38.8929 | 5189 | 5089 | 5.0 | 0.20 | 351 | 2.545 | / | / | 13.10 | 13.07 | / | / | -20.75 | / | / | 33.89 | 60.0 |
| 65060 UGC11599 | 56.0555 | -17.1753 | 289.9503 | 64.9857 | 4452 | 4208 | 3.1 | 0.68 | 377 | 2.702 | / | / | 11.53 | 11.62 | / | / | -22.29 | / | / | 33.97 | 62.4 |
| 65086 UGC11604 | 100.8958 | 14.8531 | 13.8430 | 36.8215 | 1426 | 1273 | 4.0 | 0.66 | 309 | 2.605 | / | / | 9.70 | 9.71 | / | / | -21.34 | / | / | 31.05 | 16.2 |
| 65131 PGC0065131 | 40.4787 | -26.4282 | 258.7513 | 56.5769 | 3900 | 3651 | 1.2 | 0.26 | 380 | 2.586 | / | / | 11.96 | 12.01 | / | / | -21.15 | / | / | 33.20 | 43.6 |
| 65150 UGC11613 | 98.9359 | 13.1972 | 11.8700 | 38.8035 | 2670 | 2517 | 6.1 | 0.20 | 211 | 2.324 | 14.06 | 13.40 | 14.10 | 14.10 | 14.11 | -18.71 | -18.59 | 32.84 | 37.0 | 32.72 | 34.9 |
| 65211 P0065211 | 92.6084 | 8.3127 | 5.4472 | 45.1083 | 2856 | 2673 | 5.0 | 0.46 | 284 | 2.496 | / | / | 12.62 | 12.58 | / | / | -20.27 | / | / | 32.87 | 37.6 |
| 65249 AGC033738 | 14.3435 | -36.0695 | 236.2687 | 37.5003 | 2713 | 2497 | 4.0 | 0.30 | 241 | 2.394 | 11.88 | 11.71 | 12.26 | 12.32 | 12.38 | -19.34 | -19.27 | 31.72 | 22.1 | 31.60 | 20.8 |
| 65255 UGC11635 | 113.5500 | 22.1975 | 21.5405 | 24.4091 | 4801 | 4765 | 3.6 | 0.44 | 488 | 2.725 | 11.51 | 11.15 | 11.69 | 11.74 | 11.81 | -22.36 | -22.51 | 34.22 | 69.9 | 34.34 | 73.9 |
| 65258 AGC033741 | 14.5442 | -36.1050 | 236.4488 | 37.5849 | 2716 | 2500 | 6.7 | 0.61 | 241 | 2.475 | 11.75 | 11.79 | 12.34 | 12.43 | 12.47 | -20.09 | -20.07 | 32.57 | 32.7 | 32.52 | 31.9 |
| 65295 NGC006943 | 325.9551 | -35.2971 | 216.0641 | 3.2957 | 3113 | 3073 | 5.9 | 0.50 | 400 | 2.654 | 10.42 | 10.33 | 10.92 | 11.00 | 11.02 | -21.71 | -21.82 | 32.75 | 35.5 | 32.84 | 37.0 |
| 65375 NGC6962 | 47.4062 | -25.3728 | 270.0623 | 58.3072 | 4222 | 3965 | 1.7 | 0.66 | 475 | 2.794 | 10.62 | 10.55 | 11.09 | 11.18 | 11.23 | -22.98 | -23.18 | 34.27 | 71.4 | 34.45 | 77.7 |
| 65506 AGC600138 | 40.5098 | -29.4824 | 259.9096 | 53.5952 | 6015 | 5810 | 5.0 | 0.20 | 473 | 2.675 | 12.97 | 12.37 | 12.76 | 12.79 | 12.95 | -21.90 | -22.02 | 34.94 | 97.1 | 34.94 | 97.4 |
| 65642 UGC11648 | 102.7488 | 14.2070 | 12.9405 | 35.0605 | 3364 | 3232 | 9.7 | 0.28 | 283 | 2.461 | / | / | 12.94 | 12.91 | / | / | -19.93 | / | / | 32.86 | 37.3 |
| 65683 UGC11647 | 64.0017 | -17.0565 | 304.8911 | 61.4218 | 8000 | 7853 | 5.9 | 0.20 | 466 | 2.668 | 13.58 | 12.93 | 13.06 | 13.11 | 13.39 | -21.84 | -21.96 | 35.34 | 117.1 | 35.21 | 110.4 |
| 65834 UGC11656 | 59.1805 | -21.8501 | 292.0114 | 59.5441 | 4584 | 4322 | 5.9 | 0.20 | 267 | 2.427 | 14.11 | 13.77 | 14.24 | 14.30 | 14.40 | -19.64 | -19.59 | 34.09 | 65.8 | 33.96 | 61.9 |
| 65887 UGC11662 | 65.0060 | -18.2748 | 304.9722 | 59.8732 | 5320 | 5078 | 3.7 | 0.70 | 263 | 2.557 | 12.41 | 12.48 | 12.92 | 13.03 | 13.12 | -20.83 | -20.87 | 34.00 | 63.0 | 33.97 | 62.2 |
| 65960 AGC600179 | 31.4197 | -36.3741 | 251.8429 | 44.7629 | 1474 | 1193 | 5.0 | 0.26 | 254 | 2.412 | 11.40 | 11.17 | 12.16 | 12.21 | 12.04 | -19.50 | -19.45 | 31.55 | 20.4 | 31.65 | 21.4 |
| 66094 UGC11677 | 64.3021 | -20.4123 | 301.5037 | 58.5107 | 4960 | 4703 | 6.2 | 0.50 | 338 | 2.583 | / | / | 13.11 | 13.20 | / | / | -21.12 | / | / | 34.41 | 76.2 |
| 66239 ES342-013 | 5.6778 | -42.7625 | 236.4073 | 28.0445 | 2635 | 2426 | 1.0 | 0.30 | 184 | 2.276 | 12.35 | 12.32 | 13.09 | 13.18 | 13.11 | -18.28 | -18.13 | 31.38 | 18.9 | 31.30 | 18.2 |
| 66242 AGC610018 | 46.7137 | -32.3131 | 269.1116 | 51.3619 | 2233 | 1929 | 4.1 | 0.46 | 187 | 2.315 | 13.12 | 13.15 | 14.01 | 14.09 | 13.98 | -18.63 | -18.51 | 32.62 | 33.4 | 32.61 | 33.3 |
| 66366 UGC11701 | 59.2756 | -26.0953 | 289.1365 | 55.5869 | 6116 | 5882 | 3.9 | 0.71 | 195 | 2.433 | / | / | 13.25 | 13.36 | / | / | -19.66 | / | / | 33.05 | 40.8 |
| 66396 UGC11706 | 65.0136 | -22.4320 | 300.4677 | 56.4594 | 4724 | 4454 | 3.3 | 0.22 | 369 | 2.569 | 13.55 | 13.02 | 13.46 | 13.49 | 13.62 | -20.93 | -20.98 | 34.63 | 84.3 | 34.58 | 82.4 |
| 66407 NGC07046 | 53.9457 | -29.8906 | 279.5500 | 53.2432 | 4165 | 3881 | 5.9 | 0.71 | 271 | 2.576 | / | / | 12.49 | 12.59 | / | / | -21.06 | / | / | 33.70 | 55.0 |
| 66434 UGC11711 | 67.0090 | -21.3570 | 304.3197 | 56.2772 | 8971 | 8848 | 6.0 | 0.20 | 400 | 2.602 | / | / | 14.49 | 14.55 | / | / | -21.31 | / | / | 36.09 | 164.9 |
| 66461 UGC11712 | 50.5980 | -32.1982 | 274.3763 | 51.3592 | 5801 | 5559 | 3.1 | 0.50 | 419 | 2.677 | 12.15 | 12.03 | 12.63 | 12.72 | 12.73 | -21.92 | -22.04 | 34.73 | 88.5 | 34.89 | 94.9 |
| 66478 UGC11738 | 117.5157 | 23.3605 | 22.6204 | 20.7041 | 4229 | 4195 | 4.0 | 0.50 | 281 | 2.504 | 13.34 | 13.21 | 13.70 | 13.78 | 13.86 | -20.34 | -20.35 | 34.26 | 71.2 | 34.21 | 69.4 |
| 66546 UGC11719 | 66.1237 | -23.0037 | 301.4239 | 55.4160 | 8566 | 8421 | 2.1 | 0.30 | 485 | 2.697 | / | / | 13.44 | 13.51 | / | / | -22.24 | / | / | 35.97 | 156.2 |
| 66548 AGC310060 | 73.9969 | -16.6557 | 318.5541 | 55.0529 | 936 | 625 | 1.0 | 0.42 | 149 | 2.206 | / | / | 13.46 | 13.52 | / | / | -17.44 | / | / | 30.96 | 15.6 |
| 66622 UGC11731 | 71.1057 | -19.8715 | 311.1868 | 54.9105 | 4955 | 4691 | 2.1 | 0.28 | 369 | 2.576 | 12.68 | 12.26 | 12.93 | 12.98 | 12.98 | -21.00 | -21.05 | 34.03 | 64.0 | 34.11 | 66.2 |
| 66738 PGC0066738 | 49.0326 | -35.7887 | 272.0103 | 47.8623 | 2937 | 2629 | 7.4 | 0.20 | 199 | 2.299 | / | / | 14.91 | 14.98 | / | / | -18.34 | / | / | 33.37 | 47.1 |
| 66784 NGC007059 | 334.6949 | -42.4348 | 224.6022 | 8.2892 | 1734 | 1615 | 5.6 | 0.32 | 260 | 2.429 | 12.37 | 12.26 | 11.89 | 11.95 | 12.49 | -19.66 | -19.62 | 32.16 | 27.0 | 31.57 | 20.6 |
| 66812 AGC034475 | 5.4164 | -46.3843 | 239.2796 | 25.4799 | 2661 | 2443 | 5.0 | 0.65 | 236 | 2.482 | 11.35 | 11.41 | 11.97 | 12.05 | 12.09 | -20.14 | -20.13 | 32.24 | 28.1 | 32.19 | 27.5 |
| 66836 NGC007064 | 344.1623 | -44.8185 | 229.2855 | 13.8987 | 895 | 692 | 5.1 | 0.20 | 153 | 2.185 | 11.89 | 11.93 | 13.07 | 13.09 | 12.86 | -17.44 | -17.23 | 30.30 | 11.5 | 30.32 | 11.6 |
| 66880 UGC11758 | 66.7487 | -26.3291 | 299.1181 | 52.3280 | 8635 | 8483 | 4.2 | 0.20 | 612 | 2.787 | / | / | 12.81 | 12.84 | / | / | -23.11 | / | / | 36.19 | 173.3 |
| 66969 UGC11766 | 73.6616 | -21.6080 | 311.9745 | 51.9936 | 5323 | 5061 | 1.1 | 0.35 | 438 | 2.661 | 12.53 | 12.22 | 12.82 | 12.88 | 12.91 | -21.77 | -21.88 | 34.77 | 89.8 | 34.89 | 95.1 |

| PGC Name | l | b | sgl | sgb | v_{hel} | v_{mod} | t | b/a | w_{max} | $\log w_{max}^2$ | I | I* | [3.6] | [3.6]* | $C_{[3.6]}$ | Mc | $M_{[3.6]}$ | μ_C | dC | $\mu_{[3.6]}$ | $d_{[3.6]}$ |
|-----------------|----------|----------|----------|---------|-----------|-----------|-----|------|-----------|------------------|-------|-------|-------|--------|-------------|--------|-------------|---------|-------|---------------|-------------|
| 66972 NGC007091 | 7.2280 | -47.5239 | 241.1393 | 25.5875 | 2565 | 2337 | 7.9 | 0.71 | 121 | 2.226 | / | / | 13.45 | 13.56 | / | / | -17.64 | / | / | 31.19 | 17.3 |
| 66986 UGC11768 | 71.4845 | -23.6867 | 307.2903 | 51.8629 | 6610 | 6382 | 4.0 | 0.20 | 426 | 2.629 | 13.72 | 13.12 | 13.55 | 13.59 | 13.72 | -21.49 | -21.57 | 35.32 | 115.9 | 35.33 | 116.2 |
| 67045 NGC007090 | 341.2957 | -45.3852 | 229.0135 | 11.8144 | 846 | 689 | 5.0 | 0.20 | 198 | 2.297 | 9.84 | 9.74 | 10.59 | 10.65 | 10.55 | -18.46 | -18.32 | 29.01 | 6.3 | 28.97 | 6.2 |
| 67078 ES287-043 | 356.3500 | -47.9590 | 236.4336 | 19.6904 | 2489 | 2291 | 5.9 | 0.22 | 178 | 2.252 | 13.32 | 13.28 | 14.08 | 14.16 | 14.08 | -18.05 | -17.89 | 32.13 | 26.7 | 32.05 | 25.7 |
| 67205 UGC11794 | 67.5332 | -29.4044 | 297.4530 | 49.3558 | 5850 | 5588 | 2.0 | 0.34 | 340 | 2.549 | 13.07 | 12.78 | 13.32 | 13.39 | 13.45 | -20.76 | -20.79 | 34.26 | 71.2 | 34.27 | 71.3 |
| 67246 UGC11799 | 90.7506 | -7.1326 | 343.4287 | 44.6788 | 5342 | 5132 | 4.5 | 0.69 | 332 | 2.653 | / | / | 12.52 | 12.55 | / | / | -21.80 | / | / | 34.45 | 77.6 |
| 67258 ES403-017 | 8.0069 | -49.5221 | 243.0928 | 24.5259 | 2708 | 2475 | 5.1 | 0.47 | 124 | 2.139 | 13.73 | 13.93 | 14.92 | 15.02 | 14.83 | -17.02 | -16.78 | 31.85 | 23.5 | 31.81 | 23.0 |
| 67335 ES403-024 | 7.9755 | -50.0361 | 243.4671 | 24.1409 | 2609 | 2374 | 6.0 | 0.36 | 143 | 2.177 | / | / | 14.61 | 14.71 | / | / | -17.15 | / | / | 31.86 | 23.5 |
| 67347 UGC11818 | 109.9976 | 14.4043 | 12.9781 | 28.0341 | 2404 | 2271 | 5.0 | 0.62 | 283 | 2.546 | 12.01 | 10.93 | 11.66 | 11.60 | 11.62 | -20.73 | -20.76 | 32.36 | 29.6 | 32.37 | 29.8 |
| 67373 ES403-031 | 7.0883 | -50.3176 | 243.2354 | 23.5432 | 2529 | 2294 | 4.0 | 0.41 | 136 | 2.164 | 14.39 | 14.54 | 15.39 | 15.49 | 15.37 | -17.25 | -17.03 | 32.63 | 33.6 | 32.53 | 32.1 |
| 67495 UGC011833 | 85.5579 | -15.3702 | 329.8060 | 46.3934 | 5232 | 4985 | 5.9 | 0.20 | 354 | 2.549 | / | / | 14.12 | 14.15 | / | / | -20.79 | / | / | 35.08 | 103.8 |
| 67532 NGC007140 | 338.7925 | -47.1540 | 230.0610 | 9.5644 | 2981 | 2844 | 3.8 | 0.54 | 291 | 2.530 | 10.98 | 11.03 | 11.36 | 11.45 | 11.61 | -20.58 | -20.60 | 32.19 | 27.5 | 32.06 | 25.8 |
| 67550 UGC11838 | 81.7237 | -19.9160 | 321.3682 | 47.2211 | 3496 | 3196 | 6.5 | 0.20 | 246 | 2.391 | 13.68 | 13.37 | 14.29 | 14.35 | 14.21 | -19.32 | -19.24 | 33.56 | 51.6 | 33.64 | 53.5 |
| 67556 UGC11839 | 87.3167 | -13.7617 | 332.9528 | 45.5549 | 5942 | 5721 | 4.0 | 0.23 | 453 | 2.660 | 13.28 | 12.59 | 12.89 | 12.92 | 13.12 | -21.76 | -21.87 | 34.97 | 98.7 | 34.91 | 96.1 |
| 67605 ES145-025 | 335.9156 | -46.5531 | 228.8357 | 7.9017 | 1837 | 1697 | 9.0 | 0.39 | 118 | 2.099 | / | / | 14.61 | 14.71 | / | / | -16.39 | / | / | 31.10 | 16.6 |
| 67619 UGC11844 | 72.0523 | -29.7331 | 302.0219 | 46.8545 | 7377 | 7160 | 2.0 | 0.49 | 507 | 2.756 | / | / | 12.29 | 12.38 | / | / | -22.81 | / | / | 35.35 | 117.5 |
| 67727 UGC11862 | 89.7224 | -12.4854 | 335.8945 | 43.8963 | 5843 | 5624 | 7.5 | 0.26 | 349 | 2.549 | / | / | 13.54 | 13.57 | / | / | -20.79 | / | / | 34.46 | 78.1 |
| 67823 NGC07177 | 75.3669 | -28.9582 | 305.9543 | 45.6092 | 1149 | 803 | 2.5 | 0.69 | 288 | 2.591 | 10.20 | 10.26 | 10.71 | 10.78 | 10.89 | -21.14 | -21.20 | 32.03 | 25.4 | 31.99 | 25.0 |
| 67835 ES404-017 | 9.4406 | -52.9331 | 246.3347 | 22.6252 | 2515 | 2268 | 7.6 | 0.33 | 187 | 2.288 | 13.85 | 13.88 | 14.99 | 15.08 | 14.83 | -18.38 | -18.23 | 33.23 | 44.3 | 33.35 | 46.8 |
| 67839 NGC007171 | 43.4565 | -47.9258 | 266.7738 | 35.6446 | 2724 | 2408 | 3.1 | 0.51 | 345 | 2.595 | 11.24 | 11.21 | 11.84 | 11.92 | 11.92 | -21.18 | -21.24 | 33.12 | 42.1 | 33.20 | 43.6 |
| 67842 ES404-018 | 13.9353 | -52.9257 | 248.6185 | 24.3432 | 2271 | 2010 | 6.8 | 0.20 | 163 | 2.212 | 13.86 | 13.83 | 15.09 | 15.17 | 14.85 | -17.69 | -17.50 | 32.55 | 32.3 | 32.69 | 34.5 |
| 67846 ES466-036 | 15.6748 | -52.8951 | 249.5318 | 24.9854 | 2379 | 2115 | 1.5 | 0.55 | 266 | 2.493 | 12.71 | 12.77 | 13.37 | 13.46 | 13.48 | -20.24 | -20.24 | 33.76 | 56.4 | 33.75 | 56.4 |
| 67893 AGC034977 | 32.5105 | -51.1134 | 259.1560 | 31.1588 | 1789 | 1483 | 8.2 | 0.26 | 131 | 2.124 | 13.91 | 14.02 | 14.80 | 14.89 | 14.81 | -16.89 | -16.64 | 31.70 | 21.9 | 31.52 | 20.2 |
| 67904 AGC034988 | 32.8912 | -51.1112 | 259.4222 | 31.2313 | 2623 | 2325 | 4.5 | 0.25 | 524 | 2.724 | 10.15 | 9.66 | 10.36 | 10.39 | 10.38 | -22.35 | -22.50 | 32.74 | 35.3 | 32.91 | 38.2 |
| 67920 AGC034989 | 30.3768 | -51.6560 | 257.8875 | 30.2221 | 1716 | 1414 | 5.9 | 0.46 | 110 | 2.084 | 13.93 | 14.14 | 15.43 | 15.53 | 15.18 | -16.53 | -16.25 | 31.71 | 22.0 | 31.78 | 22.7 |
| 67932 IC005156 | 11.8604 | -53.4043 | 247.8679 | 23.2010 | 2496 | 2242 | 2.2 | 0.40 | 365 | 2.590 | 11.12 | 10.99 | 11.58 | 11.65 | 11.68 | -21.13 | -21.19 | 32.83 | 36.8 | 32.87 | 37.4 |
| 67943 NGC007188 | 33.7358 | -51.1400 | 260.0269 | 31.3534 | 1760 | 1451 | 3.5 | 0.43 | 152 | 2.217 | / | / | 13.19 | 13.28 | / | / | -17.55 | / | / | 30.83 | 14.7 |
| 67954 AGC035005 | 14.4740 | -53.4637 | 249.2544 | 24.1037 | 2535 | 2275 | 5.0 | 0.39 | 266 | 2.452 | 12.12 | 12.07 | 12.88 | 12.95 | 12.87 | -19.88 | -19.85 | 32.76 | 35.6 | 32.82 | 36.6 |
| 67966 UGC11893 | 88.8275 | -15.6218 | 331.4369 | 43.4509 | 5589 | 5351 | 6.3 | 0.21 | 606 | 2.784 | 12.59 | 11.70 | 12.29 | 12.29 | 12.36 | -22.89 | -23.08 | 35.36 | 118.0 | 35.55 | 128.7 |
| 67977 UGC011895 | 91.2708 | -12.6432 | 336.4466 | 42.4310 | 4727 | 4479 | 3.1 | 0.64 | 334 | 2.629 | 11.99 | 11.76 | 12.35 | 12.42 | 12.45 | -21.49 | -21.57 | 33.99 | 62.7 | 34.06 | 65.0 |
| 68044 UGC011918 | 112.7770 | 15.5267 | 14.2142 | 25.3415 | 4097 | 4004 | 5.2 | 0.32 | 322 | 2.522 | / | / | 13.39 | 13.35 | / | / | -20.53 | / | / | 33.95 | 61.6 |
| 68128 NGC007205 | 334.8242 | -48.3603 | 230.3464 | 6.6507 | 1686 | 1540 | 4.0 | 0.47 | 317 | 2.546 | 9.98 | 9.96 | 10.31 | 10.38 | 10.54 | -20.73 | -20.76 | 31.27 | 18.0 | 31.15 | 17.0 |
| 68163 UGC11921 | 74.3943 | -32.8252 | 301.5774 | 43.1848 | 1674 | 1324 | 9.9 | 0.37 | 141 | 2.172 | / | / | 14.32 | 14.40 | / | / | -17.11 | / | / | 31.51 | 20.1 |
| 68199 AGC620014 | 40.0996 | -51.3433 | 264.6515 | 31.9988 | 1657 | 1335 | 5.6 | 0.44 | 263 | 2.458 | 11.23 | 11.22 | 11.67 | 11.74 | 11.84 | -19.93 | -19.90 | 31.77 | 22.6 | 31.64 | 21.3 |
| 68246 UGC11941 | 86.1876 | -21.3780 | 322.8556 | 42.9219 | 6850 | 6632 | 4.0 | 0.26 | 277 | 2.448 | 14.85 | 14.59 | 15.27 | 15.36 | 15.33 | -19.84 | -19.81 | 35.28 | 113.9 | 35.32 | 116.1 |
| 68248 UGC11946 | 96.3140 | -8.1398 | 344.1239 | 39.0975 | 5529 | 5324 | 5.2 | 0.64 | 354 | 2.655 | 12.54 | 12.27 | 12.81 | 12.88 | 12.94 | -21.72 | -21.82 | 34.73 | 88.4 | 34.82 | 92.2 |

| PGC Name | l | b | sgl | sgb | v_{hel} | v_{mod} | t | b/a | w_{nrx} | $\log w_{nrx}^2$ | I | I* | [3.6] | [3.6]* | $C_{[3.6]}$ | Mc | $M_{[3.6]}$ | μC | dC | $\mu_{[3.6]}$ | $d_{[3.6]}$ |
|------------------|----------|----------|----------|---------|-----------|-----------|-----|------|-----------|------------------|-------|-------|-------|--------|-------------|--------|-------------|---------|-------|---------------|-------------|
| 68305 ESI46-014 | 328.5879 | -46.3885 | 227.3465 | 3.0765 | 1694 | 1574 | 6.5 | 0.20 | 120 | 2.079 | 13.98 | 14.10 | 14.98 | 15.02 | 14.92 | -16.48 | -16.20 | 31.40 | 19.0 | 31.22 | 17.5 |
| 68345 AGC035176 | 24.0012 | -55.0989 | 255.4274 | 25.5789 | 2597 | 2314 | 5.2 | 0.20 | 318 | 2.502 | 12.28 | 11.93 | 12.40 | 12.44 | 12.55 | -20.33 | -20.33 | 32.90 | 38.0 | 32.80 | 36.3 |
| 68381 UGC0011961 | 94.3649 | -11.8376 | 338.8167 | 39.8604 | 4203 | 3949 | 3.2 | 0.26 | 426 | 2.636 | 12.82 | 12.18 | 12.50 | 12.52 | 12.72 | -21.55 | -21.64 | 34.32 | 73.2 | 34.24 | 70.5 |
| 68389 IC0005176 | 322.9963 | -43.6854 | 223.9727 | -0.3190 | 1749 | 1657 | 4.5 | 0.20 | 360 | 2.556 | 11.23 | 10.82 | 11.15 | 11.18 | 11.37 | -20.82 | -20.86 | 32.19 | 27.5 | 32.05 | 25.7 |
| 68413 IC001441 | 91.5464 | -15.8795 | 332.5696 | 40.9588 | 5133 | 4883 | 2.7 | 0.55 | 325 | 2.581 | / | / | 13.23 | 13.31 | / | / | -21.10 | / | / | / | 79.9 |
| 68429 UGC11967 | 89.3318 | -18.8828 | 327.7536 | 41.5804 | 5036 | 4772 | 7.5 | 0.20 | 279 | 2.446 | / | / | 14.13 | 14.19 | / | / | -19.78 | / | / | / | 64.2 |
| 68442 UGC11968 | 79.5867 | -30.2488 | 308.3954 | 42.1404 | 1461 | 1112 | 4.0 | 0.70 | 379 | 2.716 | 11.09 | 11.15 | 11.14 | 11.22 | 11.56 | -22.28 | -22.42 | 33.88 | 59.6 | 33.69 | 54.8 |
| 68455 IC5179 | 6.5024 | -55.9274 | 247.1503 | 19.2634 | 3413 | 3180 | 4.0 | 0.48 | 396 | 2.646 | 10.78 | 10.72 | 10.78 | 10.86 | 11.16 | -21.64 | -21.73 | 32.82 | 36.6 | 32.61 | 33.3 |
| 68482 UGC11973 | 94.2916 | -12.6145 | 337.8311 | 39.6742 | 4216 | 3959 | 3.9 | 0.28 | 494 | 2.703 | 11.17 | 10.51 | 11.33 | 11.35 | 11.28 | -22.15 | -22.29 | 33.47 | 49.4 | 33.69 | 54.7 |
| 68511 NGC007247 | 29.7947 | -55.2533 | 258.8912 | 26.7174 | 2475 | 2178 | 3.1 | 0.56 | 251 | 2.473 | 11.68 | 11.75 | 12.08 | 12.17 | 12.32 | -20.06 | -20.04 | 32.39 | 30.1 | 32.22 | 27.7 |
| 68617 UGC11994 | 90.0771 | -19.8016 | 327.1014 | 40.5331 | 4876 | 4606 | 4.1 | 0.20 | 425 | 2.628 | 12.47 | 11.90 | 12.51 | 12.54 | 12.58 | -21.48 | -21.56 | 34.11 | 66.4 | 34.18 | 68.7 |
| 68618 IC0005201 | 350.3262 | -54.8463 | 240.3034 | 12.7861 | 915 | 699 | 6.1 | 0.45 | 182 | 2.301 | 10.80 | 10.92 | 11.64 | 11.72 | 11.68 | -18.50 | -18.37 | 30.18 | 10.8 | 30.09 | 10.4 |
| 68658 NGC07264 | 92.1803 | -17.4220 | 331.0413 | 39.7788 | 4278 | 4003 | 3.1 | 0.22 | 527 | 2.724 | 12.37 | 11.71 | 12.07 | 12.09 | 12.27 | -22.35 | -22.50 | 34.70 | 87.0 | 34.71 | 87.4 |
| 68704 AGC035331 | 36.0919 | -55.4536 | 262.8161 | 27.5210 | 2674 | 2367 | 6.7 | 0.28 | 158 | 2.208 | 14.51 | 14.55 | 15.76 | 15.85 | 15.55 | -17.65 | -17.45 | 33.22 | 44.1 | 33.34 | 46.5 |
| 68727 UGC12010 | 69.7135 | -41.5443 | 291.1523 | 37.9547 | 2815 | 2468 | 2.0 | 0.22 | 201 | 2.305 | / | / | 13.80 | 13.86 | / | / | -18.41 | / | / | / | 28.5 |
| 68843 UGC12034 | 95.0715 | -14.5547 | 335.8174 | 38.2995 | 4544 | 4287 | 3.2 | 0.35 | 339 | 2.551 | 12.08 | 11.71 | 12.57 | 12.62 | 12.52 | -20.77 | -20.80 | 33.32 | 46.2 | 33.47 | 49.5 |
| 68872 PGC068872 | 27.3275 | -49.8360 | 277.6577 | 33.1804 | 7630 | 7416 | 5.0 | 0.20 | 415 | 2.618 | 13.43 | 12.89 | 13.46 | 13.52 | 13.57 | -21.38 | -21.46 | 35.04 | 102.1 | 35.13 | 106.1 |
| 68875 E533-028 | 58.6127 | -57.5003 | 259.0652 | 24.3825 | 2578 | 2283 | 4.6 | 0.52 | 219 | 2.400 | 12.47 | 12.56 | 13.13 | 13.22 | 13.25 | -19.40 | -19.33 | 32.67 | 34.1 | 32.57 | 32.6 |
| 68942 UGC12045 | 80.7471 | -33.7626 | 306.0307 | 38.9642 | 2899 | 2557 | 4.0 | 0.54 | 244 | 2.453 | 12.46 | 12.47 | 13.09 | 13.18 | 13.18 | -19.89 | -19.85 | 33.09 | 41.5 | 33.06 | 41.0 |
| 68977 UGC12054 | 73.2274 | -41.0642 | 294.3202 | 37.0170 | 2081 | 1724 | 3.0 | 0.25 | 199 | 2.303 | 13.60 | 13.41 | 14.38 | 14.43 | 14.27 | -18.52 | -18.39 | 32.81 | 36.5 | 32.85 | 37.1 |
| 69161 NGC007307 | 357.9289 | -58.6043 | 245.9218 | 14.0466 | 2089 | 1853 | 6.0 | 0.23 | 228 | 2.361 | 11.89 | 11.76 | 12.61 | 12.68 | 12.58 | -19.04 | -18.95 | 31.62 | 21.1 | 31.63 | 21.2 |
| 69253 NGC007314 | 27.1344 | -59.7421 | 259.1643 | 22.0140 | 1427 | 1123 | 4.0 | 0.39 | 300 | 2.504 | 10.10 | 10.02 | 10.51 | 10.58 | 10.67 | -20.35 | -20.35 | 31.01 | 15.9 | 30.93 | 15.3 |
| 69284 AGC320265 | 80.2001 | -37.4039 | 302.4539 | 36.6249 | 7101 | 6857 | 3.7 | 0.25 | 289 | 2.465 | 14.73 | 14.45 | 14.88 | 14.96 | 15.07 | -20.00 | -19.97 | 35.17 | 108.0 | 35.07 | 103.4 |
| 69327 NGC07331 | 93.7221 | -20.7242 | 328.0068 | 37.0625 | 816 | 491 | 3.9 | 0.44 | 501 | 2.739 | 8.16 | 7.90 | 8.37 | 8.41 | 8.52 | -22.48 | -22.64 | 31.00 | 15.9 | 31.05 | 16.2 |
| 69349 NGC07328 | 77.6185 | -40.2713 | 298.2597 | 35.7286 | 2824 | 2474 | 2.1 | 0.47 | 309 | 2.534 | 11.87 | 11.76 | 12.23 | 12.30 | 12.39 | -20.62 | -20.64 | 33.03 | 40.4 | 32.97 | 39.3 |
| 69364 UGC12122 | 87.4629 | -29.7271 | 314.6582 | 37.2794 | 1353 | 1004 | 4.0 | 0.28 | 329 | 2.525 | 10.94 | 10.68 | 10.92 | 10.97 | 11.19 | -20.54 | -20.56 | 31.74 | 22.2 | 31.53 | 20.2 |
| 69367 UGC12123 | 88.3884 | -28.5766 | 316.4254 | 37.2938 | 4079 | 3767 | 6.1 | 0.21 | 187 | 2.273 | 14.58 | 14.48 | 15.53 | 15.62 | 15.40 | -18.24 | -18.09 | 33.68 | 54.4 | 33.77 | 56.7 |
| 69383 UGC12135 | 113.2684 | 12.2123 | 10.5596 | 24.8330 | 4063 | 3951 | 5.8 | 0.29 | 281 | 2.459 | 13.69 | 12.86 | 13.34 | 13.33 | 13.46 | -19.93 | -19.90 | 33.42 | 48.3 | 33.27 | 45.0 |
| 69404 AGC620157 | 60.9412 | -51.9983 | 279.6565 | 30.5382 | 2915 | 2574 | 8.0 | 0.32 | 231 | 2.378 | / | / | 12.01 | 12.09 | / | / | -19.12 | / | / | / | 17.5 |
| 69428 UGC12133 | 76.4770 | -42.0598 | 296.0991 | 34.8199 | 7427 | 7191 | 5.8 | 0.20 | 443 | 2.647 | 13.46 | 12.81 | 13.33 | 13.37 | 13.46 | -21.64 | -21.74 | 35.20 | 109.8 | 35.27 | 113.1 |
| 69443 NGC07347 | 78.6401 | -40.2734 | 299.0059 | 35.2404 | 2246 | 1889 | 4.4 | 0.22 | 253 | 2.406 | 12.66 | 12.42 | 12.88 | 12.93 | 13.04 | -19.45 | -19.39 | 32.50 | 31.6 | 32.33 | 29.2 |
| 69448 AGC620162 | 65.4731 | -50.0621 | 283.5254 | 31.4710 | 2968 | 2624 | 4.0 | 0.61 | 208 | 2.412 | 12.09 | 12.19 | 12.77 | 12.86 | 12.89 | -19.50 | -19.45 | 32.40 | 30.2 | 32.32 | 29.1 |
| 69453 NGC007329 | 320.9726 | -45.7899 | 225.8652 | -2.0262 | 3252 | 3174 | 3.6 | 0.66 | 369 | 2.684 | 10.72 | 10.80 | 11.17 | 11.26 | 11.40 | -21.98 | -22.11 | 33.41 | 48.0 | 33.41 | 48.2 |
| 69472 UGC12160 | 114.7362 | 14.4114 | 12.9974 | 23.4446 | 1555 | 1423 | 5.8 | 0.64 | 235 | 2.477 | 12.15 | 11.42 | 11.89 | 11.86 | 12.01 | -20.10 | -20.08 | 32.11 | 26.4 | 31.95 | 24.5 |
| 69539 NGC007361 | 19.3044 | -61.5963 | 256.3346 | 18.6850 | 1249 | 958 | 4.6 | 0.24 | 211 | 2.328 | 11.47 | 11.39 | 12.39 | 12.45 | 12.27 | -18.74 | -18.63 | 31.02 | 16.0 | 31.08 | 16.5 |
| 69561 UGC12165 | 94.0288 | -22.5621 | 326.1107 | 35.9956 | 6525 | 6295 | 4.1 | 0.20 | 325 | 2.512 | 13.84 | 13.39 | 13.69 | 13.75 | 13.94 | -20.42 | -20.43 | 34.42 | 76.6 | 34.27 | 71.3 |

| PGC Name | l | b | sgl | sgb | v_{hel} | v_{mod} | t | b/a | w_{mz} | $\log w_{mz}^2$ | I | I* | [3.6] | [3.6]* | $C_{[3.6]}$ | M_C | $M_{[3.6]}$ | μ_C | d_C | $\mu_{[3.6]}$ | $d_{[3.6]}$ | |
|------------------|----------|----------|----------|---------|-----------|-----------|-----|------|----------|-----------------|-------|-------|-------|--------|-------------|--------|-------------|---------|-------|---------------|-------------|------|
| 69605 UGC12173 | 97.1125 | -18.0161 | 332.6703 | 35.2229 | 4774 | 4512 | 5.4 | 0.51 | 354 | 2.606 | 11.84 | 11.67 | 12.33 | 12.40 | 12.39 | -21.28 | -21.35 | 33.71 | 55.3 | 33.82 | 58.0 | |
| 69650 UGC12178 | 75.9630 | -44.6199 | 293.9494 | 32.9464 | 1930 | 1568 | 8.0 | 0.50 | 214 | 2.384 | / | / | 12.68 | 12.75 | / | / | -19.18 | / | / | / | 31.93 | 24.3 |
| 69661 NGC007368 | 359.8121 | -61.1730 | 248.5706 | 13.1188 | 2351 | 2108 | 3.1 | 0.22 | 358 | 2.555 | 11.48 | 11.13 | 11.44 | 11.49 | 11.67 | -20.81 | -20.85 | 32.50 | 31.6 | 32.35 | 29.5 | |
| 69691 AGC620175 | 50.5654 | -58.1345 | 271.8683 | 25.4937 | 2599 | 2265 | 7.1 | 0.20 | 179 | 2.253 | / | / | 14.92 | 14.99 | / | / | -17.90 | / | / | / | 32.92 | 38.3 |
| 69707 IC0005249 | 321.8832 | -47.4628 | 227.6047 | -1.6180 | 2366 | 2265 | 6.9 | 0.20 | 217 | 2.336 | 13.11 | 12.94 | 13.91 | 13.98 | 13.81 | -18.82 | -18.71 | 32.65 | 33.8 | 32.71 | 34.8 | |
| 69734 NGC07378 | 54.6892 | -57.2223 | 274.4077 | 26.1774 | 2558 | 2222 | 2.2 | 0.56 | 223 | 2.419 | 11.99 | 12.05 | 12.34 | 12.43 | 12.61 | -19.58 | -19.52 | 32.19 | 27.4 | 31.96 | 24.6 | |
| 69759 E346-001 | 358.8559 | -61.6504 | 248.6355 | 12.4606 | 2334 | 2092 | 5.1 | 0.20 | 253 | 2.403 | 13.09 | 12.86 | 13.28 | 13.34 | 13.46 | -19.43 | -19.36 | 32.91 | 38.2 | 32.72 | 35.0 | |
| 69797 UGC12204 | 99.0332 | -16.9080 | 334.7218 | 33.9071 | 6725 | 6525 | 4.0 | 0.22 | 371 | 2.572 | 14.06 | 13.50 | 13.91 | 13.96 | 14.09 | -20.96 | -21.01 | 35.16 | 107.5 | 35.11 | 105.1 | |
| 69934 UGC12234 | 96.5484 | -23.0596 | 326.8067 | 33.6901 | 6306 | 6070 | 4.0 | 0.54 | 410 | 2.679 | / | / | 11.49 | 11.59 | / | / | -22.06 | / | / | / | 33.70 | 55.0 |
| 69994 NGC07410 | 358.0216 | -62.8297 | 249.3033 | 11.4047 | 1740 | 1492 | 1.0 | 0.29 | 577 | 2.772 | 10.50 | 10.10 | 9.80 | 9.83 | 10.35 | -22.79 | -22.97 | 33.15 | 42.7 | 32.82 | 36.7 | |
| 69998 ES346-014 | 0.2723 | -63.1738 | 250.2510 | 11.9531 | 2693 | 2450 | 6.6 | 0.20 | 204 | 2.310 | 13.90 | 13.79 | 14.81 | 14.88 | 14.69 | -18.58 | -18.45 | 33.29 | 45.5 | 33.38 | 47.3 | |
| 70009 UGC12249 | 94.0291 | -27.9301 | 320.3619 | 33.4457 | 7551 | 7343 | 5.9 | 0.20 | 296 | 2.471 | 14.73 | 14.36 | 15.02 | 15.10 | 15.09 | -20.05 | -20.03 | 35.24 | 111.9 | 35.29 | 114.0 | |
| 70025 AGC620200 | 65.8681 | -54.9822 | 281.7682 | 26.7900 | 2859 | 2514 | 3.1 | 0.25 | 361 | 2.563 | 11.22 | 10.88 | 11.64 | 11.69 | 11.64 | -20.88 | -20.93 | 32.53 | 32.1 | 32.63 | 33.6 | |
| 70026 UGC12252 | 95.9543 | -24.9688 | 324.4637 | 33.3381 | 7136 | 6922 | 6.4 | 0.24 | 290 | 2.466 | 14.66 | 14.37 | 15.15 | 15.23 | 15.16 | -20.00 | -19.98 | 35.26 | 112.9 | 35.38 | 118.9 | |
| 70027 NGC007412 | 351.9249 | -61.8760 | 246.8048 | 9.7097 | 1710 | 1476 | 3.2 | 0.65 | 132 | 2.233 | 10.60 | 10.83 | 11.14 | 11.24 | 11.40 | -17.88 | -17.71 | 29.29 | 7.2 | 28.95 | 6.2 | |
| 70070 IC0005269B | 5.1900 | -64.0451 | 252.4527 | 12.9074 | 1666 | 1402 | 5.5 | 0.22 | 218 | 2.340 | 11.89 | 11.76 | 12.82 | 12.88 | 12.68 | -18.85 | -18.75 | 31.53 | 20.2 | 31.63 | 21.2 | |
| 70075 NGC07418A | 4.0200 | -63.9430 | 252.0006 | 12.6262 | 2107 | 1849 | 6.5 | 0.50 | 182 | 2.314 | / | / | 14.11 | 14.20 | / | / | -18.49 | / | / | / | 32.71 | 34.8 |
| 70102 ES603-031 | 46.3140 | -62.1756 | 269.4702 | 21.4996 | 2267 | 1941 | 1.0 | 0.54 | 168 | 2.291 | / | / | 14.37 | 14.46 | / | / | -18.27 | / | / | / | 32.75 | 35.6 |
| 70107 UGC12265 | 89.4737 | -35.5799 | 310.2240 | 32.3914 | 5755 | 5471 | 2.3 | 0.38 | 198 | 2.322 | / | / | 13.93 | 14.03 | / | / | -18.57 | / | / | / | 32.62 | 33.4 |
| 70128 IC0005271 | 10.7928 | -64.7656 | 254.8265 | 13.9280 | 1710 | 1435 | 3.0 | 0.39 | 343 | 2.562 | 10.39 | 10.29 | 10.87 | 10.93 | 10.97 | -20.88 | -20.92 | 31.85 | 23.4 | 31.85 | 23.5 | |
| 70175 UGC12281 | 85.6434 | -41.0049 | 303.0892 | 31.1061 | 2568 | 2213 | 7.5 | 0.20 | 248 | 2.394 | 12.79 | 12.49 | 13.40 | 13.44 | 13.32 | -19.35 | -19.28 | 32.68 | 34.4 | 32.74 | 35.4 | |
| 70184 IC0005273 | 1.6417 | -64.2376 | 251.4702 | 11.6786 | 1293 | 1033 | 5.7 | 0.67 | 192 | 2.404 | 10.54 | 10.73 | 11.23 | 11.32 | 11.39 | -19.43 | -19.37 | 30.82 | 14.6 | 30.69 | 13.7 | |
| 70213 NGC7448 | 87.5659 | -39.1242 | 305.8716 | 31.2994 | 2195 | 1838 | 5.0 | 0.45 | 276 | 2.481 | 10.81 | 10.76 | 11.36 | 11.39 | 11.43 | -20.14 | -20.13 | 31.57 | 20.6 | 31.51 | 20.1 | |
| 70266 UGC12307 | 85.5336 | -42.0055 | 302.1886 | 30.4661 | 2825 | 2472 | 9.8 | 0.25 | 209 | 2.325 | / | / | 14.86 | 14.89 | / | / | -18.60 | / | / | / | 33.54 | 51.0 |
| 70271 UGC12308 | 86.7443 | -40.6685 | 304.0413 | 30.7323 | 2237 | 1879 | 5.8 | 0.22 | 218 | 2.340 | 13.30 | 13.10 | 14.25 | 14.31 | 14.05 | -18.85 | -18.75 | 32.93 | 38.5 | 33.09 | 41.4 | |
| 70291 UGC12316 | 88.0411 | -39.3540 | 305.9525 | 30.8711 | 2371 | 2016 | 3.1 | 0.33 | 232 | 2.382 | 11.91 | 11.79 | 12.56 | 12.63 | 12.56 | -19.23 | -19.15 | 31.80 | 22.9 | 31.78 | 22.7 | |
| 70301 UGC12320 | 96.7653 | -26.4915 | 323.2462 | 31.9957 | 6624 | 6389 | 5.9 | 0.20 | 312 | 2.494 | 14.37 | 13.96 | 14.18 | 14.25 | 14.47 | -20.26 | -20.25 | 34.81 | 91.6 | 34.61 | 83.4 | |
| 70304 NGC007456 | 357.1847 | -64.1598 | 250.1081 | 10.2716 | 1198 | 946 | 6.0 | 0.35 | 221 | 2.365 | 10.99 | 11.01 | 11.83 | 11.90 | 11.81 | -19.08 | -18.99 | 30.89 | 15.1 | 30.89 | 15.1 | |
| 70324 NGC007462 | 354.4072 | -63.7977 | 249.0599 | 9.5303 | 1064 | 817 | 3.6 | 0.22 | 179 | 2.255 | 10.90 | 10.88 | 11.92 | 11.99 | 11.79 | -18.08 | -17.92 | 29.87 | 9.4 | 29.91 | 9.6 | |
| 70371 AGC0035868 | 22.7213 | -66.2293 | 259.9645 | 15.2708 | 1760 | 1465 | 9.0 | 0.43 | 147 | 2.203 | / | / | 15.59 | 15.68 | / | / | -17.41 | / | / | / | 33.12 | 42.0 |
| 70433 UGC12350 | 89.5516 | -39.0315 | 307.1161 | 30.1856 | 2135 | 1778 | 8.6 | 0.29 | 186 | 2.280 | 12.69 | 12.56 | 13.96 | 14.02 | 13.64 | -18.31 | -18.16 | 31.95 | 24.5 | 32.19 | 27.4 | |
| 70460 UGC12355 | 94.3611 | -32.3918 | 316.0206 | 30.8977 | 7720 | 7510 | 5.9 | 0.28 | 277 | 2.452 | 14.52 | 14.04 | 14.86 | 14.92 | 14.84 | -19.87 | -19.84 | 34.79 | 90.8 | 34.89 | 94.9 | |
| 70538 UGC12388 | 87.6424 | -42.8789 | 302.6997 | 28.7379 | 4594 | 4272 | 7.0 | 0.30 | 245 | 2.401 | / | / | 14.58 | 14.65 | / | / | -19.34 | / | / | / | 34.07 | 65.0 |
| 70565 ES469-015 | 17.3477 | -67.3271 | 258.5692 | 13.3058 | 1634 | 1346 | 3.5 | 0.22 | 207 | 2.318 | 12.94 | 12.84 | 13.45 | 13.52 | 13.54 | -18.66 | -18.54 | 32.20 | 27.5 | 32.06 | 25.8 | |
| 70569 NGC07497 | 91.3766 | -38.3415 | 308.7607 | 29.4996 | 1704 | 1345 | 6.2 | 0.26 | 264 | 2.428 | 11.09 | 10.69 | 11.53 | 11.56 | 11.48 | -19.65 | -19.61 | 31.13 | 16.9 | 31.16 | 17.1 | |
| 70582 ES407-007 | 3.2504 | -66.5499 | 253.6327 | 10.5421 | 1631 | 1366 | 3.1 | 0.36 | 260 | 2.436 | 12.05 | 12.00 | 12.22 | 12.30 | 12.52 | -19.72 | -19.68 | 32.25 | 28.2 | 31.98 | 24.9 | |

| PGC Name | l | b | sgl | sgb | v_{hel} | v_{mod} | t | b/a | w_{mz} | $\log w_{mz}^2$ | I | I* | [3.6] | [3.6]* | $C_{[3.6]}$ | M_C | $M_{[3.6]}$ | μ_C | dC | $\mu_{[3.6]}$ | $d_{[3.6]}$ |
|-----------------|----------|----------|----------|---------|-----------|-----------|-----|------|----------|-----------------|-------|-------|-------|--------|-------------|--------|-------------|---------|-------|---------------|-------------|
| 70588 NGC007496 | 347.8353 | -63.8011 | 247.4505 | 7.1062 | 1650 | 1419 | 3.2 | 0.63 | 152 | 2.283 | / | / | 11.05 | 11.15 | / | / | -18.19 | / | / | 29.34 | 7.4 |
| 70664 UGC12410 | 99.0024 | -27.1814 | 323.5679 | 29.9018 | 7095 | 6877 | 5.8 | 0.20 | 435 | 2.638 | 13.90 | 13.32 | 13.30 | 13.35 | 13.71 | -21.57 | -21.66 | 35.39 | 119.8 | 35.16 | 107.4 |
| 70697 AGC035947 | 0.8791 | -66.9051 | 253.2289 | 9.6225 | 1569 | 1308 | 6.7 | 0.38 | 192 | 2.308 | 12.66 | 12.72 | 13.69 | 13.77 | 13.60 | -18.57 | -18.44 | 32.17 | 27.2 | 32.22 | 27.7 |
| 70702 IC001474 | 83.3802 | -49.3441 | 295.2536 | 26.1233 | 3490 | 3145 | 5.8 | 0.50 | 255 | 2.459 | 12.98 | 12.90 | 12.98 | 13.06 | 13.35 | -19.93 | -19.91 | 33.31 | 45.9 | 32.99 | 39.7 |
| 70714 NGC07513 | 23.9595 | -68.2735 | 261.2961 | 13.6139 | 1566 | 1268 | 3.2 | 0.59 | 223 | 2.434 | 10.58 | 10.68 | 11.20 | 11.29 | 11.34 | -19.71 | -19.66 | 31.05 | 16.2 | 30.95 | 15.5 |
| 70734 UGC12430 | 98.4606 | -29.1772 | 321.2687 | 29.4325 | 3700 | 3386 | 6.5 | 0.20 | 226 | 2.354 | 13.51 | 13.20 | 14.20 | 14.26 | 14.08 | -18.98 | -18.88 | 33.08 | 41.4 | 33.17 | 43.1 |
| 70786 UGC12442 | 82.7612 | -50.6616 | 293.9737 | 25.3715 | 2674 | 2317 | 3.6 | 0.31 | 308 | 2.501 | 12.18 | 11.94 | 12.43 | 12.49 | 12.58 | -20.32 | -20.32 | 32.91 | 38.2 | 32.83 | 36.8 |
| 70795 NGC7541 | 82.8436 | -50.6545 | 294.0232 | 25.3437 | 2679 | 2323 | 4.7 | 0.32 | 422 | 2.640 | 10.58 | 10.25 | 10.52 | 10.57 | 10.78 | -21.58 | -21.68 | 32.37 | 29.7 | 32.26 | 28.3 |
| 70800 NGC007531 | 346.4176 | -64.4907 | 247.7454 | 6.2277 | 1598 | 1367 | 4.0 | 0.52 | 324 | 2.570 | 10.34 | 10.37 | 10.96 | 11.04 | 11.06 | -20.95 | -21.00 | 32.02 | 25.3 | 32.04 | 25.6 |
| 70803 UGC12451 | 83.6360 | -49.9360 | 294.9649 | 25.5663 | 3640 | 3298 | 9.8 | 0.22 | 172 | 2.237 | 14.00 | 13.88 | 14.98 | 15.06 | 14.82 | -17.92 | -17.74 | 32.76 | 35.6 | 32.82 | 36.7 |
| 70823 UGC12458 | 99.6940 | -27.5438 | 323.5006 | 29.1910 | 6857 | 6630 | 4.1 | 0.23 | 396 | 2.601 | 14.22 | 13.75 | 13.91 | 13.98 | 14.23 | -21.23 | -21.30 | 35.58 | 130.9 | 35.44 | 122.5 |
| 70880 UGC12467 | 85.1041 | -49.0832 | 296.3828 | 25.5724 | 3513 | 3168 | 8.0 | 0.25 | 198 | 2.302 | 13.70 | 13.53 | 14.61 | 14.68 | 14.45 | -18.51 | -18.38 | 32.98 | 39.5 | 33.08 | 41.4 |
| 70927 P0070927 | 85.8334 | -48.8335 | 296.9600 | 25.4302 | 3592 | 3249 | 5.0 | 0.64 | 180 | 2.359 | 13.57 | 13.62 | 14.41 | 14.50 | 14.42 | -19.03 | -18.94 | 33.48 | 49.7 | 33.48 | 49.7 |
| 70966 AGC035993 | 6.2431 | -68.5490 | 255.8687 | 9.8657 | 2745 | 2485 | 5.1 | 0.56 | 225 | 2.427 | 12.36 | 12.47 | 13.06 | 13.15 | 13.17 | -19.64 | -19.59 | 32.83 | 36.9 | 32.77 | 35.8 |
| 70981 UGC12483 | 89.3371 | -45.3372 | 301.5864 | 26.1791 | 4128 | 3796 | 3.5 | 0.64 | 239 | 2.484 | 12.78 | 12.89 | 13.26 | 13.37 | 13.49 | -20.16 | -20.15 | 33.70 | 54.9 | 33.57 | 51.8 |
| 70996 NGC07591 | 85.7656 | -49.4436 | 296.4636 | 25.0148 | 4954 | 4639 | 3.6 | 0.50 | 382 | 2.637 | 11.85 | 11.69 | 11.85 | 11.93 | 12.18 | -21.56 | -21.65 | 33.78 | 56.9 | 33.63 | 53.2 |
| 71034 UGC12494 | 86.2011 | -49.2790 | 296.8161 | 24.9407 | 4206 | 3874 | 6.7 | 0.30 | 208 | 2.330 | 13.81 | 13.65 | 14.60 | 14.68 | 14.52 | -18.76 | -18.65 | 33.31 | 45.8 | 33.36 | 47.1 |
| 71047 NGC7606 | 69.0994 | -61.2842 | 280.9335 | 20.3082 | 2232 | 1884 | 3.0 | 0.41 | 505 | 2.734 | 9.97 | 9.75 | 10.30 | 10.36 | 10.42 | -22.44 | -22.59 | 32.87 | 37.5 | 32.98 | 39.4 |
| 71049 UGC12501 | 89.3188 | -45.9620 | 301.0631 | 25.7678 | 3824 | 3486 | 3.0 | 0.27 | 258 | 2.419 | 13.74 | 13.55 | 14.09 | 14.16 | 14.22 | -19.57 | -19.52 | 33.84 | 58.6 | 33.74 | 56.0 |
| 71051 IC005309 | 87.2932 | -48.2758 | 298.1572 | 25.1601 | 4182 | 3850 | 3.1 | 0.48 | 270 | 2.479 | 12.59 | 12.53 | 13.06 | 13.15 | 13.20 | -20.12 | -20.11 | 33.35 | 46.8 | 33.29 | 45.6 |
| 71052 UGC12497 | 86.9672 | -48.6189 | 297.7211 | 25.0676 | 3779 | 3439 | 9.9 | 0.29 | 160 | 2.214 | 14.06 | 13.97 | 14.81 | 14.89 | 14.79 | -17.71 | -17.52 | 32.51 | 31.7 | 32.42 | 30.5 |
| 71055 UGC12500 | 87.5014 | -48.0785 | 298.4198 | 25.2017 | 3531 | 3187 | 3.7 | 0.28 | 279 | 2.455 | 12.86 | 12.63 | 13.16 | 13.22 | 13.29 | -19.90 | -19.87 | 33.21 | 43.9 | 33.12 | 42.1 |
| 71066 NGC07599 | 348.0900 | -65.9064 | 249.3315 | 6.1298 | 1688 | 1452 | 5.2 | 0.35 | 283 | 2.471 | 10.39 | 10.31 | 10.83 | 10.90 | 10.96 | -20.05 | -20.03 | 31.01 | 15.9 | 30.93 | 15.3 |
| 71087 UGC12511 | 89.0256 | -46.5585 | 300.4243 | 25.5122 | 3557 | 3214 | 5.9 | 0.55 | 241 | 2.450 | 12.52 | 12.58 | 13.24 | 13.34 | 13.32 | -19.86 | -19.83 | 33.20 | 43.7 | 33.20 | 43.6 |
| 71102 UGC12519 | 93.0082 | -41.5481 | 306.7390 | 26.5564 | 4382 | 4058 | 4.5 | 0.26 | 307 | 2.494 | 12.69 | 12.44 | 13.02 | 13.09 | 13.13 | -20.25 | -20.25 | 33.41 | 48.1 | 33.38 | 47.5 |
| 71155 UGC12535 | 87.9316 | -48.4516 | 298.3502 | 24.7356 | 4217 | 3886 | 4.0 | 0.23 | 187 | 2.274 | 13.98 | 13.84 | 14.19 | 14.27 | 14.42 | -18.26 | -18.11 | 32.70 | 34.6 | 32.39 | 30.1 |
| 71159 AGC330260 | 87.8934 | -48.5266 | 298.2719 | 24.7009 | 3889 | 3551 | 4.0 | 0.40 | 148 | 2.200 | 13.79 | 13.82 | 14.51 | 14.61 | 14.57 | -17.58 | -17.38 | 32.16 | 27.0 | 31.99 | 25.0 |
| 71171 P0071171 | 87.4648 | -49.0821 | 297.6203 | 24.5078 | 3998 | 3662 | 3.0 | 0.39 | 204 | 2.336 | 13.57 | 13.44 | 13.78 | 13.86 | 14.01 | -18.82 | -18.71 | 32.85 | 37.1 | 32.58 | 32.8 |
| 71181 UGC12539 | 88.0946 | -48.4721 | 298.4175 | 24.6441 | 3768 | 3428 | 3.1 | 0.40 | 366 | 2.593 | 11.91 | 11.71 | 12.41 | 12.48 | 12.45 | -21.16 | -21.22 | 33.65 | 53.6 | 33.75 | 56.3 |
| 71197 AGC330277 | 88.7610 | -47.8377 | 299.2597 | 24.7658 | 3599 | 3256 | 2.9 | 0.44 | 169 | 2.266 | / | / | 14.77 | 14.87 | / | / | -18.02 | / | / | 32.92 | 38.4 |
| 71201 AGC330282 | 89.0527 | -47.5449 | 299.6426 | 24.8247 | 3523 | 3179 | 4.2 | 0.72 | 118 | 2.222 | / | / | 14.53 | 14.64 | / | / | -17.59 | / | / | 32.24 | 28.0 |
| 71220 NGC07640 | 105.2405 | -18.9374 | 334.7408 | 27.6627 | 370 | 62 | 5.3 | 0.23 | 233 | 2.370 | 10.76 | 10.48 | 10.93 | 10.96 | 11.09 | -19.13 | -19.04 | 30.22 | 11.1 | 30.01 | 10.0 |
| 71260 UGC12562 | 91.1053 | -45.5502 | 302.3199 | 25.1080 | 3861 | 3524 | 7.9 | 0.27 | 153 | 2.193 | 14.62 | 14.64 | 15.63 | 15.73 | 15.53 | -17.51 | -17.31 | 33.07 | 41.1 | 33.06 | 41.0 |
| 71262 UGC12561 | 89.1748 | -47.9949 | 299.3440 | 24.4564 | 3741 | 3401 | 7.8 | 0.32 | 184 | 2.279 | 14.24 | 14.23 | 15.20 | 15.29 | 15.11 | -18.30 | -18.15 | 33.45 | 48.9 | 33.49 | 50.0 |
| 71430 IC0005321 | 53.5442 | -68.3584 | 272.3556 | 15.1953 | 2872 | 2553 | 1.8 | 0.59 | 197 | 2.379 | 13.02 | 13.14 | 13.59 | 13.69 | 13.78 | -19.20 | -19.12 | 33.00 | 39.8 | 32.84 | 37.0 |
| 71529 AGC330473 | 89.8910 | -49.8401 | 298.2288 | 22.8493 | 3524 | 3180 | 4.8 | 0.67 | 157 | 2.316 | 13.75 | 13.82 | 14.28 | 14.37 | 14.46 | -18.64 | -18.52 | 33.12 | 42.1 | 32.92 | 38.3 |

| PGC Name | l | b | sgl | sgb | v_{hel} | v_{mod} | t | b/a | w_{max} | $\log w_{max}^2$ | I | I* | [3.6] | [3.6]* | $C_{[3.6]}$ | M_C | $M_{[3.6]}$ | μ_C | d_C | $\mu_{[3.6]}$ | $d_{[3.6]}$ | |
|------------------|----------|----------|----------|---------|-----------|-----------|-----|------|-----------|------------------|-------|-------|-------|--------|-------------|--------|-------------|---------|-------|---------------|-------------|------|
| 71597 UGC12631 | 101.4244 | -32.3623 | 319.3766 | 25.7157 | 9183 | 9041 | 3.0 | 0.34 | 451 | 2.672 | 13.19 | 12.86 | 13.38 | 13.47 | 13.53 | -21.88 | -21.99 | 35.52 | 127.2 | 35.65 | 135.0 | |
| 71619 UGC12639 | 102.8429 | -29.4712 | 322.8563 | 25.8678 | 4548 | 4255 | 3.2 | 0.65 | 132 | 2.231 | / | / | 13.44 | 13.53 | / | / | -17.68 | / | / | / | 31.21 | 17.5 |
| 71636 UGC12641 | 98.4670 | -38.7652 | 311.9019 | 24.6936 | 2696 | 2351 | 4.0 | 0.28 | 173 | 2.247 | 14.01 | 13.91 | 14.77 | 14.84 | 14.73 | -18.01 | -17.84 | 32.75 | 35.5 | 32.70 | 34.6 | |
| 71688 UGC12650 | 104.0752 | -27.5254 | 325.3177 | 25.6567 | 5099 | 4825 | 5.8 | 0.23 | 309 | 2.493 | 13.48 | 13.08 | 13.58 | 13.63 | 13.72 | -20.25 | -20.24 | 34.02 | 63.6 | 33.94 | 61.5 | |
| 71728 NGC007694 | 82.1431 | -59.2365 | 287.9534 | 18.8449 | 2280 | 1926 | / | 0.53 | 138 | 2.203 | 12.18 | 12.33 | 13.20 | 13.30 | 13.17 | -17.60 | -17.40 | 30.77 | 14.3 | 30.71 | 13.8 | |
| 71729 NGC007689 | 325.6333 | -59.4532 | 239.7954 | 1.2722 | 1971 | 1801 | 5.9 | 0.64 | 239 | 2.486 | 10.82 | 10.97 | 11.49 | 11.58 | 11.64 | -20.19 | -20.18 | 31.83 | 23.2 | 31.76 | 22.5 | |
| 71753 UGC12667 | 103.5651 | -29.8760 | 322.7342 | 25.1293 | 3812 | 3504 | 5.8 | 0.64 | 225 | 2.456 | 12.30 | 12.34 | 12.82 | 12.92 | 12.99 | -19.91 | -19.88 | 32.92 | 38.4 | 32.82 | 36.7 | |
| 71754 P0071754 | 108.8653 | -15.5674 | 339.4502 | 25.3018 | 4809 | 4573 | 3.6 | 0.41 | 240 | 2.411 | 13.61 | 13.42 | 13.74 | 13.81 | 13.98 | -19.50 | -19.44 | 33.52 | 50.5 | 33.29 | 45.6 | |
| 71784 AGC630216 | 80.5103 | -60.9102 | 286.2251 | 17.9644 | 2214 | 1861 | 3.7 | 0.37 | 329 | 2.540 | 11.82 | 11.67 | 12.60 | 12.66 | 12.52 | -20.68 | -20.70 | 33.22 | 44.1 | 33.40 | 48.0 | |
| 71795 UGC12678 | 102.2860 | -33.4705 | 318.6409 | 24.5720 | 8963 | 8810 | 3.0 | 0.24 | 505 | 2.707 | 13.39 | 12.84 | 13.61 | 13.68 | 13.62 | -22.19 | -22.33 | 35.96 | 155.6 | 36.26 | 178.4 | |
| 71804 UGC12681 | 98.4927 | -41.1405 | 309.7094 | 23.4151 | 1479 | 1120 | 4.2 | 0.50 | 129 | 2.164 | 13.91 | 14.02 | 14.97 | 15.06 | 14.89 | -17.25 | -17.03 | 32.15 | 27.0 | 32.10 | 26.2 | |
| 71838 UGC12692 | 99.8254 | -39.1612 | 312.1297 | 23.5849 | 2194 | 1844 | 5.9 | 0.26 | 225 | 2.359 | 13.39 | 13.22 | 13.65 | 13.71 | 13.83 | -19.03 | -18.93 | 32.88 | 37.6 | 32.66 | 34.0 | |
| 71839 UGC12693 | 104.8891 | -27.8201 | 325.3238 | 24.8780 | 4971 | 4694 | 5.9 | 0.20 | 220 | 2.342 | 14.51 | 14.26 | 15.39 | 15.46 | 15.21 | -18.88 | -18.77 | 34.14 | 67.3 | 34.32 | 73.3 | |
| 71866 NGC007713 | 353.8020 | -70.8770 | 254.6550 | 5.1268 | 692 | 431 | 6.7 | 0.46 | 178 | 2.293 | 10.48 | 10.59 | 11.44 | 11.47 | 11.39 | -18.43 | -18.29 | 29.82 | 9.2 | 29.76 | 8.9 | |
| 71880 UGC12701 | 103.3497 | -32.0680 | 320.4564 | 24.3804 | 8858 | 8704 | 5.9 | 0.26 | 358 | 2.561 | 14.42 | 14.01 | 14.21 | 14.30 | 14.52 | -20.86 | -20.90 | 35.50 | 126.0 | 35.36 | 118.0 | |
| 71881 ES347-029 | 351.5310 | -70.4872 | 253.8987 | 4.7414 | 1568 | 1315 | 7.9 | 0.41 | 199 | 2.331 | 12.61 | 12.68 | 13.85 | 13.93 | 13.65 | -18.77 | -18.65 | 32.43 | 30.6 | 32.60 | 33.2 | |
| 71895 UGC12707 | 98.7285 | -41.8162 | 309.1933 | 22.9027 | 2610 | 2261 | 3.9 | 0.54 | 178 | 2.315 | 13.10 | 13.17 | 14.12 | 14.21 | 14.04 | -18.62 | -18.50 | 32.68 | 34.3 | 32.73 | 35.2 | |
| 71948 ES240-011 | 332.9523 | -64.8836 | 245.8645 | 0.7823 | 2839 | 2645 | 4.9 | 0.20 | 551 | 2.741 | 10.97 | 10.37 | 11.01 | 11.03 | 11.06 | -22.50 | -22.67 | 33.60 | 52.4 | 33.75 | 56.3 | |
| 72001 AGC630233 | 79.7095 | -63.1211 | 284.5981 | 16.3481 | 2016 | 1665 | 4.9 | 0.31 | 302 | 2.494 | 10.65 | 10.49 | 11.15 | 11.16 | 11.19 | -20.25 | -20.25 | 31.44 | 19.4 | 31.41 | 19.2 | |
| 72006 PGC0072006 | 80.7361 | -62.5091 | 285.3614 | 16.5904 | 2048 | 1696 | 9.0 | 0.46 | 140 | 2.189 | / | / | 15.06 | 15.16 | / | / | -17.27 | / | / | / | 32.44 | 30.8 |
| 72009 NGC07723 | 69.2380 | -67.9058 | 278.3083 | 14.1787 | 1860 | 1520 | 3.1 | 0.68 | 314 | 2.624 | 10.17 | 10.28 | 10.73 | 10.82 | 10.91 | -21.44 | -21.53 | 32.36 | 29.7 | 32.36 | 29.6 | |
| 72024 UGC12721 | 103.7122 | -33.0460 | 319.6315 | 23.6859 | 7611 | 7404 | 3.0 | 0.44 | 394 | 2.634 | 12.93 | 12.73 | 13.30 | 13.39 | 13.42 | -21.53 | -21.62 | 35.04 | 102.0 | 35.16 | 107.5 | |
| 72115 AGC330768 | 103.6225 | -34.6751 | 317.9977 | 23.0455 | 9409 | 9276 | 4.5 | 0.49 | 425 | 2.680 | 13.06 | 12.96 | 12.64 | 12.76 | 13.24 | -21.95 | -22.07 | 35.29 | 114.5 | 34.96 | 98.3 | |
| 72169 AGC330778 | 104.5956 | -33.0694 | 319.9503 | 23.0054 | 7409 | 7196 | 3.0 | 0.29 | 377 | 2.587 | 13.78 | 13.43 | 13.60 | 13.67 | 13.92 | -21.10 | -21.16 | 35.13 | 105.9 | 34.97 | 98.5 | |
| 72233 UGC12755 | 105.3271 | -32.2108 | 321.0753 | 22.7985 | 8794 | 8640 | 3.1 | 0.54 | 503 | 2.767 | 12.45 | 12.24 | 12.92 | 13.02 | 12.99 | -22.74 | -22.91 | 35.87 | 149.1 | 36.17 | 171.7 | |
| 72237 UGC12754 | 104.5092 | -34.3688 | 318.6408 | 22.5201 | 750 | 403 | 5.9 | 0.68 | 183 | 2.388 | 10.48 | 10.58 | 11.50 | 11.53 | 11.41 | -19.29 | -19.22 | 30.70 | 13.8 | 30.75 | 14.1 | |
| 72252 AGC630257 | 82.5618 | -63.6377 | 285.3774 | 15.1916 | 2114 | 1765 | 5.0 | 0.51 | 155 | 2.248 | 12.69 | 12.85 | 13.67 | 13.77 | 13.66 | -18.01 | -17.85 | 31.68 | 21.7 | 31.62 | 21.1 | |
| 72325 UGC12769 | 88.6497 | -59.6700 | 290.3201 | 16.3898 | 2083 | 1728 | 8.0 | 0.42 | 126 | 2.134 | / | / | 15.97 | 16.07 | / | / | -16.73 | / | / | / | 32.82 | 36.7 |
| 72367 UGC12777 | 93.6208 | -55.3404 | 295.5117 | 17.4769 | 2927 | 2578 | 5.5 | 0.49 | 218 | 2.388 | 11.94 | 11.97 | 12.48 | 12.57 | 12.63 | -19.29 | -19.21 | 31.92 | 24.3 | 31.79 | 22.8 | |
| 72411 AGC330918 | 106.2357 | -32.3938 | 321.2277 | 22.0217 | 9034 | 8892 | 4.2 | 0.45 | 367 | 2.605 | 13.23 | 13.08 | 13.59 | 13.71 | 13.75 | -21.26 | -21.34 | 35.12 | 105.5 | 35.19 | 109.2 | |
| 72438 P0072438 | 105.9789 | -33.3383 | 320.2017 | 21.8402 | 9295 | 9162 | 5.0 | 0.31 | 398 | 2.613 | 13.66 | 13.34 | 13.60 | 13.69 | 13.89 | -21.33 | -21.41 | 35.33 | 116.3 | 35.26 | 112.6 | |
| 72443 ES149-001 | 319.2566 | -57.9933 | 237.9088 | -4.3589 | 1905 | 1753 | 8.0 | 0.23 | 187 | 2.275 | / | / | 13.41 | 13.48 | / | / | -18.11 | / | / | / | 31.60 | 20.8 |
| 72491 NGC007757 | 94.7422 | -55.2328 | 296.0327 | 17.0623 | 2952 | 2604 | 5.3 | 0.69 | 139 | 2.272 | 12.10 | 12.28 | 12.66 | 12.76 | 12.89 | -18.23 | -18.08 | 31.12 | 16.7 | 30.84 | 14.7 | |
| 72506 UGC12792 | 106.0898 | -34.0341 | 319.5583 | 21.4727 | 11531 | 11515 | 3.1 | 0.47 | 421 | 2.670 | 13.05 | 12.88 | 13.37 | 13.50 | 13.55 | -21.85 | -21.97 | 35.53 | 127.5 | 35.65 | 135.1 | |
| 72599 UGC12807 | 109.3835 | -25.4947 | 329.2377 | 21.9386 | 12343 | 12402 | 7.6 | 0.20 | 379 | 2.579 | 15.11 | 14.59 | 15.07 | 15.16 | 15.24 | -21.03 | -21.08 | 36.45 | 195.0 | 36.51 | 200.8 | |
| 72632 UGC12814 | 112.9122 | -12.6208 | 343.5875 | 22.1796 | 5794 | 5603 | 6.0 | 0.20 | 347 | 2.540 | 13.97 | 13.37 | 13.90 | 13.93 | 14.02 | -20.68 | -20.70 | 34.77 | 90.1 | 34.76 | 89.4 | |

| PGC Name | l | b | sgl | sgb | v_{hel} | v_{mod} | t | b/a | w_{max} | $\log w_{max}^{\dagger}$ | I | I* | [3.6] | [3.6]* | $C_{[3.6]}$ | M_C | $M_{[3.6]}$ | μ_C | dC | $\mu_{[3.6]}$ | $d_{[3.6]}$ |
|-----------------|----------|----------|----------|----------|-----------|-----------|-----|------|-----------|--------------------------|-------|-------|-------|--------|-------------|--------|-------------|---------|-------|---------------|-------------|
| 72633 AGC330965 | 105.9524 | -36.2244 | 317.3730 | 20.6652 | 9959 | 9854 | 4.2 | 0.71 | 229 | 2.506 | 14.29 | 14.39 | 14.76 | 14.91 | 15.02 | -20.37 | -20.37 | 35.50 | 126.1 | 35.45 | 123.2 |
| 72734 PG0072734 | 121.8483 | 23.2789 | 22.4519 | 16.7280 | 5818 | 5835 | 6.2 | 0.21 | 300 | 2.478 | / | / | 14.86 | 14.90 | / | / | -20.10 | / | / | 35.14 | 106.7 |
| 72784 AGC330996 | 107.5301 | -33.7236 | 320.3750 | 20.5006 | 7967 | 7778 | 3.0 | 0.48 | 344 | 2.584 | 13.81 | 13.74 | 14.19 | 14.30 | 14.38 | -21.07 | -21.13 | 35.58 | 130.7 | 35.62 | 132.9 |
| 72957 ES012-010 | 305.3777 | -35.2980 | 214.8380 | -13.4242 | 1941 | 1943 | 7.7 | 0.64 | 211 | 2.432 | 13.17 | 13.15 | 13.78 | 13.85 | 13.86 | -19.69 | -19.65 | 33.59 | 52.3 | 33.55 | 51.2 |
| 72968 AGC331021 | 108.1786 | -34.0942 | 320.2338 | 19.8608 | 7906 | 7715 | 4.0 | 0.27 | 321 | 2.514 | 14.30 | 14.04 | 14.76 | 14.86 | 14.81 | -20.44 | -20.45 | 35.36 | 117.9 | 35.48 | 124.8 |
| 72983 UGC12857 | 95.9604 | -58.6262 | 293.7712 | 14.3756 | 2456 | 2105 | 4.0 | 0.22 | 233 | 2.370 | 12.58 | 12.42 | 12.99 | 13.05 | 13.09 | -19.12 | -19.04 | 32.23 | 27.9 | 32.10 | 26.2 |
| 73049 NGC007793 | 4.5157 | -77.1712 | 261.3011 | 3.1214 | 227 | 0 | 7.4 | 0.65 | 162 | 2.320 | 8.40 | 8.60 | 9.23 | 9.27 | 9.29 | -18.67 | -18.55 | 27.96 | 3.9 | 27.82 | 3.7 |
| 75289 AGC150063 | 195.2978 | -17.7214 | 337.0971 | -56.6963 | 8198 | 8376 | 4.8 | 0.21 | 352 | 2.547 | 14.69 | 14.06 | 14.42 | 14.47 | 14.63 | -20.74 | -20.77 | 35.49 | 125.6 | 35.42 | 121.1 |
| 79913 PG0079913 | 235.1633 | 9.5107 | 116.1994 | -72.3673 | 6560 | 6942 | 5.4 | 0.20 | 426 | 2.629 | / | / | 13.05 | 13.10 | / | / | -21.57 | / | / | 34.79 | 91.0 |
| 85512 P0085512 | 102.7082 | -33.5380 | 318.7466 | 24.2267 | 8036 | 7844 | 4.7 | 0.55 | 234 | 2.439 | / | / | 15.76 | 15.88 | / | / | -19.71 | / | / | 35.79 | 144.2 |
| 85551 P0085551 | 103.2945 | -33.2898 | 319.2262 | 23.8960 | 8743 | 8582 | 1.9 | 0.47 | 338 | 2.574 | 14.48 | 14.37 | 14.35 | 14.47 | 14.79 | -20.99 | -21.04 | 35.93 | 153.2 | 35.70 | 137.9 |
| 85610 P0085610 | 103.6305 | -33.3087 | 319.3405 | 23.6347 | 8004 | 7812 | 2.3 | 0.71 | 171 | 2.376 | 15.33 | 15.45 | 15.79 | 15.93 | 16.06 | -19.19 | -19.10 | 35.35 | 117.6 | 35.18 | 108.7 |
| 86266 P0086266 | 166.8226 | -15.4697 | 345.7623 | -30.0246 | 4662 | 4613 | 4.2 | 0.66 | 233 | 2.483 | / | / | 13.68 | 13.65 | / | / | -20.14 | / | / | 33.85 | 59.0 |
| 86269 P0086269 | 172.7348 | -11.4149 | 350.4657 | -35.8503 | 3389 | 3358 | 3.2 | 0.66 | 333 | 2.638 | / | / | 11.68 | 11.61 | / | / | -21.66 | / | / | 33.31 | 45.8 |
| 86285 P0086285 | 206.3955 | -5.7400 | 0.4608 | -69.1349 | 2902 | 3029 | 3.2 | 0.46 | 538 | 2.774 | 11.20 | 9.99 | 10.34 | 10.26 | 10.49 | -22.80 | -22.98 | 33.32 | 46.1 | 33.28 | 45.3 |
| 86290 P0086290 | 40.4707 | 7.9917 | 165.8634 | 82.9536 | 3385 | 3275 | 5.0 | 0.32 | 274 | 2.452 | / | / | 13.56 | 13.58 | / | / | -19.84 | / | / | 33.47 | 49.5 |
| 86633 PG0086633 | 232.4206 | 70.6041 | 91.7194 | -13.0005 | 3759 | 4134 | 4.8 | 0.40 | 284 | 2.482 | / | / | 14.63 | 14.72 | / | / | -20.14 | / | / | 34.99 | 99.4 |
| 89942 PG0089942 | 137.5050 | 6.3526 | 6.3290 | 0.5646 | 3168 | 3077 | 5.0 | 0.26 | 325 | 2.518 | / | / | 11.73 | 11.60 | / | / | -20.49 | / | / | 32.10 | 26.2 |
| 90023 P0090023 | 204.3876 | -14.8652 | 337.4070 | -65.8737 | 4317 | 4417 | 2.0 | 0.66 | 301 | 2.594 | / | / | 12.58 | 12.63 | / | / | -21.23 | / | / | 33.93 | 61.0 |
| 90392 P0090392 | 88.7312 | -6.6350 | 343.3010 | 46.7425 | 4078 | 3840 | 5.0 | 0.31 | 265 | 2.436 | / | / | 12.56 | 12.51 | / | / | -19.69 | / | / | 32.21 | 27.7 |
| 90402 P0090402 | 110.4855 | 13.3220 | 11.7536 | 27.5625 | 2526 | 2389 | 5.0 | 0.51 | 269 | 2.486 | / | / | 11.62 | 11.50 | / | / | -20.18 | / | / | 31.68 | 21.7 |
| 90453 AGC101097 | 112.6246 | -28.9805 | 326.6992 | 18.0961 | 4954 | 4687 | 5.9 | 0.20 | 170 | 2.230 | 15.68 | 15.61 | 16.49 | 16.58 | 16.45 | -17.86 | -17.68 | 34.37 | 74.9 | 34.35 | 74.0 |
| 90540 PG0090540 | 140.0527 | -63.7343 | 296.4380 | -6.8519 | 2224 | 1924 | 7.9 | 0.20 | 116 | 2.064 | / | / | 16.84 | 16.94 | / | / | -16.05 | / | / | 33.03 | 40.3 |
| 90548 PG0090548 | 128.7055 | -11.3176 | 347.7022 | 7.1933 | 6039 | 5901 | 6.2 | 0.34 | 233 | 2.385 | / | / | 15.79 | 15.84 | / | / | -19.19 | / | / | 35.18 | 108.4 |
| 90553 PG0090553 | 144.6848 | -58.9656 | 301.1978 | -9.1817 | 2607 | 2321 | 7.6 | 0.20 | 151 | 2.179 | / | / | 16.31 | 16.39 | / | / | -17.17 | / | / | 33.62 | 52.9 |
| 90564 AGC110840 | 136.2487 | -27.5502 | 332.4910 | -1.9295 | 5778 | 5596 | 6.3 | 0.20 | 197 | 2.294 | 15.43 | 15.29 | 16.12 | 16.22 | 16.11 | -18.44 | -18.30 | 34.62 | 84.1 | 34.63 | 84.2 |
| 90591 AGC121120 | 141.0323 | -26.4331 | 333.9844 | -6.0764 | 11721 | 11823 | 6.2 | 0.20 | 352 | 2.547 | / | / | 14.98 | 15.07 | / | / | -20.76 | / | / | 36.06 | 163.0 |
| 90592 AGC121109 | 140.1581 | -23.6986 | 336.6632 | -5.0781 | 7667 | 7575 | 6.2 | 0.20 | 226 | 2.354 | / | / | 15.91 | 16.01 | / | / | -18.88 | / | / | 35.03 | 101.4 |
| 90595 PG0090595 | 138.8962 | -19.6194 | 340.6339 | -3.5487 | 5828 | 5684 | 6.2 | 0.28 | 321 | 2.515 | / | / | 15.23 | 15.31 | / | / | -20.46 | / | / | 35.98 | 157.3 |
| 90653 AGC121048 | 156.4742 | -28.4394 | 332.0075 | -19.7834 | 6786 | 6703 | 6.2 | 0.20 | 242 | 2.384 | / | / | 15.08 | 15.13 | / | / | -19.17 | / | / | 34.40 | 75.9 |
| 90694 PG0090694 | 205.1601 | -47.3320 | 291.1634 | -44.7966 | 1686 | 1575 | 7.9 | 0.20 | 131 | 2.117 | / | / | 15.21 | 15.30 | / | / | -16.57 | / | / | 31.87 | 23.7 |
| 90695 AGC130398 | 173.1980 | -28.9533 | 329.0894 | -34.2199 | 6379 | 6344 | 6.2 | 0.20 | 269 | 2.430 | 15.38 | 14.47 | 14.84 | 14.83 | 15.02 | -19.67 | -19.62 | 34.77 | 90.1 | 34.56 | 81.8 |
| 90717 AGC140146 | 194.2565 | -29.3804 | 319.4508 | -51.2086 | 10072 | 10274 | 6.7 | 0.20 | 316 | 2.500 | / | / | 15.31 | 15.40 | / | / | -20.31 | / | / | 35.92 | 153.0 |
| 90726 AGC140148 | 197.4670 | -26.5592 | 321.1597 | -55.0748 | 8486 | 8638 | 6.7 | 0.20 | 356 | 2.551 | / | / | 14.41 | 14.48 | / | / | -20.81 | / | / | 35.46 | 123.5 |
| 90737 PG0090737 | 200.5778 | -19.5049 | 330.6182 | -60.8164 | 4351 | 4413 | 6.2 | 0.20 | 235 | 2.371 | / | / | 15.58 | 15.63 | / | / | -19.05 | / | / | 34.80 | 91.1 |
| 90751 PG0090751 | 147.0954 | 22.0668 | 23.1545 | -6.5600 | 4296 | 4345 | 7.9 | 0.20 | 188 | 2.274 | / | / | 16.66 | 16.73 | / | / | -18.10 | / | / | 34.96 | 98.3 |

| PGC Name | l | b | sgl | sgb | v_{hel} | v_{mod} | t | b/a | w_{max} | $\log w_{max}^*$ | I | I* | [3.6] | [3.6]* | $C_{[3.6]}$ | M_C | $M_{[3.6]}$ | μ_C | dC | $\mu_{[3.6]}$ | $d_{[3.6]}$ | |
|----------|-----------|----------|----------|----------|-----------|-----------|-------|------|-----------|------------------|-------|-------|-------|--------|-------------|--------|-------------|---------|-------|---------------|-------------|-------|
| 90766 | PG0090766 | 147.3165 | 25.2443 | 26.3400 | -6.2194 | 5407 | 5.6 | 0.20 | 208 | 2.318 | / | / | 16.29 | 16.38 | / | -18.53 | / | / | / | 35.05 | 102.3 | |
| 90771 | AGC170342 | 193.3573 | 14.4005 | 31.7723 | -50.4090 | 6867 | 5.6 | 0.38 | 161 | 2.232 | / | / | 16.62 | 16.74 | / | -17.69 | / | / | / | 34.53 | 80.6 | |
| 90775 | AGC170343 | 184.9992 | 19.2657 | 32.4630 | -41.0613 | 7595 | 6.2 | 0.20 | 239 | 2.378 | 15.38 | 15.12 | 15.86 | 15.95 | 15.89 | -19.20 | -19.12 | 35.20 | 109.7 | 35.23 | 110.9 | |
| 90776 | AGC170355 | 187.6639 | 18.3219 | 32.9334 | -43.7321 | 3387 | 3460 | 6.7 | 0.20 | 170 | 2.230 | / | / | 16.39 | 16.47 | / | -17.68 | / | / | / | 34.23 | 70.2 |
| 90778 | AGC170344 | 195.2194 | 15.5180 | 34.7509 | -51.3871 | 9642 | 10055 | 4.8 | 0.33 | 431 | 2.651 | / | / | 13.94 | 14.04 | / | -21.78 | / | / | / | 36.05 | 162.0 |
| 90783 | AGC170345 | 190.5213 | 20.1206 | 37.0188 | -45.1496 | 6475 | 6752 | 5.6 | 0.24 | 204 | 2.314 | / | / | 16.18 | 16.28 | / | -18.49 | / | / | / | 34.90 | 95.4 |
| 90784 | AGC170357 | 198.7274 | 18.1338 | 41.3680 | -52.6275 | 8662 | 9052 | 6.7 | 0.56 | 310 | 2.564 | / | / | 15.16 | 15.28 | / | -20.94 | / | / | / | 36.49 | 198.6 |
| 90789 | AGC170346 | 187.3435 | 23.2287 | 38.4619 | -40.9941 | 8134 | 8476 | 5.6 | 0.24 | 355 | 2.554 | 14.57 | 14.20 | 14.22 | 14.30 | 14.63 | -20.80 | -20.84 | 35.55 | 128.8 | 35.30 | 114.8 |
| 90795 | AGC170358 | 191.7501 | 24.2458 | 42.6840 | -43.7477 | 6853 | 7165 | 6.2 | 0.23 | 205 | 2.314 | 15.77 | 15.66 | 17.06 | 17.16 | 16.76 | -18.62 | -18.50 | 35.50 | 125.8 | 35.87 | 149.0 |
| 90796 | AGC170376 | 183.6671 | 26.6260 | 39.9081 | -36.3705 | 8544 | 8904 | 5.6 | 0.21 | 348 | 2.543 | 14.55 | 14.13 | 14.68 | 14.76 | 14.81 | -20.70 | -20.73 | 35.63 | 133.6 | 35.68 | 136.6 |
| 90800 | AGC170377 | 196.8507 | 23.6400 | 46.2180 | -47.7510 | 13676 | 14379 | 5.6 | 0.20 | 509 | 2.707 | 14.43 | 13.79 | 14.08 | 14.18 | 14.35 | -22.19 | -22.33 | 36.74 | 223.3 | 36.81 | 230.2 |
| 90801 | PG0090801 | 180.2240 | 28.3892 | 39.8577 | -32.8447 | 3877 | 4075 | 6.7 | 0.20 | 157 | 2.196 | / | / | 16.47 | 16.56 | / | -17.34 | / | / | / | 33.97 | 62.3 |
| 90803 | AGC170350 | 187.9046 | 26.7216 | 42.6425 | -39.4845 | 5311 | 5568 | 5.6 | 0.20 | 215 | 2.332 | 14.97 | 14.75 | 15.72 | 15.80 | 15.63 | -18.79 | -18.67 | 34.48 | 78.8 | 34.58 | 82.3 |
| 90806 | AGC170359 | 183.9461 | 27.8399 | 41.3462 | -35.9383 | 6065 | 6334 | 5.6 | 0.21 | 204 | 2.310 | 15.62 | 15.47 | 16.54 | 16.64 | 16.40 | -18.58 | -18.46 | 35.08 | 103.9 | 35.25 | 112.0 |
| 90811 | PG0090811 | 184.9012 | 28.1325 | 42.2190 | -36.4871 | 4153 | 4374 | 6.7 | 0.25 | 190 | 2.284 | / | / | 16.17 | 16.26 | / | -18.20 | / | / | / | 34.56 | 81.7 |
| 90815 | PG0090815 | 212.9715 | 19.3105 | 61.3370 | -60.7082 | 2549 | 2807 | 6.7 | 0.26 | 159 | 2.208 | / | / | 16.50 | 16.59 | / | -17.45 | / | / | / | 34.12 | 66.7 |
| 90817 | AGC180619 | 184.9967 | 29.5995 | 43.7839 | -35.7382 | 5587 | 5852 | 6.7 | 0.21 | 191 | 2.282 | / | / | 16.73 | 16.82 | / | -18.18 | / | / | / | 35.14 | 106.9 |
| 90831 | AGC180597 | 201.9617 | 26.9811 | 54.6758 | -48.6009 | 11291 | 11868 | 6.6 | 0.20 | 386 | 2.587 | 15.31 | 14.82 | 15.02 | 15.11 | 15.34 | -21.10 | -21.16 | 36.63 | 211.8 | 36.54 | 203.1 |
| 90844 | AGC180602 | 201.8658 | 29.8145 | 57.2307 | -46.3526 | 4703 | 5005 | 5.4 | 0.20 | 227 | 2.356 | 14.12 | 13.90 | 14.60 | 14.67 | 14.65 | -19.00 | -18.90 | 33.68 | 54.6 | 33.63 | 53.2 |
| 90927 | PG0090927 | 248.8651 | 25.3578 | 122.5764 | -52.0499 | 4625 | 5024 | 5.6 | 0.20 | 224 | 2.350 | / | / | 15.74 | 15.81 | / | -18.85 | / | / | / | 34.78 | 90.2 |
| 90941 | PG0090941 | 249.1564 | 29.1122 | 119.5110 | -48.8317 | 2352 | 2714 | 6.7 | 0.22 | 163 | 2.214 | / | / | 15.35 | 15.43 | / | -17.52 | / | / | / | 32.97 | 39.3 |
| 91580 | AGC270321 | 29.0679 | 27.2113 | 127.6838 | 62.8161 | 10625 | 10923 | 5.6 | 0.20 | 507 | 2.705 | / | / | 13.97 | 14.03 | / | -22.31 | / | / | / | 36.62 | 211.2 |
| 91586 | AGC270322 | 28.1236 | 24.5659 | 133.2499 | 64.0529 | 6320 | 6415 | 5.6 | 0.32 | 231 | 2.378 | / | / | 15.57 | 15.65 | / | -19.12 | / | / | / | 34.90 | 95.5 |
| 91594 | AGC270323 | 36.1728 | 24.6941 | 119.0889 | 68.7218 | 9057 | 9237 | 6.2 | 0.21 | 230 | 2.363 | / | / | 16.25 | 16.34 | / | -18.97 | / | / | / | 35.48 | 124.8 |
| 91621 | AGC280104 | 43.2744 | 16.8856 | 110.4137 | 78.7007 | 6547 | 6559 | 6.2 | 0.20 | 329 | 2.517 | / | / | 13.84 | 13.89 | / | -20.48 | / | / | / | 34.46 | 78.1 |
| 91630 | AGC280105 | 53.4177 | 16.4543 | 60.2160 | 78.2633 | 5302 | 5248 | 6.2 | 0.23 | 175 | 2.246 | / | / | 16.02 | 16.10 | / | -17.83 | / | / | / | 34.00 | 63.2 |
| 91643 | PG0091643 | 72.3212 | 16.7092 | 25.2057 | 63.4773 | 4889 | 4796 | 5.6 | 0.23 | 235 | 2.374 | / | / | 15.56 | 15.63 | / | -19.08 | / | / | / | 34.83 | 92.6 |
| 91656 | PG0091656 | 85.7269 | 16.1884 | 18.0493 | 51.1857 | 3750 | 3624 | 5.6 | 0.23 | 206 | 2.317 | / | / | 14.07 | 14.13 | / | -18.52 | / | / | / | 32.67 | 34.1 |
| 91661 | PG0091661 | 95.8447 | 19.5746 | 20.5357 | 41.1263 | 5579 | 5522 | 6.2 | 0.23 | 292 | 2.468 | / | / | 14.83 | 14.90 | / | -20.00 | / | / | / | 35.04 | 101.7 |
| 91705 | AGC310299 | 69.7711 | -21.6539 | 307.5148 | 54.4346 | 5376 | 5119 | 6.7 | 0.25 | 212 | 2.331 | / | / | 15.86 | 15.94 | / | -18.66 | / | / | / | 34.72 | 88.0 |
| 91731 | AGC320524 | 81.2011 | -26.8104 | 313.1585 | 43.4112 | 7209 | 6988 | 5.6 | 0.20 | 241 | 2.382 | / | / | 15.42 | 15.50 | / | -19.16 | / | / | / | 34.78 | 90.4 |
| 91742 | PG0091742 | 112.8577 | 12.3702 | 10.7238 | 25.2377 | 2600 | 2464 | 8.0 | 0.31 | 277 | 2.456 | / | / | 13.86 | 13.81 | / | -19.88 | / | / | / | 33.74 | 56.0 |
| 91747 | AGC320540 | 93.7370 | -21.7141 | 326.9027 | 36.6160 | 6583 | 6358 | 6.5 | 0.20 | 230 | 2.362 | 15.20 | 14.94 | 15.70 | 15.78 | 15.72 | -19.05 | -18.96 | 34.85 | 93.5 | 34.87 | 94.0 |
| 91755 | PG0091755 | 115.3911 | 14.7352 | 13.3581 | 22.8149 | 1554 | 1426 | 7.9 | 0.22 | 115 | 2.063 | / | / | 15.10 | 15.14 | / | -16.04 | / | / | / | 31.17 | 17.2 |
| 91777 | PG0091777 | 101.2703 | -19.7397 | 332.4499 | 30.9319 | 5075 | 4819 | 5.6 | 0.51 | 211 | 2.381 | / | / | 15.02 | 15.10 | / | -19.15 | / | / | / | 34.33 | 73.5 |
| 91787 | AGC331184 | 101.0005 | -24.3943 | 327.3461 | 29.4263 | 5215 | 4949 | 6.7 | 0.42 | 186 | 2.303 | / | / | 15.95 | 16.05 | / | -18.38 | / | / | / | 34.53 | 80.7 |

| PGC Name | l | b | sgl | sgb | v_{hel} | v_{mod} | t | b/a | w_{mx} | $\log w_{mx}^2$ | I | I* | [3.6] | [3.6]* | $C_{[3.6]}$ | M_C | $M_{[3.6]}$ | μ_C | d_C | $\mu_{[3.6]}$ | $d_{[3.6]}$ |
|-------------------|----------|----------|----------|----------|-----------|-----------|-----|------|----------|-----------------|-------|-------|-------|--------|-------------|--------|-------------|---------|-------|---------------|-------------|
| 91814 AGC331095 | 104.8941 | -32.4017 | 320.7237 | 23.0545 | 7166 | 6946 | 5.8 | 0.20 | 239 | 2.379 | 14.48 | 14.16 | 14.83 | 14.91 | 14.89 | -19.21 | -19.12 | 34.15 | 67.6 | 34.11 | 66.4 |
| 92378 PG0092378 | 305.4105 | 26.3650 | 152.2162 | -7.7963 | 5917 | 6308 | 5.6 | 0.20 | 179 | 2.253 | / | / | 16.25 | 16.35 | / | / | -17.90 | / | / | 34.34 | 73.7 |
| 93031 AGC331412 | 88.1675 | -49.1344 | 297.9364 | 24.1453 | 3476 | 3131 | 5.0 | 0.20 | 139 | 2.143 | 15.54 | 15.48 | 16.39 | 16.47 | 16.33 | -17.07 | -16.83 | 33.43 | 48.5 | 33.34 | 46.5 |
| 93038 AGC111414 | 127.1261 | -29.2062 | 329.6929 | 5.7722 | 11281 | 11306 | 5.9 | 0.20 | 266 | 2.425 | 16.24 | 15.94 | 17.21 | 17.32 | 16.98 | -19.63 | -19.58 | 36.82 | 231.5 | 37.26 | 283.2 |
| 97023 PG0097023 | 156.5597 | -10.6228 | 350.9615 | -19.9618 | 5596 | 5551 | 4.6 | 0.45 | 226 | 2.394 | / | / | 13.00 | 12.99 | / | / | -19.28 | / | / | 32.27 | 28.5 |
| 97032 PG0097032 | 154.8363 | -4.5206 | 357.2666 | -17.8225 | 4471 | 4418 | 3.8 | 0.41 | 286 | 2.487 | / | / | 12.93 | 12.86 | / | / | -20.19 | / | / | 33.08 | 41.3 |
| 97067 AGC140130 | 153.7948 | 8.3948 | 10.5016 | -15.1862 | 4378 | 4383 | 3.8 | 0.36 | 266 | 2.446 | / | / | 13.19 | 13.13 | / | / | -19.78 | / | / | 32.94 | 38.8 |
| 97081 P0097081 | 183.0480 | -10.6915 | 351.1414 | -45.9847 | 5584 | 5652 | 4.6 | 0.66 | 209 | 2.435 | / | / | 13.40 | 13.39 | / | / | -19.68 | / | / | 33.11 | 41.8 |
| 97109 P0097109 | 160.6087 | 10.7270 | 14.1538 | -21.3966 | 5991 | 6080 | 4.6 | 0.69 | 118 | 2.203 | / | / | 13.15 | 13.23 | / | / | -17.41 | / | / | 30.64 | 13.4 |
| 97136 P0097136 | 196.1165 | -6.4126 | 358.0570 | -58.9440 | 3496 | 3590 | 3.8 | 0.43 | 286 | 2.492 | / | / | 13.45 | 13.48 | / | / | -20.23 | / | / | 33.77 | 56.7 |
| 97187 P0097187 | 185.7905 | 13.2472 | 25.4846 | -44.3052 | 5208 | 5395 | 3.8 | 0.39 | 344 | 2.564 | / | / | 13.77 | 13.85 | / | / | -20.93 | / | / | 34.90 | 95.6 |
| 100768 P0100768 | 184.6150 | -23.4928 | 332.6465 | -45.4951 | 4369 | 4349 | 5.0 | 0.34 | 295 | 2.488 | / | / | 13.24 | 13.22 | / | / | -20.19 | / | / | 33.45 | 49.0 |
| 142820 P0142820 | 202.4506 | 29.4515 | 57.4875 | -46.9519 | 5092 | 5405 | 5.0 | 0.29 | 190 | 2.289 | 14.90 | 14.85 | 15.80 | 15.90 | 15.73 | -18.39 | -18.25 | 34.17 | 68.2 | 34.23 | 70.1 |
| 155511 P0155511 | 268.7063 | 28.3644 | 136.8443 | -37.1849 | 3876 | 4271 | 3.4 | 0.38 | 209 | 2.345 | / | / | 15.50 | 15.59 | / | / | -18.80 | / | / | 34.49 | 79.1 |
| 165356 PG0165356 | 135.8526 | 8.1351 | 7.9253 | 2.3860 | 3164 | 3076 | 5.0 | 0.52 | 264 | 2.481 | / | / | 12.51 | 12.41 | / | / | -20.13 | / | / | 32.55 | 32.3 |
| 165788 P0165788 | 51.0923 | 7.0218 | 10.9604 | 86.2370 | 5101 | 4994 | 5.0 | 0.56 | 348 | 2.614 | / | / | 12.78 | 12.79 | / | / | -21.43 | / | / | 34.30 | 72.6 |
| 166472 P0166472 | 134.9564 | 13.1972 | 12.8786 | 3.7776 | 4302 | 4260 | 5.0 | 0.65 | 234 | 2.480 | / | / | 13.83 | 13.84 | / | / | -20.11 | / | / | 34.03 | 63.8 |
| 166559 P0166559 | 51.8668 | 11.1056 | 47.4319 | 83.4695 | 4428 | 4325 | 5.0 | 0.38 | 282 | 2.475 | / | / | 14.16 | 14.21 | / | / | -20.07 | / | / | 34.37 | 74.8 |
| 166628 P0166628 | 40.3702 | -10.1956 | 247.0658 | 72.0733 | 5893 | 5753 | 3.8 | 0.71 | 83 | 2.063 | / | / | 13.59 | 13.65 | / | / | -16.04 | / | / | 29.68 | 8.6 |
| 166755 PG0166755 | 114.1865 | 14.9675 | 13.5995 | 23.9814 | 2453 | 2332 | 5.0 | 0.48 | 275 | 2.487 | / | / | 12.34 | 12.29 | / | / | -20.19 | / | / | 32.49 | 31.5 |
| 166758 P0166758 | 110.8214 | 8.8628 | 6.7439 | 27.1226 | 4354 | 4325 | 5.0 | 0.45 | 396 | 2.638 | / | / | 12.19 | 12.14 | / | / | -21.66 | / | / | 33.86 | 59.2 |
| 166785 P0166785 | 118.5547 | 7.5976 | 5.8553 | 19.4084 | 4645 | 4533 | 5.0 | 0.24 | 316 | 2.504 | / | / | 13.72 | 13.67 | / | / | -20.35 | / | / | 34.09 | 65.8 |
| 169662 AGC330925 | 106.1253 | -33.1704 | 320.4205 | 21.7960 | 8307 | 8131 | 3.3 | 0.26 | 355 | 2.557 | 14.46 | 14.12 | 14.76 | 14.85 | 14.84 | -20.82 | -20.86 | 35.81 | 145.0 | 35.92 | 152.7 |
| 906205 P0906205 | 246.1023 | 22.7733 | 121.6248 | -55.6174 | 4810 | 5203 | 2.3 | 0.30 | 297 | 2.484 | / | / | 13.89 | 13.96 | / | / | -20.16 | / | / | 34.20 | 69.2 |
| 1059326 PG1059326 | 338.8609 | 52.5643 | 126.4886 | 17.9840 | 2740 | 3023 | 3.6 | 0.44 | 199 | 2.337 | / | / | 15.28 | 15.37 | / | / | -18.71 | / | / | 34.16 | 68.0 |
| 1210567 AGC121506 | 168.7141 | -51.1898 | 305.9313 | -24.1931 | 6022 | 5880 | 1.6 | 0.35 | 193 | 2.305 | / | / | 14.98 | 15.09 | / | / | -18.41 | / | / | 33.55 | 51.2 |
| 1809186 AGC331322 | 105.3831 | -33.1355 | 320.1819 | 22.3778 | 9200 | 9063 | 3.0 | 0.35 | 281 | 2.469 | 14.42 | 14.25 | 14.80 | 14.91 | 14.94 | -20.03 | -20.01 | 35.07 | 103.2 | 35.06 | 102.7 |

TABLE C.1: Distance measurements for 1935 galaxies observed with Spitzer for which we have all the parameters requested (in particular W_{mx} , b/a, [3.6] and, for 1511 galaxies, I) to compute an estimate (Complete table online): (1) Principal Galaxy Catalog number, (2) Common name, (3) galactic longitude, degrees, (4) galactic latitude, degrees, (5) supergalactic longitude, degrees, (6) supergalactic latitude, degrees, (7) heliocentric velocities, km s^{-1} , (8) velocity with respect to the cosmic microwave background modified for the cosmology, km s^{-1} , (9) numerical morphological type, (10) axial ratio, (11) HI linewidth, km s^{-1} , (12) logarithm of the de-projected HI linewidth, km s^{-1} , (13) I band magnitude, mag (Vega system), (14) $I^{b,i,k}$, I band magnitude corrected for extinctions and k-corrected, mag (AB system), (15) [3.6] band magnitude, mag (AB system), (16) [3.6] b,i,k,a , extinctions, aperture and k-corrected [3.6] band magnitude, mag (AB system), (17) pseudo apparent magnitude at [3.6], mag, (18) pseudo absolute magnitude at [3.6], mag, (19) apparent magnitude at [3.6], mag, (20) absolute magnitude at [3.6], mag, (21) distance modulus corrected for the selection bias obtained with the color adjusted TF relation, mag, (22) selection bias corrected distance estimates obtained with the color adjusted TFR, Mpc, (23) distance modulus corrected for the selection bias obtained with the TFR, mag, (24) selection bias corrected distance estimates obtained with the TFR, Mpc.

Appendix D

Abbreviations and Acronyms

| | |
|--------------------------------|--|
| 2LPT | S econd O rders L agrangian P erturbation T heory |
| 2MASS | T wo M icron A ll S ky S urvey |
| ΛCDM | L ambda C old D ark M atter |
| A1 | A bell 1367 |
| A2 | A bell 2634/66 |
| A4 | A bell 400 |
| ART | A daptive R efinement T ree |
| An | A ntlia |
| BC | B olometric C orrection |
| BFJR | B aryonic F aber- J ackson R elation |
| BTFR | B aryonic T ully- F isher R elation |
| Ca | C ancer |
| Calib | C alibrator subsample |
| Co | C oma |
| Ce | C entaurus |
| CDM | C old D ark M atter |
| CHP | C arnegie H ubble P rogram |
| CIC | C loud I n C ell |
| CLUES | C onstrained L ocal U nivers E S imulations |
| CFS | C osmicflows with S pitzer |
| CF2 | C osmicflows- 2 |
| CMB | C osmic M icrowave B ackground |
| CR | C onstrained R ealization |
| DTFR | D irect T ully- F isher R elation |
| EDD | E xtragalactic D istance D atabase |
| F | F ornax |
| FG | F lat G alaxies |
| FJR | F aber- J ackson R elation |
| FP | F undamental P lane |
| FWHM | F ull W idth at H alf M aximum |
| GADGET | G ALaxies with D ark matter and G as int E ract |
| HDM | H ot D ark M atter |

| | |
|-----------------------|---|
| H | Hydra |
| HSB | High Surface Brightness |
| ICECoRE | Initial Conditions & Constrained Realizations |
| IRAC | InfraRed Array Camera |
| ITFR | Inverse Tully-Fisher Relation |
| ISB | Intermediate Surface Brightness |
| LMC | Large Magellanic Cloud |
| LPT | Lagrangian Perturbation Theory |
| LSB | Low Surface Brightness |
| LVL | Local Volume Large galaxy survey |
| M | Miscellaneous |
| mag | magnitude |
| Mpc | Megaparsec |
| NGP | Nearest Grid Point |
| pc | parsec |
| Pe | Pegasus |
| Pi | Pisces |
| PL, P | cepheid Period Luminosity |
| PSCz | Point Source Color redshift survey |
| RC3 | Third Reference Catalog |
| RR | Random Realization |
| RZA | Reverse Zel'dovich Approximation |
| SBF, S | Surface Brightness Fluctuation |
| SDSS | Sloan Digital Sky Survey |
| SINGS | Spitzer Infrared Nearby Galaxies Survey |
| SNIa, SN | SuperNovae of type Ia |
| SNIa-H | SuperNovae of type Ia Host subsample |
| SPH | Smooth Particle Hydrodynamics |
| S⁴G | Spitzer Survey of Stellar Structures in Galaxies |
| SB | Surface Brightness |
| SEE | Standard Error of the Estimate |
| SGL,B,X,Y,Z | Supergalactic Longitude, Latitude (B), X, Y, Z coordinates |
| sr | steradian |
| TC12 | Tully & Courtois 2012 |
| TF | Tully-Fisher |
| TFR | Tully-Fisher Relation |
| TRGB, T | Tip of the Red Giant Branch |
| TSC | Triangular Shape Cloud |
| U | Ursa Major |
| V | Virgo |
| WDM | Warm Dark Matter |
| WF | Wiener-Filter |
| WISE | Wide-Field Infrared Survey Explorer |
| WIMP | Weakly Interacting Massive Particle |
| WMAP | Wilkinson Microwave Anisotropy Probe |
| ZoA | Zone of Avoidance |
| ZP | Zero Point calibrator |

Appendix E

Physical Constants and Units

Physical Constants:

- Constant of Boltzmann: $\mathbf{k_B} = 1.380\ 65 \times 10^{-23} \text{ J K}^{-1}$
- Constant of Rydberg associated with the hydrogen: $\mathbf{R_H} = 1.097 \times 10^7 \text{ m}^{-1}$
- Gravitational constant: $\mathbf{G} = 6.673\ 84 \pm 0.000\ 80 \times 10^{-11} \text{ m}^3 \text{ kg}^{-1} \text{ s}^{-2}$
- Vacuum speed of Light: $\mathbf{c} = 2.997\ 924\ 58 \times 10^8 \text{ m s}^{-1}$

Units:

- Megaparsec, kiloparsec, parsec: \mathbf{Mpc} , \mathbf{kpc} , \mathbf{pc} ,
 $1 \text{ Mpc} = 10^3 \text{ kpc} = 10^6 \text{ pc} = 3.085\ 68 \times 10^{19} \text{ m}$
- Solar Luminosity: $\mathbf{L_\odot}$, $1 L_\odot = 3.839 \times 10^{26} \text{ W}$
- Solar Mass: $\mathbf{M_\odot}$, $1 M_\odot = 1.988\ 4 \pm 0.000\ 2 \times 10^{30} \text{ kg}$
- arcminutes: $\mathbf{arcmin} / ' , 1' = 4.629\ 63 \times 10^{-5} \text{ rad}$
- arcseconds: $\mathbf{arcsec} / '' , 1'' = \frac{1'}{60} = 7.716\ 05 \times 10^{-7} \text{ rad}$
- jansky: \mathbf{Jy} , $1 Jy = 10^{-26} \text{ W m}^{-2} \text{ Hz}^{-1}$

Other:

- Number Pi: π , $\mathbf{\Pi} = 3.141\ 592\ 653\ 59\dots$

Appendix F

Symbols and Mathematical Functions

Symbols:

| | |
|-----------------------|--|
| $[3.6]$ | apparent magnitude in the [3.6] band |
| $[3.6]_0$ | apparent magnitude in the [3.6] band obtained with the "sky" value |
| $[3.6]_+$ | apparent magnitude in the [3.6] band obtained with the "sky" value plus its uncertainty |
| $[3.6]_-$ | apparent magnitude in the [3.6] band obtained with the "sky" value minus its uncertainty |
| $[3.6]^{b,k,i,a}$ | corrected apparent magnitude in the [3.6] band |
| $[3.6]_{26.5}$ | apparent magnitude at the 26.5 mag arcsec ⁻² isophote at [3.6] |
| $[3.6]_{ext}$ | extrapolated apparent magnitude in the [3.6] band |
| $[3.6]_{tot}$ | total (asymptotic) apparent magnitude in the [3.6] band |
| α | disk scale length / slope of the Schechter luminosity function |
| α, β, i, j | indices |
| $\gamma_{[3.6]}$ | correction factor for internal extinction at 3.6 |
| γ_λ | correction factor for internal extinction at λ |
| δ | overdensity or perturbation density field |
| $\tilde{\delta}$ | spatial dependent part of the overdensity |
| δ_0 | overdensity today |
| δ^{CR} | constrained realization of the density field |
| δ^{RR} | random realization of the density field |
| δ^{WF} | wiener-filter estimate of the mean density field |
| Δ | radial peculiar velocity uncertainty |
| $\Delta\nu$ | spectral resolution after smoothing |

| | |
|---|---|
| $\Delta[3.6]^{color}, \Delta M_{[3.6]}^{color}$ | color correction term |
| Δvar | uncertainty on the variable var |
| ϵ | constraint error/uncertainty |
| $\zeta, \Psi, \Psi_T, \Psi_R$ | correlation function |
| η | correlation vector |
| λ | wavelength / HI linewidth adjustment parameter |
| λ_e | emitted wavelength |
| λ_r | received wavelength |
| λ_{rh} | hypothetical received wavelength in the case of sole expansion |
| Λ | cosmological constant |
| μ | distance modulus / surface brightness |
| $\langle \mu \rangle$ | average surface brightness |
| $\mu_{[3.6]}$ | distance modulus obtained with the Tully-Fisher relation |
| μ_0, L_0 | disk central surface brightness in magnitude / in intensity units |
| $\mu_0^{[3.6],a}$ | disk central surface brightness corrected for aperture at 3.6 μm |
| $\mu_0^{[3.6],a,i}$ | disk central surface brightness totally corrected at 3.6 μm |
| μ_{20} | surface brightness at the isophote encompassing 20% of the total light |
| $\langle \mu_{20} \rangle$ | average surface brightness within the radius enclosing 20% of the total light |
| μ_{80} | surface brightness at the isophote encompassing 80% of the total light |
| μ^c | bias corrected distance modulus |
| μ_C | distance modulus obtained with the color corrected Tully-Fisher relation |
| μ_e | effective surface brightness |
| $\langle \mu_e \rangle$ | average effective surface brightness |
| $\langle \mu_{SN} \rangle$ | distance modulus obtained with Type Ia Supernovae |
| $\langle \mu_{TF} \rangle$ | distance modulus obtained with the Tully-Fisher relation |
| ξ | autocorrelation function of the perturbation density field |
| ρ | density |
| $\bar{\rho}$ | mean density |
| ρ_m | matter density |
| ρ_{m0} | matter density today |
| n_s | spectral index |
| ρ_r | radiation density |
| ρ_{r0} | radiation density today |
| σ | variance / standard deviation |
| σ_0 | velocity dispersion |

| | |
|--------------------------------|--|
| σ_8 | normalization parameter |
| $\sigma_{b/a}$ | uncertainty of the axial ratio |
| σ_m | root mean square deviations from the rational function fit |
| σ_{NL} | sigma non-linear |
| σ_{sky} | uncertainty on the "sky" |
| σ_x, σ_y | variances of x and y variables |
| Φ | gravitational potential |
| Φ^* | normalization of the Schechter luminosity function |
| ϕ | gravitational potential due to fluctuations |
| ψ | displacement field |
| ψ_0 | displacement field today |
| Ω_Λ | dark energy density parameter |
| Ω_K | scalar curvature density parameter |
| Ω_m | matter density parameter |
| Ω_r | radiation density parameter |
| ω | constant linking pressure and mass / white noise field |
| a | scale factor |
| a, b, c | trio of constants |
| a_1, a_2, a_3, a_4 | quatuor of constants |
| a_0 | scale factor today |
| $\dot{a}, \ddot{a}, \dddot{a}$ | first, second and third derivatives of the scale factor with respect to time |
| a_{20} | radius of the isophotal level encompassing 20% of the total light |
| $a_{26.5}$ | radius of the isophotal level 26.5 magnitudes per square arcsecond at [3.6] |
| a_{80} | radius of the isophotal level encompassing 80% of the total light |
| a_e, r_e | effective radius |
| $A_a^{[3.6]}$ | aperture correction in the [3.6] band |
| $A_b^{[3.6]}$ | galactic extinction correction in the [3.6] band |
| A_b^λ | galactic extinction correction for the wavelength λ |
| $A_i^{[3.6]}$ | internal extinction correction in the [3.6] band |
| $A_k^{[3.6]}$ | k-correction in the [3.6] band |
| A_b^I | galactic extinction correction in the I band |
| A_i^I | internal extinction correction in the I band |
| A_k^I | k-correction in the I band |
| b | galactic latitude / bias |
| $\frac{b}{a}, b/a$ | axial ratio |
| c | vacuum speed of light / constraint |
| $corr$ | correlation coefficient |

| | |
|------------------------|--|
| cov | covariance |
| cst | constant |
| C | conversion factor / constraint plus its uncertainty |
| $C^{[3.6]}$ | intrinsic extinction factor |
| $C_{[3.6]}$ | color adjusted magnitude or pseudo-apparent magnitude |
| C_{82} | concentration index |
| C_ℓ | cutoff factor |
| $d_{[3.6]}$ | distance obtained with the Tully-Fisher relation |
| d_C | distance obtained with the color corrected Tully-Fisher relation |
| d_{25} | diameter at the B-isophote of 25 magnitudes per square arcsecond |
| D | distance |
| D_0 | distance today |
| D_+ | increasing solution of the second-order differential equation on the time dependent part of the overdensity |
| D_{+0} | increasing solution of the second-order differential equation on the time dependent part of the overdensity, value today |
| D_\pm | general solution of the second-order differential equation on the time dependent part of the overdensity |
| D_L | luminosity distance |
| D_n | diameter of the isophote encompassing 20.75 magnitudes per square arcsecond |
| err_{var} | errors on the variable var |
| E, U | energy |
| E_k | kinetic energy |
| E_p | potential energy |
| $E(B - V)$ | reddening |
| f | growth rate / probability distribution function / underlying field / probability of the estimate to be wrong |
| f^{CR} | constrained realization of the underlying field |
| f^{WF} | wiener-filter estimate of the underlying field |
| \tilde{f}^{RR} | random underlying field |
| \tilde{f}^{WF} | wiener-filter estimate of the random underlying field |
| F | gravitational force / flux / decomposition factor of underlying fields or of their models |
| F_0 | instrumental zero point |
| F_{HI} | flux integrated within the HI profile |
| $F_{[3.6]}, F_{[4.5]}$ | flux in [3.6] and [4.5] Spitzer bands |
| G | universal gravitational constant |
| h | Hubble constant divided by one hundred |

| | |
|---|---|
| H | (generalized) Hubble constant / Hamiltonian |
| $H_\alpha, H_\beta, H_\gamma, H_\delta, H_\epsilon$ | hydrogen lines of the Balmer series |
| H_0 | Hubble constant (today) |
| i | inclination |
| I | apparent magnitude in the I-band |
| $I^{b,i,k}$ | corrected apparent magnitude in the I-band |
| j_0 | jerk parameter |
| j_0, j_1 | Bessel functions |
| k | curvature of space / Fourier mode or wavevector |
| k_B | constant of Boltzmann |
| k_r, k_L, k_v, k_s | parameters reflecting density, luminosity and kinematic structures of galaxies ; k_s is inversely proportional to the product of the first three parameters |
| K | scalar curvature |
| l, b | galactic coordinates |
| L | length / luminosity |
| L^* | characteristic luminosity of the Schechter function |
| L_\odot | solar luminosity |
| L_{lim} | luminosity of the limiting isophote |
| m | mass / apparent magnitude |
| m_r | apparent magnitude at the galactocentric radius r |
| m_T | total apparent magnitude |
| \bar{m} | fluctuation magnitude |
| M | absolute magnitude |
| M^* | characteristic magnitude of the Schechter function |
| M_* | stellar mass |
| M_\odot | solar mass |
| $M_{[3.6]}^{b,i,k,a}$ | corrected absolute magnitude at $3.6 \mu\text{m}$ |
| $M_{C[3.6]}$ | color adjusted magnitude or pseudo-apparent magnitude |
| $M_{baryonic}$ | baryonic mass |
| M_{gas} | gas mass |
| n | number of particles, bodies, constraints, points, galaxies |
| N | noise |
| \bar{N} | fluctuation star counts |
| p | probability (not to belong to the theoretical gaussian) |
| P | pressure / power spectrum / period |
| PA | position angle |
| q_0 | deceleration parameter / statistical axial ratio for a galaxy viewed edge-on |

| | |
|------------------------|---|
| $\langle r \rangle$ | true distance |
| r | proper coordinate / galactocentric radius / distance estimate |
| $\hat{\mathbf{r}}$ | normalized directional vector |
| r_{lim} | radius of the limiting isophote |
| R, \tilde{R} | residual |
| $R_{[3.6]}$ | factor accounting for the shift to Spitzer passband centroid |
| R_λ | factor accounting for the shift to a photometric passband (wavelength λ) centroid |
| R_H | constant of Rydberg associated with the hydrogen |
| SGL, SGB | spherical supergalactic coordinates |
| SGX, SGY, SGZ | cartesian supergalactic coordinates |
| s | path, geodesic |
| S | signal / "sky" |
| $stddev$ | standard deviation (scatter) |
| t | time, morphological type |
| T | period / temperature |
| u | peculiar velocity |
| U, B, V, G, R, R_C | |
| I, I_C, Z, Y, J, H | |
| K, K_s, K' | photometric band |
| v | velocity |
| v_{hel} | heliocentric velocity |
| v_{mod} | velocity with respect to the cosmic microwave background corrected for cosmological effects |
| v_{pec} | (radial) peculiar velocity |
| $v_{pec\ c}$ | "corrected" radial peculiar velocity |
| v_{CMB} | velocity with respect to the cosmic microwave background |
| v^{CR} | constrained realization of the velocity field |
| v^{RR} | random realization of the velocity field |
| v^{WF} | wiener-filter estimate of the velocity field |
| V | volume |
| w | phase space |
| W | linewidth of the 21-cm line |
| W_{m50} | HI profile width at 50% of the mean flux within the velocity range encompassing 90% of the total HI flux |
| W_{m50}^c, W_{mx} | partially corrected HI linewidth |
| $W_{t,m50}, W_{c,m50}$ | HI linewidth adjustment parameter |
| W_{mx} | non de-projected corrected HI linewidth |
| W_{mx}^i | fully corrected HI linewidth, corresponds to twice the rotational |

| | |
|--------------------|--|
| | velocity of a galaxy |
| x | comoving coordinate |
| x, y | set of variables to model data |
| \bar{x}, \bar{y} | means of x and y variables |
| x_E | eulerian coordinate |
| x_L | lagrangian coordinate |
| z | redshift |
| z_{cos} | cosmological redshift |
| z_{extra} | extra term in the observational redshift not due to the sole expansion |
| z_{obs} | observational redshift |
| z_{pec} | peculiar redshift |
| z_{pt} | zeropoint |
| \bar{z}_{pt} | mean zeropoint |

Mathematical Functions:

| | |
|--|--|
| \wedge | vectorial product |
| $[function, H]$ | Poisson bracket |
| $\int var(var')dvar'$ | integral of the variable var with respect to the variable var' |
| \sum_n | summation over n |
| δ_{ij}^K | Kronecker symbol |
| $\langle var var' \rangle$ | average over the volume / correlation function of the variables var and var' |
| $\dot{var}, \ddot{var}, \overset{\cdot}{\ddot{var}}$ | first, second and third derivatives with respect to time of the variable var |
| $\frac{d}{d var}$ | total derivative with respect to the variable var |
| $\frac{\partial}{\partial var}$ | partial derivative with respect to the variable var |
| $(\frac{\partial}{\partial var})_{var'}$ | partial derivative with respect to the variable var with the prime variable var' fixed |
| ∇ | divergence |
| ∇^2 | laplacian |
| cos, sin | trigonometric cosinus and sinus functions |
| $e^{function}, \exp()$ | exponential function |
| $\ln()$ | Neperian logarithm |
| $\log()$ | decimal logarithm |

Bibliography

- Aaronson, M.; Huchra, J.; and Mould, J. *The infrared luminosity/ $H I$ velocity-width relation and its application to the distance scale*. *ApJ*, 229:1–13, 1979.
- Abazajian, K.; Adelman-McCarthy, J. K.; Agüeros, M. A.; Allam, S. S.; Anderson, S. F.; Annis, J.; Bahcall, N. A.; Baldry, I. K.; Bastian, S.; Berlind, A.; et al. *The First Data Release of the Sloan Digital Sky Survey*. *AJ*, 126:2081–2086, 2003.
- Adler, R. J., *The Geometry of Random Fields*, 1981.
- Alimi, J.-M.; Bouillot, V.; Rasera, Y.; Reverdy, V.; Corasaniti, P.-S.; Balmes, I.; Requena, S.; Delaruelle, X.; and Richet, J.-N. *DEUS Full Observable $\{\Lambda\}$ CDM Universe Simulation: the numerical challenge*. ArXiv e-prints 1206.2838, 2012.
- Amanullah, R.; Lidman, C.; Rubin, D.; Aldering, G.; Astier, P.; Barbary, K.; Burns, M. S.; Conley, A.; Dawson, K. S.; Deustua, S. E.; et al. *Spectra and Hubble Space Telescope Light Curves of Six Type Ia Supernovae at $0.511 < z < 1.12$ and the Union2 Compilation*. *ApJ*, 716:712–738, 2010.
- Angulo, R. E.; Springel, V.; White, S. D. M.; Jenkins, A.; Baugh, C. M.; and Frenk, C. S. *Scaling relations for galaxy clusters in the Millennium-XXL simulation*. *MNRAS*, 426:2046–2062, 2012a.
- Angulo, R. E.; Springel, V.; White, S. D. M.; Jenkins, A.; Baugh, C. M.; and Frenk, C. S. *Scaling relations for galaxy clusters in the Millennium-XXL simulation*. *MNRAS*, 426:2046–2062, 2012b.
- Appel, A. W. *An Efficient Program for Many-Body Simulation*. *SIAM Journal on Scientific and Statistical Computing*, vol. 6, no. 1, January 1985, p. 85–103., 6:85–103, 1985.
- Bahcall, N. A. *Superclustering and the large-scale structure of the Universe*. *Advances in Space Research*, 3:367–377, 1984.
- Bailin, J. and Harris, W. E. *Galaxy concentrations are trimodal*. *MNRAS*, 385:1835–1845, 2008.
- Baldry, I. K.; Glazebrook, K.; Brinkmann, J.; Ivezić, Ž.; Lupton, R. H.; Nichol, R. C.; and Szalay, A. S. *Quantifying the Bimodal Color-Magnitude Distribution of Galaxies*. *ApJ*, 600:681–694, 2004.
- Bardeen, J. M.; Bond, J. R.; Kaiser, N.; and Szalay, A. S. *The statistics of peaks of Gaussian random fields*. *ApJ*, 304:15–61, 1986.
- Barnes, J. and Hut, P. *A hierarchical $O(N \log N)$ force-calculation algorithm*. *Nature*, 324:446–449, 1986.

- Baugh, C. M. *Luminosity Bias: From Haloes to Galaxies*. PASA, 30:e030, 2013.
- Bedregal, A. G.; Aragón-Salamanca, A.; and Merrifield, M. R. *The Tully-Fisher relation for S0 galaxies*. MNRAS, 373:1125–1140, 2006.
- Behroozi, P. S.; Conroy, C.; and Wechsler, R. H. *A Comprehensive Analysis of Uncertainties Affecting the Stellar Mass-Halo Mass Relation for $0 < z < 4$* . ApJ, 717:379–403, 2010.
- Bell, E. F. and de Blok, W. J. G. *The bimodal spiral galaxy surface brightness distribution*. MNRAS, 311:668–672, 2000.
- Bertone, G. *The moment of truth for WIMP dark matter*. Nature, 468:389–393, 2010.
- Bertschinger, E. *Multiscale Gaussian Random Fields and Their Application to Cosmological Simulations*. ApJS, 137:1–20, 2001.
- Bhattacharya, S., *Cosmology using galaxy cluster peculiar velocities*, 2008.
- Binney, J. and Tremaine, S., *Galactic dynamics*, 1987.
- Birrell, J. and Rafelski, J. *Boltzmann Equation Solver Adapted to Emergent Chemical Non-equilibrium*. ArXiv e-prints, 2014.
- Bistolos, V. and Hoffman, Y. *Nonlinear Constrained Realizations of the Large-Scale Structure*. ApJ, 492:439, 1998.
- Blakeslee, J. P.; Cantiello, M.; Mei, S.; Côté, P.; Barber DeGraaff, R.; Ferrarese, L.; Jordán, A.; Peng, E. W.; Tonry, J. L.; and Worthey, G. *Surface Brightness Fluctuations in the Hubble Space Telescope ACS/WFC F814W Bandpass and an Update on Galaxy Distances*. ApJ, 724:657–668, 2010.
- Blanton, M. R. and Roweis, S. *K-Corrections and Filter Transformations in the Ultraviolet, Optical, and Near-Infrared*. AJ, 133:734–754, 2007.
- Bothun, G. D. and Mould, J. R. *Sources of error in the Tully-Fisher relation - Reducing the scatter with CCD I-band surface photometry of spiral galaxies*. ApJ, 313:629–643, 1987.
- Bottinelli, L.; Gouguenheim, L.; Paturel, G.; and Teerikorpi, P. *The Malmquist bias and the value of H_0 from the Tully-Fisher relation*. A&A, 156:157–171, 1986.
- Brammer, G. B.; Whitaker, K. E.; van Dokkum, P. G.; Marchesini, D.; Labbé, I.; Franx, M.; Kriek, M.; Quadri, R. F.; Illingworth, G.; Lee, K.-S.; et al. *The Dead Sequence: A Clear Bimodality in Galaxy Colors from $z = 0$ to $z = 2.5$* . ApJL, 706:L173–L177, 2009.
- Brook, C. B.; Di Cintio, A.; Knebe, A.; Gottlöber, S.; Hoffman, Y.; and Yepes, G. *The stellar-to-halo mass relation for Local Group galaxies*. ArXiv e-prints, 2013.
- Burstein, D.; Faber, S. M.; and Dressler, A. *Evidence from the motions of galaxies for a large-scale, large-amplitude flow toward the great attractor*. ApJ, 354:18–32, 1990.
- Caputi, K. I.; McLure, R. J.; Dunlop, J. S.; Cirasuolo, M.; and Schael, A. M. *Further constraints on the evolution of K_s -selected galaxies in the GOODS/CDFS field*. MNRAS, 366:609–623, 2006.
- Cardelli, J. A.; Clayton, G. C.; and Mathis, J. S. *The relationship between infrared, optical, and ultraviolet extinction*. ApJ, 345:245–256, 1989.

- Carroll, S. M.; Press, W. H.; and Turner, E. L. *The cosmological constant*. ARA&A, 30:499–542, 1992.
- Catinella, B.; Kauffmann, G.; Schiminovich, D.; Lemonias, J.; Scannapieco, C.; Wang, J.; Fabello, S.; Hummels, C.; Moran, S. M.; Wu, R.; et al. *The GALEX Arecibo SDSS Survey - IV. Baryonic mass-velocity-size relations of massive galaxies*. MNRAS, 420:1959–1976, 2012.
- Chamaraux, P.; Cayatte, V.; Balkowski, C.; and Fontanelli, P. *A connection between the Perseus-Pisces supercluster and the A 569 cloud?* A&A, 229:340–350, 1990.
- Chiba, T. and Nakamura, T. *The Luminosity Distance, the Equation of State, and the Geometry of the Universe*. Progress of Theoretical Physics, 100:1077–1082, 1998.
- Chilingarian, I. V.; Melchior, A.-L.; and Zolotukhin, I. Y. *Analytical approximations of K-corrections in optical and near-infrared bands*. MNRAS, 405:1409–1420, 2010.
- Chincarini, G. *Large-scale structure of the universe*. The Messenger, 26:14–15, 1981.
- Cole, S.; Lacey, C. G.; Baugh, C. M.; and Frenk, C. S. *Hierarchical galaxy formation*. MNRAS, 319:168–204, 2000.
- Colless, M.; Saglia, R. P.; Burstein, D.; Davies, R. L.; McMahan, R. K.; and Wegner, G. *The peculiar motions of early-type galaxies in two distant regions - VII. Peculiar velocities and bulk motions*. MNRAS, 321:277–305, 2001.
- Courteau, S. *Optical Rotation Curves and Linewidths for Tully-Fisher Applications*. AJ, 114:2402, 1997.
- Courteau, S.; Dutton, A. A.; van den Bosch, F. C.; MacArthur, L. A.; Dekel, A.; McIntosh, D. H.; and Dale, D. A. *Scaling Relations of Spiral Galaxies*. ApJ, 671:203–225, 2007.
- Courtois, H. M.; Hoffman, Y.; Tully, R. B.; and Gottlöber, S. *Three-dimensional Velocity and Density Reconstructions of the Local Universe with Cosmicflows-1*. ApJ, 744:43, 2012.
- Courtois, H. M.; Pomarède, D.; Tully, R. B.; Hoffman, Y.; and Courtois, D. *Cosmography of the Local Universe*. AJ, 146:69, 2013.
- Courtois, H. M. and Tully, R. B. *Cosmic Flows surveys and CLUES simulations*. Astronomische Nachrichten, 333:436, 2012a.
- Courtois, H. M. and Tully, R. B. *Cosmicflows-2: Type Ia Supernova Calibration and H_0* . ApJ, 749:174, 2012b.
- Courtois, H. M.; Tully, R. B.; Fisher, J. R.; Bonhomme, N.; Zavodny, M.; and Barnes, A. *The Extragalactic Distance Database: All Digital H I Profile Catalog*. AJ, 138:1938–1956, 2009.
- Courtois, H. M.; Tully, R. B.; and Héraudeau, P. *Cosmic flows: University of Hawaii 2.2-m I-band photometry*. MNRAS, 415:1935–1942, 2011a.
- Courtois, H. M.; Tully, R. B.; Makarov, D. I.; Mitronova, S.; Koribalski, B.; Karachentsev, I. D.; and Fisher, J. R. *Cosmic Flows: Green Bank Telescope and Parkes H I observations*. MNRAS, 414:2005–2016, 2011b.
- Cowie, L. L.; Gardner, J. P.; Hu, E. M.; Songaila, A.; Hodapp, K.-W.; and Wainscoat, R. J. *The Hawaii K-band galaxy survey. 1: Deep K-band imaging*. ApJ, 434:114–127, 1994.

- Cox, T. J. and Loeb, A. *The collision between the Milky Way and Andromeda*. MNRAS, 386:461–474, 2008.
- da Costa, L. N.; Freudling, W.; Wegner, G.; Giovanelli, R.; Haynes, M. P.; and Salzer, J. J. *The Mass Distribution in the Nearby Universe*. ApJL, 468:L5, 1996.
- da Costa, L. N.; Nusser, A.; Freudling, W.; Giovanelli, R.; Haynes, M. P.; Salzer, J. J.; and Wegner, G. *Comparison of the SFI peculiar velocities with the IRAS 1.2-Jy gravity field*. MNRAS, 299:425–432, 1998.
- Dale, D. A.; Bendo, G. J.; Engelbracht, C. W.; Gordon, K. D.; Regan, M. W.; Armus, L.; Cannon, J. M.; Calzetti, D.; Draine, B. T.; Helou, G.; et al. *Infrared Spectral Energy Distributions of Nearby Galaxies*. ApJ, 633:857–870, 2005.
- Dale, D. A.; Cohen, S. A.; Johnson, L. C.; Schuster, M. D.; Calzetti, D.; Engelbracht, C. W.; Gil de Paz, A.; Kennicutt, R. C.; Lee, J. C.; Begum, A.; et al. *The Spitzer Local Volume Legacy: Survey Description and Infrared Photometry*. ApJ, 703:517–556, 2009.
- Dale, D. A.; Gil de Paz, A.; Gordon, K. D.; Hanson, H. M.; Armus, L.; Bendo, G. J.; Bianchi, L.; Block, M.; Boissier, S.; Boselli, A.; et al. *An Ultraviolet-to-Radio Broadband Spectral Atlas of Nearby Galaxies*. ApJ, 655:863–884, 2007.
- Davis, M.; Efstathiou, G.; Frenk, C. S.; and White, S. D. M. *The evolution of large-scale structure in a universe dominated by cold dark matter*. ApJ, 292:371–394, 1985.
- de Jong, R. S. *Near-infrared and optical broadband surface photometry of 86 face-on disk dominated galaxies. II. A two-dimensional method to determine bulge and disk parameters*. A&A Supplement Series, 118:557–573, 1996a.
- de Jong, R. S. *Near-infrared and optical broadband surface photometry of 86 face-on disk dominated galaxies. III. The statistics of the disk and bulge parameters*. A&A, 313:45–64, 1996b.
- de Vaucouleurs, G. *Evidence for a local supergalaxy*. AJ, 58:30, 1953.
- de Vaucouleurs, G. *Contributions to the galaxy photometry. I - Standard total magnitudes, luminosity curves, and photometric parameters of 115 bright galaxies in the B system from detailed surface photometry*. ApJS, 33:211–218, 1977.
- Dehnen, W. *A Very Fast and Momentum-conserving Tree Code*. ApJL, 536:L39–L42, 2000.
- Dekel, A. *Dynamics of Cosmic Flows*. ARA&A, 32:371–418, 1994.
- Dekel, A.; Eldar, A.; Kolatt, T.; Yahil, A.; Willick, J. A.; Faber, S. M.; Courteau, S.; and Burstein, D. *POTENT Reconstruction from Mark III Velocities*. ApJ, 522:1–38, 1999.
- Desmond, H. *The baryonic Tully-Fisher Relation predicted by cold dark matter cosmogony*. ArXiv e-prints, 2012.
- Doumler, T.; Courtois, H.; Gottlöber, S.; and Hoffman, Y. *Reconstructing cosmological initial conditions from galaxy peculiar velocities - II. The effect of observational errors*. MNRAS, 430:902–911, 2013a.
- Doumler, T.; Gottlöber, S.; Hoffman, Y.; and Courtois, H. *Reconstructing cosmological initial conditions from galaxy peculiar velocities - III. Constrained simulations*. MNRAS, 430:912–923, 2013b.

- Doumler, T.; Hoffman, Y.; Courtois, H.; and Gottlöber, S. *Reconstructing cosmological initial conditions from galaxy peculiar velocities - I. Reverse Zeldovich Approximation*. MNRAS, 430:888–901, 2013c.
- Draine, B. T. and Lee, H. M. *Optical properties of interstellar graphite and silicate grains*. ApJ, 285:89–108, 1984.
- Dressler, A. *The Dn-sigma relation for bulges of disk galaxies - A new, independent measure of the Hubble constant*. ApJ, 317:1–10, 1987.
- Dutton, A. A. *The baryonic Tully-Fisher relation and galactic outflows*. MNRAS, 424:3123–3128, 2012.
- Eddington, A. S. *On a formula for correcting statistics for the effects of a known error of observation*. MNRAS, 73:359–360, 1913.
- Efstathiou, G. *Fred Hoyle: Contributions to the Theory of Galaxy Formation*. ArXiv Astrophysics e-prints, 2003.
- Efstathiou, G.; Davis, M.; White, S. D. M.; and Frenk, C. S. *Numerical techniques for large cosmological N-body simulations*. ApJS, 57:241–260, 1985.
- Einasto, J.; Suhhonenko, I.; Hütsi, G.; Saar, E.; Einasto, M.; Liivamägi, L. J.; Müller, V.; Starobinsky, A. A.; Tago, E.; and Tempel, E. *Towards understanding the structure of voids in the cosmic web*. A&A, 534:A128, 2011.
- Ekholm, T.; Lanoix, P.; Teerikorpi, P.; Fouqué, P.; and Paturel, G. *Investigations of the Local Supercluster velocity field. III. Tracing the backside infall with distance moduli from the direct Tully-Fisher relation*. A&A, 355:835–847, 2000.
- Erdoğan, P.; Lahav, O.; Huchra, J. P.; Colless, M.; Cutri, R. M.; Falco, E.; George, T.; Jarrett, T.; Jones, D. H.; Macri, L. M.; et al. *Reconstructed density and velocity fields from the 2MASS Redshift Survey*. MNRAS, 373:45–64, 2006.
- Erwin, P.; Pohlen, M.; and Beckman, J. E. *The Outer Disks of Early-Type Galaxies. I. Surface-Brightness Profiles of Barred Galaxies*. AJ, 135:20–54, 2008.
- Eskew, M.; Zaritsky, D.; and Meidt, S. *Converting from 3.6 and 4.5 μm Fluxes to Stellar Mass*. AJ, 143:139, 2012.
- Faber, S. M. and Jackson, R. E. *Velocity dispersions and mass-to-light ratios for elliptical galaxies*. ApJ, 204:668–683, 1976.
- Fazio, G. G.; Hora, J. L.; Allen, L. E.; Ashby, M. L. N.; Barmby, P.; Deutsch, L. K.; Huang, J.-S.; Kleiner, S.; Marengo, M.; Megeath, S. T.; et al. *The Infrared Array Camera (IRAC) for the Spitzer Space Telescope*. ApJS, 154:10–17, 2004.
- Feindt, U.; Kerschhaggl, M.; Kowalski, M.; Aldering, G.; Antilogus, P.; Aragon, C.; Bailey, S.; Baltay, C.; Bongard, S.; Buton, C.; et al. *Measuring cosmic bulk flows with Type Ia supernovae from the Nearby Supernova Factory*. A&A, 560:A90, 2013.
- Fisher, K. B.; Lahav, O.; Hoffman, Y.; Lynden-Bell, D.; and Zaroubi, S. *Wiener reconstruction of density, velocity and potential fields from all-sky galaxy redshift surveys*. MNRAS, 272:885–908, 1995.

- Fixsen, D. J.; Cheng, E. S.; Gales, J. M.; Mather, J. C.; Shafer, R. A.; and Wright, E. L. *The Cosmic Microwave Background Spectrum from the Full COBE FIRAS Data Set*. ApJ, 473:576, 1996.
- Focardi, P.; Marano, B.; and Vettolani, G. *The north extension of the Perseus supercluster*. A&A, 136:178–180, 1984.
- Folatelli, G.; Phillips, M. M.; Burns, C. R.; Contreras, C.; Hamuy, M.; Freedman, W. L.; Persson, S. E.; Stritzinger, M.; Suntzeff, N. B.; Krisciunas, K.; et al. *The Carnegie Supernova Project: Analysis of the First Sample of Low-Redshift Type-Ia Supernovae*. AJ, 139:120–144, 2010.
- Forero-Romero, J. E.; Hoffman, Y.; Yepes, G.; Gottlöber, S.; Piontek, R.; Klypin, A.; and Steinmetz, M. *The dark matter assembly of the Local Group in constrained cosmological simulations of a Λ cold dark matter universe*. MNRAS, 417:1434–1443, 2011.
- Fosalba, P.; Crocce, M.; Gaztanaga, E.; and Castander, F. J. *The MICE Grand Challenge Lightcone Simulation I: Dark matter clustering*. ArXiv e-prints, 2013.
- Freedman, W. L. and Madore, B. F. *The Hubble Constant*. ARA&A, 48:673–710, 2010.
- Freedman, W. L.; Madore, B. F.; Gibson, B. K.; Ferrarese, L.; Kelson, D. D.; Sakai, S.; Mould, J. R.; Kennicutt, R. C., Jr.; Ford, H. C.; Graham, J. A.; et al. *Final Results from the Hubble Space Telescope Key Project to Measure the Hubble Constant*. ApJ, 553:47–72, 2001.
- Freedman, W. L.; Madore, B. F.; Scowcroft, V.; Burns, C.; Monson, A.; Persson, S. E.; Seibert, M.; and Rigby, J. *Carnegie Hubble Program: A Mid-infrared Calibration of the Hubble Constant*. ApJ, 758:24, 2012.
- Freedman, W. L.; Madore, B. F.; Scowcroft, V.; Monson, A.; Persson, S. E.; Seibert, M.; Rigby, J. R.; Sturch, L.; and Stetson, P. *The Carnegie Hubble Program*. AJ, 142:192, 2011.
- Freeman, K. C. *On the Disks of Spiral and so Galaxies*. ApJ, 160:811, 1970.
- Frei, Z. and Gunn, J. E. *Generating colors and K corrections from existing catalog data*. AJ, 108:1476–1485, 1994.
- Friedmann, A. *Über die Krümmung des Raumes*. Zeitschrift für Physik, 10:377–386, 1922.
- Ganon, G. and Hoffman, Y. *Constrained realizations of Gaussian fields - Reconstruction of the large-scale structure*. ApJL, 415:L5–L8, 1993.
- Garrison-Kimmel, S.; Boylan-Kolchin, M.; Bullock, J.; and Lee, K. *ELVIS: Exploring the Local Volume in Simulations*. ArXiv e-prints, 2013.
- Garrison-Kimmel, S.; Boylan-Kolchin, M.; Bullock, J. S.; and Lee, K. *ELVIS: Exploring the Local Volume in Simulations*. MNRAS, 438:2578–2596, 2014.
- Giovanelli, R.; Haynes, M. P.; Herter, T.; Vogt, N. P.; da Costa, L. N.; Freudling, W.; Salzer, J. J.; and Wegner, G. *The I Band Tully-Fisher Relation for Cluster Galaxies: a Template Relation, its Scatter and Bias Corrections*. AJ, 113:53–79, 1997a.
- Giovanelli, R.; Haynes, M. P.; Herter, T.; Vogt, N. P.; Wegner, G.; Salzer, J. J.; da Costa, L. N.; and Freudling, W. *The I band Tully-Fisher relation for cluster galaxies: data presentation*. AJ, 113:22–52, 1997b.

- Giovanelli, R.; Haynes, M. P.; Salzer, J. J.; Wegner, G.; da Costa, L. N.; and Freudling, W. *Dependence on Luminosity of Photometric Properties of Disk Galaxies: Surface Brightness, Size, and Internal Extinction*. AJ, 110:1059, 1995.
- Gottlöber, S.; Hoffman, Y.; and Yepes, G. *Constrained Local Universe Simulations (CLUES)*. ArXiv e-prints, 2010.
- Gould, A. *Selection, covariance, and Malmquist bias*. ApJL, 412:L55–L58, 1993.
- Gunn, J. E. *The Friedmann models and optical observations in cosmology*. page 1, 1978.
- Gunn, J. E. and Gott, J. R., III. *On the Infall of Matter Into Clusters of Galaxies and Some Effects on Their Evolution*. ApJ, 176:1, 1972.
- Hahn, O. and Abel, T. *Multi-scale initial conditions for cosmological simulations*. MNRAS, 415:2101–2121, 2011.
- Hall, M.; Courteau, S.; Dutton, A. A.; McDonald, M.; and Zhu, Y. *An investigation of Sloan Digital Sky Survey imaging data and multiband scaling relations of spiral galaxies*. MNRAS, 425:2741–2765, 2012.
- Hamann, J. and Hasenkamp, J. *A new life for sterile neutrinos: resolving inconsistencies using hot dark matter*. JCAP, 10:044, 2013.
- Hamuy, M.; Phillips, M. M.; Maza, J.; Suntzeff, N. B.; Schommer, R. A.; and Aviles, R. *A Hubble diagram of distant type Ia supernovae*. AJ, 109:1–13, 1995.
- Han, M. *I-band CCD surface photometry of spiral galaxies in 16 nearby clusters*. ApJS, 81:35–47, 1992a.
- Han, M. *The large-scale velocity field beyond the local supercluster*. ApJ, 395:75–90, 1992b.
- Hattori, M. *Is the universe gravitationally dominated by non-baryonic dark matter?* pages 447–448, 1994.
- Heath, D. J. *The growth of density perturbations in zero pressure Friedmann-Lemaître universes*. MNRAS, 179:351–358, 1977.
- Heitmann, K.; Lukić, Z.; Fasel, P.; Habib, S.; Warren, M. S.; White, M.; Ahrens, J.; Ankeny, L.; Armstrong, R.; O’Shea, B.; et al. *The cosmic code comparison project*. Computational Science and Discovery, 1(1):015003, 2008.
- Heitmann, K.; Ricker, P. M.; Warren, M. S.; and Habib, S. *Robustness of Cosmological Simulations. I. Large-Scale Structure*. ApJS, 160:28–58, 2005.
- Hendry, M. A. and Simmons, J. F. L. *Optimal galaxy distance estimators*. ApJ, 435:515–527, 1994.
- Heß, S.; Kitaura, F.-S.; and Gottlöber, S. *Simulating structure formation of the Local Universe*. MNRAS, 435:2065–2076, 2013.
- Hicken, M.; Wood-Vasey, W. M.; Blondin, S.; Challis, P.; Jha, S.; Kelly, P. L.; Rest, A.; and Kirshner, R. P. *Improved Dark Energy Constraints from ~100 New CfA Supernova Type Ia Light Curves*. ApJ, 700:1097–1140, 2009.

- Hinshaw, G.; Larson, D.; Komatsu, E.; Spergel, D. N.; Bennett, C. L.; Dunkley, J.; Nolta, M. R.; Halpern, M.; Hill, R. S.; Odegard, N.; et al. *Nine-year Wilkinson Microwave Anisotropy Probe (WMAP) Observations: Cosmological Parameter Results*. ApJS, 208:19, 2013.
- Hoffman, Y. *Gaussian Fields and Constrained Simulations of the Large-Scale Structure*. In Martínez, V. J.; Saar, E.; Martínez-González, E.; and Pons-Bordería, M.-J., editors, *Data Analysis in Cosmology*, volume 665 of *Lecture Notes in Physics*, Berlin Springer Verlag, pages 565–583. 2009.
- Hoffman, Y.; Lahav, O.; Yepes, G.; and Dover, Y. *The future of the local large scale structure: the roles of dark matter and dark energy*. JCAP, 10:016, 2007.
- Hoffman, Y. and Ribak, E. *Constrained realizations of Gaussian fields - A simple algorithm*. ApJL, 380:L5–L8, 1991.
- Hoffman, Y. and Ribak, E. *Primordial Gaussian perturbation fields - Constrained realizations*. ApJ, 384:448–452, 1992.
- Holmberg, E. *A photographic photometry of extragalactic nebulae*. Meddelanden fran Lunds Astronomiska Observatorium Serie II, 136:1, 1958.
- Huang, J.-S.; Ashby, M. L. N.; Barmby, P.; Brodwin, M.; Brown, M. J. I.; Caldwell, N.; Cool, R. J.; Eisenhardt, P.; Eisenstein, D.; Fazio, G. G.; et al. *The Local Galaxy 8 μm Luminosity Function*. ApJ, 664:840–849, 2007.
- Hubble, E. *A Relation between Distance and Radial Velocity among Extra-Galactic Nebulae*. Contributions from the Mount Wilson Observatory, vol. 3, pp.23–28, 3:23–28, 1929.
- Huchra, J. P.; Macri, L. M.; Masters, K. L.; Jarrett, T. H.; Berlind, P.; Calkins, M.; Crook, A. C.; Cutri, R.; Erdoğdu, P.; Falco, E.; et al. *The 2MASS Redshift Survey: Description and Data Release*. ApJS, 199:26, 2012.
- Hudson, M. J. *Optical galaxies within 8000 km s⁻¹. III. Inhomogeneous Malmquist bias corrections and the Great Attractor*. MNRAS, 266:468–474, 1994.
- Huizinga, J. E., *Extinction studies of spiral galaxies*, 1994.
- Iocco, F. *WIMP Dark Matter and the First Stars*. 1294:66–69, 2010.
- Jacobs, B. A.; Rizzi, L.; Tully, R. B.; Shaya, E. J.; Makarov, D. I.; and Makarova, L. *The Extragalactic Distance Database: Color-Magnitude Diagrams*. AJ, 138:332–337, 2009.
- Jacoby, G. H.; Branch, D.; Ciardullo, R.; Davies, R. L.; Harris, W. E.; Pierce, M. J.; Pritchett, C. J.; Tonry, J. L.; and Welch, D. L. *A critical review of selected techniques for measuring extragalactic distances*. PASP, 104:599–662, 1992.
- Jeong, K. S.; Kawasaki, M.; and Takahashi, F. *Axions as hot and cold dark matter*. JCAP, 2:046, 2014.
- Jha, S.; Riess, A. G.; and Kirshner, R. P. *Improved Distances to Type Ia Supernovae with Multicolor Light-Curve Shapes: MLCS2k2*. ApJ, 659:122–148, 2007.
- Johnston, S. and Deboer, D. *Testing of focal plane array technologies for ASKAP*. ATNF Proposal, page 1450, 2008.

- Kaiser, N. *Clustering in real space and in redshift space*. MNRAS, 227:1–21, 1987.
- Kaiser, N.; Aussel, H.; Burke, B. E.; Boesgaard, H.; Chambers, K.; Chun, M. R.; Heasley, J. N.; Hodapp, K.-W.; Hunt, B.; Jedicke, R.; et al. *Pan-STARRS: A Large Synoptic Survey Telescope Array*. 4836:154–164, 2002.
- Karachentsev, I. D.; Karachentseva, V. E.; Kudrya, Y. N.; Sharina, M. E.; and Parnovskij, S. L. *The revised Flat Galaxy Catalogue*. Bulletin of the Special Astrophysics Observatory, 47:5, 1999.
- Karachentsev, I. D.; Kashibadze, O. G.; Makarov, D. I.; and Tully, R. B. *The Hubble flow around the Local Group*. MNRAS, 393:1265–1274, 2009.
- Karachentsev, I. D.; Mitronova, S. N.; Karachentseva, V. E.; Kudrya, Y. N.; and Jarrett, T. H. *The 2MASS Tully-Fisher relation for flat edge-on galaxies*. A&A, 396:431–438, 2002.
- Karachentsev, I. D. and Nasonova, O. G. *The observed infall of galaxies towards the Virgo cluster*. MNRAS, 405:1075–1083, 2010.
- Karachentsev, I. D.; Nasonova, O. G.; and Courtois, H. M. *Fast Motions of Galaxies in the Coma I Cloud: A Case of Dark Attractor?* ApJ, 743:123, 2011.
- Karachentsev, I. D.; Nasonova, O. G.; and Courtois, H. M. *Anatomy of Ursa Majoris*. MNRAS, 429:2264–2273, 2013.
- Kashlinsky, A.; Atrio-Barandela, F.; and Ebeling, H. *Measuring bulk motion of X-ray clusters via the kinematic Sunyaev-Zeldovich effect: summarizing the "dark flow" evidence and its implications*. ArXiv e-prints, 2012.
- Kashlinsky, A.; Atrio-Barandela, F.; Ebeling, H.; Edge, A.; and Kocevski, D. *A New Measurement of the Bulk Flow of X-Ray Luminous Clusters of Galaxies*. ApJL, 712:L81–L85, 2010.
- Kent, S. M. *CCD surface photometry of field Galaxies. II - Bulge/disk decompositions*. ApJS, 59:115–159, 1985.
- Kitaura, F.-S. *The initial conditions of the Universe from constrained simulations*. MNRAS, 429:L84–L88, 2013.
- Kitaura, F.-S.; Erdoğan, P.; Nuza, S. E.; Khalatyan, A.; Angulo, R. E.; Hoffman, Y.; and Gottlöber, S. *Cosmic structure and dynamics of the local Universe*. MNRAS, 427:L35–L39, 2012.
- Kitaura, F.-S. and Heß, S. *Cosmological structure formation with augmented Lagrangian perturbation theory*. MNRAS, 435:L78–L82, 2013.
- Kitaura, F. S.; Jasche, J.; Li, C.; Enßlin, T. A.; Metcalf, R. B.; Wandelt, B. D.; Lemson, G.; and White, S. D. M. *Cosmic cartography of the large-scale structure with Sloan Digital Sky Survey data release 6*. MNRAS, 400:183–203, 2009.
- Klypin, A.; Hoffman, Y.; Kravtsov, A. V.; and Gottlöber, S. *Constrained Simulations of the Real Universe: The Local Supercluster*. ApJ, 596:19–33, 2003.
- Klypin, A.; Kravtsov, A. V.; Valenzuela, O.; and Prada, F. *Where Are the Missing Galactic Satellites?* ApJ, 522:82–92, 1999.

- Klypin, A.; Prada, F.; Yepes, G.; Hess, S.; and Gottlober, S. *Halo Abundance Matching: accuracy and conditions for numerical convergence*. ArXiv e-prints, 2013.
- Klypin, A. A. and Shandarin, S. F. *Three-dimensional numerical model of the formation of large-scale structure in the Universe*. MNRAS, 204:891–907, 1983.
- Klypin, A. A.; Trujillo-Gomez, S.; and Primack, J. *Dark Matter Halos in the Standard Cosmological Model: Results from the Bolshoi Simulation*. ApJ, 740:102, 2011.
- Knebe, A.; Libeskind, N. I.; Pearce, F.; Behroozi, P.; Casado, J.; Dolag, K.; Dominguez-Tenreiro, R.; Elahi, P.; Lux, H.; Muldrew, S. I.; et al. *Galaxies going MAD: the Galaxy-Finder Comparison Project*. MNRAS, 428:2039–2052, 2013.
- Knebe, A.; Wagner, C.; Knollmann, S.; Diekershoff, T.; and Krause, F. *On the Starting Redshift Cosmological Simulations: Focusing on Halo Properties*. ApJ, 698:266–274, 2009.
- Knollmann, S. R. and Knebe, A. *AHF: Amiga’s Halo Finder*. ApJS, 182:608–624, 2009.
- Kolatt, T.; Dekel, A.; Ganon, G.; and Willick, J. A. *Simulating Our Cosmological Neighborhood: Mock Catalogs for Velocity Analysis*. ApJ, 458:419, 1996.
- Kolb, E. W.; Salopek, D. S.; and Turner, M. S. *Origin of density fluctuations in extended inflation*. PRD, 42:3925–3935, 1990.
- Komatsu, E.; Dunkley, J.; Nolta, M. R.; Bennett, C. L.; Gold, B.; Hinshaw, G.; Jarosik, N.; Larson, D.; Limon, M.; Page, L.; et al. *Five-Year Wilkinson Microwave Anisotropy Probe Observations: Cosmological Interpretation*. ApJS, 180:330–376, 2009.
- Komatsu, E.; Smith, K. M.; Dunkley, J.; Bennett, C. L.; Gold, B.; Hinshaw, G.; Jarosik, N.; Larson, D.; Nolta, M. R.; Page, L.; et al. *Seven-year Wilkinson Microwave Anisotropy Probe (WMAP) Observations: Cosmological Interpretation*. ApJS, 192:18, 2011.
- Kowal, C. T. *Absolute magnitudes of supernovae*. AJ, 73:1021–1024, 1968.
- Kraan-Korteweg, R. C.; Cayette, V.; Balkowski, C.; Fairall, A. P.; and Henning, P. A. *The 3-Dimensional Galaxy Distribution in the ZOA from Hydra/Antlia to the Great Attractor Region*. 67:99, 1994.
- Krauss, L. M. *Big Bang Nucleosynthesis and Dark Matter: Baryons and Neutrinos*. page 65, 1995.
- Kravtsov, A. V.; Klypin, A. A.; and Khokhlov, A. M. *Adaptive Refinement Tree: A New High-Resolution N-Body Code for Cosmological Simulations*. ApJS, 111:73, 1997.
- Lahav, O.; Santiago, B. X.; Webster, A. M.; Strauss, M. A.; Davis, M.; Dressler, A.; and Huchra, J. P. *The supergalactic plane revisited with the Optical Redshift Survey*. MNRAS, 312:166–176, 2000.
- Landy, S. D. and Szalay, A. S. *A general analytical solution to the problem of Malmquist bias due to lognormal distance errors*. ApJ, 391:494–501, 1992.
- Larson, D.; Dunkley, J.; Hinshaw, G.; Komatsu, E.; Nolta, M. R.; Bennett, C. L.; Gold, B.; Halpern, M.; Hill, R. S.; Jarosik, N.; et al. *Seven-year Wilkinson Microwave Anisotropy Probe (WMAP) Observations: Power Spectra and WMAP-derived Parameters*. ApJS, 192:16, 2011.

- Lavaux, G. *Precision constrained simulation of the local Universe*. MNRAS, 406:1007–1013, 2010.
- Lavaux, G.; Afshordi, N.; and Hudson, M. J. *First measurement of the bulk flow of nearby galaxies using the cosmic microwave background*. MNRAS, 430:1617–1635, 2013.
- Lavaux, G.; Mohayaee, R.; Colombi, S.; Tully, R. B.; Bernardeau, F.; and Silk, J. *Observational biases in Lagrangian reconstructions of cosmic velocity fields*. MNRAS, 383:1292–1318, 2008.
- Lavaux, G.; Tully, R. B.; Mohayaee, R.; and Colombi, S. *Cosmic Flow From Two Micron All-Sky Redshift Survey: the Origin of Cosmic Microwave Background Dipole and Implications for Λ CDM Cosmology*. ApJ, 709:483–498, 2010.
- Lee, M. G.; Freedman, W. L.; and Madore, B. F. *The Tip of the Red Giant Branch as a Distance Indicator for Resolved Galaxies*. ApJ, 417:553, 1993.
- Leeuwin, F.; Combes, F.; and Binney, J. *N-body simulations with perturbation particles. I - Method and tests*. MNRAS, 262:1013–1022, 1993.
- Lemaître, G. *Expansion of the universe, A homogeneous universe of constant mass and increasing radius accounting for the radial velocity of extra-galactic nebulae*. MNRAS, 91:483–490, 1931a.
- Lemaître, G. *Expansion of the universe, The expanding universe*. MNRAS, 91:490–501, 1931b.
- Libeskind, N. I.; Di Cintio, A.; Knebe, A.; Yepes, G.; Gottlöber, S.; Steinmetz, M.; Hoffman, Y.; and Martínez-Vaquero, L. A. *Cold versus Warm Dark Matter Simulations of a Galaxy Group*. PASA, 30:e039, 2013.
- Longair, M. S. and Einasto, J. *The large scale structure of the universe; Proceedings of the Symposium, Tallin, Estonian SSR, September 12-16, 1977*. 79, 1978.
- Lynden-Bell, D.; Burstein, D.; Davies, R. L.; Dressler, A.; and Faber, S. M. *On best distance estimators and galaxy streaming*. 4:307–316, 1988a.
- Lynden-Bell, D.; Faber, S. M.; Burstein, D.; Davies, R. L.; Dressler, A.; Terlevich, R. J.; and Wegner, G. *Spectroscopy and photometry of elliptical galaxies. V - Galaxy streaming toward the new supergalactic center*. ApJ, 326:19–49, 1988b.
- MacArthur, L. A.; Courteau, S.; and Holtzman, J. A. *Structure of Disk-dominated Galaxies. I. Bulge/Disk Parameters, Simulations, and Secular Evolution*. ApJ, 582:689–722, 2003.
- Makarov, D.; Makarova, L.; Rizzi, L.; Tully, R. B.; Dolphin, A. E.; Sakai, S.; and Shaya, E. J. *Tip of the Red Giant Branch Distances. I. Optimization of a Maximum Likelihood Algorithm*. AJ, 132:2729–2742, 2006.
- Martínez, H. J.; O’Mill, A. L.; and Lambas, D. G. *The evolution of the bimodal colour distribution of galaxies in Sloan Digital Sky Survey groups*. MNRAS, 372:253–258, 2006.
- Marzke, R. O.; Huchra, J. P.; and Geller, M. J. *Large-Scale Structure at Low Galactic Latitude*. AJ, 112:1803, 1996.
- Masters, K. L.; Springob, C. M.; Haynes, M. P.; and Giovanelli, R. *SFI++ I: A New I-Band Tully-Fisher Template, the Cluster Peculiar Velocity Dispersion, and H_0* . ApJ, 653:861–880, 2006.

- Mathewson, D. S.; Ford, V. L.; and Buchhorn, M. *A southern sky survey of the peculiar velocities of 1355 spiral galaxies*. *ApJS*, 81:413–659, 1992.
- Mathis, H.; Lemson, G.; Springel, V.; Kauffmann, G.; White, S. D. M.; Eldar, A.; and Dekel, A. *Simulating the formation of the local galaxy population*. *MNRAS*, 333:739–762, 2002.
- McDonald, M.; Courteau, S.; and Tully, R. B. *Bulge-disc decompositions and structural bimodality of Ursa Major cluster spiral galaxies*. *MNRAS*, 393:628–640, 2009a.
- McDonald, M.; Courteau, S.; and Tully, R. B. *The near-IR luminosity function and bimodal surface brightness distributions of Virgo cluster galaxies*. *MNRAS*, 394:2022–2042, 2009b.
- McGaugh, S. S. *The number, luminosity and mass density of spiral galaxies as a function of surface brightness*. *MNRAS*, 280:337–354, 1996.
- McGaugh, S. S. *The Baryonic Tully-Fisher Relation of Gas-rich Galaxies as a Test of Λ CDM and MOND*. *AJ*, 143:40, 2012.
- McGaugh, S. S.; Bothun, G. D.; and Schombert, J. M. *Galaxy Selection and the Surface Brightness Distribution*. *AJ*, 110:573, 1995.
- McGaugh, S. S. and de Blok, W. J. G. *Gas Mass Fractions and the Evolution of Spiral Galaxies*. *ApJ*, 481:689, 1997.
- McGaugh, S. S.; Schombert, J. M.; Bothun, G. D.; and de Blok, W. J. G. *The Baryonic Tully-Fisher Relation*. *ApJL*, 533:L99–L102, 2000.
- Meidt, S. E.; Schinnerer, E.; Knapen, J. H.; Bosma, A.; Athanassoula, E.; Sheth, K.; Buta, R. J.; Zaritsky, D.; Laurikainen, E.; Elmegreen, D.; et al. *Reconstructing the Stellar Mass Distributions of Galaxies Using S^4G IRAC 3.6 and 4.5 μ m Images. I. Correcting for Contamination by Polycyclic Aromatic Hydrocarbons, Hot Dust, and Intermediate-age Stars*. *ApJ*, 744:17, 2012.
- Mestel, L. *On the galactic law of rotation*. *MNRAS*, 126:553, 1963.
- Meyerdierks, H. *A cloud-Galaxy collision - Observation and theory*. *A&A*, 251:269–275, 1991.
- Milgrom, M. *A modification of the Newtonian dynamics - Implications for galaxies*. *ApJ*, 270:371–389, 1983a.
- Milgrom, M. *A Modification of the Newtonian Dynamics - Implications for Galaxy Systems*. *ApJ*, 270:384, 1983b.
- Milgrom, M. *A modification of the Newtonian dynamics as a possible alternative to the hidden mass hypothesis*. *ApJ*, 270:365–370, 1983c.
- Milvang-Jensen, B. and Jørgensen, I. *Galaxy Surface Photometry*. *Baltic Astronomy*, 8:535–574, 1999.
- Mitronova, S. N.; Karachentsev, I. D.; Karachentseva, V. E.; Jarrett, T. H.; and Kudrya, Y. N. *The 2MASS-selected Flat Galaxy Catalog*. *Bulletin of the Special Astrophysics Observatory*, 57:5–163, 2004.
- Mocz, P.; Green, A.; Malacari, M.; and Glazebrook, K. *The Tully-Fisher relation for 25 000 Sloan Digital Sky Survey galaxies as a function of environment*. *MNRAS*, 425:296–310, 2012.

- Monson, A. J.; Freedman, W. L.; Madore, B. F.; Persson, S. E.; Scowcroft, V.; Seibert, M.; and Rigby, J. R. *The Carnegie Hubble Program: The Leavitt Law at 3.6 and 4.5 μm in the Milky Way*. ApJ, 759:146, 2012.
- Moore, B.; Ghigna, S.; Governato, F.; Lake, G.; Quinn, T.; Stadel, J.; and Tozzi, P. *Dark Matter Substructure within Galactic Halos*. ApJL, 524:L19–L22, 1999.
- Mosenkov, A. V.; Sotnikova, N. Y.; and Reshetnikov, V. P. *2MASS photometry of edge-on spiral galaxies - I. Sample and general results*. MNRAS, 401:559–576, 2010.
- Moster, B. P.; Somerville, R. S.; Maubetsch, C.; van den Bosch, F. C.; Macciò, A. V.; Naab, T.; and Oser, L. *Constraints on the Relationship between Stellar Mass and Halo Mass at Low and High Redshift*. ApJ, 710:903–923, 2010.
- Muñoz-Mateos, J. C.; Gil de Paz, A.; Zamorano, J.; Boissier, S.; Dale, D. A.; Pérez-González, P. G.; Gallejo, J.; Madore, B. F.; Bendo, G.; Boselli, A.; et al. *Radial Distribution of Stars, Gas, and Dust in SINGS Galaxies. I. Surface Photometry and Morphology*. ApJ, 703:1569, 2009.
- Noordermeer, E. and Verheijen, M. A. W. *The high-mass end of the Tully-Fisher relation*. MNRAS, 381:1463–1472, 2007.
- Nusser, A. *Boundary-value problems in cosmological dynamics*. Physica D Nonlinear Phenomena, 237:2158–2161, 2008.
- Nusser, A. and Davis, M. *The Cosmological Bulk Flow: Consistency with ΛCDM and $z = 0$ Constraints on σ_8 and γ* . ApJ, 736:93, 2011.
- Nuza, S. E.; Hoeft, M.; van Weeren, R. J.; Gottlöber, S.; and Yepes, G. *How many radio relics await discovery?* MNRAS, 420:2006–2019, 2012.
- Obreschkow, D. and Meyer, M. *Precise Tully-Fisher Relations without Galaxy Inclinations*. ApJ, 777:140, 2013.
- Oke, J. B. and Sandage, A. *Energy Distributions, K Corrections, and the Stebbins-Whitford Effect for Giant Elliptical Galaxies*. ApJ, 154:21, 1968.
- Oort, J. H. *The evolution of large-scale structures in the universe. I*. Sterne und Weltraum, 21:456–461, 1982.
- Ootsubo, T.; Onaka, T.; Yamamura, I.; Tanabé, T.; Roellig, T. L.; Chan, K.-W.; and Matsumoto, T. *IRTS observation of the mid-infrared spectrum of the zodiacal emission*. Earth, Planets, and Space, 50:507–511, 1998.
- Pantoja, C. A.; Alschuler, D. R.; Giovanardi, C.; and Giovanelli, R. *21-cm Line Observations of Galaxies in the Zone of Avoidance*. AJ, 113:905–936, 1997.
- Paturel, G.; Petit, C.; Prugniel, P.; Theureau, G.; Rousseau, J.; Brouty, M.; Dubois, P.; and Cambrésy, L. *HYPERLEDA. I. Identification and designation of galaxies*. A&A, 412:45–55, 2003.
- Peacock, J. A., Cosmological Physics, 1999.
- Peebles, P. J. E., The large-scale structure of the universe, 1980.
- Peebles, P. J. E., Principles of Physical Cosmology, 1993.

- Peebles, P. J. E.; Phelps, S. D.; Shaya, E. J.; and Tully, R. B. *Radial and Transverse Velocities of Nearby Galaxies*. ApJ, 554:104–113, 2001.
- Peebles, P. J. E. and Tully, R. B. *The Variety of Solutions for Dynamics in the Local Group*. ArXiv e-prints, 2013.
- Perlmutter, S.; Aldering, G.; Boyle, B. J.; Castro, P. G.; Couch, W. J.; Deustua, S.; Fabbro, S.; Ellis, R. S.; Filippenko, A. V.; Fruchter, A.; et al. *Measurements of Omega and Lambda from 42 High-Redshift Supernovae*. 1998.
- Perlmutter, S.; Aldering, G.; Goldhaber, G.; Knop, R. A.; Nugent, P.; Castro, P. G.; Deustua, S.; Fabbro, S.; Goobar, A.; Groom, D. E.; et al. *Measurements of Omega and Lambda from 42 High-Redshift Supernovae*. ApJ, 517:565–586, 1999.
- Petry, C. E.; Impey, C. D.; and Foltz, C. B. *Small-Scale Structure in the Ly alpha Forest at High Redshift*. ApJ, 494:60, 1998.
- Phillips, M. M. *The absolute magnitudes of Type IA supernovae*. ApJL, 413:L105–L108, 1993.
- Pierce, M. J. and Tully, R. B. *Distances to the Virgo and Ursa Major clusters and a determination of H_0* . ApJ, 330:579–581, 1988.
- Pizagno, J.; Prada, F.; Weinberg, D. H.; Rix, H.-W.; Pogge, R. W.; Grebel, E. K.; Harbeck, D.; Blanton, M.; Brinkmann, J.; and Gunn, J. E. *The Tully-Fisher Relation and its Residuals for a Broadly Selected Sample of Galaxies*. AJ, 134:945–972, 2007.
- Planck Collaboration. *Planck 2013 results. XVI. Cosmological parameters*. ArXiv e-prints, 2013.
- Pomarède, D.; Courtois, H.; and Tully, R. B. *Visualization of structures and cosmic flows in the local Universe*. 289:323–326, 2013.
- Power, C. and Knebe, A. *The impact of box size on the properties of dark matter haloes in cosmological simulations*. MNRAS, 370:691–701, 2006.
- Prada, F.; Klypin, A. A.; Cuesta, A. J.; Betancort-Rijo, J. E.; and Primack, J. *Halo concentrations in the standard Λ cold dark matter cosmology*. MNRAS, 423:3018–3030, 2012.
- Press, W. H. and Schechter, P. *Formation of Galaxies and Clusters of Galaxies by Self-Similar Gravitational Condensation*. ApJ, 187:425–438, 1974.
- Prieto, J. L.; Rest, A.; and Suntzeff, N. B. *A New Method to Calibrate the Magnitudes of Type Ia Supernovae at Maximum Light*. ApJ, 647:501–512, 2006.
- Prunet, S.; Pichon, C.; Aubert, D.; Pogosyan, D.; Teyssier, R.; and Gottloeber, S. *Initial Conditions For Large Cosmological Simulations*. ApJS, 178:179–188, 2008.
- Rauch, M.; Sargent, W. L. W.; and Barlow, T. A. *Small-Scale Structure at High Redshift. I. Glimpses of the Interstellar Medium at Redshift ~ 3.5* . ApJ, 515:500–505, 1999.
- Rauch, M.; Sargent, W. L. W.; Barlow, T. A.; and Carswell, R. F. *Small-Scale Structure at High Redshift. III. The Clumpiness of the Intergalactic Medium on Subkiloparsec Scales*. ApJ, 562:76–87, 2001.

- Rawle, T. D.; Lucey, J. R.; Smith, R. J.; and Head, J. T. C. G. *S0 galaxies in the Coma cluster: environmental dependence of the S0 offset from the Tully-Fisher relation*. MNRAS, 433:2667–2692, 2013.
- Reach, W. T.; Megeath, S. T.; Cohen, M.; Hora, J.; Carey, S.; Surace, J.; Willner, S. P.; Barmby, P.; Wilson, G.; Glaccum, W.; et al. *Absolute Calibration of the Infrared Array Camera on the Spitzer Space Telescope*. PASP, 117:978–990, 2005.
- Reisenegger, A.; Quintana, H.; Proust, D.; and Slezak, E. *Dynamics and mass of the Shapley Supercluster, the largest bound structure in the local Universe*. The Messenger, 107:18–23, 2002.
- Riess, A. G.; Filippenko, A. V.; Challis, P.; Clocchiatti, A.; Diercks, A.; Garnavich, P. M.; Gilliland, R. L.; Hogan, C. J.; Jha, S.; Kirshner, R. P.; et al. *Observational Evidence from Supernovae for an Accelerating Universe and a Cosmological Constant*. AJ, 116:1009–1038, 1998.
- Riess, A. G.; Macri, L.; Casertano, S.; Lampeitl, H.; Ferguson, H. C.; Filippenko, A. V.; Jha, S. W.; Li, W.; and Chornock, R. *A 3% Solution: Determination of the Hubble Constant with the Hubble Space Telescope and Wide Field Camera 3*. ApJ, 730:119, 2011.
- Riess, A. G.; Macri, L.; Casertano, S.; Sosey, M.; Lampeitl, H.; Ferguson, H. C.; Filippenko, A. V.; Jha, S. W.; Li, W.; Chornock, R.; et al. *A Redetermination of the Hubble Constant with the Hubble Space Telescope from a Differential Distance Ladder*. ApJ, 699:539–563, 2009.
- Riess, A. G.; Press, W. H.; and Kirshner, R. P. *Using Type IA supernova light curve shapes to measure the Hubble constant*. ApJL, 438:L17–L20, 1995.
- Rizzi, L.; Tully, R. B.; Makarov, D.; Makarova, L.; Dolphin, A. E.; Sakai, S.; and Shaya, E. J. *Tip of the Red Giant Branch Distances. II. Zero-Point Calibration*. ApJ, 661:815–829, 2007.
- Robertson, H. P. *Relativistic Cosmology*. Reviews of Modern Physics, 5:62–90, 1933.
- Robertson, H. P. *Kinematics and World-Structure*. ApJ, 82:284, 1935.
- Robertson, H. P. *Kinematics and World-Structure II*. ApJ, 83:187, 1936a.
- Robertson, H. P. *Kinematics and World-Structure III*. ApJ, 83:257, 1936b.
- Rowan-Robinson, M., *The cosmological distance ladder: Distance and time in the universe*, 1985.
- Rubin, V. C.; Burstein, D.; Ford, W. K., Jr.; and Thonnard, N. *Rotation velocities of 16 SA galaxies and a comparison of Sa, Sb, and SC rotation properties*. ApJ, 289:81–98, 1985.
- Rybicki, G. B. and Press, W. H. *Interpolation, realization, and reconstruction of noisy, irregularly sampled data*. ApJ, 398:169–176.
- Sandage, A. *Bias properties of extragalactic distance indicators. 1: The Hubble constant does not increase outward*. ApJ, 430:1–12, 1994.
- Saunders, W.; Sutherland, W. J.; Maddox, S. J.; Keeble, O.; Oliver, S. J.; Rowan-Robinson, M.; McMahan, R. G.; Efstathiou, G. P.; Tadros, H.; White, S. D. M.; et al. *The PSCz catalogue*. MNRAS, 317:55–63, 2000.

- Scannapieco, C.; Tissera, P. B.; White, S. D. M.; and Springel, V. *Feedback and metal enrichment in cosmological smoothed particle hydrodynamics simulations - I. A model for chemical enrichment*. MNRAS, 364:552–564, 2005.
- Schechter, P. *An analytic expression for the luminosity function for galaxies*. ApJ, 203:297–306, 1976.
- Schlafly, E. F. and Finkbeiner, D. P. *Measuring Reddening with Sloan Digital Sky Survey Stellar Spectra and Recalibrating SFD*. ApJ, 737:103, 2011.
- Schlegel, D. J.; Finkbeiner, D. P.; and Davis, M. *Maps of Dust Infrared Emission for Use in Estimation of Reddening and Cosmic Microwave Background Radiation Foregrounds*. ApJ, 500:525, 1998.
- Schombert, J. *ARCHANGEL Galaxy Photometry System*. ArXiv Astrophysics e-prints, 2007.
- Schombert, J. and Smith, A. *The Structure of Galaxies I: Surface Photometry Techniques*. PASA, 29:174–192, 2012.
- Schweizer, F. *Colliding and Merging Galaxies. III. The Dynamically Young Merger Remnant NGC 3921*. AJ, 111:109, 1996.
- Sersic, J. L. *The H II regions as distance indicators*. The Observatory, 79:54–56, 1959.
- Shaya, E. J.; Peebles, P. J. E.; and Tully, R. B. *Action Principle Solutions for Galaxy Motions within 3000 Kilometers per Second*. ApJ, 454:15, 1995.
- Sheth, K.; Regan, M.; Hinz, J. L.; Gil de Paz, A.; Menéndez-Delmestre, K.; Muñoz-Mateos, J.-C.; Seibert, M.; Kim, T.; Laurikainen, E.; Salo, H.; et al. *The Spitzer Survey of Stellar Structure in Galaxies (S⁴G)*. PASP, 122:1397–1414, 2010.
- Sheth, R. K. and Diaferio, A. *Peculiar velocities of galaxies and clusters*. MNRAS, 322:901–917, 2001.
- Silk, J.; Szalay, A. S.; and Zel'dovich, Y. B. *The large-scale structure of the universe*. Scientific American, 249:56–64, 1983.
- Silva, L.; Granato, G. L.; Bressan, A.; and Danese, L. *Modeling the Effects of Dust on Galactic Spectral Energy Distributions from the Ultraviolet to the Millimeter Band*. ApJ, 509:103–117, 1998.
- Smith, J. A.; Tucker, D. L.; Kent, S.; Richmond, M. W.; Fukugita, M.; Ichikawa, T.; Ichikawa, S.-i.; Jorgensen, A. M.; Uomoto, A.; Gunn, J. E.; et al. *The u'g'r'i'z' Standard-Star System*. AJ, 123:2121–2144, 2002.
- Sorce, J. G.; Courtois, H. M.; Gottlöber, S.; Hoffman, Y.; and Tully, R. B. *Simulations of the Local Universe constrained by observational peculiar velocities*. MNRAS, 437:3586–3595, 2014.
- Sorce, J. G.; Courtois, H. M.; Sheth, K.; and Tully, R. B. *Bimodality of galaxy disc central surface brightness distribution in the Spitzer 3.6 μ m band*. MNRAS, 433:751–758, 2013a.
- Sorce, J. G.; Courtois, H. M.; and Tully, R. B. *The Mid-infrared Tully-Fisher Relation: Spitzer Surface Photometry*. AJ, 144:133, 2012a.

- Sorce, J. G.; Courtois, H. M.; Tully, R. B.; Seibert, M.; Scowcroft, V.; Freedman, W. L.; Madore, B. F.; Persson, S. E.; Monson, A.; and Rigby, J. *Calibration of the Mid-infrared Tully-Fisher Relation*. ApJ, 765:94, 2013b.
- Sorce, J. G.; Tully, R. B.; and Courtois, H. M. *The Mid-infrared Tully-Fisher Relation: Calibration of the Type Ia Supernova Scale and H_0* . ApJL, 758:L12, 2012b.
- Spergel, D. N.; Bean, R.; Doré, O.; Nolta, M. R.; Bennett, C. L.; Dunkley, J.; Hinshaw, G.; Jarosik, N.; Komatsu, E.; Page, L.; et al. *Three-Year Wilkinson Microwave Anisotropy Probe (WMAP) Observations: Implications for Cosmology*. ApJS, 170:377–408, 2007.
- Springel, V. *The cosmological simulation code GADGET-2*. MNRAS, 364:1105–1134, 2005.
- Springel, V.; White, S. D. M.; Jenkins, A.; Frenk, C. S.; Yoshida, N.; Gao, L.; Navarro, J.; Thacker, R.; Croton, D.; Helly, J.; et al. *Simulations of the formation, evolution and clustering of galaxies and quasars*. Nature, 435:629–636, 2005.
- Springob, C. M.; Masters, K. L.; Haynes, M. P.; Giovanelli, R.; and Marinoni, C. *SFI++ II. A New I-Band Tully-Fisher Catalog, Derivation of Peculiar Velocities, and Data Set Properties*. ApJS, 172:599–614, 2007.
- Stoughton, C.; Lupton, R. H.; Bernardi, M.; Blanton, M. R.; Burles, S.; Castander, F. J.; Connolly, A. J.; Eisenstein, D. J.; Frieman, J. A.; Hennessy, G. S.; et al. *Sloan Digital Sky Survey: Early Data Release*. AJ, 123:485–548, 2002.
- Strauss, M. A. and Willick, J. A. *The density and peculiar velocity fields of nearby galaxies*. Physics Reports, 261:271–431, 1995.
- Sunyaev, R. A. and Zeldovich, I. B. *Microwave background radiation as a probe of the contemporary structure and history of the universe*. ARA&A, 18:537–560, 1980.
- Sunyaev, R. A. and Zeldovich, Y. B. *Small-Scale Fluctuations of Relic Radiation*. APSS, 7:3–19, 1970.
- Swaters, R. A.; Sanders, R. H.; and McGaugh, S. S. *Testing Modified Newtonian Dynamics with Rotation Curves of Dwarf and Low Surface Brightness Galaxies*. ApJ, 718:380–391, 2010.
- Teerikorpi, P. *Theoretical aspects in the use of the inverse Tully-Fisher relation for distance determination*. A&A, 234:1–4, 1990.
- Teerikorpi, P. *On general Malmquist corrections to direct and inverse Tully-Fisher distance moduli*. A&A, 280:443–450, 1993.
- Teerikorpi, P. *The inverse Tully-Fisher relation*. Astrophysical Letters and Communications, 31:263, 1995.
- Teerikorpi, P. *Observational Selection Bias Affecting the Determination of the Extragalactic Distance Scale*. ARA&A, 35:101–136, 1997.
- Teyssier, R. *Cosmological hydrodynamics with adaptive mesh refinement. A new high resolution code called RAMSES*. A&A, 385:337–364, 2002.
- Thompson, R. I. *Tests and constraints on theories of galaxy formation and evolution*. APSS, 284:353–356, 2003.

- Tielens, A. G. G. M. *Interstellar Polycyclic Aromatic Hydrocarbon Molecules*. ARA&A, 46:289–337, 2008.
- Tikhonov, A. V. and Klypin, A. *The emptiness of voids: yet another overabundance problem for the Λ cold dark matter model*. MNRAS, 395:1915–1924, 2009.
- Tonry, J. L.; Dressler, A.; Blakeslee, J. P.; Ajhar, E. A.; Fletcher, A. B.; Luppino, G. A.; Metzger, M. R.; and Moore, C. B. *The SBF Survey of Galaxy Distances. IV. SBF Magnitudes, Colors, and Distances*. ApJ, 546:681–693, 2001.
- Torres-Flores, S.; Mendes de Oliveira, C.; Plana, H.; Amram, P.; and Epinat, B. *The Tully-Fisher relations for Hickson compact group galaxies*. MNRAS, 432:3085–3096, 2013.
- Tully, R. *Galaxies: Lighthouses in the Shoals of Dark Halos*. ArXiv e-prints, 2010.
- Tully, R. B. *Our CMB Motion: The Role of the Local Void*. In Metcalfe, N. and Shanks, T., editors, Cosmic Frontiers, volume 379 of ASPCS, page 24. 2007.
- Tully, R. B., The Local Velocity Anomaly, 2008a. page 3.
- Tully, R. B. *The Local Void is Really Empty*. In J. Davies & M. Disney, editor, IAU Symposium, volume 244 of IAU Symposium, pages 146–151. 2008b.
- Tully, R. B. and Courtois, H. M. *Cosmicflows-2: I-band Luminosity-H I Linewidth Calibration*. ApJ, 749:78, 2012.
- Tully, R. B.; Courtois, H. M.; Dolphin, A. E.; Fisher, J. R.; Héraudeau, P.; Jacobs, B. A.; Karachentsev, I. D.; Makarov, D.; Makarova, L.; Mitronova, S.; et al. *Cosmicflows-2: The Data*. AJ, 146:86, 2013.
- Tully, R. B. and Fisher, J. R. *A new method of determining distances to galaxies*. A&A, 54:661–673, 1977.
- Tully, R. B. and Fouque, P. *The extragalactic distance scale. I - Corrections to fundamental observables*. ApJS, 58:67–80, 1985.
- Tully, R. B.; Mould, J. R.; and Aaronson, M. *A color-magnitude relation for spiral galaxies*. ApJ, 257:527–537, 1982.
- Tully, R. B. and Pierce, M. J. *Distances to Galaxies from the Correlation between Luminosities and Line Widths. III. Cluster Template and Global Measurement of H_0* . ApJ, 533:744–780, 2000.
- Tully, R. B.; Pierce, M. J.; Huang, J.-S.; Saunders, W.; Verheijen, M. A. W.; and Witchalls, P. L. *Global Extinction in Spiral Galaxies*. AJ, 115:2264–2272, 1998.
- Tully, R. B.; Rizzi, L.; Shaya, E. J.; Courtois, H. M.; Makarov, D. I.; and Jacobs, B. A. *The Extragalactic Distance Database*. AJ, 138:323–331, 2009.
- Tully, R. B.; Shaya, E. J.; Karachentsev, I. D.; Courtois, H. M.; Kocevski, D. D.; Rizzi, L.; and Peel, A. *Our Peculiar Motion Away from the Local Void*. ApJ, 676:184–205, 2008.
- Tully, R. B. and Verheijen, M. A. W. *The Ursa Major Cluster of Galaxies. II. Bimodality of the Distribution of Central Surface Brightnesses*. ApJ, 484:145, 1997.

- Tully, R. B.; Verheijen, M. A. W.; Pierce, M. J.; Huang, J.-S.; and Wainscoat, R. J. *The Ursa Major Cluster of Galaxies. I. Cluster Definition and Photometric Data*. AJ, 112:2471, 1996.
- Turnbull, S. J.; Hudson, M. J.; Feldman, H. A.; Hicken, M.; Kirshner, R. P.; and Watkins, R. *Cosmic flows in the nearby universe from Type Ia supernovae*. MNRAS, 420:447–454, 2012.
- Verheijen, M. A. W.; Oosterloo, T. A.; van Cappellen, W. A.; Bakker, L.; Ivashina, M. V.; and van der Hulst, J. M. *Apertif, a focal plane array for the WSRT*. 1035:265–271, 2008.
- Watson, W. A.; Iliev, I. T.; Diego, J. M.; Gottlöber, S.; Knebe, A.; Martínez-González, E.; and Yepes, G. *Statistics of extreme objects in the Juropa Hubble Volume simulation*. ArXiv e-prints, 2013.
- Werner, M. W.; Roellig, T. L.; Low, F. J.; Rieke, G. H.; Rieke, M.; Hoffmann, W. F.; Young, E.; Houck, J. R.; Brandl, B.; Fazio, G. G.; et al. *The Spitzer Space Telescope Mission*. ApJS, 154:1–9, 2004.
- Wetzel, A. R.; Tinker, J. L.; and Conroy, C. *Galaxy evolution in groups and clusters: star formation rates, red sequence fractions and the persistent bimodality*. MNRAS, 424:232–243, 2012.
- Whitaker, K. E.; Labbé, I.; van Dokkum, P. G.; Brammer, G.; Kriek, M.; Marchesini, D.; Quadri, R. F.; Franx, M.; Muzzin, A.; Williams, R. J.; et al. *The NEWFIRM Medium-band Survey: Photometric Catalogs, Redshifts, and the Bimodal Color Distribution of Galaxies out to $z \sim 3$* . ApJ, 735:86, 2011.
- White, S. D. M.; Frenk, C. S.; and Davis, M. *Clustering in a neutrino-dominated universe*. ApJL, 274:L1–L5, 1983.
- Williams, M. J.; Bureau, M.; and Cappellari, M. *The Tully-Fisher relations of early-type spiral and S0 galaxies*. MNRAS, 409:1330–1346, 2010.
- Willick, J. A. *Statistical bias in distance and peculiar velocity estimation. 1: The 'calibration' problem*. ApJS, 92:1–31, 1994.
- Willick, J. A.; Courteau, S.; Faber, S. M.; Burstein, D.; and Dekel, A. *Homogeneous Velocity-Distance Data for Peculiar Velocity Analysis. I. Calibration of Cluster Samples*. ApJ, 446:12, 1995.
- Willick, J. A.; Courteau, S.; Faber, S. M.; Burstein, D.; Dekel, A.; and Kolatt, T. *Mark III Catalog of Galaxy Peculiar Velocities (Willick+ 1997)*. VizieR Online Data Catalog, 7198:0, 1996.
- Wright, E. L. *WISE the Wide-field Infrared Survey Explorer*. In Zinnecker, H.; Epchtein, N.; and Rauer, H., editors, EAS Publications Series, volume 33 of EAS Publications Series, pages 57–62. 2008.
- Xia, J.-Q.; Vitagliano, V.; Liberati, S.; and Viel, M. *Cosmography beyond standard candles and rulers*. PRD, 85(4):043520, 2012.
- Xu, G. *A New Parallel N-Body Gravity Solver: TPM*. ApJS, 98:355, 1995.

- Zaritsky, D.; Courtois, H.; Muñoz-Mateos, J.-C.; Sorce, J.; Erroz-Ferrer, S.; Comerón, S.; Gadotti, D. A.; Gil de Paz, A.; Hinz, J. L.; Laurikainen, E.; et al. *The Baryonic Tully-Fisher Relationship for S^4G Galaxies and the "Condensed" Baryon Fraction of Galaxies*. ArXiv e-prints, 2014.
- Zaroubi, S. *Reconstructing the ZOA from Galaxy Peculiar Velocities*. In R. C. Kraan-Korteweg, P. A. Henning, & H. Andernach, editor, *Mapping the Hidden Universe: The Universe behind the Milky Way - The Universe in HI*, volume 218 of ASPCS, page 173. 2000.
- Zaroubi, S. *Unbiased reconstruction of the large-scale structure*. MNRAS, 331:901–908, 2002.
- Zaroubi, S.; Hoffman, Y.; and Dekel, A. *Wiener Reconstruction of Large-Scale Structure from Peculiar Velocities*. ApJ, 520:413–425, 1999.
- Zaroubi, S.; Hoffman, Y.; Fisher, K. B.; and Lahav, O. *Wiener Reconstruction of the Large-Scale Structure*. ApJ, 449:446, 1995.
- Zavala, J.; Jing, Y. P.; Faltenbacher, A.; Yepes, G.; Hoffman, Y.; Gottlöber, S.; and Catinella, B. *The Velocity Function in the Local Environment from Λ CDM and Λ WDM Constrained Simulations*. ApJ, 700:1779–1793, 2009.
- Zel'dovich, Y. B. *Gravitational instability: An approximate theory for large density perturbations*. A&A, 5:84–89, 1970.
- Zemp, M.; Stadel, J.; Moore, B.; and Carollo, C. M. *An optimum time-stepping scheme for N-body simulations*. MNRAS, 376:273–286, 2007.
- Zhong, G. H.; Liang, Y. C.; Liu, F. S.; Hammer, F.; Hu, J. Y.; Chen, X. Y.; Deng, L. C.; and Zhang, B. *A large sample of low surface brightness disc galaxies from the SDSS - I. The sample and the stellar populations*. MNRAS, 391:986–999, 2008.
- Zwicky, F. *Die Rotverschiebung von extragalaktischen Nebeln*. Helvetica Physica Acta, 6:110–127, 1933.

Acknowledgements

Completing a PhD is a road ahead with its challenges but this long road has been worthwhile. I would like to thank every single person who walked alongside me on this tortuous path. First of all, I would like to acknowledge the persons who supervised my scientific work. In that sense thanks go to H el ene Courtois, Stefan Gottl ober, Brent Tully and Yehuda Hoffman who answered every single question I had, helped me develop my criticism and my research abilities and welcomed me in their collaborations to accomplish this work. I would like to add Matthias Steinmetz, Gustavo Yepes and Christophe Dujardin who also contributed to the successful proceedings of my PhD. Special thanks go to my referee. The members I have not mentioned yet are Corinne Augier and Cristiano Porciani.

This thesis required lots of codes implying developers. I am thus particularly in debt to James Schombert for ARCHANGEL, Timur Doumler for ICECORE (but also for the german language), Steffen Knollmann for GINNUNGAGAP, Volker Springel for GADGET, Alexander Knebe for Amiga halo finder and Daniel Pomar ede for SDvision. Because this thesis work is the result of two international collaborations, Cosmicflows and CLUES, I am grateful to the different universities and institutes who welcomed me for several months at a time. I want to mention the Universities of Hawaii, Potsdam and Lyon and the Institutes for Astronomy and of Nuclear Physics as well as the Leibniz-Institute for Astrophysics. With these different locations over the world comes a multitude of persons to thank. Also I thank Noam Libeskind, Steffen Hess, Francisco-Shu Kitaura, Jabran Zahid, Kirsten Larson and Alain Khayat. I would like to add to this list Don Neil, Mark Seibert, Barry Madore, Wendy Freedman, Victoria Scowcroft, Igor Karachentsev, Kartik Sheth, Dennis Zaritsky and Tom Jarrett and all the others that I may have forgotten and to whom I present my deepest apologizes. I would like to give a special thank to Sylvie Flores who assumed the role of my PhD godmother during these three years and was always able to discern when I was in my most distressing times, hence needed support.

This thesis used lots of computer facilities and thanks go to people in charge of the maintenance of such computing systems in Potsdam, in Lyon, in Hawaii and in Munich. This work also made use of powerful databases (NED, EDD and HyperLeda), thanks go to their founders. I think that it is worthwhile mentioning the numerous wonderful persons that I met at conferences and that I will never forget. Unfortunately this page will not be enough to mention all of them but I want to express how much I enjoyed meeting every single one of them.

Then there are lots of persons upstream this thesis to thank beginning with the teacher I had the year before the last in grammar school, and continuing with all the physics teachers I had after that subsequently in (junior) high schools, preparatory school and at the Ecole Normale Sup erieure de Lyon. I would like to thank Roy Gal and Lisa Kewley for being my supervisors for my first long term internship in astrophysics.

Last but not least, come the persons who have continuously followed the flows with me, to whom I owe everything: my parents. A very special thank goes to Pierre who always supported me during these three years and never doubted of me even when I would. He helped me go through the most difficult times bringing light, joy and love into my life.

Declaration of independent work

I hereby declare that this thesis is the product of my own independent work and that I have listed all the literature and resources that have been used.

Déclaration sur l'honneur

Je certifie que cette thèse est le fruit de mon propre travail et qu'elle a été rédigée sans autre aide que les sources et références dûment citées.

Selbständigkeitserklärung

Hiermit versichere ich, dass ich die vorliegende Arbeit selbständig verfasst und keine anderen als die angegebenen Quellen und Hilfsmittel benutzt habe.

Jenny Sorce
Lyon, 12 06 2014

The scientific results presented in this thesis have been or will be published in ApJ, ApJL, AJ and MNRAS journals as an ensemble of papers. ([Sorce et al., 2014](#), [2013a](#), [2012a](#), [2013b](#), [2012b](#), and others are in preparation)